Springer Theses
Recognizing Outstanding Ph.D. Research

Ismael Moreno-Gomez

A Phenomenological Mathematical Modelling Framework for the Degradation of Bioresorbable Composites

Springer

Springer Theses

Recognizing Outstanding Ph.D. Research

Aims and Scope

The series "Springer Theses" brings together a selection of the very best Ph.D. theses from around the world and across the physical sciences. Nominated and endorsed by two recognized specialists, each published volume has been selected for its scientific excellence and the high impact of its contents for the pertinent field of research. For greater accessibility to non-specialists, the published versions include an extended introduction, as well as a foreword by the student's supervisor explaining the special relevance of the work for the field. As a whole, the series will provide a valuable resource both for newcomers to the research fields described, and for other scientists seeking detailed background information on special questions. Finally, it provides an accredited documentation of the valuable contributions made by today's younger generation of scientists.

Theses are accepted into the series by invited nomination only and must fulfill all of the following criteria

- They must be written in good English.
- The topic should fall within the confines of Chemistry, Physics, Earth Sciences, Engineering and related interdisciplinary fields such as Materials, Nanoscience, Chemical Engineering, Complex Systems and Biophysics.
- The work reported in the thesis must represent a significant scientific advance.
- If the thesis includes previously published material, permission to reproduce this must be gained from the respective copyright holder.
- They must have been examined and passed during the 12 months prior to nomination.
- Each thesis should include a foreword by the supervisor outlining the significance of its content.
- The theses should have a clearly defined structure including an introduction accessible to scientists not expert in that particular field.

More information about this series at http://www.springer.com/series/8790

Ismael Moreno-Gomez

A Phenomenological Mathematical Modelling Framework for the Degradation of Bioresorbable Composites

Doctoral Thesis accepted by
the University of Cambridge, Cambridge, UK

Springer

Author
Dr. Ismael Moreno-Gomez
Department of Materials Science
and Metallurgy
University of Cambridge
Cambridge, UK

Supervisors
Prof. Ruth E. Cameron
Department of Materials Science
and Metallurgy
University of Cambridge
Cambridge, UK

Prof. Serena M. Best
Department of Materials Science
and Metallurgy
University of Cambridge
Cambridge, UK

ISSN 2190-5053 ISSN 2190-5061 (electronic)
Springer Theses
ISBN 978-3-030-04989-8 ISBN 978-3-030-04990-4 (eBook)
https://doi.org/10.1007/978-3-030-04990-4

Library of Congress Control Number: 2018962399

This Springer imprint is published by the registered company Springer Nature Switzerland AG
The registered company address is: Gewerbestrasse 11, 6330 Cham, Switzerland

There are men who struggle for a day and they are good.
There are men who struggle for a year and they are better.
There are men who struggle many years, and they are better still.
But there are those who struggle all their lives:
These are the indispensable ones.

Excerpt from *"The Mother"* by Bertolt Brecht.

To my family,
for always been there.
To my dad,
wish you were here.
To Olga,
for the many special moments to come.

Supervisor's Foreword

Resorbable composites, which combine biodegradable polyesters and calcium-based ceramics, have significant therapeutic potential as tissue engineering scaffolds, as temporary implants and as drug-loaded matrices for controlled release. However, their degradation is complex and the rate of resorption depends on multiple connected factors such as the shape and size of the device, polymer chemistry and molecular weight, particle phase, size, volume fraction, distribution and pH-dependent dissolution properties. Understanding and ultimately predicting the degradation of resorbable composites are of central importance if we are to fully unlock the promise of these materials.

Computational models play a key role in modern materials science research as they allow us to deepen the understanding of complex materials behaviours. Despite the numerous advantages that a thorough understanding of bioresorbable composites in general, and their degradation behaviour in particular would bring to patients, many questions remain unanswered.

Analytic models of the degradation of certain composites were first proposed by Prof. Jingzhe Pan of Leicester University in 2011. In this thesis, Ismael Moreno-Gomez takes this approach as a start point and develops it to create a generalised model that mathematically represents the interwoven phenomena present during degradation. He next compiles a comprehensive database of quantitative degradation data mined from the existing literature, adds information from novel controlled experiments and then draws all three strands together to generate new insights into the complex factors as play.

This is an exciting body of research of great value to the field. I am delighted that Dr. Moreno-Gomez has been awarded the prestigious Springer Thesis Prize—a very well-deserved recognition of his important work.

Cambridge, UK
October 2018

Prof. Ruth E. Cameron

Abstract

Understanding and, ultimately, predicting the degradation of bioresorbable composites made of biodegradable polyesters and calcium-based ceramics are paramount in order to fully unlock the potential of these materials, which are heavily used in orthopaedic applications and also being considered for stents.

A modelling framework which characterises the degradation of bioresorbable composites was generated by generalising a computational model previously reported in the literature. The framework uses mathematical expressions to represent the interwoven phenomena present during degradation. Three ceramic-specific models were then created by particularising the framework for three common calcium-based fillers, namely tricalcium phosphate (TCP), hydroxyapatite (HA) and calcium carbonate (CC). In these models, the degradation of a bioresorbable composite is described with four parameters: the non-catalytic and auto-catalytic polymer degradation rates, k_1 and k_2' respectively, and the ceramic dissolution rate and exponent, A_d and θ respectively.

A comprehensive data mining exercise was carried out by surveying the existing literature in order to obtain quantitative degradation data for bioresorbable composites containing TCP, HA and CC. This resulted in a database with a variety of case studies. Subsequently, each case study was analysed using the corresponding ceramic-specific model returning a set of values for the four degradation constants. Both cases with agreement and disagreement between model prediction and experimental data were studied. 76% of the 107 analysed case studies displayed the expected behaviour.

In general terms, the analysis of the harvested data with the models showed that a wide range of degradation behaviours can be attained using different polymeric matrix–ceramic filler combinations. Furthermore, the existence of discrepancies in degradation behaviour between a priori similar bioresorbable composites became apparent, highlighting the high number of hidden factors affecting composite degradation such as polymer tacticity or ceramic impurities. The analysis of the case studies also highlighted that the ceramic dissolution rate needed to depict the portrayed degradation behaviours is significantly higher than that reported for

ceramics alone in dissolution studies under physiological conditions, indicating that studies of the filler elements alone do not provide a complete picture. Lastly, the computational analysis provided insight into the complex influence of factors such as sample porosity and degradation protocol in the degradation behaviour.

In addition to the computational analysis of literature data, an experimental degradation study was carried out with nanocomposites made of calcium carbonate and poly(D,L-lactide-co-glycolide). This study showed the existence of a clear buffering effect with the addition of the ceramic filler and confirmed the assumptions employed in the modelling framework in this particular bioresorbable composite. The detailed nature and modest size of these data enabled a more precise and thorough analysis using the CC composites' degradation model.

In summary, the modelling framework is able to capture the main degradation behaviour of bioresorbable composites and also point to factors responsible for dissimilar behaviours. The degradation maps generated with the values of k_1, k_2', A_d and θ output by the models appear to be a good tool to summarise, classify and facilitate the analysis and search of specific bioresorbable composites.

Acknowledgements

First and foremost, I would like to thank Prof. Ruth E. Cameron and Prof. Serena M. Best for their guidance, patient, support and encouragement during the last four years. The work of this thesis would not have been possible without the technical assistance provided by Andrew Moss and Mary Vickers (XRD), Simon Griggs (SEM) and Rob Cornell (Polymer Laboratory).

I would like to acknowledge "La Caixa" Foundation and Lucideon for the financial support during my Ph.D. studies. Additionally, I would also like to thank my industrial supervisor Dr. Xiang Zhang for his assistance and encouragement, Dr. Anke Husmann for her advice and insights into modelling and effective ways of communicating results, Dr. Masato Ueda for the generous supply of the calcium carbonate nanoparticles and Prof. Jingzhe Pan for his advice and help during the initial stages of the project.

I would also like to thank Miss Malavika Nair and Miss Saoirse Bryar for their contributions to the understanding of dissolution of hydroxyapatite and tricalcium phosphate during their Part III projects in the Cambridge Centre for Medical Materials.

Finally, I would like to thank my friends, family and members of the CCMM for their constant encouragement and continued support.

Contents

List of Figures

List of Tables

Chapter 1
Introduction

1.1 Background and Motivation

With an ageing population [1] and an increasing rate of sports related injuries [2], the need for a steady and reliable source of good quality materials for orthopaedic applications seems paramount. Currently, the three main commercially available types of orthopaedic implants are: non-degradable implants, biodegradable polymeric implants and bioresorbable composites or biocomposites, that is composites made of biodegradable polymers and calcium-based fillers. Figure 1.1 depicts the different types of interference screws for anterior cruciate ligament (ACL) reconstruction manufactured by Stryker [3].

The analysis of ACL reconstruction interference screws, which can be used as a representative case of the overall trend in orthopaedic implants, has not shown unanimous consensus regarding the relative performance of the different types of screws. Although most clinical output studies reported a similar performance for both resorbable and non-resorbable implants [4, 5], other studies reported a slightly better performance of the titanium implants [6]. Traditionally, the preferred option by medical consultants has been non-degradable implants [7], probably due to the complications of degradable implants such as delayed inflammation, sinus formation and fluid accumulation [8, 9].

Despite the numerous theoretical advantages of the bioresorbable and bioactive implants when compared with the non-degradable implants, such as the lack of requirement for a second surgery to remove the implant, biocompatibility and bone growth stimulation [10], in practical terms these advantages have not been translated to the patients. One of the main concerns halting a wider use of biodegradable polymer implants and biocomposites is related to its, sometimes, unreliable and unpredictable degradation behaviour. The current approach is to overengineer these implants in order to avoid early failure. For example, Drogset et al. reported a residual screw tract in implanted poly(L-lactide) screws that showed no bone ingrowth several years after surgery [6], pointing to a extremely slow degradation profile and thus, sacrificing

I. Moreno-Gomez, *A Phenomenological Mathematical Modelling Framework for the Degradation of Bioresorbable Composites*,
Springer Theses, https://doi.org/10.1007/978-3-030-04990-4_1

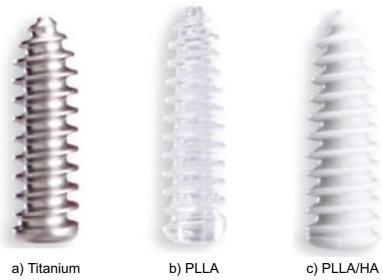

Fig. 1.1 Three commercially available interference screws for anterior cruciate ligament reconstruction from Stryker [3]: **a** made of titanium, **b** made of poly(L-lactide) (PLLA) and **c** made of poly(L-lactide) and hydroxyapatite (PLLA/HA)

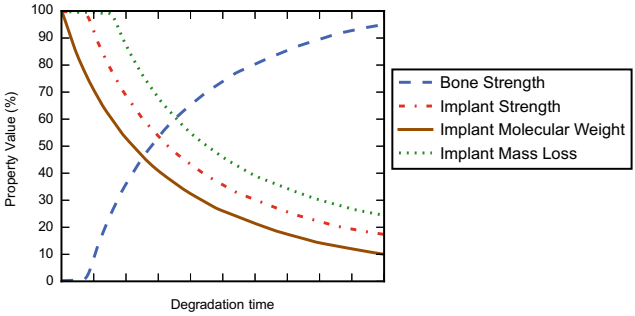

Fig. 1.2 Idealized relationship between strengths of a biodegradable implant and bone for an optimum load transfer. Also included the relationship between implant mass loss, molecular weight and strength. Adapted from [13, 14]

the advantages related to the biodegradability of the material, indicating that such materials are not ideal for fixation devices [11].

The ideal material candidate should remain sufficiently strong after implantation in order to bear the applied mechanical loads and ensure a correct fixation. As tissue heals and is able to support increasing mechanical loads, the implant should degrade to facilitate the load transfer. After the healing has finished, the implant should completely degrade and be replaced by the native tissue [12]. Figure 1.2 characterises this ideal behaviour in terms of both bone and implant properties.

Regrettably, the degradation behaviour of biocomposites is not yet well understood, with a priori similar poly(L-lactide) and hydroxyapatite biocomposites, such as the ones studied by Verheyen et al. [15] and Shikinami and Okuno [16] showing notable differences in their degradation behaviour, partially due to the great variety of factors which play a role in this degradation process, ranging from particle shape [17] to sample porosity [18] including properties like particle size [19], solubility product of the filler [20] or molecular ratio of monomers in the polymeric matrix [21], creating a complex picture through interactions and interwoven responses.

Experimental studies of the degradation behaviour displayed by biocomposites require a high demand of resources as they can span up to several years with heavily time-consuming characterisation for each timepoint. This excessive cost combined with the endless number of possibilities, in terms of polymer-ceramic combinations, suggest that using a simple trial and error approach to find the biocomposite with an adequate degradation profile for a given application seems a daunting and colossal task pointing to the convenience of using, where possible, data already available in literature.

The degradation of biocomposites presents a combination of factors, such as clinical relevance, complexity, existence of a significant amount of published data and proximity to polymer degradation, a heavily modelled phenomenon, which makes it an attractive problem for computational modelling. Surprisingly, there are very few published modelling efforts dealing with the different aspects of biocomposites. In terms of degradation, the mathematical model developed by Pan et al. for composites made of polyesters and tricalcium phosphate [22, 23] showed promised in advancing the understanding of the mechanisms involved in the degradation of biocomposites, bringing closer the possibility of having customised biocomposites with a particular degradation profile for a certain injury with the subsequent advantages for the patients.

1.2 Aims of the Thesis

Given the abovementioned necessity of improving the understanding of the mechanisms governing the degradation of biocomposites in order to unlock their full potential, improve their reliability and open the possibility of implant customisation, the general objective of this thesis is to contribute to this furthering of the degradation understanding by means of analysis of available biocomposite degradation data with a customised computational tool.

The specific aims of this thesis are:

- Development of a general modelling framework for the degradation of biocomposites made of biodegradable polyesters and calcium-based ceramics based on the mathematical model proposed by Pan et al. [22, 23]. This modelling framework will employ different expressions to characterise the interwoven mechanisms present during degradation as a function of time.
- Analysis of the aforementioned general modelling framework with particular focus on discussing the employed assumptions and subsequent inherent limitations, in addition to the modelling framework advantages.
- Development and computational implementation of three ceramic-specific models resulting from the particularisation of the general modelling framework for common calcium-based ceramics, namely tricalcium phosphate (TCP), hydroxyapatite (HA) and calcium carbonate (CC).
- Creation of a database of quantitative degradation data for biocomposites with a polyester matrix and either tricalcium phosphate, hydroxyapatite or calcium carbonate as a filler containing information pertaining to the polymer, ceramic and

sample characteristics in addition to protocol and measurements of degradation by surveying and harvesting the available published literature.
- Analysis of the harvested degradation data with the ceramic-specific models, including the study of case studies showing both compliant and non-compliant behaviour with the modelling framework predictions to establish the influence on biocomposite degradation of a series of factors such as ceramic addition, sample porosity and degradation protocol.
- Production, characterisation and in vitro degradation of nanocomposites made of poly(D,L-lactide-co-glycolide) and calcium carbonate with several ceramic particle sizes and ceramic weight fractions to study their effect on composite degradation behaviour and compare those measured effects to the modelling framework assumptions.

1.3 Structure of the Thesis

This thesis is divided in eight chapters, with this first one serving as an introduction to the work.

Chapter 2 contains a brief review of the relevant literature, including a summary of the biocomposite degradation mechanisms and an overview of the published computational models concerning the degradation of biocomposites.

Chapter 3 introduces a mathematical modelling framework for the degradation of bioresorbable composites containing calcium-based fillers. This modelling framework is based on the computational model proposed by Pan et al. [22, 23] for the degradation of composites made of polyesters and tricalcium phosphate. In addition to the general framework, three ceramic-specific models, resulting from the particularisation of this framework for three common calcium-based fillers, namely tricalcium phosphate (TCP), hydroxyapatite (HA) and calcium carbonate (CC), are reported.

Chapters 4, 5 and 7 constitute an unit. These three chapters share a similar structure and contain the analysis of the qualitative degradation data harvested from literature using the ceramic-specific models introduced in Chap. 3. In Chap. 4, the analysed data pertain to bioresorbable composites containing tricalcium phosphate, whereas in Chap. 5, the composites contain hydroxyapatite and in Chap. 7, calcium carbonate.

Chapter 6 presents an experimental study of the in vitro degradation of nanocomposites made of poly(D,L-lactide-co-glycolide) and calcium carbonate.

Chapter 7, in addition to the abovementioned analysis of the harvested CC composites degradation data, discusses a detailed analysis of the Chap. 6 nanocomposites.

Lastly, Chap. 8 summarises the key findings of this work and outlines a series of suggestions for future work stemming from this thesis.

References

1. Suzman, R., Beard, J. (2011). Global health and aging. Technical Report 11-7737, World Health Organization.
2. Health and Social Care Information Centre (2012). *Provisional monthly hospital episode statistics for admitted patient care, outpatients and accident and emergency data - April 2012*. Technical report, National Health Service.
3. Stryker (2004). Fixation devices for ACL reconstruction. Commercial brochure. Retrieved September 1, 2016 from http://www.stryker.com/emea/Solutions/ACLRepair/UniversalACLInstrumentationSystem/index.htm.
4. Myers, P., Logan, M., Stokes, A., Boyd, K., & Watts, M. (2008). Bioabsorbable versus titanium interference screws with hamstring autograft in anterior cruciate ligament reconstruction: a prospective randomized trial with 2-year follow-up. *Arthroscopy: The Journal of Arthroscopic & Related Surgery 24*(7), 817–823.
5. Emond, C. E., Woelber, E. B., Kurd, S. K., Ciccotti, M. G., & Cohen, S. B. (2011). A comparison of the results of anterior cruciate ligament reconstruction using bioabsorbable versus metal interference screws: a meta-analysis. *JBJS*, *93*(6), 572–580.
6. Drogset, J. O., Straume, L. G., Bjørkmo, I., & Myhr, G. (2011). A prospective randomized study of ACL-reconstructions using bone-patellar tendon-bone grafts fixed with bioabsorbable or metal interference screws. *Knee Surgery, Sports Traumatology, Arthroscopy*, *19*(5), 753–759.
7. Kontakis, G. M., Pagkalos, J. E., Tosounidis, T. I., Melissas, J., & Katonis, P. (2007). Bioabsorbable materials in orthopaedics. *Acta Orthopaedica Belgica*, *73*(2), 159.
8. Ambrose, C. G., & Clanton, T. O. (2004). Bioabsorbable implants: review of clinical experience in orthopedic surgery. *Annals of Biomedical Engineering*, *32*(1), 171–177.
9. Amini, A. R., Wallace, J. S., & Nukavarapu, S. P. (2011). Short-term and long-term effects of orthopedic biodegradable implants. *Journal of Long-term Effects of Medical Implants 21*(2).
10. Hench, L. L., & Polak, J. M. (2002). Third-generation biomedical materials. *Science*, *295*(5557), 1014–1017.
11. Walton, M., & Cotton, N. J. (2007). Long-term in vivo degradation of poly-L-lactide (PLLA) in bone. *Journal of Biomaterials Applications*, *21*(4), 395–411.
12. Weiler, A., Hoffmann, R. F., Stähelin, A. C., Helling, H.-J., & Südkamp, N. P. (2000). Biodegradable implants in sports medicine: the biological base. *Arthroscopy*, *16*(3), 305–321.
13. Disegi, J. A., & Wyss, H. (1989). Implant materials for fracture fixation: a clinical perspective. *Orthopedics*, *12*(1), 75–79.
14. Pietrzak, W. S., Verstynen, M. L., & Sarver, D. R. (1997). Bioabsorbable fixation devices: status for the craniomaxillofacial surgeon. *The Journal of Craniofacial Surgery*, *8*(2), 92–96.
15. Verheyen, C., De Wijn, J., Van Blitterswijk, C., & De Groot, K. (1992). Evaluation of hydroxylapatite/poly(L-lactide) composites: mechanical behavior. *Journal of Biomedical Materials Research*, *26*(10), 1277–1296.
16. Shikinami, Y., & Okuno, M. (1999). Bioresorbable devices made of forged composites of hydroxyapatite (HA) particles and poly-L-lactide (PLLA): part I. Basic characteristics. *Biomaterials*, *20*(9), 859–877.
17. Tsunoda, M. (2003). Degradation of poly(DL-lactic acid-co-glycolic acid) containing calcium carbonate and hydroxyapatite fillers-effect of size and shape of the fillers. *Dental Materials Journal*, *22*(3), 371–382.
18. Deng, X., Sui, G., Zhao, M., Chen, G., & Yang, X. (2007). Poly(L-lactic acid)/hydroxyapatite hybrid nanofibrous scaffolds prepared by electrospinning. *Journal of Biomaterials Science, Polymer Edition*, *18*(1), 117–130.
19. Yang, Z., Best, S. M., & Cameron, R. E. (2009). The influence of α-tricalcium phosphate nanoparticles and microparticles on the degradation of poly(D, L-lactide-co-glycolide). *Advanced Materials*, *21*(38–39), 3900–3904.
20. Ara, M., Watanabe, M., & Imai, Y. (2002). Effect of blending calcium compounds on hydrolytic degradation of poly(DL-lactic acid-co-glycolic acid). *Biomaterials*, *23*(12), 2479–2483.

21. Kikuchi, M., Koyama, Y., Yamada, T., Imamura, Y., Okada, T., Shirahama, N., et al. (2004). Development of guided bone regeneration membrane composed of β-tricalcium phosphate and poly(L-lactide-co-glycolide-co-ε-caprolactone) composites. *Biomaterials*, *25*(28), 5979–5986.
22. Pan, J., Han, X., Niu, W., & Cameron, R. E. (2011). A model for biodegradation of composite materials made of polyesters and tricalcium phosphates. *Biomaterials*, *32*(9), 2248–2255.
23. Pan, J. (2014). *Modelling degradation of bioresorbable polymeric medical devices*. Elsevier.

Chapter 2
Literature Review

This chapter briefly discusses relevant literature on the degradation mechanisms of bioresorbable composites and the computational models developed to characterise them. As mentioned in the introductory chapter, the harvest and analysis of published experimental degradation data from bioresorbable composites is one of the main objectives of this thesis. Therefore, a majority of the literature on biocomposite degradation is presented in the following chapters and to avoid repetition, only introductory literature is included here.

2.1 Degradation Mechanisms of Bioresorbable Composite

A bioresorbable composite, or biocomposite, can be defined as a composite that "can be disintegrated, eroded, dissolved, broken down and/or experience chain scission to produce degradation products that the body can 'resorb', i.e. degradation products that can be metabolised and enter the general metabolic pathways of the body" [1, 2]. Biocomposites, currently being widely investigated for orthopaedic applications [3], usually have a biodegradable polymeric matrix and a calcium-based sparingly soluble ceramic filler.

2.1.1 Biodegradable Polymeric Matrixes

Biodegradable polymers have been widely researched since 1974, which marked their first clinical application as sutures [4]. A significant part of that research has focused on homopolymers and copolymers of α-hydroxy-acids, such as lactic and glycolic acid, and most recently again on poly(ε-caprolactone), all of them with approved status for use in the biomedical field by the FDA [5–7].

I. Moreno-Gomez, *A Phenomenological Mathematical Modelling Framework for the Degradation of Bioresorbable Composites*,
Springer Theses, https://doi.org/10.1007/978-3-030-04990-4_2

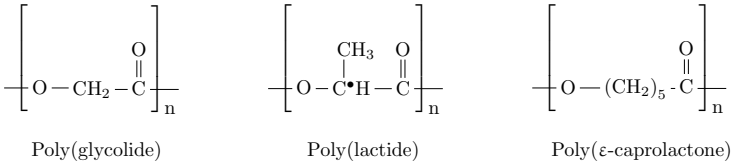

Fig. 2.1 Structures of poly(lactide), poly(glycolide) and poly(ε-caprolactone). "n" is the number of repeating units. • indicates the position of the chiral centre in the poly(lactide) repeating unit

Table 2.1 Physical properties of various biodegradable polymers. T_m is the melting temperature, T_g is the glass transition temperature, σ is the tensile strength and t_{deg} is the time to complete resorption. Adapted from [5, 6]

Polymer	T_m (°C)	T_g (°C)	σ (MPa)	t_{deg} (months)
PLLA	185	60	85	>24
PDLLA	Amorphous	55	40	(12...16)
PGA	226	40	80	(6...12)
P(D,L)LGA(50:50)	Amorphous	45	47	(1...2)
P(D,L)LGA(75:25)	Amorphous	52	47	(4...5)
PCL	61	−63	30	>24

Physico-chemical Properties

Poly(lactide) (PLA) and poly(glycolide) (PGA) are the main homopolymers of the poly(α-hydroxy-acids) and their monomers can be combined to form poly(lactide-co-glycolide) (PLGA). All of them, in addition to poly(ε-caprolactone) (PCL), present backbone ester linkages (RCOOR'). The structures of poly(glycolide), poly(lactide) and poly(ε-caprolactone) repeating units are depicted in Fig. 2.1.

The presence of a methyl group in the central carbon causes chirality in lactide, resulting in two stereo-isomeric forms: L-lactide, the natural occurring isomer in humans [8], and D-lactide. Thus, poly(lactide) (PLA) exists in three forms: poly(L-lactide) (PLLA), poly(D-lactide) (PDLA) and racemic mixture of D,L-PLA (PDLLA), all of them with different values of properties such as crystallinity, tensile strength and degradation rate [9]. The existence of two lactide stereo-isomers and the possibility of copolymerising several different monomers open the door to attain a wide range of properties. Table 2.1 highlights this range reporting several physical properties for a selection of biopolymers, including different homo- and copolymers of poly(lactide).

Degradation Mechanisms: Molecular Level

Poly(α-hydroxy-acids) and poly(ε-caprolactone) degrade by hydrolysis of the backbone ester bonds (RCOOR′) in an aqueous environment [10], yielding a carboxylic acid (RCOOH) and an alcohol (R′OH). This reaction can be catalysed by a base or an acid as seen in Fig. 2.2.

The resulting carboxylic end groups can experience dissociation, increasing the local acidity, which in turn catalyses the hydrolysis reaction. This phenomenon,

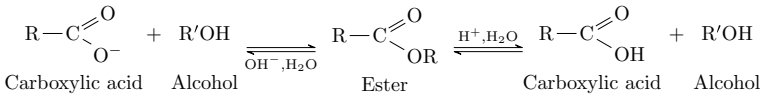

Fig. 2.2 General schematic of base (OH^-) and acid (H^+) catalysed hydrolysis of an ester yielding a carboxylic acid and an alcohol, from [11]

known as autocatalysis, has been widely observed in poly(α-hydroxy-acids) [12, 13]. For poly(ε-caprolactone) conflicting information has been published with Pitt et al. reporting the presence of autocatalysis in PCL hydrolysis [14] and Siparsky et al. reporting its absence [15].

The chain scissions caused by the hydrolysis can either be random or end-scissions, i.e. hydrolysis can happen to a random ester bond or to the final bond in the chain. Shih found that poly(ε-caprolactone) experiences random scission while poly(D,L-lactide) presents a significantly higher proportion of end-scission, also called unzipping [16, 17]. Additional research has found both evidences of unzipping in poly(lactide) [18] and random scission [19] in an acidic medium. Park reported random scission for poly(lactide-co-glycolide), probably due to a preferential hydrolysis of glycolide units [20]. Gleadall et al. concluded that a mixture of both random and end scission is necessary to accommodate both mass loss and molecular weight reduction observed during degradation of bioresorbable polyesters [21].

Degradation Mechanisms: Macroscopic Level

Polymer hydrolysis is activated by the presence of water and thus, heavily dependent on water diffusion into the material. Macroscopically, degradation can be either surface or bulk, with bulk degradation being either homogeneous or heterogeneous [22]. Surface degradation occurs when the water entrance is slower than the hydrolysis rate, so hydrolysis is confined to the device surface. Bulk degradation occurs when water penetration is greater than the hydrolysis rate, so hydrolysis happens in the whole device. If the degradation rate is constant throughout the device, it is considered homogeneous, whereas if the inner part degrades faster than the outer part, it is considered heterogeneous. Figure 2.3 contains schematic representation of the three degradation types.

Considering the water ingress/hydrolysis rate interaction, von Burkersroda et al. calculated a critical device dimension, L_{critical}, which marks the transition from bulk to surface degradation. L_{critical} is approximately 10 cm for poly(α-hydroxy-acids) and 1.3 cm for poly(ε-caprolactone) [23], suggesting that the degradation of medical devices made of these materials will proceed through bulk degradation.

Li and co-workers have extensively studied the degradation of devices made of several poly(α-hydroxy-acids) such as poly(D,L-lactide) [24], poly(D,L-lactic-co-glycolic acid), poly(L-lactic-co-glycolic acid) [25] and poly(L-lactide) [26], characterising the mechanism as heterogeneous bulk degradation. Similarly, Hurrell and colleagues analysed the degradation of poly(glycolide) [27–29], arriving at the same conclusion. Huang et al. found that poly(ε-caprolactone) and PCL-based copolymer

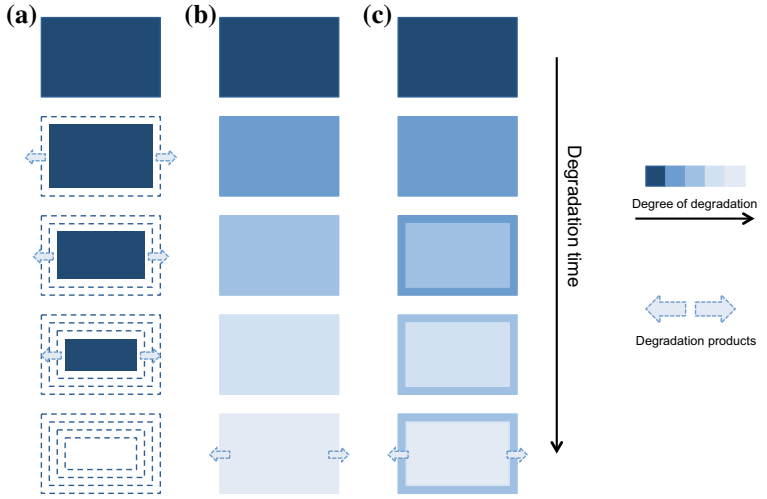

Fig. 2.3 Schematic models of different types of degradation: **a** surface degradation, **b** homogeneous bulk degradation and **c** heterogeneous bulk degradation, adapted from Farrar [22]

and blends experience homogeneous degradation unless D,L-lactide is present [30]. Grizzi et al. observed that device size has a significant influence in the difference of degradation rates between the core and the surface with bigger devices experiencing larger dissimilarity [31].

Heterogeneous bulk degradation, also known as autocatalytic bulk degradation, is generally divided in four stages. Firstly, water diffuses into the device and polymer hydrolysis starts. Then, degradation continues throughout the sample but oligomers and monomers at the surface are able to diffuse out, while those in the centre are trapped and act as a catalyst, accelerating the reaction, resulting in a highly-degraded core encapsulated in a less-degraded shell. In a third stage, the shell breaks and releases the acidic degradation products and lastly, the shell remains also degrade [24–29]. For homogeneous degradation, the sequence of events is similar but the difference between core and surface is not observed [7].

The factors affecting the degradation of biodegradable polymers, which have been extensively investigated [10, 32–35], are numerous and include hydrophilicity, crystallinity, molecular weight, sample size, processing history, sterilisation method, porosity and presence of additives, plasticisers and residual monomers among material factors and pH, ionic concentration, temperature, fluid flow rate and mechanical loading among environmental factors.

Table 2.2 Physico-chemical properties of various calcium-based ceramic fillers. Ca/P and Ca/C are the molar ratio of calcium to phosphorus and calcium to carbon, $-\log_{10}(K_{sp})$ is negative base 10 logarithm of the solubility product and ρ_{cer} is the ceramic density. Adapted from [39, 40]

Ceramic	Chemical formula	Ca/P or Ca/C ratio (mol mol^{-1})	$-\log_{10}(K_{sp})$ at 37 °C	ρ_{cer} (g cm^{-3})
HA	$Ca_{10}(PO_4)_6(OH)_2$	1.67	117.2	3.16
α-TCP	$Ca_3(PO_4)_2$	1.5	25.5	2.86
β-TCP	$Ca_3(PO_4)_2$	1.5	29.5	3.07
β-CC	$CaCO_3$	1	8.56	2.71
λ-CC	$CaCO_3$	1	8.42	2.95
μ-CC	$CaCO_3$	1	8.02	2.65

2.1.2 Calcium-Base Ceramic Fillers

The chemical similarity of the mineral component of human bone to hydroxyapatite, a calcium phosphate, has motivated researchers to investigate calcium-based ceramics as bone substitutes [36]. Most of the research has focused on calcium phosphates, particularly hydroxyapatite (HA) and tricalcium phosphate (TCP) [37] with some studies also investigating calcium carbonate (CC) [38].

Physico-chemical Properties

Calcium phosphates, also known as calcium orthophosphates (CaP), are salts of (ortho)phosphoric acid (H_3PO_4), while calcium carbonates (CC) are salts of carbonic acid (H_2CO_3). CaP contain Ca^{2+} ions and HPO_4^{2-} or PO_4^{2-} ions and CC contain Ca^{2+} ions and CO_3^{2-} ions. Several physico-chemical properties for selected calcium phosphates and calcium carbonates are included in Table 2.2. The significant variation in properties such as solubility and density suggests a wide range of behaviours.

Degradation Mechanism: Dissolution

Both calcium phosphates and calcium carbonate degrade by dissolution in an aqueous media [40, 41]. The solubility of these calcium-based ceramics is affected by several ceramic factors, such as Ca^{2+}:anion ratio, crystal structure, crystallinity, lattice defects, phase purity, presence of foreign ions, chemical composition and porosity [40, 41] as well as environmental factors, such as pH, activity of biological macromolecules, temperature and media ionic strength [37].

The dissolution of these calcium-based ceramics has been widely researched, usually by fixing most of the abovementioned variables and controlling the remaining, particularly composition, pH and undersaturation. The undersaturation of a sparingly soluble salt, σ, which changes with the specific experimental conditions, can be expressed using the ionic activity product I_P, and the solubility product, K_{sp}:

$$\sigma = 1 - \left(\frac{I_P}{K_{sp}}\right)^{\frac{1}{\eta}} = 1 - \left(\frac{\prod_{i=1}^{n} C_i^{m_i}}{K_{sp}}\right)^{\frac{1}{\eta}} \quad (1) \qquad (2.1)$$

with η, the sum of multiplicities of the n different ions in the ceramic chemical composition: $\eta = \sum_{i=1}^{n} m_i$ and the ionic product activity calculated as $\prod_{i=1}^{n} C_i^{m_i}$ with C_i, the concentration of dissolved ion i and m_i, the multiplicity of the ith ion in the ceramic chemical composition.

The dissolution rate measured in these experiments, J, which is a function of the undersaturation, can be expressed as:

$$J = A_d f(\sigma) \qquad (\text{mol m}^{-2}\,\text{s}^{-1} \text{ or mol s}^{-1}) \qquad (2.2)$$

with A_d the dissolution rate constant and a given function depending on the dominant dissolution mechanism [42, 43]. Generally, the dissolution mechanism is found by identifying the value of the constant n for the obtained experimental data using an empirical power law of the undersaturation σ:

$$J = A_d \sigma^n \qquad (\text{mol m}^{-2}\,\text{s}^{-1} \text{ or mol s}^{-1}) \qquad (2.3)$$

with n, the effective reaction order for a given experimental set up and A_d, the abovementioned dissolution rate constant [42, 44].

Hydroxyapatites: Thomann et al. studied pure hydroxyapatite at constant pH and high undersaturation in a wide pH range finding dissolution governed by diffusion of calcium and/or phosphate ions ($n = 1.34$) [45]. Tang et al. observed a change in dominant dissolution mechanism for hydroxyapatite from $n = 2$ at the initial stages to $n = 9$ [46] as dissolution progressed. Lastly, Christoffersen et al. noted the presence of a variety of mechanisms in HA dissolution with dominance of polynuclear dissolution, giving n values from 2.9 to 4.7 [47]. Carbonated hydroxyapatite with a 3.06% CO_3^{2-} showed dissolution controlled by surface diffusion ($n = 1.9$) at low undersaturation [48]. Chin and Nancollas observed surface controlled dissolution following spiral dislocation ($n = 2$) in fluoroapatite, as opposed to hydroxyapatite, which showed polynucleation-controlled dissolution ($n = 6$) [49]. An attempt to build a general hydroxyapatite dissolution mechanisms model by agglutinating different individual mechanisms was undertaken by Dorozhkin [50].

Tricalcium phosphate: Bohner et al. studied β-TCP and found diffusion-controlled dissolution at the initial stages with different pH values ($n = 2$), and a more complex situation for latter stages in variable pH, indicating a mix of mechanisms ($n = 8.31$) [51]. Tang et al. observed surface-pit (polynucleation) controlled dissolution ($n = 5.5$) using commercially available β-TCP over a range of undersaturation using the constant composition method [52]. Lastly, Ito et al. reported also polynucleation dissolution ($n \approx 4.9$) at acidic pH in zinc-containing β-TCP discs [53].

Table 2.3 A selection of dissolution mechanisms with their corresponding kinetic profiles and effective reaction orders, n [42, 43, 51] for common calcium-based ceramics

Dissolution mechanism	Kinetic form	Effective reaction order	Ceramics and References
Volume (ion) diffusion	$J = A_d\sigma$	$n = 1$	HA [45]; α-TCP [54]
Surface diffusion	$J = A_d\sigma^2$	$n = 2$	HA [46]; Carbonated HA [48]; β-TCP [51]; α-TCP [54, 55]; CC [40]
Spiral dissolution by surface diffusion	$J = A_d\sigma^{\frac{1}{2}}\ln(1-\sigma)$ $\approx A_d\sigma^2$	$n \approx 2$	Fluoro-HA [49]
Polynucleation dissolution (surface pit)	$J = A_d\sigma^{\frac{2}{3}}\left(-\ln(1-\sigma)\right)^{\frac{1}{6}}$ $\exp\left(\frac{A}{\ln(1-\sigma)}\right)$	$n > 2$	HA: $n = (2.7\ldots4.9)$ [47], $n = 6$ [49], $n = 9$ [46]; β-TCP: $n = 4.9$ [53], $n = 5.5$ [52], $n = 8.3$ [51]; CC [40]

The dissolution of α-TCP was studies by Ginebra et al. and was found to be surface-diffusion controlled initially and become ion-diffusion controlled through the hydrated layer formed around the reactants in later stages [54]. Durucan and Brown also observed a surface-diffusion controlled dissolution for α-TCP [55].

Calcium carbonate: Morse et al. found a mixture of dissolution mechanisms for the different $CaCO_3$ allotropes, with prevalence of transport controlled mechanisms at low pH and presence of more complex kinetics at higher pH values [40].

Table 2.3 summarises the main characteristics of the different dissolution mechanisms including examples of calcium-based ceramics displaying said mechanisms.

2.1.3 Degradation Behaviour of Bioresorbable Composites

The degradation behaviour of bioresorbable composites is a complex phenomenon not yet well understood, with a number of factors, pertaining to the polymeric matrix, the ceramic filler and the interactions between both, playing a role in the degradation process. Although biocomposites tend to present a different degradation behaviour than their pure polymer counterparts, conflicting findings have been reported, such as experimental studies describing biocomposites with both lower [56, 57] and higher degradation kinetics [58, 59] than the corresponding pure polymer scaffolds.

Due to the complexity, rather than providing a brief discussion and considering that one of the principal aims of this thesis is to contribute to the biocomposite degradation understanding with the analysis of biocomposite degradation data, Chaps. 4, 5 and 7 present a detailed study of the influence on biocomposite degradation of factors such as ceramic addition, sample porosity and degradation protocol for bioresorbable composites containing tricalcium phosphate (TCP),

hydroxyapatite (HA) and calcium carbonate (CC), respectively. In addition, Chap. 3 presents and discussed the expected biocomposite degradation behaviour during the analysis of the modelling framework.

2.2 Computational Models Concerning the Degradation Behaviour of Bioresorbable Composites

Computational models play a key role in modern materials science research as they allow to deepen the understanding of complex materials behaviours [60]. The degradation behaviour of biodegradable polymers has garnered significant attention from the modelling community since the 80s when the first simple mechanistic models appeared [14]. Sadly, the degradation behaviour of biocomposites has not sparked the same interest and there are scarce examples of such models in literature.

Monitoring the molecular weight of the polymeric matrix in biocomposites has been frequently used as a technique to characterise the degradation of biocomposites [61, 62]. As a significant number of the biodegradable polymers degradation models aim to provide a characterisation of the evolution of the molecular weight over time, these computational models have been included in this review as the employed modelling approaches could be of interest for the modelling of biocomposite degradation.

2.2.1 Models for Biodegradable Polymers

Literature provides abundant examples of models for multiple aspects of biodegradable polymers such as mechanical properties [63–65], drug delivery [66, 67], bone tissue formation [68] and degradation behaviour among others. To keep this review as concise and relevant as possible, only computational models for degradation behaviour are included. A mathematical description is included solely for mechanistic models with a deterministic approach as the composite degradation models presented in this thesis employ said approach.

The development of mathematical models for chain scission in biodegradable polymers with bulk degradation started in the 80s with Pitt and co-workers proposing, in 1981 and 1987, simple mechanistic models for autocatalytic [14] and non-catalytic [69] hydrolysis using the following expressions for polymer chain scissions rate, R_s ($\mathrm{mol\,m^{-3}}$):

$$\frac{\mathrm{d}R_s}{\mathrm{d}t} = k_2 C_\mathrm{e} C_{\mathrm{H_2O}} C_\mathrm{COOH} \qquad (\mathrm{mol\,m^{-3}\,s^{-1}}) \tag{2.4}$$

and

$$\frac{\mathrm{d}R_s}{\mathrm{d}t} = k_1 C_\mathrm{e} C_{\mathrm{H_2O}} \qquad (\mathrm{mol\,m^{-3}\,s^{-1}}) \tag{2.5}$$

respectively, with C_e, the concentration of ester bonds (mol m^{-3}); C_{H_2O}, the concentration of water (mol m^{-3}); C_{COOH}, the concentration of carboxylic acid end groups (mol m^{-3}) and k_1 (m^3 mol^{-1} s^{-1}) and k_2 (m^6 mol^{-2} s^{-1}), the non-catalytic and autocatalytic polymer hydrolysis rate constants respectively.

The autocatalytic model, which considered the concentration of carboxylic end groups as catalyst, was modified in 1998 by Siparsky et al. and in 2007 by Lyu et al. to include the concentration of hydrogen ions as catalyst instead of the chain ends concentration, using the equilibrium dissociation condition for weak acids [15, 70] giving the following expression:

$$\begin{aligned}\frac{dR_s}{dt} &= k_2 C_e C_{H_2O} C_{H^+} \\ &= k_2 K_a^{0.5} C_e C_{H_2O} C_{COOH}^{0.5} \qquad (\text{mol m}^{-3}\,\text{s}^{-1})\end{aligned} \tag{2.6}$$

with C_{H^+}, the concentration of hydrogen ions (mol m^{-3}); K_a, the equilibrium constant for the deprotonation reaction of the carboxylic end groups (mol m^{-3}) and k_2, C_e, C_{H_2O} and C_{COOH}, the abovementioned magnitudes. A good summary of these initial modelling efforts, including analytical solutions and a critical analysis, can be found in the review written by Farrar [22]. More complex mechanistic models, still employing a deterministic approach, capable of characterising full molecular weight distribution in bulk-degrading polymers, were developed by Batycky et al. in 1997 for non-catalytic hydrolysis including a distinction between end and random scissions [71] and by Antheunis and co-workers in 2009 for autocatalytic hydrolysis [72, 73].

The last few years have seen numerous modelling contributions employing a deterministic approach, either aiming to generate a model as general as possible, such as Rothstein et al. with a model combining bulk and surface degradation [74], or trying to customise the model as much as possible, such as Casalini et al. with a model for the degradation of poly(lactide-co-glycolide) microspheres, using the approach of Perale et al. [75], which included autocatalysis and oligomer diffusion within the matrix with a molecular weight dependent diffusion coefficient [76]. Similarly, Busatto and co-workers proposed models for both homogeneous and heterogeneous degradation of poly(lactide-co-glycolide) microspheres considering the three possible bond types present in the polymer [77, 78].

A stochastic approach for modelling bulk-degrading polymers was pioneered by Göpferich in 1997 using a Monte Carlo technique and considering erosion, also referred as mass loss [79]. In 2002, Siepmann et al. modified the model to include drug release rate without including autocatalytic hydrolysis or monomer and oligomers diffusion through the matrix [80]. In 2011, Chen et al. proposed a model with stochastic hydrolysis and mass transport to simulate both polymeric degradation and erosion considering autocatalysis [81]. Modelling attempts combining atomistic bulk approaches with quantum chemical approaches for hydrolytic degradation of aliphatic polymers have also been investigated by Hofmann et al. [82] and Entrialgo-Castaño et al. [83].

A significant amount of effort over the last few years has been dedicated by the Mechanics of Materials research group at Leicester University to comprehensively model the behaviour of biodegradable polymers with bulk degradation. These efforts are specially relevant because of the strong relationship with the modelling approach employed in this thesis.

In 2008, Wang et al. proposed a mechanistic model with a deterministic approach consisting of a set of simplified reaction-diffusion equations considering both autocatalytic and non-catalytic hydrolysis and including two adimensional parameters employed to generate biodegradation maps which indicated the conditions for having degradation controlled by autocatalytic hydrolysis, non-catalytic hydrolysis or oligomer diffusion [84, 85]. The rate of chain scissions and the monomer diffusion were modelled using, respectively, the following expressions:

$$\frac{\mathrm{d}R_s}{\mathrm{d}t} = k_1 C_\mathrm{e} + k_2 C_\mathrm{e} C_\mathrm{m}^n \qquad (\mathrm{mol\,m^{-3}\,s^{-1}}) \tag{2.7}$$

and

$$\frac{\mathrm{d}C_\mathrm{m}}{\mathrm{d}t} = \frac{\mathrm{d}R_m}{\mathrm{d}t} + \mathrm{div}_{x_i}[D\mathrm{grad}_{x_i}(C_\mathrm{m})] \qquad (\mathrm{mol\,m^{-3}\,s^{-1}}) \tag{2.8}$$

with C_e, the concentration of ester bonds ($\mathrm{mol\,m^{-3}}$); C_m, the concentration of monomers ($\mathrm{mol\,m^{-3}}$); n, the dissociation degree ($\mathrm{mol\,mol^{-1}}$); R_m, the monomer production rate ($\mathrm{mol\,m^{-3}\,s^{-1}}$); D, the diffusion coefficient ($\mathrm{m^2\,s^{-1}}$); and k_1 ($\mathrm{s^{-1}}$) and k_2 ($\mathrm{m^3\,mol^{-1}\,s^{-1}}$), the non-catalytic and autocatalytic polymer hydrolysis rate constants respectively. Han and Pan expanded the model in 2009 by including a characterisation of polymer crystallisation during degradation [86, 87] and the effect of temperature on degradation [87, 88]. In 2010, Wang et al. coupled an entropy spring model to the original model to obtain the characterisation of the Young's modulus as a function of polymer degradation [85, 89].

Han and Pan proposed a major development in 2011, with the addition of the distinction between random and end scission mechanisms in both autocatalytic and non-catalytic hydrolysis, changing to a stochastic approach for polymer chain scission and oligomer production using a kinetic Monte Carlo scheme coupled with a finite differences approach for the diffusion equation, resulting in the capability to compute the evolution of the molecular weight distribution over degradation time [87, 90]. In 2012, Gleadall et al. generated a simplified version of the 2009 model to characterise the hydrolysis-induced crystallisation in biodegradable polymers [91, 92]. A year later, Han and Pan used a simple version of the model in a commercial finite element package (COMSOL Multiphysics) to analyse degradation of medical devices with complex geometries [93]. A detailed and complete description of updated and harmonised versions of the abovementioned models was published by Pan in book format [44].

Further work by Gleadall and co-workers encompassed a simple ready-to-use simulation tool in Excel to analyse different chain scission scenarios in 2013 [92, 94] and the modification of the deterministic version of the model in 2014 to include four

hydrolysis mechanisms: non-catalytic random scission, non-catalytic end scission, autocatalytic random scission, and autocatalytic end scission using the following expressions for chain scissions rate and diffusion respectively:

$$\frac{\mathrm{d}R_s}{\mathrm{d}t} = k_{\mathrm{r1}}C_{\mathrm{e}} + k_{\mathrm{e1}}C_{\mathrm{end}} + k_{\mathrm{r2}}C_{\mathrm{e}}\left(\frac{C_{\mathrm{acid}}}{1-X_{\mathrm{c}}}\right)^n + k_{\mathrm{e2}}C_{\mathrm{end}}\left(\frac{C_{\mathrm{acid}}}{1-X_{\mathrm{c}}}\right)^n \quad (\mathrm{mol\,m^{-3}\,s^{-1}}) \tag{2.9}$$

and

$$\frac{\mathrm{d}C_a}{\mathrm{d}t} = \frac{\mathrm{d}R_a}{\mathrm{d}t} + \mathrm{div}_{x_i}[D\mathrm{grad}_{x_i}(C_{\mathrm{a}})] \quad (\mathrm{mol\,m^{-3}\,s^{-1}}) \tag{2.10}$$

with C_{e}, the concentration of ester bonds ($\mathrm{mol\,m^{-3}}$); C_{end}, the concentration of chain ends ($\mathrm{mol\,m^{-3}}$); C_{acid}, the concentration of carboxylic end groups ($\mathrm{mol\,m^{-3}}$); X_{c}, the degree of crystallinity (1); the subscript in the transport equation "a" being either "m" or "ol", to represent monomer or oligomer diffusion: $R_{\mathrm{m/ol}}$, the monomer/oligomer production rate ($\mathrm{mol\,m^{-3}\,s^{-1}}$) and $C_{\mathrm{m/ol}}$, the concentration of monomers/oligomers ($\mathrm{mol\,m^{-3}}$); D, the diffusion coefficient ($\mathrm{m^2\,s^{-1}}$) and k_{r1} and k_{e1} ($\mathrm{s^{-1}}$), the random and end non-catalytic rates and k_{r2} and k_{e2} ($\mathrm{m^3\,mol^{-1}\,s^{-1}}$), the random and end autocatalytic rates. This new version was employed to analyse the effect of random scissions, end scissions, autocatalysis, initial molecular weight and residual monomer on degradation behaviour [21, 92, 95]. In 2015, Gleadall and co-workers explored a totally different approach using an atomic-scale finite element method to analyse the Young's modulus of amorphous polymer structures during degradation [92, 96, 97]. In 2017, a simple version of the model was adapted to analyse the degradation of bioresorbable polymeric stents using Abaqus/Standard [98] and lastly in 2018 the same simple version was coupled with erosion to simulate drug release during degradation [99].

2.2.2 Models for Bioresorbable Composites

Despite numerous advantages that a thorough understanding of biocomposites in general, and their degradation behaviour in particular would bring to patients, there are documented really few modelling attempts for this type of material. The modelling of mechanical properties in bioresorbable composites has received some attention in recent years. Ebrahimian-Hosseinabadi et al. employed two simple semi-empirical models to describe the elastic module of poly(lactide-co-glycolide)–nano-biphasic calcium phosphate composites [100] and Doyle et al. proposed a finite element model to characterise the elastic properties of poly(ε-caprolactone)–β-TCP scaffolds [101].

To the author's knowledge, only two significant attempts to model the degradation of bioresorbable composites have been published: a model for the degradation of composites made of polyesters and TCP proposed by Pan et al. with equations for both polymer hydrolysis and ceramic dissolution [44, 102] and a simple mechanistic model proposed by Kobayashi and Yamaji for poly(L-lactide)–β-TCP composites

in which polymer hydrolysis is water-controlled, and the unique role attributed to the ceramic filler is the increase in water content within the portions of the matrix surrounding the particles [59]. Considering numerous studies attributing buffering capacity to calcium-based ceramics during composite degradation [56, 103, 104], assigning only a water capture capability to the ceramic phase did not seem a complete characterisation of the degradation phenomena. The mathematical description of the ceramic role in composite degradation proposed by Pan et al. seemed more comprehensive, making said model attractive as a base for a general modelling framework intended to be use for the analysis of the vast amount of available literature data. A full description of Pan et al.'s model will be provided in Chap. 3.

In summary, this chapter contained a review of the relevant literature on degradation mechanisms for both biodegradable polymer and calcium-based ceramics. Additionally, an overview of the different available models for the degradation behaviour of biodegradable polymers was presented and lastly, the two available models for biocomposite degradation were introduced. Of the two computational models, Pan et al.'s model [44, 102] presented the best features to become the foundation of the general modelling framework for the degradation of biocomposites that will be discussed in Chap. 3.

References

1. Williams, D. (1999). *The Williams dictionary of biomaterials*. Liverpool University Press.
2. Arshady, R. (2003). *Biodegradable polymers*, Citus Reference Series. Citus Books.
3. Neumann, M., & Epple, M. (2006). Composites of calcium phosphate and polymers as bone substitution materials. *European Journal of Trauma*, *32*(2), 125–131.
4. Horton, C. E., Adamson, J., Mladick, R., & Carraway, J. (1974). Vicryl synthetic absorbable sutures. *The American Surgeon*, *40*(12), 729–731.
5. Middleton, J. C., & Tipton, A. J. (2000). Synthetic biodegradable polymers as orthopedic devices. *Biomaterials*, *21*(23), 2335–2346.
6. Van de Velde, K., & Kiekens, P. (2002). Biopolymers: Overview of several properties and consequences on their applications. *Polymer Testing*, *21*(4), 433–442.
7. Woodruff, M. A., & Hutmacher, D. W. (2010). The return of a forgotten polymer-polycaprolactone in the 21st century. *Progress in Polymer Science*, *35*(10), 1217–1256.
8. Södergård, A., & Stolt, M. (2002). Properties of lactic acid based polymers and their correlation with composition. *Progress in Polymer Science*, *27*(6), 1123–1163.
9. Vert, M., Schwarch, G., & Coudane, J. (1995). Present and future of PLA polymers. *Journal of Macromolecular Science, Part A: Pure and Applied Chemistry*, *32*(4), 787–796.
10. Cameron, R., & Kamvari-Moghaddam, A. (2012). Synthetic bioresorbable polymers. In *Durability and Reliability of Medical Polymers* (pp. 96–118). Elsevier.
11. Smith, M. B., & March, J. (2006). *March's advanced organic chemistry*. New York: Wiley.
12. Li, S., et al. (1999). Hydrolytic degradation characteristics of aliphatic polyesters derived from lactic and glycolic acids. *Journal of Biomedical Materials Research*, *48*(3), 342–353.
13. Pitt, G., Gratzl, M., Kimmel, G., Surles, J., & Sohindler, A. (1981). Aliphatic polyesters II. The degradation of poly(DL-lactide), poly(ε-caprolactone), and their copolymers in vivo. *Biomaterials*, *2*(4), 215–220.
14. Pitt, C. G., Chasalow, F., Hibionada, Y., Klimas, D., & Schindler, A. (1981). Aliphatic polyesters. I. The degradation of poly(ε-caprolactone) in vivo. *Journal of Applied Polymer Science*, *26*(11), 3779–3787.

15. Siparsky, G. L., Voorhees, K. J., & Miao, F. (1998). Hydrolysis of polylactic acid (PLA) and polycaprolactone (PCL) in aqueous acetonitrile solutions: Autocatalysis. *Journal of Environmental Polymer Degradation*, *6*(1), 31–41.
16. Shih, C. (1995a). Chain-end scission in acid catalyzed hydrolysis of poly(D, L-lactide) in solution. *Journal of Controlled Release*, *34*(1), 9–15.
17. Shih, C. (1995b). A graphical method for the determination of the mode of hydrolysis of biodegradable polymers. *Pharmaceutical Research*, *12*(12), 2036–2040.
18. De Jong, S., Arias, E. R., Rijkers, D., Van Nostrum, C., Kettenes-Van den Bosch, J., & Hennink, W. (2001). New insights into the hydrolytic degradation of poly(lactic acid): Participation of the alcohol terminus. *Polymer*, *42*(7), 2795–2802.
19. Belbella, A., Vauthier, C., Fessi, H., Devissaguet, J.-P., & Puisieux, F. (1996). In vitro degradation of nanospheres from poly(D, L-lactides) of different molecular weights and polydispersities. *International Journal of Pharmaceutics*, *129*(1–2), 95–102.
20. Park, T. G. (1995). Degradation of poly(lactic-co-glycolic acid) microspheres: Effect of copolymer composition. *Biomaterials*, *16*(15), 1123–1130.
21. Gleadall, A., Pan, J., Kruft, M.-A., & Kellomäki, M. (2014). Degradation mechanisms of bioresorbable polyesters. Part 1. Effects of random scission, end scission and autocatalysis. *Acta Biomaterialia*, *10*(5), 2223–2232.
22. Farrar, D. (2008). Modelling of the degradation process for bioresorbable polymers. In *Degradation rate of bioresorbable materials* (pp. 183–206). Elsevier.
23. von Burkersroda, F., Schedl, L., & Göpferich, A. (2002). Why degradable polymers undergo surface erosion or bulk erosion. *Biomaterials*, *23*(21), 4221–4231.
24. Li, S., Garreau, H., & Vert, M. (1990a). Structure-property relationships in the case of the degradation of massive poly(α-hydroxy acids) in aqueous media. Part 1: Poly(DL-lactic acid). *Journal of Materials Science: Materials in Medicine*, *1*, 123–130.
25. Li, S., Garreau, H., & Vert, M. (1990). Structure-property relationships in the case of the degradation of massive poly(α-hydroxy acids) in aqueous media. Part 2: Degradation of lactide-glycolide copolymers: PLA37.5GA25 and PLA75GA25. *Journal of Materials Science: Materials in Medicine*, *1*(3), 131–139.
26. Li, S., Garreau, H., & Vert, M. (1990c). Structure-property relationships in the case of the degradation of massive poly(α-hydroxy acids) in aqueous media: Part 3: Influence of the morphology of poly(L-lactic acid). *Journal of Materials Science: Materials in Medicine*, *1*, 198–206.
27. Hurrell, S., & Cameron, R. E. (2001). Polyglycolide: Degradation and drug release. Part I: Changes in morphology during degradation. *Journal of Materials Science: Materials in Medicine*, *12*(9), 811–816.
28. Hurrell, S., & Cameron, R. E. (2001). Polyglycolide: Degradation and drug release. Part II: Drug release. *Journal of Materials Science: Materials in Medicine*, *12*(9), 817–820.
29. Hurrell, S., Milroy, G. E., & Cameron, R. E. (2003). The distribution of water in degrading polyglycolide. Part I: Sample size and drug release. *Journal of Materials Science: Materials in Medicine*, *14*(5), 457–464.
30. Huang, M.-H., Li, S., Hutmacher, D. W., Coudane, J., & Vert, M. (2006). Degradation characteristics of poly(ε-caprolactone)-based copolymers and blends. *Journal of Applied Polymer Science*, *102*(2), 1681–1687.
31. Grizzi, I., Garreau, H., Li, S., & Vert, M. (1995). Hydrolytic degradation of devices based on poly(DL-lactic acid) size-dependence. *Biomaterials*, *16*(4), 305–311.
32. Alexis, F. (2005). Factors affecting the degradation and drug-release mechanism of poly(lactic acid) and poly[(lactic acid)-co-(glycolic acid)]. *Polymer International*, *54*(1), 36–46.
33. Li, S., & Vert, M. (2002). Biodegradation of aliphatic polyesters. *Degradable polymers* (pp. 71–131). Berlin: Springer.
34. Lyu, S., & Untereker, D. (2009). Degradability of polymers for implantable biomedical devices. *International Journal of Molecular Sciences*, *10*(9), 4033–4065.
35. Engineer, C., Parikh, J., & Raval, A. (2011). Review on hydrolytic degradation behavior of biodegradable polymers from controlled drug delivery system. *Trends in Biomaterials and Artificial Organs*, *25*(2).

36. Dorozhkin, S. V. (2009). Calcium orthophosphates in nature, biology and medicine. *Materials*, *2*(2), 399–498.
37. Dorozhkin, S. V. (2010). Bioceramics of calcium orthophosphates. *Biomaterials*, *31*(7), 1465–1485.
38. Cotton, N. J., Egan, M. J., & Brunelle, J. E. (2008). Composites of poly(DL-lactide-co-glycolide) and calcium carbonate: In vitro evaluation for use in orthopedic applications. *Journal of Biomedical Materials Research Part A*, *85*(1), 195–205.
39. Dorozhkin, S. V., & Epple, M. (2002). Biological and medical significance of calcium phosphates. *Angewandte Chemie International Edition*, *41*(17), 3130–3146.
40. Morse, J. W., Arvidson, R. S., & Lüttge, A. (2007). Calcium carbonate formation and dissolution. *Chemical Reviews*, *107*(2), 342–381.
41. Bohner, M. (2000). Calcium orthophosphates in medicine: From ceramics to calcium phosphate cements. *Injury*, *31*, D37–D47.
42. Hayakawa, S. (2015). In vitro degradation behavior of hydroxyapatite. In M. Mucalo (Ed.), *Hydroxyapatite (HAp) for biomedical applications*, chapter 4 (pp. 85–105). Elsevier.
43. Wu, W., & Nancollas, G. H. (1999). Determination of interfacial tension from crystallization and dissolution data: A comparison with other methods. *Advances in Colloid and Interface Science*, *79*(2–3), 229–279.
44. Pan, J. (2014). *Modelling degradation of bioresorbable polymeric medical devices*. Elsevier.
45. Thomann, J., Voegel, J., & Gramain, P. (1993). Quantitative model for the dissolution of calcium hydroxyapatite with a permselective ionic interface. *Journal of Colloid and Interface Science*, *157*(2), 369–374.
46. Tang, R., Wang, L., & Nancollas, G. H. (2004b). Size-effects in the dissolution of hydroxyapatite: An understanding of biological demineralization. *Journal of Materials Chemistry*, *14*(14), 2341–2346.
47. Christoffersen, J., Christoffersen, M. R., & Johansen, T. (1996). Some new aspects of surface nucleation applied to the growth and dissolution of fluorapatite and hydroxyapatite. *Journal of Crystal Growth*, *163*(3), 304–310.
48. Tang, R., Henneman, Z. J., & Nancollas, G. H. (2003). Constant composition kinetics study of carbonated apatite dissolution. *Journal of Crystal Growth*, *249*(3–4), 614–624.
49. Chin, K. A., & Nancollas, G. H. (1991). Dissolution of fluorapatite. A constant-composition kinetics study. *Langmuir*, *7*(10), 2175–2179.
50. Dorozhkin, S. V. (2002). A review on the dissolution models of calcium apatites. *Progress in Crystal Growth and Characterization of Materials*, *44*(1), 45–61.
51. Bohner, M., Lemaître, J., & Ring, T. A. (1997). Kinetics of dissolution of β-tricalcium phosphate. *Journal of Colloid and Interface Science*, *190*(1), 37–48.
52. Tang, R., Wu, W., Haas, M., & Nancollas, G. H. (2001). Kinetics of dissolution of β-tricalcium phosphate. *Langmuir*, *17*(11), 3480–3485.
53. Ito, A., Senda, K., Sogo, Y., Oyane, A., Yamazaki, A., & LeGeros, R. Z. (2006). Dissolution rate of zinc-containing β-tricalcium phosphate ceramics. *Biomedical Materials*, *1*(3), 134.
54. Ginebra, M.-P., Fernández, E., Driessens, F., & Planell, J. A. (1999). Modeling of the hydrolysis of α-tricalcium phosphate. *Journal of the American Ceramic Society*, *82*(10), 2808–2812.
55. Durucan, C., & Brown, P. W. (2002). Kinetic model for α-tricalcium phosphate hydrolysis. *Journal of the American Ceramic Society*, *85*(8), 2013–2018.
56. Agrawal, C. M., & Athanasiou, K. A. (1997). Technique to control pH in vicinity of biodegrading PLA-PGA implants. *Journal of Biomedical Materials Research*, *38*(2), 105–114.
57. Yang, Z., Best, S. M., & Cameron, R. E. (2009). The influence of α-tricalcium phosphate nanoparticles and microparticles on the degradation of poly(D, L-lactide-co-glycolide). *Advanced Materials*, *21*(38–39), 3900–3904.
58. Furukawa, T., Matsusue, Y., Yasunaga, T., Shikinami, Y., Okuno, M., & Nakamura, T. (2000). Biodegradation behavior of ultra-high-strength hydroxyapatite/poly(L-lactide) composite rods for internal fixation of bone fractures. *Biomaterials*, *21*(9), 889–898.
59. Kobayashi, S., & Yamaji, S. (2014). Analytical prediction of hydrolysis behavior of tricalcium phosphate/poly-L-lactic acid composites in simulated body environment. *Advanced Composite Materials*, *23*(3), 211–223.

60. Barber, Z. (2005). Chapter 1: General aspects of materials modelling. *Introduction to materials modelling*. Maney Publishing London.
61. Imai, Y., Nagai, M., & Watanabe, M. (1999b). Degradation of composite materials composed of tricalcium phosphate and a new type of block polyester containing a poly(L-lactic acid) segment. *Journal of Biomaterials Science, Polymer Edition*, *10*(4), 421–432.
62. Shikinami, Y., & Okuno, M. (1999). Bioresorbable devices made of forged composites of hydroxyapatite (HA) particles and poly-L-lactide (PLLA): Part I. Basic characteristics. *Biomaterials*, *20*(9), 859–877.
63. Soares, J. S., Moore, J. E, Jr., & Rajagopal, K. R. (2008). Constitutive framework for biodegradable polymers with applications to biodegradable stents. *Asaio Journal*, *54*(3), 295–301.
64. da Silva Soares, J. F. (2008). *Constitutive modeling for biodegradable polymers for application in endovascular stents*. Texas A&M University.
65. Bergström, J. S., & Hayman, D. (2015). An overview of mechanical properties and material modeling of polylactide (PLA) for medical applications. *Annals of Biomedical Engineering*, *44*, 330–340.
66. Göpferich, A. (1996). Mechanisms of polymer degradation and erosion. *Biomaterials*, *17*(2), 103–114.
67. Lao, L. L., Peppas, N. A., Boey, F. Y. C., & Venkatraman, S. S. (2011). Modeling of drug release from bulk-degrading polymers. *International Journal of Pharmaceutics*, *418*(1), 28–41.
68. Milan, J.-L., Planell, J. A., & Lacroix, D. (2010). Simulation of bone tissue formation within a porous scaffold under dynamic compression. *Biomechanics and Modeling in Mechanobiology*, *9*(5), 583–596.
69. Pitt, C. G., & Zhong-Wei, G. (1987). Modification of the rates of chain cleavage of poly(ε-caprolactone) and related polyesters in the solid state. *Journal of Controlled Release*, *4*(4), 283–292.
70. Lyu, S., Schley, J., Loy, B., Lind, D., Hobot, C., Sparer, R., et al. (2007). Kinetics and time-temperature equivalence of polymer degradation. *Biomacromolecules*, *8*(7), 2301–2310.
71. Batycky, R. P., Hanes, J., Langer, R., & Edwards, D. A. (1997). A theoretical model of erosion and macromolecular drug release from biodegrading microspheres. *Journal of Pharmaceutical Sciences*, *86*(12), 1464–1477.
72. Antheunis, H., van der Meer, J.-C., de Geus, M., Kingma, W., & Koning, C. E. (2009). Improved mathematical model for the hydrolytic degradation of aliphatic polyesters. *Macromolecules*, *42*(7), 2462–2471.
73. Antheunis, H., van der Meer, J.-C., de Geus, M., Heise, A., & Koning, C. E. (2010). Autocatalytic equation describing the change in molecular weight during hydrolytic degradation of aliphatic polyesters. *Biomacromolecules*, *11*(4), 1118–1124.
74. Rothstein, S. N., Federspiel, W. J., & Little, S. R. (2009). A unified mathematical model for the prediction of controlled release from surface and bulk eroding polymer matrices. *Biomaterials*, *30*(8), 1657–1664.
75. Perale, G., Arosio, P., Moscatelli, D., Barri, V., Müller, M., MacCagnan, S., et al. (2009). A new model of resorbable device degradation and drug release: Transient 1-dimension diffusional model. *Journal of Controlled Release*, *136*(3), 196–205.
76. Casalini, T., Rossi, F., Lazzari, S., Perale, G., & Masi, M. (2014). Mathematical modeling of PLGA microparticles: From polymer degradation to drug release. *Molecular Pharmaceutics*, *11*(11), 4036–4048.
77. Busatto, C., Berkenwald, E., Mariano, N., Casis, N., Luna, J., & Estenoz, D. (2016). Homogeneous hydrolytic degradation of poly(lactic-co-glycolic acid) microspheres: Mathematical modeling. *Polymer Degradation and Stability*, *125*, 12–20.
78. Busatto, C., Pesoa, J., Helbling, I., Luna, J., & Estenoz, D. (2017). Heterogeneous hydrolytic degradation of poly(lactic-co-glycolic acid) microspheres: Mathematical modeling. *Journal of Applied Polymer Science*, *134*(43).
79. Göpferich, A. (1997). Polymer bulk erosion. *Macromolecules*, *30*(9), 2598–2604.

80. Siepmann, J., Faisant, N., & Benoit, J.-P. (2002). A new mathematical model quantifying drug release from bioerodible microparticles using Monte Carlo simulations. *Pharmaceutical Research*, *19*(12), 1885–1893.
81. Chen, Y., Zhou, S., & Li, Q. (2011). Mathematical modeling of degradation for bulk-erosive polymers: Applications in tissue engineering scaffolds and drug delivery systems. *Acta Biomaterialia*, *7*(3), 1140–1149.
82. Hofmann, D., Entrialgo-Castaño, M., Kratz, K., & Lendlein, A. (2009). Knowledge-based approach towards hydrolytic degradation of polymer-based biomaterials. *Advanced Materials*, *21*(32–33), 3237–3245.
83. Entrialgo-Castaño, M., Salvucci, A. E., Lendlein, A., & Hofmann, D. (2008). An atomistic modeling and quantum mechanical approach to the hydrolytic degradation of aliphatic polyesters. *Macromolecular Symposia*, *269*(1), 47–64.
84. Wang, Y., Pan, J., Han, X., Sinka, C., & Ding, L. (2008). A phenomenological model for the degradation of biodegradable polymers. *Biomaterials*, *29*(23), 3393–3401.
85. Wang, Y. (2009). *Modelling degradation of bioresorbable polymeric devices*. Ph.D. thesis, Department of Engineering, University of Leicester.
86. Han, X., & Pan, J. (2009). A model for simultaneous crystallisation and biodegradation of biodegradable polymers. *Biomaterials*, *30*(3), 423–430.
87. Han, X. (2011). *Degradation models for polyesters and their composites*. Ph.D. thesis, Univeristy of Leicester.
88. Han, X., Pan, J., Buchanan, F., Weir, N., & Farrar, D. (2010). Analysis of degradation data of poly(L-lactide-co-L, D-lactide) and poly(L-lactide) obtained at elevated and physiological temperatures using mathematical models. *Acta Biomaterialia*, *6*(10), 3882–3889.
89. Wang, Y., Han, X., Pan, J., & Sinka, C. (2010a). An entropy spring model for the Youngs modulus change of biodegradable polymers during biodegradation. *Journal of the Mechanical Behavior of Biomedical Materials*, *3*(1), 14–21.
90. Han, X., & Pan, J. (2011). Polymer chain scission, oligomer production and diffusion: A two-scale model for degradation of bioresorbable polyesters. *Acta Biomaterialia*, *7*(2), 538–547.
91. Gleadall, A., Pan, J., & Atkinson, H. (2012). A simplified theory of crystallisation induced by polymer chain scissions for biodegradable polyesters. *Polymer Degradation and Stability*, *97*(9), 1616–1620.
92. Gleadall, A. C. (2015). *Modelling degradation of biodegradable polymers and their mechanical properties*. Ph.D. thesis, Department of Engineering, University of Leicester.
93. Han, X., & Pan, J. (2013). Finite element analysis of degradation of biodegradable medical devices. *OA Biotechnology*, *2*(3), 22.
94. Gleadall, A., & Pan, J. (2013). Computer simulation of polymer chain scission in biodegradable polymers. *Journal of Biotechnology and Biomaterials*.
95. Gleadall, A., Pan, J., Kruft, M.-A., & Kellomäki, M. (2014). Degradation mechanisms of bioresorbable polyesters. Part 2. Effects of initial molecular weight and residual monomer. *Acta Biomaterialia*, *10*(5), 2233–2240.
96. Gleadall, A., Pan, J., Ding, L., Kruft, M.-A., & Curcó, D. (2015a). An atomic finite element model for biodegradable polymers. Part 1. Formulation of the finite elements. *Journal of the Mechanical Behavior of Biomedical Materials*, *51*, 409–420.
97. Gleadall, A., Pan, J., & Kruft, M.-A. (2015b). An atomic finite element model for biodegradable polymers. Part 2. A model for change in youngs modulus due to polymer chain scission. *Journal of the Mechanical Behavior of Biomedical Materials*, *51*, 237–247.
98. Shine, R., Shirazi, R. N., Ronan, W., Sweeney, C. A., Kelly, N., Rochev, Y. A., et al. (2017). Modeling of biodegradable polyesters with applications to coronary stents. *Journal of Medical Devices*, *11*(2), 021007.
99. Sevim, K., & Pan, J. (2018). A model for hydrolytic degradation and erosion of biodegradable polymers. *Acta Biomaterialia*, *66*, 192–199.
100. Ebrahimian-Hosseinabadi, M., Ashrafizadeh, F., Etemadifar, M., & Venkatraman, S. S. (2011). Evaluating and modeling the mechanical properties of the prepared PLGA/nano-BCP composite scaffolds for bone tissue engineering. *Journal of Materials Science and Technology*, *27*(12), 1105–1112.

101. Doyle, H., Lohfeld, S., & McHugh, P. (2014). Predicting the elastic properties of selective laser sintered PCL/β-TCP bone scaffold materials using computational modelling. *Annals of Biomedical Engineering*, *42*(3), 661–677.
102. Pan, J., Han, X., Niu, W., & Cameron, R. E. (2011). A model for biodegradation of composite materials made of polyesters and tricalcium phosphates. *Biomaterials*, *32*(9), 2248–2255.
103. Van der Meer, S., De Wijn, J., & Wolke, J. (1996). The influence of basic filler materials on the degradation of amorphous D-and L-lactide copolymer. *Journal of Materials Science: Materials in Medicine*, *7*(6), 359–361.
104. Ara, M., Watanabe, M., & Imai, Y. (2002). Effect of blending calcium compounds on hydrolytic degradation of poly(DL-lactic acid-co-glycolic acid). *Biomaterials*, *23*(12), 2479–2483.

Chapter 3
Degradation of Bioresorbable Composites: The Models

This chapter discusses the development of computational degradation models for different bioresorbable composite materials. The models were developed in a two-stage process. Firstly, a general modelling framework was generated and analysed and secondly, this general framework was particularised for specific ceramic fillers yielding the degradation models.

The first section, Sect. 3.1, presents the general modelling framework, which acted as a universal model, and arose from a generalisation of the degradation model for composites made of biodegradable polyesters and tricalcium phosphates proposed by Pan et al. [1, 2]. The analysis of this framework is also included in this section. This analysis highlighted all the components which affect the composite degradation and how those components are interconnected. This generic framework can be tailored to mimic the degradation of various composites with different biodegradable polymeric matrixes and calcium-based materials fillers and thus using this general framework as a template, degradation models for specific composites may be generated.

After the presentation and discussion of the general framework and its main features in the first section, the second section, Sect. 3.2, discusses three specific models for three given composites. These models were derived through the particularisation of the general modelling framework. The first specific model deals with composites made of tricalcium phosphate (TCP) [1] whereas the second and third models deal with hydroxyapatite (HA) and calcium carbonate (CC) composites respectively. For each one of the three models, two different sets of equations are included. The first set of equations, composed of dimensional equations, is the customisation of the general modelling case to the composite of interest. The second set of equations, composed of non-dimensional equations, is an nondimensionalisation of the first set in order to facilitate the computational resolution using numerical techniques. The numerical methods used are indicated and briefly discussed. For conciseness, a thorough description only of the first model, the TCP model, is included.

I. Moreno-Gomez, *A Phenomenological Mathematical Modelling Framework for the Degradation of Bioresorbable Composites*,
Springer Theses, https://doi.org/10.1007/978-3-030-04990-4_3

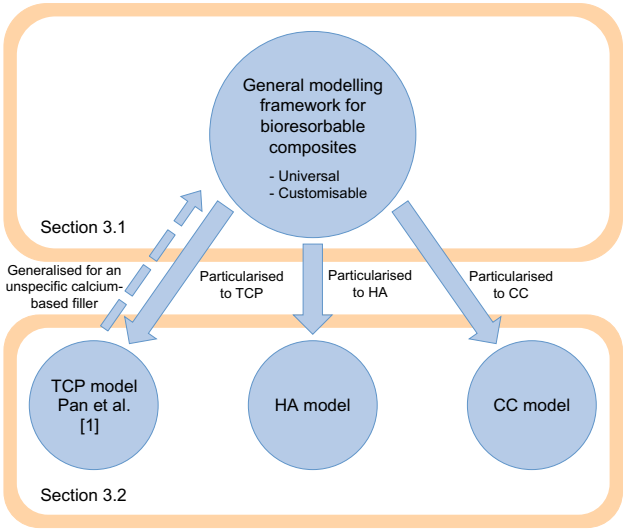

Fig. 3.1 Schematic representation of the relationships between the general modelling framework and the three models for specific ceramic fillers: the tricalcium phosphate (TCP) model, the hydroxyapatite (HA) model and the calcium carbonate (CC) model

Figure 3.1 reflects the relationships between the general modelling framework and the specific models discussed in this chapter. Chronologically Pan et al. developed the first model [1], a model for composites made of biodegradable polyester and tricalcium phosphate. This thesis describes the subsequent development of the general framework through abstraction from this TCP model. Once this framework was established, two new specific models were then produced for two cases of interest: hydroxyapatite and calcium carbonate.

In order to attain a global and complete picture of the approach employed in the composite degradation modelling, Sect. 3.3 discusses the construction and characterisation of the representative unit cell used as a representation of the whole composite sample in the modelling framework and subsequently, in the three ceramic-specific degradation models.

In the same manner, in order to provide an overview of the constituent elements of the degradation models, Sect. 3.4 includes a compilation of all these constituent elements classified according to two criteria: dependence and type. In terms of dependence, the constituent elements can be composite, polymer or ceramic dependent. In terms of type, the constituent elements can be variables, constants or derived constants.

The fifth and last section of the chapter, Sect. 3.5, includes a description of the method of use for the specific composite degradation models presented in Sect. 3.2. In order to run the computational simulations and further the insight into composite

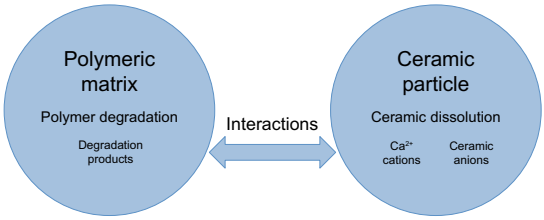

Fig. 3.2 Schematic representation of the relationships between the two main elements and its processes involved in composite degradation

degradation, experimental composite degradation data were harvested from the available literature. The literature search and data extraction methods are presented and discussed here and lastly, the data analysis process employed with the harvested literature data in this work is described.

3.1 Degradation Modelling Framework for Biodegradable Composites

The modelling framework discussed in this chapter aims to characterise the degradation behaviour of composites made of biodegradable polymer matrices and calcium-based ceramic fillers. The framework provides a mathematical description of the different interwoven phenomena that govern the time-dependent composite degradation behaviour based on the model proposed by Pan et al. for TCP-polyester composites [1, 2].

A first step towards the construction of the modelling framework was the identification of both the principal elements in the system to be modelled and the interactions between those elements. In the studied system, biodegradable composites, there are two main elements. Figure 3.2 contains a schematic representation of these elements and their interactions.

The first element, the polymeric matrix, experiences degradation by polymer backbone scission. The second element, the calcium-based ceramic filler, experiences dissolution resulting in the release of its constituent ions, including Ca^{2+}. Some of the released ions may react with the by-products of the polymer degradation giving rise to a complex interwoven evolution of both polymer degradation and ceramic dissolution.

In order to provide a realistic characterisation of the degradation process, accurate ways of modelling both elements, and their time-dependent processes, in addition to the interactions between both were needed. The framework modelled the whole physical composite sample using a representative unit cell. This unit cell consists of a representative calcium-based ceramic particle surrounded by polymer phase. Figure 3.3 shows an example of a representative unit cell for a composite made of spherical ceramic particles. The unit cell volume, V_{unit} (m^3), results from the addition of the polymer and initial ceramic volumes, V_{pol} (m^3) and V_{cer0} (m^3) respectively. All these

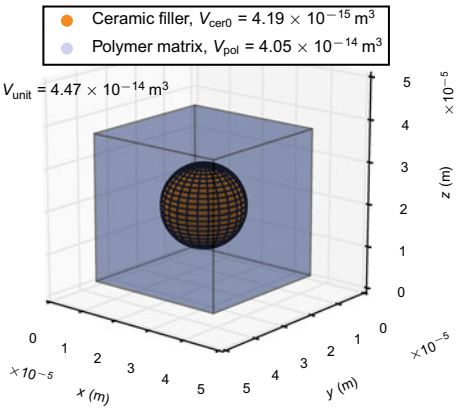

Fig. 3.3 Example of a representative unit cell used in the modelling framework to characterise the whole composite. V_{pol} and V_{cer0} are the polymer and initial ceramic volumes respectively, and both add to V_{unit}, the volume of the unit cell. The unit cell depicted in this figure corresponds to a poly(L-lactide)–20%wtβ-tricalcium phosphate composite. The ceramic particles have spherical shape and an average particle size (diameter) of 20 μm

volumes are calculated using different parameters of the constituent matrix and filler materials. A detailed description of the unit cell with the necessary mathematical characterisation is discussed later in Sect. 3.3.

In these biodegradable composites, the matrix is usually made of a biodegradable polyester, a specific type of biodegradable polymer. Polyesters are polymers with linear long chains which include a R-COOH group in their repeating unit. Figure 3.4a depicts a poly(L-lactic acid) (PLLA) molecule, whose repeating unit has the molecular formula $C_3H_4O_2$, as an illustrative example of biodegradable polyesters. Green dots are used to signal the ester bond in each repeating unit. PLLA is a commonly used polymer in bioresorbable composites which belongs to the poly-α-hydroxy-acids family. In the presence of water, polyester chains degrade by ester bond hydrolysis. Figure 3.4b shows the structure of the initial PLLA molecule (Fig. 3.4a) after the scission of its second ester bond resulting in two shorter PLLA chains. The incorporated water molecule is highlighted in orange. The scission rate of the ester bonds can be used as a polymer degradation characterising parameter.

Polyester molecules can also experience dissociation of the hydrogen ion in the carboxylic end group as shown in Fig. 3.4c. The hydrogen ions released from the ester bonds are highlighted in magenta. The acidic environment created by the released hydrogen ions affects the polymer degradation rate, causing an increase in its magnitude, i.e. the by-products of the polymer degradation speed up further degradation. The acid dissociation of the carboxylic end groups can be represented by an equilibrium expression at physiological temperature as:

$$\text{R-COOH} \underset{K_a}{\overset{37^\circ\text{C}}{\rightleftharpoons}} \text{R-COO}^- + \text{H}^+ \tag{3.1}$$

where K_a is the acid dissociation constant for the chosen polymer at 37 °C (mol m^3).[1]

[1] In this work, acid dissociation constants are always expressed in terms of concentrations instead of in terms of activity and therefore K_a has concentration units [4], usually reported as mol/L which can be easily converted to mol m^{-3}.

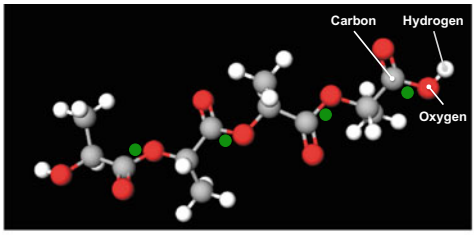

(a) 3D representation of a poly(L-lactic acid) molecule with ester bonds marked with green dots. C atoms depicted in grey, O atoms in red and H atoms in white.

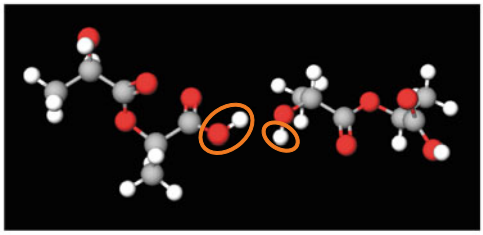

(b) 3D representation of poly(L-lactic acid) molecules resulting from the cleavage of a longer chain. The atoms of the H_2O molecule consumed in the bond hydrolysis are highlighted in orange.

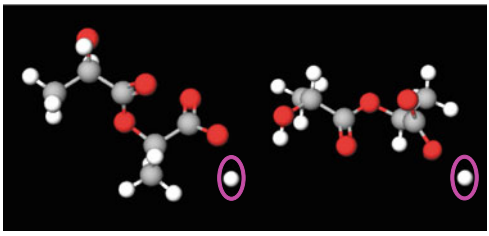

(c) 3D representation of poly(L-lactic acid) molecules after acid dissociation of the ester bond hydrogens. The released hydrogen atoms are highlighted in magenta.

Fig. 3.4 Illustration of a polyester molecule undergoing degradation by ester bond hydrolysis. 3D representation of the molecules created with MolView [3]

The effect of the released hydrogen ions due to the acid dissociation of the carboxylic end groups points to the necessity of including two different contributions in the mathematical characterisation of the polymer backbone scission rate. The first component needs to reflect the non-catalytic degradation and should depend only on the number of ester bonds present in the polymer phase at a given time. The second component needs to reflect the autocatalytic degradation and should also depend on the quantity of hydrogen ions at a given time.

Considering these two contributions, the polymer degradation can take the following expression, previously used by Wang et al. [5, 6] and Pan et al. [1, 2]:

$$\frac{\mathrm{d}R_s}{\mathrm{d}t} = k_1 C_\mathrm{e} + k_2' C_\mathrm{e} C_{\mathrm{H}^+} \qquad (\mathrm{mol\,m^{-3}\,s^{-1}}) \tag{3.2}$$

where R_s is the concentration of chain scissions ($\mathrm{mol\,m^{-3}}$); k_1, the non-catalytic degradation rate constant ($\mathrm{s^{-1}}$); k_2', the autocatalytic degradation rate constant ($\mathrm{m^3\,mol^{-1}\,s^{-1}}$); C_e, the concentration of ester bonds ($\mathrm{mol\,m^{-3}}$) and C_{H^+}, the concentration of hydrogen ions ($\mathrm{mol\,m^{-3}}$), with all the concentrations defined per unit of polymer phase volume, rather than per unit of composite volume. This mathematical expression of the polymer degradation does not include the concentration of water molecules, C_{H_2O} ($\mathrm{mol\,m^{-3}}$), as polymer degradation is assumed to be independent of the water content with an excess of water in the polymer phase.

The dissociation of the carboxylic end groups, which results in an increase of hydrogen ions, can be represented as:

$$K_a = \frac{[H^+][R-COO^-]}{[R-COOH]} \qquad (\mathrm{mol\,m^{-3}}) \tag{3.3}$$

where K_a is the polymer dissociation constant at a given temperature ($\mathrm{mol\,m^{-3}}$); [*R-COO*$^-$], the concentration of dissociated chains ($\mathrm{mol\,m^{-3}}$) and [*R-COOH*], the concentration of non-dissociated chains ($\mathrm{mol\,m^{-3}}$) with all the concentrations defined per unit of polymer phase volume.

The quantity of chains per unit of volume at a given point in time can be characterised as:

$$C_{chain} = C_{chain0} + R_s = [R\text{-}COOH] + [R\text{-}COO^-] \qquad (\mathrm{mol\,m^{-3}}) \tag{3.4}$$

where C_{chain} is the concentration of polymer chains at a given time ($\mathrm{mol\,m^{-3}}$); C_{chain0}, the polymer chains concentration at the time origin ($\mathrm{mol\,m^{-3}}$) and R_s, the concentration of chain scissions at a given time ($\mathrm{mol\,m^{-3}}$) with the concentrations also defined per unit of polymer phase volume.

Lastly, the number-average molecular weight of the polymer phase, M_n (Da), can be expressed as the ratio between the concentration of total molar mass in the polymer phase and the concentration of polymer chains at a given time:

$$M_n = \frac{C_{e0} M_{unit}}{C_{chain0} + R_s} \qquad (\mathrm{Da}) \tag{3.5}$$

with C_{e0}, the initial concentration of ester bonds ($\mathrm{mol\,m^{-3}}$); M_{unit}, the molar mass associated to one ester bond (Da); C_{chain0}, the concentration of polymer chains at the time origin ($\mathrm{mol\,m^{-3}}$) and R_s, the concentration of chain scissions at a given time ($\mathrm{mol\,m^{-3}}$), with the concentration defined per unit volume of polymer.

As noted by Pan, experimentally measured M_n values tend to exclude the short chains as they are too small to be detected using techniques such as gel permeation chromatography (GPC) [2]. Considering this, the number-average molecular weight of the polymer phase, M_n (Da), can be characterised, when short chains are excluded, as the ratio between the concentration of total molar mass in the polymer phase associated to long chains and the concentration of long polymer chains at a given time:

$$M_{\mathrm{n}} = \frac{(C_{\mathrm{e0}} - R_{ol})M_{\mathrm{unit}}}{C_{\mathrm{chain0}} + R_s - \frac{R_{ol}}{m}} \quad \text{(Da)} \tag{3.6}$$

with C_{e0}, the initial concentration of ester bonds in long chains ($\mathrm{mol\,m^{-3}}$); R_{ol}, the concentration of ester bonds in short chains at a given time ($\mathrm{mol\,m^{-3}}$); M_{unit}, the molar mass associated to one ester bond (Da); C_{chain0}, the concentration of long polymer chains at the time origin ($\mathrm{mol\,m^{-3}}$); R_s, the concentration of chain scissions at a given time ($\mathrm{mol\,m^{-3}}$) and m, the average degree of pseudo-polymerisation of the short chains (1) with all the concentration per unit of volume of the polymer phase. The relationship between the concentration of chain scissions, R_s, and the concentration of ester bonds in short chains, R_{ol}, is determined by the polymer scission type such as random, end or a mixture of both.

Equations 3.2–3.4 and 3.6 fully describe the general behaviour of the biodegradable polymers commonly used in composites and were employed in the modelling framework to mathematically describe the polymeric matrix during composite degradation. Equation 3.2 characterises the polymer degradation behaviour taking into account both its non-catalytic and autocatalytic components. A specific polymer is completely characterised with only two parameters: the appropriate values of non-catalytic and autocatalytic degradation rate constants, k_1 ($\mathrm{s^{-1}}$) and k_2' ($\mathrm{m^3\,mol^{-1}\,s^{-1}}$).

The calcium-based ceramic fillers used in these composites are, usually, sparingly soluble ceramics. This type of ceramic is characterised by a sustained, albeit slow, dissolution in an aqueous media. In this framework, the ceramic dissolution is modelled by means of the degree of undersaturation, σ (1),[2] with the following expression, previously used by Wang and Nancollas [7, 8] and Tang et al. [9, 10]:

$$\sigma = 1 - \left(\frac{I_{\mathrm{P}}}{K_{\mathrm{sp}}}\right)^{\frac{1}{\eta}} = 1 - \left(\frac{\prod_{i=1}^{n} C_i^{m_i}}{K_{\mathrm{sp}}}\right)^{\frac{1}{\eta}} \quad (1) \tag{3.7}$$

where I_{P} is the ionic activity product ($\mathrm{mol^{\eta}\,m^{-3\eta}}$); K_{sp}, the solubility product of the calcium-based ceramic filler ($\mathrm{mol^{\eta}\,m^{-3\eta}}$)[3] and η, the sum of multiplicities of the n different ions in the ceramic chemical composition: $\eta = \sum_{i=1}^{n} m_i$ ($\mathrm{mol\,mol^{-1}}$). The ionic product activity is calculated as $\prod_{i=1}^{n} C_i^{m_i}$ with C_i, the concentration of dissolved ion i ($\mathrm{mol\,m^{-3}}$) and m_i, the multiplicity of the ith ion in the ceramic chemical composition ($\mathrm{mol\ mol^{-1}}$).

The undersaturation represents the deviation of the actual quantity of dissolution products from the equilibrium quantity of dissolved ions at a given time and is a

[2] In this work, dimensionless units are expressed with the symbol "1" and usually displayed between parentheses: (1).

[3] The definition and mathematical expression of the solubility product K_{sp} is given in Appendix A.2.

measure of the driving force for continuous dissolution. The ceramic dissolution rate J, defined as the number of molecules dissolved from the particle per unit area of the ceramic surface per unit time, can be represented by a power law approximation of the undersaturation:

$$J = A_{\mathrm{d}}\sigma^{\theta} = A_{\mathrm{d}}\left(1 - \left(\frac{I_{\mathrm{P}}}{K_{\mathrm{sp}}}\right)^{\frac{1}{\eta}}\right)^{\theta} \qquad (\mathrm{mol\,m^{-2}\,s^{-1}}) \tag{3.8}$$

where J is the dissolution rate ($\mathrm{mol\,m^{-2}\,s^{-1}}$); σ, the aforementioned undersaturation (1); A_d ($\mathrm{mol\,m^{-2}\,s^{-1}}$) and θ (1) the rate and coefficient of the power law respectively. This power law approximation can represent a variety of dissolution mechanisms commonly observed in these materials [2, 11].

The variation in concentration of dissolved ceramic molecules in the polymer phase, C_{cer} ($\mathrm{mol\,m^{-3}}$), with respect to time can be derived from the ceramic filler dissolution rate, J ($\mathrm{mol\,m^{-2}\,s^{-1}}$), using S_{cer} ($\mathrm{m^3}$) and V_{pol} ($\mathrm{m^3}$), the ceramic particle surface area and the polymer phase volume in the representative unit cell respectively:

$$\frac{\mathrm{d}C_{\mathrm{cer}}}{\mathrm{d}t} = \frac{1}{V_{\mathrm{pol}}}S_{\mathrm{cer}}J \qquad (\mathrm{mol\,m^{-3}\,s^{-1}}) \tag{3.9}$$

A more convenient notation can be achieved using the total area of interface per unit of volume in the composite a_{cer} ($\mathrm{m^2\,m^{-3}}$), $a_{\mathrm{cer}} = {}^{S_{\mathrm{cer}}}/_{V_{\mathrm{unit}}}$, and the ratio between the polymer phase and unit cell volumes expressed as function of the initial ceramic volume fraction, f_{cer0} ($\mathrm{m^3\,m^{-3}}$): ${}^{V_{\mathrm{pol}}}/_{V_{\mathrm{unit}}} = {}^{(V_{\mathrm{unit}} - V_{\mathrm{cer0}})}/_{V_{\mathrm{unit}}} = 1 - {}^{V_{\mathrm{cer0}}}/_{V_{\mathrm{unit}}} = 1 - f_{\mathrm{cer0}}$.

$$\frac{\mathrm{d}C_{\mathrm{cer}}}{\mathrm{d}t} = \frac{1}{V_{\mathrm{pol}}}S_{\mathrm{cer}}J = \frac{V_{\mathrm{unit}}}{V_{\mathrm{pol}}}a_{\mathrm{cer}}J = \frac{a_{\mathrm{cer}}}{1 - f_{\mathrm{cer0}}}A_{\mathrm{d}}\sigma^{\theta} \qquad (\mathrm{mol\,m^{-3}\,s^{-1}}) \tag{3.10}$$

where σ is the aforementioned undersaturation (1); A_{d} ($\mathrm{mol\,m^{-2}\,s^{-1}}$) and θ (1) the rate and coefficient of the power dissolution law respectively.

The variation in calcium ions concentration in the polymer phase, $[Ca^{2+}]$ ($\mathrm{mol\,m^{-3}}$), with respect to time is directly proportional to the variation in concentration of dissolved ceramic molecules; with $I_{\mathrm{cer}}^{\mathrm{Ca}}$ ($\mathrm{mol\,mol^{-1}}$), the number of calcium ions per molecule of the calcium-based ceramic filler, as the proportionality constant:

$$\frac{\mathrm{d}[Ca^{2+}]}{\mathrm{d}t} = I_{\mathrm{cer}}^{\mathrm{Ca}}\frac{\mathrm{d}C_{\mathrm{cer}}}{\mathrm{d}t} = I_{\mathrm{cer}}^{\mathrm{Ca}}\frac{a_{\mathrm{cer}}}{1 - f_{\mathrm{cer0}}}A_{\mathrm{d}}\sigma^{\theta} \qquad (\mathrm{mol\,m^{-3}\,s^{-1}}) \tag{3.11}$$

with a_{cer} the total area of interface per unit of volume in the composite ($\mathrm{m^2\,m^{-3}}$); f_{cer0}, the initial ceramic volume fraction ($\mathrm{m^3\,m^{-3}}$); σ, the aforementioned undersaturation (1); A_d ($\mathrm{mol\,m^{-2}\,s^{-1}}$) and θ (1) the rate and coefficient of the power dissolution law respectively.

The reduction rate of the ceramic volume in the unit cell can be expressed as a function of the released ceramic molecules and the volume of those ceramic molecules:

$$\frac{\mathrm{d}V_{\mathrm{cer}}}{\mathrm{d}t} = -S_{\mathrm{cer}} J\, \Omega_{\mathrm{cer}} = -\frac{\Omega_{\mathrm{cer}}}{I_{\mathrm{cer}}^{\mathrm{Ca}}} V_{\mathrm{pol}} \frac{\mathrm{d}[Ca^{2+}]}{\mathrm{d}t} \qquad (\mathrm{m^3\,s^{-1}}) \tag{3.12}$$

where S_{cer} is the surface area of the representative ceramic particle ($\mathrm{m^2}$); J, the ceramic dissolution rate ($\mathrm{mol\,m^{-2}\,s^{-1}}$); Ω_{cer}, the ceramic molar volume ($\mathrm{m^3\,mol^{-1}}$); $I_{\mathrm{cer}}^{\mathrm{Ca}}$, the number of calcium ions per molecule of the calcium-based ceramic filler ($\mathrm{mol\,mol^{-1}}$); V_{pol}, the volume of the polymer phase in the representative unit and $\frac{\mathrm{d}[Ca^{2+}]}{\mathrm{d}t}$ the variation of concentration of calcium ions with respect to time ($\mathrm{mol\,m^{-3}\,s^{-1}}$).

As the ceramic dissolution is a surface mediated phenomenon, it is of interest to characterise the evolution of the total area of interface between the ceramic and the polymer per unit of composite volume with respect to time. This rate can be easily calculated using the definition of a_{cer} ($a_{\mathrm{cer}} = {}^{S_{\mathrm{cer}}}/_{V_{\mathrm{unit}}}$) ($\mathrm{m^2\,m^{-3}}$), the calculus chain rule, Eq. 3.12 and expressing ${}^{V_{\mathrm{pol}}}/_{V_{\mathrm{unit}}}$ as $1 - f_{\mathrm{cer0}}$:

$$\begin{aligned}
\frac{\mathrm{d}a_{\mathrm{cer}}}{\mathrm{d}t} &= \frac{\mathrm{d}S_{\mathrm{cer}}}{\mathrm{d}t}\frac{1}{V_{\mathrm{unit}}} = \frac{\mathrm{d}S_{\mathrm{cer}}}{\mathrm{d}V_{\mathrm{cer}}}\frac{\mathrm{d}V_{\mathrm{cer}}}{\mathrm{d}t}\frac{1}{V_{\mathrm{unit}}} \\
&= -\frac{\mathrm{d}S_{\mathrm{cer}}}{\mathrm{d}V_{\mathrm{cer}}}\frac{\Omega_{\mathrm{cer}}}{I_{\mathrm{cer}}^{\mathrm{Ca}}}\frac{V_{\mathrm{pol}}}{V_{\mathrm{unit}}}\frac{\mathrm{d}[Ca^{2+}]}{\mathrm{d}t} \\
&= -k_{\mathrm{geom}}\frac{\Omega_{\mathrm{cer}}}{I_{\mathrm{cer}}^{\mathrm{Ca}}}(1 - f_{\mathrm{cer0}})\frac{\mathrm{d}[Ca^{2+}]}{\mathrm{d}t} \qquad (\mathrm{mol\,m^{-3}\,s^{-1}})
\end{aligned} \tag{3.13}$$

where k_{geom} is a geometry dependent constant ($\mathrm{m^{-1}}$); Ω_{cer}, the ceramic molar volume ($\mathrm{m^3\,mol^{-1}}$); $I_{\mathrm{cer}}^{\mathrm{Ca}}$, the number of calcium ions per molecule of the calcium-based ceramic filler ($\mathrm{mol\,mol^{-1}}$); f_{cer0}, the initial ceramic volume fraction ($\mathrm{m^3\,m^{-3}}$) and $\frac{\mathrm{d}[Ca^{2+}]}{\mathrm{d}t}$, the variation of concentration of calcium ions with respect to time ($\mathrm{mol\,m^{-3}\,s^{-1}}$).

The reduction of a_{cer} with respect to time depends on the geometry of the particle through the constant k_{geom}, which captures how the particle surface area varies with its volume: $k_{\mathrm{geom}} = \frac{\mathrm{d}S_{\mathrm{cer}}}{\mathrm{d}V_{\mathrm{cer}}}$ ($\mathrm{m^{-1}}$).

Equations 3.11 and 3.13 characterise completely the ceramic behaviour and for a given ceramic just two parameters are needed to attain this characterisation: A_{d} ($\mathrm{mol\,m^{-2}\,s^{-1}}$) and θ (1), respectively the rate and exponent of the power dissolution law.

After characterising the polymer degradation and ceramic dissolution, the framework needed to model the different interactions between both elements. In the next paragraphs these interactions are explored and mathematically characterised.

As previously mentioned, the dissolution process of the calcium-based ceramic results in the release of negatively charged ions, as well as Ca^{2+} ions. These anions will vary depending on the specific ceramic employed in the composite. As an illustrative example, the use of tricalcium phosphate (Ca_3PO_4) causes the release of

both phosphate (PO_4^{3-}) and calcium (Ca^{2+}) ions whereas the use of calcium carbonate ($CaCO_3$) causes the release of both carbonate (CO_3^{2-}) and calcium (Ca^{2+}) ions instead.

The released anions are available to react with the hydrogen ions, a by-product of the polymeric matrix degradation, to produce different compounds following the inverse acid deprotonation route. In a general case, the ceramic releases from one to several types of negatively charged ions, B^{n-}. These B^{n-} ions undergo recombination with hydrogen ions as follows:

$$B^{n-} + H^+ \underset{K_n}{\overset{37^\circ C}{\rightleftharpoons}} HB^{(n-1)-} \tag{3.14a}$$

$$\cdots \tag{3.14b}$$

$$H_{n-1}B^- + H^+ \underset{K_1}{\overset{37^\circ C}{\rightleftharpoons}} H_nB \tag{3.14c}$$

with $K_1, \ldots, K_n$ being the first, ..., nth deprotonation constants of the polyprotic acid composed of B ions.

The recombination of hydrogen ions with B^{n-} ions causes a decrease of local environmental acidity, provoking a reduction of the autocatalytic component of the polymer degradation. This buffering effect was incorporated into the mathematical framework using the equilibrium constants of all the involved deprotonation reactions, $K_1, \ldots, K_n$ expressed as ion concentrations ($\mathrm{mol\,m^{-3}}$). As previously mentioned, these reactions change depending on the chosen ceramic filler. The final number of reactions for a given ion will be equal to the negative charge (n^-) of the released anion B^{n-}.

$$K_n = \frac{[H^+][B^{n-}]}{[HB^{(n-1)-}]} \qquad (\mathrm{mol\,m^{-3}}) \tag{3.15a}$$

$$\cdots \tag{3.15b}$$

$$K_1 = \frac{[H^+][H_{n-1}B^-]}{[H_nB]} \qquad (\mathrm{mol\,m^{-3}}) \tag{3.15c}$$

When the calcium-based ceramic contains more than one anion, the individual buffering effect of each anion needs to be incorporated using the method described in the set of Eqs. 3.15, resulting in as many set of equations as different released ceramic anions.

In order to complete the framework, the mass conservation equations needed to be included. Assuming stoichiometric ceramic dissolution, the ratio between the amount, in concentration units, of anions (either in its uncombined state, $[B^{n-}]$ ($\mathrm{mol\,m^{-3}}$), or recombined as any of the elements present in the polyprotic acid deprotonation route, $[HB^{(n-1)-}]$ ($\mathrm{mol\,m^{-3}}$), ..., $[H_nB]$ ($\mathrm{mol\,m^{-3}}$)) and the amount of Ca^{2+} cations, also in concentration units ($\mathrm{mol\,m^{-3}}$), should be equal to the ratio of the two ions in the ceramic chemical composition. This equality can be expressed mathematically as:

$$\frac{I_{cer}^{B}}{I_{cer}^{Ca}}[Ca^{2+}] = [B^{n-}] + [HB^{(n-1)-}] + \cdots + [H_nB] \qquad (\text{mol m}^{-3}) \qquad (3.16)$$

with I_{cer}^{B}, the number of B ions per molecule of calcium-based ceramic filler (mol mol^{-1}) and I_{cer}^{Ca}, the number of calcium ions per molecule of calcium-based ceramic filler (mol mol^{-1}). Similarly to the set of Eqs. 3.15, the modelling framework needs to incorporate as many Eqs. 3.16 as different types of released ceramic anions.

The last equation of the framework was given by the conservation of hydrogen ions. Assuming negligible hydrogen ion diffusion from the outer layer of the composite, the initial hydrogen ion quantity, in concentration units, plus the amount produced by the polymer degradation, also in concentration units, should equal the total amount of hydrogen ions, either in its free state, $[H^+]$ (mol m^{-3}), or in its recombined states $[HB^{(n-1)-}]$ (mol m^{-3}), ..., $[H_nB]$ (mol m^{-3}). As each chain that releases a hydrogen ion becomes dissociated the equality can be expressed as:

$$[H^+] + [HB^{(n-1)-}] + \cdots + n[H_nB] = [R\text{-}COO^-] + \Delta C_{H_0^+} \qquad (\text{mol m}^{-3}) \qquad (3.17)$$

with $[R\text{-}COO^-]$ the concentration of dissociated chains (mol m^{-3}) and $\Delta C_{H_0^+}$ the initial hydrogen ions concentration not resulting from carboxylic end groups dissociation (mol m^{-3}). In a similar fashion to Eqs. 3.15 and 3.16, if the ceramic releases more than one anion, all of them need to be consider in the mathematical expression of the hydrogen mass conservation.

In summary, the general modelling framework encompassed a series of equations which reflect the matrix and filler behaviours and their interactions during degradation using the mechanisms outlined by Pan et al. for TCP-polyester composites [1, 2]. Figure 3.5 depicts a schematic representation of these master equations grouped according to two different criteria.

Each green block corresponds to one of the nine master equations which form the general modelling framework. The first classification is given by the blue blocks or rows. Equations enclosed in the same blue block or row characterise the same physical reality, which is explicitly mentioned above the equations.

A second classification, corresponding to the mathematical characteristics of the master equations is given by the red blocks or columns. This classification criteria is relevant when attempting to solve the system of equations (Sect. 3.2 outlines and discusses the particularities of finding a numerical solution for each specific model). The left column includes the three time-dependent differential equations: the polymer scission equation, the calcium ions concentration equation and the particle dissolution equation. The second column includes the non-time-dependent (non-differential) equations: equilibrium constants equations that model all the buffering reactions and matter conservation equations for both the calcium and hydrogen ions.

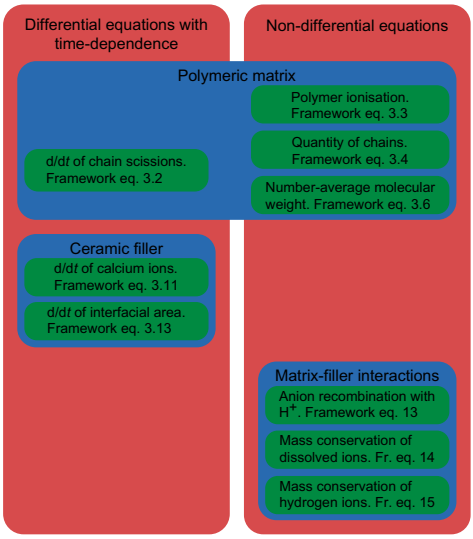

Fig. 3.5 Schematic representation of the master equations included in the general modelling framework grouped according to their physical meaning and mathematical characteristics

This general modelling framework gave rise to different specific models when particularised for different calcium-based ceramics. As previously mentioned, the specific anions released by each filler determine the particular form of the equations used to characterise the matrix-filler interactions, included in Fig. 3.5 bottom right blue box.

The particularisation of the general modelling framework for three different calcium-based ceramics, namely tricalcium phosphate, hydroxyapatite and calcium carbonate is presented and described in Sect. 3.2 but before introducing the ceramic-specific models, an analysis of the modelling framework is presented.

3.1.1 Analysis of the Modelling Framework

The analysis of the modelling framework is divided into two different parts. Firstly, the main assumptions employed, either explicitly or implicitly, in the mathematical characterisation of both polymer matrix and ceramic filler during the generation of the modelling framework are discussed. In addition, the associated limitations stemming from these assumptions, are also considered. Secondly, a list of advantages resulting from the use of the modelling framework is also presented.

The main assumptions made in the characterisation of the polymeric matrix employed in the general modelling are:

- Polymer scission with water excess: the polymer scission rate was modelled using Eq. 3.2 $\left({}^{dR_x}/_{dt} = k_1 C_e + k_2' C_e C_{H^+}\right)$. The water concentration is deemed to be high enough to ensure water is not a limiting factor in polymer scission as conveyed

by the absence of the concentration of water molecules, C_{H_2O} ($\mathrm{mol\,m^{-3}}$), in this equation.

- Given polymer scission type: the equation used to calculate the number-average molecular weight excludes short chains and considers only the long ones. The relationship between the concentration of short chains and the concentration of polymer scissions is determined by the type of polymer scission. For example, in a polymeric matrix with preferential end scission, also known as unzipping, all the scissions will produce short chains while in a polymeric matrix with random scission only a few of them will produce short chains. For practicality, in this work the polymer scission type was fixed as a mixture of random and preferential end scission, which might not be valid for all the polymeric matrixes.
- Absence of crystallinity in the polymer phase: none of the polymer related equations of the modelling framework considers the presence of crystalline phase. This assumption does not pose any shortcomings in the characterisation of amorphous polymers such as most poly(lactide-co-glycolide) and poly(D,L-lactide) matrixes or polymeric matrixes with low degree of crystallinity such as certain poly(L-lactide) copolymers. Conversely, this assumption could lead to mischaracterisations of semi-crystalline polymeric matrixes with an initial high degree of crystallisation or matrixes experiencing a significant amount of crystallisation during polymer degradation.
- Negligible diffusion of polymer degradation products: monomers, oligomers and hydrogen ions resulting from polymer chain scissions and acid dissociation of ester hydrogen atoms during the polymeric matrix degradation are assumed to remain inside the composite sample, as exemplified by Eq. 3.17 in the modelling framework, which models the mass conservation of hydrogen ions and considers only two possible fates for a given hydrogen ion: either the hydrogen ion remains as a free hydrogen ion or recombines with one of the released ceramic anions. The existence of exclusively these two possibilities rules out the diffusion of hydrogen ions from inside the composite towards the surrounding environment. This assumption could lead to underestimations of the autocatalytic polymer degradation rate k_2' as biodegradable polymers often experience diffusion of the polymer degradation products towards the surrounding environment, at least in the outer layer of the sample, as reported by Grizzi et al. [12] lowering the concentration of hydrogen ions available to catalyse the hydrolytic polymer chain scissions.
- No significant swelling: the unit cell volume, V_{unit} ($\mathrm{m^3}$), and the polymer and initial ceramic volumes, V_{pol} ($\mathrm{m^3}$) and V_{cer0} ($\mathrm{m^3}$) are calculated prior to the start of degradation using materials properties for non-swollen matrixes and fillers as discussed later in Sect. 3.3. As these volumes are not changed during composite degradation, the representation is valid only if there is no significant swelling.

Similarly, the main assumptions made in the characterisation of the ceramic filler employed in the general modelling framework are:

- Adequate representative ceramic particle size: the contribution of the ceramic phase was characterised in the modelling framework employing a unique representative particle size. In most cases, composites contain fillers with a broad

particle size distribution and the representative particle size was computed as a Sauter mean diameter using the available information as described in Sect. 3.5.2 as part of the data extraction methods. The validity of this representation is determined by both the quantity and quality of the available particle size information. A representative particle size of a poorly characterised ceramic filler could result in a misrepresentation of the composite sample.

- Composite spatial homogeneity: the use of a representative unit cell consisting of one ceramic particle with the representative particle size surrounded by a determined quantity of polymer phase, as described in Sect. 3.3, produces average values, representing the whole composite sample, as output of the computational simulations. These simulated results are representative of the reality only when the composite sample is fully represented by the unit cell and that requires certain homogeneity in the composite, i.e. that the spatial distribution of ceramic particles is even throughout the polymeric matrix and that each particle is fully surrounded by polymer phase. For composites with a strong deviation from this assumption, e.g composites with agglomeration of the ceramic particles, the use of this modelling framework does not pose an accurate representation.
- Sufficient diffusion of dissolved ceramic ions: the ceramic anions and calcium cations released during the ceramic filler dissolution are assumed to diffuse fast enough to result in an uniform concentration throughout the whole unit cell, i.e. the distance between the ceramic particle surface and the confines of the representative unit cell is of the same magnitude or smaller than the distance that the dissolved ceramic ions can diffuse in the analysed time step. In cases deviating from this assumption, the use of this modelling framework could lead to underestimations of the ceramic dissolution rate A_{d}.

A non-exhaustive list of advantages of the framework includes:

- Versatility: the mathematical expressions used in the modelling framework to characterise the different elements involved in composite degradation hold for a variety of materials. The polymeric degradation expression is widely accepted as an accurate way of characterising several members of the poly-α-hydroxy-acids family [1, 2, 5]. The ceramic dissolution law has been widely used to characterise calcium-based materials [7, 9, 10]. These factors make the modelling framework suitable for the analysis of a wide range of composites with different polymeric matrix and ceramic filler combinations.
- Low computational cost: the use of a representative unit cell to characterise a whole composite significantly reduces the computational cost of the simulations. This characteristic allows the data analysis to be carried out in a reasonable timescale. A single simulation of any of the specific models presented in the next section (Sect. 3.2) took on average from 180 to 300 s in a commercially available laptop (2012 MacBook Pro with processor Intel Core i7 at 2.9 GHz and 8 GB at 1600 MHz DDR3 SDRAM).
- Modularity and simplicity: the relative simplicity of the modular approach employed in this modelling framework, dividing the characterisation of composite

degradation in three different independent blocks, allows the introduction of modifications and improvements with ease.

Having now presented the analysis of the main assumptions and advantages of the general modelling framework, the next section discusses the specific degradation models obtained with the particularisation of the general framework for tricalcium phosphate, hydroxyapatite and calcium carbonate.

3.2 Degradation Models for Bioresorbable Composites with Common Calcium-based Materials as Filler

In this section, complete models with all the constituent equations for several common calcium-based materials are presented. As previously mentioned, only the numerical solution of the tricalcium phosphate (TCP) model is thoroughly described. Brief remarks about the singularities of the numerical solutions of the hydroxyapatite (HA) and calcium carbonate (CC) models are included.

3.2.1 Tricalcium Phosphate (TCP) Composites Degradation Model

This degradation model for composites made of biodegradable polymer and tricalcium phosphate ($Ca_3(PO_4)_2$) spherical particles results from the particularisation of the general modelling framework employing TCP as ceramic filler. Although the modelling framework was based on the TCP model proposed by Pan et al. [1, 2], the version discussed here presents some minor differences with the original, which are summarised before the discussion of the numerical solution.

The TCP composites degradation model is given as a set of eleven governing equations, which expresses the relationships amongst eleven variables. For clarity, the same nomenclature adopted by Pan et al. [2], is employed here. The eleven variables, named x_1, x_2, …, and x_{11} represent eleven magnitudes of interest to understand the composite degradation phenomena. These magnitudes are:

- $x_1 = R_s$, concentration of polymer chain scissions ($\mathrm{mol\,m^{-3}}$).
- $x_2 = [H^+] = C_{\mathrm{H}^+}$, concentration of hydrogen ions ($\mathrm{mol\,m^{-3}}$).
- $x_3 = [Ca^{2+}]$, concentration of calcium ions ($\mathrm{mol\,m^{-3}}$).
- $x_4 = [PO_4^{3-}]$, concentration of phosphate ions ($\mathrm{mol\,m^{-3}}$).
- $x_5 = [R\text{-}COOH]$, concentration of non-dissociated carboxylic end group chains ($\mathrm{mol\,m^{-3}}$).
- $x_6 = [R\text{-}COO^-]$, concentration of dissociated carboxylic end group chains ($\mathrm{mol\,m^{-3}}$).
- $x_7 = [HPO_4^{2-}]$, concentration of hydrogen phosphate ions ($\mathrm{mol\,m^{-3}}$).

- $x_8 = [H_2PO_4^-]$, concentration of dihydrogen phosphate ions ($\mathrm{mol\,m^{-3}}$).
- $x_9 = [H_3PO_4]$, concentration of phosphoric acid ($\mathrm{mol\,m^{-3}}$).
- $x_{10} = a_{\mathrm{TCP}}$, total area of interface between the ceramic and polymer phases per unit of composite volume, i.e. concentration of interfacial area in the composite ($\mathrm{m^2\,m^{-3}}$). $a_{\mathrm{TCP}} = \frac{S_{\mathrm{cer}}}{V_{\mathrm{unit}}}$; with S_{cer}, the ceramic representative particle surface area ($\mathrm{m^2}$) and V_{unit}, the unit cell volume ($\mathrm{m^3}$).
- $x_{11} = M_{\mathrm{n}}$, number-average molecular weight of the polymer phase (Da).

It is worth noting that all the concentrations, except the interface area, are defined in the polymer phase, i.e. per unit of volume of the polymer phase, not per unit of volume of composite.

The eleven constituent equations of the TCP degradation model are listed below in their dimensional form. As mentioned, the equations stem from the particularisation of the general modelling framework (see Sect. 3.1) for tricalcium phosphate. The nomenclature employed in the modelling framework section was selected to highlight the physical meaning of the composite model equations, whereas the nomenclature used in this section was selected to highlight the mathematical aspects and distinguish clearly between variables or unknown model outputs and constant parameters or known model inputs. To facilitate the transition from the general modelling framework nomenclature to this chapter nomenclature, the equations are included in both.

The equations are presented, as mentioned in the modelling framework description, divided into two different groups according to their time-dependence. The first group of equations includes the three differential equations which show the time-dependence of R_s/x_1, $[Ca^{2+}]/x_3$ and a_{TCP}/x_{10}.

The first differential equation of the TCP model characterises the variation of polymer chain scissions concentration in the polymer phase, R_s/x_1 ($\mathrm{mol\,m^{-3}}$), over time. Framework equation 3.2 particularised for a given type of polymer scission excluding short polymer chains is used to describe the R_s/x_1 rate:

$$\frac{\mathrm{d}R_s}{\mathrm{d}t} = C_{\mathrm{e0}}\left[1-\alpha\left(\frac{R_s}{C_{\mathrm{e0}}}\right)^{\beta}\right](k_1 + k_2' C_{\mathrm{H^+}}) \qquad (\mathrm{mol\,m^{-3}\,s^{-1}}) \qquad (3.18a)$$

$$\frac{\mathrm{d}x_1}{\mathrm{d}t} = C_{\mathrm{e0}}\left[1-\alpha\left(\frac{x_1}{C_{\mathrm{e0}}}\right)^{\beta}\right](k_1 + k_2' x_2) \qquad (\mathrm{mol\,m^{-3}\,s^{-1}}) \qquad (3.18b)$$

with C_{e0}, the initial concentration of ester bonds in long chains in the polymer phase ($\mathrm{mol\,m^{-3}}$); α (1) and β (1), the empirical parameters used to characterise the polymer scission type and subsequent production of short chains by chain scission; k_1 ($\mathrm{s^{-1}}$) and k_2' ($\mathrm{m^3\,mol^{-1}\,s^{-1}}$), the non-catalytic and autocatalytic polymer hydrolysis rate constants respectively and $C_{\mathrm{H^+}}/x_2$, the concentration of hydrogen ions in the polymer phase ($\mathrm{mol\,m^{-3}}$).

The second differential equation characterises the evolution over time of the calcium ions concentration in the polymer phase, $[Ca^{2+}]/x_3$ ($\mathrm{mol\,m^{-3}}$) as a function of the concentration of interfacial area in the composite volume, a_{TCP}/x_{10} ($\mathrm{m^2\,m^{-3}}$)

and the undersaturation, σ (1). This equation results from the particularisation of framework equation 3.11 for TCP ($Ca_3(PO_4)_2$), where the number of calcium ions per TCP molecule is $I_{\text{cer}}^{\text{Ca}} = 3\ (\text{mol mol}^{-1})$, the ionic product is $I_{\text{P}} = [Ca^{2+}]^3[PO_4^{3-}]^2$ ($\text{mol}^5\,\text{m}^{-15}$) or $I_{\text{P}} = x_3^3 x_4^2$ ($\text{mol}^5\,\text{m}^{-15}$) and the total number of ions in a TCP molecule is $\eta = 5\ (\text{mol mol}^{-1})$:

$$\frac{\text{d}[Ca^{2+}]}{\text{d}t} = 3\frac{a_{\text{TCP}}}{1 - f_{\text{TCP0}}} A_{\text{d}} \left[1 - \left(\frac{[Ca^{2+}]^3[PO_4^{3-}]^2}{K_{\text{sp}}}\right)^{\frac{1}{5}}\right]^{\theta} \quad (\text{mol m}^{-3}\,\text{s}^{-1}) \tag{3.19a}$$

$$\frac{\text{d}x_3}{\text{d}t} = 3\frac{x_{10}}{1 - f_{\text{TCP0}}} A_{\text{d}} \left[1 - \left(\frac{x_3^3 x_4^2}{K_{\text{sp}}}\right)^{\frac{1}{5}}\right]^{\theta} \quad (\text{mol m}^{-3}\,\text{s}^{-1}) \tag{3.19b}$$

with f_{TCP0}, the initial volume fraction of TCP in the composite ($\text{m}^3\,\text{m}^{-3}$); K_{sp}, the TCP solubility product at 37 °C ($\text{mol}^5\,\text{m}^{-15}$) and A_{d} and θ, the rate constant ($\text{mol m}^{-2}\,\text{s}^{-1}$) and exponent (1) of the TCP dissolution power law.

The third differential equation describes the change of the concentration of interfacial area in the composite volume, a_{TCP}/x_{10} ($\text{m}^2\,\text{m}^{-3}$), with respect to time as a function of the calcium ions concentration rate $\frac{\text{d}[Ca^{2+}]}{\text{d}t}/\frac{\text{d}x_3}{\text{d}t}$ (mol m^{-3}). The equation is obtained particularising framework equation 3.13 for spherical particles, by adapting k_{geom}.

For a spherical particle, the surface area, volume and their derivatives with respect to the particle radius r (m) can be expressed as:

$$S_{\text{cer}} = 4\pi r^2 \quad (\text{m}^2) \qquad \frac{\text{d}S_{\text{cer}}}{\text{d}r} = 8\pi r \quad (\text{m})$$
$$V_{\text{cer}} = \frac{4}{3}\pi r^3 \quad (\text{m}^3) \qquad \frac{\text{d}V_{\text{cer}}}{\text{d}r} = 4\pi r^2 \quad (\text{m}^2)$$

with r the particle radius, i.e. half of the particle size. r can also be expressed as a function of a_{TCP}: $r = (\frac{V_{\text{unit}} a_{\text{TCP}}}{4\pi})^{\frac{1}{2}}$ (m).

The value of k_{geom} for spherical particles is:

$$k_{\text{geom}} = \frac{\text{d}S_{\text{cer}}}{\text{d}V_{\text{cer}}} = \frac{\text{d}S_{\text{cer}}}{\text{d}r}\frac{\text{d}r}{\text{d}V_{\text{cer}}} = \frac{8\pi r}{4\pi r^2}$$
$$= \frac{2}{r} = 4\pi^{\frac{1}{2}} \left(\frac{1}{V_{\text{unit}}}\right)^{\frac{1}{2}} \left(\frac{1}{a_{\text{TCP}}}\right)^{\frac{1}{2}} \quad (\text{m}^{-1}) \tag{3.20}$$

Substituting the value of k_{geom} for spherical particles in framework equation 3.13 yields the desired description:

$$\frac{da_{TCP}}{dt} = -\frac{4\pi^{\frac{1}{2}}}{3}\left(\frac{1}{V_{unit}}\right)^{\frac{1}{2}} \Omega_{TCP}(1 - f_{TCP0})\left(\frac{1}{a_{TCP}}\right)^{\frac{1}{2}} \frac{d[Ca^{2+}]}{dt} \quad (m^2\, m^{-3}\, s^{-1}) \tag{3.21a}$$

$$\frac{dx_{10}}{dt} = -\frac{4\pi^{\frac{1}{2}}}{3}\left(\frac{1}{V_{unit}}\right)^{\frac{1}{2}} \Omega_{TCP}(1 - f_{TCP0})\left(\frac{1}{x_{10}}\right)^{\frac{1}{2}} \frac{dx_3}{dt} \quad (m^2\, m^{-3}\, s^{-1}) \tag{3.21b}$$

with V_{unit}, the volume of the representative unit (m^3); Ω_{TCP}, the TCP molar volume ($m^3\, mol^{-1}$) and f_{TCP0}, the initial TCP volume fraction ($m^3\, m^{-3}$).

The second group includes the remaining eight equations coming from equilibrium constant relationships, matter conservation and the computation of the number-average molecular weight. These equations lack time dependency relationships but relate the other eight variables with R_s/x_1, $[Ca^{2+}]/x_3$ and a_{TCP}/x_{10}.

The first two equations in this second group complete the polymer degradation characterisation. The fourth TCP model equation, which is the first one not including time-dependency, describes the equilibrium relationship between the hydrogen ions concentration, $[H^+]/x_2$ ($mol\, m^{-3}$) and the concentration of dissociated and undissociated end group chains, $[R\text{-}COO^-]/x_6$ ($mol\, m^{-3}$) and $[R\text{-}COOH]/x_5$ ($mol\, m^{-3}$). Framework equation 3.3 without any modification is used to describe this relationship:

$$K_a = \frac{[H^+][R\text{-}COO^-]}{[R\text{-}COOH]} \quad (mol\, m^{-3}) \tag{3.22a}$$

$$K_a = \frac{x_2 x_6}{x_5} \quad (mol\, m^{-3}) \tag{3.22b}$$

with K_a, the equilibrium constant for the deprotonation reaction of the carboxylic end group for the chosen polymer, also known as polymer acid dissociation constant ($mol\, m^{-3}$) at 37 °C.

The fifth equation relates the concentration of dissociated and undissociated end group chains, $[R\text{-}COO^-]/x_6$ ($mol\, m^{-3}$) and $[R\text{-}COOH]/x_5$ ($mol\, m^{-3}$) to the concentration of chain scissions, R_s/x_1 ($mol\, m^{-3}$). Unmodified framework equation 3.4 describes the relationship:

$$[R\text{-}COOH] + [R\text{-}COO^-] = C_{chain0} + R_s \quad (mol\, m^{-3}) \tag{3.23a}$$

$$x_6 + x_5 = C_{chain0} + x_1 \quad (mol\, m^{-3}) \tag{3.23b}$$

with C_{chain0}, the initial concentration of polymer chains in the polymer phase ($mol\, m^{-3}$).

TCP dissolution results in the release of both phosphate, PO_4^{3-}, and calcium, Ca^{2+}, ions. Phosphate anions recombine with the available hydrogen ions, buffering the local acidity. The recombination of anions follows the inverse orthophosphoric acid

(H_3PO_4) deprotonation route. The next three equations characterise this buffering effect.

Framework set of equation 3.15 particularised for phosphate ions with $B^{n-} = PO_4^{3-}$, describe the relationship between hydrogen ions concentration, $[H^+]/x_2$ ($\mathrm{mol\,m^{-3}}$), free phosphate ion concentration, $[PO_4^{3-}]/x_4$ ($\mathrm{mol\,m^{-3}}$) and partially to fully recombined phosphate ion concentrations, $[HPO_4^{2-}]/x_7$ ($\mathrm{mol\,m^{-3}}$), $[H_2PO_4^-]/x_8$ ($\mathrm{mol\,m^{-3}}$) and $[H_3PO_4]/x_9$ ($\mathrm{mol\,m^{-3}}$). As the total anion charge is $n = 3$ three equations are needed to completely characterise the different recombination reactions:

$$K_3 = \frac{[H^+][PO_4^{3-}]}{[HPO_4^{2-}]} \qquad (\mathrm{mol\,m^{-3}}) \tag{3.24a}$$

$$K_3 = \frac{x_2 x_4}{x_7} \qquad (\mathrm{mol\,m^{-3}}) \tag{3.24b}$$

$$K_2 = \frac{[H^+][HPO_4^{2-}]}{[H_2PO_4^-]} \qquad (\mathrm{mol\,m^{-3}}) \tag{3.25a}$$

$$K_2 = \frac{x_2 x_7}{x_8} \qquad (\mathrm{mol\,m^{-3}}) \tag{3.25b}$$

$$K_1 = \frac{[H^+][H_2PO_4^-]}{[H_3PO_4]} \qquad (\mathrm{mol\,m^{-3}}) \tag{3.26a}$$

$$K_1 = \frac{x_2 x_8}{x_9} \qquad (\mathrm{mol\,m^{-3}}) \tag{3.26b}$$

with K_3, K_2, K_1, the equilibrium constants for the deprotonation reactions at 37 °C of hydrogen phosphate ion ($\mathrm{mol\,m^{-3}}$), dihydrogen phosphate ion ($\mathrm{mol\,m^{-3}}$) and phosphoric acid ($\mathrm{mol\,m^{-3}}$) respectively.

Assuming stoichiometric ceramic dissolution, the concentration of calcium ions, $[Ca^{2+}]/x_3$ ($\mathrm{mol\,m^{-3}}$) can be related to the concentration of free phosphate ions, $[PO_4^{3-}]/x_4$ ($\mathrm{mol\,m^{-3}}$) and recombined phosphate ions in all the recombination states, $[HPO_4^{2-}]/x_7$ ($\mathrm{mol\,m^{-3}}$), $[H_2PO_4^-]/x_8$ ($\mathrm{mol\,m^{-3}}$) and $[H_3PO_4]/x_9$ ($\mathrm{mol\,m^{-3}}$). Framework equation 3.16 particularised for TCP using $I_{\mathrm{cer}}^{\mathrm{B}} = I_{\mathrm{cer}}^{\mathrm{PO_4}} = 2$ ($\mathrm{mol\,mol^{-1}}$), $I_{\mathrm{cer}}^{\mathrm{Ca}} = 3$ ($\mathrm{mol\,mol^{-1}}$) and $B^{n-} = PO_4^{3-}$ describes the relationship:

$$\frac{2}{3}[Ca^{2+}] = [PO_4^{3-}] + [HPO_4^{2-}] + [H_2PO_4^-] + [H_3PO_4] \qquad (\mathrm{mol\,m^{-3}}) \tag{3.27a}$$

$$\frac{2}{3}x_3 = x_4 + x_7 + x_8 + x_9 \qquad (\mathrm{mol\,m^{-3}}) \tag{3.27b}$$

The next equation in the TCP model relates the concentration of free hydrogen ions, $[H^+]/x_2$ ($\mathrm{mol\,m^{-3}}$); recombined hydrogen ions in all the different

recombination states, $[H^+]/x_2$ (mol m^{-3}), $[HPO_4^{2-}]/x_7$ (mol m^{-3}), $[H_2PO_4^-]/x_8$ (mol m^{-3}) and $[H_3PO_4]/x_9$ (mol m^{-3}) to the concentration of dissociated chains, $[R\text{-}COO^-]/x_6$ (mol m^{-3}). Framework equation 3.17 particularised for $B^{n-} = PO_4^{3-}$ is used to describe the mass conservation relationship of hydrogen ions:

$$[H^+] + [HPO_4^{2-}] + 2[H_2PO_4^-] + 3[H_3PO_4] = [R\text{-}COO^-] + \Delta C_{H_0^+} \quad (\text{mol m}^{-3}) \tag{3.28a}$$

$$x_2 + x_7 + 2x_8 + 3x_9 = x_6 + \Delta C_{H_0^+} \quad (\text{mol m}^{-3}) \tag{3.28b}$$

with $\Delta C_{H_0^+}$, the part of hydrogen ions concentration at the time origin not coming from the dissociation of the carboxylic group ends: $\Delta C_{H_0^+} = C_{H_0^+} - x_6(t = 0)$.

The last equation of the TCP model characterises the relationship between number-average molecular weight of the polymer phase, M_n/x_{11} (Da), and the concentration of chain scissions, R_s/x_1 (mol m^{-3}). Framework equation 3.6 particularised for a given type of polymer scission using an empirical relation to characterise the production of short chains $\left({}^{R_{ol}}/_{C_{e0}} = \alpha({}^{R_s}/_{C_{e0}})^{\beta}\right)$ describes this relationship:

$$M_n = \frac{C_{e0}\left[1 - \alpha\left(\frac{R_s}{C_{e0}}\right)^{\beta}\right]M_{unit}}{C_{chain0} + R_s - \frac{C_{e0}}{m}\alpha\left(\frac{R_s}{C_{e0}}\right)^{\beta}} \quad (\text{Da}) \tag{3.29a}$$

$$x_{11} = \frac{C_{e0}\left[1 - \alpha\left(\frac{x_1}{C_{e0}}\right)^{\beta}\right]M_{unit}}{C_{chain0} + R_s - \frac{C_{e0}}{m}\alpha\left(\frac{x_1}{C_{e0}}\right)^{\beta}} \quad (\text{Da}) \tag{3.29b}$$

with C_{e0}, the initial concentration of ester bonds in long chains in the polymer phase (mol m^{-3}); α (1) and β (1), the empirical parameters used to characterise the polymer scission type and subsequent production of short chains by chain scission; M_{unit}, the molar mass associated to one ester bond (Da); C_{chain0}, the initial concentration of long polymer chains in the polymer phase (mol m^{-3}) and m, the average degree of pseudo-polymerisation of the short chains (1).

The set of eleven equations, from Eq. 3.18 to Eq. 3.29 excluding Eq. 3.20, fully stated, the differences with the original TCP model [1, 2] are summarised below:

- Use of $\Delta C_{H_0^+}$ ($\Delta C_{H_0^+} = C_{H_0^+} - x_6(t = 0)$) instead of $C_{H_0^+}$ in Eq. 3.28a/3.28b to differentiate between hydrogen coming from carboxylic end dissociation and hydrogen coming from other sources and attain a balanced expression at the time origin.
- Employment of a modified equation to compute pure polymer degradation, with the differences stemming from the determination of number of chains. The variation of polymer chain scissions concentration in the polymer phase, R_s (mol m^{-3}), over time for pure polymer degradation was computed as:

$$\frac{dR_s}{dt} = C_{e0}\left[1 - \alpha\left(\frac{R_s}{C_{e0}}\right)^{\beta}\right]\left(k_1 + k_2'\left(\left[K_a(C_{chain0} + R_s) + 0.25K_a^2\right]^{\frac{1}{2}} - 0.5K_a\right)\right) \quad (\text{mol m}^{-3}\,\text{s}^{-1}) \tag{3.30}$$

instead of:

$$\frac{\mathrm{d}R_s}{\mathrm{d}t} = C_{e0}\left[1-\alpha\left(\frac{R_s}{C_{e0}}\right)^{\beta}\right]\left(k_1 + k_2'\left[K_a(C_{chain0}+R_s)\right]^{\frac{1}{2}}\right) \quad (\mathrm{mol\,m^{-3}\,s^{-1}}) \tag{3.31}$$

with C_{e0}, the initial concentration of ester bonds in long chains in the polymer phase ($\mathrm{mol\,m^{-3}}$); α (1) and β (1), the empirical parameters used to characterise the polymer scission type and subsequent production of short chains by chain scission; k_1 ($\mathrm{s^{-1}}$) and k_2' ($\mathrm{m^3\,mol^{-1}\,s^{-1}}$), the non-catalytic and autocatalytic polymer hydrolysis rate constants respectively; K_a, the equilibrium constant for the deprotonation reaction of the carboxylic end group for the chosen polymer, also known as polymer acid dissociation constant ($\mathrm{mol\,m^{-3}}$) at 37 °C and C_{chain0}, the initial concentration of polymer chains in the polymer phase ($\mathrm{mol\,m^{-3}}$).

- The use of a different set of initial values for the eleven modelling variables, also stemming from a slightly different chains number consideration. Said used initial values are specified in Sect. 4.1.

The set of eleven equations, from Eq. 3.18 to Eq. 3.29 excluding Eq. 3.20, fully characterise the degradation of TCP composites. The appropriate numerical methods employed to solve this system of equations are outlined and discussed in the following paragraphs.

Numerical Solution of the TCP Composites Degradation Model

The following paragraphs discuss the numerical solution of the model, i.e. the generation of a set of values for the eleven variables that satisfy the set of equations at a given time t. The discussion is structured in two parts. Firstly, the non-dimensional variables are introduced and the nondimensionalisation process applied to the equations is analysed. Secondly, the implemented numerical solver of the non-dimensional set of equations is discussed.

For the numerical integration of the equations, Pan recommend expressing them in a non-dimensional form for convenience [2]. Following this recommendation a set of non-dimensional variables based on the dimensional ones is defined:

- $\bar{x}_1 = \frac{x_1}{C_{e0}} = \frac{R_s}{C_{e0}} = \bar{R}_s$, nondimensionalised concentration of chain scissions (1).
- $\bar{x}_2 = \frac{x_2}{(C_{H^+})_{pH=7.4}} = \frac{C_{H^+}}{(C_{H^+})_{pH=7.4}} = \bar{C}_{H^+}$, nondimensionalised concentration of hydrogen ions (1).
- $\bar{x}_3 = \frac{x_3}{[Ca^{2+}]_{eq}} = \frac{[Ca^{2+}]}{[Ca^{2+}]_{eq}} = [\overline{Ca}^{2+}]$, nondimensionalised concentration of calcium ions (1).
- $\bar{x}_4 = \frac{x_4}{(C_{H^+})_{pH=7.4}} = \frac{[PO_4^{3-}]}{(C_{H^+})_{pH=7.4}} = [\overline{PO}_4^{3-}]$, nondimensionalised concentration of phosphate ions (1).
- $\bar{x}_5 = \frac{x_5}{C_{e0}} = \frac{[R\text{-}COOH]}{C_{e0}} = [\overline{R\text{-}COOH}]$, nondimensionalised concentration of non-dissociated carboxylic end group chains (1).
- $\bar{x}_6 = \frac{x_6}{C_{e0}} = \frac{[R\text{-}COO^-]}{C_{e0}} = [\overline{R\text{-}COO}^-]$, nondimensionalised concentration of dissociated carboxylic end group chains (1).
- $\bar{x}_7 = \frac{x_7}{(C_{H^+})_{pH=7.4}} = \frac{[HPO_4^{2-}]}{(C_{H^+})_{pH=7.4}} = [\overline{HPO}_4^{2-}]$, nondimensionalised concentration of hydrogen phosphate ions (1).

- $\bar{x}_8 = \frac{x_8}{(C_{H^+})_{pH=7.4}} = \frac{[H_2PO_4^-]}{(C_{H^+})_{pH=7.4}} = [\overline{H_2PO_4^-}]$, nondimensionalised concentration of dihydrogen phosphate ions (1).
- $\bar{x}_9 = \frac{x_9}{(C_{H^+})_{pH=7.4}} = \frac{[H_3PO_4]}{(C_{H^+})_{pH=7.4}} = [\overline{H_3PO_4}]$, nondimensionalised concentration of phosphoric acid (1).
- $\bar{x}_{10} = \frac{x_{10}}{a_{TCP0}} = \frac{a_{TCP}}{a_{TCP0}} = \overline{a}_{TCP}$, nondimensionalised total area of interface between the two phases per unit of volume of the composite (1).
- $\bar{x}_{11} = \frac{x_{11}}{M_{n0}} = \frac{M_n}{M_{n0}} = \overline{M}_n$, nondimensionalised number-average molecular weight (1).

with the concentrations $x_1, \ldots, x_9$ defined per unit of polymer phase.

For the nondimensionalisation process five different constants were used: $(C_{H^+})_{pH=7.4}$, the hydrogen ions concentration at a pH of 7.4 ($mol\,m^{-3}$); $[Ca^{2+}]_{eq}$, the calcium ions concentration at dissolution equilibrium ($mol\,m^{-3}$); C_{e0}, the concentration of ester bonds in long chains at the time origin in the polymer phase ($mol\,m^{-3}$), a_{TCP0}, the value of a_{TCP} at the time origin ($m^2\,m^{-3}$) and M_{n0}, the number-average molecular weight of the polymer phase at the time origin (Da).

Using this set of non-dimensional variables, a set of eleven non-dimensional equations was generated by substituting the dimensional variables for their non-dimensional counterparts. The non-dimensional equations are presented in two different groups. The first group includes the non-dimensional versions of the three differential equations and the second group includes the non-dimensional version of the other eight equations.

The $\bar{x}_1$, $\bar{x}_3$ and $\bar{x}_{10}$ time-dependent equations are presented next, starting with the non-dimensional version of Eq. 3.18b:

$$\frac{d\bar{x}_1}{d\bar{t}} = (1 - \alpha\bar{x}_1^{\beta})(\bar{k}_1 + \bar{x}_2) \qquad (1) \qquad (3.32)$$

with $\bar{k}_1 = \frac{k_1}{k_2'(C_{H^+})_{pH=7.4}}$ (1) and $\bar{t} = tk_2'(C_{H^+})_{pH=7.4}$ (1).

Secondly, the non-dimensional version of Eq. 3.19b:

$$\frac{d\bar{x}_3}{d\bar{t}} = \frac{3a_{TCP0}A_d}{k_2'(C_{H^+})_{pH=7.4}[Ca^{2+}]_{eq}(1-f_{TCP0})}\bar{x}_{10}\left(1 - \left(\frac{\bar{x}_3^3\bar{x}_4^2}{\frac{K_{sp}}{[Ca^{2+}]_{eq}^3[(C_{H^+})_{pH=7.4}]^2}}\right)^{\frac{1}{5}}\right)^{\theta}$$
$$= S_{TCP}\bar{x}_{10}\sigma^{\theta} \qquad (1) \qquad (3.33)$$

with $S_{TCP} = \frac{3a_{TCP0}A_d}{k_2'(C_{H^+})_{pH=7.4}[Ca^{2+}]_{eq}(1-f_{TCP0})}$ (1), $\sigma^{\theta} = \left(1 - \left(\frac{\bar{x}_3^3\bar{x}_4^2}{\bar{K}_{sp}}\right)^{\frac{1}{5}}\right)^{\theta}$ (1) and $\bar{K}_{sp} = \frac{K_{sp}}{[Ca^{2+}]_{eq}^3[(C_{H_+})_{pH=7.4}]^2}$ (1).

And lastly, the non-dimensional version of Eq. 3.21b:

$$\frac{d\bar{x}_{10}}{d\bar{t}} = \frac{-4\pi^{\frac{1}{2}}\Omega_{TCP}(1-f_{TCP0})[Ca^{2+}]_{eq}}{3V_{unit}^{\frac{1}{2}}a_{TCP0}^{\frac{3}{2}}}\frac{d\bar{x}_3}{d\bar{t}}\bar{x}_{10}^{-\frac{1}{2}}$$
$$= K_{a_{TCP}}\frac{d\bar{x}_3}{d\bar{t}}\bar{x}_{10}^{-\frac{1}{2}} \qquad (1) \qquad (3.34)$$

with $K_{a_{\mathrm{TCP}}} = \frac{-4\pi^{\frac{1}{2}}\Omega_{\mathrm{TCP}}(1-f_{\mathrm{TCP0}})[Ca^{2+}]_{\mathrm{eq}}}{3V_{\mathrm{unit}}^{\frac{1}{2}}a_{\mathrm{TCP0}}^{\frac{3}{2}}}$ (1).

The other eight non-dimensional equations of the TCP model relate $\bar{x}_1, \bar{x}_3$ and $\bar{x}_{10}$ to $\bar{x}_2, \bar{x}_4, \bar{x}_5, \bar{x}_6, \bar{x}_7, \bar{x}_8, \bar{x}_9$ and $\bar{x}_{11}$. Firstly, the non-dimensional version of Eq. 3.22b:

$$\bar{K}_{\mathrm{a}} = \frac{\bar{x}_2\bar{x}_6}{\bar{x}_5} \qquad (1) \tag{3.35}$$

with $\bar{K}_{\mathrm{a}} = \frac{K_{\mathrm{a}}}{(C_{\mathrm{H}^+})_{\mathrm{pH}=7.4}}$ (1).

Followed by the non-dimensional version of Eq. 3.23b:

$$\bar{x}_6 + \bar{x}_5 = \frac{M_{\mathrm{unit}}}{M_{\mathrm{n0}}} + \bar{x}_1 \qquad (1) \tag{3.36}$$

with $\frac{M_{\mathrm{unit}}}{M_{\mathrm{n0}}} = \frac{C_{\mathrm{chain0}}}{C_{\mathrm{e0}}} = N_{\mathrm{dp0}}^{-1}$ (1) where M_{unit}, is the molar mass associated to one ester bond (Da); M_{n0}, the number-average molecular weight at the time origin (Da) and N_{dp0}, the initial average degree of pseudo-polymerisation (Da Da^{-1}).

Non-dimensional version of Eqs. 3.24b, 3.25b and 3.26b:

$$\bar{K}_3 = \frac{\bar{x}_2\bar{x}_4}{\bar{x}_7} \qquad (1) \tag{3.37}$$

$$\bar{K}_2 = \frac{\bar{x}_2\bar{x}_7}{\bar{x}_8} \qquad (1) \tag{3.38}$$

$$\bar{K}_1 = \frac{\bar{x}_2\bar{x}_8}{\bar{x}_9} \qquad (1) \tag{3.39}$$

with $\bar{K}_3 = \frac{K_3}{(C_{\mathrm{H}^+})_{\mathrm{pH}=7.4}}$ (1), $\bar{K}_2 = \frac{K_2}{(C_{\mathrm{H}^+})_{\mathrm{pH}=7.4}}$ (1), $\bar{K}_1 = \frac{K_1}{(C_{\mathrm{H}^+})_{\mathrm{pH}=7.4}}$ (1).

Non-dimensional version of Eq. 3.27b:

$$\frac{2}{3}\bar{x}_3 K_{\text{Ca-H}} = \bar{x}_4 + \bar{x}_7 + \bar{x}_8 + \bar{x}_9 \qquad (1) \tag{3.40}$$

with $K_{\text{Ca-H}} = \frac{[Ca^{2+}]_{\mathrm{eq}}}{(C_{\mathrm{H}^+})_{\mathrm{pH}=7.4}}$ (1).

Non-dimensional version of Eq. 3.28b:

$$\bar{x}_2 + \bar{x}_7 + 2\bar{x}_8 + 3\bar{x}_9 = \bar{x}_6 K_{\text{Ce0-H}} + \Delta\bar{C}_{\mathrm{H}_0^+} \qquad (1) \tag{3.41}$$

with $K_{\text{Ce0-H}} = \frac{C_{\mathrm{e0}}}{(C_{\mathrm{H}^+})_{\mathrm{pH}=7.4}}$ (1) and $\Delta\bar{C}_{\mathrm{H}_0^+} = \bar{C}_{\mathrm{H}_0^+} - \bar{x}_6(t=0)K_{\text{Ce0-H}} = \frac{C_{\mathrm{H}_0^+}}{(C_{\mathrm{H}^+})_{\mathrm{pH}=7.4}} - \bar{x}_6(t=0)K_{\text{Ce0-H}}$ (1).

And lastly, the non-dimensional version of Eq. 3.29b:

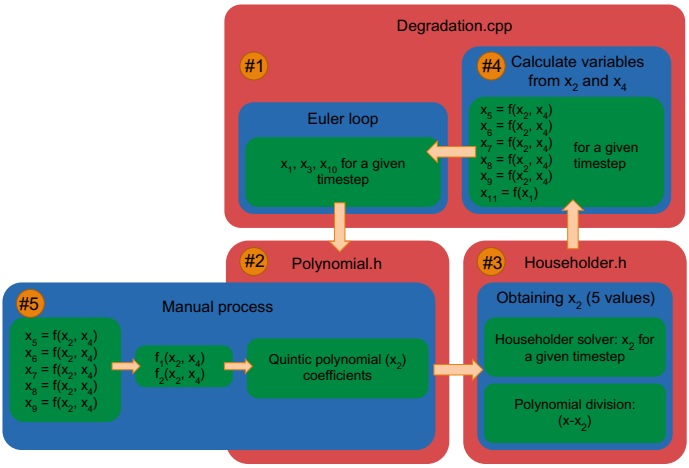

Fig. 3.6 Schematic visual representation of the different steps included in the implemented numerical solver. The green coloured boxes describe the specific mathematical instructions needed, the blue coloured boxes include the abstract general actions and the red coloured boxes indicate the C++ files containing those numerical instructions

$$\bar{x}_{11} = \frac{1 - \alpha \bar{x}_1^{\beta}}{1 + N_{\mathrm{dp0}}\left(\bar{x}_1 - \left(\frac{\alpha}{m}\right)\bar{x}_1^{\beta}\right)} \qquad (1) \qquad (3.42)$$

with $\frac{M_{\mathrm{unit}}}{M_{\mathrm{n0}}} = \frac{C_{\mathrm{chain0}}}{C_{\mathrm{e0}}} = N_{\mathrm{dp0}}^{-1}$ and N_{dp0}, the initial average degree of pseudo-polymerisation (Da Da^{-1}).[4]

Once the eleven equations are expressed in an non-dimensional form, the numerical solution of the system can be explored. Figure 3.6 depicts a visual schematic representation of the different steps, grouped in blocks, of the numerical solver employed to obtain the evolution of the different variables over time.

The graphic representation is structured in three different levels: the lowest level represented by the green boxes indicates the necessary specific mathematical operations to execute the high level instruction, described in the medium level blue boxes. The uppermost level, depicted using red boxes, includes information about the file structure of the C++ implementation, indicating the particular file that computes the designated instruction. This core numerical solver implemented in C++ was linked to a Python interface to facilitate the data input and output.

The workflow of the numerical solver follows an anticlockwise direction, starting with an Euler loop situated in the top left corner of the figure and identified as number #1. In each iteration of the Euler loop, a new set of $\bar{x}_1$, $\bar{x}_3$ and $\bar{x}_{10}$ values corresponding to a time-step t_{n}, is obtained using the values of the variables at $t_{\mathrm{n}-1}$ and the three time-dependent equations. For illustrative purposes, the first equation of the Euler

[4]Information about the definition and description of the average degree of pseudo-polymerisation, N_{dp0}, can be found in Appendix A.4.

loop can be expressed as: $\bar{x}_1(\bar{t}+\Delta\bar{t}) = \bar{x}_1(\bar{t}) + \frac{\mathrm{d}\bar{x}_1}{\mathrm{d}\bar{t}}\Delta\bar{t}$. It is worth noting that this time-step must be small enough to ensure the convergence of the solution.

After calculating the values of $\bar{x}_1$, $\bar{x}_3$ and $\bar{x}_{10}$ for a given time-step, the values of the remaining variables need to be computed. The numerical solver calculated those values by computing first the coefficients of the 5th degree $\bar{x}_2$ polynomial at t_n. The 5th degree polynomial is then used to calculate the correct value of $\bar{x}_2$. This step is identified in Fig. 3.6 as number #2 and implemented in the *polynomial.h* file.

The five $\bar{x}_2$ solutions to this 5th degree polynomial are obtained with a customised Householder root-finding algorithm, implemented in the *householder.h* file and identified as number #3 in the figure. From these five values, the selection of the only $\bar{x}_2$ value with physical meaning provides the desired value of $\bar{x}_2$.

Once the correct $\bar{x}_2$ value is calculated the $\bar{x}_4$, $\bar{x}_7$, $\bar{x}_8$, $\bar{x}_9$, $\bar{x}_6$ and $\bar{x}_5$ values are computed using mathematical relationships derived from the non-dimensional equations. Lastly, the value of $\bar{x}_{11}$ is computed. These calculations were implemented in the *degradation.h* file and correspond to number #4 in the figure. After a complete cycle, the whole process is repeated again and the values at $t_{\mathrm{n}+1}$ are calculated using the values at t_n.

The general expression of the 5th degree $\bar{x}_2$ polynomial used to calculate the value of $\bar{x}_2$ in each time-step was derived manually from the seven equations relating $\bar{x}_2$, $\bar{x}_4$, $\bar{x}_5$, $\bar{x}_6$, $\bar{x}_7$, $\bar{x}_8$ and $\bar{x}_9$ to $\bar{x}_1$, $\bar{x}_3$ and $\bar{x}_{10}$. This polynomial provides a solution for a system with seven variables and seven equations. This step can be found in Fig. 3.6 labelled as number #5 and was carried out only once, i.e. this step does not belong to the cycle.

The first step employed for solving this system of seven equations with seven variable, i.e. generating the 5th degree $\bar{x}_2$ polynomial, is to express $\bar{x}_5$, $\bar{x}_6$, $\bar{x}_7$, $\bar{x}_8$ and $\bar{x}_9$ as functions of $\bar{x}_2$ and $\bar{x}_4$:

Rearranging Eq. 3.35, $\bar{x}_5$ can be expressed as a function of $\bar{x}_2$ and $\bar{x}_6$:

$$\bar{x}_5 = \frac{\bar{x}_2\bar{x}_6}{\bar{K}_\mathrm{a}} \tag{3.43}$$

$\bar{x}_6$ can also expressed as a function of $\bar{x}_2$ by expressing $\bar{x}_5$ as a function of both $\bar{x}_2$ and $\bar{x}_6$, as described in Eq. 3.43, and then rearranging Eq. 3.36:

$$\bar{x}_6 = \left(\frac{M_\mathrm{unit}}{M_\mathrm{n0}} + \bar{x}_1\right)\frac{\bar{K}_\mathrm{a}}{\bar{K}_\mathrm{a} + \bar{x}_2} \tag{3.44}$$

$\bar{x}_7$, $\bar{x}_8$ and $\bar{x}_9$ can be expressed as functions of $\bar{x}_2$ and $\bar{x}_4$ with a series of simple arrangement and substitutions. For instance, $\bar{x}_7$ can be expressed as a function of $\bar{x}_2$ and $\bar{x}_4$ by rearranging Eq. 3.37:

$$\bar{x}_7 = \frac{\bar{x}_2\bar{x}_4}{\bar{K}_3} \tag{3.45}$$

In a similar fashion, by rearranging Eq. 3.38 and using Eq. 3.45, $\bar{x}_7$ can be expressed as a function of $\bar{x}_2$ and $\bar{x}_4$:

$$\bar{x}_8 = \frac{\bar{x}_2\bar{x}_7}{\bar{K}_2} = \frac{\bar{x}_2\bar{x}_2\bar{x}_4}{\bar{K}_2\bar{K}_3} = \frac{\bar{x}_2^2\bar{x}_4}{\bar{K}_2\bar{K}_3} \tag{3.46}$$

And finally, by rearranging Eq. 3.39 and using Eq. 3.46, $\bar{x}_7$ can be expressed as a function of $\bar{x}_2$ and $\bar{x}_4$:

$$\bar{x}_9 = \frac{\bar{x}_2\bar{x}_8}{\bar{K}_1} = \frac{\bar{x}_2\bar{x}_2\bar{x}_2\bar{x}_4}{\bar{K}_1\bar{K}_2\bar{K}_3} = \frac{\bar{x}_2^3\bar{x}_4}{\bar{K}_1\bar{K}_2\bar{K}_3} \tag{3.47}$$

Once $\bar{x}_5$, $\bar{x}_6$, $\bar{x}_7$, $\bar{x}_8$ and $\bar{x}_9$ are expressed as functions of $\bar{x}_2$ and $\bar{x}_4$, the appropriate substitutions in Eqs. 3.40 and 3.41 result in a reduction from a system with seven variables to a system with two variables formed by the following two equations:

$$\bar{x}_4 + \frac{\bar{x}_2\bar{x}_4}{\bar{K}_3} + \frac{\bar{x}_2^2\bar{x}_4}{\bar{K}_2\bar{K}_3} + \frac{\bar{x}_2^3\bar{x}_4}{\bar{K}_1\bar{K}_2\bar{K}_3} = \frac{2}{3}\bar{x}_3 K_{\text{Ca-H}} \tag{3.48}$$

$$\bar{x}_2 + \frac{\bar{x}_2\bar{x}_4}{\bar{K}_3} + 2\frac{\bar{x}_2^2\bar{x}_4}{\bar{K}_2\bar{K}_3} + 3\frac{\bar{x}_2^3\bar{x}_4}{\bar{K}_1\bar{K}_2\bar{K}_3} - \left(\frac{M_{\text{unit}}}{M_{\text{n0}}} + \bar{x}_1\right)\frac{\bar{K}_{\text{a}}}{\bar{K}_{\text{a}} + \bar{x}_2} K_{\text{Ce0-H}} = \bar{C}_{\text{H}_0^+} \tag{3.49}$$

Extracting common factor $\bar{x}_4$ in the left hand side of Eq. 3.48 and dividing the right hand side by the resulting expression from the common factor extraction, $\bar{x}_4$ is expressed as a function of $\bar{x}_2$. Introducing this value in Eq. 3.49 yields the desired 5th degree polynomial of $\bar{x}_2$, $A + B\bar{x}_2 + C\bar{x}_2^2 + D\bar{x}_2^3 + E\bar{x}_2^4 + F\bar{x}_2^5$ with:

$$A = -\left((M_{\text{unit}} + \bar{x}_1 M_{\text{n0}})K_{\text{Ce0-H}} + \Delta\bar{C}_{\text{H}_0^+} M_{\text{n0}}\right)\bar{K}_1\bar{K}_2\bar{K}_3\bar{K}_{\text{a}} \tag{3.50a}$$

$$\begin{aligned} B = &-\left((M_{\text{unit}} + \bar{x}_1 M_{\text{n0}})K_{\text{Ce0-H}} + \Delta\bar{C}_{\text{H}_0^+} M_{\text{n0}}\right)\bar{K}_1\bar{K}_2\bar{K}_{\text{a}} \\ &+ M_{\text{n0}}\bar{K}_1\bar{K}_2\left(\frac{2}{3}\bar{x}_3 K_{\text{Ca-H}}\bar{K}_{\text{a}} + \bar{K}_3(\bar{K}_{\text{a}} - \Delta\bar{C}_{\text{H}_0^+})\right) \end{aligned} \tag{3.50b}$$

$$\begin{aligned} C = &-\left((M_{\text{unit}} + \bar{x}_1 M_{\text{n0}})K_{\text{Ce0-H}} + \Delta\bar{C}_{\text{H}_0^+} M_{\text{n0}}\right)\bar{K}_1\bar{K}_{\text{a}} \\ &+ M_{\text{n0}}\bar{K}_1\left(\frac{2}{3}\bar{x}_3 K_{\text{Ca-H}}(\bar{K}_2 + 2\bar{K}_{\text{a}}) + \bar{K}_2(\bar{K}_3 + \bar{K}_{\text{a}} - \Delta\bar{C}_{\text{H}_0^+})\right) \end{aligned} \tag{3.50c}$$

$$D = -\left((M_{\text{unit}} + \bar{x}_1 M_{\text{n0}})K_{\text{C}_{\text{e0}}\text{-H}} + \Delta\bar{C}_{\text{H}_0^+} M_{\text{n0}}\right)\bar{K}_{\text{a}} + M_{\text{n0}}\left(\frac{2}{3}\bar{x}_3 K_{\text{Ca-H}}(2\bar{K}_1 + 3\bar{K}_{\text{a}}) + \bar{K}_1(\bar{K}_2 + \bar{K}_{\text{a}} - \Delta\bar{C}_{\text{H}_0^+})\right) \quad (3.50\text{d})$$

$$E = M_{\text{n0}}(2\bar{x}_3 K_{\text{Ca-H}} + \bar{K}_1 + \bar{K}_{\text{a}} - \Delta\bar{C}_{\text{H}_0^+}) \quad (3.50\text{e})$$

$$F = M_{\text{n0}} \quad (3.50\text{f})$$

In summary, the complete solution of the system of equations at a generic time-step t_{n} was achieved in a two-stage process: firstly, the computation of the values of $\bar{x}_1$, $\bar{x}_3$ and $\bar{x}_{10}$ using the values of the variables at the previous time-step, $t_{\text{n}-1}$, and secondly, the calculation of the $\bar{x}_2$ value using the 5th degree polynomial, followed by the calculation of the remaining variables values at time-step t_{n}.

Once all the values for time-step t_{n} were known, the process started again with a new increment of time Δt giving the next time-step, $t_{\text{n+1}}$ ($t_{\text{n+1}} = t_{\text{n}} + \Delta t$). This process was repeated until either the number-average molecular weight of the polymer phase reached a set limit or the maximum allowed number of steps was achieved.

In a nutshell, the degradation model for tricalcium phosphate composites, presented in this section, fully captures the TCP degradation phenomena using a set of eleven equations. The numerical solution of the model, also included in this section, provides the evolution of eleven magnitudes of interest over time. Of special interest due to its prevailing use as composite degradation measurement, is the evolution of the number-average molecular weight of the polymer phase, M_{n}, over time. For a given tricalcium phosphate case study, the degradation is characterised exclusively by a set of four values for k_1, k_2', A_{d} and θ, with k_1 (s^{-1}) and k_2' ($\text{m}^3\,\text{mol}^{-1}\,\text{s}^{-1}$) the non-catalytic and autocatalytic polymer hydrolysis rate constants respectively, and A_{d} ($\text{mol}\,\text{m}^{-2}\,\text{s}^{-1}$) and θ (1), the rate constant and exponent of the TCP dissolution power law respectively. In order to obtain the evolution over time for the above-mentioned eleven magnitudes of interest, only a series of polymer-dependent, ceramic-dependent and composite-dependent constants, in addition to the initial values of the eleven variables are needed.

3.2.2 Hydroxyapatite (HA) Composites Degradation Model

Using the modelling framework presented in Sect. 3.1, a set of governing equations is proposed in order to characterise the degradation of composites containing spherical hydroxyapatite (HA) particles as filler. For clarity and continuity purposes, the same nomenclature used in Sect. 3.2.1 is employed in this section.

For HA, whose chemical composition is $\text{Ca}_{10}(\text{PO}_4)_6(\text{OH})_2$, the composite degradation model includes thirteen variables, named $x_1, x_2, \ldots, x_{12}$ and x_{13}. The first nine

variables represent the same magnitudes than in the TCP model (see Sect. 3.2.1). The other four variables symbolise the following magnitudes:

- $x_{10} = a_{\mathrm{HA}}$, total area of interface between the particle, in this case hydroxyapatite, and the polymeric matrix per unit of volume of the composite ($\mathrm{m^2\,m^{-3}}$).
- $x_{11} = [OH^-] = C_{\mathrm{OH^-}}$, concentration of hydroxide ions in the polymer phase ($\mathrm{mol\,m^{-3}}$).
- $x_{12} = [H_2O]$, concentration in the polymer phase of water molecules formed from the hydroxide ions released by the hydroxyapatite ($\mathrm{mol\,m^{-3}}$).
- $x_{13} = M_{\mathrm{n}}$, number-average molecular weight of the polymer phase (Da).

Hydroxyapatite, similarly to tricalcium phosphate, is a calcium orthophosphate and therefore releases, during dissolution, Ca^{2+} and PO_4^{3+} ions [13], resulting in significant similarities between the HA model presented here and the TCP model presented in Sect. 3.2.1. The differences between the two models arise from the release of OH^- ions, exclusive of hydroxyapatite, and the distinct number and ratio of constituent ions in the two ceramics, with hydroxyapatite having $I_{\mathrm{cer}}^{\mathrm{Ca}} = 10\ (\mathrm{mol\,mol^{-1}})$ and $I_{\mathrm{cer}}^{\mathrm{PO_4}} = 6\ (\mathrm{mol\,mol^{-1}})$ [13], instead of 3 and $2\,\mathrm{mol\,mol^{-1}}$ respectively.

Following the same structure employed in the TCP model, the presentation of equations is divided into two groups. Firstly, the three differential equation are introduced, followed by the non-differential equations in a second group. The first group of equations show the dependence of x_1, x_3 and x_{10} with respect to time. The first equation of this group, which describes the variation of the concentration of chain scissions in the polymer phase, x_1 ($\mathrm{mol\,m^{-3}}$), with respect to time does not change with the ceramic filler. Conversely, the second and third equations present some differences with respect to the TCP model equations due to the use of a different ceramic.

Framework equation 3.2 particularised for a given type of polymer scission excluding short chains describes the x_1 rate:

$$\frac{\mathrm{d}x_1}{\mathrm{d}t} = C_{\mathrm{e0}}\left[1 - \alpha\left(\frac{x_1}{C_{\mathrm{e0}}}\right)^{\beta}\right](k_1 + k_2' x_2) \qquad (\mathrm{mol\,m^{-3}\,s^{-1}}) \qquad (3.51)$$

with C_{e0}, the initial concentration of ester bonds in long chains in the polymer phase ($\mathrm{mol\,m^{-3}}$); α (1) and β (1), the empirical parameters used to characterise the polymer scission type and the subsequent production of short chains by chain scission; k_1 ($\mathrm{s^{-1}}$) and k_2' ($\mathrm{m^3\,mol^{-1}\,s^{-1}}$), the non-catalytic and autocatalytic polymer hydrolysis rate constants respectively and x_2, the concentration of hydrogen ions in the polymer phase ($\mathrm{mol\,m^{-3}}$).

Framework equation 3.11 particularised for HA ($Ca_{10}(PO_4)_6(OH)_2$) with the number of calcium ions per HA molecule $I_{\mathrm{cer}}^{\mathrm{Ca}} = 10\ (\mathrm{mol\,mol^{-1}})$, the ionic product $I_{\mathrm{P}} = x_3^{10} x_4^6 x_{11}^2$ ($\mathrm{mol^{18}\,m^{-54}}$) and total number of ions in a HA molecule $\eta = 18$ ($\mathrm{mol\,mol^{-1}}$) describes the variation of the concentration of calcium ions in the polymer phase, x_3 with time:

$$\frac{\mathrm{d}x_3}{\mathrm{d}t} = 10\frac{x_{10}}{1-f_{\mathrm{HA0}}}A_{\mathrm{d}}\left[1-\left(\frac{x_3^{10}x_4^6x_{11}^2}{K_{\mathrm{sp}}}\right)^{\frac{1}{18}}\right]^{\theta} \qquad (\mathrm{mol\,m^{-3}\,s^{-1}}) \qquad (3.52)$$

with f_{HA0}, the initial volume fraction of HA in the composite ($\mathrm{m^3\,m^{-3}}$); K_{sp}, the HA solubility product at 37 °C ($\mathrm{mol^{18}\,m^{-54}}$) and A_{d} and θ, the rate constant ($\mathrm{mol\,m^{-2}\,s^{-1}}$) and exponent (1) of the HA dissolution power law respectively.

Framework equation 3.13 particularised for spherical particles as shown in Sect. 3.2.1 using the HA value of calcium ions per ceramic molecule, $I_{\mathrm{cer}}^{\mathrm{Ca}} = 10$ ($\mathrm{mol\,mol^{-1}}$) is used to characterise the rate of interfacial area per unit of composite volume, x_{10}:

$$\frac{\mathrm{d}x_{10}}{\mathrm{d}t} = -\frac{4\pi^{\frac{1}{2}}}{10}\left(\frac{1}{V_{\mathrm{unit}}}\right)^{\frac{1}{2}}\Omega_{\mathrm{HA}}(1-f_{\mathrm{HA0}})\left(\frac{1}{x_{10}}\right)^{\frac{1}{2}}\frac{\mathrm{d}x_3}{\mathrm{d}t} \qquad (\mathrm{m^2\,m^{-3}\,s^{-1}}) \qquad (3.53)$$

with V_{unit}, the volume of the representative unit ($\mathrm{m^3}$); Ω_{HA}, the HA molar volume ($\mathrm{m\,mol^{-1}}$) and f_{HA0}, the initial HA volume fraction ($\mathrm{m^3\,m^{-3}}$).

The second group includes the remaining ten equations, which express the relations between the other ten variables and the three time-dependent variables. The first two equation of the second group complete the characterisation of the polymer phase, with framework equations 3.3 and 3.4 without any modifications:

$$K_{\mathrm{a}} = \frac{x_2x_6}{x_5} \qquad (\mathrm{mol\,m^{-3}}) \qquad (3.54)$$

$$x_6 + x_5 = C_{\mathrm{chain0}} + x_1 \qquad (\mathrm{mol\,m^{-3}}) \qquad (3.55)$$

with K_{a}, the equilibrium constant for the deprotonation reaction of the carboxylic end group for the chosen polymer at 37 °C ($\mathrm{mol\,m^{-3}}$) and C_{chain0}, the initial concentration of polymer chains in the polymer phase ($\mathrm{mol\,m^{-3}}$).

The dissolution of the HA particles results in the release of two different anions: phosphate ions, $\mathrm{PO_4^{3-}}$, and hydroxide ions, $\mathrm{OH^-}$. Having two anions entails the presence of two sets of equilibrium constants for deprotonation reactions, two equation for the mass conservation of a released anion and two sources of terms for the hydrogen mass conservation equation.

The relationship between the concentration of hydrogen ions, x_2 ($\mathrm{mol\,m^{-3}}$); free phosphate ions, x_4 ($\mathrm{mol\,m^{-3}}$) and recombined phosphate ions in all their recombining states, x_7 ($\mathrm{mol\,m^{-3}}$), x_8 ($\mathrm{mol\,m^{-3}}$) and x_9 ($\mathrm{mol\,m^{-3}}$) is the same relationship used in the TCP model and therefore is described by the particularisation of framework equation 3.15 with $\mathrm{B_1^{n_{1-}}} = \mathrm{PO_4^{3-}}$:

$$K_3 = \frac{x_2x_4}{x_7} \qquad (\mathrm{mol\,m^{-3}}) \qquad (3.56)$$

$$K_2 = \frac{x_2x_7}{x_8} \qquad (\mathrm{mol\,m^{-3}}) \qquad (3.57)$$

$$K_1 = \frac{x_2 x_8}{x_9} \qquad (\mathrm{mol\,m^{-3}}) \tag{3.58}$$

with K_3, K_2, K_1, the equilibrium constants for the deprotonation reactions at 37 °C of hydrogen phosphate ion ($\mathrm{mol\,m^{-3}}$), dihydrogen phosphate ion ($\mathrm{mol\,m^{-3}}$) and phosphoric acid ($\mathrm{mol\,m^{-3}}$) respectively.

The hydroxide ions also undergo recombination with the available hydrogen ions. The relationship between the concentration of hydrogen ions, x_2 ($\mathrm{mol\,m^{-3}}$) and the concentration of hydroxide ions, x_{11} ($\mathrm{mol\,m^{-3}}$), is described by the particularisation of framework equation 3.15 with $\mathrm{B}_2^{\mathrm{n}_2-} = \mathrm{OH}^-$:

$$K_\mathrm{w} = x_2 x_{11} \qquad (\mathrm{mol\,m^{-3}}) \tag{3.59}$$

with K_w, the equilibrium constant for the self-ionisation of water at 37 °C ($\mathrm{mol\,m^{-3}}$) [14].

Framework equation 3.16 particularised for HA using $I_\mathrm{cer}^{\mathrm{B}_1} = I_\mathrm{cer}^{\mathrm{PO_4}} = 6\,(\mathrm{mol\,mol^{-1}})$, $I_\mathrm{cer}^{\mathrm{Ca}} = 10\,(\mathrm{mol\,mol^{-1}})$ and $\mathrm{B}_1^{\mathrm{n}_1-} = \mathrm{PO}_4^{3-}$ describes the mass conservation relationship of the calcium ions and the phosphate ions in all their recombining states using units of concentration:

$$\frac{3}{5}x_3 = x_4 + x_7 + x_8 + x_9 \qquad (\mathrm{mol\,m^{-3}}) \tag{3.60}$$

Framework equation 3.16 particularised for HA using $I_\mathrm{cer}^{\mathrm{B}_2} = I_\mathrm{cer}^{\mathrm{OH}} = 2\,(\mathrm{mol\,mol^{-1}})$, $I_\mathrm{cer}^{\mathrm{Ca}} = 10\,(\mathrm{mol\,mol^{-1}})$ and $\mathrm{B}_2^{\mathrm{n}_2-} = \mathrm{OH}^-$ describes the mass conservation relationship of the calcium ions and the hydroxide ions in all their recombining states using units of concentration:

$$\frac{1}{5}x_3 + \Delta C_{\mathrm{OH}_0^-} = x_{11} + x_{12} \qquad (\mathrm{mol\,m^{-3}}) \tag{3.61}$$

with $\Delta C_{\mathrm{OH}_0^-}$, the hydroxide ions concentration at the time origin, i.e., the initial hydroxide ions concentration resulting from water self-ionisation instead of HA dissolution ($\mathrm{mol\,m^{-3}}$). This extra term appears because OH^-, the released ion considered in this mass conservation relationship with calcium ions, is an existing ion already present in the system as one of the buffer constituent ions. Conversely, in Eq. 3.60, the studied ceramic ion is a foreign ion, not existing any other source of origin for the ion in the system.

Framework equation 3.17 particularised for HA using $\mathrm{B}_1^{\mathrm{n}_1-} = \mathrm{PO}_4^{3-}$ and $\mathrm{B}_2^{\mathrm{n}_2-} = \mathrm{OH}^-$ describes the mass conservation relationship of the hydrogen ions in units of concentration:

$$x_2 + x_7 + 2x_8 + 3x_9 + x_{12} = x_6 + \Delta C_{\mathrm{H}_0^+} \qquad (\mathrm{mol\,m^{-3}}) \tag{3.62}$$

with $\Delta C_{\mathrm{H}_0^+}$, the non carboxylic ends dissociation hydrogen ions concentration at the time origin, which includes a contribution from the water self-ionisation ($\mathrm{mol\,m^{-3}}$).

The last equation of the HA model, which is common to the TCP model, describes the relationship between the number-average molecular weight of the polymer phase, x_{13} (Da), and the concentration of chain scissions, x_1 (mol m^{-3}). Framework equation 3.6 particularised for a given type of polymer scission using an empirical reaction to characterise the production of short chains $\left({}^{R_{ol}}/_{C_{e0}} = \alpha({}^{R_s}/_{C_{e0}})^{\beta}\right)$ gives:

$$x_{13} = \frac{C_{e0}\left[1 - \alpha\left(\frac{x_1}{C_{e0}}\right)^{\beta}\right]M_{\text{unit}}}{C_{\text{chain0}} + R_s - \frac{C_{e0}}{m}\alpha\left(\frac{x_1}{C_{e0}}\right)^{\beta}} \quad \text{(Da)} \tag{3.63}$$

with C_{e0}, the initial concentration of ester bonds in long chains in the polymer phase (mol m^{-3}); α (1) and β (1), the empirical parameters used to characterise the polymer scission type and the subsequent production of short chains by chain scission; M_{unit}, the molar mass associated to one ester bond (Da); C_{chain0}, the initial concentration of long polymer chains in the polymer phase (mol m^{-3}) and m, the average degree of pseudo-polymerisation of the short chains (1).

The set of thirteen equations comprising from Eq. 3.51 to Eq. 3.63 characterise the degradation of HA composites. In order to solve the system of equations the same nondimensionalisation procedure was employed. The following set of nondimensional variables can be defined for the nondimensionalisation procedure:

- $\bar{x}_1 = \frac{x_1}{C_{e0}} = \frac{R_s}{C_{e0}} = \bar{R}_s$, nondimensionalised concentration of chain scissions (1).
- $\bar{x}_2 = \frac{x_2}{(C_{H^+})_{pH=7.4}} = \frac{C_{H^+}}{(C_{H^+})_{pH=7.4}} = \bar{C}_{H^+}$, nondimensionalised concentration of hydrogen ions (1).
- $\bar{x}_3 = \frac{x_3}{[Ca^{2+}]_{eq}} = \frac{[Ca^{2+}]}{[Ca^{2+}]_{eq}} = [\overline{Ca}^{2+}]$, nondimensionalised concentration of calcium ions (1).
- $\bar{x}_4 = \frac{x_4}{(C_{H^+})_{pH=7.4}} = \frac{[PO_4^{3-}]}{(C_{H^+})_{pH=7.4}} = [\overline{PO_4}^{3-}]$, nondimensionalised concentration of phosphate ions (1).
- $\bar{x}_5 = \frac{x_5}{C_{e0}} = \frac{[R\text{-}COOH]}{C_{e0}} = [\overline{R\text{-}COOH}]$, nondimensionalised concentration of non-dissociated carboxylic end group chains (1).
- $\bar{x}_6 = \frac{x_6}{C_{e0}} = \frac{[R\text{-}COO^-]}{C_{e0}} = [\overline{R\text{-}COO}^-]$, nondimensionalised concentration of dissociated carboxylic end group chains (1).
- $\bar{x}_7 = \frac{x_7}{(C_{H^+})_{pH=7.4}} = \frac{[HPO_4^{2-}]}{(C_{H^+})_{pH=7.4}} = [\overline{HPO_4}^{2-}]$, nondimensionalised concentration of hydrogen phosphate ions (1).
- $\bar{x}_8 = \frac{x_8}{(C_{H^+})_{pH=7.4}} = \frac{[H_2PO_4^-]}{(C_{H^+})_{pH=7.4}} = [\overline{H_2PO_4}^-]$, nondimensionalised concentration of dihydrogen phosphate ions (1).
- $\bar{x}_9 = \frac{x_9}{(C_{H^+})_{pH=7.4}} = \frac{[H_3PO_4]}{(C_{H^+})_{pH=7.4}} = [\overline{H_3PO_4}]$, nondimensionalised concentration of phosphoric acid (1).
- $\bar{x}_{10} = \frac{x_{10}}{a_{HA0}} = \frac{a_{HA}}{a_{HA0}} = \bar{a}_{HA}$, nondimensionalised total area of interface between the two phases, hydroxyapatite and polymer, per unit of volume of the composite (1).
- $\bar{x}_{11} = \frac{x_{11}}{(C_{OH^-})_{pH=7.4}} = \frac{C_{OH^-}}{(C_{OH^-})_{pH=7.4}} = \bar{C}_{OH^-}$, nondimensionalised concentration of hydroxide ions (1).

- $\bar{x}_{12} = \frac{x_{12}}{(C_{OH^-})_{pH=7.4}} = \frac{[H_2O]}{(C_{OH^-})_{pH=7.4}} = [\overline{H_2O}]$, nondimensionalised concentration of water molecules coming from the dissolved hydroxide ions (1).
- $\bar{x}_{13} = \frac{x_{13}}{M_{n0}} = \frac{M_n}{M_{n0}} = \overline{M}_n$, nondimensionalised number-average molecular weight (1).

with $x_1, \ldots, x_9$, x_{11} and x_{12} concentrations defined per unit of polymer phase.

For the adimensionalisation process, six different constants were used: $(C_{H^+})_{pH=7.4}$, the hydrogen ions concentration at a pH equals to 7.4 (mol m^{-3}); $(C_{OH^-})_{pH=7.4}$, the hydroxide ions concentration at a pH equals to 7.4 (mol m^{-3}); $[Ca^{2+}]_{eq}$, the calcium ions concentration at equilibrium (mol m^{-3}); C_{e0}, the concentration in the polymer phase of ester bonds belonging to long chains (mol m^{-3}); a_{HA0}, the value of a_{HA} at the time origin (m^2 m^{-3}) and M_{n0}, the number-average molecular weight at the time origin (Da).

Using this set of non-dimensional variables the following equations were obtained. Firstly the nondimensionalised differential equations are presented, starting with the non-dimensional version of Eq. 3.51:

$$\frac{d\bar{x}_1}{d\bar{t}} = (1 - \alpha \bar{x}_1^{\beta})(\bar{k}_1 + \bar{x}_2) \qquad (1) \qquad (3.64)$$

with $\bar{k}_1 = \frac{k_1}{k_2'(C_{H^+})_{pH=7.4}}$ (1) and $\bar{t} = tk_2'(C_{H^+})_{pH=7.4}$ (1).

Followed by, the non-dimensional version of Eq. 3.52:

$$\frac{d\bar{x}_3}{d\bar{t}} = \frac{10 a_{HA0} A_d}{k_2'(C_{H^+})_{pH=7.4}[Ca^{2+}]_{eq}(1 - f_{HA0})} \bar{x}_{10} \left(1 - \left(\frac{\bar{x}_3^{10}\bar{x}_4^6\bar{x}_{11}^2}{\frac{K_{sp}}{[Ca^{2+}]_{eq}^{10}[(C_{H^+})_{pH=7.4}]^6[(C_{OH^-})_{pH=7.4}]^2}}\right)^{\frac{1}{18}}\right)^{\theta}$$
$$= S_{HA}\bar{x}_{10}\sigma^{\theta} \qquad (1) \qquad (3.65)$$

with $S_{HA} = \frac{10 a_{HA0} A_d}{k_2'(C_{H^+})_{pH=7.4}[Ca^{2+}]_{eq}(1-f_{HA0})}$ (1), $\sigma^{\theta} = \left(1 - \left(\frac{\bar{x}_3^{10}\bar{x}_4^6\bar{x}_{11}^2}{\bar{K}_{sp}}\right)^{\frac{1}{18}}\right)^{\theta}$ (1) and $\bar{K}_{sp} = \frac{K_{sp}}{[Ca^{2+}]_{eq}^{10}[(C_{H^+})_{pH=7.4}]^6[(C_{OH^-})_{pH=7.4}]^2}$ (1).

Ending with the non-dimensional version of Eq. 3.53:

$$\frac{d\bar{x}_{10}}{d\bar{t}} = \frac{-4\pi^{\frac{1}{2}}\Omega_{HA}(1 - f_{HA0})[Ca^{2+}]_{eq}}{10 V_{unit}^{\frac{1}{2}} a_{HA0}^{\frac{3}{2}}} \frac{d\bar{x}_3}{d\bar{t}} \bar{x}_{10}^{-\frac{1}{2}}$$
$$= K_{a_{HA}} \frac{d\bar{x}_3}{d\bar{t}} \bar{x}_{10}^{-\frac{1}{2}} \qquad (1) \qquad (3.66)$$

with $K_{a_{HA}} = \frac{-4\pi^{\frac{1}{2}}\Omega_{HA}(1-f_{HA0})[Ca^{2+}]_{eq}}{10 V_{unit}^{\frac{1}{2}} a_{HA0}^{\frac{3}{2}}}$ (1);

The other ten equations, relating the three time-dependent variables with the other ten variables, are presented in their nondimensionalised for in a second group, starting with the non-dimensional version of Eq. 3.54:

$$\bar{K}_{\mathrm{a}} = \frac{\bar{x}_2 \bar{x}_6}{\bar{x}_5} \qquad (1) \tag{3.67}$$

with $\bar{K}_{\mathrm{a}} = \frac{K_{\mathrm{a}}}{(C_{\mathrm{H}^+})_{\mathrm{pH}=7.4}}$ (1).

Non-dimensional version of Eq. 3.55:

$$\bar{x}_6 + \bar{x}_5 = \frac{M_{\mathrm{unit}}}{M_{\mathrm{n0}}} + \bar{x}_1 \qquad (1) \tag{3.68}$$

with $\frac{M_{\mathrm{unit}}}{M_{\mathrm{n0}}} = \frac{C_{\mathrm{chain0}}}{C_{\mathrm{e0}}} = N_{\mathrm{dp0}}^{-1}$ (1) where M_{unit}, is the molar mass associated to one ester bond (Da); M_{n0}, the number-average molecular weight at the time origin (Da) and N_{dp0}, the initial average degree of pseudo-polymerisation ($\mathrm{Da\,Da^{-1}}$).

Non-dimensional version of Eqs. 3.56–3.58:

$$\bar{K}_3 = \frac{\bar{x}_2 \bar{x}_4}{\bar{x}_7} \qquad (1) \tag{3.69}$$

$$\bar{K}_2 = \frac{\bar{x}_2 \bar{x}_7}{\bar{x}_8} \qquad (1) \tag{3.70}$$

$$\bar{K}_1 = \frac{\bar{x}_2 \bar{x}_8}{\bar{x}_9} \qquad (1) \tag{3.71}$$

with $\bar{K}_3 = \frac{K_3}{(C_{\mathrm{H}^+})_{\mathrm{pH}=7.4}}$ (1), $\bar{K}_2 = \frac{K_2}{(C_{\mathrm{H}^+})_{\mathrm{pH}=7.4}}$ (1), $\bar{K}_1 = \frac{K_1}{(C_{\mathrm{H}^+})_{\mathrm{pH}=7.4}}$ (1).

Non-dimensional version of Eq. 3.59:

$$\bar{K}_{\mathrm{w}} = \bar{x}_2 \bar{x}_{11} \qquad (1) \tag{3.72}$$

with $\bar{K}_{\mathrm{w}} = \frac{K_{\mathrm{w}}}{(C_{\mathrm{H}^+})_{\mathrm{pH}=7.4}(C_{\mathrm{OH}^-})_{\mathrm{pH}=7.4}}$ (1).

Non-dimensional version of Eq. 3.60:

$$\frac{3}{5}\bar{x}_3 K_{\text{Ca-H}} = \bar{x}_4 + \bar{x}_7 + \bar{x}_8 + \bar{x}_9 \qquad (1) \tag{3.73}$$

with $K_{\text{Ca-H}} = \frac{[Ca^{2+}]_{\mathrm{eq}}}{(C_{\mathrm{H}^+})_{\mathrm{pH}=7.4}}$ (1).

Non-dimensional version of Eq. 3.61:

$$\frac{1}{5}\bar{x}_3 K_{\text{Ca-OH}} + \Delta\bar{C}_{\mathrm{OH}_0^-} = \bar{x}_{11} + \bar{x}_{12} \qquad (1) \tag{3.74}$$

with $K_{\text{Ca-OH}} = \frac{[Ca^{2+}]_{\mathrm{eq}}}{(C_{\mathrm{OH}^-})_{\mathrm{pH}=7.4}}$ (1) and $\Delta\bar{C}_{\mathrm{OH}_0^-} = \frac{C_{\mathrm{OH}_0^-}}{(C_{OH^-})_{pH=7.4}}$ (1).

Non-dimensional version of Eq. 3.62:

$$\bar{x}_2 + \bar{x}_7 + 2\bar{x}_8 + 3\bar{x}_9 + \bar{x}_{12} K_{\text{OH-H}} = \bar{x}_6 K_{\mathrm{C_{e0}\text{-}H}} + \Delta\bar{C}_{\mathrm{H}_0^+} \qquad (1) \tag{3.75}$$

with $K_{\text{OH-H}} = \frac{(C_{\text{OH}^-})_{\text{pH}=7.4}}{(C_{\text{H}^+})_{\text{pH}=7.4}}$ (1), $K_{\text{Ce0-H}} = \frac{C_{\text{e0}}}{(C_{\text{H}^+})_{\text{pH}=7.4}}$ (1) and
$\Delta\bar{C}_{\text{H}_0^+} = \bar{C}_{\text{H}_0^+} - \bar{x}_6(t=0)K_{\text{Ce0-H}} = \frac{C_{\text{H}_0^+}}{(C_{\text{H}^+})_{\text{pH}=7.4}} - \bar{x}_6(t=0)K_{\text{Ce0-H}}$ (1).

And lastly, the non-dimensional version of Eq. 3.63:

$$\bar{x}_{13} = \frac{1-\alpha\bar{x}_1^{\beta}}{1+N_{\text{dp0}}\left(\bar{x}_1 - \left(\frac{\alpha}{m}\right)\bar{x}_1^{\beta}\right)} \qquad \text{(Da)} \tag{3.76}$$

with $\frac{M_{\text{unit}}}{M_{\text{n0}}} = \frac{C_{\text{chain0}}}{C_{\text{e0}}} = N_{\text{dp0}}^{-1}$ and N_{dp0}, the initial average degree of pseudo-polymerisation ($\text{Da}\,\text{Da}^{-1}$).

To attain the numerical solution of the system of equations a similar approach than the one used for the TCP system was used (see Sect. 3.2.1). In this case the yielded $\bar{x}_2$ polynomial is a 6th degree polynomial, $A + B\bar{x}_2 + C\bar{x}_2^2 + D\bar{x}_2^3 + E\bar{x}_2^4 + F\bar{x}_2^5 + G\bar{x}_2^6$ with:

$$A = -5M_{\text{n0}}\bar{K}_1\bar{K}_2\bar{K}_3\bar{K}_{\text{a}}\bar{K}_{\text{w}}K_{\text{OH-H}} \tag{3.77a}$$

$$B = -\Big((M_{\text{unit}} + \bar{x}_1 M_{\text{n0}})K_{\text{Ce0-H}} + \Delta\bar{C}_{\text{H}_0^+}M_{\text{n0}} - \Delta\bar{C}_{\text{OH}_0^-}K_{\text{OH-H}}M_{\text{n0}}\Big)5\bar{K}_1\bar{K}_2\bar{K}_3\bar{K}_{\text{a}} + M_{\text{n0}}\bar{K}_1\bar{K}_2\bar{K}_3\bar{K}_{\text{a}}\bar{x}_3K_{\text{Ca-H}} - 5M_{\text{n0}}\bar{K}_1\bar{K}_2\bar{K}_{\text{w}}K_{\text{OH-H}}(\bar{K}_{\text{a}} + \bar{K}_3) \tag{3.77b}$$

$$C = -\Big((M_{\text{unit}} + \bar{x}_1 M_{\text{n0}})K_{\text{Ce0-H}} + \Delta\bar{C}_{\text{H}_0^+}M_{\text{n0}} - \Delta\bar{C}_{\text{OH}_0^-}K_{\text{OH-H}}M_{\text{n0}}\Big)5\bar{K}_1\bar{K}_2\bar{K}_{\text{a}} + M_{\text{n0}}\bar{K}_1\bar{K}_2\Big(\bar{x}_3K_{\text{Ca-H}}(4\bar{K}_{\text{a}} + \bar{K}_3) - 5\bar{K}_3(\Delta\bar{C}_{\text{H}_0^+} - \Delta\bar{C}_{\text{OH}_0^-}K_{\text{OH-H}}) + 5\bar{K}_3\bar{K}_{\text{a}}\Big) - 5M_{\text{n0}}\bar{K}_1\bar{K}_{\text{w}}K_{\text{OH-H}}(\bar{K}_{\text{a}} + \bar{K}_2) \tag{3.77c}$$

$$D = -\Big((M_{\text{unit}} + \bar{x}_1 M_{\text{n0}})K_{\text{Ce0-H}} + \Delta\bar{C}_{\text{H}_0^+}M_{\text{n0}} - \Delta\bar{C}_{\text{OH}_0^-}K_{\text{OH-H}}M_{\text{n0}}\Big)5\bar{K}_1\bar{K}_{\text{a}} + M_{\text{n0}}\bar{K}_1\Big(\bar{x}_3K_{\text{Ca-H}}(7\bar{K}_{\text{a}} + 4\bar{K}_2) - 5\bar{K}_2(\Delta\bar{C}_{\text{H}_0^+} - \Delta\bar{C}_{\text{OH}_0^-}K_{\text{OH-H}}) + 5\bar{K}_2(\bar{K}_{\text{a}} + \bar{K}_3)\Big) - 5M_{\text{n0}}\bar{K}_{\text{w}}K_{\text{OH-H}}(\bar{K}_{\text{a}} + \bar{K}_1) \tag{3.77d}$$

$$E = -\Big((M_{\text{unit}} + \bar{x}_1 M_{\text{n0}})K_{\text{Ce0-H}} + \Delta\bar{C}_{\text{H}_0^+}M_{\text{n0}} - \Delta\bar{C}_{\text{OH}_0^-}K_{\text{OH-H}}M_{\text{n0}}\Big)5\bar{K}_{\text{a}} + M_{\text{n0}}\Big(\bar{x}_3K_{\text{Ca-H}}(10\bar{K}_{\text{a}} + 7\bar{K}_1) - 5\bar{K}_1(\Delta\bar{C}_{\text{H}_0^+} - \Delta\bar{C}_{\text{OH}_0^-}K_{\text{OH-H}}) + 5\bar{K}_1(\bar{K}_{\text{a}} + \bar{K}_2)\Big) - 5M_{\text{n0}}\bar{K}_{\text{w}}K_{\text{OH-H}} \tag{3.77e}$$

$$F = M_{\text{n0}}\Big(10\bar{x}_3K_{\text{Ca-H}} - 5(\Delta\bar{C}_{\text{H}_0^+} - \Delta\bar{C}_{\text{OH}_0^-}K_{\text{OH-H}}) + 5(\bar{K}_{\text{a}} + \bar{K}_1)\Big) \tag{3.77f}$$

$$G = 5M_{n0} \tag{3.77g}$$

The six roots of the polynomial were found with a customised implementation of a Householder root-finding algorithm and the $\bar{x}_2$ value with physical meaning was used to solve the system of equations using a procedure similar to the one employed in the TCP model.

In summary, this section presented and discussed the degradation model for hydroxyapatite composites, which fully captures the HA degradation phenomena using a set of thirteen equations. The numerical solution of the model, briefly discussed here too, provides the evolution of the thirteen degradation magnitudes of interest over time. Similarly to the TCP model, the evolution of the number-average molecular weight of the polymer phase, M_n, over time is of special interest due to its prevailing use as composite degradation measurement. For a given hydroxyapatite case study, the degradation is defined exclusively by a set of four values for k_1, k_2', A_d and θ, with k_1 (s^{-1}) and k_2' ($m^3\,mol^{-1}\,s^{-1}$) the non-catalytic and autocatalytic polymer hydrolysis rate constants respectively; and A_d ($mol\,m^{-2}\,s^{-1}$) and θ (1), the rate constant and exponent of the TCP dissolution power law respectively; requiring just a series of polymer-dependent, ceramic-dependent and composite-dependent constants, in addition to the initial values of the thirteen variables to provide the evolution over time of the complete composite degradation characterisation.

3.2.3 Calcium Carbonate (CC) Composites Degradation Model

The particularisation of the general modelling framework for composites containing spherical particles made of calcium carbonate, whose chemical composition is $CaCO_3$, produces a set of ten governing equations. In a similar fashion to Sects. 3.2.1 and 3.2.2, the variables are named x_1, x_2, …, and x_{10}. x_1, x_2, x_3, x_5, and x_6 represent the same magnitudes than in the TCP model (see Sect. 3.2.1) and HA model (see Sect. 3.2.2). x_4, x_7, x_8, x_9 and x_{10} represent different magnitudes due to the change in anions resulting from ceramic dissolution:

- $x_4 = [CO_3^{2-}]$, concentration of carbonate ions in the polymer phase ($mol\,m^{-3}$).
- $x_7 = [HCO_3^-]$, concentration of hydrogen carbonate ions in the polymer phase ($mol\,m^{-3}$).
- $x_8 = [H_2CO_3]$, concentration of carbonic acid in the polymer phase ($mol\,m^{-3}$).
- $x_9 = a_{CC}$, total area of interface between the two phases, calcium carbonate and polymer, per unit of volume of the composite ($m^2\,m^{-3}$).
- $x_{10} = M_n$, number-average molecular weight of the polymer phase (Da).

Calcium carbonate, as opposed to tricalcium phosphate and hydroxyapatite, is not a calcium orthophosphate and therefore releases Ca^{2+} and CO_3^{2-} ions, instead of PO_4^{3-} ions, during dissolution. The presence of carbonate ions causes significant

changes and differences with respect to the previous TCP and HA models, described in Sects. 3.2.1 and 3.2.2 respectively.

In the first group, the equations showing the time-dependence of x_1, x_3 and x_9 are introduced. The second and third equations present slight variations with respect to the previous models due to the different filler chemistry. Framework equation 3.2 particularised for a given type of scissions excluding short chains is used to describe the variation of x_1 over time:

$$\frac{\mathrm{d}x_1}{\mathrm{d}t} = C_{e0}\left[1 - \alpha\left(\frac{x_1}{C_{e0}}\right)^{\beta}\right](k_1 + k_2' x_2) \qquad (\mathrm{mol\,m^{-3}\,s^{-1}}) \qquad (3.78)$$

with C_{e0}, the initial concentration in the polymer phase of ester bonds in long chains ($\mathrm{mol\,m^{-3}}$); α (1) and β (1), the empirical parameters used to characterise the polymer scission type and the subsequent production of short chains by chain scission; k_1 ($\mathrm{s^{-1}}$) and k_2' ($\mathrm{m^3\,mol^{-1}\,s^{-1}}$), the non-catalytic and autocatalytic polymer hydrolysis rate constants respectively and x_2, the concentration of hydrogen ions in the polymer phase ($\mathrm{mol\,m^{-3}}$).

Framework equation 3.11 particularised for CC ($CaCO_3$) with the number of calcium ions per CC molecule $I_{cer}^{Ca} = 1$ ($\mathrm{mol\,mol^{-1}}$), the ionic product $I_P = x_3 x_4$ ($\mathrm{mol^2\,m^6}$) and the total number of ions in a CC molecule $\eta = 2$ ($\mathrm{mol\,mol^{-1}}$) is used to describe the variation of x_3 with time:

$$\frac{\mathrm{d}x_3}{\mathrm{d}t} = \frac{x_9}{1 - f_{CC0}} A_d \left[1 - \left(\frac{x_3 x_4}{K_{sp}}\right)^{\frac{1}{2}}\right]^{\theta} \qquad (\mathrm{mol\,m^{-3}\,s^{-1}}) \qquad (3.79)$$

with f_{CC0}, the initial volume fraction of CC in the composite ($\mathrm{m^3\,m^{-3}}$); K_{sp}, the CC solubility product at 37 °C ($\mathrm{mol^2\,m^{-6}}$) and A_d and θ, the rate constant ($\mathrm{mol\,m^{-2}\,s^{-1}}$) and exponent (1) of the CC dissolution power law respectively.

Framework equation 3.13 particularised for spherical particles as shown in Sect. 3.2.1 and with $I_{cer}^{Ca} = 1$ ($\mathrm{mol\,mol^{-1}}$) is used to characterise the rate of x_9:

$$\frac{\mathrm{d}x_9}{\mathrm{d}t} = -4\pi^{\frac{1}{2}}\left(\frac{1}{V_{unit}}\right)^{\frac{1}{2}} \Omega_{CC}(1 - f_{CC0})\left(\frac{1}{x_9}\right)^{\frac{1}{2}} \frac{\mathrm{d}x_3}{\mathrm{d}t} \qquad (\mathrm{m^2\,m^{-3}\,s^{-1}}) \qquad (3.80)$$

with V_{unit}, the volume of the representative unit ($\mathrm{m^3}$); Ω_{CC}, the CC molar volume ($\mathrm{m^3\,mol^{-1}}$) and f_{CC0}, the initial CC volume fraction ($\mathrm{m^3\,m^{-3}}$).

The second group of equations encompasses the remaining seven equations, relating x_2, x_4, x_5, x_6, x_7, x_8 and x_{10} and to x_1, x_3 and x_9. The first two equation of this group describe the other relevant characteristics of the polymer phase using the unmodified framework equations 3.3 and 3.4:

$$K_a = \frac{x_2 x_6}{x_5} \qquad (\mathrm{mol\,m^{-3}}) \qquad (3.81)$$

$$x_6 + x_5 = C_{\text{chain0}} + x_1 \qquad (\text{mol m}^{-3}) \tag{3.82}$$

with K_a, the equilibrium constant for the deprotonation reaction of the carboxylic end group for the chosen polymer at 37 °C (mol m^{-3}) and C_{chain0}, the initial concentration of polymer chains in the polymer phase (mol m^{-3}).

The dissolution of the CC particles results in the release of carbonate ions, CO_3^{2-} [15]. These anions can bind available hydrogen ions following the inverse deprotonation route of carbonic acid. The relationship between the concentrations of hydrogen ions, x_2 (mol m^{-3}); free carbonate ions, x_4 (mol m^{-3}) and recombined carbonate ions in all their states, x_7 (mol m^{-3}) and x_8 (mol m^{-3}) is described by the particularisation of framework equation 3.15 using $B^{n-} = CO_3^{2-}$:

$$K_2 = \frac{x_2 x_4}{x_7} \qquad [16] \quad (\text{mol m}^{-3}) \tag{3.83}$$

$$K_1 = \frac{x_2 x_7}{x_8} \qquad [17] \quad (\text{mol m}^{-3}) \tag{3.84}$$

with K_2, K_1, the equilibrium constants for the deprotonation reactions at 37 °C of hydrogen carbonate ion (mol m^{-3}) and carbonic acid (mol m^{-3}) respectively.

Framework equation 3.16 particularised for CC using $I_{\text{cer}}^{B_1} = I_{\text{cer}}^{CO_3} = 1$ (mol mol^{-1}), $I_{\text{cer}}^{Ca} = 1$ (mol mol^{-1}) and $B^{n-} = CO_3^{2-}$ describes the mass conservation relationship of the concentrations of calcium ions, x_4 (mol m^{-3}) and carbonate ions in all their recombining states, x_7 (mol m^{-3}) and x_8 (mol m^{-3}):

$$x_3 = x_4 + x_7 + x_8 \qquad (\text{mol m}^{-3}) \tag{3.85}$$

Framework equation 3.17 particularised for CC using $B^{n-} = CO_3^{2-}$ describes the mass conservation relationship of hydrogen ions in units of concentration:

$$x_2 + x_7 + 2x_8 = x_6 + \Delta C_{H_0^+} \qquad (\text{mol m}^{-3}) \tag{3.86}$$

with $\Delta C_{H_0^+}$, the hydrogen ions concentration at the time origin, i.e., the initial hydrogen ions concentration not resulting from carboxylic end groups dissolution (mol m^{-3}).

The last equation of the CC model expresses the number-average molecular weight, x_{10} (Da), as a function of the concentration of chain scissions, x_1 (mol m^{-3}), using the framework equation 3.6 particularised for a given type of polymer scission using the empirical relationship ${}^{R_{oi}}/_{C_{e0}} = \alpha({}^{R_s}/_{C_{e0}})^{\beta}$ to characterise the production of short chains:

$$x_{10} = \frac{C_{e0}\left[1 - \alpha\left(\frac{x_1}{C_{e0}}\right)^{\beta}\right] M_{\text{unit}}}{C_{\text{chain0}} + R_s - \frac{C_{e0}}{m}\alpha\left(\frac{x_1}{C_{e0}}\right)^{\beta}} \qquad (\text{Da}) \tag{3.87}$$

with C_{e0}, the initial concentration in the polymer phase of ester bonds in long chains (mol m^{-3}); α (1) and β (1), the empirical parameters used to characterise the polymer

scission type and the subsequent production of short chains by chain scission; M_{unit}, the molar mass associated to one ester bond (Da); C_{chain0}, the initial concentration of long polymer chains in the polymer phase (mol m^{-3}) and m, the average degree of pseudo-polymerisation of the short chains (1).

The next step in order to solve the system of equation is the application of the nondimensionalisation procedure to the set of ten equations comprising from Eqs. 3.78 to 3.87. The set of non-dimensional variables is defined as follows:

- $\bar{x}_1 = \frac{x_1}{C_{e0}} = \frac{R_s}{C_{e0}} = \bar{R}_s$, nondimensionalised concentration of chain scissions (1).
- $\bar{x}_2 = \frac{x_2}{(C_{H^+})_{pH=7.4}} = \frac{C_{H^+}}{(C_{H^+})_{pH=7.4}} = \bar{C}_{H^+}$, nondimensionalised concentration of hydrogen ions (1).
- $\bar{x}_3 = \frac{x_3}{[Ca^{2+}]_{eq}} = \frac{[Ca^{2+}]}{[Ca^{2+}]_{eq}} = [\overline{Ca}^{2+}]$, nondimensionalised concentration of calcium ions (1).
- $\bar{x}_4 = \frac{x_4}{(C_{H^+})_{pH=7.4}} = \frac{[CO_3^{2-}]}{(C_{H^+})_{pH=7.4}} = [\overline{CO}_3^{2-}]$, nondimensionalised concentration of carbonate ions (1).
- $\bar{x}_5 = \frac{x_5}{C_{e0}} = \frac{[R\text{-}COOH]}{C_{e0}} = [\overline{R\text{-}COOH}]$, nondimensionalised concentration of non-dissociated carboxylic end group chains (1).
- $\bar{x}_6 = \frac{x_6}{C_{e0}} = \frac{[R\text{-}COO^-]}{C_{e0}} = [\overline{R\text{-}COO}^-]$, nondimensionalised concentration of dissociated carboxylic end group chains (1).
- $\bar{x}_7 = \frac{x_7}{(C_{H^+})_{pH=7.4}} = \frac{[HCO_3^-]}{(C_{H^+})_{pH=7.4}} = [\overline{HCO}_3^-]$, nondimensionalised concentration of hydrogen carbonate ions (1).
- $\bar{x}_8 = \frac{x_8}{(C_{H^+})_{pH=7.4}} = \frac{[H_2CO_3]}{(C_{H^+})_{pH=7.4}} = [\overline{H_2CO}_3]$, nondimensionalised concentration of carbonic acid (1).
- $\bar{x}_9 = \frac{x_9}{a_{CC0}} = \frac{a_{CC}}{a_{CC0}} = \bar{a}_{CC}$, nondimensionalised total area of interface between the two phases, calcium carbonate and polymer, per unit of volume of the composite (1).
- $\bar{x}_{10} = \frac{x_{10}}{M_{n0}} = \frac{M_n}{M_{n0}} = \overline{M}_n$, nondimensionalised number-average molecular weight (1).

with the concentrations $x_1, \ldots, x_8$ defined per unit of polymer phase.

During the adimensionalisation process five different constants were used: $(C_{H^+})_{pH=7.4}$, the hydrogen ions concentration at a pH equals to 7.4 (mol m^{-3}); $[Ca^{2+}]_{eq}$, the calcium ions concentration at dissolution equilibrium (mol m^{-3}); C_{e0}, the concentration in the polymer phase of ester bonds in long chains at the time origin (mol m^{-3}); a_{CC0}, the value of a_{CC} at the time origin (m^2 m^{-3}) and M_{n0}, the polymer number-average molecular weight at the time origin (Da).

With this set of non-dimensional variables the following set of non-dimensional equations was obtained. Firstly, the three nondimensionalised differential equations are listed, starting with the non-dimensional version of Eq. 3.78:

$$\frac{d\bar{x}_1}{d\bar{t}} = (1 - \alpha \bar{x}_1^{\beta})(\bar{k}_1 + \bar{x}_2) \qquad (1) \qquad (3.88)$$

with $\bar{k}_1 = \frac{k_1}{k_2'(C_{H^+})_{pH=7.4}}$ (1) and $\bar{t} = tk_2'(C_{H^+})_{pH=7.4}$ (1).

Secondly, the non-dimensional version of Eq. 3.79:

$$\frac{\mathrm{d}\bar{x}_3}{\mathrm{d}\bar{t}} = \frac{a_{\mathrm{CC0}}A_{\mathrm{d}}}{k_2'(C_{\mathrm{H}^+})_{\mathrm{pH}=7.4}[Ca^{2+}]_{\mathrm{eq}}(1-f_{\mathrm{CC0}})}\bar{x}_{10}\left(1-\left(\frac{\bar{x}_3\bar{x}_4}{\frac{K_{\mathrm{sp}}}{[Ca^{2+}]_{\mathrm{eq}}[(C_{\mathrm{H}^+})_{\mathrm{pH}=7.4}]}}\right)^{\frac{1}{2}}\right)^{\theta}$$
$$= S_{\mathrm{CC}}\bar{x}_9\sigma^{\theta} \quad (1) \qquad (3.89)$$

with $S_{\mathrm{CC}} = \frac{a_{\mathrm{CC0}}A_{\mathrm{d}}}{k_2'(C_{\mathrm{H}^+})_{\mathrm{pH}=7.4}[Ca^{2+}]_{\mathrm{eq}}(1-f_{\mathrm{CC0}})}$ (1), $\sigma^{\theta} = \left(1-\left(\frac{\bar{x}_3\bar{x}_4}{\bar{K}_{\mathrm{sp}}}\right)^{\frac{1}{2}}\right)^{\theta}$ (1) and $\bar{K}_{\mathrm{sp}} = \frac{K_{\mathrm{sp}}}{[Ca^{2+}]_{\mathrm{eq}}[(C_{\mathrm{H}^+})_{\mathrm{pH}=7.4}]}$ (1).

And finally, the non-dimensional version of Eq. 3.80:

$$\frac{\mathrm{d}\bar{x}_9}{\mathrm{d}\bar{t}} = \frac{-4\pi^{\frac{1}{2}}\Omega_{\mathrm{CC}}(1-f_{\mathrm{CC0}})[Ca^{2+}]_{\mathrm{eq}}}{V_{\mathrm{unit}}^{\frac{1}{2}}a_{\mathrm{CC0}}^{\frac{3}{2}}}\frac{\mathrm{d}\bar{x}_3}{\mathrm{d}\bar{t}}\bar{x}_{10}^{-\frac{1}{2}}$$
$$= K_{\mathrm{a_{CC}}}\frac{\mathrm{d}\bar{x}_3}{\mathrm{d}\bar{t}}\bar{x}_9^{-\frac{1}{2}} \quad (1) \qquad (3.90)$$

with $K_{\mathrm{a_{CC}}} = \frac{-4\pi^{\frac{1}{2}}\Omega_{\mathrm{CC}}(1-f_{\mathrm{CC0}})[Ca^{2+}]_{\mathrm{eq}}}{V_{\mathrm{unit}}^{\frac{1}{2}}a_{\mathrm{CC0}}^{\frac{3}{2}}}$ (1).

The second group of nondimensionalised equations, formed by seven equations, is presented here:

Non-dimensional version of Eq. 3.81:

$$\bar{K}_{\mathrm{a}} = \frac{\bar{x}_2\bar{x}_6}{\bar{x}_5} \quad (1) \qquad (3.91)$$

with $\bar{K}_{\mathrm{a}} = \frac{K_{\mathrm{a}}}{(C_{\mathrm{H}^+})_{\mathrm{pH}=7.4}}$ (1).

Non-dimensional version of Eq. 3.82:

$$\bar{x}_6 + \bar{x}_5 = \frac{M_{\mathrm{unit}}}{M_{\mathrm{n0}}} + \bar{x}_1 \quad (1) \qquad (3.92)$$

with $\frac{M_{\mathrm{unit}}}{M_{\mathrm{n0}}} = \frac{C_{\mathrm{chain0}}}{C_{\mathrm{e0}}} = N_{\mathrm{dp0}}^{-1}$ (1) where M_{unit}, is the molar mass associated to one ester bond (Da); M_{n0}, the number-average molecular weight at the time origin (Da) and N_{dp0}, the initial average degree of pseudo-polymerisation ($\mathrm{Da\,Da^{-1}}$).

Non-dimensional version of Eqs. 3.83 and 3.84:

$$\bar{K}_2 = \frac{\bar{x}_2\bar{x}_4}{\bar{x}_7} \quad (1) \qquad (3.93)$$

$$\bar{K}_1 = \frac{\bar{x}_2\bar{x}_7}{\bar{x}_8} \quad (1) \qquad (3.94)$$

with $\bar{K}_1 = \frac{K_1}{(C_{H^+})_{pH=7.4}}$ (1) and $\bar{K}_2 = \frac{K_2}{(C_{H^+})_{pH=7.4}}$ (1).

Non-dimensional version of Eq. 3.85:

$$\bar{x}_3 K_{\text{Ca-H}} = \bar{x}_4 + \bar{x}_7 + \bar{x}_8 \qquad (1) \qquad (3.95)$$

with $K_{\text{Ca-H}} = \frac{[Ca^{2+}]_{eq}}{(C_{H^+})_{pH=7.4}}$ (1).

Non-dimensional version of Eq. 3.86:

$$\bar{x}_2 + \bar{x}_7 + 2\bar{x}_8 = \bar{x}_6 K_{C_{e0}\text{-H}} + \Delta\bar{C}_{H_0^+} \qquad (1) \qquad (3.96)$$

with $K_{C_{e0}\text{-H}} = \frac{C_{e0}}{(C_{H^+})_{pH=7.4}}$ (1) and $\Delta\bar{C}_{H_0^+} = \bar{C}_{H_0^+} - \bar{x}_6(t=0)K_{C_{e0}\text{-H}} = \frac{C_{H_0^+}}{(C_{H^+})_{pH=7.4}} - \bar{x}_6(t=0)K_{C_{e0}\text{-H}}$ (1).

And finally, the non-dimensional version of Eq. 3.87:

$$\bar{x}_{10} = \frac{1 - \alpha\bar{x}_1^{\beta}}{1 + N_{dp0}\left(\bar{x}_1 - \left(\frac{\alpha}{m}\right)\bar{x}_1^{\beta}\right)} \qquad (\text{Da}) \qquad (3.97)$$

with $\frac{M_{unit}}{M_{n0}} = \frac{C_{chain0}}{C_{e0}} = N_{dp0}^{-1}$ and N_{dp0}, the initial average degree of pseudo-polymerisation ($\text{Da}\,\text{Da}^{-1}$).

In a similar fashion, in order to solve the system of equations the same procedure than before was applied (see Sect. 3.2.1). In the CC model the yielded $\bar{x}_2$ polynomial is a 4th degree polynomial, $A + B\bar{x}_2 + C\bar{x}_2^2 + D\bar{x}_2^3 + E\bar{x}_2^4$ with:

$$A = -\left((M_{unit} + \bar{x}_1 M_{n0})K_{C_{e0}\text{-H}} + \Delta\bar{C}_{H_0^+}M_{n0}\right)\bar{K}_1\bar{K}_2\bar{K}_a \qquad (3.98a)$$

$$B = -\left((M_{unit} + \bar{x}_1 M_{n0})K_{C_{e0}\text{-H}} + \Delta\bar{C}_{H_0^+}M_{n0}\right)\bar{K}_1\bar{K}_a + M_{n0}\bar{K}_1\left(\bar{x}_3 K_{\text{Ca-H}}\bar{K}_a + \bar{K}_2(\bar{K}_a - \Delta\bar{C}_{H_0^+})\right) \qquad (3.98b)$$

$$C = -\left((M_{unit} + \bar{x}_1 M_{n0})K_{C_{e0}\text{-H}} + \Delta\bar{C}_{H_0^+}M_{n0}\right)\bar{K}_a + M_{n0}\left(\bar{x}_3 K_{\text{Ca-H}}(\bar{K}_1 + 2\bar{K}_a) + \bar{K}_1(\bar{K}_2 + \bar{K}_a - \Delta\bar{C}_{H_0^+})\right) \qquad (3.98c)$$

$$D = M_{n0}(2\bar{x}_3 K_{\text{Ca-H}} + \bar{K}_1 + \bar{K}_a - \Delta\bar{C}_{H_0^+}) \qquad (3.98d)$$

$$E = M_{n0} \qquad (3.98e)$$

The four $\bar{x}_2$ values were found using a fourth degree customised Householder root-finding algorithm. After selecting the $\bar{x}_2$ value with physical meaning all the other variables were calculated following the approach explained in Sect. 3.2.1.

This section, the last one concerned with the presentation of composite degradation models, introduced and discussed the degradation model for calcium carbonate composites. Briefly, the model fully captures the CC degradation phenomena using a set of ten equations, which provides the evolution of ten magnitudes of interest over time, when numerically solved. Similarly to the previous models, the evolution over time of the number-average molecular weight of the polymer phase, M_n, is specially interesting due to its common use as composite degradation measurement. For a given calcium carbonate case study, the degradation is defined exclusively by a set of four values for k_1, k_2', A_d and θ, with k_1 (s^{-1}) and k_2' ($m^3\,mol^{-1}\,s^{-1}$) the non-catalytic and autocatalytic polymer hydrolysis rate constants respectively, and A_d ($mol\,m^{-2}\,s^{-1}$) and θ (1), the rate constant and exponent of the TCP dissolution power law respectively. The use of a series of polymer-dependent, ceramic-dependent and composite-dependent constants, in addition to the initial values of the ten variables allows the computation of the degradation magnitudes of interest.

3.3 Characterisation of the Representative Unit Cell

As introduced in Sect. 3.1, the modelling framework and, subsequently the ceramic-specific degradation models derived from it, employ an unit cell as representation of the composite sample. This section discusses in detail the characterisation of this unit cell.

The representative unit cell is composed of a ceramic particle surrounded by a determined quantity of polymer phase. In order to fully characterise this unit cell, the following parameters are needed:

- Representative ceramic particle size, d_0 (m): diameter of the spherical particle which conveys the initial properties of the ceramic particle size distribution in terms of surface to volume ratio. The initial ceramic volume, V_{cer0} (m^3), can be easily computed using d_0, as $V_{cer0} = \frac{\pi}{6} d_0^3$. In the implemented computational models, the representative ceramic particle size was calculated beforehand following the process explained in Sect. 3.5.2 and then directly input into the corresponding model.
- Quantity of polymer surrounding the particle, V_{pol}: corresponding amount of polymer phase assigned to a representative particle. Conventionally, in the published experimental degradation data, composites are reported as having a ceramic weight fraction or percentage in the composite, f_{wCer0}, where a value of $f_{wCer0} = 20\,wt\,\%$ means that the undegraded composite has a $20\,wt\,\%$ of ceramic and of $80\,wt\,\%$ polymer. V_{pol} can be expressed as a function of f_{wCer0} as shown below.
- Unit cell volume, V_{unit}: the volume occupied by the constituent elements of the unit cell at the time origin, i.e. the initial ceramic particle and the surrounding polymer. When two of the three elements are known, it is trivial to compute the remaining using $V_{unit} = V_{pol} + \frac{\pi}{6} d_0^3$.

V_{unit} (m^3) and V_{pol} (m^3) can be computed using f_{wCer0} (wt %) following a series of steps. Firstly, the ceramic volume fraction can be expressed in an analogous manner to the ceramic weight fraction ($f_{\text{wCer0}} = {}^{m_{\text{cer0}}}/_{m_{\text{comp}}}$) as:

$$f_{\text{cer0}} = \frac{V_{\text{cer0}}}{V_{\text{unit}}} = \frac{\frac{\pi}{6} d_0^3}{V_{\text{unit}}} \qquad (\text{m}^3\,\text{m}^{-3}) \tag{3.99}$$

The volume of the unit cell, V_{unit} (m^3), can be easily characterised as function of f_{wCer0} using Eq. 3.99 and the relationship between the ceramic volume fraction and weight fraction, $F_{\text{wtov}} = {}^{f_{\text{cer0}}}/_{f_{\text{wCer0}}}$:

$$V_{\text{unit}} = \frac{\frac{\pi}{6} d_0^3}{f_{\text{cer0}}} = \frac{\frac{\pi}{6} d_0^3}{f_{\text{wCer0}} F_{\text{wtov}}} \qquad (\text{m}^3) \tag{3.100}$$

Using the polymer density, ρ_{pol} ($\text{kg}\,\text{m}^{-3}$) ($\rho_{\text{pol}} = \frac{m_{\text{pol}}}{V_{\text{pol}}}$), and the ceramic density ρ_{cer} ($\text{kg}\,\text{m}^{-3}$) ($\rho_{\text{cer}} = \frac{m_{\text{cer}}}{V_{\text{cer}}}$), the expression of F_{wtov} can be expressed as:

$$F_{\text{wtov}} = \frac{f_{\text{cer0}}}{f_{\text{wCer0}}} = \frac{V_{\text{cer0}} m_{\text{comp}}}{V_{\text{comp}} m_{\text{cer0}}} = \frac{\frac{m_{\text{cer0}}}{\rho_{\text{cer}}} m_{\text{comp}}}{\frac{m_{\text{comp}}}{\rho_{\text{comp}}} m_{\text{cer0}}} = \frac{\rho_{\text{comp}}}{\rho_{\text{cer}}} \qquad (1) \tag{3.101}$$

The density of the composite, ρ_{comp} ($\text{kg}\,\text{m}^{-3}$) ($\rho_{\text{comp}} = \frac{m_{\text{comp}}}{V_{\text{comp}}}$), can be calculated assuming linear mixture of volumes as:

$$\begin{aligned}
\rho_{\text{comp}} &= \frac{m_{\text{comp}}}{V_{\text{comp}}} = \frac{m_{\text{pol}} + m_{\text{cer0}}}{V_{\text{pol}} + V_{\text{cer0}}} = \frac{m_{\text{pol}} + m_{\text{cer0}}}{\frac{m_{\text{pol}}}{\rho_{\text{pol}}} + \frac{m_{\text{cer0}}}{\rho_{\text{cer}}}} \\
&= \frac{\left(m_{\text{pol}} + m_{\text{cer0}}\right) \rho_{\text{pol}} \rho_{\text{cer}}}{m_{\text{pol}} \rho_{\text{cer}} + m_{\text{cer0}} \rho_{\text{pol}}} \\
&= \frac{m_{\text{comp}} \rho_{\text{pol}} \rho_{\text{cer}}}{\left(1 - f_{\text{wCer0}}\right) m_{\text{comp}} \rho_{\text{cer}} + f_{\text{wCer0}} m_{\text{comp}} \rho_{\text{pol}}} \\
&= \frac{\rho_{\text{pol}} \rho_{\text{cer}}}{\left(1 - f_{\text{wCer0}}\right) \rho_{\text{cer}} + f_{\text{wCer0}} \rho_{\text{pol}}} \qquad (\text{kg}\,\text{m}^{-3})
\end{aligned} \tag{3.102}$$

Lastly, the substitution of Eq. 3.102 in 3.101 gives the final expression of F_{wtov}:

$$\begin{aligned}
F_{\text{wtov}} &= \frac{\rho_{\text{pol}} \rho_{\text{cer}}}{\rho_{\text{cer}} \left(\left(1 - f_{\text{wCer0}}\right) \rho_{\text{cer}} + f_{\text{wCer0}} \rho_{\text{pol}} \right)} \\
&= \frac{\rho_{\text{pol}}}{\left(1 - f_{\text{wCer0}}\right) \rho_{\text{cer}} + f_{\text{wCer0}} \rho_{\text{pol}}} \qquad (1)
\end{aligned} \tag{3.103}$$

with the polymer density, ρ_{pol} ($\text{kg}\,\text{m}^{-3}$), and the ceramic density ρ_{cer} ($\text{kg}\,\text{m}^{-3}$), defined by the polymer and ceramic types employed in the composite and the initial ceramic weight fraction, f_{wCer0} (wt %) defined by the specific given composite sample.

Equations 3.103, 3.100 and $V_{pol} = V_{unit} - \frac{\pi}{6} d_0^3$ provide all the necessary information to express the unit cell parameters with known constants and parameters for a given composite. During composite degradation, the modelling framework assumes that V_{unit} remains unchanged over time and therefore that no significant swelling occurs. The polymer volume, V_{pol}, is also assumed to remain constant during composite degradation. Although the ceramic volume in the unit cell, V_{cer} (m^3), decreases over time as the ceramic dissolution progresses, the change is modest due to the sparingly soluble behaviour of the considered calcium-based ceramics. Thus, it seems reasonable to assume that the polymer volume also remains constant given a constant V_{unit} over time.

After presenting both the key parameters and calculation process of the representative unit cell, an analysis of how the unit cell reflects changes in composite samples is discussed. Figure 3.7 shows the effect of having different ceramic weight fractions or percentages, f_{wCer0} (wt %), and different representative particle sizes, d_0 (m) on the representative unit cell for a poly(L-lactide)–β-tricalcium phosphate composite.

Nine different unit cells, representing a variety of d_0–f_{wCer0} combinations, are included in Fig. 3.7, where the x–axis conveys the ceramic weight fraction, f_{wCer0} (wt %) and the y–axis conveys the representative ceramic particle size, d_0 (m) of the representative unit cells. In order to evaluate the effect of these two defining parameters on the characteristics of the resulting representative unit cell and subsequent composite degradation behaviour, it is convenient to analyse the properties related to them.

As ceramic dissolution is a surface area mediated phenomenon, the ratio of initial ceramic surface area, S_{cer0} (m^2), to initial ceramic volume, V_{cer0} (m^3), can be used to express potential contribution of different ceramic particles. This ratio can be expressed as a function of the ceramic representative particle size, d_0 (m), as:

$$\frac{S_{cer0}}{V_{cer0}} = \frac{6\pi d_0^2}{\pi d_0^3} = \frac{6}{d_0} \qquad (m^{-1}) \tag{3.104}$$

To assess the differences between unit cells with different quantities of polymer and ceramic phases, the ratio between initial ceramic volume, V_{cer0} (m^3), and polymer volume, V_{pol} (m^3), can be employed. Using Eq. 3.99 and the relationship between the ceramic volume fraction and weight fraction, $F_{wtov} = {}^{f_{cer0}}/_{f_{wCer0}}$, this ratio can be expressed as a function of f_{wCer0} (wt %), the ceramic weight fraction of the composite as:

$$\frac{V_{cer0}}{V_{pol}} = \frac{V_{unit} f_{cer0}}{V_{pol}} = \frac{f_{cer0}}{1 - f_{cer0}} = \frac{F_{wtov} f_{wCer0}}{1 - F_{wtov} f_{wCer0}} \qquad (m) \tag{3.105}$$

Equations 3.104 and 3.105 highlight the properties controlled by each one of the two composite defining parameters. These relationships translate into certain properties in the rows and columns of Fig. 3.7. Unit cells sharing the same row present the same ceramic particle size, d_0 (m), and different ceramic weight fraction, f_{wCer0} (wt %), which results in the unit cells having the same ${}^{S_{cer0}}/_{V_{cer0}}$ ratio and increasing

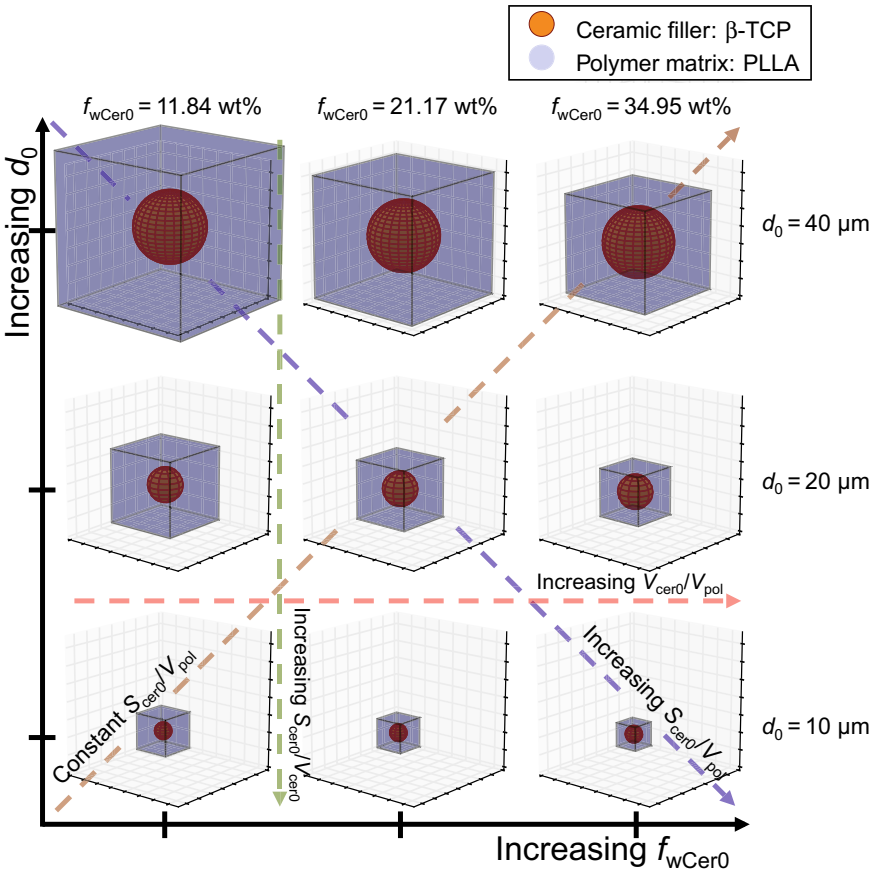

Fig. 3.7 The effect of varying ceramic weight fraction or percentage, f_{wCer0} (wt %), and representative particle size, d_0 (m), on the representative unit cell for composite samples made of poly(L-lactide) and β-tricalcium phosphate. The distance between two consecutive marks in any axis of a single representative unit cell is 5 μm, for a total length of 75 μm in each axis

V_{cer0}/V_{pol} ratio with increasing ceramic weight fraction f_{wCer0} as pointed by the red dashed arrow line. In a similar fashion, unit cells sharing the same column present the same ceramic weight fraction, f_{wCer0} (wt %), and different ceramic particle size, d_0 (m), which results in those cell having the same V_{cer0}/V_{pol} and decreasing values of S_{cer0}/V_{cer0} with increasing ceramic particle size, d_0 as pointed by the green dashed arrow line.

As previously mentioned, ceramic dissolution is a surface mediated phenomenon, while polymer degradation is a bulk phenomena. Thus, a good parameter to characterise composite degradation could be given by the ratio of ceramic surface area, S_{cer0} (m^2), and polymer volume, V_{pol} (m^3) in the unit cell. This ratio is controlled exclusively by the ceramic particle size, d_0 (m) and the ceramic weight fraction, f_{wCer0} (wt %), and can be calculated as the combination of the previous two ratios as:

$$\frac{S_{cer0}}{V_{pol}} = \frac{S_{cer0}}{V_{cer0}} \frac{V_{cer0}}{V_{pol}} \qquad (m^{-1}) \tag{3.106}$$

A poly(L-lactide)-β-tricalcium phosphate composite sample with $d_0 = 20\,\mu m$ and $f_{wCer0} = 21.17\,wt\,\%$ would be represented by the unit cell depicted at the centre of Fig. 3.7. The remaining d_0–f_{wCer0} combinations depicted in the image, have been chosen in such a way, that the unit cells situated either below or on the right next to the central one, represent an increase by a factor of 2 of the ${}^{S_{cer0}}/_{V_{pol}}$ value, when compared with the central unit cell. Although the final effect is the same in both movements, doubling of the value of the ${}^{S_{cer0}}/_{V_{pol}}$ ratio, the origin is different: the unit cell situated below have the same value of ${}^{V_{cer0}}/_{V_{pol}}$ and twice the value of ${}^{S_{cer0}}/_{V_{cer0}}$, while the unit cell situated to the right has the same value of ${}^{S_{cer0}}/_{V_{cer0}}$ and twice the value of ${}^{V_{cer0}}/_{V_{pol}}$. Therefore, a movement to the next unit cell in the diagonal identified with a dashed blue arrow line results in a quadruplication of the ${}^{S_{cer0}}/_{V_{pol}}$ value. Conversely, the three unit cells situated in the opposite diagonal, identified with a dashed brown arrow line, share the exact same value of ${}^{S_{cer0}}/_{V_{pol}}$ despite their obvious differences in representative particle size d_0 and ceramic weight fraction f_{wCer0}.

In summary, the unit cell construction represents the properties of the composite samples in terms of ${}^{S_{cer0}}/_{V_{cer0}}$ and ${}^{V_{cer0}}/_{V_{pol}}$ using just the representative particle size d_0 and the initial ceramic weight fraction f_{wCer0}, reflecting the potential composite degradation behaviour of those composites.

3.4 Constituent Elements of the Bioresorbable Composites Degradation Models

After presenting the construction and analysis of the representative unit cell, this sections contains a classification of all the different constituent elements found in the composite degradation models. In both the general modelling framework, discussed in Sect. 3.1, and the ceramic-specific degradation models, discussed in section and Sect. 3.2, the constituent elements can be classified according to both their dependence and type into the following categories:

- Composite degradation variables: magnitudes of interest employed to represent composite degradation. As the degradation models characterise different composites, these variables differ between models. The composite degradation variables found in all the specific degradation models, i.e. the TCP, HA and CC models, are:
  - R_s, concentration of polymer chain scissions ($mol\,m^{-3}$).
  - $[H^+] = C_{H^+}$, concentration of hydrogen ions ($mol\,m^{-3}$).
  - $[Ca^{2+}]$, concentration of calcium ions ($mol\,m^{-3}$).

- $[R\text{-}COOH]$, concentration of non-dissociated carboxylic end group chains ($\mathrm{mol\,m^{-3}}$).
- $[R\text{-}COO^-]$, concentration of dissociated carboxylic end group chains ($\mathrm{mol\,m^{-3}}$).
- $a_{\mathrm{TCP/HA/CC}}$, total area of interface between the ceramic and polymer phases per unit of composite volume ($\mathrm{m^2\,m^{-3}}$).
- M_{n}, number-average molecular weight of the polymer phase (Da).

The following degradation variables are also found in the two models with a calcium orthophosphate as ceramic filler, i.e. the TCP and HA models:

- $[PO_4^{3-}]$, concentration of phosphate ions ($\mathrm{mol\,m^{-3}}$).
- $[HPO_4^{2-}]$, concentration of hydrogen phosphate ions ($\mathrm{mol\,m^{-3}}$).
- $[H_2PO_4^-]$, concentration of dihydrogen phosphate ions ($\mathrm{mol\,m^{-3}}$).
- $[H_3PO_4]$, concentration of phosphoric acid ($\mathrm{mol\,m^{-3}}$).

In the TCP degradation model only the eleven composite degradation variables listed so far can be found, while two more variables are present in the HA model:

- $[OH^-] = C_{\mathrm{OH^-}}$, concentration of hydroxide ions in the polymer phase ($\mathrm{mol\,m^{-3}}$).
- $[H_2O]$, concentration in the polymer phase of water molecules formed from the hydroxide ions released by the hydroxyapatite ($\mathrm{mol\,m^{-3}}$).

Lastly, the following three variables can be found exclusively in the CC model:

- $[CO_3^{2-}]$, concentration of carbonate ions in the polymer phase ($\mathrm{mol\,m^{-3}}$).
- $[HCO_3^-]$, concentration of hydrogen carbonate ions in the polymer phase ($\mathrm{mol\,m^{-3}}$).
- $[H_2CO_3]$, concentration of carbonic acid in the polymer phase ($\mathrm{mol\,m^{-3}}$).

The complete sets of equations for the TCP, HA and CC models are reported in Sects. 3.2.1–3.2.3 respectively. In those equations, the composite degradation variables can be easily identified as all of them use symbols of the type x_i, instead of the symbols presented here, to highlight the differences between variables and constants.

- Composite-dependent constants: set of parameters which characterise a specific composite sample. Usually, the composite-dependent constants are exclusive of that particular composite sample and not shared with other composite samples. The following composite-dependent constants can be found in the models:

  - M_{n0}, (Da), number-average molecular weight of the polymer phase at the time origin.
  - d_0 (m), representative ceramic particle size.
  - f_{wCer0} (wt %), ceramic weight fraction in the composite.
  - $\Delta C_{\mathrm{H_0^+}}$ ($\mathrm{mol\,m^{-3}}$), the initial hydrogen ions concentration not resulting from carboxylic end groups dissociation .
  - $\Delta C_{\mathrm{OH_0^-}}$ ($\mathrm{mol\,m^{-3}}$), the initial hydroxide ions concentration.
  - α (1), empirical rate of production of short chains by chain scission.
  - β (1), empirical exponent of production of short chains by chain scission.

- m (1), average degree of pseudo-polymerisation of the short chains.
- k_1 (s^{-1}), non-catalytic polymer hydrolysis rate.
- k_2' ($m^3\,mol^{-1}\,s^{-1}$), autocatalytic polymer hydrolysis rate.
- A_d (s^{-1}), rate of the ceramic dissolution power law.
- θ ($m^3\,mol^{-1}\,s^{-1}$), exponent of the ceramic dissolution power law.

The group of composite-dependent constants formed by α, β and m represent the scission type of the polymeric matrix of the composite sample and the group formed by the four composite degradation constants k_1, k_2', A_d and θ represent the overall degradation behaviour of the composite sample.

- Composite-derived constants: set of parameters which also characterise the composite sample and can be derived using composite-dependent constants in addition to polymer-dependent and ceramic-dependent constants:
  - f_{cer0} ($m^3\,m^{-3}$), initial ceramic volume fraction in the composite, which can be calculated as: $f_{cer0} = \frac{f_{wCer0}\rho_{pol}}{(1-f_{wCer0})\rho_{cer}+f_{wCer0}\rho_{pol}}$.
  - V_{unit} (m^3), volume of the representative unit cell, which can be computed as: $V_{unit} = \frac{\pi d_0^3}{6 f_{cer0}}$.
  - V_{cer0} (m^3), volume occupied initially by the ceramic phase in the representative unit cell, which can be computed as: $V_{cer0} = \frac{\pi}{6} d_0^3$.
  - V_{pol} (m^3), volume occupied by the polymer phase in the representative unit cell, which can be computed as: $V_{pol} = V_{unit} - V_{cer0}$.
- Polymer-dependent constants: set of constants determined by the polymer matrix of the composite. If several composite samples share the same polymeric matrix, those samples also share the same values of the polymer-dependent constants. The polymer-dependent constants found in the degradation models are:
  - ρ_{pol} ($kg\,m^{-3}$), polymer density.
  - K_a ($mol\,m^{-3}$), polymer acid dissociation constant at 37 °C, usually reported as the base 10 logarithm of the reciprocal of K_a, pK_a with $pK_a = -\log_{10}(K_a)$.
  - M_{unit} (Da), average molar mass associated to one ester bond in the polymeric matrix.
- Polymer-derived constants: set of parameters which are also employed to characterise the polymer matrix. The polymer-derived constants can be calculated using composite-dependent constants and polymer-dependent constants:
  - C_{e0} ($mol\,m^{-3}$), initial concentration in the polymer phase of ester bonds in long chains, can be computed as: $C_{e0} = {}^{\rho_{pol}}/_{M_{unit}}$.
  - R_{ol} ($mol\,m^{-3}$), concentration of ester bonds in short chains at a given time, can be computed as ${}^{R_{ol}}/_{C_{e0}} = \alpha({}^{R_s}/_{C_{e0}})^{\beta}$.
  - C_{chain0} ($mol\,m^{-3}$), concentration of long polymer chains in the polymer phase at the time origin, can be computed as: $C_{chain0} = {}^{\rho_{pol}}/_{M_{n0}}$.
  - N_{dp0} ($Da\,Da^{-1}$), initial average degree of pseudo-polymerisation, can be computed as: $N_{dp0} = \frac{M_{n0}}{M_{unit}} = \frac{C_{e0}}{C_{chain0}}$.

- Ceramic-dependent constants: set of constants determined by the ceramic filler of the composite. Similarly to the polymer-dependent constants, if several composite samples share the same ceramic filler, those sample also share the same values of the ceramic-dependent constants. The degradation models contain the following ceramic-dependent constants:
  - ρ_{cer} ($kg\,m^{-3}$), ceramic density.
  - M_{cer} ($g\,mol^{-1}$), ceramic molar mass.
  - K_{sp} (($mol^{\eta}\,m^{-3\eta}$) with η the sum of multiplicities of the different ions in the ceramic chemical composition), ceramic solubility product, usually expressed as the a base 10 logarithm of reciprocal of K_{sp}, pK_{sp} with $pK_{sp} = -\log_{10}(K_{sp})$.[5]
  - $[Ca^{2+}]_{eq}|_{cer}$ ($mol\,m^{-3}$), ceramic calcium equilibrium concentration.[6]
  - K_i ($mol\,m^{-3}$), acid dissociation constants at 37 °C associated to the ceramic released anions, usually reported as the base 10 logarithm of the reciprocal of K_i, pK_i with $pK_i = -\log_{10}(K_i)$.
- Ceramic-derived constants: set of parameters also used to characterise the ceramic filler that can be derived from composite ceramic-dependent constants.
  - Ω_{cer} ($m^3\,mol^{-1}$), ceramic molar volume, which can be computed as: $\Omega_{cer} = {}^{M_{cer}}/_{\rho_{cer}}$. As the ceramic molar volume is only one ceramic-derived constant, it is reported with the ceramic-dependent constants.

In order to compute the composite degradation simulations using the specific degradation models presented in Sect. 3.2, just the initial values of the composite degradation variables in addition to the values of the composite-dependent constants, polymer-dependent constants and ceramic-dependent constants are needed.

3.5 Using the Bioresorbable Composites Degradation Models

This section includes the instructions of use for the three specific composite degradation models presented in Sect. 3.2. These computational models employ experimental composite degradation data in order to provide information about the degradation behaviour of calcium-based biocomposites. The process followed to obtain this desired composite degradation information can be divided in three different stages:

1. Data harvesting: the first stage is concerned with the search, extraction and treatment of experimental degradation data for use in the computational models. After

[5] Information about the definition and calculation of the ceramic solubility product can be found in Appendix A.2.

[6] Information about the definition and calculation of the ceramic calcium equilibrium concentration can also be found in Appendix A.2.

the completion of the data harvesting stage, the experimental composite degradation data are ready for use with their corresponding specific model (TCP, HA or CC).
2. Data analysis: the second stage deals with the extraction of degradation information from the harvested experimental data. In a nutshell, this step deals with the computation of the set of values for the degradation constants k_1, k_2', A_d and θ that most closely represents the number-average molecular weight versus time curve of a given piece of harvested experimental data.
3. Results generation: the third and final stage gathers the information obtained during the previous stage and presents it in several formats according to the increasing level of complexity of the different analyses.

In the next pages, an in-depth description of the three distinct stages of the method of use of the specific composite degradation models is provided. Before the in-depth descriptions and due to the hierarchical structure of composite degradation data, the precise nomenclature employed when referring to these data is included for reference.

3.5.1 Nomenclature Employed in the Use of the Models

Composite experimental degradation data are key when using the models to further the knowledge of biocomposite degradation. Although simple in nature, some of the analysis performed with the models require different ways of grouping and connecting these experimental data. In order to clarify the subtleties associated with each type of experimental data grouping, the specific nomenclature adopted in this work is included here:

- System (of composites): specific combination of a polymeric matrix and a ceramic filler, i.e. composites which share exactly the same polymeric matrix and ceramic filler. An example of a system would be poly(L-lactide)–pure hydroxyapatite composites. Pure polymer samples sharing the polymeric matrix of the system are considered part of that given system as samples having a ceramic weight fraction equals to zero.
- Family: combination of systems which share polymeric matrix and ceramic filler names, i.e. composites which share similar polymeric matrixes and similar ceramic fillers.
  When the matrix is a copolymer, samples with different monomer ratios are considered part of the same family but not part of the same system, i.e., a poly(D,L-lactide-co-glycolide)(50:50)–α-tricalcium phosphate sample and a poly(D,L-lactide-co-glycolide)(75:25)–α-tricalcium phosphate sample belong to the same family, poly(D,L-lactide-co-glycolide)– tricalcium phosphate, but to different systems. In a similar fashion, when the ceramic can present several allotropes, samples with different allotropes are considered part of the same family, i.e., a poly(D,L-lactide-co-glycolide)(75:25)–α-tricalcium phosphate sample and a poly(D,L-lactide-co-glycolide)(75:25)–β-tricalcium phosphate sample belong

to the same family, poly(D,L-lactide-co-glycolide)– tricalcium phosphate, but to different systems.

- Occurrence (also experimental data occurrence): experimental data reporting the evolution of degradation over time for a particular pure polymer or composite sample. Several occurrences from the same system in the same experimental study will form a case study. The occurrences will differ from each other in properties like ceramic weight fraction, polymer initial molecular weight, and so on.
- Case (of a system): a case or case study is a cluster of experimental data from a given experimental study which belong to one particular system. Typically, a case study of a system includes several experimental occurrences, with a minimum of one pure polymer occurrence and one composite occurrence.

3.5.2 Composite Degradation Data Harvesting Process

As previously mentioned, the composite degradation models require experimental data in order to provide information about the degradation behaviour of calcium-based biocomposites. The data harvesting process, used to provide these data, consists of two parts: data search and data extraction and treatment.

Data Search

Firstly, a search for composite experimental data available in literature was conducted. The scope of the search is defined as: "quantitative degradation data at physiological temperature from composites made of polyesters and either tricalcium phosphate or hydroxyapatite or calcium carbonate". The following degradation measurements are considered quantitative during the search:

- Molecular weight of the polymer phase: this degradation measurement is considered the gold standard, as the comparison with the results output by the computational models is direct. Although the degradation models output number-average molecular weight, M_n (Da), other molecular weight averages such as weight-average, M_w (Da), and viscosity-average, M_v (Da) are also considered. Molecular weight was the most abundant quantitative degradation data type in the harvested literature data.
- pH, $pH(t)$: data reporting the evolution of the degradation buffer pH value over time are considered a valid and accurate degradation measurement when the data present a sudden onset of the pH drop after an initial plateau at physiological pH. This sudden drop of the pH value is caused by the acidity associated to the burst release of the composite degradation products. This burst release can be related to a critical polymer molecular weight allowing for a comparison between the results output by the degradation models and the experimental degradation data. pH data was the second most abundant quantitative degradation data type in the harvested literature data.
- Weight loss or mass loss, $W_L(t)$ or $M_L(t)$: similarly, when the experimental degradation data present a sudden weight or mass loss, pointing again to a burst release

of the composite degradation products, the weight loss or mass loss data are considered valid quantitative degradation data. The weight or mass loss caused by the burst release can also be related to a critical polymer molecular weight allowing for a comparison between experimental data and the outcome of the models.

- Mechanical properties, such as flexural strength $\sigma_{\text{flexural}}(t)$ (Pa) and yield strength $\sigma_{\text{y}}(t)$ (Pa): the evolution of flexural strength and yield strength over time is closely related to the composite molecular weight and therefore flexural strength and yield strength data are also considered valid quantitative degradation data.

Google scholar (https://scholar.google.co.uk/) was employed as search engine with the following keywords: "degradation", "composite", "biodegradable polymer", "hydroxyapatite", "tricalcium phosphate", "calcium carbonate", "lactide", "caprolactone", "glycolide", "molecular weight". All the results returned by the search were scanned for the following cues.

1. Polymer matrix and ceramic filler within the scope of this project.
2. Experimental degradation data of a quantitative nature, as defined above.
3. Characterisation, at least basic, of both polymer and ceramic phases.

Articles which presented the above-mentioned cues were used for data extraction. Before the data extraction and to broaden the reach of the search, both the references and citations of these articles were included as candidates in the search process.

Data Extraction

After the search stage, the data were extracted from the selected literature. Several pieces of information were harvested from each published article. Table 3.1 summarises the information extracted from selected literature.

Table 3.1a contains the extracted pieces of information reflecting the properties of the polymer matrix and the ceramic filler, while Table 3.1b includes the extracted characteristics of the composite samples, the degradation protocol and degradation measurements. These pieces of information can be classified into two different broad categories, namely input data and output data. Input data consisted of information needed to characterise the composite before degradation and can be found in Table 3.1a above the dash line. The input data are enough to define the values of the composite-dependent, polymer-dependent and ceramic-dependent constants. The output data, found in Table 3.1b and the two rows below the dash line in Table 3.1a, provided a characterisation of the composite during and after degradation and information about the degradation process itself. The names chosen for the two categories, input and output data relate to their use in the computational model. Input data were fed to the model to start the simulation and output data were compared to the generated simulations or used during the analyses with the aim of relating certain properties with degradation traits.

Both input and output data are needed in a specific format for use in the models. Most of the magnitudes can be harvested directly in the correct format but two of them, namely polymer molecular weight and ceramic representative particle size, usually require some adjustments. Polymer molecular weight data are part of both

Table 3.1 Information extracted from the selected literature

(a) Polymer and ceramic characteristics extracted from the selected literature data

Polymer characteristics	Ceramic characteristics
Type	Type
Copolymer monomer ratio	Weight percentage
Initial molecular weight	Particle size distribution
	Particle shape
Manufacturing process	Manufacturing process
Manufacturer	Manufacturer

(b) Sample characteristics, degradation protocol and degradation measurements extracted from the selected literature data

Sample characteristics	Degradation protocol	Degradation measurements
Morphology	Buffer media or animal	Molecular weight or
Porosity	Buffer to sample ratio or implantation site	pH or
Fabrication method	Buffer replacement or implantation protocol	Weight/mass loss or
Author	Shaking protocol or extraction protocol	Mechanical properties

input and output data. The initial molecular weight, part of input data, is used to characterise the pre-degradation composite molecular weight. The computational models employed number-average initial molecular weight, M_{n0} (Da) or $M_n(t = 0)$ (Da). For the comparison between the simulation and output experimental data at different time-points also the number-average molecular weight, $M_n(t)$ (Da), is used.

When the found literature data contained $M_n(t)$, the number-average molecular weights were used without any modifications, but in most cases some processing steps were needed as the molecular weight data were reported using another average. The different modifications applied to the molecular weight data depending on the provided information are listed here:

- Weight-average molecular weight, $M_w(t)$ (Da) and dispersity, $Đ(t)$[7] ($\mathrm{Da\,Da^{-1}}$): the number-average molecular weight, $M_n(t)$ (Da), is computed as the ratio between the weight-average molecular weight and the dispersity for the initial and subsequent time-points:

$$M_n(t) = \frac{M_w(t)}{Đ(t)} \qquad \text{(Da)} \tag{3.107}$$

- Weight-average molecular weight, $M_w(t)$ (Da), and initial dispersity, $Đ_0$ ($\mathrm{Da\,Da^{-1}}$): the dispersity is assumed to remain constant over time with a value of $Đ_0$. The

[7] Formerly known as polydispersity or polydispersity index, *PD* or *PDI*, with $PD(t)$ or $PDI(t) = {}^{M_w(t)}/_{M_n(t)}$ ($\mathrm{Da\,Da^{-1}}$). In Chaps. 4, 5 and 7, the deprecated nomenclature, polydispersity index *PDI*, is employed when referring to harvested data in order to maintain coherency with the nomenclature used by the authors.

number-average molecular weight, $M_n(t)$ (Da), is computed as the ratio between weight-average molecular weight and initial dispersity for the initial and subsequent time-points:

$$M_n(t) = \frac{M_w(t)}{Đ_0} \quad \text{(Da)} \tag{3.108}$$

- Weight-average molecular weight, $M_w(t)$ (Da): when the dispersity is not reported the employed value of $Đ$ is extracted from literature data of similar polymers and assumed to remain constant at a value of $Đ_a$ over time. The number-average molecular weight, $M_n(t)$ (Da), is computed as the ratio between weight-average molecular weight and assumed dispersity for all time-points:

$$M_n(t) = \frac{M_w(t)}{Đ_a} \quad \text{(Da)} \tag{3.109}$$

- Viscosity-average molecular weight, $M_v(t)$ (Da) and dispersity, $Đ$(t): the ratio between viscosity-average molecular weight, $M_v(t)$, and weight-average molecular weight, $M_w(t)$, is extracted from literature data of similar polymeric matrixes and assumed to remain constant at a value of $\frac{M_{v0}}{M_{w0}}$. The number-average molecular weight, $M_n(t)$ (Da) is then calculated as:

$$M_n(t) = \frac{M_v(t)}{M_{v0}} \frac{M_{w0}}{Đ(t)} \quad \text{(Da)} \tag{3.110}$$

- Viscosity average molecular weight, $M_v(t)$ (Da): the relationship between viscosity-average and number-average molecular weights, $R_{\mathbf{MvMn}}$ is extracted from literature data of similar polymeric matrixes and assumed to be time independent. The number-average molecular weight, $M_n(t)$ (Da), is then computed as the ratio between the viscosity-average molecular weight and the assumed $R_{\mathbf{MvMn}}$ ratio:

$$M_n(t) = \frac{M_v(t)}{R_{MvMn}} \quad \text{(Da)} \tag{3.111}$$

A similar approach was followed when the degradation measurements presented other formats.

- Inherent viscosity, $I.V.(t)$ (dL/g): the relationship between number-average molecular weight, $M_n(t)$ (Da), and inherent viscosity is determined using an empirical relationship with reference data of similar polymer matrixes taken from literature.
- pH, $pH(t)$ and initial molecular weight, either number-average (M_{n0} (Da)) or weight average (M_{w0} (Da): the number-average molecular weight is estimated using an empirical relationship between pH and number-average molecular weight determined with reference data of similar polymers. This relationship provides the value of number-average molecular weight corresponding to the pH drop, i.e the value of the number-average critical molecular weight $M_{n\,critical}$ (Da), resulting in a number-average molecular weight curve with two points, the initial molecular

weight and the critical molecular weight:

$$M_{\mathrm{n}}(t=0) = M_{\mathrm{n0}} \quad \text{(Da)} \tag{3.112}$$

$$M_{\mathrm{n}}(t = t_{\mathrm{pH\ drop}}) = M_{\mathrm{n\ critical}} \quad \text{(Da)} \tag{3.113}$$

This method was previously employed by Pan et al. with their TCP degradation model [1].

- Weight or mass loss, $W_{\mathrm{L}}(t)$ or $m_{\mathrm{L}}(t)$ (wt%) and initial molecular weight, either weight-average, M_{w} (Da), or number-average, M_{n} (Da): similarly, the number-average molecular weight is estimated using an empirical relationship between weight or mass loss and number-average molecular weight determined with reference data of similar polymers. The relationship also provides the number-average molecular weight associated to the sudden weight or mass loss, i.e. the number-average critical molecular weight $M_{\mathrm{n\ critical}}$, resulting again in a number-average molecular weight curve with two points:

$$M_{\mathrm{n}}(t=0) = M_{\mathrm{n0}} \quad \text{(Da)} \tag{3.114}$$

$$M_{\mathrm{n}}(t = t_{\mathrm{W/M\ loss\ burst}}) = M_{\mathrm{n\ critical}} \quad \text{(Da)} \tag{3.115}$$

pH and weight or mass loss, employed as measurements of composite degradation, are intrinsically related. The release of composite degradation products is the root cause of the evolution of both magnitudes, pH and weight or mass loss, making them two different representations of the same phenomenon. Pan et al. also employed this relationship between weight or mass loss and number-average molecule weight with their TCP degradation model [1].

- Flexural strength, $\sigma_{\mathrm{flexural}}$ (Pa) or yield strength, σ_{y} (Pa): a relationship between the reported mechanical property and number-average molecular weight, M_{n} (Da), is used based on literature data of similar polymer matrixes:

$$M_{\mathrm{n}}(t) = f\left(\sigma_{\mathrm{flexural/y}}(t)\right) \quad \text{(Da)} \tag{3.116}$$

This method was employed only with two case studies.

As mentioned in Sects. 3.1 and 3.3, the ceramic filler is characterised in the model using a representative particle size. This representative particle size captures the behaviour of the whole particle size distribution in terms of both volume and surface area. The processing methods used to obtain the representative particle size depending on the data available are explained below:

- Particle size distribution: when the ceramic particle size distribution is provided, the representative particle size is computed as the Sauter mean diameter (*SMD*) of the distribution assuming spherical particles:

$$SMD = D[3,2] = d_{32} = \frac{d_v^3}{d_s^2} = 6\frac{\sum_{i=1}^{N} \frac{\pi}{6} d_i^3}{\sum_{i=1}^{N} \pi d_i^2} = 6\frac{\sum_{i=1}^{N} V_i}{\sum_{i=1}^{N} A_i} \quad \text{(m)} \tag{3.117}$$

being d_v (m), the volume equivalent particle diameter; d_s (m), the surface equivalent particle diameter and V_i (m^3), A_i (m^2), and d_i (m), the volume, surface area and diameter of the ith particle respectively.[8]

- Boundary sizes of the distribution: when only the boundary or boundaries of the particle size distribution are provided, the representative particle size is computed as the Sauter mean diameter (*SMD*) assuming a specific distribution type of spherical particles. If both the lower and upper boundaries of the particle size distribution are provided, it is assumed that 85% of the particles fall within the distribution limits. If only the upper boundary is provided, the lower limit is considered zero and it is also assumed that 85% of the particles fall within the distribution limits considering that only positive sizes have a physical meaning. Three different types of distribution are considered depending on the employed ceramic fabrication method:
  - Normal distribution, between the lower and upper boundaries $f_n(x_l, x_u)$ or between zero and the upper boundary $f_n(x_u)$: the normal or Gaussian distribution is employed when the ceramic fabrication method is unspecified or of a chemical nature. For $f_n(x_l, x_u)$, the mean and standard deviation are defined as $\mu = \frac{x_l + x_u}{2}$ and $\sigma = \frac{x_u - x_l}{3}$ respectively and for $f_n(x_u)$, the mean and standard deviation are defined as $\mu = \frac{x_u}{2}$ and $\sigma = \frac{x_u}{3}$ respectively.
  - Weibull distribution, between the lower and upper boundaries $f_{wd}(x_l, x_u)$ or between zero and the upper boundary $f_{wd}(x_u)$: the Weibull or Rosin-Rammler distribution is used with ceramic fabrication methods including a final comminution step. For $f_{wd}(x_l, x_u)$, the scale parameter is defined as $\lambda = \frac{x_l + x_u}{2} + \frac{x_u - x_l}{3}$, while for $f_{wd}(x_u)$, the scale parameter is defined as $\lambda = \frac{x_u}{2} + \frac{x_u}{3}$. In both cases, the shape factor is defined as $k = 2$.
  - Acicular distribution, $f_a(x_l, x_u, y_l, y_u)$: when the particles have an acicular shape, the distribution of particles is generated using two independent normal distributions for the particle width, x (m), and length, y (m), considering the particles as cylinders. In the width normal distribution the mean and standard deviation are defined as $\mu = \frac{x_l + x_u}{2}$ and $\sigma = \frac{x_u - x_l}{3}$ respectively and in the length normal distribution the mean and standard deviation are defined as $\mu = \frac{y_l + y_u}{2}$ and $\sigma = \frac{y_u - y_l}{3}$ respectively. The volume of the acicular particle is estimated as $V = \frac{\pi}{4} x^2 y$ and the surface area as $S = \pi x y$.
- Average particle size, d_{mean} or d (m): in most publications, the ceramic particle size distribution is characterised by an average particle size without further insight into calculation method or average type. In these cases, the representative particle size is assumed to be equal to this reported average particle size.

[8] The description and mathematical derivation of the Sauter mean diameter, d_{32}, can be found in Appendix A.5.

- Scanning electron microscopy (SEM) or micro X-ray computed tomography (μ-CT) images, SEM images (m) or μ-CT (m): when the characterisation of the ceramic particle size distribution is done with images, originated either by SEM or μ-CT, the representative particle size is computed as the Sauter mean diameter, d_{32} (m), of the particle distribution depicted in those images assuming spherical particles.

After the pre-treatment, both input and output data were stored in *.csv* files. For input data files several experimental occurrences were included in the same file with each row represented a different experimental occurrence. For output data each experimental occurrence was stored in a separate *.csv* file.

3.5.3 Composite Degradation Data Analysis Process

Once the data harvesting stage had been completed and format compatibility of both input and output data had been attained, input and output data were fed to a computational program which run the data analysis process. This program uses an algorithm which aims to find a set of degradation parameters ensuring the closest match possible between simulated data and associated output data for a given input data.

This algorithm can be seen from the mathematical point of view as a fitting algorithm with the objective of minimising the difference between simulated data and experimental results. Figure 3.8 shows the data analysis process flow chart. The analysis or fitting process, usually applied to one case study of a system at a time, has two main stages, namely pure polymer data analysis and composite data analysis. As discussed in Sect. 3.2, the models characterise composite degradation with four values for the degradation constants k_1, k_2', A_d and θ; where k_1 (s^{-1}) and k_2' ($\mathrm{m}^3\,\mathrm{mol}^{-1}\,\mathrm{s}^{-1}$) are the non-catalytic and autocatalytic polymer degradation rate constants respectively, and A_d ($\mathrm{mol\,m}^{-2}\,\mathrm{s}^{-1}$) and θ (1) the ceramic degradation rate and exponent respectively. The outcome of the fitting algorithm is a quadruple or 4-tuple with the values of these four parameters for each experimental case study.

The first stage, pure polymer data analysis, depicted in the left green block of Fig. 3.8 searches for the pair or pairs of values for the polymer degradation rate constants, k_1 and k_2', which characterise pure polymer data degradation. During this first stage the ceramic parameters, A_d and θ, are not considered as they do not influence the degradation of pure polymer occurrences.

This pure polymer data analysis commences after the data have been pre-treated as described in Sect. 3.5.2 and are ready to be input into the computational models, including the transformation of the original experimental degradation data into a M_n–t curve. The first step of the process is the definition of the polymer region of interest, polymer ROI, by providing four values: $\mathrm{k}_{1\,\mathrm{min}}$, $\mathrm{k}_{1\,\mathrm{max}}$, $\mathrm{k}'_{2\,\mathrm{min}}$ and $\mathrm{k}'_{2\,\mathrm{max}}$. These values of the polymer degradation constants define the following boundary cases: ($\mathrm{k}_{1\,\mathrm{min}}$, 0), ($\mathrm{k}_{1\,\mathrm{max}}$, 0), (0, $\mathrm{k}'_{2\,\mathrm{max}}$) and (0, $\mathrm{k}'_{2\,\mathrm{max}}$) where $\mathrm{k}_{1\,\mathrm{min}}$ and $\mathrm{k}'_{2\,\mathrm{min}}$ are

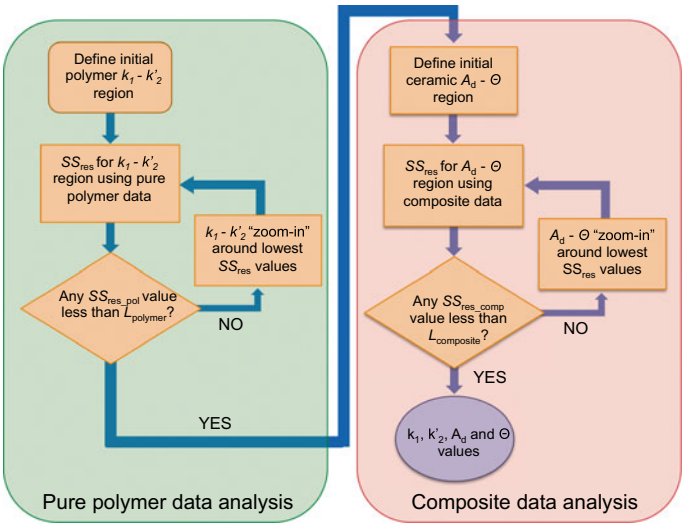

Fig. 3.8 Flow chart depicting the data fitting process

underestimations of the experimentally measured pure polymer degradation rate for the solely non-catalytic and solely autocatalytic degradation types respectively. In a similar fashion, $k_{1\,max}$ and $k'_{2\,max}$ are overestimations for the solely non-catalytic and solely autocatalytic degradation types respectively. Figure 3.9a depicts an example of the appearance of the polymer region of interest enclosed by these four points in the k_1–k'_2 plane.

From the definition of the polymer ROI, it follows that the real polymer degradation rate constants for the particular case study of a given system A (k_{1A} and k'_{2A}), shared by all the occurrences of the case study, lie within this region of interest. The second step was the computation of degradation simulations for a grid of points spaced δ_k in both k_1 and k'_2 directions and spanning the whole region of interest using the computational models presented in Sect. 3.2. The simulations are then ranked according to their goodness of fit with respect to the pure polymer data. The parameter used to measure the goodness of fit for each fitting was a normalised weighted sum of squared residuals, defined as:

$$SS_{\text{res}}^{\text{pol}} = \frac{1}{m_{\text{pol}}} \sum_{i=0}^{m_{\text{pol}}} k_{\text{WL}}(t_i) \left(\frac{M_{\text{n pol}}^{\text{sim}}(t_i) - M_{\text{n pol}}^{\text{exp}}(t_i)}{M_{\text{n pol}}^{\text{exp}}(t_0)} \right)^2 \tag{3.118}$$

where $M_{\text{n pol}}^{\text{sim}}(t)$ and $M_{\text{n pol}}^{\text{exp}}(t)$ are respectively, the computationally predicted and harvested experimentally measured number-average molecular weights over time for the pure polymer occurrence; t_0 indicates time origin; $k_{\text{WL}}(t_i)$ is a weighting factor assigning heavier importance to low mass loss values and m_{pol} is the number of experimental time-points in the pure polymer occurrence.

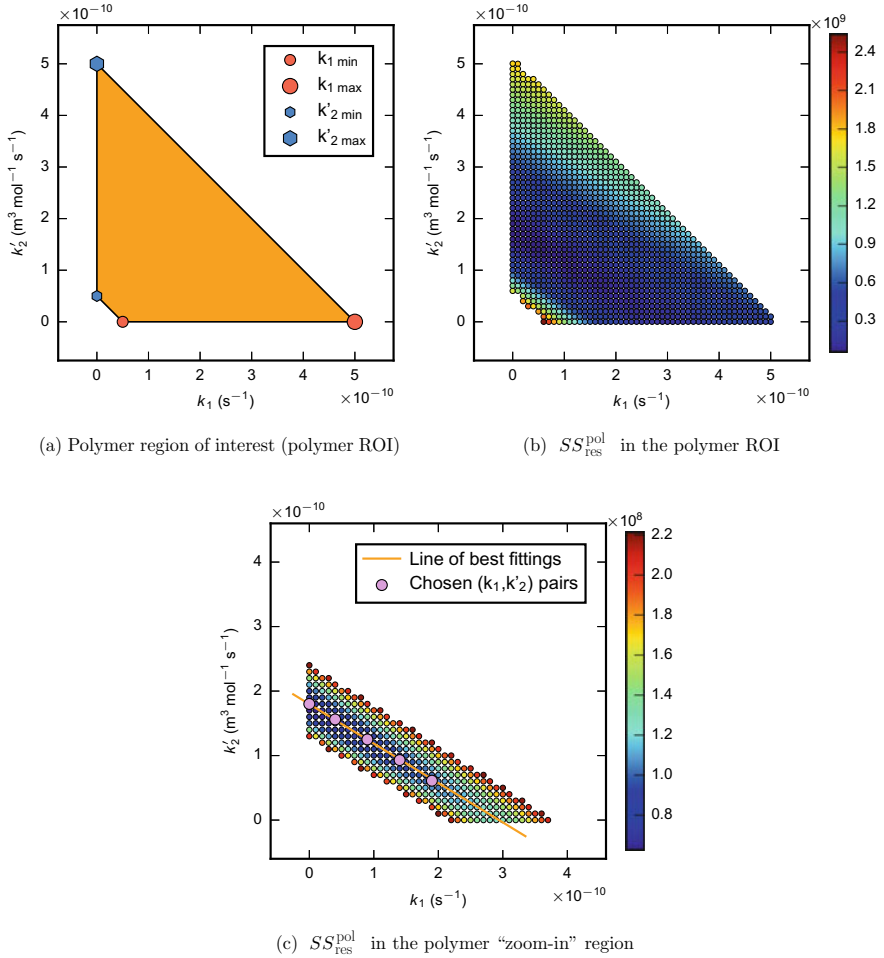

(a) Polymer region of interest (polymer ROI)

(b) $SS_{\text{res}}^{\text{pol}}$ in the polymer ROI

(c) $SS_{\text{res}}^{\text{pol}}$ in the polymer "zoom-in" region

Fig. 3.9 Different steps in the pure polymer data analysis stage

Figure 3.9b exhibits a graphical representation of the goodness of fit for a particular example. The colour of each simulated point (k_1, k_2') represents its $SS_{\text{res}}^{\text{pol}}$ value. A dark blue colour indicates a low $SS_{\text{res}}^{\text{pol}}$ value when compared to the rest of the points in the polymer ROI and therefore implies that the differences between the simulation and the experimental data are the least significant amongst the simulated points. A bright red colour represents a high $SS_{\text{res}}^{\text{pol}}$ value, implying a significant mismatch between simulation and experimental data.

After the initial analysis, the fitting algorithm enters a loop in which a "zoom-in" is applied to the original polymer ROI, identifying a subregion of interest and running the same instructions on a finer grid. The subregion is computed as the

region that contains the bottom $x\%$ of $SS_{\text{res}}^{\text{pol}}$ values. In a typical "zoom-in" step, δ_k was reduced by a factor of one to five and x was set to a value ranging from (10...25)%. Figure 3.9c includes the result of the "zoom-in" process on the region of interest depicted in Fig. 3.9b with x equals to 25. A line of "best fittings" is also included, as usually the same polymer degradation behaviour could be achieved with a range of (k_1, k_2') combinations with different values of non-catalytic to autocatalytic degradation rates ratio (k_1/k_2'). The points depicted in magenta represent the 3 to 5 pairs of values, highlighting the differences in k_1/k_2' ratio, output by the pure polymer data analysis.

After completing the first stage, the pure polymer data analysis, the fitting algorithm returns a pair or several pairs of values $(\mathrm{k}_1, \mathrm{k}_2')$ for the analysed case study as mentioned above. Then, the algorithm moves to the second stage, composite data analysis, represented in the right red block in Fig. 3.8, which follows a similar set of instructions, in order to find the correct values of A_d and θ for the case study, with the k_1 and k_2' values generated by the first stage. The real values of A_d and θ are contained in the ceramic region of interest (ceramic ROI). θ values range from 1 to 4 and thus, include the reported values for several dissolution mechanisms [11, 18]. The range of A_d values stem from reference values of minimum reported dissolution rate for a given ceramic, as lower boundary, and physical constraints such as complete dissolution in the analysed degradation time as upper boundary. Figure 3.10 shows a ceramic region of interest in the A_d–θ plane for a given pair of $(\mathrm{k}_1, \mathrm{k}_2')$.

The parameter used to measure the goodness of fit in this stage, $SS_{\text{res}}^{\text{comp}}$, is updated to include both the pure polymer and composite samples occurrences:

$$SS_{\text{res}}^{\text{comp}} = \frac{1}{\sum_{j=1}^{n} m_j} \sum_{j=1}^{n} \sum_{i=1}^{m_j} k_{\mathrm{WL\,j}}(t_i) \left(\frac{M_{\mathrm{n}j}^{\text{sim}}(t_i) - M_{\mathrm{n}j}^{\text{exp}}(t_i)}{M_{\mathrm{n}j}^{\text{exp}}(t_0)} \right)^2 \tag{3.119}$$

where $M_{\mathrm{n}j}^{\text{sim}}(t)$ and $M_{\mathrm{n}j}^{\text{exp}}(t)$ are respectively, the computationally predicted and harvested experimentally measured number-average molecular weights over time for the jth occurrence, with m_j, the number of experimental time-points for the jth occurrence and n, the number of occurrences for the system case study; t_0 indicates time origin and $k_{\mathrm{WL\,j}}(t_i)$ is a weighting factor assigning heavier importance to low mass loss values for the jth occurrence.

Figure 3.10b, c contain an example of the evaluation of the simulations in both the ceramic ROI and in the subregion selected after a refinement iteration. The final outcome of the fitting process algorithm is one or several quadruples or 4-tuples containing k_1, k_2', A_d and θ for the analysed case study. The output quadruples are those which present values of $SS_{\text{res}}^{\text{comp}}$ below a defined arbitrary threshold. The final reported one corresponds to the 4-tuple which best fits experimental information in terms of final ceramic particle size.

θ Value

A grid of θ values, as explained above and depicted in Fig. 3.10b, was employed during the analysis of experimental data with the three ceramic-specific models for

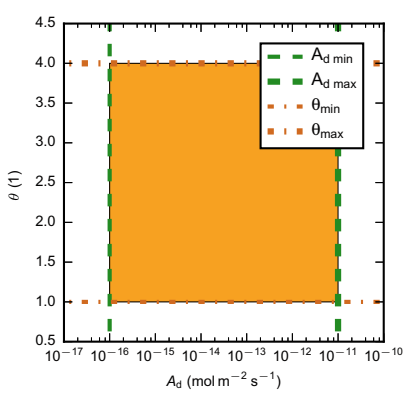

(a) Ceramic region of interest (ceramic ROI)

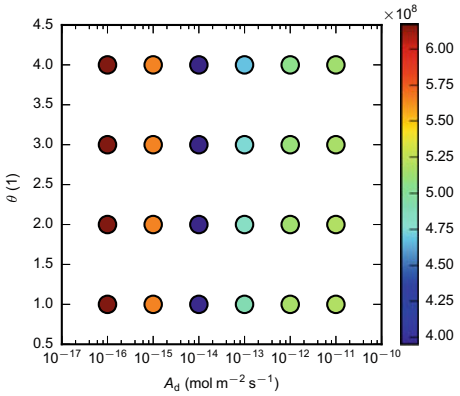

(b) $SS_{\text{res}}^{\text{comp}}$ in the ceramic ROI

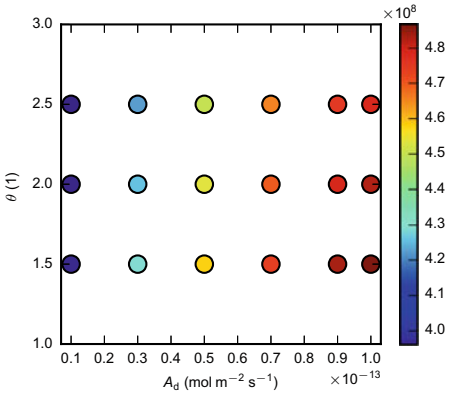

(c) $SS_{\text{res}}^{\text{comp}}$ in the ceramic "zoom-in" region

Fig. 3.10 Different steps in the composite data analysis stage

the first few case studies of each type. The little influence of θ in the composite data analysis became apparent, as pointed by the same colour of all points with same A_{d} value in Fig. 3.10c. Subsequently, given the incapability of the models to ascertain the dominant dissolution mechanism in each case study, reflected by the θ value, and to decrease the computational cost of the simulations, a value of $\theta = 2$ was fixed for the remaining analyses.

Range of Goodnesses of Fit

Figure 3.11 includes examples of the different goodnesses of fit found during data analysis. Four different categories were considered: excellent (Fig. 3.11a), good (Fig. 3.11b), fair (Fig. 3.11c) and poor (Fig. 3.11d).

Of all the analysed case studies, around 80% presented excellent or good goodness of fit with the remaining 20% distributed 3:1 between fair and poor goodness of fit. The 5% with poor fitting were included as the actual polymer degradation rate

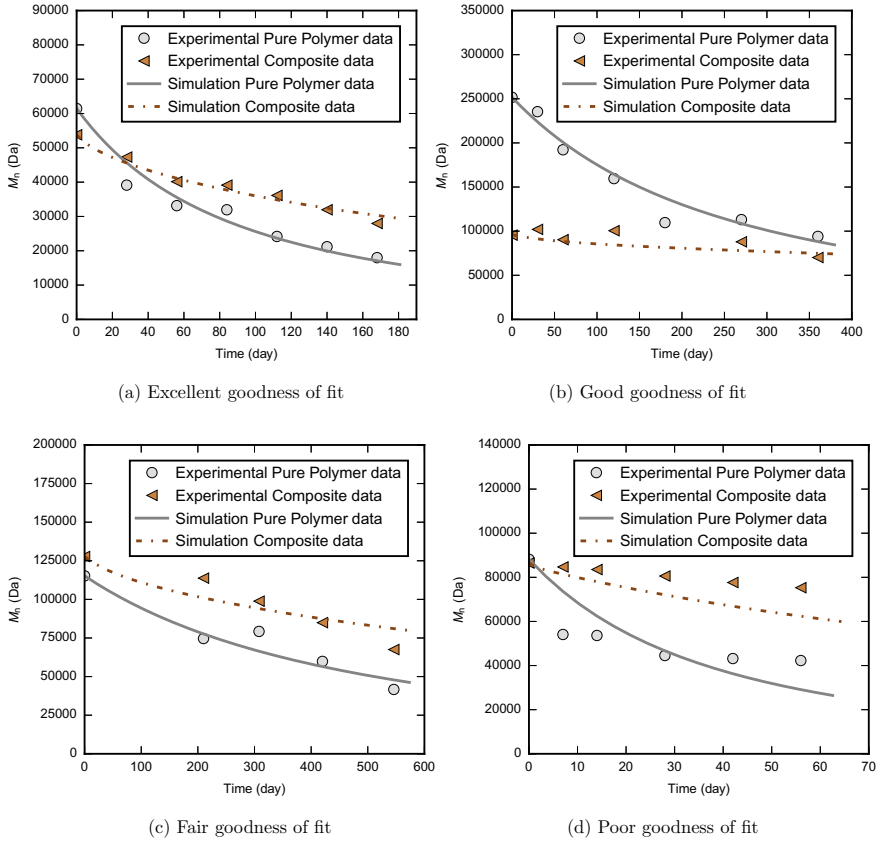

(a) Excellent goodness of fit

(b) Good goodness of fit

(c) Fair goodness of fit

(d) Poor goodness of fit

Fig. 3.11 Different types of goodness of fit observed during data analysis with the three ceramic-specific models

values (k_1, k_2') are probably of a similar order of magnitude because the bulk of the discrepancies comes from a mismatch in degradation curve shape stemming from a different random to end scissions ratio [19], which can be hard to ascertain from experimental data.

3.5.4 Types of Results Generated by the Degradation Models

After the presentation of the data analysis, the different types of results generated by the models are presented here. These results have a hierarchical structure, with increasing level of complexity, which is depicted in Fig. 3.12.

The first level of results, the simplest and most elemental, acts as a backbone for superior levels. Figure 3.12a depicts an example of this type of results. In essence,

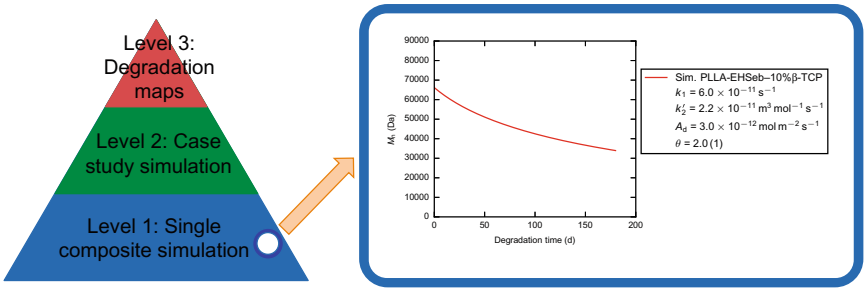

(a) Results level 1: single composite degradation simulation

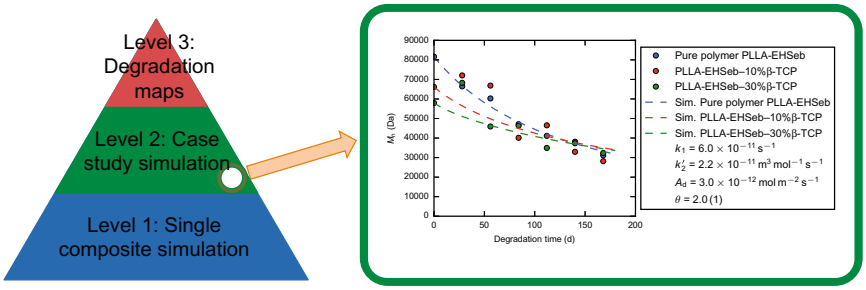

(b) Results level 2: case study simulation

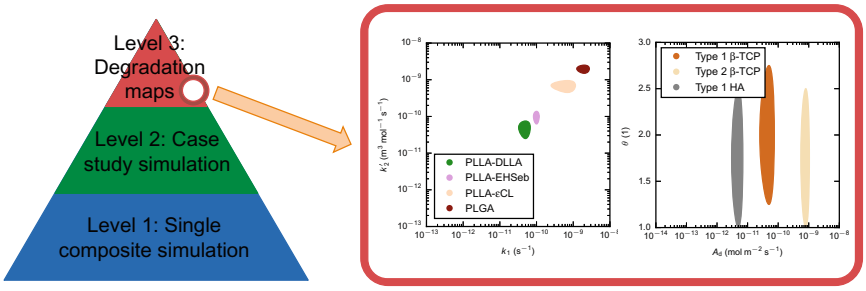

(c) Results level 3: degradation maps

Fig. 3.12 Hierarchical structure of the results generated with the biocomposites data analysis, ordered by increasing level of complexity

the results in this first level correspond to the output of the computational degradation models presented in Sect. 3.2. Providing all the necessary constants, composite input data and initial values of the variables as explained in Sect. 3.4, the evolution of the magnitudes used to characterise the degradation of the composite sample is calculated for a given set of values for the four degradation parameters k_1, k'_2, A_d and θ.

When several of these first level simulations are joined together and use to characterise the experimental occurrences of a particular case study, a level 2 result is formed. An example of a level 2 result, for a case study with a poly(L-lactide) copolymer matrix and β-tricalcium phosphate filler, is depicted in Fig. 3.12b. These

results are generated using the data analysis process presented in Sect. 3.5.3 and represent the first useful type of results in terms of providing insight into the degradation mechanisms of biocomposites.

The uppermost level, level number 3, consists of the most complex and elaborated type of results. This type, named degradation maps, condense information about a significant number of case studies by representing each one with their four values of the degradation constants k_1, k_2', A_d and θ. Figure 3.12c presents an example of a polymer and ceramic maps for several case studies. This type of results are output by the more general high-level analyses undertaken in Chaps. 4, 5 and 7 using harvested experimental data.

In summary, this chapter has presented a general modelling framework for calcium-based biocomposites degradation, followed by three ceramic-specific composite degradation models generated by particularising the general framework for tricalcium phosphate, hydroxyapatite and calcium carbonate. The representative unit cell, employed by the developed models to characterise composite samples, was also introduced and analysed. Then, the constituent elements of the degradation models were presented compiled in a list and classified according to their dependence and type. Lastly, the methods of use of these models were presented. In the next three chapters, the use of these models with harvested experimental data is discussed. Chapter 4 deals with the analysis of tricalcium phosphate composites, Chap. 5 with the analysis of hydroxyapatite composites and finally, Chap. 7 with the analysis of calcium carbonate composites.

References

1. Pan, J., Han, X., Niu, W., & Cameron, R. E. (2011). A model for biodegradation of composite materials made of polyesters and tricalcium phosphates. *Biomaterials*, *32*(9), 2248–2255.
2. Pan, J. (2014). *Modelling degradation of bioresorbable polymeric medical devices*. Elsevier.
3. Bergwerf, H. (2014). *MolView online application*. Retrieved September 1, 2016 from http://molview.org/.
4. Popov, K., Rönkkömäki, H., & Lajunen, L. H. (2006). Guidelines for NMR measurements for determination of high and low pK_a values (IUPAC Technical Report). *Pure and Applied Chemistry*, *78*(3), 663–675.
5. Wang, Y., Pan, J., Han, X., Sinka, C., & Ding, L. (2008). A phenomenological model for the degradation of biodegradable polymers. *Biomaterials*, *29*(23), 3393–3401.
6. Wang, Y. (2009). *Modelling degradation of bioresorbable polymeric devices*. Ph.D. thesis, Department of Engineering, University of Leicester.
7. Wang, L., & Nancollas, G. H. (2008). Calcium orthophosphates: crystallization and dissolution. *Chemical Reviews*, *108*(11), 4628–4669.
8. Wang, L., Tang, R., Bonstein, T., Orme, C. A., Bush, P. J., & Nancollas, G. H. (2005). A new model for nanoscale enamel dissolution. *The Journal of Physical Chemistry B*, *109*(2), 999–1005.
9. Tang, R., Orme, C. A., & Nancollas, G. H. (2004a). Dissolution of crystallites: surface energetic control and size effects. *ChemPhysChem*, *5*(5), 688–696.
10. Tang, R., Wang, L., & Nancollas, G. H. (2004b). Size-effects in the dissolution of hydroxyapatite: an understanding of biological demineralization. *Journal of Materials Chemistry*, *14*(14), 2341–2346.

11. Hayakawa, S. (2015). In vitro degradation behavior of hydroxyapatite. In M. Mucalo (Ed.), *Hydroxyapatite (HAp) for biomedical applications* (Vol. 4, pp. 85–105). Elsevier.
12. Grizzi, I., Garreau, H., Li, S., & Vert, M. (1995). Hydrolytic degradation of devices based on poly(DL-lactic acid) size-dependence. *Biomaterials*, *16*(4), 305–311.
13. Dorozhkin, S. V. (2010). Bioceramics of calcium orthophosphates. *Biomaterials*, *31*(7), 1465–1485.
14. Marshall, W. L., & Franck, E. (1981). Ion product of water substance, 0–1000 °C, 1–10,000 bars new international formulation and its background. *Journal of Physical and Chemical Reference Data*, *10*(2), 295–304.
15. Morse, J. W., Arvidson, R. S., & Lüttge, A. (2007). Calcium carbonate formation and dissolution. *Chemical Reviews*, *107*(2), 342–381.
16. Harned, H. S., & Scholes, S. R, Jr. (1941). The ionization constant of HCO_3^- from 0 to 50°. *Journal of the American Chemical Society*, *63*(6), 1706–1709.
17. Harned, H. S., & Davis, R., Jr. (1943). The ionization constant of carbonic acid in water and the solubility of carbon dioxide in water and aqueous salt solutions from 0 to 50°. *Journal of the American Chemical Society*, *65*(10), 2030–2037.
18. Bohner, M., Lemaître, J., & Ring, T. A. (1997). Kinetics of dissolution of β-tricalcium phosphate. *Journal of Colloid and Interface Science*, *190*(1), 37–48.
19. Gleadall, A., Pan, J., Kruft, M.-A., & Kellomäki, M. (2014a). Degradation mechanisms of bioresorbable polyesters. Part 1. Effects of random scission, end scission and autocatalysis. *Acta Biomaterialia*, *10*(5), 2223–2232.

Chapter 4
Degradation of Bioresorbable Composites: Tricalcium Phosphate Case Studies

As previously mentioned in the introductory chapter, studying the degradation of biocomposites is a time and resource-consuming process. Therefore it is logical to try and maximise the information that can be extracted from already published experimental data. Although inaccurate and incomplete information in composite characterisation are to be expected, analysing these published degradation data with the computational models obtained from the general modelling framework based on an extended version of Pan et al.'s TCP-polyester composite degradation model [1] and presented in Chap. 3 is, in the author's opinion, still a worthy approach. By doing so, a global degradation map for biocomposites can be built. This map, albeit incomplete, will aid understanding of the biocomposite degradation mechanisms and highlight areas of particular interest due to their appropriate degradation profiles.

A thorough search of composite degradation data available in literature was carried out in order to provide the necessary information for the computational models. The search focuses on composite samples made of biodegradable polyester matrixes, with special emphasis on poly(α-hydroxy)acids, and three different ceramic fillers: two calcium orthophosphates, namely tricalcium phosphate (TCP) and hydroxyapatite (HA), and a carbonate, namely calcium carbonate (CC). The data mining includes only studies which reported quantitative degradation measurements, preferably evolution of polymer molecular weight over time; although some other physical magnitudes employed to report degradation, e.g. pH or mass loss, have also been considered.

This chapter is the first one of a series of three (Chaps. 4, 5 and 7) presenting the analysis of literature data using the ceramic-specific computational models introduced in Chap. 3. Each chapter focuses on a different ceramic filler, starting with tricalcium phosphate in the present chapter, followed by hydroxyapatite in Chap. 5 and calcium carbonate in Chap. 7.

The present chapter is divided in seven different sections. Those section can be broadly grouped into two blocks. The first block encompassing the first four sections include the information needed a priori to run simulations while the last three sections, part of the second block, focus on the presentation and analysis of the results output

I. Moreno-Gomez, *A Phenomenological Mathematical Modelling Framework for the Degradation of Bioresorbable Composites*,
Springer Theses, https://doi.org/10.1007/978-3-030-04990-4_4

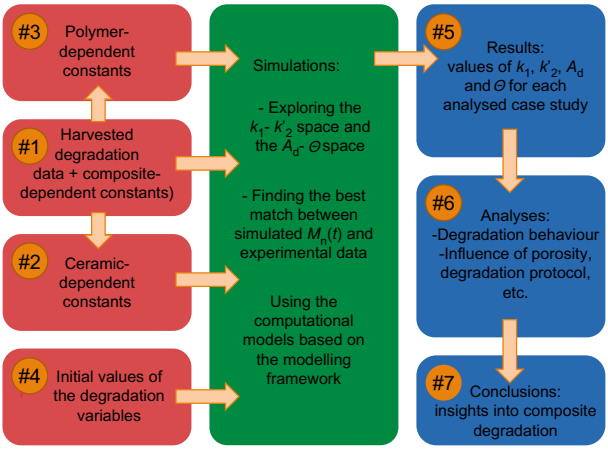

Fig. 4.1 Schematic showing the relationship between the structure of this chapter and the workflow of the composite degradation modelling

by the computational model. Figure 4.1 exhibits a schematic of the chapter structure highlighting the fit of each section in the general workflow.

The first block, depicted with its elements coloured in a red shade, contains the first four sections. The initial section, Sect. 4.1, includes the degradation data harvested from literature according to the methods described in Sect. 3.5.2. A polymer type and a ceramic type are part of the information extracted for each case study. The computational model employs constants associated with both the specific polymer type and the specific ceramic type for each case study. Those ceramic-dependent and polymer-dependent constants for the different tricalcium phosphate and polymer types encountered during the literature search are reported in Sects. 4.2 and 4.3 respectively. The fourth and last section of this block, Sect. 4.4, includes the values at the time origin of variables included in the TCP composites degradation model. Thus, these four sections contain all the necessary information to run the composite degradation simulations.

The computational model, the TCP composites degradation model in this case, employs all the abovementioned information to generate the results following the process described in Sect. 3.5.3. This stage in the modelling workflow is represented in Fig. 4.1 by a green shade element. For both practicality and lack of space, the different steps of the results generation process for the analysed case studies are not shown here.

The second part, depicted in a blue shade, consists of Sects. 4.5–4.7 dealing with a posteriori information. Firstly, the results output by the computational model are shown in a visual format in Sect. 4.5. Additional information obtained during the data harvesting and employed during composite degradation analysis is included in Appendix B.1. Secondly, a series of analyses of the results examining the degradation behaviour, in addition to the influence of several factors on said behaviour are

presented in Sect. 4.6. Finally, the main conclusions and insights obtained from all the analyses of the results are included in Sect. 4.7. This structure, albeit with minor changes, is also used in Chaps. 5 and 7.

4.1 Degradation Data from Tricalcium Phosphate Composites and Composite-Dependent Constants for the Tricalcium Phosphate Composites Model

This section contains the experimental data concerning the degradation of tricalcium phosphate composites and the values of the composite-dependent constants for the TCP data. The experimental degradation data are presented in a tabular format, including several composite-dependent constants employed as modelling input in addition to information about the reported quantitative degradation measurements and ceramic characterisation for each case study. The harvested data resulted from a search of the available literature conducted according to the method described in Sect. 3.5.2. Briefly, combinations including "tricalcium phosphate composite" in addition to other keywords are employed. Once a relevant article is found, both references and citations are also checked.

The degradation data can be grouped in two different categories: polymer characteristics and ceramic characteristics. The first category includes several characterising parameters of the polymeric matrix such as polymer type, molar ratio of monomers for the case of copolymers, initial number-average molecular weight, M_{n0} (kDa) and type of reported data reflecting composite degradation. The second category includes several characterising parameters of the ceramic filler such as ceramic type, ceramic weight fraction of the undegraded composite samples, f_{w0} (wt %), ceramic representative particle size, d_0 (μm) and ceramic data available to compute the ceramic representative particle size. The extracted data were processed as described in Sect. 3.5.2. Although the computational model employs input values in international system units, M_{n0} and d_0 are reported here using multiples for convenience due to the usual range encountered in literature for both variables.

Some of the extracted polymer and ceramic characterising parameters are composite-dependent constants, such as initial number-average molecular weight, M_{n0} (kDa); ceramic weight fraction of the undegraded composite samples, f_{w0} (wt %) and ceramic representative particle size, d_0 (μm), while others define the polymer-dependent constants, such as polymer type and molar ratio of monomers in copolymers or the ceramic-dependent constants, such as ceramic type. The remaining composite-dependent constants, excluding the composite degradation constants k_1, k_2', A_d and θ, are also presented in this section.

The data included in this section exclusively contains information fed to the computational model. Other relevant information, mostly concerning composite characteristics rather than polymer or ceramic characteristics, was also harvested for each studied composite degradation case. Those characteristics included fabrication

method, sample morphology and structure, as well as sample degradation protocol. Although these factors may affect composite degradation behaviour, they are not explicitly represented in the modelling framework. These pieces of information are included in Appendix B.1.

Table 4.1 presents the input degradation information extracted from the harvested literature data and employed to analyse the degradation of tricalcium phosphate composites using the TCP composites degradation model presented in Sect. 3.2.1. The data are ordered alphabetically by polymer type including first the homopolymers, followed by copolymers and blends. For similar polymer types, enantiopure matrixes are presented first. When several cases concerned the same polymeric matrix the cases are ordered according to ceramic type and initial polymer molecular weight. Each row in the table represents one case study and is separated from the rest by either a solid or a dashed line. A dashed line is used when consecutive cases were generated by the same author or research group and a solid line is used when there is no known author relationship. Tricalcium phosphate type is described using abbreviations. Briefly, TCP stands for tricalcium phosphate and the preceding Greek letter indicates the allotrope. The prefix "a" indicates low crystallinity. A complete list of tricalcium phosphate types including full denominations can be found in Table 4.2.

As previously mentioned, Table 4.1 includes three of the composite-dependent constants for each tricalcium phosphate case study. The values of the remaining nine composite-dependent constants for the case studies are discussed here. Water self-ionisation is not considered in the TCP composites degradation model, and thus, the value of the initial hydroxide ions concentration, $\Delta C_{\mathrm{OH}_0^-}$ ($\mathrm{mol\,m^{-3}}$), is not needed.

Similarly, ignoring the small contribution to the initial hydrogen ions concentration that results from the water self-ionisation and assuming no other hydrogen ions sources in the composites samples apart from the acid dissociation experienced by the polymer chains, the initial hydrogen ions concentration not resulting from carboxylic end groups dissociation, $\Delta C_{\mathrm{H}_0^+}$, takes the value $0\,\mathrm{mol\,m^{-3}}$.

In terms of polymer scission type, the tricalcium phosphates case studies were assumed to experience a mixture of random and end scission, as done by Pan et al. [1], which is characterised by:

- Empirical rate of production of short chains by chain scission, $\alpha = 0.4(1)$.
- Empirical exponent of production of short chains by chain scission, $\beta = 1(1)$.
- Average degree of pseudo-polymerisation of the short chains, $m = 4(1)$.

Finding the defining values of the last four composite-dependent parameters, the composite degradation constants k_1, k_2', A_d and θ, for each case study is the aim of the analysis process applied to these harvested degradation data. These values are the outcome of the composite degradation simulations and can be found in Sect. 4.5.

Table 4.1 Summary of data found in literature on degradation of composites made of biodegradable polymer and tricalcium phosphate. *CMR* is the molar ratio of the different monomers in a copolymer, M_{n0} is the sample initial number-average molecular weight, f_{w0} is the initial ceramic weight fraction of a composite sample and d_0 is the ceramic representative particle size of the undegraded composite sample. Further abbreviations employed in columns labelled "Data" can be found in Sect. 3.5.2. Abbreviations used to specify the tricalcium phosphate type can be found in Table 4.2. A dashed line between rows indicates that data displayed in those consecutive rows belong to the same researcher or research group. A solid line between rows indicates no known author relationship for the data

Polymer characteristics				Ceramic characteristics				Case code and reference
Type	CMR (mol %)	M_{n0} (kDa)	Data	Type	f_{w0} (wt %)	d_0 (μm)	Data	
Poly(L-lactide)	–	67.17	$M_n(t)$	–	0	–	d_{mean} in text	Kobayashi β-TCP [2]
	–	60.80		β-TCP	4.7	2.22		
	–	57.60		β-TCP	9.1	2.40		
	–	59.52		β-TCP	13.3	2.68		
Poly(L-lactide)	–	68.00	$M_v(t_0)$	–	0	–	$f_{wb}(125)$ μm	Aunoble β-TCP [3]
	–	46.00		β-TCP	60	103		
Poly(L-lactide)	–	251.70	$M_w(t)$ and $PDI(t)$	–	0	–	SEM images	Adamus β-TCP [4]
	–	95.49		β-TCP	52	1.1		
Poly(L-lactide)	–	351.37	$M_w(t)$ and $PDI(t)$	β-TCP	66.7	2.41	d_{mean} in text	Kang 07 S β-TCP [5]
Poly(L-lactide)	–	351.37	$M_w(t)$ and $PDI(t)$	β-TCP	66.7	2.41	d_{mean} in text	Kang 07 F β-TCP [5]
Poly(L-lactide)	–	580.00	$M_n(t)$	β-TCP	65	2.41	d_{mean} in text	Kang 09 F β-TCP [6]
Poly(L-lactide)	–	580.00	$M_n(t)$	β-TCP	65	2.41	d_{mean} in text	Kang 09 FL β-TCP [6]

(continued)

Table 4.1 (continued)

Polymer characteristics				Ceramic characteristics				Case code and reference
Type	CMR (mol%)	M_{n0} (kDa)	Data	Type	f_{w0} (wt%)	d_0 (μ m)	Data	
Poly(D,L-lactide)	4:96	36.89	$M_w(t)$	–	0	–	$d_{\text{Vol mean}}$ in text	Daculsi Vit β-TCP [7]
	4:96	43.75		β-TCP	10	40		
	4:96	37.23		β-TCP	24	40		
Poly(D,L-lactide)	4:96	36.89	$M_w(t)$	–	0	–	$d_{\text{Vol mean}}$ in text	Daculsi Viv β-TCP [7]
	4:96	43.75		β-TCP	10	40		
	4:96	37.23		β-TCP	24	40		
Poly(D,L-lactide)	4:96	37.00	$\%M_n(t)$ and M_{n0}	–	0	–	$f_n(50, 125)$ μm	Niemela LD β-TCP [8]
	4:96	26.00		β-TCP	20	100		
Poly(D,L-lactide)	50:50	18.30	$M_w(t)$ and $PDI(t_0)$	–	0	–	d_{mean} in text	Zheng aβ-TCP [9]
	50:50	19.25		aβ-TCP	25	0.72		
	50:50	22.82		aβ-TCP	33	0.72		
	50:50	23.49		aβ-TCP	50	0.72		
Poly(D,L-lactide)	50:50	30.00	$W_L(t)$	–	0	–	$f_{wd}(50, 199)$ μm	Lin β-TCP [10]
	50:50	30.00		β-TCP	30	166		
	50:50	30.00		β-TCP	35	166		
	50:50	30.00		β-TCP	40	166		
	50:50	30.00		β-TCP	45	166		
	50:50	30.00		β-TCP	50	166		
	50:50	30.00		β-TCP	55	166		
	50:50	30.00		β-TCP	60	166		

(continued)

Table 4.1 (continued)

Polymer characteristics				Ceramic characteristics				Case code and reference
Type	CMR (mol%)	M_{n0} (kDa)	Data	Type	f_{w0} (wt%)	d_0 (μ m)	Data	
Poly(D,L-lactide)	50:50	88.13	$M_w(t)$	–	0	–	d_{mean} in text	Heidemann β-TCP [11]
	50:50	92.88		β-TCP	26	2.2		
Poly(L-co-D,L-lactide)	70:30	26.35	$M_w(t)$ and $I.V.(t_0)$	–	0	–	$f_n(50, 125)$ μm	Niemela LDL β-TCP [12]
	70:30	23.26		β-TCP	20	100		
Poly(L-co-D,L-lactide)	70:30	46.15	$M_n(t)$	α-TCP	45	163	$f_n(200)$ μm	Ignatius P α-TCP [13]
Poly(L-co-D,L-lactide)	70:30	68.33	$M_w(t)$	–	0	–	$f_n(200)$ μm	Ignatius D β-TCP [14]
	70:30	87.71		β-TCP	10	163		
	70:30	66.50		β-TCP	30	163		
Poly(L-co-D,L-lactide)	70:30	204.92	$I.V.(t)$ for PP	–	0	–	$f_n(75, 106)$ μm	Haaparanta 3wt β-TCP [15]
	70:30	204.92		β-TCP	5	93		
	70:30	204.92		β-TCP	10	93		
	70:30	204.92		β-TCP	20	93		
Poly(L-co-D,L-lactide)	70:30	211.69	$I.V.(t)$ for PP	–	0	–	$f_n(75, 106)$ μm	Haaparanta 2wt β-TCP [15]
	70:30	211.69		β-TCP	5	93		
	70:30	211.69		β-TCP	10	93		
	70:30	211.69		β-TCP	20	93		
Poly(L-lactide-co-ε-caprolactone)	70:30	90.00	$M_w(t)$ and $PDI(t_0)$	–	0	–	SEM image	Ahola 13 β-TCP [16]
	70:30	69.00		β-TCP	54.35	19		
	70:30	70.00		β-TCP	65.22	19		

(continued)

Table 4.1 (continued)

Polymer characteristics				Ceramic characteristics				Case code and reference
Type	CMR (mol %)	M_{n0} (kDa)	Data	Type	f_{w0} (wt %)	d_0 (μ m)	Data	
Poly(L-lactide-co-ε-caprolactone)	70:30	90.98	$M_n(t)$	–	0	–	SEM image	Ahola 12 β-TCP [17]
	70:30	87.97		β-TCP	10	19		
	70:30	78.57		β-TCP	20	19		
	70:30	74.44		β-TCP	35	19		
	70:30	69.55		β-TCP	50	19		
Poly(L-lactide-co-ε-caprolactone)	92:8	39.12	$M_w(t)$	–	0	–	SEM image	Kikuchi PLCL β-TCP [18]
	92:8	43.71		β-TCP	50	4		
Poly(L-lactide-co-glycolide)	70:30	65.00	$M_n(t)$	–	0	–	SEM images	Yang F. β-TCP [19]
	70:30	54.50		β-TCP	30	9		
Poly(L-lactide-co-glycolide)	70:30	160.30	$M_n(t)$	β-TCP	41.5	3.22	d_{mean} in text	Yang Y. S β-TCP [20]
Poly(L-lactide-co-glycolide)	70:30	160.30	$M_n(t)$	β-TCP	41.5	3.22	d_{mean} in text	Yang Y. D β-TCP [20]
Poly(L-lactide-co-glycolide)	70.7:29.3	24.79	$M_w(t)$ and $PDI(t_0)$	–	0	–	SEM images	Jin β-TCP [21]
	70.7:29.3	19.50		β-TCP	10	5		
	70.7:29.3	26.12		β-TCP	30	5		
Poly(D,L-lactide-co-glycolide)	44.6:55.4	8.60	$\%M_w(t)$ and $PDI(t_0)$	–	0	–	Assumed	Ara β-TCP [22]
	44.6:55.4	10.00		β-TCP	30	30		

(continued)

Table 4.1 (continued)

Polymer characteristics				Ceramic characteristics				Case code and reference
Type	CMR (mol%)	M_{n0} (kDa)	Data	Type	f_{w0} (wt%)	d_0 (μ m)	Data	
Poly(D,L-lactide-co-glycolide)	50:50	34.00	$W_L(t)$, $pH(t)$ and M_n as-received	–	0	–	Particle size distribution in composite	Bennett nC α-TCP [23]
	50:50	34.00		α-TCP	27.1	0.8		
Poly(D,L-lactide-co-glycolide)	50:50	34.00	$W_L(t)$, $pH(t)$ and M_n as-received	–	0	–	Particle size distribution in composite	Bennett nC $D_2$50 α-TCP [23]
	50:50	34.00		α-TCP	27.1	0.8		
Poly(D,L-lactide-co-glycolide)	50:50	34.00	$W_L(t)$, $pH(t)$ and M_n as-received	–	0	–	Particle size distribution in composite	Bennett nC $D_2$100 α-TCP [23]
	50:50	34.00		α-TCP	27.1	0.8		
Poly(D,L-lactide-co-glycolide)	50:50	34.00	$W_L(t)$, $pH(t)$ and M_n as-received	–	0	–	Particle size distribution in composite	Bennett iC α-TCP [23]
	50:50	40.80		α-TCP	31.5	5.4		
Poly(D,L-lactide-co-glycolide)	50:50	34.00	$W_L(t)$, $pH(t)$ and M_n as-received	–	0	–	Particle size distribution in composite	Bennett mC α-TCP [23]
	50:50	34.00		α-TCP	30.2	49		

(continued)

Table 4.1 (continued)

Polymer characteristics				Ceramic characteristics				Case code and reference
Type	CMR (mol %)	M_{n0} (kDa)	Data	Type	f_{w0} (wt %)	d_0 (μ m)	Data	
Poly(D,L-lactide-co-glycolide)	50:50	34.00	$W_L(t)$, $pH(t)$ and M_n as-received	–	0	–	Particle size distribution in composite	Bennett mC $D_2$50 α-TCP [23]
	50:50	34.00		α-TCP	30.2	49		
Poly(D,L-lactide-co-glycolide)	50:50	34.00	$W_L(t)$, $pH(t)$ and M_n as-received	–	0	–	Particle size distribution in composite	Bennett mC $D_2$100 α-TCP [23]
	50:50	34.00		α-TCP	30.2	49		
Poly(D,L-lactide-co-glycolide)	50:50	34.50	$W_L(t)$, $pH(t)$ and M_w as-received	–	0	–	Particle size distribution	Ege α-TCP [24, 25]
	50:50	34.50		α-TCP	25.24	0.333		
Poly(D,L-lactide-co-glycolide)	50:50	34.50	$W_L(t)$, $pH(t)$ and M_w as-received	–	0	–	Particle size distribution	Yang Z. 5050 nC α-TCP [26, 27]
	50:50	34.50		α-TCP	22.38	0.57		
	50:50	34.50		α-TCP	30.82	0.57		
	50:50	34.50		α-TCP	40.25	0.57		
Poly(D,L-lactide-co-glycolide)	50:50	34.50	$W_L(t)$, $pH(t)$ and M_w as-received	–	0	–	SEM image	Yang Z. 5050 mC α-TCP [26, 27]
	50:50	34.50		α-TCP	32.40	19		

(continued)

Table 4.1 (continued)

Polymer characteristics				Ceramic characteristics				Case code and reference
Type	CMR (mol %)	M_{n0} (kDa)	Data	Type	f_{w0} (wt %)	d_0 (μ m)	Data	
Poly(D,L-lactide-co-glycolide)	50:50	36.00	$W_L(t)$, $pH(t)$ and M_n as-received	–	0	–	Particle size distribution	Mellon α-TCP [28]
	50:50	36.00		α-TCP	20	6.02		
	50:50	36.00		α-TCP	60	6.02		
Poly(D,L-lactide-co-glycolide)	50:50	36.50	$pH(t)$ and M_w as-received	–	0	–	Analysis in [23]	Barrett α-TCP [29, 30]
	50:50	36.50		α-TCP	10.25	1.5		
	50:50	36.50		α-TCP	20.51	1.5		
	50:50	36.50		α-TCP	30.77	1.5		
	50:50	36.50		α-TCP	41.02	1.5		
Poly(D,L-lactide-co-glycolide)	50:50	68.50	$W_L(t)$, $pH(t)$ and M_w as-received	–	0	–	μ-CT images	Ehrenfried α-TCP [31]
	50:50	68.50		α-TCP	5	175		
	50:50	68.50		α-TCP	10	175		
	50:50	68.50		α-TCP	15	175		
	50:50	68.50		α-TCP	20	175		
	50:50	68.50		α-TCP	30	175		
	50:50	68.50		α-TCP	40	175		
Poly(D,L-lactide-co-glycolide)	50:50	34.50	$W_L(t)$, $pH(t)$ and M_w as-received	–	0	–	Particle size distribution	Ege β-TCP [25]
	50:50	34.50		β-TCP	19.45	0.648		

(continued)

Table 4.1 (continued)

Polymer characteristics				Ceramic characteristics				Case code and reference
Type	CMR (mol %)	M_{n0} (kDa)	Data	Type	f_{w0} (wt %)	d_0 (μ m)	Data	
Poly(D,L-lactide-co-glycolide)	50:50	36.00	$W_L(t)$, $pH(t)$ and M_n as-received	–	0	–	Particle size distribution	Mellon β-TCP [28]
	50:50	36.00		β-TCP	40	4.02		
Poly(D,L-lactide-co-glycolide)	75:25	60.00	$W_L(t)$, $pH(t)$ and M_w as-received	–	0	–	Particle size distribution	Yang Z. 7525 nC α-TCP [27]
	75:25	60.00		α-TCP	22.38	0.57		
	75:25	60.00		α-TCP	30.82	0.57		
	75:25	60.00		α-TCP	40.25	0.57		
Poly(D,L-lactide-co-glycolide)	75:25	60.00	$W_L(t)$, $pH(t)$ and M_w as-received	–	0	–	SEM image	Yang Z. 7525 mC α-TCP [27]
	75:25	60.00		α-TCP	32.40	19		
Poly(L-lactide)/poly(ethylene: hexamethylene/sebacate) block copolymer	75.3:24.7	27.28	$M_w(t)$ and $PDI(t)$	–	0	–	d_{mean} in text	Imai L100 β-TCP [32]
	75.3:24.7	32.44		β-TCP	10	5.3		
	75.3:24.7	29.35		β-TCP	30	5.3		

(continued)

Table 4.1 (continued)

Polymer characteristics				Ceramic characteristics				Case code and reference
Type	CMR (mol %)	M_{n0} (kDa)	Data	Type	f_{w0} (wt %)	d_0 (μ m)	Data	
Poly(L-lactide)/ poly(ethylene: hexamethylene/sebacate) block copolymer	75.3:24.7	28.28	$M_w(t)$ and $PDI(t)$	–	0	–	d_{mean} in text	Imai L250 β-TCP [32]
	75.3:24.7	35.01		β-TCP	10	5.3		
	75.3:24.7	31.12		β-TCP	30	5.3		
Poly(L-lactide)/ poly(ethylene: hexamethylene/sebacate) block copolymer	75.3:24.7	70.14	$M_w(t)$	–	0	–	d_{mean} in text	Kikuchi T800 β-TCP [33]
	75.3:24.7	47.81		β-TCP	75	0.3		
Poly(L-lactide)/ poly(ethylene: hexamethylene/sebacate) block copolymer	75.3:24.7	70.14	$M_w(t)$	–	0	–	d_{mean} in text	Kikuchi T1100 β-TCP [33]
	75.3:24.7	66.00		β-TCP	75	1		

(continued)

Table 4.1 (continued)

Polymer characteristics				Ceramic characteristics				Case code and reference
Type	CMR (mol %)	M_{n0} (kDa)	Data	Type	f_{w0} (wt %)	d_0 (μ m)	Data	
Poly(L-lactide)/ poly(ethylene: hex-amethylene/sebacate) block copolymer	98.3:1.7	81.66	$M_n(t)$	–	0	–	d_{mean} in text	Imai H100 β-TCP [34]
	98.3:1.7	66.15		β-TCP	10	5.3		
	98.3:1.7	57.92		β-TCP	30	5.3		
Poly(L-lactide)/ poly(ethylene: hex-amethylene/sebacate) block copolymer	98.3:1.7	61.47	$M_n(t)$	–	0	–	d_{mean} in text	Imai H250 β-TCP [34]
	98.3:1.7	84.00		β-TCP	10	5.3		
	98.3:1.7	53.80		β-TCP	30	5.3		
Poly(L-lactide-co-glycolide-co-ε-caprolactone)	75:11:14	120.35	$M_w(t)$	–	0	–	SEM image	Kikuchi PLGC β-TCP [18]
	75:11:14	126.29		β-TCP	60	4		

Table 4.2 Abbreviations and descriptions of the different types of tricalcium phosphate encountered in the harvested degradation data

Abbreviation	Description
α-TCP	Highly crystalline alpha tricalcium phosphate
β-TCP	Highly crystalline beta tricalcium phosphate
aβ-TCP	Amorphous or low crystallinity beta tricalcium phosphate

4.2 Tricalcium Phosphate Information and Ceramic-Dependent Constants for the Tricalcium Phosphate Composites Degradation Model

This section presents the different types of tricalcium phosphate found in the harvested literature and their associated values of the ceramic-dependent parameters. The TCP computational model derived from the modelling framework, presented in Sect. 3.2.1, employs chemical relationships to characterise the interactions between ceramic filler and polymeric matrix resulting in a versatile model capable of dealing with different types of tricalcium phosphate.

Tricalcium phosphate (TCP), whose chemical formula is $Ca_3(PO_4)_2$, has several allotropes, namely α, β and α′. The three distinct polymorphs are stable at different temperatures, with the transition from β-TCP to α-TCP occurring at 1125 °C [35] and the transition from α-TCP to α′-TCP at 1430 °C but with α′-TCP unable to survive quenching [35].

Although the three allotropes share exactly the same chemical composition, $Ca_3(PO_4)_2$, and therefore release Ca^{2+} and $(PO_4)^{3-}$ ions during dissolution, the polymorphs have different crystallographic properties with β-TCP having a rhombohedral space group $R3c$ [35], α-TCP a monoclinic space group $P2_1/a$ [35] and α′-TCP a hexagonal space group $P6_3/mmc$ [35]. These differences in structure affect the ceramic parameters used in the computational model.

Usually when prepared through a conventional wet chemistry route, the TCP fabrication method includes a high temperature sintering step with this temperature defined accordingly to the sought after TCP allotrope [25]. As a result, it is not common to find low crystallinity α- or β-TCP, which would differ in properties from their high crystallinity counterparts. Table 4.2 reports the abbreviations used to designate each one of the tricalcium phosphate types encountered in the harvested tricalcium phosphate composites degradation data.

The modelling framework uses several parameters that are ceramic-dependent, namely ceramic molar mass, M_{cer}; ceramic density, ρ_{cer}; ceramic molar volume, Ω_{cer}; ceramic solubility expressed as a negative base 10 logarithm of the ionic product at

Table 4.3 Values of the ceramic-dependent parameters used in the tricalcium phosphate model. Acid dissociation expressed as the negative base 10 logarithm of the acid dissociation constant, $pK_i = -\log_{10}(K_i)$ with K_i in mol dm^{-3}. Solubility expressed as the negative base 10 logarithm of the ionic product at equilibrium of Ca_3PO_4 with concentrations in mol dm^{-3}. $|_{\alpha/\beta/a\beta}$ used to denote the value of a magnitude particularised for a specific TCP polymorph

Constant (unit)	Quantity	Value	Reference
pK_1 (1)	First logarithmic phosphoric acid dissociation constant at 37 °C	2.21	[36]
pK_2 (1)	Second logarithmic phosphoric acid dissociation constant at 37 °C	7.18	[37]
pK_3 (1)	Third logarithmic phosphoric acid dissociation constant at 37 °C	12.23	[38]
M_{TCP} (g mol^{-1})	TCP molar mass	310.177	[39]
$-\log_{10}(K_{sp})\|_{\alpha}$ (1)	α-TCP solubility at 37 °C	25.5	[40]
$-\log_{10}(K_{sp})\|_{a\beta-\beta}$ (1)	aβ-TCP and β-TCP solubility at 37 °C	29.5	[40]
$[Ca^{2+}]_{eq}\|_{\alpha}$ (mol m^{-3})	α-TCP equilibrium calcium concentration at 37 °C	9.342×10^{-3}	Appendix A.2.1
$[Ca^{2+}]_{eq}\|_{a\beta-\beta}$ (mol m^{-3})	aβ-TCP and β-TCP equilibrium calcium concentration at 37 °C	1.481×10^{-3}	Appendix A.2.1
$\rho_{TCP}\|_{\alpha}$ (kg m^{-3})	α-TCP density	2860	[40]
$\rho_{TCP}\|_{\beta}$ (kg m^{-3})	β-TCP density	3070	[40]
$\rho_{TCP}\|_{a\beta}$ (kg m^{-3})	aβ-TCP density	2456	⊤
$\Omega_{TCP}\|_{\alpha}$ (m^3 mol^{-1})	α-TCP molar volume	1.085×10^{-4}	†
$\Omega_{TCP}\|_{a\beta}$ (m^3 mol^{-1})	aβ-TCP molar volume	1.262×10^{-4}	†
$\Omega_{TCP}\|_{\beta}$ (m^3 mol^{-1})	β-TCP molar volume	1.010×10^{-4}	†

⊤ Data not reported. Assuming density is 80% of β-TCP density
† Calculated as the ratio between M_{TCP} and ρ_{TCP} ($\Omega_{TCP} = {}^{M_{TCP}}/_{\rho_{TCP}}$)

equilibrium, $-\log_{10}(K_{sp})$; ceramic calcium equilibrium concentration, $[Ca^{2+}]_{eq}|_{cer}$ and acid dissociation constants associated to the released anions, pK_i. The values of these ceramic-dependent constants for the encountered tricalcium phosphate types are presented in Table 4.3.

4.3 Biodegradable Polymers Information and Polymer-Dependent Constants for the Composites Degradation Modelling Framework

This section includes the values of the polymer-dependent constant for all the polymer matrixes present in the harvested degradation data from Chaps. 4, 5 and 7. All the computational models derived from the modelling framework use the same mathematical representation to characterise polymer degradation and are able to accommodate a range of different polymeric matrixes. Thus, these constants are common across the three ceramic-specific composites degradation models presented in Sects. 3.2.1–3.2.3.

The values of the three polymer-dependent parameters, namely polymer density, ρ_{pol}; polymer acid dissociation constant, K_{a} and molar mass associated to one ester bond in the polymeric matrix, M_{unit} are reported, in addition to the semi structural formula of the repeating unit(s), in Table 4.4 for all the different polymer types encountered in all the analysed degradation data.

4.4 Initial Values for the TCP Composites Degradation Model Variables

Having now presented the values of the composite-dependent, ceramic-dependent and polymer-dependent constants in Sects. 4.1, 4.2, 4.3 respectively, only the initial values of the degradation variables used in the TCP composites degradation model, discussed in Sect. 3.2.1, are needed in order to simulate the degradation of tricalcium phosphate composites. This section includes those values.

The values of the eleven degradation variables at the time origin, which are listed below, arise from two assumptions: firstly, that both ceramic dissolution and polymer scission start at the time origin and secondly, that the polymer phase has attained carboxylic end acid dissociation equilibrium at the time origin with the initial hydrogen ions concentration not resulting from carboxylic end groups dissociation, $\Delta C_{\text{H}_0^+} = 0\,\text{mol}\,\text{m}^{-3}$.

- $x_1|_{t=0} = R_{s0} = 0$, initial concentration of polymer chain scissions ($\text{mol}\,\text{m}^{-3}$).
- $x_2|_{t=0} = [H^+]_0 = C_{\text{H}_0^+} = -0.5K_{\text{a}} + \sqrt{0.25K_{\text{a}}^2 + K_{\text{a}}C_{\text{chain0}}}$, initial concentration of hydrogen ions ($\text{mol}\,\text{m}^{-3}$).
- $x_3|_{t=0} = [Ca^{2+}]_0 = 0$, initial concentration of calcium ions ($\text{mol}\,\text{m}^{-3}$).
- $x_4|_{t=0} = [PO_4^{3-}]_0 = 0$, initial concentration of phosphate ions ($\text{mol}\,\text{m}^{-3}$).
- $x_5|_{t=0} = [R\text{-}COOH]_0 = C_{\text{chain0}} - \left(-0.5K_{\text{a}} + \sqrt{0.25K_{\text{a}}^2 + K_{\text{a}}C_{\text{chain0}}}\right)$, initial concentration of non-dissociated carboxylic end group chains ($\text{mol}\,\text{m}^{-3}$).
- $x_6|_{t=0} = [R\text{-}COO^-]_0 = -0.5K_{\text{a}} + \sqrt{0.25K_{\text{a}}^2 + K_{\text{a}}C_{\text{chain0}}}$, initial concentration of dissociated carboxylic end group chains ($\text{mol}\,\text{m}^{-3}$).

Table 4.4 Polymer specific parameters used in the models stemming from the composites degradation modelling framework. *CMR* is the molar ratio of the different monomers in a copolymer, M_{unit} is the average molar mass associated to one ester bond, pK_a is the negative base 10 logarithm of the polymer acid dissociation constant at 37 °C and ρ_{pol} is the polymer density reported as midpoint of the typical density interval. The repeating unit or units are reported using semi structural formulas

Type	CMR	M_{unit} ($g\,mol^{-1}$)	pK_a (1)	ρ_{pol} ($kg\,m^{-3}$)	Repeating unit(s)	Reference
Poly(ε-caprolactone)	–	114.144	4.88⋆	1128	$-\left(O-(CH_2)_5-C(=O)\right)_n-$	[69, 70]
Poly(glycolide)	–	58.036	3.83*	1600	$-\left(O-CH_2-C(=O)\right)_n-$	[69, 70]
Poly(L-lactide)	–	72.063	3.87^	1270	$-\left(O-C^{\bullet}H(CH_3)-C(=O)\right)_n-$	[69, 70]
Poly(D,L-lactide)	4:96 50:50	72.063 72.063	3.87^ 3.87^	1260+ 1260	$-\left(O-C^{\bullet}H(CH_3)-C(=O)\right)_{n,m}-$	[69, 70] [69, 70]
Poly(L-co-D,L-lactide)	70:30	72.063	3.87^	1267†	$-\left(O-C^{\bullet}H(CH_3)-C(=O)\right)_{n,m}-$	[69, 70]
Poly(L-lactide-co-ε-caprolactone)	28.4:71.6 70:30 86.4:13.6 92:8	102.193† 84.687† 77.786† 75.429†	4.32† 4.01† 3.93† 3.90†	1200⊓ 1280‡ 1280‡ 1280‡	$-\left(O-C^{\bullet}H(CH_3)-C(=O)\right)_n-$ $-\left(O-(CH_2)_5-C(=O)\right)_m-$	[69] [69, 71] [69, 71] [69, 71]
Poly(D,L-lactide-co-ε-caprolactone)	60:40	88.895†	4.06†	1270⊔	$-\left(O-C^{\bullet}H(CH_3)-C(=O)\right)_{n,m}-$ $-\left(O-(CH_2)_5-C(=O)\right)_o-$	[69, 70]

(continued)

Table 4.4 (continued)

Type	CMR	M_{unit} ($g\,mol^{-1}$)	pK_a (1)	ρ_{pol} ($kg\,m^{-3}$)	Repeating Unit(s)	Reference
Poly(L-lactide-co-glycolide)	70:30	67.855[†]	3.86[†]	1310[†]	$-\left(O-C^{\bullet}H(CH_3)-C(=O)\right)_n-$	[69, 70]
	70.7:29.3	67.953[†]	3.86[†]	1310[†]	$-\left(O-CH_2-C(=O)\right)_m-$	[69, 70]
Poly(D,L-lactide-co-glycolide)	44.6:55.4	64.292[†]	3.85[†]	1350[◇]	$-\left(O-C^{\bullet}H(CH_3)-C(=O)\right)_{n,m}-$	[69, 70]
	47:53	64.629[†]	3.85[†]	1350[◇]		[69, 70]
	50:50	65.050[†]	3.85[†]	1350		[69, 70]
	75:25	68.556[†]	3.86[†]	1300	$-\left(O-CH_2-C(=O)\right)_o-$	[69, 70]
	85:15	69.959[†]	3.86[†]	1290		[69, 72]
	95:5	71.362[†]	3.87[†]	1290[◁]		[69, 72]
Poly(L-lactide)/ poly(ethylene:hexamethylene/ sebacate) block copolymer)	75.3:24.7	90.444[†]	3.98[†]	1.224[†]	$-\left(O-(CH_2)_2\right)_m-$	[69, 73] App. A.7
	98.3:1.7	73.328[†]	3.88[†]	1.266[†]	$-\left(O-(CH_2)_6\right)_o-$	[69, 73] App. A.7
					$-\left(O-C^{\bullet}H(CH_3)-C(=O)\right)_n-$	
					$-\left(O-C(=O)-(CH_2)_8-C(=O)\right)_p-$	

(continued)

Table 4.4 (continued)

Type	CMR	M_{unit} ($g\,mol^{-1}$)	pK_a (1)	ρ_{pol} ($kg\,m^{-3}$)	Repeating Unit(s)	Reference
Poly(L-lactide-co-glycolide co-ε-caprolactone)	75:11:14	76.411†	3.92†	1300∨	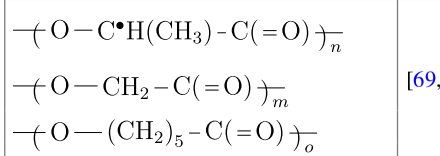	[69, 70]
Poly(D,L-lactide-co-glycolide co-ε-caprolactone)	46.7:25.1:28.2	80.405†	3.98†	1300∨	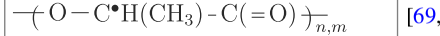	[69, 70]
	42:42:16	72.905†	3.92†	1300∨	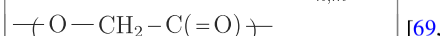	[69, 70]
	61.0:32.9:6.1	70.020†	3.88†	1300∨	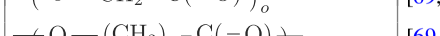	[69, 70]

†Parameter calculated as a weighted average using homopolymer data and *CMR* monomer ratios as proportionality constants. For pK_a values, the weighted average is calculated with K_a values. Further details can be found in Appendix A.3
⋆ Calculated using linear interpolation between the pK_a values reported at 30 and 40 °C
∗ pK_a value reported at 37.5 °C
∧ Calculated using linear interpolation between the pK_a values reported at 35 and 40 °C
• Chiral centre present in the poly(lactide) repeating unit
+ Assumed equal to PDLLA(50:50)
⊓ Assumed value
⊔ Assumed equal to PLLA density
‡ Assumed equal to PLAεCL (86:14) density
◇ Assumed equal to P(D,L)LGA (50:50) density
∨ Assumed equal to P(D,L)LGA (75:25) density
◁ Assumed equal to P(D,L)LGA (85:15) density

- $x_7|_{t=0} = [HPO_4^{2-}]_0 = 0$, initial concentration of hydrogenphosphate ions (mol m^{-3}).
- $x_8|_{t=0} = [H_2PO_4^-]_0 = 0$, initial concentration of dihydrogenphosphate ions (mol m^{-3}).
- $x_9|_{t=0} = [H_3PO_4]_0 = 0$, initial concentration of phosphoric acid (mol m^{-3}).
- $x_{10}|_{t=0} = a_{TCP0} = \frac{\pi d_0^2}{V_{unit}}$, initial concentration of interfacial area in the composite (m^2 m^{-3}).
- $x_{11}|_{t=0} = M_{n0}$, initial polymer number-average molecular weight (Da).

where the concentrations $x_1,\ldots,x_9$ are defined in the polymer phase, K_a is the polymer acid dissociation constant at 37 °C (mol m^{-3}); C_{chain0}, the polymer chains concentration at the time origin (mol m^{-3}); d_0, the representative particle size (m) and V_{unit}, the volume of the representative unit cell (m^3).

4.5 Results of the Tricalcium Phosphate Composites Degradation Model

The results output by the TCP composites degradation model after running the simulations with the TCP degradation data reported in Sect. 4.1 are presented in this section. These results have been grouped in four different blocks, according to their polymeric matrixes: poly(L-lactide), poly(D,L-lactide) homo- or copolymer, polylactide-co-glycolide and "miscellaneous polymers". The chosen visual representation, aimed at facilitating the analysis, includes three different graphs: a polymer degradation map, a ceramic degradation map and a 3D plot exploring the polymer-ceramic degradation space. The polymer degradation map provides information about degradation aspects of the matrix by representing each case as a point by their duplet (k_1, k_2') in the k_1–k_2' plane. Likewise, the ceramic degradation map provides information about degradation aspects of the tricalcium phosphate filler by representing each case as a point by their duplet (A_d, θ) in the A_d–θ plane. Lastly, each case is represented as a triplet (k_1, k_2', A_d) in the (k_1–k_2'–A_d) degradation space. Each analysed tricalcium phosphate composite degradation case is always represented by the same unique combination of marker and colour, with the colour shade being an indication of the polymeric matrix group the case belongs to: blue for poly(L-lactide), green for poly(D,L-lactide) homo- or copolymer and red for poly(lactide-co-glycolide). The legend included in each visual representation of the results is common for the three displayed graphs: k_1–k_2' map, A_d–θ plane and k_1–k_2'–A_d plot. For clarity purposes, the results associated with one polymeric matrix have been split into several groups when an excessive amount of data resulted in difficulty interpreting the graphs.

Uniqueness of model parameters, k_1, k_2', A_d and θ: As explained in Sect. 3.5.3, usually several (k_1, k_2') pairs provide a good fitting for pure polymer data alone. Subsequently, during composite data analysis there is a possibility of having more than one (k_1, k_2', A_d, θ) 4-tuple with a good fitting, as higher k_2' values can be compensated with higher A_d values, i.e. cases displaying both high autocatalytic polymer

degradation rate k_2' and high dissolution rate A_d can have the same molecular weight reduction profile as cases with both low k_2' and A_d. The likelihood of having multiple solutions for a given case dramatically decreases with more than one composite sample. For TCP cases with multiple solutions, the chosen and reported 4-tuple was selected considering typical dissolution profiles, in terms of remaining ceramic weight fraction, found in literature for similar TCP composites.

4.5.1 Poly(L-lactide) Matrix

TCP case studies with a poly(L-lactide) matrix were analysed, despite PLLA being a semi-crystalline polymer, because samples were either amorphous or presented a crystalline fraction of less than 10% with no evidence of degradation-induced crystallisation over time.

Figure 4.2 shows the visual representation of the modelling results for the poly(L-lactide)-TCP case studies. This visual representation consists of three degradation maps: a polymer degradation map, showing the obtained k_1 and k_2' values, in Fig. 4.2a, a ceramic degradation map, with the A_d and θ values in Fig. 4.2b and lastly, a representation of the 3D degradation space (k_1–k_2'–A_d) in Fig. 4.2c. The poly(L-lactide) group contained data from Kobayashi and Yamaji [2], Aunoble et al. [3], Adamus et al. [4] and Kang et al. [5, 6].

The polymer degradation map in Fig. 4.2a showed some clustering, with most (k_1, k_2') duplets falling inside the bottom left quarter of the polymer degradation map. Conversely, the ceramic map in Fig. 4.2b showed no clustering, apart from the four cases authored by Kang et al. (case codes starting with Kang: □, ⬟, ⬣ and ⬢). Appendix B.1.1 contains the above-mentioned TCP-PLLA results in a tabular format. Additionally, it includes several composite characteristics for each analysed case study, necessary for discussion Sect. 4.6.

4.5.2 Poly(D,L-lactide) and Poly(D,L-lactide) Copolymers Matrixes

The visual representation of the results output by the TCP composites degradation model (Sect. 3.2.1) for case studies with a poly(D,L-lactide) homo- or copolymer matrix is shown in Fig. 4.3. This group encompassed data from Daculsi et al. [7], Niemel et al. [8, 12], Zheng et al. [9], Lin et al. [10], Heidemann et al. [11], Ignatius et al. [13, 14] and Haaparanta et al. [15]. Figure 4.3a exhibits the polymer degradation map, Fig. 4.3b the ceramic degradation map and Fig. 4.3c the representation in the 3D degradation space.

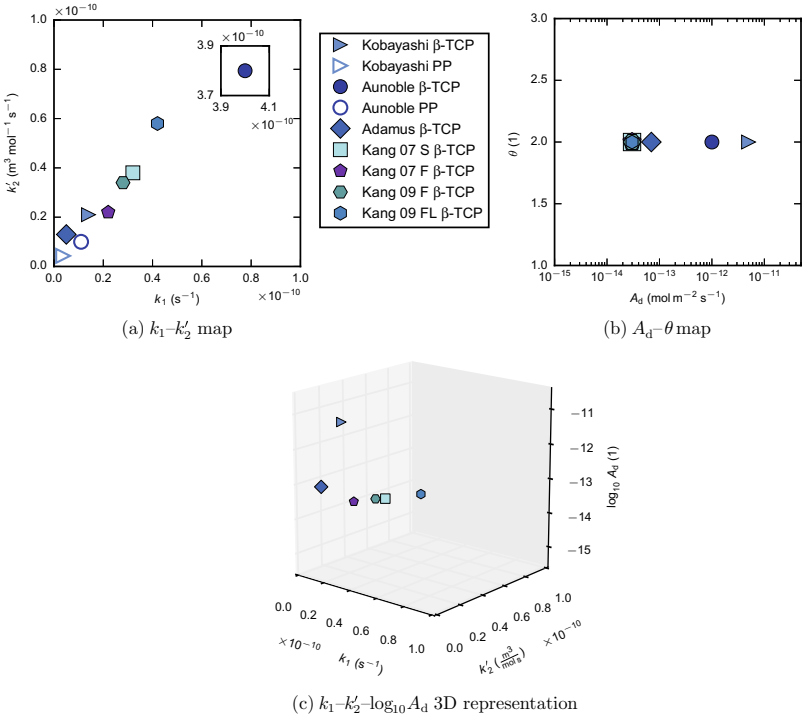

(a) k_1–k_2' map

(b) A_d–θ map

(c) k_1–k_2'–$\log_{10}A_d$ 3D representation

Fig. 4.2 Results output by the TCP composites degradation model for data with a poly(L-lactide) matrix. k_1 is the non-catalytic polymer degradation rate, k_2' is the autocatalytic polymer degradation rate, A_d is the ceramic dissolution rate and θ is the power ceramic dissolution law exponent. The tricalcium phosphate type used in each case study is indicated in the legend by the abbreviation found at the end of the case study code. The meaning of the abbreviations can be found in Table 4.2. Black inset plots correspond to regions situated outside the limits defined in the main plot

Both the polymer degradation map (Fig. 4.3a) and the ceramic degradation map (Fig. 4.3b) showed clustering of the degradation data, with two clusters present in each degradation map. Appendix B.1.2 contains the above-mentioned TCP-PDLLA results in a tabular format. Additionally, it includes several composite characteristics for each analysed case study, necessary for discussion Sect. 4.6.

4.5.3 Poly-lactide-co-glycolide Matrix

The visual representation of the results for case studies with a poly(lactide-co-glycolide) matrix has been split into two different groups to aid visualisation: the CCMM (Cambridge Centre for Medical Materials) group and the remaining data group. The visual representation of the CCMM group, which contained data

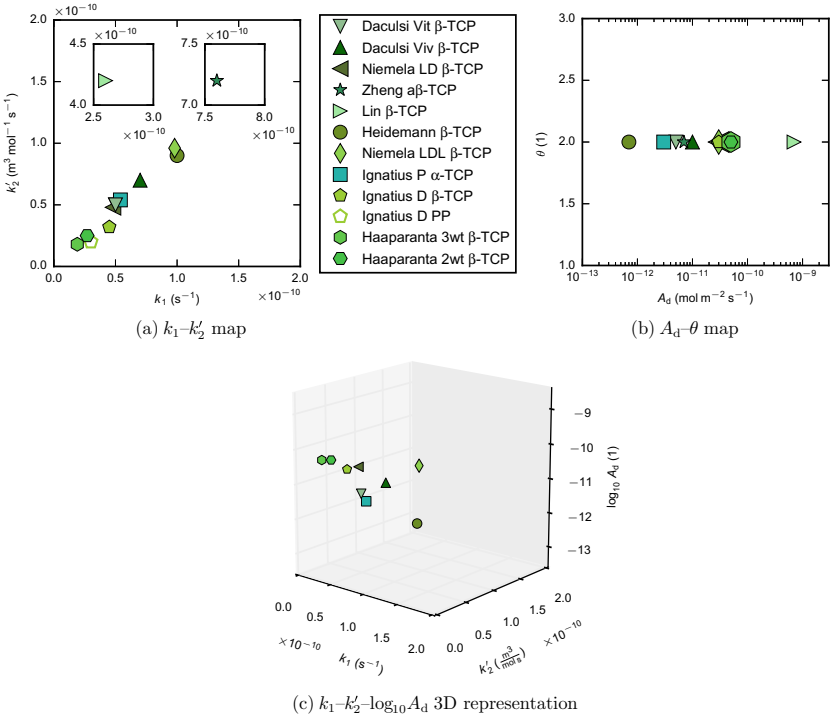

(a) k_1–k_2' map

(b) A_d–θ map

(c) k_1–k_2'–$\log_{10}A_d$ 3D representation

Fig. 4.3 Results output by the TCP composites degradation model for data with a poly(D,L-lactide) homo- or copolymer matrix. k_1 is the non-catalytic polymer degradation rate, k_2' is the autocatalytic polymer degradation rate, A_d is the ceramic dissolution rate and θ is the power ceramic dissolution law exponent. The tricalcium phosphate type used in each case study is indicated in the legend by the abbreviation found at the end of the case study code. The meaning of the abbreviations can be found in Table 4.2. Black inset plots correspond to regions situated outside the limits defined in the main plot

from Bennett [23], Ege et al. [24, 25], Yang et al. [26, 27], Mellon [28], Barrett, [29, 30] and Ehrenfried et al. [31], is shown in Fig. 4.4. Figure 4.4a contains the polymer degradation map, Fig. 4.4b the ceramic degradation map and Fig. 4.4c the 3D degradation space plot.

The CCMM group polymer degradation map showed significant clustering of the data in two different levels: pairs of case studies sharing the same (k_1, k_2') coordinates and a high number of case studies sharing the same region in the k_1–k_2' map. The first clustering level was a result of those cases sharing the same pure polymer data, e.g. Bennett nC D_L50 α-TCP (■) and Bennett mC D_L50 α-TCP (●) contained the same pure polymer occurrence. The second and higher level came from the similarity of the employed polymers in a majority of these case studies. The ceramic degradation map showed less clustering due to the higher diversity of the employed ceramics.

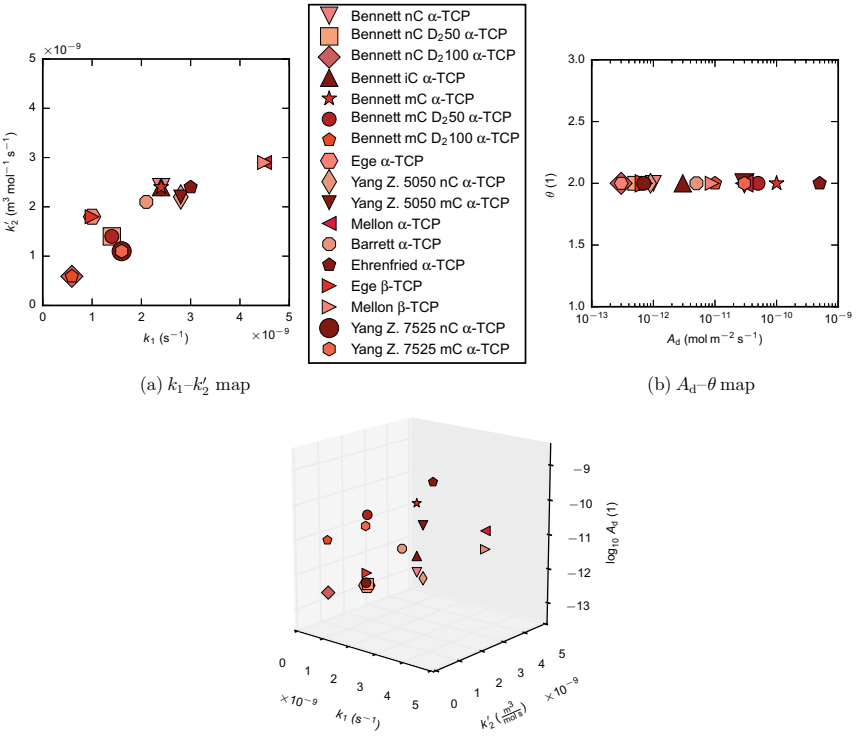

(a) k_1–k_2' map

(b) A_d–θ map

(c) k_1–k_2'–$\log_{10}A_d$ 3D representation

Fig. 4.4 Results output by the TCP composites degradation model for data with a poly(lactide-co-glycolide) matrix: case studies from the CCMM group. k_1 is the non-catalytic polymer degradation rate, k_2' is the autocatalytic polymer degradation rate, A_d is the ceramic dissolution rate and θ is the power ceramic dissolution law exponent. The tricalcium phosphate type used in each case study is indicated in the legend by the abbreviation found at the end of the case study code. The meaning of the abbreviations can be found in Table 4.2

The second visual representation, with the remaining data group results, is shown in Fig. 4.5, with the polymer degradation map in Fig. 4.5a, the ceramic degradation map in Fig. 4.5b and the 3D plot in Fig. 4.5c. This group encompassed data from Yang et al. [19], Yang et al. [20], Jin et al. [21] and Ara et al. [22].

The visual representation of the remaining poly(lactide-co-glycolide) data presented only one cluster, in the left hand corner of the k_1–k_2' map. Appendix B.1.3 contains the above-mentioned TCP-PLGA results in a tabular format. Additionally, it includes several composite characteristics for each analysed case study, necessary for discussion Sect. 4.6.

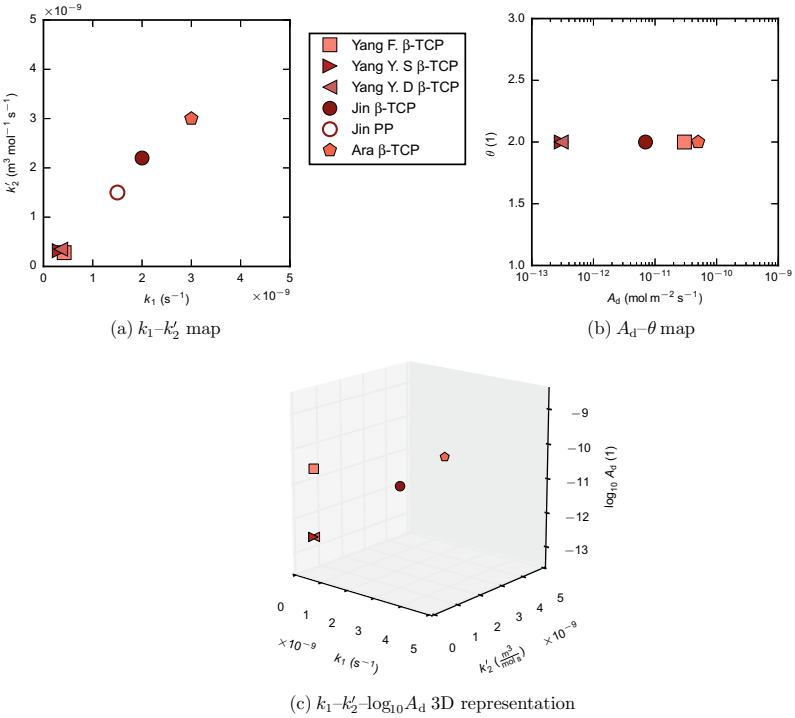

(a) k_1–k_2' map

(b) A_d–θ map

(c) k_1–k_2'–$\log_{10}A_d$ 3D representation

Fig. 4.5 Results output by the TCP composites degradation model for data with a poly(lactide-co-glycolide) matrix: remaining case studies data. k_1 is the non-catalytic polymer degradation rate, k_2' is the autocatalytic polymer degradation rate, A_d is the ceramic dissolution rate and θ is the power ceramic dissolution law exponent. The tricalcium phosphate type used in each case study is indicated in the legend by the abbreviation found at the end of the case study code. The meaning of the abbreviations can be found in Table 4.2

4.5.4 Miscellaneous Polymers Matrixes

Lastly, the visual representation of the results for case studies with miscellaneous polymer matrixes, included in Fig. 4.6, contains the polymer degradation map (Fig. 4.6a), the ceramic degradation map (Fig. 4.6b) and the 3D degradation space plot (Fig. 4.6c). The miscellaneous polymer matrixes group encompassed data from Ahola et al. with a poly(L-lactide-co-ε-caprolactone) matrix (□, ○, ●) [16, 17], data from Kikuchi et al. [18, 33] also with a poly(L-lactide-co-ε-caprolactone) matrix (◁) in addition to a poly(L-lactide-co-glycolide- co-ε-caprolactone) matrix (▷) and a poly(L-lactide)/poly(ethylene:hexamethylene/sebacate) block copolymer matrix (●, ★) and lastly data from Imai et al. also with a poly(L-lactide)/poly(ethylene: hexamethylene/sebacate) block copolymer (◊, ◆, ⬡, ⬢) [32, 34].

The visual representation showed clustering in both the polymer and ceramic degradation maps. In the polymer degradation map, the clustering was especially

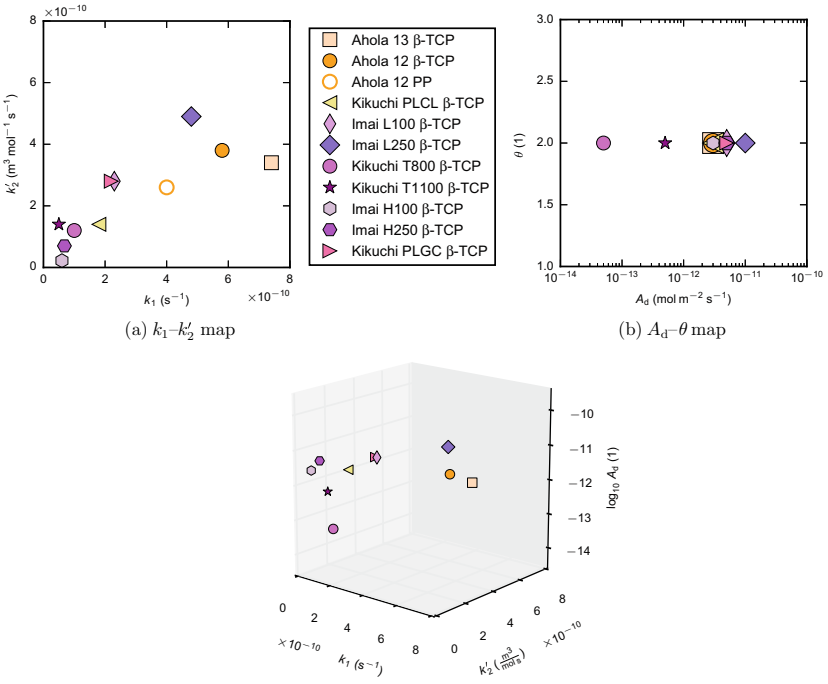

(a) k_1–k_2' map

(b) A_d–θ map

(c) k_1–k_2'–$\log_{10}A_d$ 3D representation

Fig. 4.6 Results output by the TCP composites degradation model for data with a miscellaneous polymer matrix. k_1 is the non-catalytic polymer degradation rate, k_2' is the autocatalytic polymer degradation rate, A_d is the ceramic dissolution rate and θ is the power ceramic dissolution law exponent. The tricalcium phosphate type used in each case study is indicated in the legend by the abbreviation found at the end of the case study code. The meaning of the abbreviations can be found in Table 4.2

marked for case studies sharing poly(L-lactide)/poly(ethylene:hexamethylene/sebacate) block copolymer as their polymeric matrix. Appendix B.1.4 contains the above-mentioned TCP-misc. polymers results in a tabular format. Additionally, it includes several composite characteristics for each analysed case study, necessary for discussion Sect. 4.6.

4.6 Discussion of the Modelling Results for Tricalcium Phosphate Composites Degradation Data

This section includes the analysis and discussion of the modelling results reported in Sect. 4.5. In the first place, an overview of the capabilities of the degradation models, using the TCP composites degradation model as an example, is presented.

This overview highlights the intended model usage and includes examples with real TCP experimental data. Secondly, a compilation of all the TCP modelling results in addition to an initial analysis are introduced. After this initial analysis, four in-depth analyses are reported: tricalcium phosphate dissolution, effect of TCP addition on composite degradation behaviour, influence of sample structure and influence of degradation protocol. Lastly, a summary of the main insights resulting from the analyses is presented. The structure of this section is replicated, with the exception of the model capabilities overview, in Chaps. 5 and 7.

4.6.1 Overview of the Capabilities of the Model

This section presents the capabilities of the degradation models derived from the general modelling framework, using the TCP composites degradation model presented in Sect. 3.2.1 as an example. This presentation is structured in three parts. Firstly, the predicted effect of different composite parameters on composite degradation is discussed using a set of simulations and secondly, the outcome of the data analysis process for one of the case studies presented in Sect. 4.5 is included and the fitting process employed to obtain the values of the composite degradation constants is explained. Finally, a summary of the implications derived from the ideal functioning of the models is presented. After the presentation of the model capabilities, the analysis of data which do not conform with the predicted behaviour is discussed.

Figure 4.7 exhibits the predicted degradation curves, reporting the variation of the number-average molecular weight over time, for a poly(D,L-lactide)(50:50)–β-tricalcium phosphate case study comprising five samples: a pure polymer sample, and four composite samples. Three of the composite samples share the same ceramic representative particle size, $d_0 = 10\,\mu\text{m}$, while having increasing values of ceramic weight percentage, $f_{\text{wCer0}} = 5$, 10 and 20 wt %. The fourth composite sample has a d_0 of 20 μm and a f_{wCer0} of 20 wt %. The five samples share the same polymeric matrix and ceramic filler and thus, the same values of composite degradation constants. The chosen values for the non-catalytic and autocatalytic polymer degradation constants, k_1 and k_2', are $2\times10^{-10}\,\text{s}^{-1}$ and $2\times10^{-10}\,\text{m}^3\,\text{mol}^{-1}\,\text{s}^{-1}$ respectively, while the chosen values for the rate and exponent of the ceramic dissolution power law, A_d and θ, are $2\times10^{-11}\,\text{mol}\,\text{m}^{-2}\,\text{s}^{-1}$ and 2.0(1) respectively.

As discussed in Sect. 3.3, the computational model captures the degradation properties of a composite employing a representative unit cell calculated using the values of d_0 and f_{wCer0}. This unit cell characterises the ratio between the initial ceramic surface area and the polymer volume, $S_{\text{cer0}}/V_{\text{pol}}$, which is used as a characterising parameter of the composite degradation. Figure 4.7 also includes the representative unit cells of the five samples part of the simulated case study. The simulated case study allows the study of two phenomena: the effect of having an increasing ceramic weight fraction while keeping d_0 constant, and the effect of increasing the ceramic representative particle size while keeping f_{wCer0} constant. When the composite degradation constants k_1, k_2', A_d and θ are kept constant, an increasing ceramic weight fraction

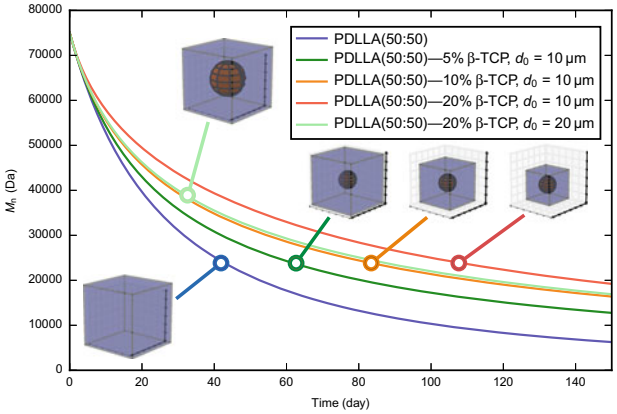

Fig. 4.7 Predicted evolution of the number-average molecular weight, M_n (Da) for the different samples of a poly(D,L-lactide)(50:50)–β-tricalcium phosphate case study. d_0 is the ceramic representative particle size. The ceramic weight fraction f_{wCer0} is indicated as the percentage between the polymer and ceramic abbreviations for each sample in the legend. All the samples share the same values of the composite degradation constants: $k_1 = 2 \times 10^{-10}\,s^{-1}$, $k_2' = 2 \times 10^{-10} m^3\,mol^{-1}\,s^{-1}$, $A_d = 2 \times 10^{-11} mol\,m^{-2}\,s^{-1}$ and $\theta = 2.0(1)$

results in a slower molecular weight reduction over time. Conversely, an increasing ceramic representative particle size results in a faster molecular weight reduction over time.

These results can be explained considering the expression of the polymer scission rate: $\frac{dR_s}{dt} = k_1 C_e + k_2' C_e C_{H^+}$, where C_e and C_{H^+} are the concentrations in the polymer phase of ester bonds and free hydrogen ions respectively. Having the same polymer matrix in all the simulated samples implies that the values of C_e, k_1 and k_2' are shared across all of them, and therefore the differences in molecular weight reduction rate arise from the value of the concentration of free hydrogen ions, C_{H^+}. The value of the concentration of free hydrogen ions changes because a fraction of the released ceramic ions bind to these free hydrogen ions decreasing the value of C_{H^+}. This reduction is proportional to the value of S_{cer0}/V_{pol} in the composites. Having more ceramic surface area available for a given quantity of polymer results in more released ceramic ions when the ceramic degradation constants A_d and θ are kept constant. Both increasing the ceramic weight fraction and decreasing the ceramic particle size increase the S_{cer0}/V_{pol} value and thus, cause the abovementioned degradation behaviour.

The analysis just described reveals that although the effect of the ceramic addition could be seen, seemingly, as a reduction of the polymer degradation rate, the actual degradation behaviour stems from a more complex reality. All the samples in the case study share indeed the the same values of the polymer degradation rates k_1 and k_2'. Thus and to avoid confusion, the term polymer degradation rate is reserved, in this work, for the non-catalytic and autocatalytic polymer degradation rates k_1 and k_2' respectively.

Having now discussed the predicted changes in composite degradation with varying ceramic representative particle size d_0 and ceramic weight percentage f_{wCer0}, the outcome of the data analysis process for the Imai H250 β-TCP case study [34] is presented. Figure 4.8 includes the experimental and simulated degradation curves for Imai H250 β-TCP, which includes a pure polymer sample and two composite samples with different values of ceramic weight fraction. This case study has poly(L-lactide)/poly(ethylene:hexamethylene/sebacate) block copolymer (98.3:1.7) as polymeric matrix and high crystallinity β-TCP as ceramic filler. Imai H250 β-TCP is a representative fitting of the different ones encountered during the analysis process, with some fittings being better and some being worse than this one. Imai H250 β-TCP is also an example of conforming data in which the addition of a ceramic filler causes a reduction in the molecular weight reduction rate of the composites as predicted by the computational model. When case studies present this behaviour they are referred to, in this work, as cases with a buffering effect.

As mentioned in Sect. 3.5.3, the data analysis process was divided in two different stages. Firstly, the pure polymer analysis, in which the experimental pure polymer occurrence was used to find the values of the polymer degradation constants k_1 and k_2'. In the case depicted in Fig. 4.8, the pure polymer experimental and simulated data are depicted in two different shades of blue. The chosen simulation corresponds to: $k_1 = 6.8\times10^{-11}\,\text{s}^{-1}$ and $k_2' = 7.0\times10^{-11}\,\text{m}^3\,\text{mol}^{-1}\,\text{s}^{-1}$. The second stage, the composite data analysis, used the experimental composite occurrences depicted in green and red to find the values of the ceramic degradation constants A_d and θ. The chosen simulations employ $A_\text{d} = 5\times10^{-12}\,\text{mol}\,\text{m}^{-2}\,\text{s}^{-1}$ and $\theta = 2.0(1)$ with the values of k_1 and k_2' found in the previous stage. In addition to the features explained in Fig. 4.7,

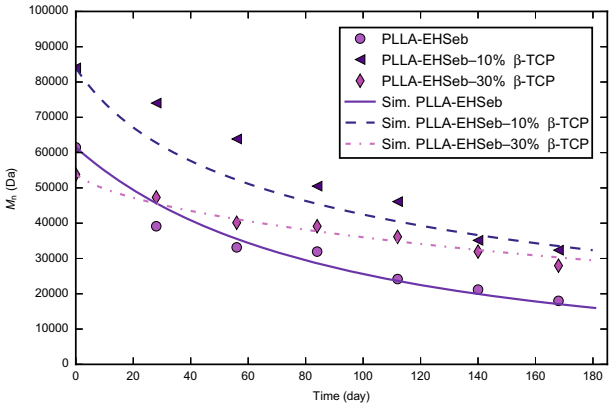

Fig. 4.8 Analysis of conforming data: experimental data and simulations for the Imai H250 β-TCP case study [34]. The following values of composite degradation constants were used for the simulations: $k_1 = 6.8\times10^{-11}\text{s}^{-1}$, $k_2' = 7\times10^{-11}\text{m}^3\ \text{mol}^{-1}\ \text{s}^{-1}$, $A_\text{d} = 5\times10^{-12}\text{mol}\,\text{m}^{-2}\ \text{s}^{-1}$ and $\theta = 2.0(1)$. M_n is the number average molecular weight. PLLA-EHSeb abbreviates poly(L-lactide)/poly(ethylene:hexamethylene/sebacate) block copolymer

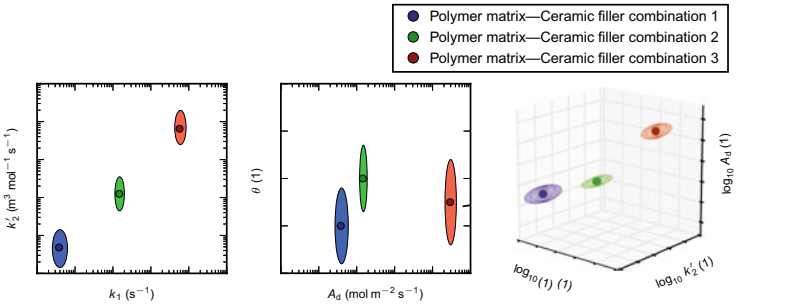

(a) k_1–k_2' map (b) A_d–θ map (c) k_1–k_2'–$\log_{10}A_d$ 3D representation

Fig. 4.9 Variation of the predicted results for three different polymer–ceramic combinations if the model could fully capture the composite degradation behaviour. k_1 is the non-catalytic polymer degradation rate, k_2' is the autocatalytic polymer degradation rate, A_d is the ceramic dissolution rate and θ is the power ceramic dissolution law exponent

the real data analysis shows that the computational model was capable of dealing with different initial molecular weights in one case study.

Lastly, assuming that a case study is comprehensively characterised by a combination of a polymeric matrix and a ceramic filler, for example poly(L-lactide) and highly crystalline β-tricalcium phosphate, and that the model perfectly captures all the aspects of composite degradation, the ideal outcome of the model for three of these polymer-ceramic combinations is shown in Fig. 4.9, with the polymer degradation map in Fig. 4.9a, the ceramic degradation map in Fig. 4.9b and the 3D plot in the k_1–k_2'–A_d in Fig. 4.9c.

With a perfect capture of the degradation behaviour by the model, all the poly(L-lactide)−high crystallinity β-TCP cases would share the same values of the four degradation parameters, k_1, k_2', A_d and θ, which characterise composite degradation and thus, all of them would be represented by the darker blue dots while the darker green and red dots would depict two other polymer-ceramic combinations. Some of the expected variation is included in the ellipses depicted in a lighter shade. The variability in k_2' is expected due to the variations in morphology and porosity of the samples, whereas the variability in θ is expected due to the low sensitivity of the model to changes in θ.

Analysis of Non-conforming Data

Some of the analysed data did not follow the expected abovementioned behaviour and required a different analysis process. Figure 4.10 depicts an example of this process, with the Kobayashi β-TCP case study [2]. The non-conforming data was called, in this work, data with no-buffering effect, because the addition of a ceramic filler does not cause a reduction in the molecular weight reduction rate of the composites.

In non-buffering cases, the analysis process was also divided in two different stages: pure polymer data analysis and composite data analysis. The pure polymer data analysis stage, depicted in Fig. 4.10a, was more complex than usual. The normal

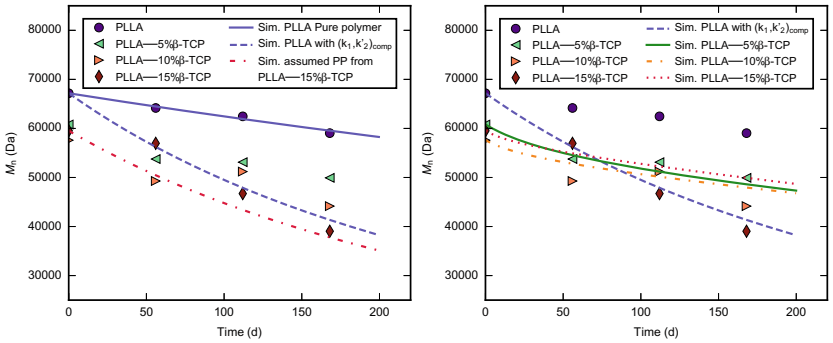

(a) Pure polymer data analysis (b) Composite data analysis

Fig. 4.10 Analysis of non-conforming data: experimental data and simulations for the Kobayashi β-TCP case study [2]. The following values of composite degradation constants were used for the simulations: $k_1 = 1.4 \times 10^{-11}\,\mathrm{s}^{-1}$, $k_2' = 2.1 \times 10^{-11}\,\mathrm{m}^3\,\mathrm{mol}^{-1}\,\mathrm{s}^{-1}$, $A_\mathrm{d} = 5 \times 10^{-12}\,\mathrm{mol\,m}^{-2}\,\mathrm{s}^{-1}$ and $\theta = 2.0(1)$ with the following pure polymer degradation constants: $k_1 = 3.7 \times 10^{-12}\,\mathrm{s}^{-1}$ and $k_2' = 4.3 \times 10^{-12}\,\mathrm{m}^3\,\mathrm{mol}^{-1}\,\mathrm{s}^{-1}$. M_n is the number-average molecular weight. PLLA abbreviates poly(L-lactide)

analysis of the pure polymer occurrence from Kobayashi β-TCP yielded a duplet of (k_1, k_2') values, which are the ones employed in the continuous blue line simulation labelled "PLLA Pure polymer". In case studies with a non-buffering effect, the pure polymer occurrence had the lowest molecular weight reduction rate and thus those values could not be used for the composite data analysis.

In order to find the (k_1, k_2') values of the composites occurrences, a plausible theoretical pure polymer data was inferred and analysed from the composite data. These plausible polymer data is depicted with a dash-dotted red line in the figure labelled "assumed PP from PLLA–15%β-TCP". This step was also employed in cases without a pure polymer occurrence. The subsequent analysis gave a valid set of values for k_1 and k_2'. For completeness, the appearance of the pure polymer data with these (k_1, k_2') values has been included in a dash-dotted blue line labelled "PLLA with $(\mathrm{k_1}, \mathrm{k'_2})_\mathrm{comp}$". As a result of the pure polymer analysis, there are two sets of values: $(\mathrm{k_1}, \mathrm{k'_2})_\mathrm{PP}$, which only characterised the pure polymer occurrence, and $(\mathrm{k_1}, \mathrm{k'_2})_\mathrm{comp}$, which characterised the composite occurrences and were employed in the composite data analysis. This composite data analysis, included in Fig. 4.10b, followed the usual procedure to find the correct values of A_d and θ using the duplet $(\mathrm{k_1}, \mathrm{k'_2})_\mathrm{comp}$.

4.6.2 Modelling Results Overview and Initial Discussion

In order to provide an overview of the modelling results, a compilation of all the tricalcium phosphate biocomposites results collated in a single set of graphs, containing

a polymer map, a ceramic map and a $\log_{10}k_1$–$\log_{10}k_2'$–$\log_{10}A_d$ 3D plot, is included in Fig. 4.11. For clarity and due to the numerous data points, individual graph legends have been omitted. Legends including all the data points can be found in Sect. 4.5. As a replacement and to facilitate the analysis, coloured regions enclosing a majority of the results for cases with poly(L-lactide) (PLLA), poly(D,L-lactide) homo- or copolymer (PDLLA) and poly(lactide-co-glycolide) (PLGA) matrixes have been added in both the polymer map (Fig. 4.11a) and 3D plot (Fig. 4.11c).

Figure 4.11a exhibits the global polymer degradation map for tricalcium phosphate biocomposites, containing the values of the non-catalytic polymer degradation rate k_1 and the autocatalytic polymer degradation rate k_2' for each analysed case study. The three main groups of polymeric matrixes, namely poly(L-lactide), poly(D,L-lactide) homo- or copolymer and poly-(lactide-co-glycolide), are highlighted using coloured ellipses enclosing the majority of the corresponding data. As a general trend and despite the existing overlapping among the different coloured regions, PLGA exhibited a faster degradation than PDLLA, which in turn degraded faster than PLLA. This order in polymer degradation rates matched the usual behaviour for polymeric scaffolds, as previously reported by Neuendorf et al. [41] and Middleton and Tipton [42].

The polymer degradation map also shows a clear correlation between the values of the non-catalytic and autocatalytic polymer degradation rates, k_1 and k_2' respectively, as all the analysed tricalcium phosphate cases lie in the region surrounding the map diagonal. This behaviour points to a coexistence of both types of polymer degradation in all the analysed cases. The use of logarithmic axes in this visual representation makes less apparent that some particular cases showed a marked non-catalytic behaviour, such as Ahola 13 β-TCP (□) [16] or Imai H100 β-TCP (⬡) [34] both with $k_1/k_2' > 2$, while others showed a marked autocatalytic behaviour, such as Adamus β-TCP (◆) [4] or Kikuchi T1100 β(★) [33] both with $k_1/k_2' < 0.5$.

A significant spread for both k_1 (s^{-1}), the non-catalytic degradation rate and k_2' ($m^3\,mol^{-1}\,s^{-1}$), the autocatalytic polymer degradation rate, with values spanning nearly four orders of magnitude, from 10^{-12} to 10^{-8}, for both polymer degradation constants was depicted in the k_1–k_2' map. This variability translated into a significant difference in degradation timescale and mechanical performance over time for different composites. At the low degradation end, for example, the Adamus β-TCP case study (◆) [4], a composite made of commercially available poly(L-lactide) and commercially available β-TCP, which still maintained 90% of their initial flexural strength value after being degraded for twelve months. Similarly, the Kobayashi β-TCP case study (▶) [2], also with commercially available poly(L-lactide) and commercially available β-TCP, which experienced reductions in M_n ranging from 15 to 30% after 24 weeks of degradation. These two cases represented tricalcium phosphate biocomposites with the ability to maintain their integrity for significantly long periods of time, probably, up to several years.

On the high degradation end, the Ara β-TCP case (⬟) [22], with a poly(D,L-lactide-co-glycolide)(44.6:55.4) matrix and commercially available β-TCP, which showed a significant mass loss of over 30% in less than four weeks. The Mellon α-TCP case (◀) [28], with commercially available poly(D,L-lactide-co-glycolide)(50:50) and

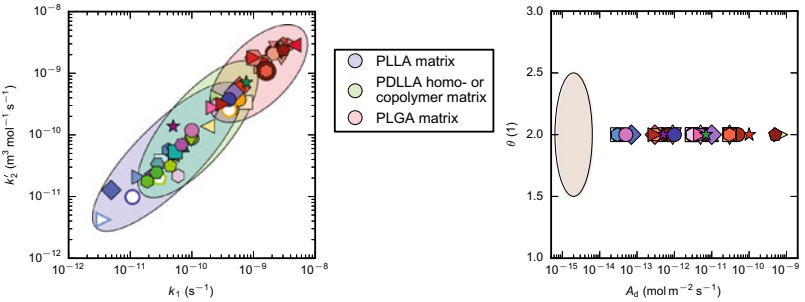

(a) k_1–k_2' map (b) A_d–θ map

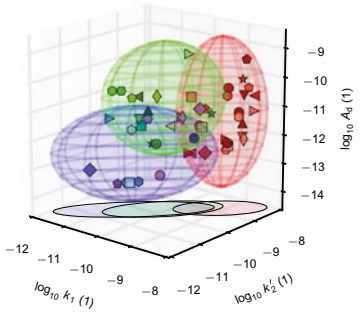

(c) $\log_{10}k_1$–$\log_{10}k_2'$–$\log_{10}A_d$ 3D representation

Fig. 4.11 Global degradation maps containing results output by the TCP composites degradation model for all the analysed case studies. k_1 is the non-catalytic polymer degradation rate, k_2' is the autocatalytic polymer degradation rate, A_d is the ceramic dissolution rate and θ is the power ceramic dissolution law exponent. Coloured ellipses, for the k_1–k_2' map, or ellipsoids, for the $\log_{10}k_1$–$\log_{10}k_2'$–$\log_{10}A_d$ plot, enclose the majority of the case studies for usual polymeric matrixes. The beige coloured region in the A_d–θ map represents experimental dissolution data for highly crystalline β-tricalcium phosphate at 37 °C and different initial pH ranging from 5.0 to 7.0 in free drift experiments measured by Bryar [43]

in-house produced α-TCP, behaved similarly, reporting a mass loss of over 70% in a month for the composite sample with lower ceramic content. These case studies, at the right hand corner of the polymer degradation map, represented tricalcium phosphate biocomposites that could be completely reabsorbed in a short period of time of just a few weeks.

Figure 4.11b shows the ceramic degradation map, including dissolution rate A_d (mol m^{-2} s^{-1}) and power dissolution law exponent θ (1) for all tricalcium phosphate modelling results. All the analysed cases had the same value of power dissolution law exponent θ, pointing to an insensitivity of composite degradation with respect to theta in the computational model. Conversely, dissolution rate A_d presented a significant spread, spanning almost five orders of magnitude (from 10^{-14} to over 10^{-9}), indicating a high sensitivity of the simulation degradation profiles with respect to the value of dissolution rate A_d. The marker colours used in this visual representation, as

previously mentioned, convey information solely about the case studies polymeric matrixes. Data for the dissolution of β-TCP with high crystallinity at 37 °C and different initial pH ranging from 5.0 to 7.0 in free drift experiments measured by Bryar [43] is represented by the beige region.

An initial inspection showed both no obvious direct correlation between polymeric matrix and tricalcium phosphate dissolution behaviour, and higher A_d values than those reported for β-tricalcium phosphate in several free drift experiments [43]. As polymer matrix did not seem to be an important factor and there was no overlap between the reported results and the available dissolution data for tricalcium phosphate, a deeper analysis using all the available information about the different types of tricalcium phosphate employed was deemed necessary. This analysis, with its own different visual representations, follows in the next Sect. 4.6.3.

Lastly, Fig. 4.11c includes the 3D degradation space plot for tricalcium phosphate biocomposites. In a similar fashion to the ellipses in the polymer degradation map, translucent ellipsoids, encompassing a majority of the results obtained by the TCP composites degradation model, have been included for case studies with poly(L-lactide) (PLLA), poly(D,L-lactide) homo- or copolymer (PDLLA) and poly(lactide-co-glycolide) matrixes. Also similarly to the polymer degradation map, there was a significant overlap between the three ellipsoids. The region delimited by both k_1 (s^{-1}) and k_2' ($m^3\ mol^{-1}\ s^{-1}$) in the interval (10^{-11}, 10^{-10}) and A_d ($mol\ m^{-2}\ s^{-1}$) in (10^{-12}, 10^{-11}) seemed to contain a particularly high concentration of case studies.

The three general degradation maps showed a significant variability or spread in the reported composite degradation constants for the analysed tricalcium phosphate case studies. On the proviso that the modelling framework has fully captured composite degradation behaviour, all case studies sharing the same polymeric matrix-ceramic filler combination should have exactly the same values for k_1, k_2', A_d and θ. As this is clearly not the case it is worth analysing the origin of this variability.

In this case, the variability could stem from the complexity of composite degradation phenomena and the plethora of interwoven parameters which play a role in it. Although the modelling framework contain the main factors involved in composite degradation, there are a number of other factors which have not been explicitly included but do affect composite degradation. For example, two a-priori similar case studies with a poly(D,L-lactide)(50:50) matrix and β-TCP as a filler might show significantly different degradation behaviour, such as Lin β-TCP (▷) [10] and Heidemann β-TCP(●) [11] in Fig. 4.3. The distinct behaviours could arise from differences in sample structure and morphology, degradation protocol, polymer properties such as polymer crystallinity, block structure and ceramic properties such as ceramic crystallinity, purity, etc., i.e. factors defined within the experimental parameters and the use of the TCP composites degradation model would allow a systematic investigation of the influence of several of the non-included factors on composite degradation.

4.6.3 Characterisation of Tricalcium Phosphate Dissolution

Calcium phosphates in general and tricalcium phosphate in particular experience degradation by dissolution in an aqueous media [44]. Tricalcium phosphate, considered a sparingly soluble ceramic, presents a low solubility in all its allotropes as indicated by its solubility product of $-\log_{10}(K_{sp}) = 25.5$ at 37 °C for α-TCP [40] and $-\log_{10}(K_{sp}) = 29.5$ at 37 °C for β-TCP [40]. There are a variety of factors, in addition to the abovementioned crystal structure, which affect TCP dissolution such as crystallinity and lattice defects [45], porosity [46], environmental pH [47] and media composition [48].

The analysis of ceramic dissolution seems a good starting point in order to understand the influence of the addition of a sparingly soluble ceramic to a polymeric matrix, to form a biocomposite, on the degradation behaviour of those biocomposites. The modelling framework presented in Chap. 3, and all the ceramic-specific models derived from it, employed two parameters, dissolution rate A_d (mol m^{-2} s^{-1}) and power dissolution law exponent θ (1), in order to characterise ceramic dissolution, as one of the phenomena occurring during composite degradation. The global TCP composites ceramic map presented in Fig. 4.11b, as part of an initial analysis, showed the insensitivity of tricalcium phosphate composites degradation behaviour to power dissolution law exponent θ and, contrarily, the strong influence of dissolution rate A_d. In addition, the initial analysis also pointed to a lack of correlation between TCP dissolution rate and specific matrix polymer type. Considering this information, a series of analyses were carried out in order to deepen the understanding of tricalcium phosphate dissolution within composite degradation and to elucidate the influence of different tricalcium phosphate characteristics on the reported values of dissolution rate A_d.

A number of different types of tricalcium phosphate were encountered during the degradation data harvesting process. Those types differed in several characteristics such as crystal structure and degree of crystallinity. As previously mentioned, these characteristics influence the ceramic solubility and it is therefore assumed that these fillers will present different behaviour. The expected behaviour is higher dissolution for the tricalcium phosphate types with decreased crystallinity [45] and higher solubility product K_{sp}. Figure 4.12 exhibits the dissolution rate for all the TCP analysed case studies according to their tricalcium phosphate type. Tricalcium phosphate type is indicated in the figure legend using abbreviations. A complete list containing full denominations for all abbreviations is included in Table 4.2.

To facilitate the analysis, the different tricalcium phosphates types have been arranged in descending order of expected solubility. The two types of β-TCP, were coloured in shades of brown with shade intensity proportional to the expected solubility. The spread in y-axis of the data has been used exclusively to improve visual analysis and carries no physical meaning. A golden stripe shows the dissolution rate measured by Bryar [43] at 37 °C and different initial pH ranging from 5.0 to 7.0 in free drift experiments for highly crystalline β-TCP fabricated using a similar method to Ege [25].

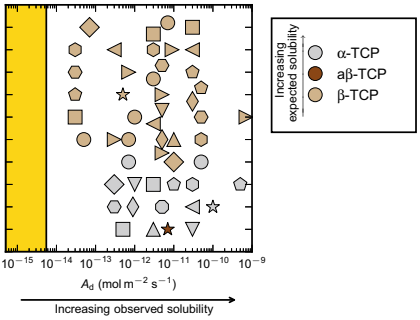

Fig. 4.12 Tricalcium phosphate dissolution rate for all the analysed case studies: influence of tricalcium phosphate type. A_d is the ceramic dissolution rate. The golden stripe corresponds to the range of dissolution rates measured by Bryar at 37 °C and different initial pH ranging from 5.0 to 7.0 in free drift experiments for highly crystalline β-tricalcium phosphate [43]

This visual representation suggested two distinct phenomena. Firstly, the dissolution rate of the different tricalcium phosphate types did not match the expected solubility behaviour as the colours of the figure should have had a majority of brown shades on the left moving on to grey as A_d increased. Instead an almost complete overlap of A_d values for both α- and β-TCP was found. Secondly, none of the reported TCP dissolution rates fell within the range measured by Bryar in free drift experiments at 37 °C and different initial pH ranging from 5.0 to 7.0 [43]. Dissolution rates for similar types of β-TCP presented a value that exceeded this measured value by up to several orders of magnitude. Bohner et al. [47] reported a much higher dissolution rate for β-TCP at constant pH = 4.2 which would agree with the TCP computational model output as during composite degradation an acid environment is generated due to the release of hydrogen ions as a result of polymer degradation. To find the cause of these phenomena both the influence of polymeric matrix and ceramic particle size will be considered.

Polymeric Matrix

The addition of a sparingly soluble ceramic, in this case tricalcium phosphate, to a polymeric matrix is expected to cause a buffering effect on composite degradation by neutralising some of the hydrogen ions released during polymer degradation, as explained in the overview of the model capabilities in Sect. 4.6.1. Figure 4.13 reports the tricalcium phosphate dissolution rate, A_d, for all the analysed case studies indicating both the polymer matrix of the case and whether a buffering effect was shown, in addition to the TCP type. The polymer matrix is indicated by the edge colour of the markers using the usual convention. A black dot in the centre of the ceramic indicates that the case study presented a buffering effect, whereas a white dot indicates a non-buffering effect. No dot indicated that the comparison of composite sample with their pure polymer counterparts could not be assessed, primary due to the absence of pure polymer data.

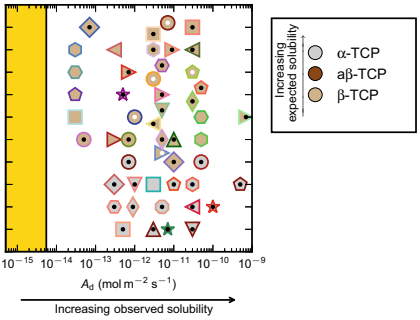

Fig. 4.13 Tricalcium phosphate dissolution rate for all the analysed case studies indicating the tricalcium phosphate types: presence of buffering effect and influence of polymeric matrix. A_d is the ceramic dissolution rate. The golden stripe corresponds to the range of dissolution rates measured by Bryar at 37 °C and different initial pH ranging from 5.0 to 7.0 in free drift experiments for highly crystalline β-tricalcium phosphate [43]. The edge colours of the markers indicate the polymeric matrix used in the case studies following the colour convention used in Sect. 4.5. Black dots represent case studies with a buffering effect, whereas white dots represent case studies with a non-buffering effect

There was no clear correlation between tricalcium phosphate type and composite degradation behaviour, in terms of buffering capacity. Conversely, there were some changes in buffering effect presence for different edge colours, pointing to a possible influence of polymeric matrix on the presence of buffering effect. It is therefore necessary to consider the factors pertaining to the polymeric matrix in order to increase the understanding of the effect of tricalcium phosphate addition on composite degradation. This analysis is presented next in Sect. 4.6.4.

Particle Size

The ceramic representative particle size is a critical parameter in composite characterisation. This size encloses relevant ceramic properties in terms of specific surface area. In addition, the ceramic representative particle size and the ceramic weight fraction will determine the size and quantities of the representative unit cell as discussed in Sect. 3.3. Figure 4.14 exhibits the relationship between representative particle size an tricalcium phosphate dissolution rate A_d for all the TCP analysed case studies.

A strong correlation is apparent between the representative particle size and the tricalcium phosphate dissolution rate A_d. The particle size was accounted for in the mathematical representation used to characterise the TCP dissolution, resulting in A_d carrying units of $\mathrm{mol\,s^{-2}}$. Therefore, the expected behaviour would be to have the same value of tricalcium phosphate dissolution rate when employing the same TCP type regardless of the particle size. But the obtained results clearly pointed to a further relevant effect of particle size.

This duplicated particle effect, in conjunction with the unexpectedly high obtained values of TCP dissolution rate, suggested a series of critical differences between the free drift experiments, i.e experimental measurements of the ions released by a

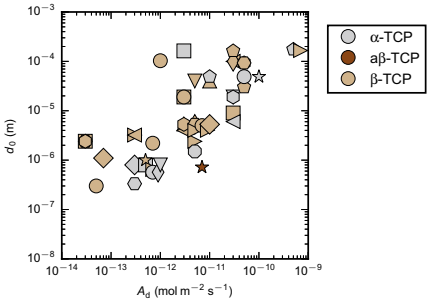

Fig. 4.14 Tricalcium phosphate dissolution rate for all the analysed case studies indicating the tricalcium phosphate types: effect of particle size. A_d is the ceramic dissolution rate and d_0 is the ceramic representative particle size of the undegraded composite sample

ceramic immersed in a solution used as reference [43], and the reality during composite degradation.

Firstly, despite water molecules surrounding the ceramic particles, in this case tricalcium phosphate, in both free drift experiments and composite degradation, the environment surrounding the particles is quite different due to the presence of a local acidity source in composite degradation. The hydrogen ions released by the polymer molecules significantly lower the pH causing a dramatic increase in tricalcium phosphate dissolution, similarly to the dissolution data reported by Bohner et al. [47], accounting for the higher than expected dissolution rate values. Although a dependency on polymer type of this phenomenon might be expected, it might not be too significant as all the studied polymers generated environments significantly different to those found in free drift experiments.

Secondly, while dissolution throughout free drift experiments barely influences the overall properties of the media due to the high buffer to dissolved ions ratio, the effect on the particle surroundings amid composite degradation is significant and closely interconnected with particle size. Two composites made with the same tricalcium phosphate type and same weight fraction but with different particle size will experience dissimilar degradation behaviours as for the composite with a smaller particle size the amount of polymer quantity assigned to each particle will be less voluminous, as explained in Sect. 3.3, and therefore the changes caused by the released ions will be more powerful which would partially account for the strong correlation between dissolution rate and particle size. Additionally, this correlation could also suggest an overestimation of the surface area of the small particles, which as part of composites would have a smaller effective surface area, giving artificially low A_d values in the analysis.

In summary, the analysis of the tricalcium phosphate dissolution showed an unexpected behaviour with both TCP allotropes showing similar dissolution rates and with higher values than those measured in free drift experiments at 37 °C and different initial pH ranging from 5.0 to 7.0 for highly crystalline β-TCP [43]. The double discrepancy of this behaviour could be explained by both the presence of a polymeric

matrix acting as a source of acidity, the influence of ceramic particle size on the definition of the surrounding environment in composite samples and the possibility of overestimation of effective surface area for small particles.

4.6.4 *Effect of Tricalcium Phosphate Addition on Composite Degradation Behaviour*

The modelling framework for biocomposites degradation presented in Chap. 3 considered as key hypothesis, that the addition of a sparingly soluble ceramic to a polymeric matrix, forming a composite, would never cause an increase in molecular weight reduction rate over time for the composite, considering pure polymer degradation rate as a baseline. This behaviour arises from the buffering effect associated with anions released during ceramic dissolution. These anions cause an alkalinisation of the environment, i.e. a reduction in the concentration of free hydrogen ions. For polymeric matrixes with heavily non-catalytic degradation, this phenomenon does not cause almost any changes; whereas for highly autocatalytic matrixes, there can be a significant reduction in degradation rate.

The harvested experimental data presented a variety of behaviours in terms of composite degradation: some composite samples degraded at the same rate than their pure polymer counterparts, while others degraded at a higher rate or at a slower rate. As the computational model used in this work predicted only a reduction in molecular weight decrease rate for composite samples, two main behaviour have been distinguished in the classification employed when analysing experimental degradation data: case studies showing a buffering effect and case studies showing a non-buffering effect. The expected behaviour, i.e. data with a buffering effect, was presented in detail in Sect. 4.6.1. Data not following the expected behaviour were classified as case studies with a non-buffering effect.

In order to characterise a group of case studies, a representative metric which combines information from the set of case studies is needed. Due to the nature of the data, a geometric mean with geometric standard deviation was selected as characterising metric of a data group, instead of the more common arithmetic mean with standard deviation. The computation and use of this metric followed the guidelines suggested by Kirkwood [49] and Limpert et al. [50]. Further details can be found in Appendix A.6.

During the different undertaken analyses, comparisons between two distinct sets of polymer degradation rates k_1 and k'_2, characterising either one or a group of case studies, were made. For example, a comparison between set A: (k_{1A}, k'_{2A}) and set B: (k_{1B}, k'_{2B}). In this situation, A was deemed to have a lower polymer degradation rate if:

- both values of the polymer degradation rates are lower for A, i.e, $(k_{1A} < k_{1B})$ and $(k'_{2A} < k'_{2B})$ or

- the euclidean distance in the k_1–k_2' plane, measured from the origin, is shorter for point A than for point B, i.e, $\left((k_{1A})^2 + (k_{2A}')^2\right)^{1/2} < \left((k_{1B})^2 + (k_{2B}')^2\right)^{1/2}$.

In order to evaluate the effect of ceramic addition on composite degradation, i.e. the presence or absence of buffering effect, only case studies containing both composite and pure polymer data have been considered. For clarity, the representation employed in this visual analysis has been slightly modified: hollow markers are used to denote cases in which ceramic addition has no buffering effect, i.e. cases in which composite samples unexpectedly had a higher molecular reduction rate than polymeric samples. Full markers are used to represent case studies with a buffering effect caused by the ceramic addition. Markers shapes and colours have been taken from the results presented in Sect. 4.5 without modification. For non-buffered case studies, which had two (k_1, k_2') duplets, one for composite samples and another one for pure polymer samples as explained in Sect. 4.6.1, only the composite duplet has been included in the k_1–k_2' map and the subsequent analysis.

Figure 4.15 shows the effect of ceramic addition on tricalcium phosphate composites degradation for all the analysed case studies, grouped by polymeric matrix into four categories: case studies with a poly(L-lactide) matrix, a poly(D,L-lactide) homo- or copolymer matrix, a poly(lactide-co-glycolide) matrix or a miscellaneous polymer matrix.

Poly(L-lactide) Matrix

The effect of tricalcium phosphate addition in composites with a poly(L-lactide) matrix is included in Fig. 4.15a, with the analysis in Table 4.5.

Of all the analysed PLLA-TCP case studies only three of them had both pure polymer and composite samples, fulfilling the requisites for the analysis of tricalcium phosphate addition in composite degradation behaviour. Two of those cases showed a non-buffering effect (Kobayashi β-TCP (▷) [2] and Aunoble β-TCP (○) [3]) while the third one showed a buffering effect (Adamus β-TCP (◆) [4]). The case studies with a non-buffering effect showed significantly higher values of polymer degradation constants k_1 and k_2' than the buffering case study.

Adamus et al. showed that the addition of β-tricalcium phosphate to the PLLA matrix resulted in a significant buffering effect. Both polymer and composite samples presented crystalline regions in the polymer phase during degradation, with both types of samples having a similar crystallinity degree. Conversely, the initial molecular weight was significantly different between pure polymer and composite samples, with the former having a much higher value that the latter [4]. This case study highlighted the ability of the model to capture composite degradation behaviour when pure polymer and composite sample had significantly different initial molecular weights and similar crystallinity degree in the polymer phase.

In order to understand the discrepancies between model predictions and experimental results for the non-buffering case studies an analysis of all the experimental data provided by the authors for Kobayashi β-TCP and Aunoble β-TCP was carried out.

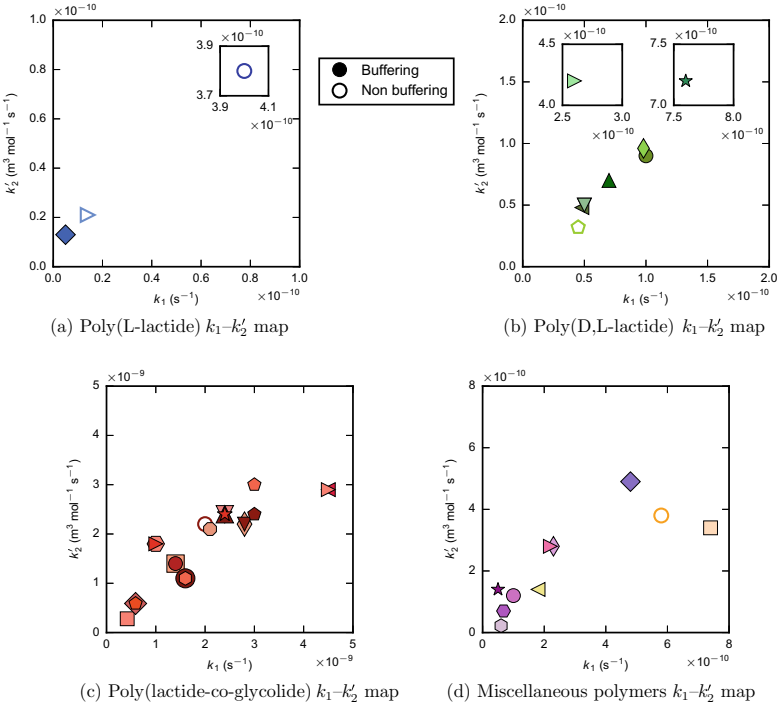

(a) Poly(L-lactide) k_1–k_2' map (b) Poly(D,L-lactide) k_1–k_2' map

(c) Poly(lactide-co-glycolide) k_1–k_2' map (d) Miscellaneous polymers k_1–k_2' map

Fig. 4.15 The effect of tricalcium phosphate addition on composite degradation for all analysed case studies. k_1 is the non-catalytic polymer degradation rate and k_2' is the autocatalytic polymer degradation rate. Full markers represent case studies showing a buffering effect, whereas hollow markers represent case studies showing a non-buffering effect. Black inset plots correspond to regions situated outside the limits defined in the main plot

Table 4.5 Analysis of tricalcium phosphate addition effect on composite degradation for case studies with a poly(L-lactide) matrix. k_1 is the non-catalytic polymer degradation rate and k_2' is the autocatalytic polymer degradation rate, with both reported as geometric mean ⁎ geometric standard deviation

Buffering effect	k_1 (s^{-1})	k_2' (m^3 mol^{-1} s^{-1})	Percentage of cases (%)	Number of cases
Yes	5.0×10^{-12}	1.3×10^{-11}	33	1
No	$(7.5 \text{ ⁎ } 10.7) \times 10^{-11}$	$(8.9 \text{ ⁎ } 7.7) \times 10^{-11}$	67	2

The Kobayashi β-TCP case study consists of one pure polymer sample and three composite samples. Kobayashi and Yamaji reported extremely low values of water absorption for all samples as can be seen in Fig. 4.16. The pure polymer occurrence showed a different behaviour with the value of water absorption plateauing after an initial increase. In contrast, composite samples had a linear increase in water content over time, with the magnitude of the increase proportional to the ceramic content of each sample. The authors modelled molecular weight drop over time using a similar

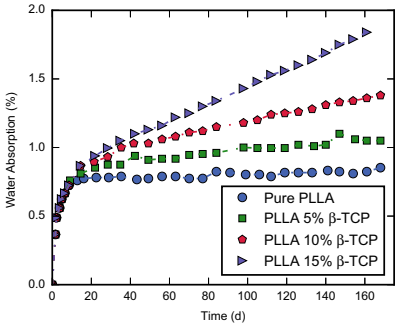

Fig. 4.16 Degradation data (water absorption over time) from Kobayashi β-TCP case study [2]. Data replotted from [2]. Dashed and dash-dotted lines are shown for clarity only. Markers and colours are specific of this visual representation

representation of polymer chain scission to the one employing in this work, but with the addition of a term representing water content as the amount of water drawn into the sample was heavily correlated with the quantity of polymer-ceramic interface. These differences in water uptake pointed to water as a degradation limiting factor for this case study, not fulfilling the TCP degradation model assumption of excess of water.

In Aunoble β-TCP the differences in porosity between pure polymer samples and composite samples with a much higher value in the latter, in addition to the in vivo degradation [3] could contribute to the lack of buffering behaviour although more information is needed in order to fully identify the behaviour origin.

In summary, different behaviours were observed for PLLA-TCP case studies with one case study showing a buffering effect and two studies showing a non-buffering effect. The TCP composites degradation model fully characterised the behaviour of the buffering effect case. The discrepancies between the experimental data and the model predictions were likely to arise from not meeting the water excess condition in the first case and having significantly different sample structures in the second case.

Poly(D,L-lactide) and Poly(D,L-lactide) Copolymers Matrixes

Figure 4.15b exhibits the effect of tricalcium phosphate addition in case studies with a poly(D,L-lactide) homo- or copolymer matrix. Table 4.6 includes the analysis of those results.

Table 4.6 Analysis of tricalcium phosphate addition effect on composite degradation for case studies with a poly(D,L-lactide) homo- or copolymer matrix. k_1 is the non-catalytic polymer degradation rate and k_2' is the autocatalytic polymer degradation rate, with both reported as geometric mean ⁎ geometric standard deviation

Buffering effect	k_1 (s^{-1})	k_2' ($m^3\ mol^{-1}\ s^{-1}$)	Percentage of cases (%)	Number of cases
Yes	$(1.2 \divideontimes 2.7) \times 10^{-10}$	$(1.2 \divideontimes 2.9) \times 10^{-10}$	87	7
No	4.5×10^{-11}	3.2×10^{-11}	13	1

A significant majority of the 8 case studies with a poly(D,L-lactide) homo- or copolymer matrix showed a buffering effect. Case studies with a buffering effect presented much higher values for the polymer degradation rates than cases with a non-buffering effect, which could suggest that at high degradation rates the buffering effect overshadowed other factors relevant for degradation. This variations in degradation behaviours emphasised the wide range of degradation properties that could be achieved by different combinations of only poly(D,L-lactide) homo- and copolymers and α- or β-tricalcium phosphate.

The extent of the buffering effect had a wide span, ranging from really mild to really strong. For example, Daculsi Vit β-TCP (▽) [7] and Daculsi Viv β-TCP (▲) [7] showed a really mild buffering effect with the composite samples having, in both case studies, a molecular weight reduction rate only slightly lower than the pure polymer counterparts.

A medium buffering effect was reported by Niemela LD β-TCP (◀) [12], Niemela LDL β-TCP (◆) [8] and Heidemann β-TCP (●) [11]. Niemel et al. reported higher water absorption for the composite sample than for the pure polymer sample in the Niemela LD β-TCP case study [12] which highlighted the validity of the model in terms of the existence of a buffering effect even considering a strong dependence between polymer scission rate and water content. Conversely, it could also mean that the model underestimated the buffering effect as composite sample would have degraded faster if the degradation is considered to be proportional to water content.

The two remaining case studies, Zheng aβ-TCP (★) [9] and Lin β-TCP (▶) [10], showed a strong buffering effect as supported by the experimental degradation data exhibited in Fig. 4.17. Zheng et al. showed that the addition of aβ-TCP cause a significant decrease in the molecular weight drop rate when comparing composite and pure polymer samples. This case study also portrayed a saturation effect, in which the addition of a 50 wt % of aβ-TCP instead of a 30 wt % of did not cause further buffering effect as can be seen in Fig. 4.17a. Lin et al. reported that the addition of β-TCP slowed down degradation, at least tripling the time for the onset of mass loss as shown in Fig. 4.17b.

Daculsi Vit β-TCP, Daculsi Viv β-TCP and Niemela LD β-TCP all shared the same commercially available matrix, poly(D,L-lactide)(4:96) from Purac Biochem B.V. (trade name Purasorb PLD9655). The TCP composites degradation model reported similar k_1 and k_2' values for the three cases, which pointed to the ability of the model to pick up similarities between case studies even when they come from different authors.

Ignatius D β-TCP (⬠) [13] was the only case study with a poly(D,L-lactide) homo- or copolymer which showed a non-buffering effect. Ignatius D β-TCP shared polymeric matrix, poly(L-co-D,L-lactide)(70:30) (trade name Resomer LR70x), with Niemela LDL β-TCP (◆) [8], which showed a buffering effect. Figure 4.18 includes the degradation, weight-average molecular weight over time, for both case studies. Niemela LDL β-TCP curves have been displaced in the x-axis (time) to allow a straight forward comparison between both case studies. Although the pure polymer curves seemed to behave similarly, the composite curves showed differences in behaviour with Ignatius D β-TCP composites showing a faster molecular weight

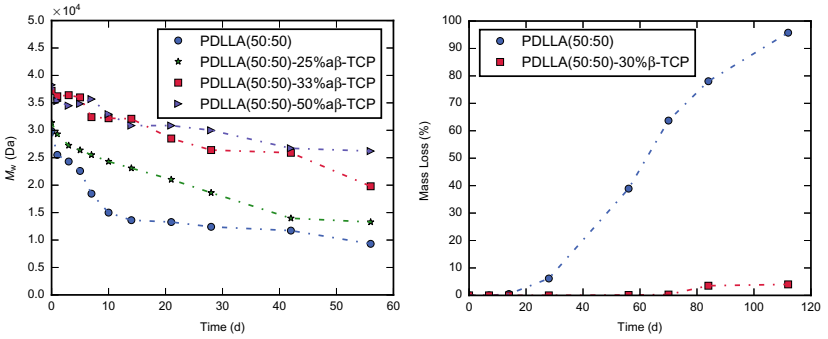

(a) M_w over time (b) Mass loss over time

Fig. 4.17 Degradation data (M_w over time and mass loss over time) from Zheng aβ-TCP [9] and Lin β-TCP [10]. Data replotted from [9, 10]. M_w is the weight average molecular weight. Dashed and dash-dotted lines are shown for clarity only. Markers and colours are specific of this visual representation

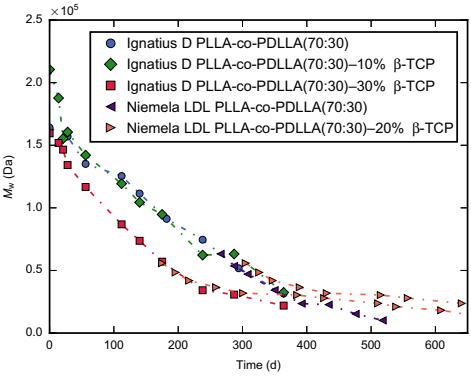

Fig. 4.18 Degradation data (M_w over time) from Ignatius D β-TCP [14] and Niemela LDL β-TCP case [12] studies. M_w is the weight average molecular weight. Data replotted from [12, 14]. Dash-dotted lines are shown for clarity only. Markers and colours are specific of this visual representation

drop. Despite the consideration of all the extra information reported by Ignatius et al. [13] and Niemel et al. [8], no particular cause could be pinned down to explain the mismatch in behaviour without further information.

In summary, a significant majority of the analysed PDLLA-TCP case studies behaved as predicted by the computational model. No apparent reason could be found to explain the behaviour of the discrepant case study which contained a polymeric matrix employed in a different case study showing a buffering effect.

Poly(lactide-co-glycolide) Matrix

For cases with a poly(lactide-co-glycolide) matrix the effect of tricalcium phosphate addition is shown in Fig. 4.15c, with the corresponding analysis in Table 4.7.

Of the 20 analysed PLGA case studies all but one displayed buffering effect. The non-buffering case study presented a higher polymer degradation rates k_1 and k_2'

Table 4.7 Analysis of tricalcium phosphate addition effect on composite degradation for case studies with a poly(lactide-co-glycolide) matrix. k_1 is the non-catalytic polymer degradation rate and k_2' is the autocatalytic polymer degradation rate, with both reported as geometric mean ⁎ geometric standard deviation

Buffering effect	k_1 (s^{-1})	k_2' ($m^3\ mol^{-1}\ s^{-1}$)	Percentage of cases (%)	Number of cases
Yes	$(1.7 \divideontimes 2.0) \times 10^{-9}$	$(1.6 \divideontimes 1.9) \times 10^{-9}$	95	19
No	2.0×10^{-9}	2.2×10^{-9}	5	1

values. There was a significant number of buffering cases with both lower and higher polymer degradation rates than the non-buffering case.

The analysis showed a significant variation within the poly(lactide-co-glycolide) buffering case studies spanning more than one order of magnitude, with the Yang F. β-TCP case (□) [19] whose matrix is poly(L-lactide-co-glycolide)(70:30) at the slow end and Mellon α-TCP (◁) [28] and Mellon β-TCP (▷) [28] whose matrix is poly(D,L-lactide-co-glycolide)(50:50) at the fast end.

Yang showed that the presence of a 50 mol % D,L-lactide instead of a 75 mol % resulted in a significant increase in polymer degradation rates as can be seen when comparing Yang Z. 5050 mC α-TCP (▼) [26, 27] and Yang Z. 5050 nC α-TCP (◊) [26, 27], both with a poly(D,L-lactide-co-glycolide)(50:50) matrix, to Yang Z. 7525 mC α-TCP (⬡) [27] and Yang Z. 7525 nC α-TCP (●) [27], both with a poly(D,L-lactide-co-glycolide)(75:25) matrix.

In addition, the model was able to capture the similarities between different case studies from the CCMM (Cambridge Centre for Medical Materials) group, as seen by the proximity of Bennett nC α-TCP (▽) [23], Bennett iC α-TCP (▲) [23], Bennett mC α-TCP (★) [23], Yang Z. 5050 nC α-TCP (◊) [26, 27], Yang Z. 5050 mC α-TCP (▼) [26, 27] and Barrett α-TCP (⬡) [29, 30], all of them with the same commercially available poly(D,L-lactide-co-glycolide)(50:50) matrix. The group also showed a significant variety of buffering effect for the different employed ceramic fillers.

The non-buffering case study, Jin α-TCP (○) [21], with a poly(L-lactide-co-glycolide) matrix had a semi-dense structure due to its fabrication method with microwave energy. This structure resulted in a gradual and significant mass loss, higher for the composite samples, which could account for the non-buffering behaviour.

In a nutshell, for the PLGA composites the model fully reflected the degradation behaviour in a 95% of the analysed case studies capturing similarities among the CCMM group data.

Miscellaneous Polymers Matrixes

Figure 4.15d shows the effect of tricalcium phosphate addition in case studies with a miscellaneous polymer matrix. The analysis is presented in Table 4.8.

All but one of the 10 case studies with a miscellaneous polymer matrix presented a buffering effect. The non-buffering case study presented higher values of the polymer

Table 4.8 Analysis of tricalcium phosphate addition effect on composite degradation for case studies with a miscellaneous polymer matrix. k_1 is the non-catalytic polymer degradation rate and k_2' is the autocatalytic polymer degradation rate, with both reported as geometric mean ⁎ geometric standard deviation

Buffering effect	k_1 (s^{-1})	k_2' ($m^3\ mol^{-1}\ s^{-1}$)	Percentage of cases (%)	Number of cases
Yes	$(1.6 \divideontimes 2.6) \times 10^{-10}$	$(1.5 \divideontimes 2.6) \times 10^{-10}$	90	9
No	5.8×10^{-10}	3.8×10^{-10}	10	1

degradation rates k_1 and k_2'. Most of the cases showing a buffering effect had a poly(L-lactide) copolymer as matrix.

Imai et al. showed that varying the ratio of monomers in a copolymer can dramatically change the composite degradation behaviour using a poly(L-lactide)/poly (ethylene: hexamethylene/sebacate) block copolymer. The two case studies with a 98.3 mol % of poly(L-lactide), Imai H100 β-TCP (⬡) [34] and Imai H250 β-TCP (⬢) [34] had a much slower degradation that Imai L100 β-TCP (◊) [32] and Imai L250 β-TCP (◆) [32], the two cases with a 75.3 mol % of poly(L-lactide).

Similarly, Kikuchi et al. [18] showed that adding glycolide to a poly(L-lactide-co-ε-caprolactone) copolymer can significantly increase the autocatalytic component of the degradation behaviour as can be seen when comparing the k_2' values of Kikuchi PLCL β-TCP (◁) [18], with a poly(L-lactide-co-ε-caprolactone) matrix, and Kikuchi PLGC β-TCP (▷) [18] with poly(L-lactide-co-glycolide-co-ε-caprolactone) matrix.

The non-buffering case study, Ahola 12 β-TCP (○) [17] shared a high degree of similarity with Ahola 13 β-TCP (□), a case study with a buffering effect albeit with a low one. Both cases had the same commercially available poly(L-lactide)-co-ε-caprolactone as matrix and the same commercially available β-TCP as filler, being the only significant difference between both cases the presence of the drug ciprofloxacin in Ahola 13 β-TCP. The presence of the drug and that poly(ε-caprolactone) has been reported to show no autocatalysis by Lam et al. [51] could explain the different behaviours.

In short, the TCP model captured the degradation behaviour of all but one cases with a miscellaneous polymer matrix, which displayed the variety of degradation behaviours that could be attained with matrix modifications. The case study with a non-buffering behaviour presented significant similarities to a low extent buffering case which suggested that the high non-catalytic polymer degradation rate of the matrix in addition to the presence of a drug as factors accounting for the non-buffering behaviour.

All Polymer Matrixes

A global analysis, including all the analysed tricalcium phosphate case studies, is reported in Table 4.9. An extremely significant majority of the 41 cases presented a buffering effect, as expected. The polymer degradation rates of the non-buffering cases were lower that those of the buffering cases, pointing to a probable prevalence of the buffering effect at higher degradation rates.

Table 4.9 Analysis of tricalcium phosphate addition effect on composite degradation for all the analysed case studies. k_1 is the non-catalytic polymer degradation rate and k_2' is the autocatalytic polymer degradation rate, with both reported as geometric mean ⁎ geometric standard deviation

Buffering effect	k_1 (s^{-1})	k_2' ($m^3\ mol^{-1}\ s^{-1}$)	Percentage of cases (%)	Number of cases
Yes	$(4.8 \divideontimes 5.3) \times 10^{-10}$	$(4.7 \divideontimes 4.8) \times 10^{-10}$	88	36
No	$(2.0 \divideontimes 7.5) \times 10^{-10}$	$(1.8 \divideontimes 6.9) \times 10^{-10}$	12	5

Conclusions

The analysis of the effect of tricalcium phosphate addition on composite degradation was discussed in this section. The analysed case studies were classified in two different categories according to their behaviour: cases showing a buffering effect and a non-buffering effect.

A significant majority, 36 out of 41, of the analysed TCP case studies displayed the expected behaviour, i.e. a buffering effect, pointing towards the validity of the TCP composites degradation model. The model also captured a great variety of behaviours within the degradation space, highlighting the numerous available possibilities. In addition, the model was also able to reflect the similarities in degradation of case studies sharing some characteristics as depicted by the data clustering. In addition, the analysis also pointed to the existence of behaviour discrepancies within similar case studies belonging to different data groups, suggesting the need for a more comprehensive characterisation of both the employed tricalcium phosphate type filler and polymeric matrix in order to identify the factors responsible for these variations.

The model was unable to characterise the behaviour of the non-buffering case studies but nevertheless pointed to plausible causes responsible for this behaviour. These causes included not meeting the water excess model condition, significant differences between pure polymer and composite samples and the use of a highly non-catalytic matrix.

4.6.5 The Influence of Sample Porosity on Degradation Behaviour

Sample structure, along with morphology, is a critical factor in composite degradation. Heterogeneous bulk degradation is commonly viewed as the dominant type of degradation in most of these polymeric matrixes as shown by Li et al. [52–54] and Hurrell and Cameron [55, 56], with the heterogeneity of the degradation caused by the autocatalysis present in the polymer hydrolysis [57, 58]. Sample structure and morphology heavily impact the distances that free hydrogen ions, which act as catalyst, need to travel in order to diffuse out of the sample and therefore it is believed that these properties will have a significant impact in composite degradation as first suggested by Grizzi et al. for polymeric scaffolds [59].

Fu et al. reported the decrease of internal acidity in polymer microspheres with a reduction in size, suggesting the presence of a distance $L_{\text{homogeneous bulk}}$, defined as the distance which allows complete diffusion of the hydrogen ions out of the sample, below which samples experience homogeneous bulk degradation [60], setting a lower boundary in terms of size for heterogeneous bulk degradation. In addition, von Burkersroda et al. confirmed the existence of a critical device dimension, L_{erosion}, above which degradable polymers experience degradation by surface erosion rather than bulk erosion [61], setting an upper boundary in terms of size for heterogeneous bulk degradation. Defining the free hydrogen ions to buffer distance, $L_{H^+\text{–buffer}}$, as the average distance for a given sample from each and every point in the polymeric matrix to the closest surface point, samples would then be expected to experience an increase in degradation rate with increasing $L_{H^+\text{–buffer}}$, in the interval defined by $L_{\text{homogeneous bulk}}$ and L_{erosion}.

A binary broad classification has been adopted to enable an assessment of how sample structure affects composite degradation. For each case study, samples were classified as either dense or non-dense, also referred as porous. This classification sacrifices accuracy for practicality, as it solely encompasses macroscopic aspects in a binary way. In order to gain full insight into the effect of structure and morphology, not only the macroscopic but also the microscopic aspects should be considered. These microscopic aspects concern ceramic particles and their surrounding microenvironment, in a similar way to the modelling framework unit cell and its boundary conditions (see Sect. 3.3). These features are extremely difficult to fully characterise from literature as such detailed information is not usually reported.

Furthermore, characterising the sample structure in a binary way is an oversimplification, as there is a spectrum of structures with gradual variations among them. For example, when analysing a solvent cast and a injection-moulded samples, both are considered dense with this binary classification, but in reality have different properties, including divergent $L_{H^+\text{–buffer}}$ values and therefore dissimilar composite degradation rates as shown by McDonald et al. [62].

Nevertheless, the use of sample porosity seems an appropriate beginning as it can usually be determined for most case studies with the information available in the literature. Figure 4.19 includes polymer degradation maps for tricalcium phosphate biocomposites conveying sample porosity, as either dense or non-dense, for all the modelled case studies. Table 4.10 summarises the analysis of the presented information by reporting relevant metrics for both dense and non-dense TCP biocomposites.

In this and following analyses, the number of cases sharing a particular trait is counted. For those calculations non-buffering case studies contribute with two sets of polymer degradation constants, one representing the pure polymer fitting and another representing the composite fitting. Although this method might cause a certain over-representation of a particular trait, as usually both pure polymer and composite samples share the same structure, degradation protocol, etc., it was preferred to the alternative of sacrificing some of the information.

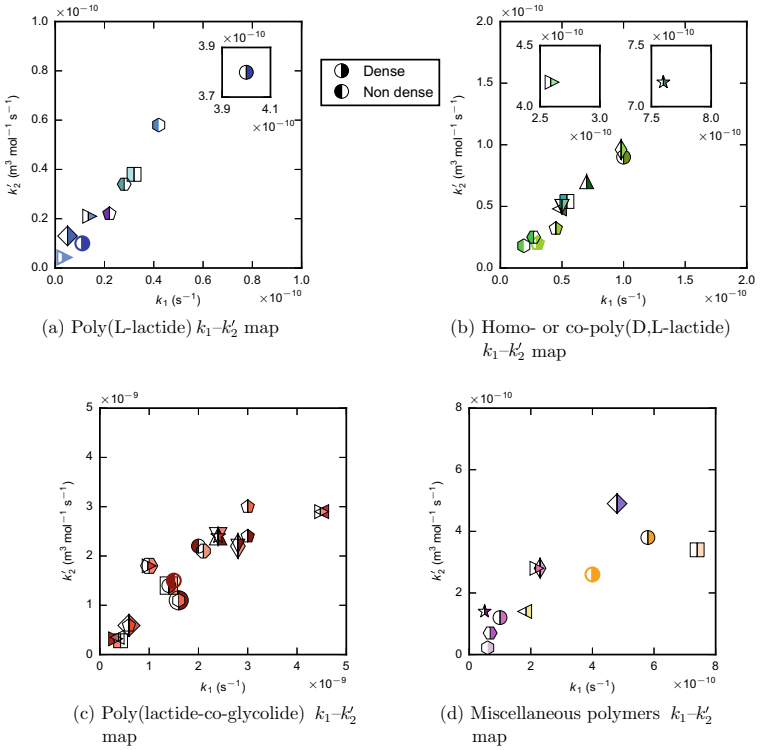

(a) Poly(L-lactide) k_1–k_2' map

(b) Homo- or co-poly(D,L-lactide) k_1–k_2' map

(c) Poly(lactide-co-glycolide) k_1–k_2' map

(d) Miscellaneous polymers k_1–k_2' map

Fig. 4.19 The influence of sample porosity on composite degradation for all the analysed tricalcium phosphate case studies. k_1 is the non-catalytic polymer degradation rate and k_2' is the autocatalytic polymer degradation rate. Right-hand side filled markers represent dense case studies, whereas left-hand side filled markers represent non dense case studies. Black inset plots correspond to regions situated outside the limits defined in the main plot

Poly(L-lactide) Matrix

The influence of sample porosity on composite degradation for case studies with a poly(L-lactide) matrix is included in Fig. 4.19a, with the corresponding analysis in the first row of Table 4.10. A slight majority of the 9 analysed case studies had a dense structure and unexpectedly presented lower values of polymer degradation rates k_1 and k_2' than the porous case studies. While the four porous case studies showed little variation, the dense case studies showed a much greater variability, with case studies degrading both slower and faster than the non-dense cases.

The combined simultaneous assessment of buffering effect, discussed in Sect. 4.6.4, and sample porosity did not provide extra information as only dense cases met the conditions for the analysis of buffering effect presence.

Table 4.10 Analysis of the influence of sample porosity on composite degradation for all the analysed tricalcium phosphate case studies. k_1 is the non-catalytic polymer degradation rate and k_2' is the autocatalytic polymer degradation rate, with both reported as geometric mean ⁎ geometric standard deviation

Case studies	k_1 (s^{-1})	k_2' ($m^3\ mol^{-1}\ s^{-1}$)	Percentage of cases (%)	Number of cases
Dense with poly(L-lactide) matrix	$(1.6 \divideontimes 6.5) \times 10^{-11}$	$(2.1 \divideontimes 5.5) \times 10^{-11}$	56	5
Non-dense with poly(L-lactide) matrix	$(3.0 \divideontimes 1.3) \times 10^{-11}$	$(3.6 \divideontimes 1.5) \times 10^{-11}$	44	4
Dense with poly(D,L-lactide) homo- or copolymer matrix	$(9.1 \divideontimes 2.7) \times 10^{-11}$	$(8.7 \divideontimes 3.2) \times 10^{-11}$	75	9
Non-dense with poly(D,L-lactide) homo- or copolymer matrix	$(3.0 \divideontimes 1.7) \times 10^{-11}$	$(2.9 \divideontimes 1.8) \times 10^{-11}$	25	3
Dense with poly(lactide-co-glycolide) matrix	$(1.9 \divideontimes 1.8) \times 10^{-9}$	$(1.7 \divideontimes 1.6) \times 10^{-9}$	78	18
Non-dense with poly(lactide-co-glycolide) matrix	$(6.8 \divideontimes 2.4) \times 10^{-10}$	$(6.4 \divideontimes 2.6) \times 10^{-10}$	22	5
Dense with miscellaneous polymers matrix	$(1.9 \divideontimes 2.6) \times 10^{-10}$	$(1.7 \divideontimes 2.5) \times 10^{-10}$	100	11
All dense data	$(3.2 \divideontimes 6.8) \times 10^{-10}$	$(3.1 \divideontimes 6.3) \times 10^{-10}$	78	43
All non-dense data	$(1.1 \divideontimes 5.5) \times 10^{-10}$	$(1.1 \divideontimes 5.3) \times 10^{-10}$	22	12

Poly(D,L-lactide) and Poly(D,L-lactide) Copolymers Matrixes

Figure 4.19b exhibits the influence of sample porosity in case studies with a poly(D,L-lactide) homo- or copolymer matrix. The analysis with the relevant metrics is reported in the second row of Table 4.10. A significant majority of the 12 case studies presented a dense structure. Contrarily to the poly(L-lactide) case studies, the values of the polymer degradation rates were higher for the dense cases. The distribution in the k_1–k_2' map had little overlap with almost all non-dense case studies in the left hand corner, pointing to the validity of the initial assumption relating higher values of $L_{H^+\text{–buffer}}$ with higher degradation rates. Regrettably, the combined simultaneous assessment of buffering effect and sample porosity did not provide extra information as only dense cases could be analysed for the presence of buffering effect.

Poly(lactide-co-glycolide) Matrix

For case studies with a poly(lactide-co-glycolide) matrix, the influence of sample porosity is shown in Fig. 4.19c, with the analysis in the third row of Table 4.10. The dense samples, which presented a majority of the 23 PLGA-TCP case studies, had significantly higher polymer degradation constants than the porous ones, suggesting again the validity of the initial hypothesis, although in this instance the specific poly(lactide-co-glycolide) matrix might have also played a role in the difference

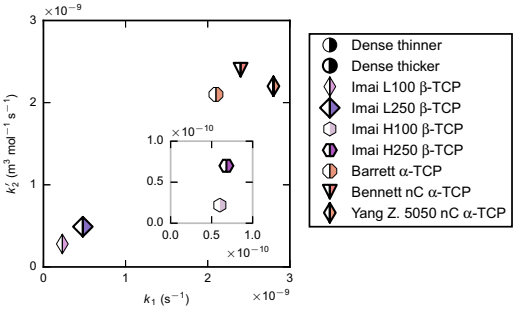

Fig. 4.20 Polymer degradation map including the tricalcium phosphate case studies used for a direct comparison of sample structure influence on composite degradation behaviour. k_1 is the non-catalytic polymer degradation rate and k_2' is the autocatalytic polymer degradation rate. Right-hand side filled markers represent dense case studies with the thickness of the marker edge proportional to the sample thickness

between the values of the dense versus non-dense polymer degradation constants. Of those with dense structure, the percentage of buffering effect presence was 100%, while the percentage ratio of buffering/non-buffering was 50:50 for porous case studies suggesting that structure might be relevant in the non-buffering PLGA-TCP case.

Miscellaneous Polymers Matrixes

Figure 4.19d contains the influence of sample porosity for case studies with a miscellaneous polymer matrix. The fourth row of Table 4.10 includes the analysis. All the cases presented a dense structure and therefore no comparison between dense and non-dense case studies could be established. Similarly, the simultaneous assessment of buffering effect and sample porosity was rendered redundant by the absence of porous cases.

All Polymer Matrixes

The analysis of the influence of sample porosity on composite degradation for all the analysed tricalcium phosphate case studies is reported in the fifth and final row of Table 4.10. Of the 55 analysed TCP case studies, a significant majority had a dense structure and those cases showed higher values of polymer degradation rates in line with the expected behaviour.

Direct Comparison

Amongst the tricalcium phosphate case studies, no data were found to allow a direct comparison between dense and non-dense samples. However a series of case studies belonging to the PLGA CCMM group in addition to case studies authored by Imai et al. allow the comparison between different $L_{H^+\text{–buffer}}$. Although all the samples presented a dense structure, the data included different thicknesses. Figure 4.20 shows all the data employed in the direct comparisons.

Imai et al. analysed two different thicknesses: 100 and 250 μ m. The thinner samples, Imai L100 β-TCP (◊) [32] and Imai H100 β-TCP (○) [34], had lower polymer degradation rate than their thicker counterparts, Imai L250 β-TCP (◈) [32] and Imai H250 β-TCP (◍) [34], portraying the expected behaviour for two different poly(L-lactide) copolymers.

Similarly, a comparison can be made amongst several cases belonging to the PLGA CCMM group data. The comparison involves Yang Z. 5050 nC α-TCP (◆) [26, 27], Bennett nC α-TCP (▼) [23] and Barrett α-TCP (◍) [29, 30]. All of them used the same commercially available poly(D,L-lactide-co-glycolide)(50:50) from Lakeshore Biomaterials and similar in-house α-TCP but different sample morphologies. Barrett and Bennett employed disks with $\Phi = 8$ mm, t = 0.9 mm and $\Phi = 3.5$ mm, t = 1 mm, respectively. Yang used films of $8 \times 8\,\text{mm}^2 \times 1$ mm.

The case studies with thicker thicknesses, which was the dimension defining $L_{H^+\text{–buffer}}$, presented higher values of polymer degradation rates than the thinner case study, pointing once again to the validity of the initial assumption.

Conclusions

The analysis of the influence of porosity on degradation behaviour for TCP composites showed mostly an agreement with the initial hypothesis that the degradation is related to the characteristic diffusional length $L_{H^+\text{–buffer}}$. The poly(D,L-lactide), poly(lactide-co-glycolide) and all polymer data analyses, in addition to the direct comparisons agreed with the expected behaviour, while the poly(L-lactide) analysis disagreed, pointing to strong enough differences amongst nominally similar polymeric matrixes from different origins to overshadow the porosity contribution to degradation behaviour.

4.6.6 The Influence of In vitro Versus In vivo Protocols on Degradation Behaviour

Degradation protocol, understood as a set of environmental specifications, is widely considered as a relevant factor affecting the degradation of polymeric scaffolds [42, 63–65] and biocomposites [66–68]. In the analysed tricalcium phosphate composites case studies, over thirty different degradation protocols were reported. In order to make the analysis feasible, a broad binary classification based on their biological characteristics, which distinguished between in vitro and in vivo degradation, has been employed.

Figure 4.21 presents the polymer degradation maps for tricalcium phosphate biocomposites providing information about their degradation protocol. Table 4.11 summarises the analysis of the influence of in vitro versus in vivo protocols on the polymer degradation constants obtained by the TCP composites degradation model for all the analysed case studies.

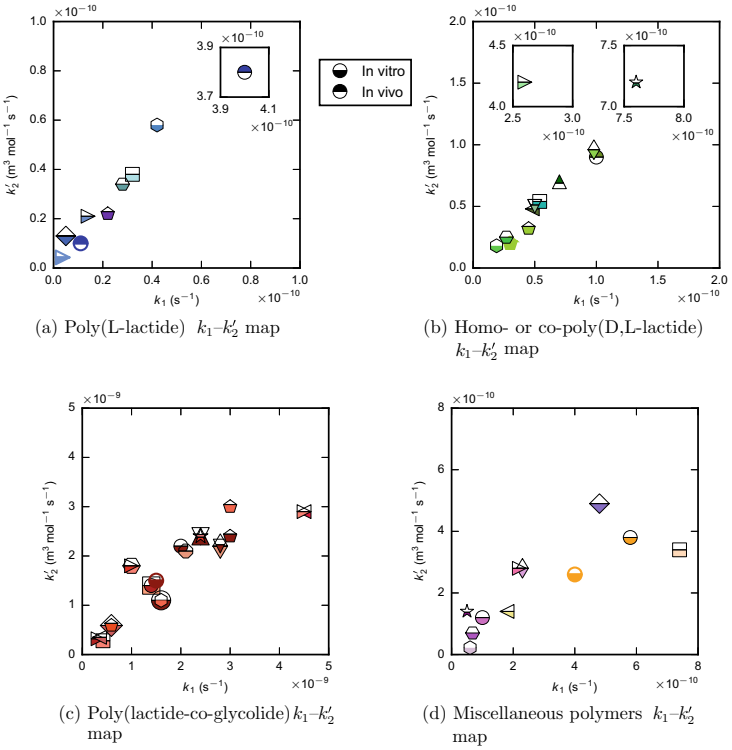

(a) Poly(L-lactide) k_1–k_2' map

(b) Homo- or co-poly(D,L-lactide) k_1–k_2' map

(c) Poly(lactide-co-glycolide) k_1–k_2' map

(d) Miscellaneous polymers k_1–k_2' map

Fig. 4.21 The influence of in vitro versus in vivo protocols on composite degradation for all the analysed tricalcium phosphate case studies. k_1 is the non-catalytic polymer degradation rate and k_2' is the autocatalytic polymer degradation rate. Bottom side filled markers represent in vitro case studies, whereas top side filled markers represent in vivo case studies. Black inset plots correspond to regions situated outside the limits defined in the main plot

Poly(L-lactide) Matrix

Figure 4.21b shows the influence of in vitro versus in vivo degradation protocol for case studies with a poly(L-lactide) matrix. The analysis is included in the first row of Table 4.11. A significant majority of the 9 analysed case studies presented in vitro degradation. The values of the polymer degradation constants k_1 and k_2' for in vitro degraded cases were lower and with smaller spread that those for in vivo degraded cases.

Poly(D,L-lactide) and Poly(D,L-lactide) Copolymers Matrix

For case studies with a poly(D,L-lactide) homo- or copolymer matrix the influence of in vitro versus in vivo protocols is depicted in Fig. 4.21b, while the analysis can be found in the second row of Table 4.11. In a similar fashion to poly(L-lactide) case studies, a significant majority of the 12 analysed case studies in this group had

Table 4.11 Analysis of the influence of in vitro versus in vivo protocols on composite degradation for all the analysed tricalcium phosphate case studies. k_1 is the non-catalytic polymer degradation rate and k_2' is the autocatalytic polymer degradation rate, with both reported as geometric mean ⁎ geometric standard deviation

Case studies	k_1 (s^{-1})	k_2' ($m^3\,mol^{-1}\,s^{-1}$)	Percentage of cases (%)	Number of cases
In vitro with poly(L-lactide) matrix	$(1.5 \divideontimes 2.6) \times 10^{-11}$	$(2.1 \divideontimes 2.3) \times 10^{-11}$	78	7
In vivo with poly(L-lactide) matrix	$(6.6 \divideontimes 12.7) \times 10^{-11}$	$(6.2 \divideontimes 13.1) \times 10^{-11}$	22	2
In vitro with poly(D,L-lactide) homo- or copolymer matrix	$(6.7 \divideontimes 3.1) \times 10^{-11}$	$(6.4 \divideontimes 3.5) \times 10^{-11}$	83	10
In vivo with poly(D,L-lactide) homo- or copolymer matrix	$(8.4 \divideontimes 1.3) \times 10^{-11}$	$(7.9 \divideontimes 1.2) \times 10^{-11}$	17	2
In vitro with poly(lactide-co-glycolide) matrix	$(1.5 \divideontimes 2.2) \times 10^{-9}$	$(1.4 \divideontimes 2.1) \times 10^{-9}$	100	23
In vitro with miscellaneous polymers matrix	$(1.9 \divideontimes 2.6) \times 10^{-10}$	$(1.7 \divideontimes 2.5) \times 10^{-10}$	100	11
All in vitro data	$(2.8 \divideontimes 6.8) \times 10^{-10}$	$(2.7 \divideontimes 6.3) \times 10^{-10}$	93	51
All in vivo data	$(7.4 \divideontimes 4.4) \times 10^{-11}$	$(7.0 \divideontimes 4.5) \times 10^{-11}$	7	4

also in vitro degradation protocol which resulted in lower polymer degradation rates, although this time with a bigger spread than the in vivo degraded cases.

Poly(lactide-co-glycolide) and Miscellaneous Polymers Matrix

Figures 4.21c, d present the results conveying the type of degradation protocol for case studies with a poly(lactide-co-glycolide) and miscellaneous polymers matrixes respectively, with the analysis included in the third and fourth rows of Table 4.11. The 23 poly(lactide-co-glycolide) and the 11 miscellaneous polymers case studies were degraded using in vitro protocols and therefore no comparison could be made.

All Polymer Matrixes

The last row of Table 4.11 includes the analysis of the influence of in vitro versus in vivo protocols when considering all the analysed tricalcium phosphate case studies. The in vitro data presented higher polymer degradation rates but the uneven split of the 55 case studies in the two categories made the comparison biased.

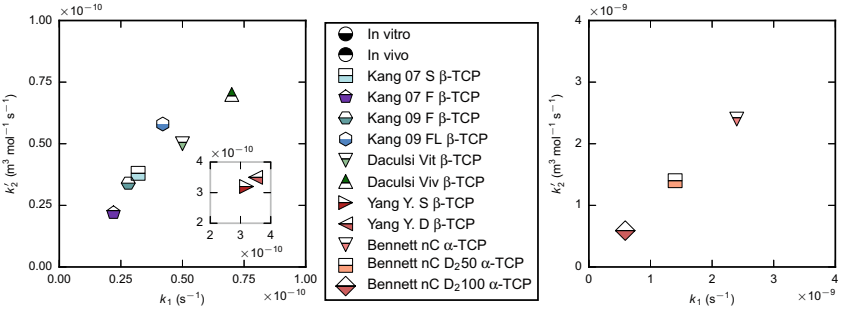

Fig. 4.22 Polymer degradation map including the tricalcium phosphate case studies used for a direct comparison of degradation protocol influence on composite degradation behaviour. k_1 is the non-catalytic polymer degradation rate and k_2' is the autocatalytic polymer degradation rate. Bottom side filled markers represent in vitro case studies, whereas top side filled markers represent in vivo case studies

Direct Comparison

The analysed tricalcium phosphate data contained several case studies which allowed a more direct comparison between different degradation protocols. The cases used in the direct comparisons shared all the characteristics apart from their degradation protocols. A polymer degradation map containing these data is included in Fig. 4.22.

Several case studies authored by Kang et al. [5, 6] allowed the comparison of three different in vitro protocol for porous poly(L-lactide) and β-TCP composites: S, F and FL. The S degradation protocol employed SBF (pH = 7.4) at 37 °C with replacement of 30 mL every 2 days, while the F protocol had constant buffer replacement at a flow rate of 0.02 mL/(mL min) and the FL had the addition of dynamic loading at 0.6 Hz and 0.1 MPa to protocol F.

The continuous buffer replacement caused a decrease in the polymer degradation rates as can be seen when comparing Kang 07 S β-TCP (⊟) [5] with S protocol and Kang 07 F β-TCP (⬟) [5] with F. The further addition of dynamic mechanical loading produced an increase in polymer degradation rates as seen in Kang 09 F β-TCP (⬭) [6] with an F protocol and Kang 09 FL β-TCP (⬙) [6] with an FL degradation protocol.

Similarly, Yang et al. researched the effect of cyclic loading in porous poly(L-lactide-co-glycolide)(70:30) and β-TCP. Including 8 h d^{-1} of cyclic loading at 1 Hz and (0.5. . .0.6) mm displacement and keeping 16 h d^{-1} of shaking at 50 rpm with PBS (pH = 7.4) at 37 °C and weekly buffer replacement caused a mild increase in degradation rate as seen when comparing Yang Y. S β-TCP (▶) [20] (no cycling load) and Yang Y. D β-TCP (◀) [20].

Bennett studied the influence of the presence of deuterated water (D_2O) in the degradation buffer for poly(D,L-lactide-co-glycolide)(50:50)–α-TCP composites. All the Bennett cases were degraded in PBS (0.01 M, pH = 7.4) fabricated with varying percentage of D_2O at 37 °C. Bennett nC α-TCP (▽) [23] was degraded in 0% D_2O, Bennett nC D2 50 α-TCP (⊟) [23] in 50% D_2O and Bennett nC D2 100 α-TCP (⬙) [23] in 100% D_2O. The addition of D_2O dramatically slowed down the degradation kinetics.

Daculsi et al. compared in vitro, PBS (0.01 M, pH = 7.4) at 37 °C, versus in vivo, condylar implantation in adult New Zealand white rabbits, degradation protocols for dense composites with both commercially available poly(D,L-lactide)(4:96) and β-TCP. In this instance, Daculsi Vit β-TCP (▽) [7] degraded in vitro presented slower polymer degradation rate than Daculsi Viv β-TCP (▲) [7], degraded in vivo.

Conclusions

The analysis of the influence of in vitro versus in vivo protocols for TCP composites did not provide great insights as a significant majority of the case studies had an in vitro degradation protocol making difficult to isolate the protocol contribution.

On the other hand, the direct comparisons offered interesting insights. For dense composites with both commercially available poly(D,L-lactide)(4:96) and β-TCP in vitro samples degraded slower than in vivo samples. For several porous composites the inclusion of loading in the in vitro degradation protocol resulted in higher polymer degradation rates. And lastly, the addition of deuterated water to the degradation buffer caused a significant decrease in the degradation rate.

4.7 Conclusions for the Tricalcium Phosphate Composites Analysis

This chapter presented the analysis of tricalcium phosphate composites degradation data harvested from literature using the computational model for TCP composites presented in Sect. 3.2.1. In the first place, the necessary information was reported, including both composite degradation data harvested from literature and tricalcium phosphate specific parameters employed by the computational model. Secondly, the results from the simulations carried out for all the case studies along with the necessary information for the analyses were presented. Then the model capabilities were discussed and lastly, the analysis of the TCP results was carried out divided in an overview and four main sections: tricalcium phosphate dissolution, effect of TCP addition on composite degradation, influence of sample porosity and finally, influence of in vitro versus in vivo degradation protocols.

The analysis of the tricalcium phosphate dissolution showed an unexpected behaviour with both TCP allotropes showing similar dissolution rates and with higher values than those measured in free drift experiments at 37 °C and different initial pH ranging from 5.0 to 7.0 for highly crystalline β-TCP [43]. The double discrepancy of this behaviour could be explained by both the presence of a polymeric matrix acting as a source of acidity, the influence of ceramic particle size on the definition of the surrounding environment in composite samples and the possibility of effective surface area overestimation for small particles.

The analysis of the effect of tricalcium phosphate addition on composite degradation provided several insights. The TCP case studies, which displayed a wide range of composite degradation behaviours, were classified into two categories: case studies presenting a buffering effect and a non-buffering effect, with 88% of the 41 cases showing the former, as predicted by the modelling framework pointing to its validity.

For the compliant case studies, the TCP computational model highlighted the wide range of both degradation constants and buffering effect extent that could be achieved by distinct combinations of polymeric matrix and tricalcium phosphate, resulting in an abundance of degradation behaviours. Considering that with a perfect capture of degradation behaviour by the model similar polymer-ceramic combinations should share the values of the four degradation constants, the analysis also pointed to the existence of behaviour discrepancies within similar case studies belonging to different data groups, suggesting the need for a more comprehensive characterisation of both the employed tricalcium phosphate type filler and polymeric matrix in order to identify the factors responsible for these variations.

For the minority of TCP case studies in which the computational model was unable to capture the degradation behaviour, a number of plausible causes were identified such as absence of water excess, important differences between pure polymer and composite samples or the employment of a highly non-catalytic matrix.

The porosity analysis for TCP composites showed, in most part, an agreement with the initial hypothesis that the degradation is related to the characteristic diffusional length $L_{H^+-\text{buffer}}$. The degradation protocols analysis did not provide clear general insights but revealed interesting information such as that for dense PDLLA–β-TCP composites in vitro degradation was slower than in vivo, that the inclusion of loading caused an increase in degradation rate for several porous composites or that, conversely, the addition of deuterated water caused a significant decrease.

The following chapter, Chap. 5 is the second chapter discussing the harvest and analysis of experimental degradation data using the computational models derived from the general framework presented in Chap. 3. In this case, the analysed composites contain hydroxyapatite as a filler.

References

1. Pan, J., Han, X., Niu, W., & Cameron, R. E. (2011). A model for biodegradation of composite materials made of polyesters and tricalcium phosphates. *Biomaterials*, *32*(9), 2248–2255.
2. Kobayashi, S., & Yamaji, S. (2014). Analytical prediction of hydrolysis behavior of tricalcium phosphate/poly-L-lactic acid composites in simulated body environment. *Advanced Composite Materials*, *23*(3), 211–223.
3. Aunoble, S., Clément, D., Frayssinet, P., Harmand, M. F., & Le Huec, J. C. (2006). Biological performance of a new β-TCP/PLLA composite material for applications in spine surgery: In vitro and in vivo studies. *Journal of Biomedical Materials Research Part A*, *78*(2), 416–422.
4. Adamus, A., et al. (2012). In vitro degradation of β-tricalcium phosphate reinforced poly (L-lactic acid). In *Materials science forum* (Vol. 714, pp. 283–290). Trans Tech Publications
5. Kang, Y., Xu, X., Yin, G., Chen, A., Liao, L., & Yao, Y., et al. (2007). A comparative study of the in vitro degradation of poly(L-lactic acid)/β-tricalcium phosphate scaffold in static and dynamic simulated body fluid. *European Polymer Journal*, *43*(5), 1768–1778.
6. Kang, Y., Yao, Y., Yin, G., Huang, Z., Liao, X., Xu, X., et al. (2009). A study on the in vitro degradation properties of poly(L-lactic acid)/β-tricalcuim phosphate (PLLA/β-TCP) scaffold under dynamic loading. *Medical Engineering & Physics*, *31*(5), 589–594.

7. Daculsi, G., Goyenvalle, E., Cognet, R., Aguado, E., & Suokas, E. O. (2011). Osteoconductive properties of poly(96L/4D-lactide)/beta-tricalcium phosphate in long term animal model. *Biomaterials*, *32*(12), 3166–3177.
8. Niemelä, T. (2005). Effect of β-tricalcium phosphate addition on the in vitro degradation of self-reinforced poly-L,D-lactide. *Polymer Degradation and Stability*, *89*(3), 492–500.
9. Zheng, X., Zhou, S., Yu, X., Li, X., Feng, B., Qu, S., et al. (2008). Effect of in vitro degradation of poly(D, L-lactide)/β-tricalcium composite on its shape-memory properties. *Journal of Biomedical Materials Research Part B: Applied Biomaterials*, *86*(1), 170–180.
10. Lin, F.-H., Chen, T.-M., Lin, C.-P., & Lee, C.-J. (1999). The merit of sintered PDLLA/TCP composites in management of bone fracture internal fixation. *Artificial Organs*, *23*(2), 186–194.
11. Heidemann, W., Jeschkeit, S., Ruffieux, K., Fischer, J. H., Wagner, M., Krüger, G., et al. (2001). Degradation of poly(D, L)lactide implants with or without addition of calciumphosphates in vivo. *Biomaterials*, *22*(17), 2371–2381.
12. Niemelä, T., Kellomäki, M., & Törmälä, P. (2004). In vitro degradation of osteoconductivepoly-L/DL-lactide/β-TCP composites. In *Key engineering materials* (Vol. 254, pp. 509–512). Trans Tech Publication
13. Ignatius, A. A., Wolf, S., Augat, P., & Claes, L. E. (2001b). Composites made of rapidly resorbable ceramics and poly(lactide) show adequate mechanical properties for use as bone substitute materials. *Journal of Biomedical Materials Research Part A*, *57*(1), 126–131.
14. Ignatius, A. A., Augat, P., & Claes, L. E. (2001a). Degradation behavior of composite pins made of tricalcium phosphate and poly(L, DL-lactide). *Journal of Biomaterials Science, Polymer Edition*, *12*(2), 185–194.
15. Haaparanta, A.-M., Haimi, S., Ellä, V., Hopper, N., Miettinen, S., Suuronen, R., et al. (2010). Porous polylactide/β-tricalcium phosphate composite scaffolds for tissue engineering applications. *Journal of Tissue Engineering and Regenerative Medicine*, *4*(5), 366–373.
16. Ahola, N., Männistö, N., Veiranto, M., Karp, M., Rich, J., Efimov, A., et al. (2013). An in vitro study of composites of poly(L-lactide-co-ε-caprolactone), β-tricalcium phosphate and ciprofloxacin intended for local treatment of osteomyelitis. *Biomatter*, *3*(2), e23162.
17. Ahola, N., Veiranto, M., Rich, J., Efimov, A., Hannula, M., Seppälä, J., et al. (2012). Hydrolytic degradation of composites of poly(L-lactide-co-ε-caprolactone)70/30 and β-tricalcium phosphate. *Journal of Biomaterials Applications*, *28*(4), 529–543.
18. Kikuchi, M., Koyama, Y., Yamada, T., Imamura, Y., Okada, T., Shirahama, N., et al. (2004). Development of guided bone regeneration membrane composed of β-tricalcium phosphate and poly(L-lactide-co-glycolide-co-ε-caprolactone) composites. *Biomaterials*, *25*(28), 5979–5986.
19. Yang, F., Cui, W., Xiong, Z., Liu, L., Bei, J., & Wang, S. (2006). Poly(L, L-lactide-co-glycolide)/tricalcium phosphate composite scaffold and its various changes during degradation in vitro. *Polymer Degradation and Stability*, *91*(12), 3065–3073.
20. Yang, Y., Zhao, Y., Tang, G., Li, H., Yuan, X., & Fan, Y. (2008). In vitro degradation of porous poly(L-lactide-co-glycolide)/β-tricalcium phosphate (PLGA/β-TCP) scaffolds under dynamic and static conditions. *Polymer Degradation and Stability*, *93*(10), 1838–1845.
21. Jin, H.-H., Min, S.-H., Song, Y.-K., Park, H.-C., & Yoon, S.-Y. (2010). Degradation behavior of poly(lactide-co-glycolide)/β-TCP composites prepared using microwave energy. *Polymer Degradation and Stability*, *95*(9), 1856–1861.
22. Ara, M., Watanabe, M., & Imai, Y. (2002). Effect of blending calcium compounds on hydrolytic degradation of poly(DL-lactic acid-co-glycolic acid). *Biomaterials*, *23*(12), 2479–2483.
23. Bennett, S. M. (2012). *Degradation mechanisms of PLGA/ α-TCP composites for orthopaedic applications*. Ph.D. thesis, Department of Materials Science and Metallurgy, University of Cambridge.
24. Ege, D., Best, S., & Cameron, R. (2014). The degradation behaviour of nanoscale HA/PLGA and α-TCP/PLGA composites. *Bioinspired, Biomimetic and Nanobiomaterials*, *3*, BBN2.
25. Ege, D. (2012). *Mechanical and degradation properties of calcium phosphate/biodegradable polymer composites*. Ph.D. thesis, Department of Materials Science and Metallurgy, University of Cambridge.

26. Yang, Z., Best, S. M., & Cameron, R. E. (2009). The influence of α-tricalcium phosphate nanoparticles and microparticles on the degradation of poly(D, L-lactide-co-glycolide). *Advanced Materials*, *21*(38–39), 3900–3904.
27. Yang, Z. (2009). *Development and characterisation of bioactive, bioresorbable α-tricalcium phosphate/poly(D,L-lactide-co-glycolide) nanocomposites for bone substitution and fixation*. Ph.D. thesis, Department of Materials Science and Metallurgy, University of Cambridge.
28. Mellon, V. (2003). *Degradation study of poly(lactide-co-glycolic) acid and alpha or beta tricalcium phosphate composites - non porous*. Unpublished research at University of Cambridge.
29. Barrett, C. E., & Cameron, R. E. (2014). X-ray microtomographic analysis of α-tricalcium phosphate-poly(lactic-co-glycolic) acid nanocomposite degradation. *Polymer*, *55*(16), 4041–4049.
30. Barrett, C. E. (2013). *The degradation behaviour of tricalcium phosphate - poly(lactide-co-glycolide) nanocomposites*. Ph.D. thesis, Department of Materials Science and Metallurgy, University of Cambridge.
31. Ehrenfried, L. M., Patel, M. H., & Cameron, R. E. (2008). The effect of tri-calcium phosphate (TCP) addition on the degradation of polylactide-co-glycolide (PLGA). *Journal of Materials Science: Materials in Medicine*, *19*(1), 459–466.
32. Imai, Y., Fukuzawa, A., & Watanabe, M. (1999a). Effect of blending tricalcium phosphate on hydrolytic degradation of a block polyester containing poly(L-lactic acid) segment. *Journal of Biomaterials Science, Polymer Edition*, *10*(7), 773–786.
33. Kikuchi, M., Koyama, Y., Takakuda, K., Miyairi, H., Shirahama, N., & Tanaka, J. (2002). In vitro change in mechanical strength of β-tricalcium phosphate/copolymerized poly-L-lactide composites and their application for guided bone regeneration. *Journal of Biomedical Materials Research*, *62*(2), 265–272.
34. Imai, Y., Nagai, M., & Watanabe, M. (1999b). Degradation of composite materials composed of tricalcium phosphate and a new type of block polyester containing a poly(L-lactic acid) segment. *Journal of Biomaterials Science, Polymer Edition*, *10*(4), 421–432.
35. Elliott, J. C. (2013). *Structure and chemistry of the apatites and other calcium orthophosphates* (Vol. 18). Elsevier.
36. Bates, R. G. (1951). First dissociation constant of phosphoric acid from 0° to 60°C: limitations of the electromotive force method for moderately strong acids. *Journal of Research of the National Bureau of Standards*, *47*, 127–134.
37. Bates, R. G., & Acree, S. (1943). pH values of certain phosphate-chloride mixtures, and the second dissociation constant of phosphoric acid from 0° to 60°C. *Journal of Research of the National Bureau of Standards*, *30*, 129–155.
38. Vanderzee, C. E., & Quist, A. S. (1961). The third dissociation constant of orthophosphoric acid. *The Journal of Physical Chemistry*, *65*(1), 118–123.
39. PubChem (2005c). *CID: 24456*. Retrieved September 1, 2016 from https://pubchem.ncbi.nlm.nih.gov/compound/Calcium_phosphate#section=Top.
40. Dorozhkin, S. V., & Epple, M. (2002). Biological and medical significance of calcium phosphates. *Angewandte Chemie International Edition*, *41*(17), 3130–3146.
41. Neuendorf, R., Saiz, E., Tomsia, A., & Ritchie, R. (2008). Adhesion between biodegradable polymers and hydroxyapatite: Relevance to synthetic bone-like materials and tissue engineering scaffolds. *Acta Biomaterialia*, *4*(5), 1288–1296.
42. Middleton, J. C., & Tipton, A. J. (2000). Synthetic biodegradable polymers as orthopedic devices. *Biomaterials*, *21*(23), 2335–2346.
43. Bryar, S. (2015). *Experimental study of the dissolution rate of β-tricalcium phosphate for use in biodegradable composites for orthopaedic applications*. Part III individual research project: Department of Materials Science and Metallurgy, University of Cambridge.
44. Bohner, M. (2000). Calcium orthophosphates in medicine: from ceramics to calcium phosphate cements. *Injury*, *31*, D37–D47.
45. Daculsi, G., LeGeros, R., LeGeros, J., & Mitre, D. (1991). Lattice defects in calcium phosphate ceramics: high resolution TEM ultrastructural study. *Journal of Applied Biomaterials*, *2*(3), 147–152.

46. LeGeros, R. Z. (1993). Biodegradation and bioresorption of calcium phosphate ceramics. *Clinical Materials*, *14*(1), 65–88.
47. Bohner, M., Lemaître, J., & Ring, T. A. (1997). Kinetics of dissolution of β-tricalcium phosphate. *Journal of Colloid and Interface Science*, *190*(1), 37–48.
48. Brazda, L., Rohanova, D., & Helebrant, A. (2008). Kinetics of dissolution of calcium phosphate (Ca-P) bioceramics. *Processing and Application of Ceramics*, *2*(1), 57–62.
49. Kirkwood, T. B. (1979). Geometric means and measures of dispersion. *Biometrics*, *35*, 908–909.
50. Limpert, E., Stahel, W. A., & Abbt, M. (2001). Log-normal distributions across the sciences: Keys and clues: On the charms of statistics, and how mechanical models resembling gambling machines offer a link to a handy way to characterize log-normal distributions, which can provide deeper insight into variability and probability-normal or log-normal: That is the question. *AIBS Bulletin*, *51*(5), 341–352.
51. Lam, C. X., Hutmacher, D. W., Schantz, J.-T., Woodruff, M. A., & Teoh, S. H. (2009). Evaluation of polycaprolactone scaffold degradation for 6 months in vitro and in vivo. *Journal of Biomedical Materials Research Part A*, *90*(3), 906–919.
52. Li, S., Garreau, H., & Vert, M. (1990a). Structure-property relationships in the case of the degradation of massive poly(α-hydroxy acids) in aqueous media. Part 1: poly(DL-lactic acid). *Journal of Materials Science: Materials in Medicine*, *1*, 123–130.
53. Li, S., Garreau, H., & Vert, M. (1990b). Structure-property relationships in the case of the degradation of massive poly(α-hydroxy acids) in aqueous media. Part 2: degradation of lactide-glycolide copolymers: PLA37.5GA25 and PLA75GA25. *Journal of Materials Science: Materials in Medicine*, *1*(3), 131–139.
54. Li, S., Garreau, H., & Vert, M. (1990c). Structure-property relationships in the case of the degradation of massive poly(α-hydroxy acids) in aqueous media: Part 3: Influence of the morphology of poly(L-lactic acid). *Journal of Materials Science: Materials in Medicine*, *1*, 198–206.
55. Hurrell, S., & Cameron, R. E. (2001a). Polyglycolide: degradation and drug release. Part I: Changes in morphology during degradation. *Journal of Materials Science: Materials in Medicine*, *12*(9), 811–816.
56. Hurrell, S., & Cameron, R. E. (2001b). Polyglycolide: degradation and drug release. Part II: Drug release. *Journal of Materials Science: Materials in Medicine*, *12*(9), 817–820.
57. Pitt, C. G., Chasalow, F., Hibionada, Y., Klimas, D., & Schindler, A. (1981a). Aliphatic polyesters. I. The degradation of poly(*varepsilon*-caprolactone) in vivo. *Journal of Applied Polymer Science*, *26*(11), 3779–3787.
58. Pitt, G., Gratzl, M., Kimmel, G., Surles, J., & Sohindler, A. (1981b). Aliphatic polyesters II. The degradation of poly(DL-lactide), poly(ε-caprolactone), and their copolymers in vivo. *Biomaterials*, *2*(4), 215–220.
59. Grizzi, I., Garreau, H., Li, S., & Vert, M. (1995). Hydrolytic degradation of devices based on poly(DL-lactic acid) size-dependence. *Biomaterials*, *16*(4), 305–311.
60. Fu, K., Pack, D. W., Klibanov, A. M., & Langer, R. (2000). Visual evidence of acidic environment within degrading poly(lactic-co-glycolic acid) (PLGA) microspheres. *Pharmaceutical Research*, *17*(1), 100–106.
61. von Burkersroda, F., Schedl, L., & Göpferich, A. (2002). Why degradable polymers undergo surface erosion or bulk erosion. *Biomaterials*, *23*(21), 4221–4231.
62. McDonald, P. F., Lyons, J. G., Geever, L. M., & Higginbotham, C. L. (2010). In vitro degradation and drug release from polymer blends based on poly(DL-lactide), poly(L-lactide-glycolide) and poly(ε-caprolactone). *Journal of Materials Science*, *45*(5), 1284–1292.
63. Vert, M., Li, S., & Garreau, H. (1991). More about the degradation of LA/GA-derived matrices in aqueous media. *Journal of Controlled Release*, *16*(1–2), 15–26.
64. Li, S., & Vert, M. (2002). *Biodegradation of aliphatic polyesters. In Degradable polymers* (pp. 71–131). Springer.
65. Alexis, F. (2005). Factors affecting the degradation and drug-release mechanism of poly(lactic acid) and poly[(lactic acid)-co-(glycolic acid)]. *Polymer International*, *54*(1), 36–46.

66. Armentano, I., Dottori, M., Fortunati, E., Mattioli, S., & Kenny, J. (2010). Biodegradable polymer matrix nanocomposites for tissue engineering: a review. *Polymer Degradation and Stability*, *95*(11), 2126–2146.
67. Rezwan, K., Chen, Q., Blaker, J., & Boccaccini, A. R. (2006). Biodegradable and bioactive porous polymer/inorganic composite scaffolds for bone tissue engineering. *Biomaterials*, *27*(18), 3413–3431.
68. Kwon, K.-A., Shepherd, J. H., Shepherd, D. V., Moreno-Gomez, I., & Best, S. M. (2016). Nanocomposites for bone repair. In E. San Thian, J. Huang & M. Aizawa, (Eds.), *Nanobioceramics for Healthcare Applications*, (Chap. 9, pp. 239–298). Singapore: World Scientific.
69. Speight, J. G., et al. (2005). *Lange's handbook of chemistry* (Vol. 1). New York: McGraw-Hill.
70. Van de Velde, K., & Kiekens, P. (2002). Biopolymers: overview of several properties and consequences on their applications. *Polymer Testing*, *21*(4), 433–442.
71. Zhu, Y., Leong, M. F., Ong, W. F., Chan-Park, M. B., & Chian, K. S. (2007). Esophageal epithelium regeneration on fibronectin grafted poly(L-lactide-co-caprolactone)(PLLC) nanofiber scaffold. *Biomaterials*, *28*(5), 861–868.
72. Mikos, A. G., Sarakinos, G., Leite, S. M., Vacant, J. P., & Langer, R. (1993). Laminated three-dimensional biodegradable foams for use in tissue engineering. *Biomaterials*, *14*(5), 323–330.
73. Scientific Polymer, Inc. (2013). *Polymer density data*. Retrieved September 1, 2016 from http://scientificpolymer.com/density-of-polymers-by-density/

Chapter 5
Degradation of Bioresorbable Composites: Hydroxyapatite Case Studies

In this chapter, the analysis of the degradation of hydroxyapatite (HA) composites using the HA composites degradation model, described in Sect. 3.2.2, is presented. The chapter follows, with minor changes, the structure of Chap. 4. Firstly, in Sect. 5.1, the HA composite degradation data harvested from literature are reported, including the necessary composite degradation input information employed by the computational model. The second section, Sect. 5.2, includes information about the different types of hydroxyapatite (HA) found in the harvested degradation data and their associated values for the ceramic-dependent constants. In order to avoid duplication, this chapter does not include the values of the polymer-dependent constants, which can be found in Sect. 4.3. The third section, Sect. 5.3, contains the initial values of the HA composites degradation model variables. Section 5.4 presents the results from the degradation simulations, i.e. the set of values obtained in each studied case for the four degradation constants: k_1, the non-catalytic polymer degradation rate; k_2', the autocatalytic polymer degradation rate; A_d, the ceramic dissolution rate and θ, the ceramic dissolution exponent. The fifth section, Sect. 5.5, contains a discussion of the results including analyses of how properties such as composite structure and degradation protocol affect composite degradation. Lastly, Sect. 5.6, the sixth and final one introduces a summary of the conclusions stemming from the HA composites degradation discussion.

5.1 Degradation Data from Hydroxyapatite Composites and Composite-Dependent Constants for the Hydroxyapatite Composites Model

This section includes information concerning the degradation of hydroxyapatite composites. The harvested degradation data which includes several composite-dependent constants for each case study are presented in a tabular format. This table is followed by the remaining composite-dependent constants which are common to all

I. Moreno-Gomez, *A Phenomenological Mathematical Modelling Framework for the Degradation of Bioresorbable Composites*, Springer Theses, https://doi.org/10.1007/978-3-030-04990-4_5

hydroxyapatite case studies. As has been mentioned in Chap. 4, the information reported here is part of the input data fed to the computational model in order to simulate composite degradation. The harvested input information, extracted using the methodology described in Sect. 3.5.2, can be grouped in two different categories: polymer characteristics and ceramic characteristics. The first category includes several characterising parameters of the polymeric matrix: polymer type, molar ratio of monomers for the case of copolymers, initial number-average molecular weight, M_{n0} and type of reported data reflecting composite degradation. The second category includes several characterising parameters of the ceramic filler: ceramic type, ceramic weight fraction of the undegraded composite samples, f_{w0}; ceramic representative particle size, d_0 and ceramic data available to compute the ceramic representative particle size.

As was previously stated, this table exclusively contains information fed to the computational model. Some other relevant information, mostly concerning composite characteristics rather than polymer or ceramic characteristics, was also harvested for each studied hydroxyapatite composite degradation case. Those characteristics included fabrication method, sample morphology and structure, as well as sample degradation protocol. Although these factors may affect composite degradation behaviour, they are not explicitly represented in the modelling framework. These pieces of information are presented in Appendix B.2 alongside the results for each analysed case study.

Table 5.1 summarises all the above-mentioned input information needed to run the simulations with the HA composites degradation model for the hydroxyapatite composites data harvested from the available literature. The data are ordered alphabetically by polymer type including first the homopolymers, followed by copolymers and blends. For similar polymer types, enantiopure matrixes are presented first. When several cases concerned the same polymeric matrix the cases were ordered according to ceramic type and initial polymer molecular weight. Each row in the table represents one case study and is separated from the rest of the table by either a solid or a dashed line. A dashed line is used when consecutive cases were generated by the same author or research group and a solid line is used when there is no known author relationship. Hydroxyapatite type is described using abbreviations. Briefly, hHA and hCHA stand for high crystallinity pure hydroxyapatite and high crystallinity carbonated hydroxyapatite, respectively. The prefixes "p" and "l" indicate partial ("p") and low ("l") crystallinity. A complete list of hydroxyapatite types including a full denomination for each abbreviation can be found in Table 5.2.

Of the twelve composite-dependent constants listed in Sect. 3.4, Table 5.1 includes three of them for each hydroxyapatite case study. The values of the remaining nine composite-dependent constants are discussed here. The HA composites degradation model considers water self-ionisation as a source of both hydroxide and hydrogen ions. And thus, both the initial hydroxide ions concentration, $\Delta C_{OH_0^-}$ and the initial hydrogen ions concentration not resulting from carboxylic end groups dissociation, $\Delta C_{H_0^+}$, take the value of $(K_w/[H^+]_0)$ mol m^{-3}, where K_w is the water self-ionisation constant at 37 °C and $[H^+]_0$ is the initial concentration of hydrogen ions.

Table 5.1 Summary of data found in literature on degradation of composites made of biodegradable polymer and hydroxyapatite. *CMR* is the molar ratio of the different monomers in a copolymer, M_{n0} is the sample initial number-average molecular weight, f_{w0} is the initial ceramic weight fraction of a composite sample and d_0 is the ceramic representative particle size of the undegraded composite sample. Further abbreviations employed in columns labelled "Data" can be found in Sect. 3.5.2. Abbreviations used to specify the hydroxyapatite type can be found in Table 5.2. A dashed line between rows indicates that data displayed in those consecutive rows belong to the same researcher or research group. A solid line between rows indicates no known author relationship for the data

Polymer characteristics				Ceramic characteristics				Case code and reference
Type	CMR (mol %)	M_{n0} (kDa)	Data	Type	f_{w0} (wt %)	d_0 (μm)	Data	
Poly(ε-caprolactone)	–	53.00	$M_n(t)$	–	0	–	f_n(40, 60) nm	Wang PCL bnHA [1]
	–	56.00		bnHA	33.3	0.052		
	–	54.00		bnHA	50	0.052		
Poly(L-lactide)	–	25.00	$\sigma_{flexural}(t)$ and $pH(t)$	–	0	–	f_{wb}(50, 200) nm	Huang hHA [2]
	–	25.00		hHA	20	0.168		
Poly(L-lactide)	–	33.20	$M_v(t)$	–	0	–	f_a(20, 40, 100, 100) nm	Wang lHA [3]
	–	32.18		lHA	10	0.047		
Poly(L-lactide)	–	33.20	$M_v(t)$	–	0	–	f_a(20, 40, 100, 100) nm	Wang gP-lHA [3]
	–	31.04		gP-lHA	9.5	0.047		

(continued)

Table 5.1 (continued)

Polymer characteristics				Ceramic characteristics				Case code and reference
Type	CMR (mol %)	M_{n0} (kDa)	Data	Type	f_{w0} (wt %)	d_0 (μm)	Data	
Poly(L-lactide)	–	79.44	M_{n0} and $W_L(t)$	–	0	–	f_a(5, 10, 20, 40) nm	Zhou lCCDHA [4]
	–	79.44		lCCDHA	25	0.012		
Poly(L-lactide)	–	73.33	$M_v(t)$	–	0	–	f_{wb}(45) μm	Verheyen 92 Vit hHA [5]
	–	83.33		hHA	30	37		
	–	76.67		hHA	50	37		
Poly(L-lactide)	–	166.67	$M_v(t)$	–	0	–	f_{wb}(45) μm	Verheyen 93 hHA [6]
	–	83.33		hHA	30	37		
	–	50.00		hHA	50	37		
Poly(L-lactide)	–	73.33	$M_v(t)$	–	0	–	f_{wb}(45) μm	Verheyen 92 Viv hHA [5]
	–	83.33		hHA	30	37		
	–	76.67		hHA	50	37		

(continued)

Table 5.1 (continued)

Polymer characteristics				Ceramic characteristics				Case code and reference
Type	CMR (mol %)	M_{n0} (kDa)	Data	Type	f_{w0} (wt %)	d_0 (μm)	Data	
Poly(L-lactide)	–	95.68	$M_n(t)$ and $\sigma_y(t)$	–	0	–	$f_n(200)$ nm	Diaz PP/C bnHA and Diaz C bnHA [7]
	–	95.68		bnHA	9.1	0.163		
	–	95.68		bnHA	23.1	0.163		
	–	95.68		bnHA	33.3	0.163		
Poly(L-lactide)	–	106.59	$M_v(t)$ and $PDI(t)$	–	0	–	d_{mean} in text	Shikinami 99 pCHA [8]
	–	103.37		pCHA	20	3		
	–	100.96		pCHA	30	3		
	–	104.00		pCHA	40	3		
	–	101.00		pCHA	50	3		
Poly(L-lactide)	–	107.18	$M_v(t)$	–	0	–	d_{mean} in text	Furukawa Med pCHA [9]
	–	102.26		pCHA	30	3		
Poly(L-lactide)	–	100.14	$M_v(t)$	pCHA	30	3	d_{mean} in text	Furukawa Sub pCHA [9]
Poly(L-lactide)	–	100.96	$M_v(t)$	pCHA	30	3	d_{mean} in text	Ishii pCHA [10]
	–	104.00		pCHA	40	3		

(continued)

Table 5.1 (continued)

Polymer characteristics				Ceramic characteristics				Case code and reference
Type	CMR (mol %)	M_{n0} (kDa)	Data	Type	f_{w0} (wt %)	d_0 (μm)	Data	
Poly(L-lactide)	–	89.71	$M_v(t)$	pCHA	30	3	d_{mean} in text	Shikinami 01 pCHA [11]
Poly(L-lactide)	– –	107.18 102.26	$M_v(t)$	– hHA	0 30	– 3	d_{mean} in text	Furukawa Med hHA [9]
Poly(L-lactide)	–	105.19	$M_v(t)$	hHA	30	3	d_{mean} in text	Furukawa Sub hHA [9]
Poly(L-lactide)	– –	120.19 104.00	$M_v(t)$	hHA hHA	30 40	3 3	d_{mean} in text	Ishii hHA [10]
Poly(L-lactide)	–	91.05	$M_v(t)$	hHA	40	3	d_{mean} in text	Shikinami 01 hHA [11]
Poly(L-lactide)	– –	174.67 174.67	$M_v(t)$	– lHA	0 10	– 0.023	f_a(15, 15, 40, 70) nm	Deng SC lHA [12]
Poly(L-lactide)	– –	174.67 174.67	$M_v(t)$	– lHA	0 10	– 0.023	f_a(15, 15, 40, 70) nm	Deng ES lHA [12]
Poly(L-lactide)	– –	178.67 178.67	$M_v(t)$	– lHA	0 10	– 0.023	f_a(15, 15, 40, 70) nm	Sui ES lHA [13]

(continued)

Table 5.1 (continued)

Polymer characteristics				Ceramic characteristics				Case code and reference
Type	CMR (mol %)	M_{n0} (kDa)	Data	Type	f_{w0} (wt %)	d_0 (μm)	Data	
Poly(L-lactide)	–	200.00	M_{w0} and $W_L(t)$	–	0	–	$f_a(20, 40, l, l)$ nm	Xu PP/C gP-lHA and Xu C gP-lHA [14]
	–	200.00		gP-lHA	2.82	0.050		
	–	200.00		gP-lHA	4.70	0.050		
	–	200.00		gP-lHA	9.40	0.050		
	–	200.00		gP-lHA	19.74	0.050		
	–	200.00		gP-lHA	28.20	0.050		
Poly(D,L-lactide)	4:96	56.11	$M_w(t)$ and $PDI(t_0)$	–	0	–	SEM images	Rakmae 13 lCHA [15]
	4:96	44.10		lCHA	20	0.02		
	4:96	29.94		lCHA	40	0.02		
Poly(D,L-lactide)	4:96	56.11	$M_w(t)$ and $PDI(t_0)$	–	0	–	SEM images	Rakmae 13 pCHA [15]
	4:96	30.06		pCHA	20	0.15		
	4:96	26.04		pCHA	40	0.15		
Poly(D,L-lactide)	4:96	56.11	$M_w(t)$ and $PDI(t_0)$	–	0	–	SEM images	Rakmae 13 hHA [15]
	4:96	20.96		hHA	20	0.3		
	4:96	18.02		hHA	40	0.3		

(continued)

Table 5.1 (continued)

Polymer characteristics				Ceramic characteristics				Case code and reference
Type	CMR (mol %)	M_{n0} (kDa)	Data	Type	f_{w0} (wt %)	d_0 (μm)	Data	
Poly(D,L-lactide)	4:96	88.18	$M_w(t)$	–	0	–	d_{mean} in text	Rakmae 12 hCHA [16]
	4:96	35.88		hCHA	20	1		
	4:96	31.18		hCHA	40	1		
Poly(D,L-lactide)	4:96	88.18	$M_w(t)$	–	0	–	d_{mean} in text	Rakmae 12 sA-hCHA [16]
	4:96	78.24		sA-hCHA	20	1		
	4:96	72.94		sA-hCHA	40	1		
Poly(D,L-lactide)	4:96	88.18	$M_w(t)$	–	0	–	d_{mean} in text	Rakmae 12 sM-hCHA [16]
	4:96	86.47		sM-hCHA	20	1		
	4:96	72.94		sM-hCHA	40	1		
Poly(D,L-lactide)	15:85	627.00	$\log(M_n(t))$	–	0	–	$f_{wb}(1, 45)$ μm	Van der Meer hHA [17]
	15:85	627.00		hHA	30	37		
	15:85	627.00		hHA	50	37		

(continued)

Table 5.1 (continued)

Polymer characteristics				Ceramic characteristics				Case code and reference
Type	CMR (mol %)	M_{n0} (kDa)	Data	Type	f_{w0} (wt %)	d_0 (μm)	Data	
Poly(D,L-lactide)	50:50 50:50	13.50 13.50	$\%M_w(t)$ and $PDI(t_0)$	– pns-lHA	0 28	– 0.082	$f_n(100)$ nm	Zou 12 Vit pns-lHA [18]
Poly(D,L-lactide)	50:50 50:50	13.50 13.50	$\%M_w(t)$ and $PDI(t_0)$	– pns-lHA	0 28	– 0.082	$f_n(100)$ nm	Zou 12 Vit pns-lHA [18]
Poly(D,L-lactide)	50:50 50:50	13.50 13.50	$\%M_w(t)$ and $PDI(t_0)$	– pns-lHA	0 28	– 0.082	$f_n(100)$ nm	Zou 12 Viv pns-lHA [18]
Poly(D,L-lactide)	50:50 50:50	13.50 13.50	$\%M_w(t)$ and $PDI(t_0)$	– pns-lHA	0 28	– 0.082	$f_n(100)$ nm	Zou 12 Viv R pns-lHA [18]
Poly(D,L-lactide) modified w COOH groups	50:50 50:50	15.90 13.50	$\%M_w(t)$ and $PDI(t_0)$	– pns-lHA	0 15.5	– 0.3	SEM images	Zou 11 C pns-lHA [19]

(continued)

Table 5.1 (continued)

Polymer characteristics				Ceramic characteristics				Case code and reference
Type	CMR (mol %)	M_{n0} (kDa)	Data	Type	f_{w0} (wt %)	d_0 (μm)	Data	
Poly(D,L-lactide) modified w COOH groups			$\%M_w(t)$ and $PDI(t_0)$				SEM images	Zou 11 C R pns-lHA [19]
	50:50	15.90		–	0	–		
	50:50	13.50		pns-lHA	15.5	0.3		
Poly(D,L-lactide) modified w OH and COOH groups			$\%M_w(t)$ and $PDI(t_0)$				SEM images	Zou 11 HC pns-lHA [19]
	50:50	14.10		–	0	–		
	50:50	13.70		pns-lHA	16.7	0.3		
Poly(D,L-lactide) modified w N, OH and COOH groups			$\%M_w(t)$ and $PDI(t_0)$				SEM images	Zou 11 AHC pns-lHA [19]
	50:50	13.80		–	0	–		
	50:50	12.60		pns-lHA	17	0.3		
Poly(D,L-lactide)	50:50	51.30	$M_v(t)$	pCHA	70	3	d_{mean} in text	Hasegawa pCHA [20]

(continued)

Table 5.1 (continued)

Polymer characteristics				Ceramic characteristics				Case code and reference
Type	CMR (mol %)	M_{n0} (kDa)	Data	Type	f_{w0} (wt %)	d_0 (μm)	Data	
Poly(D,L-lactide)	NR	144.12	$M_w(t)$	–	0	–	$f_n(20, 30)$ nm	Chen PP/C bnHA and Chen C bnHA [21]
	NR	144.12		bnHA	20	0.026		
	NR	144.12		bnHA	40	0.026		
	NR	144.12		bnHA	60	0.026		
Poly(L-co-D,L-lactide)	100:0	88.33	$M_w(t)$ and $PDI(t)$	–	0	–	d_{mean} in text	Hile hHA [22]
	70:30	95.00		hHA	25	30		
Poly(L-lactide-co-ε-caprolactone)	70:30	79.76	$M_n(t)$	–	0	–	$f_n(200)$ nm	Diaz PLCL bnHA [23]
	70:30	79.76		bnHA	9.1	0.163		
	70:30	79.76		bnHA	23.1	0.163		
	70:30	79.76		bnHA	33.3	0.163		
Poly(D,L-lactide-co-ε-caprolactone)	60:40	34.00	$M_n(t)$	–	0	–	$f_n(25, 45)$ μm	Ural NS hHA [24]
	60:40	34.00		hHA	20	37		
	60:40	34.00		hHA	40	37		
	60:40	34.00		hHA	60	37		

(continued)

Table 5.1 (continued)

Polymer characteristics				Ceramic characteristics				Case code and reference
Type	CMR (mol %)	M_{n0} (kDa)	Data	Type	f_{w0} (wt %)	d_0 (μm)	Data	
Poly(D,L-lactide-co-ε-caprolactone)	60:40	91.80	$M_n(t)$	–	0	–	$f_n(25, 45)$ μm	Ural VL hHA [24]
	60:40	91.80		hHA	20	37		
	60:40	91.80		hHA	40	37		
	60:40	91.80		hHA	60	37		
Poly(D,L-lactide-co-glycolide)	44.6:55.4	11.40	$M_n(t)$	–	0	–	d_{cube} in text	Tsunoda hHA [25]
	44.6:55.4	8.50		hHA	50	0.5		
	44.6:55.4	9.50		hHA	50	1.4		
Poly(D,L-lactide-co-glycolide)	44.6:55.4	30.00	$M_n(t)$	–	0	–	$f_{wb}(100, 150)$ μm	Li hHA [26]
	44.6:55.4	30.00		hHA	20	135		
Poly(D,L-lactide-co-glycolide)	47:53	65.60	$M_n(t)$	–	0	–	$f_n(200)$ nm	Diaz PLGA bnHA [27]
	47:53	65.60		bnHA	9.1	0.163		
	47:53	65.60		bnHA	23.1	0.163		
	47:53	65.60		bnHA	33.3	0.163		

(continued)

Table 5.1 (continued)

Polymer characteristics				Ceramic characteristics				Case code and reference
Type	CMR (mol %)	M_{n0} (kDa)	Data	Type	f_{w0} (wt %)	d_0 (μm)	Data	
Poly(D,L-lactide-co-glycolide)	50:50 50:50	30.29 30.29	$\%M_w(t)$ and $M_w(t_0)$	– hHA	0 44	– 80	Assumed	Agrawal hHA [28]
Poly(D,L-lactide-co-glycolide)	50:50 50:50	34.50 34.50	$pH(t)$ and $W_L(t)$	– pCHA	0 27.7	– 7.50	Particle size distribution	Naik pCHA [29] [30]
Poly(D,L-lactide-co-glycolide)	50:50 50:50	34.50 34.50	$pH(t)$ and $W_L(t)$	– hCHA	0 29.5	– 24.66	Particle size distribution	Naik ca hCHA [29] [30]
Poly(D,L-lactide-co-glycolide)	50:50 50:50	34.50 34.50	$pH(t)$ and $W_L(t)$	– hCHA	0 31.2	– 12.75	Particle size distribution	Naik cw hCHA [29] [30]

(continued)

Table 5.1 (continued)

Polymer characteristics				Ceramic characteristics				Case code and reference
Type	CMR (mol %)	M_{n0} (kDa)	Data	Type	f_{w0} (wt %)	d_0 (μm)	Data	
Poly(D,L-lactide-co-glycolide)			$pH(t)$ and $W_L(t)$				Particle size distribution in composite	Naik f sMP-pCHA [31] [30]
	50:50	34.50		–	0	–		
	50:50	34.50		sMP-pCHA	27.1	140.09		
Poly(D,L-lactide-co-glycolide)			$pH(t)$ and $W_L(t)$				Particle size distribution in composite	Naik c sMP-pCHA [31] [30]
	50:50	34.50		–	0	–		
	50:50	34.50		sMP-pCHA	28.8	132.99		
Poly(D,L-lactide-co-glycolide)			$pH(t)$ and $W_L(t)$				Particle size distribution in composite	Naik fca sMP-hCHA [31] [30]
	50:50	34.50		–	0	–		
	50:50	34.50		sMP-hCHA	26.0	75.10		
Poly(D,L-lactide-co-glycolide)			$pH(t)$ and $W_L(t)$				Particle size distribution in composite	Naik cca sMP-hCHA [31] [30]
	50:50	34.50		–	0	–		
	50:50	34.50		sMP-hCHA	29.9	75.73		

(continued)

Table 5.1 (continued)

Polymer characteristics				Ceramic characteristics				Case code and reference
Type	CMR (mol %)	M_{n0} (kDa)	Data	Type	f_{w0} (wt %)	d_0 (μm)	Data	
Poly(D,L-lactide-co-glycolide)	50:50 50:50	34.50 34.50	$pH(t)$, $W_L(t)$ and M_w as-received	– hCHA	0 21.52	– 0.210	Particle size distribution in composite	Ege hCHA [32]
Poly(D,L-lactide-co-glycolide)	50:50 50:50	34.50 34.50	$pH(t)$, $W_L(t)$ and M_w as-received	– hHA	0 28.55	– 0.706	Particle size distribution in composite	Ege hHA [33] [32]
Poly(D,L-lactide-co-glycolide)	75:25 75:25	77.30 77.30	$W_L(t)$ and M_{w0}	– hHA	0 20	– 3	SEM images	Lee hHA [34]
Poly(lactide-co-glycolide)	95:05 95:05	124.20 99.46	$\eta(t)$	– lHA	0 3	– 0.045	f_a(30, 30 115, 125) nm	Liuyun lHA [35]
Poly(lactide-co-glycolide)	NR NR	30.0 30.0	$W_L(t)$	– hHA	0 16.6	– 1.3	f_a(0.5, 1 7, 10) μm	Ban hHA [36]

(continued)

Table 5.1 (continued)

Polymer characteristics				Ceramic characteristics				Case code and reference
Type	CMR (mol %)	M_{n0} (kDa)	Data	Type	f_{w0} (wt %)	d_0 (μm)	Data	
Poly(L-lactide) and poly(ε-caprolactone) blend			$M_n(t)$				$f_n(100)$ nm	Rodenas CL bnHA [37]
	28.4:71.6	115.23		–	0	–		
	28.4:71.6	127.78		bnHA	16.7	0.082		
Poly(L-lactide) and poly(ε-caprolactone) blend			$M_n(t)$				$f_n(100)$ nm	Rodenas LA bnHA [37]
	86.4:13.6	106.17		–	0	–		
	86.4:13.6	150.00		bnHA	16.7	0.082		
Poly(D,L-lactide-co-glycolide) (50:50) and poly(ε-caprolactone) blend			$M_w(t)$				d_{mean} in a reference	Ji bnHA [38]
	84:16	78.87		–	0	–		
	84:16	78.87		bnHA	10.9	0.030		
	84:16	78.87		bnHA	22.1	0.030		
	84:16	78.87		bnHA	31.2	0.030		

(continued)

Table 5.1 (continued)

Polymer characteristics				Ceramic characteristics				Case code and reference
Type	CMR (mol %)	M_{n0} (kDa)	Data	Type	f_{w0} (wt %)	d_0 (μm)	Data	
Poly(D,L-lactide-co-glycolide) (65:35) and poly(ε-caprolactone) blend	71.8:28.2	39.63	$M_n(t)$	hHA	10	10	d in text	Dunn CLs hHA [39]
Poly(D,L-lactide-co-glycolide) (65:35) and poly(ε-caprolactone) blend	71.8:28.2	39.63	$M_n(t)$	hHA	10	10	d in text	Dunn CLd hHA [39]
Poly(D,L-lactide-co-glycolide) (65:35) and poly(ε-caprolactone) blend	93.9:6.1	33.39	$M_n(t)$	hHA	10	10	d in text	Dunn LGs hHA [39]
Poly(D,L-lactide-co-glycolide) (65:35) and poly(ε-caprolactone) blend	93.9:6.1	33.39	$M_n(t)$	hHA	10	10	d in text	Dunn LGd hHA [39]

Table 5.2 Abbreviations, descriptions and model assimilations of the different types of hydroxyapatite encountered in the harvested degradation data

Abbreviation	Description	Assimilated to
lCCDHA	Carbonated calcium deficient unsintered pure hydroxyapatite produced by a wet chemistry route	aCHA
lCHA	Amorphous or low crystallinity unsintered carbonated hydroxyapatite produced by a wet chemistry route	aCHA
pCHA	Partially crystalline carbonated hydroxyapatite	cCHA
sMP-pCHA	MPTMS (mercaptopropyltrimethoxysilane) modified partially crystalline carbonated hydroxyapatite	cCHA
hCHA	Highly crystalline carbonated hydroxyapatite	cCHA
sA-hCHA	APES (3-Aminopropyltriethoxysilane) modified highly crystalline carbonated hydroxyapatite	cCHA
sM-hCHA	MPTS (3-methacryloxypropyltrimethoxysilane) modified highly crystalline carbonated hydroxyapatite	cCHA
sMP-hCHA	MPTMS (mercaptopropyltrimethoxysilane) modified highly crystalline carbonated hydroxyapatite	cCHA
pns-lHA	Mixture of partially crystalline and non-stoichiometric unsintered pure hydroxyapatite produced by a wet chemistry route	aHA
lHA	Amorphous or low crystallinity unsintered pure hydroxyapatite produced by a wet chemistry route	aHA
gP-lHA	Polymer grafted lHA	aHA
bnHA	Commercially produced nano-sized pure hydroxyapatite	cHA
hHA	Highly crystalline pure hydroxyapatite	cHA

In a similar way to the tricalcium phosphate case studies, the hydroxyapatite case studies were assumed to experience a mixture of random and end scission, as previously done by Pan et al. [40]. This polymer scission type is characterised by:

- Empirical rate of production of short chains by chain scission, $\alpha = 0.4(1)$.
- Empirical exponent of production of short chains by chain scission, $\beta = 1(1)$.
- Average degree of pseudo-polymerisation of the short chains, $m = 4(1)$.

The last four composite-dependent constants are the composite degradation constants, k_1, k_2', A_d and θ. These composite degradation constants are the output of the analysis process and can be found in Sect. 5.4.

5.2 Hydroxyapatite Information and Ceramic-Dependent Constants for the Hydroxyapatite Composites Degradation Model

The composite degradation data obtained from the literature contained different types of hydroxyapatite. A description of all those types and their corresponding ceramic-dependent constants is presented in this section. The HA composites

degradation model, introduced in Sect. 3.2.2, employs chemical relationships to represent the interactions between ceramic filler and polymeric matrix. This fact enables the assimilation of all the encountered hydroxyapatite types to merely two main classes according to their chemistry: pure hydroxyapatite (HAp[1]: $Ca_{10}(PO_4)_6(OH)_2$) and carbonated hydroxyapatite (CHA: $Ca_{10}(PO_4)_6(CO_3)_x(OH)_{2-2x}$ with $x = 0.4$[2]). Both HAp and CHA can have a varying degree of crystallinity giving a total of four relevant types of hydroxyapatite for use in the computational model: crystalline HA (cHA), crystalline CHA (cCHA) and their amorphous or low crystallinity counterparts (aHA and aCHA).

Table 5.2 includes the abbreviations used to designate each one of the hydroxyapatite types encountered in the harvested composite degradation data in addition to their description. The corresponding assimilated hydroxyapatite types employed in the computational model are also included.

As has been noted, the modelling framework uses several parameters that are ceramic-dependent: ceramic molar mass, M_{cer}; ceramic density, ρ_{cer}; ceramic molar volume, Ω_{cer}; ceramic solubility expressed as a base 10 logarithm of the reciprocal of the ionic product at equilibrium, $-\log_{10}(K_{sp})$; ceramic calcium equilibrium concentration, $[Ca^{2+}]_{eq}|_{cer}$ and acid dissociation constants associated to the released anions, pK_i.

For the HA composites degradation model the employed acid dissociation constants are common to all the hydroxyapatite types, as explained in Sect. 3.2.2, due to the omission of carbonate ions in the buffering reactions. The hydroxyapatite chemical composition affects the remaining five hydroxyapatite parameters: molar mass, density, molar volume, solubility and calcium equilibrium concentration. In addition, the degree of crystallinity also affects hydroxyapatite density and hydroxyapatite molar volume resulting in one set of acid dissociation constants, two sets of values for molar mass, solubility constant and calcium equilibrium concentration, as these ceramic parameters are dependent exclusively on chemical composition, and four sets of values for density and molar volume, as these two ceramic parameters are affected by both chemical composition and density. Table 5.3 reports all these ceramic-dependent parameters for the four different relevant types of hydroxyapatite.

The HA composites degradation model also employs polymer-dependent constants, namely polymer density, ρ_{pol}; polymer dissociation constant, K_a and molar mass associated to one ester bond in the polymeric matrix, M_{unit}. These constants are common across all the models derived from the modelling framework and can be found in Sect. 4.3.

[1] HAp was chosen as abbreviation to designate pure hydroxyapatite, instead of the the more usual HA, as HA was used throughout this work as abbreviation for hydroxyapatite in a general broad sense, i.e. group of all ceramics that could be classified as hydroxyapatite, independently of their particular properties.

[2] Information about the chosen fraction of carbonate ions in carbonated hydroxyapatite can be found in Appendix A.1.

Table 5.3 Values of the ceramic-dependent parameters used in the hydroxyapatite model. Acid dissociation expressed as the negative base 10 logarithm of the acid dissociation constant, $pK_i = -\log_{10}(K_i)$ with K_i in mol dm^{-3}. Water dissociation expressed as the negative base 10 logarithm of the water dissociation constant, $pK_w = -\log_{10}(K_w)$ with K_w in mol^2 dm^{-6}. Solubility expressed as the negative base 10 logarithm of the ionic product at equilibrium of $Ca_{10}(PO_4)_6(OH)_2$ or $Ca_{10}(PO_4)_6(CO_3)_{0.4}(OH)_{1.2}$ with concentrations in mol dm^{-3}

Constant (unit)	Quantity	Value	Reference
pK_1 (1)	First logarithmic phosphoric acid dissociation constant at 37 °C	2.21	[41]
pK_2 (1)	Second logarithmic phosphoric acid dissociation constant at 37 °C	7.18	[42]
pK_3 (1)	Third logarithmic phosphoric acid dissociation constant at 37 °C	12.23	[43]
pK_w (1)	Logarithmic water dissociation constant at 37 °C	13.58	[44]
M_{aCHA} (g mol^{-1})	aHA and cHA molar mass*	1004.622	[45]
M_{acCHA} (g mol^{-1})	aCHA and cCHA molar mass⋆	1015.010	Appendix A.1
$-\log_{10}(K_{sp})\|_{acHA}$ (1)	aHA and cHA solubility at 37 °C*	117.2	[46]
$-\log_{10}(K_{sp})\|_{acCHA}$ (1)	aCHA and cCHA solubility at 37 °C⋆	116.9	[47]
$[Ca^{2+}]_{eq}\|_{acHA}$ (mol m^{-3})	aHA and cHA equilibrium calcium concentration at 37 °C	4.370×10^{-4}	Appendix A.2.2
$[Ca^{2+}]_{eq}\|_{acCHA}$ (mol m^{-3})	aCHA and cCHA equilibrium calcium concentration at 37 °C	3.392×10^{-4}	Appendix A.2.3
ρ_{cHA} (kg m^{-3})	cHA density	3160	[46]
ρ_{cCHA} (kg m^{-3})	cCHA density	3160	⊤
ρ_{aHA} (kg m^{-3})	aHA density	2528	⊥
ρ_{aCHA} (kg m^{-3})	aCHA density	2528	⊥
Ω_{aHA} (m^3 mol^{-1})	aHA molar volume	3.974×10^{-4}	†
Ω_{aCHA} (m^3 mol^{-1})	aCHA molar volume	4.015×10^{-4}	†
Ω_{cHA} (m^3 mol^{-1})	cHA molar volume	3.179×10^{-4}	†
Ω_{cCHA} (m^3 mol^{-1})	cCHA molar volume	3.212×10^{-4}	†

*Using the formula $Ca_{10}(PO_4)_6(OH)_2$

⋆Using the formula $Ca_{10}(PO_4)_6(CO_3)_x(OH)_{2-2x}$ with $x = 0.4$

⊤Data not reported. Assuming same density as cHA

⊥Data not reported. Assuming density is 80% of the cHA or cCHA density

†Calculated as the ratio between M_i and ρ_i ($\Omega_i = M_i/\rho_i$)

5.3 Initial Values for the HA Composites Degradation Model Variables

This section presents the values at the time origin of the variables employed in the HA composites degradation model. These values, in addition to the values of the composite-dependent, ceramic-dependent and polymer-dependent constants presented in Sects. 5.1, 5.2 and 4.3 respectively, are needed in order to simulate the degradation of hydroxyapatite composites. As previously stated, the HA composites model considers water self-ionisation as a source of both hydroxide and hydrogen ions and employs a value of $({}^{K_w}/_{[H^+]_0})$ mol m^{-3} for the initial hydrogen ions concentration not resulting from carboxylic end groups dissociation, $\Delta C_{H_0^+}$, with K_w the water self-ionisation constant at 37 °C and $[H^+]_0$ the initial concentration of hydrogen ions.

The initial values of the eleven degradation variables, which are listed below, arise from two assumptions: firstly, that both ceramic dissolution and polymer scission start at the time origin and secondly, that the polymer phase has attained carboxylic end acid dissociation equilibrium at the time origin.

- $x_1|_{t=0} = R_{s0} = 0$, initial concentration of polymer chain scissions (mol m^{-3}).
- $x_2|_{t=0} = [H^+]_0 = C_{H_0^+}$, initial concentration of hydrogen ions (mol m^{-3}). $x_2|_{t=0}$ takes a value equals to the positive root of the following x_2 third degree polynomial: $x_2^3 + K_a x_2^2 - (K_a C_{chain0} + K_w)x_2 - K_w K_a = 0$.
- $x_3|_{t=0} = [Ca^{2+}]_0 = 0$, initial concentration of calcium ions (mol m^{-3}).
- $x_4|_{t=0} = [PO_4^{3-}]_0 = 0$, initial concentration of phosphate ions (mol m^{-3}).
- $x_5|_{t=0} = [R\text{-}COOH]_0 = C_{chain0} - \frac{K_a C_{chain0}}{x_2|_{t=0} + K_a}$, initial concentration of non-dissociated carboxylic end group chains (mol m^{-3}).
- $x_6|_{t=0} = [R\text{-}COO^-]_0 = \frac{K_a C_{chain0}}{x_2|_{t=0} + K_a}$, initial concentration of dissociated carboxylic end group chains (mol m^{-3}).
- $x_7|_{t=0} = [HPO_4^{2-}]_0 = 0$, initial concentration of hydrogenphosphate ions (mol m^{-3}).
- $x_8|_{t=0} = [H_2PO_4^-]_0 = 0$, initial concentration of dihydrogenphosphate ions (mol m^{-3}).
- $x_9|_{t=0} = [H_3PO_4]_0 = 0$, initial concentration of phosphoric acid (mol m^{-3}).
- $x_{10}|_{t=0} = a_{HA0} = \frac{\pi d_0^2}{V_{unit}}$, initial concentration of interfacial area in the composite (m^2 m^{-3}).
- $x_{11}|_{t=0} = [OH^-]_0 = \frac{K_w}{x_2|_{t=0}}$, initial concentration of hydroxide ions (mol m^{-3}).
- $x_{12}|_{t=0} = [H_2O]_0 = 0$, initial concentration of recombined water molecules (mol m^{-3}).
- $x_{13}|_{t=0} = M_{n0}$, initial polymer number-average molecular weight (Da).

where the concentrations $x_1, \ldots, x_9$, x_{11} and x_{12} are defined in the polymer phase, K_a is the polymer acid dissociation constant at 37 °C (mol m^3); C_{chain0}, the polymer chains concentration at the time origin (mol m^{-3}); d_0, the representative particle size (m); V_{unit}, the volume of the representative unit cell (m^3) and K_w, the water self-ionisation constant at 37 °C.

5.4 Results of the Hydroxyapatite Composites Degradation Model

The results output by the HA composites degradation model after running the simulations with the HA degradation data reported in Sect. 5.1 are presented in this section. These results have been grouped in four different blocks, according to their polymeric matrixes: poly(L-lactide), poly(D,L-lactide), poly-lactide-co-glycolide and "miscellaneous polymers". The chosen visual representation, aimed at facilitating the analysis, includes three different graphs: a polymer degradation map, a ceramic degradation map and a 3D plot exploring the polymer-ceramic degradation space. The polymer degradation map provides information about degradation aspects of the matrix by representing each case as a point by their duplet (k_1, k_2') in the k_1–k_2' plane. Likewise, the ceramic degradation map provides information about degradation aspects of the filler by representing each case as a point by their duplet (A_d, θ) in the A_d–θ plane. Lastly, each case is represented as a triplet (k_1, k_2', A_d) in the $(k_1$–k_2'–$A_d)$ degradation space. Each analysed composite degradation case is always represented by the same unique combination of marker and colour, with the colour shade being an indication of the polymeric matrix group the case belongs to: blue for poly(L-lactide), green for poly(D,L-lactide) and red for poly(lactide-co-glycolide). The legend included in each visual representation of the results is common for the three displayed graphs: k_1–k_2' map, A_d–θ plane and k_1–k_2'–A_d plot. For clarity purposes, the results associated with one polymeric matrix have been split into several groups when an excessive amount of data resulted in difficulty interpreting the graphs.

Uniqueness of model parameters, k_1, k_2', A_d and θ: As explained in Sect. 4.5, there is a possibility of having multiple solutions for a given case. For HA cases with multiple solutions, the chosen and reported (k_1, k_2', A_d, θ) 4-tuple was also selected considering typical dissolution profiles, in terms of remaining ceramic weight fraction, of similar HA composites from literature.

5.4.1 Poly(L-lactide) Matrix

The results output by the HA composites degradation model for degradation data with a poly(L-lactide) matrix are presented visually, split into three different sets: data from the Takiron Co. group, data from the Leiden University and the Beijing University groups and a general set containing the remaining data. Figure 5.1 includes results from the Takiron Co. group, which contained experimental studies carried out by Shikinami and Okuno [8, 11], Furukawa et al. [9] and Ishii et al. [10].

Figure 5.1a presents the polymer degradation map for the Takiron Co. group data, Fig. 5.1b the ceramic degradation map and Fig. 5.1c the 3D plot in the k_1–k_2'–A_d degradation space. As previously mentioned, the marker-colour combinations displayed in the legend are uniquely associated with one hydroxyapatite case. The values of the polymer degradation constants k_1 and k_2' for all the Takiron Co.

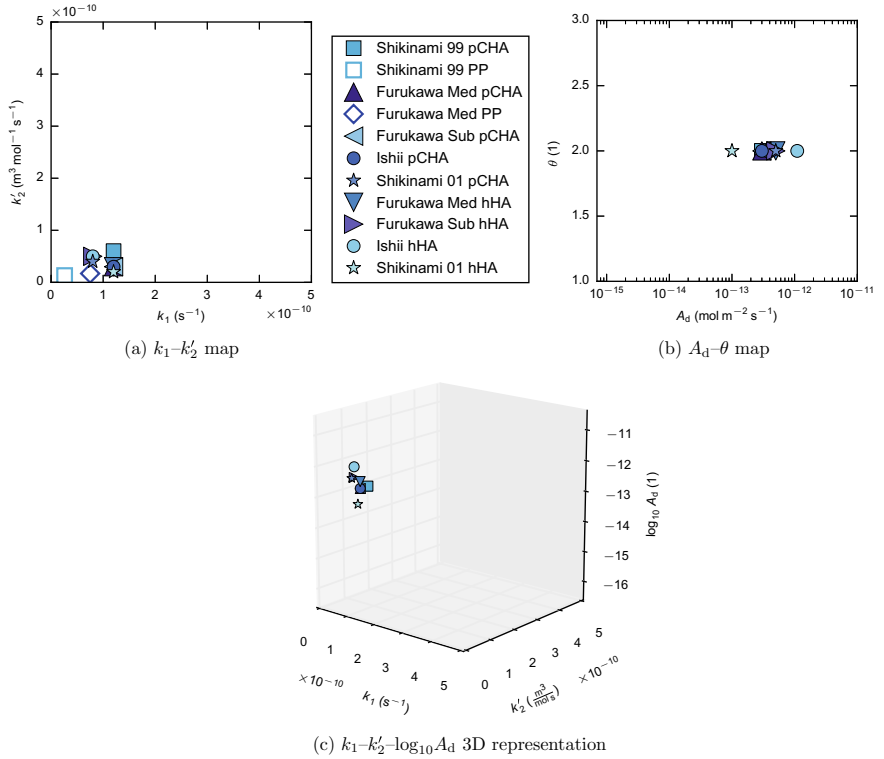

(a) k_1–k_2' map

(b) A_d–θ map

(c) k_1–k_2'–$\log_{10}A_d$ 3D representation

Fig. 5.1 Results output by the HA composites degradation model for data with a poly(L-lactide) matrix: case studies from the Takiron Co. group. k_1 is the non-catalytic polymer degradation rate, k_2' is the autocatalytic polymer degradation rate, A_d is the ceramic dissolution rate and θ is the power ceramic dissolution law exponent. The hydroxyapatite type used in each case study is indicated in the legend by the abbreviation found at the end of the case study code. The meaning of the abbreviations can be found in Table 5.2

group case studies populated a small region clustered around a single k_1–k_2' duplet. In a similar fashion, the ceramic dissolution constants A_d and θ were contained in a short A_d interval with θ equal to 2.0 showing a low sensitivity of the model to changes in θ.

Figure 5.2 reports the results for HA composites degradation data belonging to both the Leiden University and the Beijing University groups. The Leiden University group contained data from Verheyen et al. [5, 6]. The Beijing University group consisted of data from Deng et al. [12] and Sui et al. [13]. Following the usual visual representation structure, Fig. 5.2a includes the polymer degradation map, Fig. 5.2b the ceramic degradation map and Fig. 5.2b the 3D plot in the k_1–k_2'–A_d degradation space.

Figure 5.2 highlights the differences between results from the Leiden University group data and the Beijing University group data. Although the two groups presented clustering in both polymer and ceramic degradation constants, the clusters differed significantly in both size and origin.

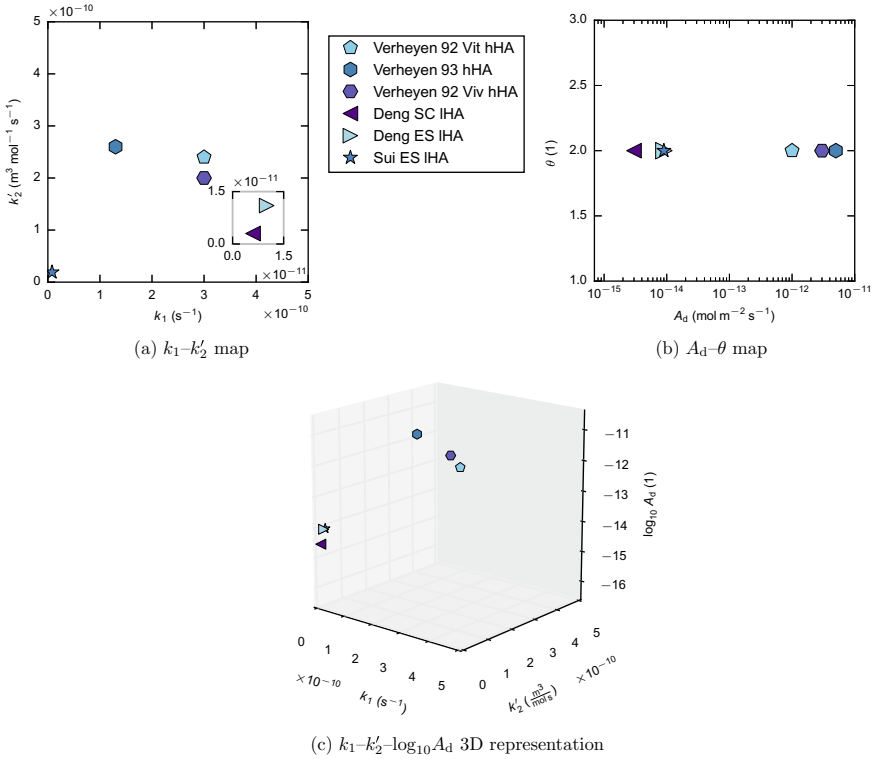

(a) k_1–k_2' map

(b) A_d–θ map

(c) k_1–k_2'–$\log_{10}A_d$ 3D representation

Fig. 5.2 Results output by the HA composites degradation model for data with a poly(L-lactide) matrix: case studies from the Leiden University group and the Beijing University group. k_1 is the non-catalytic polymer degradation rate, k_2' is the autocatalytic polymer degradation rate, A_d is the ceramic dissolution rate and θ is the power ceramic dissolution law exponent. The hydroxyapatite type used in each case study is indicated in the legend by the abbreviation found at the end of the case study code. The meaning of the abbreviations can be found in Table 5.2. Grey inset plots correspond to zoomed-up regions included to avoid amalgamation of results around the origin

Figure 5.3 presents the results corresponding to the remaining poly(L-lactide)-hydroxyapatite data. This group encompassed work from Huang et al. [2], Wang et al. [3], Zhou et al. [4], Díaz et al. [7] and Xu et al. [14]. Figure 5.3a exhibits the polymer degradation map; Fig. 5.3b the ceramic degradation map and Fig. 5.3c the 3D plot in the k_1–k_2'–A_d degradation space.

Results belonging to the remaining group data showed a broad spread in both polymer and ceramic degradation constants, without the presence of clusters, as opposed to the previously poly(L-lactide)-hydroxyapatite shown data. Appendix B.2.1 contains the above-mentioned HA-PLLA results in a tabular format. Additionally, it includes several composite characteristics for each analysed case study, necessary for discussion Sect. 5.5.

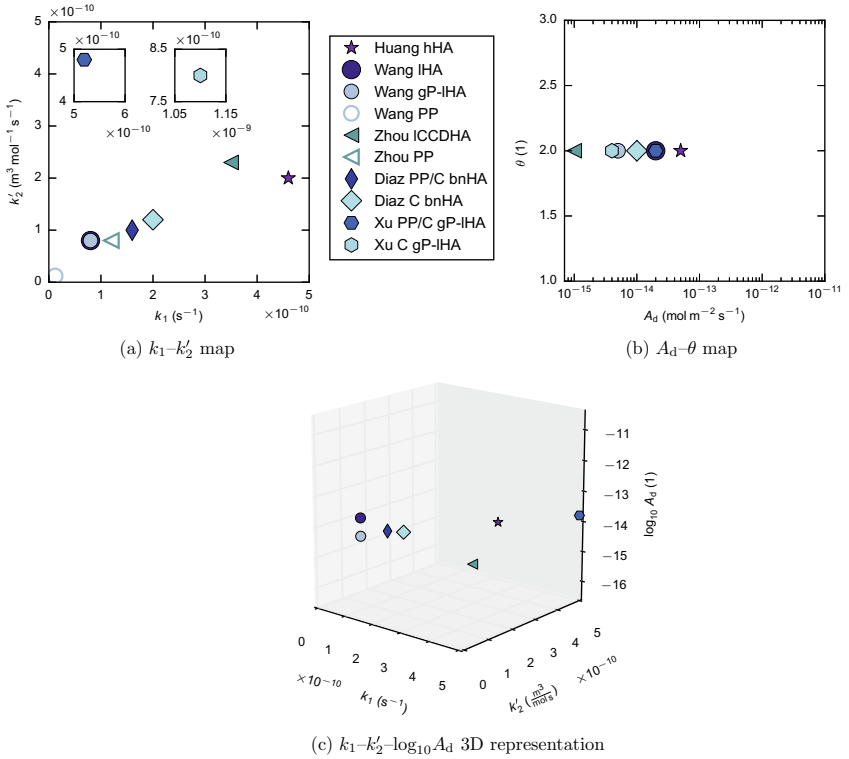

(a) k_1–k_2' map

(b) A_d–θ map

(c) k_1–k_2'–$\log_{10}A_d$ 3D representation

Fig. 5.3 Results output by the HA composites degradation model for data with a poly(L-lactide) matrix: remaining case studies data. k_1 is the non-catalytic polymer degradation rate, k_2' is the autocatalytic polymer degradation rate, A_d is the ceramic dissolution rate and θ is the power ceramic dissolution law exponent. The hydroxyapatite type used in each case study is indicated in the legend by the abbreviation found at the end of the case study code. The meaning of the abbreviations can be found in Table 5.2. Black inset plots correspond to regions situated outside the limits defined in the main plot

5.4.2 Poly(D,L-lactide) Matrix

The results from the HA composites degradation model for composites with poly(D,L-lactide) matrix are presented separated in two different sets. In the first place, data from the Southwest Jiaotong University group and in the second place, a set containing data from Suranaree University and the remaining data. Figure 5.4 exhibits the model output for data belonging to the Southwest Jiaotong University group using a polymer degradation map (Fig. 5.4a), a ceramic degradation map (Fig. 5.4b) and a 3-dimensional plot (Fig. 5.4c). This group comprised data from Zou et al. [18, 19].

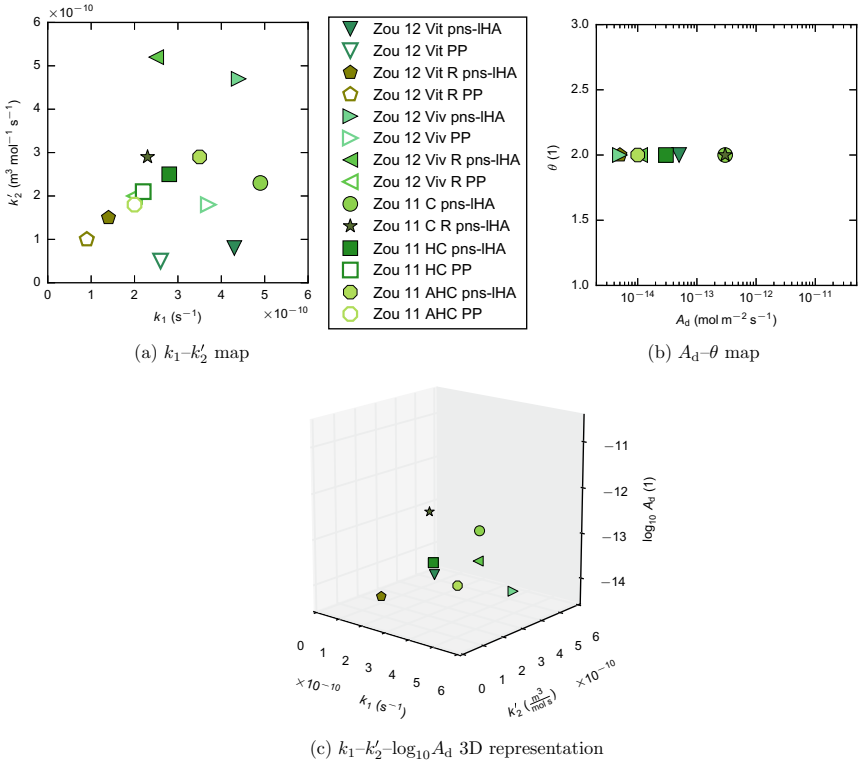

(a) k_1–k_2' map

(b) A_d–θ map

(c) k_1–k_2'–$\log_{10}A_d$ 3D representation

Fig. 5.4 Results output by the HA composites degradation model for data with a poly(D,L-lactide) matrix: case studies from the Southwest Jiaotong University group. k_1 is the non-catalytic polymer degradation rate, k_2' is the autocatalytic polymer degradation rate, A_d is the ceramic dissolution rate and θ is the power ceramic dissolution law exponent. The hydroxyapatite type used in each case study is indicated in the legend by the abbreviation found at the end of the case study code. The meaning of the abbreviations can be found in Table 5.2

The spread in both polymer and ceramic degradation constants of the results reported in Fig. 5.4 was quite significant despite the shared authorship of all the shown case studies.

Figure 5.5 combines data from the Suranaree University group and the remaining PDLLA-HA data. This set of results encompasses data authored by Rakmae et al. [15, 16], which formed the Suranaree University group and data authored by Van der Meer et al. [17] and Hasegawa et al. [20], which formed the remaining data group. The map of polymer degradation constants is presented in Fig. 5.5a, the map of ceramic degradation constants in Fig. 5.5b and the 3D k_1–k_2'–A_d plot in Fig. 5.5c.

The results showed clustering in both the k_1–k_2' and the A_d–θ maps although with dissimilar behaviour. The polymer degradation map presented one big cluster encompassing all case studies but one, whereas the ceramic dissolution map portrayed three different clusters. Appendix B.2.2 contains the above-mentioned HA-PDLLA

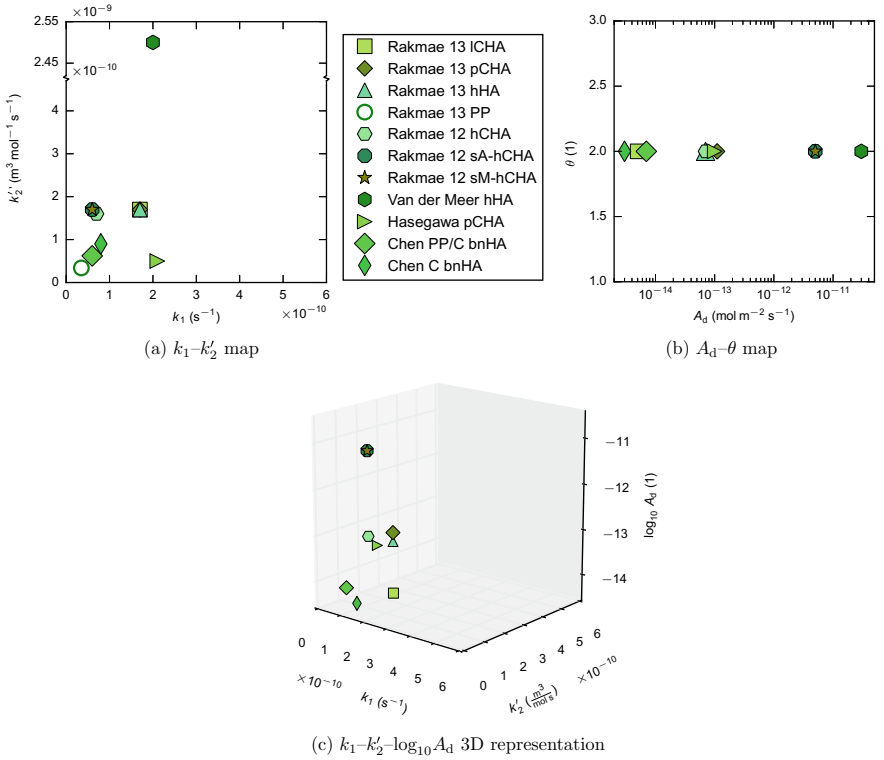

(a) k_1–k_2' map

(b) A_d–θ map

(c) k_1–k_2'–$\log_{10}A_d$ 3D representation

Fig. 5.5 Results output by the HA composites degradation model for data with a poly(D,L-lactide) matrix: case studies from Suranaree University group and remaining case studies data. k_1 is the non-catalytic polymer degradation rate, k_2' is the autocatalytic polymer degradation rate, A_d is the ceramic dissolution rate and θ is the power ceramic dissolution law exponent. The hydroxyapatite type used in each case study is indicated in the legend by the abbreviation found at the end of the case study code. The meaning of the abbreviations can be found in Table 5.2

results in a tabular format. Additionally, it includes several composite characteristics for each analysed case study, necessary for discussion Sect. 5.5.

5.4.3 *Poly-lactide-co-glycolide Matrix*

The results from the HA composites degradation model for composites with poly(lactide-co-glycolide) matrix are reported split into two different sets. Firstly, data from the CCMM group and secondly, the remaining data. Figure 5.6 visually exhibits the results for poly(D,L-lactide-co-glycolide)-hydroxyapatite composites belonging to the CCMM group, which combined data from Naik et al. [29–31] and Ege et al. [32, 33]. The polymer analysis is presented in Fig. 5.6a, followed by the ceramic analysis in Fig. 5.6b and the combined polymer-ceramic analysis in Fig. 5.6c.

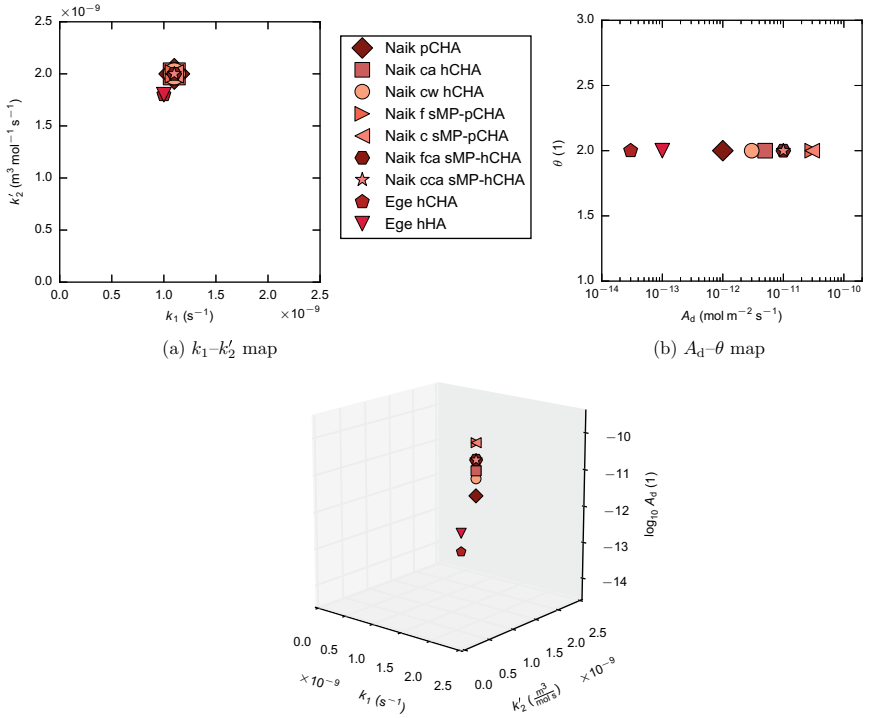

(a) k_1–k_2' map

(b) A_d–θ map

(c) k_1–k_2'–$\log_{10} A_d$ 3D representation

Fig. 5.6 Results output by the HA composites degradation model for data with a poly(lactide-co-glycolide) matrix: case studies from the CCMM group. k_1 is the non-catalytic polymer degradation rate, k_2' is the autocatalytic polymer degradation rate, A_d is the ceramic dissolution rate and θ is the power ceramic dissolution law exponent. The hydroxyapatite type used in each case study is indicated in the legend by the abbreviation found at the end of the case study code. The meaning of the abbreviations can be found in Table 5.2

The CCMM group data results showed significant clustering in the polymer degradation map as the data contained only two pure polymer occurrences, i.e. all the Naik or Ege case studies share the same pure polymer data. There was a higher spread in the ceramic degradation map.

Figure 5.7 introduces the visual representation of the remaining results for the PLGA-HA composites analysis. This set contained data from Tsunoda [25], Li and Chang [26], Díaz et al. [27], Agrawal and Athanasiou [28], Lee et al. [34], Liuyun et al. [35] and Ban et al. [36]. Figure 5.7a contains the k_1–k_2' map, Fig. 5.7b the A_d–θ map and lastly, Fig. 5.7c the representation of the k_1–k_2'–A_d degradation space.

The polymer degradation constants of the remaining PLGA-HA composites data showed clustering for a majority of the analysed case studies, with the rest showing much higher degradation rates. The ceramic degradation constants results expanded across a much wider region with the data almost evenly distributed throughout the A_d interval (10^{-14}, 10^{-11}). Appendix B.2.3 contains the above-mentioned HA-PLGA

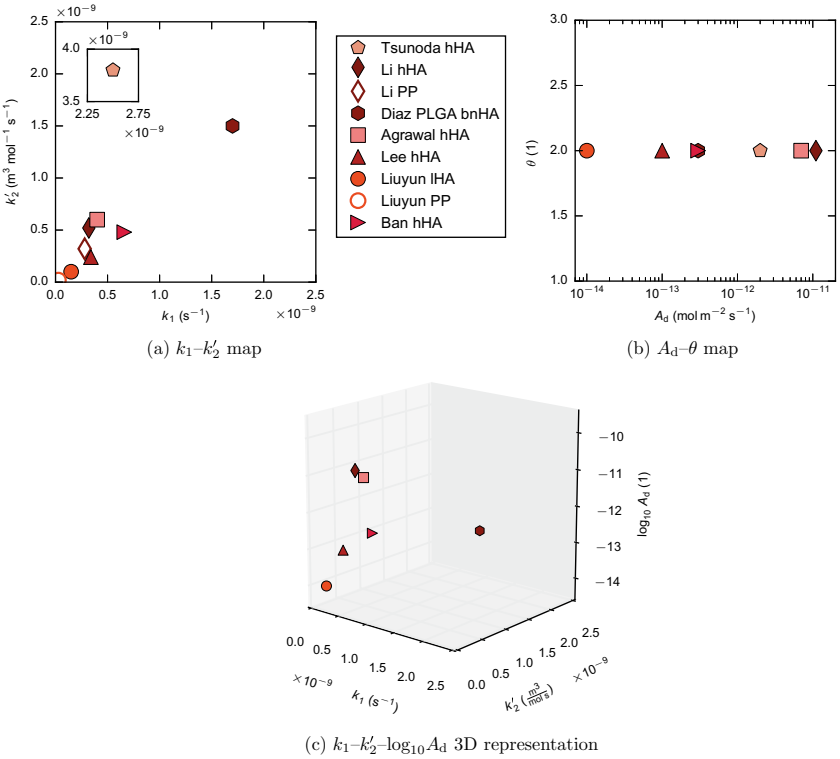

(a) k_1–k_2' map

(b) A_d–θ map

(c) k_1–k_2'–$\log_{10}A_d$ 3D representation

Fig. 5.7 Results output by the HA composites degradation model for data with a poly(lactide-co-glycolide) matrix: remaining case studies data. k_1 is the non-catalytic polymer degradation rate, k_2' is the autocatalytic polymer degradation rate, A_d is the ceramic dissolution rate and θ is the power ceramic dissolution law exponent. The hydroxyapatite type used in each case study is indicated in the legend by the abbreviation found at the end of the case study code. The meaning of the abbreviations can be found in Table 5.2. Black inset plots correspond to regions situated outside the limits defined in the main plot

results in a tabular format. Additionally, it includes several composite characteristics for each analysed case study, necessary for discussion Sect. 5.5.

5.4.4 Miscellaneous Polymers Matrixes

Figure 5.8 displays the visual representation of the results for the hydroxyapatite composites with miscellaneous polymers as matrix. Figure 5.8a shows the polymer degradation map, Fig. 5.8b the ceramic degradation map and Fig. 5.8c the 3D degradation space plot. The miscellaneous polymers data set encompassed data from

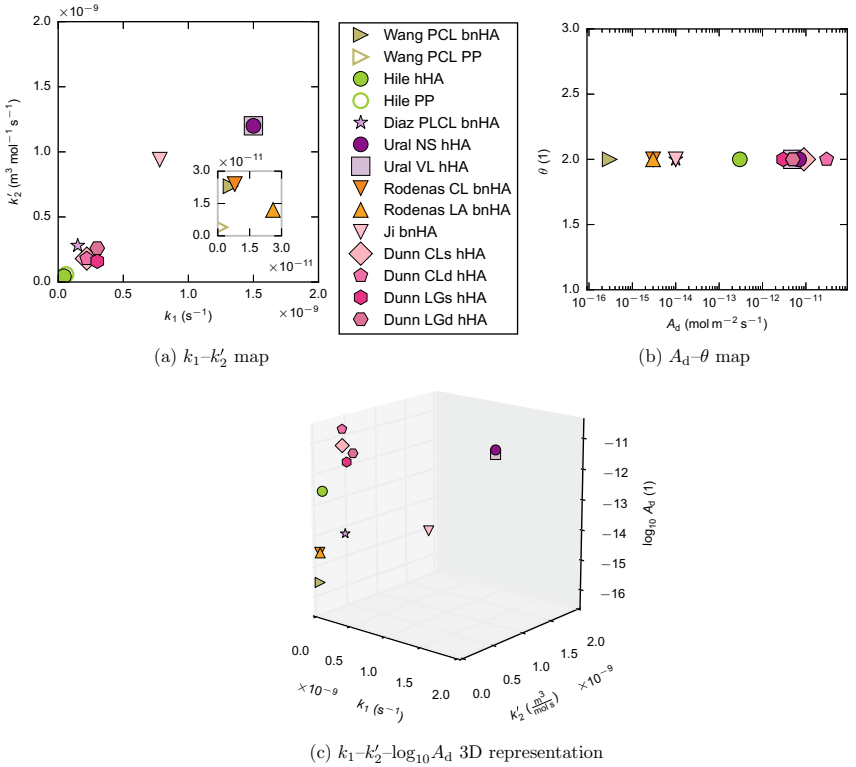

(a) k_1–k_2' map

(b) A_d–θ map

(c) k_1–k_2'–$\log_{10}A_d$ 3D representation

Fig. 5.8 Results output by the HA composites degradation model for data with a miscellaneous polymer matrix. k_1 is the non-catalytic polymer degradation rate, k_2' is the autocatalytic polymer degradation rate, A_d is the ceramic dissolution rate and θ is the power ceramic dissolution law exponent. The hydroxyapatite type used in each case study is indicated in the legend by the abbreviation found at the end of the case study code. The meaning of the abbreviations can be found in Table 5.2. Grey inset plots correspond to zoomed-up regions included to avoid amalgamation of results around the origin

Wang et al. (▶, ▷) [1] with a poly(ε-caprolactone) matrix, data from Hile et al. (●, ○) [22] with a poly(L-co-D,L-lactide) matrix, data from Díaz and Puerto (★) [23] and Ural et al. (●, □) [24] with a poly(lactide-co-ε-caprolactone) matrix, data from Rodenas-Rochina et al. (▼, ▲) [37] with a matrix made of a blend of poly(L-lactide) and poly(ε-caprolactone) and lastly data from Ji et al. (▽) [38] and Dunn et al. (◇, ⬟, ⬢, ⬣) [39] with a poly(lactide-co-glycolide)-poly(ε-caprolactone) blend as matrix.

The results showed some clustering in both polymer and ceramic degradation constants, specially for case studies sharing common authorship like Dunn CLs hHA, CLd hHA, LGs hHA, LGd hHA and Ural NS hHA, VL hHA. Appendix B.2.4 contains the above-mentioned HA-misc. Polymers results in a tabular format. Additionally, it includes several composite characteristics for each case, necessary for Sect. 5.5.

5.5 Discussion of the Modelling Results for Hydroxyapatite Composites Degradation Data

This section presents the analysis and discussion of the results reported in Sect. 5.4. Firstly, an overview of all modelling results in addition to an initial analysis are introduced. The initial analysis is followed by a series of in-depth analyses exploring hydroxyapatite dissolution as well as the effect of hydroxyapatite addition, sample structure and degradation protocol on composite degradation behaviour. Finally, a summary of the main features of hydroxyapatite composites degradation found during the analyses is presented. The discussion in this section builds on the ideas outlined in Sect. 4.6.1 on the ideal model usage.

5.5.1 Modelling Results Overview and Initial Discussion

Figure 5.9 includes a compilation of all the hydroxyapatite biocomposites modelling results collated in a single set of graphs: a polymer map, a ceramic map and a $\log_{10}k_1$–$\log_{10}k'_2$–$\log_{10}A_d$ 3D plot. Although the graph legends used in Sect. 5.4 also apply to this visual representation, they have been omitted for clarity. In lieu of those legends and to facilitate the analysis, coloured regions enclosing a majority of the results for cases with poly(L-lactide) (PLLA), poly(D,L-lactide) (PDLLA) and poly(lactide-co-glycolide) (PLGA) matrixes have been included in both the polymer map and 3D plot.

The global polymer degradation map for hydroxyapatite biocomposites, containing the non-catalytic polymer degradation rate k_1 and the autocatalytic polymer degradation rate k'_2 for each analysed case study, is shown in Fig. 5.9a. The three main groups of polymeric matrixes, namely poly(L-lactide), poly(D,L-lactide) and poly-(lactide-co-glycolide), are presented as coloured ellipses enclosing the majority of the corresponding data. In general terms, although there was a significant overlap among the different regions, polymer degradation rates could be ordered from low to high as follows: PLLA < PDLLA < PLGA. This order in polymer degradation rates matched the typical behaviour for polymeric scaffolds, as previously reported by Neuendorf et al. [49] and Middleton and Tipton [50].

The polymer degradation map also shows a clear correlation between the values of the non-catalytic and autocatalytic polymer degradation rates, k_1 and k'_2 respectively, as a significant majority of the analysed hydroxyapatite cases lie in the region surrounding the map diagonal. This behaviour points to a coexistence of both types of polymer degradation in all the analysed cases. The use of logarithmic axes in this visual representation makes less apparent that some particular cases showed a marked non-catalytic behaviour, such as Furukawa Med pCHA (▲) [9] or Zou 12 Vit pns-lHA (▼) [18] both with $k_1/k'_2 \geq 4$, while others showed a marked autocatalytic behaviour, such as Van der Meer hHA (⬢) [17], Wang PCL bnHA (▶) [1] or Rodenas CL bnHA (▼) [37], all of them with $k_1/k'_2 \leq 0.33$.

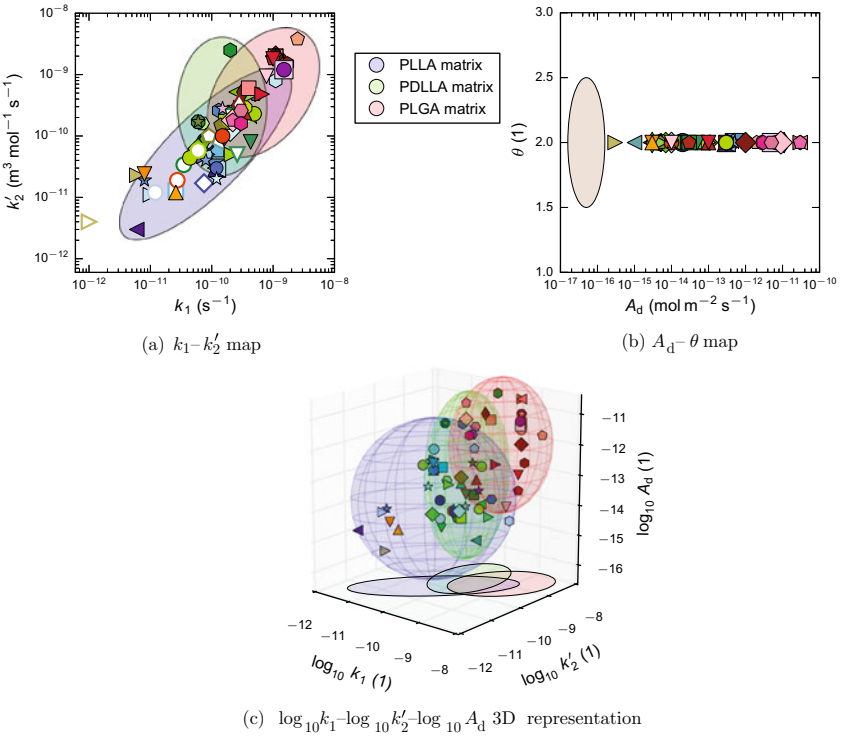

(a) k_1–k_2' map

(b) A_d–θ map

(c) $\log_{10}k_1$–$\log_{10}k_2'$–$\log_{10}A_d$ 3D representation

Fig. 5.9 Global degradation maps containing results output by the HA composites degradation model for all the analysed case studies. k_1 is the non-catalytic polymer degradation rate, k_2' is the autocatalytic polymer degradation rate, A_d is the ceramic dissolution rate and θ is the power ceramic dissolution law exponent. Coloured ellipses, for the k_1–k_2' map, or ellipsoids, for the $\log_{10}k_1$–$\log_{10}k_2'$–$\log_{10}A_d$ plot, enclose the majority of the case studies for usual polymeric matrixes. The beige coloured region in the A_d–θ map represents experimental dissolution data for highly crystalline pure hydroxyapatite at 37 °C and different initial pH ranging from 3.0 to 7.4 in free drift experiments measured by Nair [48]

This k_1–k_2' map showed a significant spread for both k_1 (s^{-1}), the non-catalytic degradation rate and k_2' (m^3 mol^{-1} s^{-1}), the autocatalytic polymer degradation rate, with values spanning nearly four orders of magnitude, from 10^{-12} to 10^{-8}, for both polymer degradation constants. This variability translated into a vast difference in degradation rate and mechanical performance over time for different composites. At the low end, for example, the Wang PCL bnHA case study (▶) [1], a biocomposite made of poly(ε-caprolactone) and commercially available nano-sized hydroxyapatite, experienced a reduction in M_w of merely 2% in a time period of six months. Similarly, the Deng SC lHA case study (◀) [12], with poly(L-lactide) and low crystallinity hydroxyapatite, showed little mass loss after having been degraded for up to eight weeks despite having a porous structure. These two cases represented biocomposites with the ability to maintain their integrity for long periods of time, probably, up to several years.

Conversely, the Van der Meer hHA case (⬢) [17], with a poly(D,L-lactide) matrix and highly crystalline pure hydroxyapatite as a filler, comprised composite samples which reached a mass loss of over 60% in less than ten days. The Tsunoda hHA case (⬟) [25], with poly(D,L-lactide-co-glycolide)(50:50) and pure hydroxyapatite, behaved similarly, reporting a mass loss of over 50% in six weeks for the composite sample with lower ceramic content. These cases, at the high end of the polymer degradation map, represented biocomposites that could be completely reabsorbed in just a few weeks.

The ceramic degradation map, including dissolution rate A_d (mol m^{-2} s^{-1}) and power dissolution law exponent θ (1) for all modelling results, is shown in Fig. 5.9b. As observed in the TCP composites analysis (Sect. 4.6.2), power dissolution law exponent θ had the same value for all the different types of hydroxyapatite found in literature. This fact pointed once again to insensitivity of the simulated degradation profiles with respect to θ. On the other hand, dissolution rate A_d presented significant variation, spanning nearly six order of magnitude (from 10^{-16} to over 10^{-11}), indicating a high sensitivity of the simulation degradation profiles with respect to A_d. The marker colours used in this visual representation, as previously mentioned, convey information solely about the case studies polymeric matrixes. Experimental dissolution data for pure hydroxyapatite with high crystallinity at 37 °C and different initial pH ranging from 3.0 to 7.4 measured in free drift experiments by Nair [48] fell in the A_d–θ space region enclosed by the beige blob. An initial inspection showed both no obvious direct correlation between polymeric matrix and ceramic dissolution behaviour, and higher A_d values than reported for pure hydroxyapatite in free drift conditions [48]. As polymer matrix did not seem to be a critical factor and there was no overlap between the reported results and the available dissolution data, a deeper analysis using all the available information about the different types of hydroxyapatite employed was deemed necessary. This analysis, with its own different visual representations is included later in this chapter in Sect. 5.5.2.

The 3D degradation space plot for hydroxyapatite biocomposites is shown in Fig. 5.9c. Translucent ellipsoids, encompassing a majority of the results obtained by the HA composites degradation model, have been included for case studies with poly(L-lactide) (PLLA), poly(D,L-lactide) (PDLLA) and poly(lactide-co-glycolide) matrixes. In a similar fashion to the polymer degradation map there was a significant overlap between the three ellipsoids. The region delimited by both k_1 (s^{-1}) and k_2' (m^3 mol^{-1} s^{-1}) in the interval (10^{-10}, 10^{-9}) and A_d (mol m^{-2} s^{-1}) in (10^{-14}, 10^{-13}) seemed to contain a particularly high concentration of cases.

Origin of the Spread in Composite Degradation Constants

The three general degradation maps showed a significant variability or spread in the reported composite degradation constants for the analysed case studies. On the proviso that the modelling framework has fully captured composite degradation behaviour, all case studies sharing the same polymeric matrix-ceramic filler combination should have exactly the same values for k_1, k_2', A_d and θ. As this is clearly not the case it is worth analysing the origin of this variability.

This variability can be traced back to two different sources. A first source, expected due to the complexity of composite degradation phenomena and the plethora of interwoven parameters which play a role in it, arises from the fact that there are a number of factors which have not been explicitly included in the modelling framework but do affect composite degradation. For example, two a-priori similar case studies with a poly(L-lactide) matrix and pure hydroxyapatite as a filler might show significantly different degradation behaviour due to differences in sample structure and morphology, degradation protocol, polymer properties such as polymer crystallinity, block structure and ceramic properties such as ceramic crystallinity, purity, etc., i.e. factors defined within the experimental parameters.

An example of this variability can be found in the results from composites with a poly(L-lactide) matrix presented in Sect. 5.4.1 (Figs. 5.1, 5.2 and 5.3). Data from the Takiron Co. group, as well as data from the Leiden University group and data from the Beijing University group presented clustering in both polymer and ceramic degradation constants but with different origin and size for the clusters. The fact that several case studies of the same group shared really similar values for k_1, k_2', A_d and θ pointed to a good representation of composite degradation phenomena in the model, whereas the differences in origin and sizes of the clusters pointed to differences in degradation behaviour for case studies belonging to different groups and presumably differences in polymeric matrix and ceramic filler rooted in different definitions of experimental parameters. This type of variability can not be avoided and is in fact used to deepen the understanding of composite degradation behaviour by carrying out different analyses of relevant parameters hidden under the label poly(L-lactide)-pure hydroxyapatite and not yet accounted for in the computational modelling framework.

A second source of variability, more troublesome in nature, was present in case studies which shared fabrication methods, degradation protocols, materials sources and authorship, with all of the above resulting in being almost identical a priori. Sometimes despite this similarity, these case studies show differences in composite degradation behaviour to an extent which can not be justified by inherent randomness in the experimental degradation studies suggesting factors undefined within the experimental parameters as culprits for this behaviour.

An example of this type of variability can be found in results from the Southwest Jiaotong University group, reported in Fig. 5.4 in Sect. 5.4.2, where most case studies shared a poly(D,L-lactide)(50:50) polymeric matrix and a mixture of partially crystalline and non-stoichiometric unsintered pure hydroxyapatite ceramic filler, both fabricated for each case study following the same protocols. Despite these similarities different case studies within the group showed significantly distinct behaviour. The cause of this variability usually remains unidentified, requiring further work to develop a thorough and full understanding of the phenomena involved in the degradation of these case studies. In the following section, the hydroxyapatite dissolution is characterised in detail.

5.5.2 Characterisation of Hydroxyapatite Dissolution

Calcium phosphates in general and hydroxyapatite in particular experience degradation by dissolution in an aqueous media [51]. Hydroxyapatite, considered a sparingly soluble ceramic, has a low solubility as indicated by its solubility product of $-\log_{10}(K_{sp}) = 117.2$ at 37 °C [46]. There are a variety of factors which affect hydroxyapatite dissolution such as crystallinity and lattice defects [52], porosity [53], environmental pH [54] and media composition [55].

The analysis of ceramic dissolution seems a good starting point in order to understand the influence of ceramic addition to a polymeric matrix, to form composite, on the degradation behaviour of those composites. The modelling framework presented in Chap. 3 employed two parameters, dissolution rate A_d (mol m^{-2} s^{-1}) and power dissolution law exponent θ (1), to characterise ceramic dissolution, as one of the phenomena occurring during composite degradation. The global HA ceramic map presented in Fig. 5.9b, as part of an initial analysis, showed the insensitivity of hydroxyapatite composite degradation behaviour to power dissolution law exponent θ and, contrarily, the strong influence of dissolution rate A_d. In addition, the initial analysis also pointed to a lack of correlation between HA dissolution rate and specific matrix polymer type. Considering this information, a series of analyses were carried out in order to deepen the understanding of hydroxyapatite dissolution within composite degradation and to elucidate the influence of different hydroxyapatite characteristics on the reported values of dissolution rate A_d.

A number of different types of hydroxyapatite were encountered during the degradation data harvesting. Those types differed in several characteristics such as chemistry, crystallinity and surface modification. As previously mentioned, these characteristics influence the ceramic solubility and it is therefore assumed that these fillers will present different behaviour. The expected behaviour is higher dissolution for the hydroxyapatite types with decreased crystallinity [52], increased number of impurities [53] and absence of surface modifications. Figure 5.10 exhibits the dissolution rate for all the HA analysed case studies according to their hydroxyapatite type. Hydroxyapatite type is indicated in the figure legend using abbreviations. A complete list containing full denominations and descriptions for all abbreviations is included in Table 5.2.

For silane modified highly crystalline carbonated hydroxyapatite all the types have been collated in one group (sm-hCHA) independently of the silane coupling agent employed. To facilitate the analysis, the different hydroxyapatite types have been split in two columns arranged in descending order of expected solubility. The first column contains different types of carbonated hydroxyapatite (CHAs), with these types coloured in shades of brown and with shade intensity proportional to the expected solubility. In a similar fashion, the second column contains different varieties of pure hydroxyapatite (HAs) in shades of grey following a similar intensity pattern. The spread in y-axis of the data has been used exclusively to improve visual analysis and carries no physical meaning. A golden stripe shows the dissolution rates measured by Nair [48] in free drift experiments at 37 °C and different initial pH

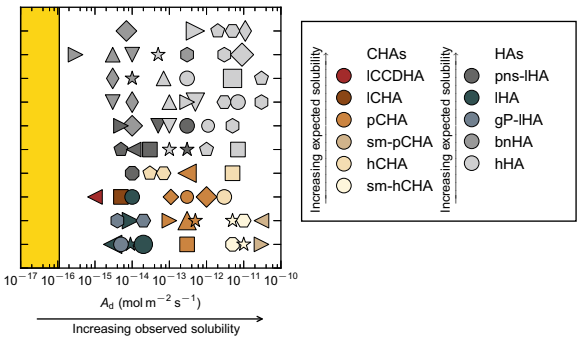

Fig. 5.10 Hydroxyapatite dissolution rate for all the analysed case studies: influence of hydroxyapatite type. A_d is the ceramic dissolution rate. The golden stripe corresponds to the range of dissolution rates measured by Nair in free drift experiments at 37 °C and different initial pH ranging from 3.0 to 7.4 for highly crystalline pure hydroxyapatite [48]

ranging from 3.0 to 7.4 for highly crystalline pure hydroxyapatite fabricated using a similar method to Ege et al. [26, 32].

This visual representation suggested the same two different phenomena seen in the TCP analysis. Firstly, the dissolution rate of the different hydroxyapatite types displayed a behaviour opposite of what was expected with darker shades on the left moving on to lighter shades as A_d increased implying larger values of dissolution rate for case studies with a higher crystallinity and purity. Secondly, none of the reported dissolution rates fell within the range measured by Nair in free drift experiments at 37 °C and initial physiological and lower pH values [48]. Dissolution rates for similar types of hydroxyapatite presented a value that exceeded this measured value by up to several orders of magnitude. This discrepancy was also observed by Yamamuro et al., who reported a much greater dissolution of hydroxyapatite when blended with poly(L-lactide) to form a composite than when immersed alone in distilled water at 37 °C with continuous stirring [56, 57], which would agree with the computational model output. To ascertain the cause of this behaviour both the influence of polymeric matrix and ceramic particle are considered.

Polymeric Matrix

The addition of a sparingly soluble ceramic to a polymeric matrix is expected to cause a buffering effect on composite degradation as explained in the overview of the model capabilities in Sect. 4.6.1. Figure 5.11 reports the hydroxyapatite dissolution rate, A_d, for all the analysed case studies indicating both the polymer matrix of the case and whether a buffering effect was shown in addition to the hydroxyapatite type. The polymer matrix is indicated by the edge colour of the markers. A black dot in the centre of the ceramic indicates that the case study presented a buffering effect, whereas a white dot indicates a non-buffering effect. No dot indicated that the comparison of composite sample with their pure polymer counterparts could not be assessed, primary due to the absence of pure polymer data.

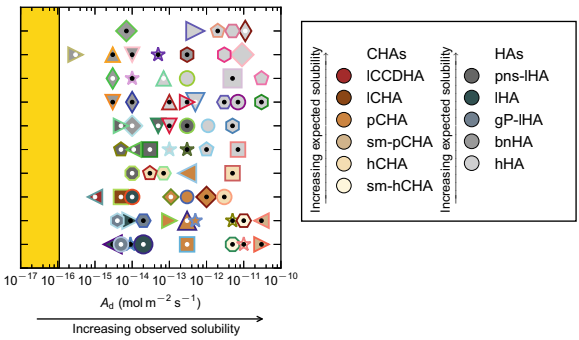

Fig. 5.11 Hydroxyapatite dissolution rate for all the analysed case studies indicating the hydroxyapatite types: presence of buffering effect and influence of polymeric matrix. A_d is the ceramic dissolution rate. The golden stripe corresponds to the range of dissolution rates measured by Nair in free drift experiments at 37 °C and different initial pH ranging from 3.0 to 7.4 for highly crystalline pure hydroxyapatite [48]. The edge colours of the markers indicate the polymeric matrix used in the case studies following the colour convention used in Sect. 5.4. Black dots represent case studies with a buffering effect, whereas white dots represent case studies with a non-buffering effect

No clear correlation between hydroxyapatite type and composite degradation behaviour, in terms of buffering capacity, became apparent. On the contrary, there were marked changes in buffering effect presence for different edge colours, pointing to a possible influence of polymeric matrix on the presence of buffering effect. This analysis is presented in Sect. 5.5.3.

Particle Size

The ceramic representative particle size is a critical parameter in composite characterisation and plays an important role in defining the representative unit cell as discussed in Sect. 3.3. Figure 5.12 exhibits the relationship between representative particle size an hydroxyapatite dissolution rate A_d for all the HA analysed case studies.

In line with the TCP analysis, there was a strong correlation between the representative particle size and the hydroxyapatite dissolution rate A_d, despite accounting for particle size in the hydroxyapatite dissolution characterisation, as reflected by A_d carrying units of mol s^{-2}. This particle effect in addition to the unexpectedly high values of HA dissolution rate obtained suggested again a series of critical differences between the reference free drift experiments [48], i.e. experimental measurements of the ions released by a ceramic immersed in a solution, and the reality during composite degradation.

In the first place, the environment surrounding the particles presents significant differences between the two states with a source of local acidity in composite degradation. The hydrogen ions released by the polymer molecules significantly lower the pH causing a dramatic increase in hydroxyapatite dissolution as reported by Yamamuro et al. [56, 57] accounting for the higher than expected dissolution rate values.

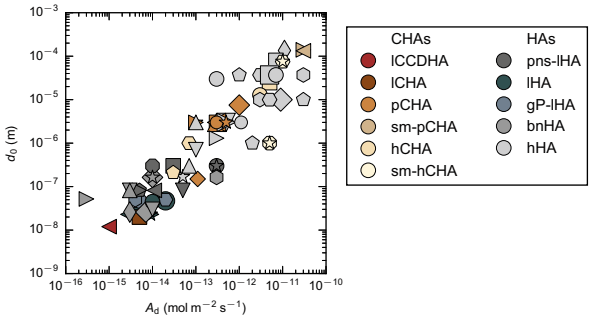

Fig. 5.12 Hydroxyapatite dissolution rate for all the analysed case studies indicating the hydroxyapatite types: effect of particle size. A_d is the ceramic dissolution rate. d_0 is the ceramic representative particle size of the undegraded composite sample

Although a dependency on polymer type of this phenomenon might be expected, it might not be too significant as all the studied polymers generated environments significantly different to those found in free drift experiments.

In the second place, while dissolution throughout free drift experiments barely influences the overall properties of the media due to the high buffer to dissolved ions ratio, the effect on the particle surroundings amid composite degradation is significant and closely interconnected with particle size as explained in Sect. 3.3, which would partially account for the strong particle size/hydroxyapatite dissolution rate correlation. In addition, this correlation could also suggest an overestimation of the surface area of small particles in composites resulting in unrealistic low values of A_d.

In summary, the analysis of the hydroxyapatite dissolution showed an unexpected behaviour with denser and purer ceramics with higher crystallinity showing higher dissolution rates than the less dense, impure, lower crystallinity ceramics and all of them showing higher values than those measured in free drift experiments at 37 °C and different initial pH ranging from 3.0 to 7.4 for highly crystalline pure hydroxyapatite [48]. The double discrepancy of this behaviour can be explained by the presence of a polymeric matrix acting as a source of acidity, the influence of ceramic particle size on the definition of the surrounding environment in composite samples and the possibility of an inaccurate size characterisation of the small particles within composites.

5.5.3 Effect of Hydroxyapatite Addition on Composite Degradation Behaviour

As explained in detail in Sect. 4.6.4, the analysis of the effect of ceramic addition requires the data to be classified as either showing a buffering effect or showing

a non-buffering effect, with the former being the expected behaviour, discussed in Sect. 4.6.1. During the different undertaken analyses comparison between two different set of polymer degradation rates k_1 and k_2', for example set A: (k_{1A}, k_{2A}') and set B: (k_{1B}, k_{2B}') were made. As explained in Sect. 4.6.4, A was deemed to have a lower polymer degradation rate if ($k_{1A} < k_{1B}$) and ($k_{2A}' < k_{2_B}'$) or the Euclidean distance in the k_1–k_2' plane, measured from the origin, is shorter for point A than for point B.

In order to evaluate the effect of ceramic addition on composite degradation, i.e. the presence or absence of buffering effect, only case studies containing both composite and pure polymer data have been considered. Full markers represent case studies showing a buffering effect, whereas hollow markers represent case studies showing a non-buffering. Markers shapes and colours have been taken from the results presented in Sect. 5.4 without modification. For non-buffered case studies, which had two (k_1, k_2') duplets, one for composite samples and another one for pure polymer

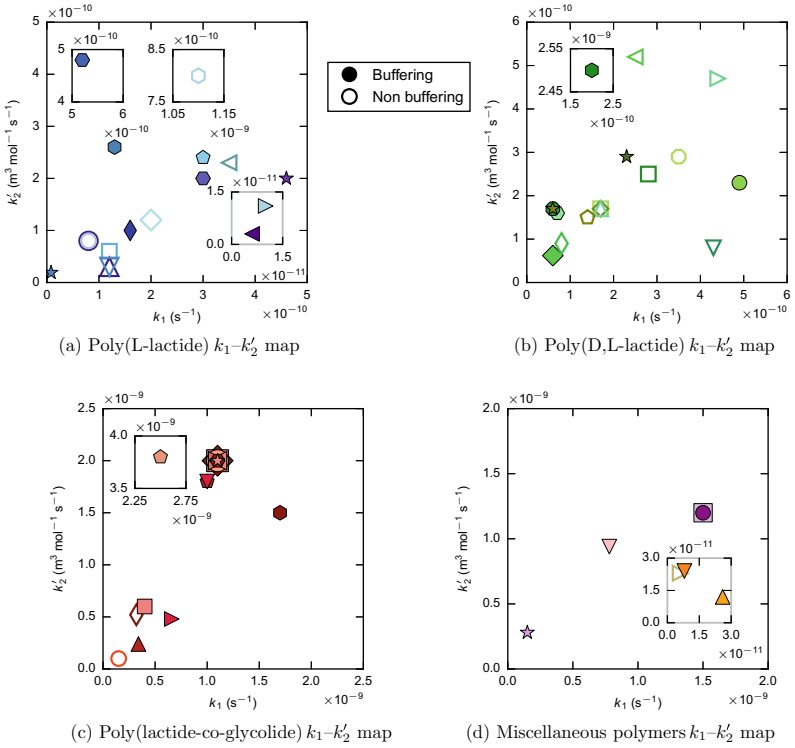

(a) Poly(L-lactide) k_1–k_2' map

(b) Poly(D,L-lactide) k_1–k_2' map

(c) Poly(lactide-co-glycolide) k_1–k_2' map

(d) Miscellaneous polymers k_1–k_2' map

Fig. 5.13 The effect of hydroxyapatite addition on composite degradation for all analysed case studies. k_1 is the non-catalytic polymer degradation rate and k_2' is the autocatalytic polymer degradation rate. Full markers represent case studies showing a buffering effect, whereas hollow markers represent case studies showing a non-buffering effect. Grey inset plots correspond to zoomed-up regions included to avoid amalgamation of results around the origin. Black inset plots correspond to regions situated outside the limits defined in the main plot

samples as explained in Sect. 4.6.1, only the composite duplet has been included in the k_1–k_2' map. Figure 5.13 shows the effect of ceramic addition on hydroxyapatite composites degradation for all the analysed case studies, grouped by polymeric matrix. Now, the inferences that can be made from the composites using this analysis are considered for each different polymer type.

Poly(L-lactide) Matrix

Figure 5.13a reports the effect of hydroxyapatite addition on composite degradation for composites with a poly(L-lactide) matrix. Table 5.4 includes the analysis of this effect reporting the degradation rate constants, k_1 and k_2' in addition to percentage and number of cases for the two possible categories. A slight majority of the 17 analysed poly(L-lactide)-hydroxyapatite cases showed a buffering effect, i.e. the expected behaviour. The polymer degradation constants, reported as geometric mean ✳ geometric standard deviation, were lower and presented a larger spread for buffering cases.

All the case studies from both the Leiden University group (Verheyen 92 Vit hHA (⬠), Verheyen 93 hHA (⬢) and Verheyen 92 Viv hHA (⬣)) [5, 6] and the Beijing University group (Deng SC lHA (◀), Deng ES lHA (▷) and Sui ES lHA (★)) [12, 13] presented both clustering of the polymer degradation rates and a buffering effect, pointing to a good capture of their behaviour by the model. The two clusters of polymer degradation rates showed a significant disparity in both size and origin. In addition, the two groups displayed also differences in the extent of the buffering effect with the Leiden University group case studies having a mild buffering effect and the Beijing University group case studies presenting a much stronger buffering effect. These two facts highlighted both the wide range of behaviours that could be achieved in composites made of poly(L-lactide) and hydroxyapatite and the ability of the model to characterise them.

The three case studies from the Leiden University group consisted of a pure polymer sample and two composite samples with different hydroxyapatite weight percentages (30% and 50%). Verheyen et al. reported, in all of them, that the extent of the buffering effect was directly proportional to the hydroxyapatite weight percentage when solely varying the ceramic-polymer ratio, i.e. that a greater buffering effect was seen in the composite sample having a higher hydroxyapatite weight percentage [5, 6], as captured by the model. In addition to this feature, the computational model

Table 5.4 Analysis of hydroxyapatite addition effect on composite degradation for case studies with a poly(L-lactide) matrix. k_1 is the non-catalytic polymer degradation rate and k_2' is the autocatalytic polymer degradation rate, with both reported as geometric mean ✳ geometric standard deviation

Buffering effect	k_1 (s^{-1})	k_2' ($m^3\ mol^{-1}\ s^{-1}$)	Percentage of cases (%)	Number of cases
Yes	$(8.4 \text{ ✳ } 6.3) \times 10^{-11}$	$(7.5 \text{ ✳ } 5.7) \times 10^{-11}$	53	9
No	$(1.7 \text{ ✳ } 2.4) \times 10^{-10}$	$(9.7 \text{ ✳ } 3.0) \times 10^{-11}$	47	8

was also able to handle the differences in initial molecular weight among the three Verheyen 93 hHA samples (100% PLLA, PLLA-30%hHA and PLLA-50%hHA).

Deng et al. showed, with two case studies: Deng ES lHA (▷) and Deng SC lHA (◁) that fabrication method affected overall degradation behaviour without modifying the effect of hydroxyapatite addition, i.e. the case studies showed different degradation profiles but in both situations a buffering effect was present in the composite samples [12].

As previously mentioned, in case studies with no buffering effect, values of degradation rate constants k_1 and k_2' shown by composite samples, instead of those shown by pure polymer samples, were employed in the degradation rate analysis. In these non-buffering cases, the k_1 and k_2' values of the composite samples were higher than their pure polymer counterparts. Poly(L-lactide) composites with buffering effect presented polymer degradation rates both significantly lower and higher that the non-buffering cases, with a significant majority of the non-buffering cases enclosed by the buffering case studies. This fact could point to the idea that hydroxyapatite addition revealed the true degradation rate of the polymeric matrix and that pure polymer samples presented an artificially slow degradation.

To ascertain the validity of this hypothesis a deeper analysis of the non-buffering case studies was necessary. Some of these cases belonged to Takiron Co. group [8–11]. This group of case studies were of particular interest for their homogeneity in experimental conditions and reproducibility in behaviour. Although only three of the nine case studies of this group contained pure polymer data, it was assumed that the remaining cases would also exhibit a non-buffering effect as the experimental degradation profiles of the composite samples seemed highly reproducible. Shikinami 99 pCHA [8], one of the two cases with pure polymer data, showed a clear lag time in experimental degradation data for the pure polymer sample as shown in Fig. 5.14. The curve showing molecular weight variation over time contained an initial plateau, lasting for 37 days, followed by a typical degradation profile. A shorter lag time was also reported for the composite sample with the lowest ceramic loading. On the contrary, immediate degradation was reported for the remaining composites of which, for clarity purposes, only the sample with 20%pCHA is included in Fig. 5.14. Furukawa Med pCHA [9] and Furukawa Med hHA [9] reported a similar duality in degradation behaviour with a lag time of 18 days present only for the pure polymer sample.

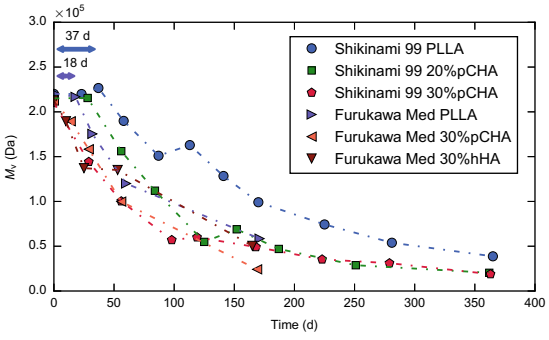

Fig. 5.14 Degradation data (M_v over time) from two case studies belonging to the Takiron Co. group [8, 9]. M_v is the viscosity average molecular weight. Data replotted from [8, 9]. Dash-dotted lines are shown for clarity only. Markers and colours are specific of this visual representation

This lag time in degradation could have been caused by a delay in water penetration due to a high density, a compact structure and a high polymer crystallinity arising from the customised forging process employed to make the samples. Although composite samples were made following the same protocol, ceramic-polymer interface could have served as a pathway for water diffusion resulting in a higher water penetration. As mentioned in Sect. 4.6.4, water diffusion could be a limiting factor in composite degradation for systems of these characteristics as hypothesised by Kobayashi and Yamaji [58].

Another interesting phenomenon in degradation behaviour for composites with poly(L-lactide) matrix was found in the data reported by Díaz et al. [7] and Xu et al. [14]. Although the types of experimental data provided (respectively, yield strength and weight loss), did not permit a unequivocally accurate analysis due to the difficulties of relating the provided data with the molecular weight, the experimental evidence pointed to a dual effect of hydroxyapatite addition on composite degradation rate. Low ceramic weight fractions caused a buffering effect as obtained in Diaz PP/C bnHA (♦) [7] and Xu PP/C gP-lHA (●) [14], whereas high ceramic weight fractions resulted in faster loss of molecular weight for composites as sample integrity was compromised with high proportion of filler as reported in Diaz C bnHA (◇) [7] and Xu C gP-lHA (○) [14].

In summary, the model was able to fully capture the behaviour of a slight majority of the PLLA case studies and pointed to water penetration and excessive hydroxyapatite addition as causes of the degradation behaviour displayed by the non-buffering PLLA cases.

Poly(D,L-lactide) Matrix

Figure 5.13b shows the outcome of adding hydroxyapatite in terms of degradation behaviour for cases with a poly(D,L-lactide) matrix with the analysis of these results reported in Table 5.5. Hydroxyapatite addition resulted in a non-buffering effect in a majority of the 17 case studies. Polymer degradation rate, measured as previously stated as distance in the k_1–k_2' plane from the origin to the point defined by the average (k_1, k_2') values, was higher for case studies with non-buffering effect, which could point to not only differences in water penetration but the presence of other phenomena.

Table 5.5 Analysis of hydroxyapatite addition effect on composite degradation for case studies with a poly(D,L-lactide) matrix. k_1 is the non-catalytic polymer degradation rate and k_2' is the autocatalytic polymer degradation rate, with both reported as geometric mean ⁎ geometric standard deviation

Buffering effect	k_1 (s^{-1})	k_2' ($m^3\ mol^{-1}\ s^{-1}$)	Percentage of cases (%)	Number of cases
Yes	$(1.2 \divideontimes 2.4) \times 10^{-10}$	$(2.4 \divideontimes 3.1) \times 10^{-10}$	41	7
No	$(2.2 \divideontimes 1.7) \times 10^{-10}$	$(2.0 \divideontimes 1.9) \times 10^{-10}$	59	10

Of the case studies which exhibited a buffering effect, Van der Meer hHA (⬢) [17] showed the one with the highest extent amongst all the analysed hydroxyapatite case studies.

An important number of the non-buffering case studies with poly(D,L-lactide) matrix belonged to Southwest Jiaotong University group [18, 19]. Case studies from this group were fabricated by means of electrospinning and therefore presented a highly porous structure. Only two cases out of eight, Zou 11 C pns-lHA (●) and Zou 11 C R pns-lHA (★), experienced a buffering effect with hydroxyapatite addition. The remaining cases (6/8) did not show a buffering effect and composite samples had an increase in molecular weight reduction rate, ranging from mild (Zou 12 Vit pns-lHA (▽), Zou 12 Vit R pns-lHA (⬠), Zou 11 HC pns-lHA (□) and Zou 11 AHC pns-lHA (○)) to severe (Zou 12 Viv pns-lHA (▷) and Zou 12 Viv R pns-lHA (◁)). An increase in molecular weight reduction rate was labelled mild when the time to reach half of the initial molecular weight (t_{50}) in composite samples was less than 30% shorter than in their pure polymer counterparts, and severe when the reduction in t_{50} varied between 50% and 70%.

Figure 5.15a reproduces the water uptake information available for cases whose code start with Zou 11 [19]. A common behaviour, in which both pure polymer and composite samples achieved a water uptake of 200% in less than two weeks, was shared across all these cases. Water uptake profiles showed a steep increase followed by a more moderate monotonous increase. Final water uptake values, ranging from 450% to more than 1300%, were higher for composite samples than for their pure polymer counterparts but high enough to consider water excess in both situations.

Zou et al. reported mass loss for a vast majority of their case studies [18, 19]. Figure 5.15b includes some of these data. A similar trend, in which pure polymer samples showed a maximum mass loss of 15% whereas composite samples reached mass loss values of (20. . .25)%, was shared across cases. This experimental evidence in addition to the presence of water excess pointed to compromised sample integrity as the main driver behind the increase in degradation rate with hydroxyapatite addition.

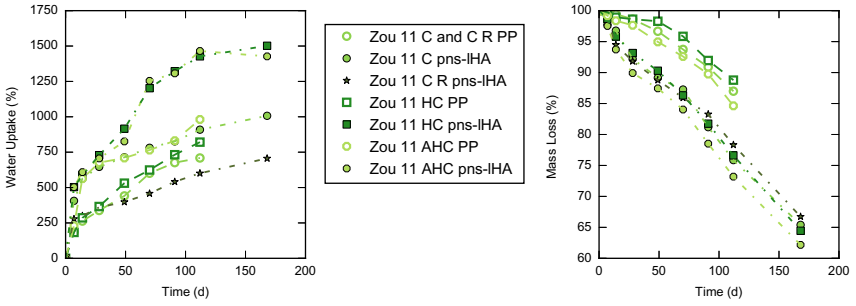

(a) Water uptake (b) Mass loss

Fig. 5.15 Degradation data (water uptake over time and mass loss over time) from Zou 11 case studies belonging to the Southwest Jiaotong University group [19]. Data replotted from [19]. Dashed and dash-dotted lines are shown for clarity only

The second relevant group of poly(D,L-lactide)-hydroxyapatite case studies, investigated by Rakmae et al. [15, 16], and referred to as Suranaree University group, showed an intriguing behaviour. The group was made up of six case studies, which could be split in two batches: Rakmae 13 and Rakmae 12. Rakmae 13, reported in [15], was formed by Rakmae 13 lCHA (□), Rakmae 13 pCHA (◇) and Rakmae 13 hHA (△). Rakmae 12, reported in [16], is formed by Rakmae 12 hCHA (⬡), Rakmae 12 sA-hCHA (●), Rakmae 12 sM-hCHA (★). Each batch shared pure polymer data, i.e. there were only two sets of pure polymer data in the group. Despite sharing the same degradation protocol and polymer source and similar fabrication method, sample structure and morphology, the two case studies batches showed opposite behaviour. Hydroxyapatite addition resulting in a non-buffering effect for Rakmae 13, whereas a buffering effect was reported for Rakmae 12.

Although composite samples showed a variety of behaviours, those variations can be accounted for by the differences in hydroxyapatite types employed in each case study. However, the differences in behaviour for pure polymer samples, ultimately responsible for the overall difference in hydroxyapatite addition effect, could not be explained without further research, as the common commercial origin of the polymer, in addition to similarities in fabrication method, degradation protocol, sample structure and morphology presumably excluded experimental variation as the source of the discrepancies in degradation behaviour.

The final insight from case studies with a poly(D,L-lactide) comes from Chen PP/C bnHA (◆) and Chen C bnHA (◊) authored by Chen et al. [21]. As with the poly(L-lactide)-hydroxyapatite studies by Díaz et al. [7] and Xu et al. [14], addition of a low weight percentage (20 wt %) of commercially available nano-hydroxyapatite caused a mild buffering effect, while addition of high weight percentages (40 wt % and 60 wt %) caused the opposite effect. Although differences in degradation behaviour between buffered and non-buffered samples, displayed as molecular weight versus time curves, were apparent, differences between samples with a common behaviour were much more subtle, probably due to the porous nature of the samples.

For the PDLLA case studies, the model captured the behaviour of a minority of the analysed cases, pointing to a variety of factors such as sample integrity, excessive hydroxyapatite addition and unusual pure polymer behaviour, as roots for the behaviour of the non-buffering PDLLA cases.

Poly(lactide-co-glycolide) Matrix

Figure 5.13c reports the effect of hydroxyapatite addition on composites with a poly(lactide-co-glycolide) matrix. Table 5.6 includes the analysis of these results. A significant majority of the 16 studied cases behaved as expected and showed a buffering effect with ceramic addition. Only two case studies, Li hHA (◊) [26] and Liuyun lHA (○) [35], exhibited a non-buffering effect.

The computed polymer degradation rates showed a marked distinction between case studies with and without buffering effect, with much lower values for the latter. This significant difference in degradation rate could suggest that at high degradation

Table 5.6 Analysis of hydroxyapatite addition effect on composite degradation for case studies with a poly(lactide-co-glycolide) matrix. k_1 is the non-catalytic polymer degradation rate and k_2' is the autocatalytic polymer degradation rate, with both reported as geometric mean ⁎ geometric standard deviation

Buffering effect	k_1 (s^{-1})	k_2' ($m^3\ mol^{-1}\ s^{-1}$)	Percentage of cases (%)	Number of cases
Yes	$(9.8 \divideontimes 1.7) \times 10^{-10}$	$(1.4 \divideontimes 2.1) \times 10^{-09}$	88	14
No	$(2.2 \divideontimes 1.7) \times 10^{-10}$	$(2.3 \divideontimes 3.2) \times 10^{-10}$	12	2

rates, the buffering effect played a more dominant role which overshadowed any other factor, whereas at low degradation rates limiting factors, such as water penetration, became more important. This coexistence of opposing factors affecting degradation would have negative implication in terms of degradation control and predictability as noted by Naik et al. [29].

Naik et al. and Ege et al. showed that the extent of the achieved buffering effect could be varied by adding different hydroxyapatite types as demonstrated by the pH over time degradation data included in Fig. 5.16. The variations in buffering effect

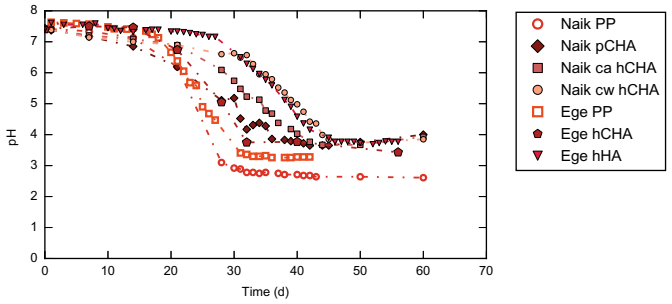

(a) Case studies with different calcining conditions

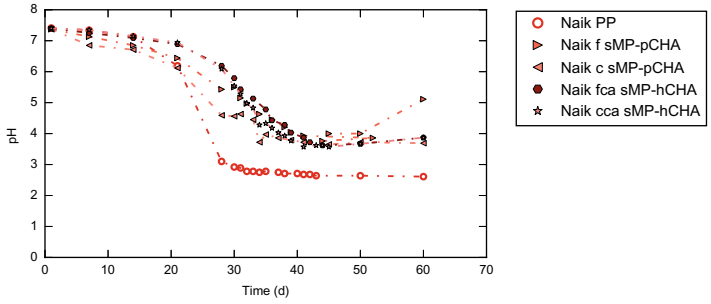

(b) Case studies with different silanisation treatment

Fig. 5.16 Degradation data (pH over time) from case studies belonging to the CCMM group data: influence of hydroxyapatite type on composite degradation. Data replotted from [29–33]. Dashed and dash-dotted lines are shown for clarity only

for case studies containing hydroxyapatite calcined in a variety of conditions can be seen in Fig. 5.16a which shows data from Naik pCHA (◆) [29, 30], Naik ca hCHA (■) [29, 30], Naik cw hCHA (●) [29, 30], Ege hCHA (⬟) [32, 33] and Ege hHA (▼). The calcining conditions for each case study can be found in Table B.7. The drop in pH, representative of the time needed by the sample to reach a critical degradation point, experienced a ample range of delays with hydroxyapatite addition. This delay ranged from a little more than 3 day for Ege hCHA (⬟), which contained pure hydroxyapatite calcined at 800 °C for 2 h in an air atmosphere, to 17 days for Naik cw hCHA (●), which contained pure hydroxyapatite calcined at 800 °C for 4 h in a wet argon atmosphere.

Naik et al. also demonstrated that the silanisation of hydroxyapatite did not have a large effect on the extent of the buffering effect as exhibited in Fig. 5.16b with degradation data from Naik f sMP-pCHA (▶) [30, 31], Naik c sMP-pCHA (◀) [30, 31], Naik fca sMP-hCA (⬣) [30, 31] and Naik cca sMP-hCHA (★) [30, 31] where the delays in pH drop were fairly similar for case studies sharing hydroxyapatite differing only in silanisation treatment such as Naik f sMP-pCHA (▶) and Naik c sMP-pCHA (◀) on one hand and Naik fca sMP-hCA (⬣) and Naik cca sMP-hCHA (★) on another.

For poly(lactide-co-glycolide)-hydroxyapatite case studies with no-buffering effect, potential explanations were found when considering all experimental data provided. Li and Chang reported, in addition to the Li hHA case study data, degradation data for composites made with two more different fillers, wollastonite and bioglass 45S5 [26]. Both the wollastonite and bioglass 45S5 composites showed a buffering effect. Achieving an opposite effect with hydroxyapatite addition could be explained by the fact that the reported solubility of both wollastonite and bioglass 45S5 was much higher than the solubility of the hydroxyapatite, pointing to a mismatch in polymer-ceramic selection regarding polymer degradation and ceramic dissolution timescales.

Regretfully, the composite degradation behaviour reported by Liuyun et al. (Liuyun lHA case study) [35] can not be accounted for in a definitive manner. Differences in differential scanning calorimetry between pure polymer and composite samples could point to a plausible underlying cause, with the development of crystalline regions within the polymer phase during degradation only in the composite sample but further research would be necessary to confirm it.

For the PLGA composites, the model fully reflected the degradation behaviour in almost all the analysed case studies and pointed to a more dominant effect of the buffering effect at high polymer degradation rates.

Miscellaneous Polymers Matrixes

The effect of hydroxyapatite addition on composite degradation for the remaining data, i.e. case studies with a miscellaneous polymer matrix, is included in Fig. 5.13c. The analysis of these results is presented in Table 5.7.

Table 5.7 Analysis of hydroxyapatite addition effect on composite degradation for case studies with a miscellaneous polymer matrix. k_1 is the non-catalytic polymer degradation rate and k_2' is the autocatalytic polymer degradation rate, with both reported as geometric mean ⁎ geometric standard deviation

Buffering effect	k_1 (s^{-1})	k_2' ($m^3\ mol^{-1}\ s^{-1}$)	Percentage of cases (%)	Number of cases
Yes	$(1.9 \divideontimes 9.2) \times 10^{-10}$	$(2.2 \divideontimes 7.9) \times 10^{-10}$	86	6
No	6.0×10^{-12}	2.3×10^{-11}	14	1

In a similar fashion to the poly(lactide-co-glycolide) cases, an important majority of the 7 cases experienced a buffering effect with hydroxyapatite addition. A non-buffering effect was reported only in one case, Wang PCL bnHA (▷) [1], which had a significantly low polymer degradation rate.

Ural et al. reported composite degradation data for two case studies: Ural NS hHA (●) [24] and Ural VL hHA (□) [24]. Both cases shared the same commercially available hydroxyapatite and had a similar polymeric matrix. The conditions of polymerisation for the poly(D,L-lactide-co-ε-caprolactone) employed as matrix in each case study differed in both atmosphere and time duration. Ural NS hHA matrix was polymerised in a N_2 atmosphere for 3 h while Ural VL hHA matrix was polymerised under vacuum for 19 h. Although the curves showing number average molecular weight (M_n) variation over time for both cases were, at a first glance, fairly distinct, the analysis with the computational model revealed that in reality both case studies were analogous as really similar sets of k_1, k_2', A_d and θ values represented accurately both cases, as shown in Fig. 5.17. Thus, the computational model showcased its ability to capture the similarities in degradation behaviour of both cases despite the mismatch in initial molecular weight, arising from the difference in polymerisation times.

A similar matrix, poly(L-lactide-co-ε-caprolactone)(70:30), was employed by Díaz and Puerto in Diaz PLCL bnHA (☆). The case study presented a fairly different behaviour highlighting the variety of behaviours that could result from changes in matrix, ceramic and scaffold properties. In a similar fashion, Rodenas-Rochina et al. demonstrated that by varying the ratio of polymers in a poly(L-lactide)-poly(εcaprolactone) blend, the degradation behaviour could be modified as seen in Rodenas CL bnHA (▽) [37] and Rodenas LA bnHA (△) [37].

The divergence from the expected behaviour showed by Wang PCL bnHA (▷) [1] could be explained by a combination of factors including proportional loss of mechanical integrity, as pointed by the presented mass loss data [1], and the low autocatalytic behaviour of poly(ε-caprolactone), as described by Lam et al. [59].

In summary, for case studies with a miscellaneous polymeric matrix, the model captured correctly the behaviour in almost all the analysed cases and pointed again to the prevalence of the buffering effect at high polymer degradation rates.

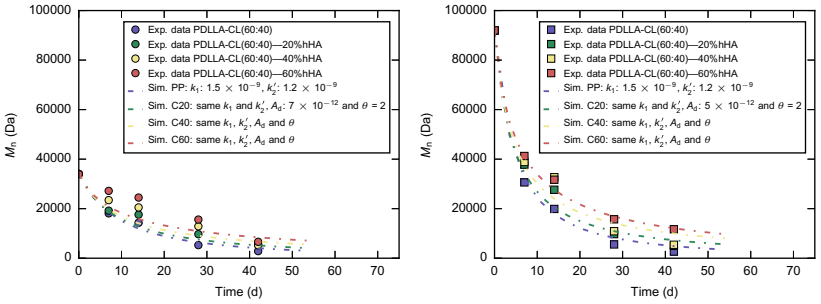

(a) Ural NS hHA case study (b) Ural VL hHA case study

Fig. 5.17 Degradation data (M_n over time) and HA composites degradation model results for case studies reported by Ural et al. [24]. M_n is the number average molecular weight. Experimental data replotted from [24]. Simulations carried out as part of this work. Marker colours are specific of this visual representation

All Polymer Matrixes

The global analysis, including all modelled case studies, is summarised in Table 5.8. A significant majority of the 57 analysed case studies presented a buffering effect and therefore showcased the expected behaviour. In addition, the buffering case studies had higher average polymer degradation rates than the non-buffering case studies. This fact could point to a greater dominance of the buffering effect with high polymer degradation rates.

Taking into account that the average k_1 and k_2' values of the pure polymer samples within the non-buffering cases would be even lower, as the polymer degradation constants of the composites were employed in this calculations, the lower average k_1 and k_2' suggested that at low polymer degradation rates the buffering effect could be overshadowed by other effects including water penetration.

Conclusions

The analysis presented in this section considered the effect of hydroxyapatite addition on composite degradation. The analysed case studies were classified into two categories: case studies showing a buffering effect and case studies showing a

Table 5.8 Analysis of hydroxyapatite addition effect on composite degradation for all the analysed case studies. k_1 is the non-catalytic polymer degradation rate and k_2' is the autocatalytic polymer degradation rate, with both reported as geometric mean ⁎ geometric standard deviation

Buffering effect	k_1 (s^{-1})	k_2' (m^3 mol^{-1} s^{-1})	Percentage of cases (%)	Number of cases
Yes	$(2.7 \divideontimes 5.4) \times 10^{-10}$	$(3.5 \divideontimes 6.0) \times 10^{-10}$	63	36
No	$(1.7 \divideontimes 2.7) \times 10^{-10}$	$(1.4 \divideontimes 2.7) \times 10^{-10}$	37	21

non-buffering effect, with the presence of a buffering effect being one of the main features derived from the composite degradation modelling framework.

36 of the 57 HA analysed case studies displayed a buffering effect, pointing towards the validity of the computational model, especially at high polymer degradation rates. A great variety of behaviours within these cases was noticed, highlighting the numerous available possibilities within the degradation space. The computational model emphasised the similarities in degradation behaviour for data coming from the same group as seen in the clustering displayed by those cases. The model also showed the ability to capture these degradation similarities even when they were hidden by different initial molecular weights.

For the 21 case studies with a non-buffering effect, the model was unable to fully characterise the behaviour but nevertheless, pointed into the right direction to identify a cause for the unexpected behaviour, being this cause usually related to an unmet model assumption such as water excess or mechanical integrity.

5.5.4 The Influence of Sample Porosity on Degradation Behaviour

Porosity, as a factor influencing the diffusional length $L_{H^+\text{–buffer}}$, is expected to affect the degradation behaviour of biocomposites as explained in Sect. 4.6.5. The influence of porosity for HA composites is included in Fig. 5.18 and the corresponding analysis in Table 5.9.

Poly(L-lactide) Matrix

The k_1–k_2' map shown in Fig. 5.18a contains information about the porosity-degradation relationship for hydroxyapatite composites with a poly(L-lactide) matrix. The corresponding analysis is presented in the first row of Table 5.9. A significant majority of the 27 analysed PLLA-HA cases had a dense structure. Unexpectedly, the polymer degradation constants k_1 and k_2' for the dense cases were lower than for the porous cases. Although a contribution towards this discrepancy could be explained with the inherent variations in polymer degradation rate due to the use of different poly(L-lactide) matrixes in terms of origin and fabrication method, including information about the buffering effect might improve the understanding of this behaviour.

Looking at the aforementioned buffering effect, discussed in Sect. 5.5.3, and sample porosity simultaneously it was found that dense case studies presented a percentage ratio of buffering/non buffering cases of 50:50, shifting to 31:69 if all Takiron Co. group cases were included assuming a similar behaviour to Shikinami 99 pCHA [8]. For porous structure case studies the buffering/non-buffering ratio was 60:40. The lower percentage ratio of buffering effect in dense cases could point to the overshadowing of porosity effect by other phenomena such as water penetration in addition

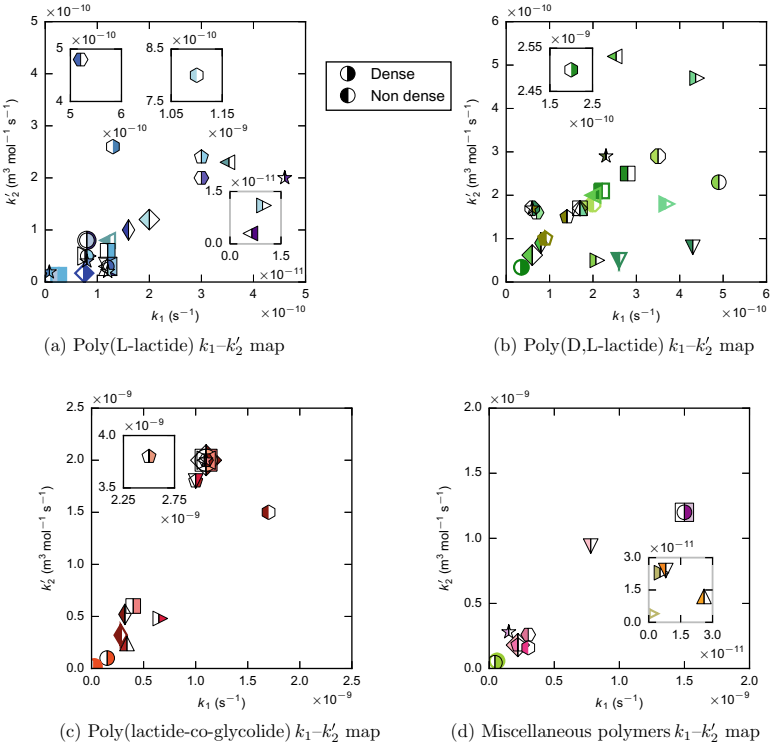

(a) Poly(L-lactide) k_1–k_2' map

(b) Poly(D,L-lactide) k_1–k_2' map

(c) Poly(lactide-co-glycolide) k_1–k_2' map

(d) Miscellaneous polymers k_1–k_2' map

Fig. 5.18 The influence of sample porosity on composite degradation for all the analysed hydroxyapatite case studies. k_1 is the non-catalytic polymer degradation rate and k_2' is the autocatalytic polymer degradation rate Right-hand side filled markers represent dense case studies, whereas left-hand side filled markers represent non dense case studies. Grey inset plots correspond to zoomed-up regions included to avoid amalgamation of results around the origin. Black inset plots correspond to regions situated outside the limits defined in the main plot

to the inherent differences in poly(L-lactide) degradation rate.

Poly(D,L-lactide) Matrix

For hydroxyapatite case studies with a poly(D,L-lactide) matrix, the polymer degradation map examining the influence of sample porosity can be found in Fig. 5.18b, whereas the analysis is included in the second row of Table 5.9. In this instance, a significant majority of the 25 cases had a porous structure. The polymer degradation rate for dense cases was again lower than for non-dense cases.

This result presented similarities with the poly(L-lactide) analysis, in the sense that the influence of sample porosity might be overshadowed by inherent variations of polymer degradation rate within the different poly(D,L-lactide) matrixes. These variations could be even higher in this matrix as the analysed case studies presented

Table 5.9 Analysis of the influence of sample porosity on composite degradation for all the analysed hydroxyapatite case studies. k_1 is the non-catalytic polymer degradation rate and k_2' is the autocatalytic polymer degradation rate, with both reported as geometric mean ⁎ geometric standard deviation

Case studies	k_1 (s^{-1})	k_2' ($m^3\ mol^{-1}\ s^{-1}$)	Percentage of cases (%)	Number of cases
Dense with poly(L-lactide) matrix	$(8.7 \divideontimes 2.8) \times 10^{-11}$	$(4.3 \divideontimes 3.2) \times 10^{-11}$	70	19
Non-dense with poly(L-lactide) matrix	$(1.3 \divideontimes 5.9) \times 10^{-10}$	$(1.1 \divideontimes 4.4) \times 10^{-10}$	30	8
Dense with poly(D,L-lactide) matrix	$(9.8 \divideontimes 1.9) \times 10^{-11}$	$(1.9 \divideontimes 3.2) \times 10^{-10}$	32	8
Non-dense with poly(D,L-lactide) matrix	$(2.2 \divideontimes 1.8) \times 10^{-10}$	$(1.6 \divideontimes 2.1) \times 10^{-10}$	68	17
Dense with poly(lactide-co-glycolide) matrix	$(6.9 \divideontimes 3.1) \times 10^{-10}$	$(9.9 \divideontimes 4.3) \times 10^{-10}$	78	14
Non-dense with poly(lactide-co-glycolide) matrix	$(4.8 \divideontimes 2.3) \times 10^{-10}$	$(4.9 \divideontimes 2.2) \times 10^{-10}$	22	4
Dense with miscellaneous polymers matrix	$(2.8 \divideontimes 7.0) \times 10^{-10}$	$(2.5 \divideontimes 6.2) \times 10^{-10}$	29	4
Non-dense with miscellaneous polymers matrix	$(6.0 \divideontimes 8.9) \times 10^{-11}$	$(7.9 \divideontimes 5.5) \times 10^{-11}$	71	10
All dense data	$(1.9 \divideontimes 4.1) \times 10^{-10}$	$(1.7 \divideontimes 6.4) \times 10^{-10}$	54	45
All non-dense data	$(1.5 \divideontimes 4.6) \times 10^{-10}$	$(1.4 \divideontimes 3.6) \times 10^{-10}$	46	39

different ratio of the two lactide enantiomeric forms, D and L, and no group with the same D-L ratio could be found in order to try and isolate the porosity effect.

Using the same approach employed with PLLA matrixes, the percentage ratio of buffering/non-buffering was 57:43 for dense case studies 30:70 for porous case studies. The higher polymer degradation rate in porous case studies in addition to the prevalence of a non-buffering effect could suggest the predominance of the effect of mechanical instability over porosity. Van der Meer hHA (◑) [17], which had both dense structure and buffering effect, presented the highest polymer degradation rate, in agreement with the expectations.

Poly(lactide-co-glycolide) Matrix

Figure 5.18c exhibits the influence of sample porosity on composite degradation for case studies with a poly(lactide-co-glycolide) matrix. The analysis of these results can be found in the third row of Table 5.9. A significant majority of the 18 cases had dense structure. For PLGA composites, the polymer degradation rate of the dense cases was higher than the non-dense cases in line with the expected behaviour. Of those with dense structure, the percentage ratio of buffering/non-buffering was 92:8, while the percentage ratio was 33:67 for porous case studies suggesting a largely true capture of the degradation behaviour by the initial hypothesis.

Miscellaneous Polymers Matrixes

For the remaining case studies, the relationship between sample porosity and composite degradation is presented in Fig. 5.18d with the corresponding analysis in the fourth row of Table 5.9. The distribution of structures in case studies with a miscellaneous polymer matrix is uneven, with a bit more than a quarter of 14 cases having dense structures and the remaining having a porous structure. Calculated polymer degradation rates values were significantly higher for dense case studies agreeing with the expectations. All dense case studies showed buffering effect, whereas one porous case showed a non-buffering effect with ceramic addition. Said case, Wang PCL bnHA (▷ and ▶) [1], had incidentally the lowest degradation rate.

All Polymeric Matrixes

A global analysis of porosity influence, including the 84 analysed hydroxyapatite case studies, is included in the fifth and final row of Table 5.9. The polymer degradation rates followed the expected behaviour with higher values for dense case studies albeit without a really notable difference. This fact might point to the validity of our initial hypothesis assuming that the data set considered is extensive enough to average out the variations associated with specific types of polymeric matrix.

Nevertheless, further experimental work is required to ascertain the complete validity of the initial hypothesis regarding the effect of sample structure on degradation behaviour, making use of a more complete and exhaustive set of composite degradation data.

Direct Comparison

Only one direct comparison between dense and porous structures was found in all the analysed case studies. The experimental degradation studies carried out by Deng et al. [12] compared the degradation behaviour of solvent-cast and electrospun composites: Deng SC lHA (◁, solvent-cast) and Deng ES lHA (▷, electrospun) shared exactly the same poly(L-lactide) matrix, nano-hydroxyapatite filler and morphology. In both cases the ceramic addition caused a buffering effect with a more prominent effect, i.e. greater difference between composite and pure polymer samples in the electrospun case Deng ES lHA. The solvent cast pure polymer sample degraded significantly

slower than electrospun pure polymer sample. Mass losses lesser than 11% were reported for all the samples.

This unexpected behaviour might suggest unaccounted phenomena related to water penetration, as water uptake was proportional to degradation rate when considering exclusively either pure polymer samples or composite samples and overall had low values, less than 12% for all the samples, suggesting water as the limiting factor for degradation. Different polymer crystallinity percentage arising from the fabrication differences could potentially explain the unusual water uptake profiles, with dense samples having higher water uptake than porous samples. All this information suggested that the difference in fabrication method not only affected the value of $L_{H^+\text{–buffer}}$ for both cases but also influenced other degradation relevant properties resulting in the unanticipated behaviour.

Conclusions

After completing the analysis of the influence of porosity on HA composites degradation behaviour, a complex picture emerged. Although the global analysis including all HA analysed case studies agreed with the initial hypothesis, pointing towards the validity of the characteristic diffusional length $L_{H^+\text{–buffer}}$, careful consideration is required as evidence pointing in the opposite direction was also found.

In summary, the poly(L-lactide) analysis, including the only direct comparison, and the poly(D,L-lactide) analysis showed an unforeseen behaviour, whereas the poly(lactide-co-glycolide) and miscellaneous polymers analyses in addition to the one considering all polymer matrixes simultaneously, revealed a behaviour compliant with the initial hypothesis. This coexistence of conflicting findings suggested that some factors, intrinsically linked to sample structure, such as water penetration or mechanical integrity, play an important role in degradation behaviour. Thus, these factors could partially or fully overshadow the porosity effect generating the encountered convoluted picture.

5.5.5 The Influence of In vitro Versus In vivo Protocols on Degradation Behaviour

The degradation protocol, being a major contributor to the environmental conditions of the samples during composite degradation, is predicted to have an effect on degradation behaviour as pointed in Sect. 4.6.6. The influence of in vitro versus in vivo degradation for all the analysed hydroxyapatite case studies is included in Fig. 5.19 with the corresponding analysis in Table 5.10.

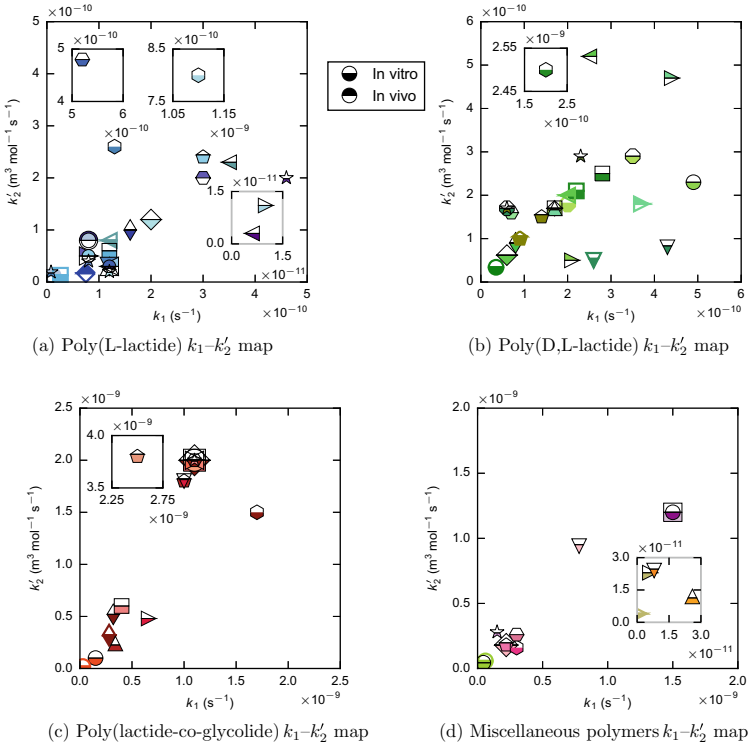

(a) Poly(L-lactide) k_1–k_2' map

(b) Poly(D,L-lactide) k_1–k_2' map

(c) Poly(lactide-co-glycolide) k_1–k_2' map

(d) Miscellaneous polymers k_1–k_2' map

Fig. 5.19 The influence of in vitro versus in vivo protocols on composite degradation for all the analysed hydroxyapatite case studies. k_1 is the non-catalytic polymer degradation rate and k_2' is the autocatalytic polymer degradation rate Bottom side filled markers represent in vitro case studies, whereas top side filled markers represent in vivo case studies. Grey inset plots correspond to zoomed-up regions included to avoid amalgamation of results around the origin. Black inset plots correspond to regions situated outside the limits defined in the main plot

Poly(L-lactide) Matrix

For hydroxyapatite composites with a poly(L-lactide) matrix the k_1–k_2' map, including information about degradation protocol, can be found in Fig. 5.19a. The analysis is presented in the first row of Table 5.10. Of the 27 analysed case studies, a majority reported in vitro degradation. These case studies exhibited higher polymer degradation rates k_1 and k_2', albeit with high variability, than the in vivo degradation cases.

Poly(D,L-lactide) Matrix

The polymer degradation map, exhibiting the influence of in vitro versus in vivo protocols, for the 25 case studies with a poly(D,L-lactide) matrix is shown in Fig. 5.19b with the corresponding analysis included in the second row of Table 5.10. Cases with in vivo degradation had higher polymer degradation rates than cases with in vitro degradation.

Table 5.10 Analysis of the influence of in vitro versus in vivo protocols on composite degradation for all the analysed hydroxyapatite case studies. k_1 is the non-catalytic polymer degradation rate and k_2' is the autocatalytic polymer degradation rate, with both reported as geometric mean ⁎ geometric standard deviation

Case studies	k_1 (s^{-1})	k_2' ($m^3\ mol^{-1}\ s^{-1}$)	Percentage of cases (%)	Number of cases
In vitro with poly(L-lactide) matrix	$(1.0 \divideontimes 4.7) \times 10^{-10}$	$(7.1 \divideontimes 4.7) \times 10^{-11}$	59	16
In vivo with poly(L-lactide) matrix	$(8.7 \divideontimes 2.2) \times 10^{-11}$	$(4.1 \divideontimes 2.2) \times 10^{-11}$	41	11
In vitro with poly(D,L-lactide) matrix	$(1.5 \divideontimes 2.1) \times 10^{-10}$	$(1.6 \divideontimes 2.4) \times 10^{-10}$	80	20
In vivo with poly(D,L-lactide) matrix	$(2.8 \divideontimes 1.4) \times 10^{-10}$	$(2.1 \divideontimes 2.6) \times 10^{-10}$	20	5
In vitro with poly(lactide-co-glycolide) matrix	$(6.3 \divideontimes 2.9) \times 10^{-10}$	$(8.5 \divideontimes 3.9) \times 10^{-10}$	100	18
In vitro with miscellaneous polymers matrix	$(9.3 \divideontimes 8.7) \times 10^{-11}$	$(1.1 \divideontimes 5.8) \times 10^{-10}$	100	14
All in vitro data	$(1.8 \divideontimes 4.8) \times 10^{-10}$	$(1.9 \divideontimes 5.2) \times 10^{-10}$	81	68
All in vivo data	$(1.3 \divideontimes 2.4) \times 10^{-10}$	$(6.8 \divideontimes 3.1) \times 10^{-11}$	19	16

Poly(lactide-co-glycolide) and Miscellaneous Polymers Matrixes

The analysed data contained only in vitro degradation case studies for both poly(lactide-co-glycolide) and miscellaneous polymers matrixes. Although no comparison between in vitro and in vivo protocols could be made, polymer degradation maps are included in Fig. 5.19c and d, respectively. The analysis is reported in Table 5.10 with information about poly(lactide-co-glycolide) and miscellaneous polymers composites in the third and fourth row, respectively.

All Polymeric Matrixes

Lastly, the global analysis including all data is presented in the final row of Table 5.10. Of the 84 cases a significant majority had in vitro degradation. Polymer degradation rates were higher for in vitro cases, probably driven by poly(D,L-lactide) and poly(lactide-co-glycolide) case studies.

Direct Comparison

Some of the analysed case studies allowed a more direct comparison between distinct degradation protocols for specific systems, as solely degradation protocol was varied during composite degradation experiments. For clarity purposes, a polymer degradation map with the relevant cases for this analysis is shown in Fig. 5.20.

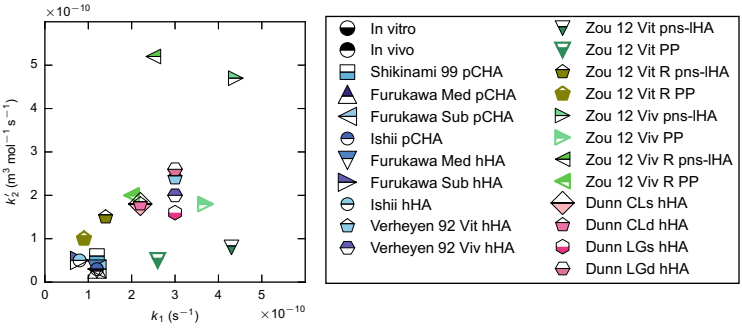

Fig. 5.20 Polymer degradation map including the hydroxyapatite case studies used for a direct comparison of degradation protocol influence on composite degradation behaviour. k_1 is the non-catalytic polymer degradation rate and k_2' is the autocatalytic polymer degradation rate Bottom side filled markers represent in vitro case studies, whereas top side filled markers represent in vivo case studies

A significant amount of data from Takiron Co. group [8–10] could be used to compare degradation behaviour under in vitro and in vivo conditions. These case studies are shown in Fig. 5.20 using blue shade markers. As several of the Takiron Co. group case studies did not include pure polymer data and the representations of the results in the k_1–k_2' map were tightly clustered, only in this instance, the original degradation data were used in order to facilitate the analysis of the degradation protocol effect. These curves, showing the variation of molecular weight over time, can be found in Fig. 5.21. Complete information about the Takiron Co. group case studies can be found in Sect. 5.4.1. Briefly, all the cases presented a dense structure with similar morphologies (cylinders with a diameter of 3.2 mm), a poly(L-lactide) matrix and either partially crystalline carbonated hydroxyapatite (pCHA) or highly crystalline pure hydroxyapatite (hHA) as a filler.

Containing pCHA, the composite sample of Shikinami 99 pCHA, degraded in vitro (PBS at 37 °C without shaking), showed a similar degradation profile to both the composite samples of Furukawa Med pCHA and Furukawa Sub pCHA, degraded in vivo (Japanese white male rabbits), as can be seen in Fig. 5.21a. The different implantation sites used in the in vivo cases had a negligible impact in the degradation profile of the composite samples. Contrarily, Fig. 5.21c showed that the pure polymer sample of Shikinami 99 pCHA presented a delayed drop in molecular weight when compared with the pure polymer sample of Furukawa Med pCHA. The Takiron Co. group case studies employing hHA showed that there was no differences in degradation profile between the composite samples of Furukawa Med hHA and Furukawa Sub hHA as seen in Fig. 5.21b. Ishii pCHA and Ishii hHA behaved similarly to Furukawa Med pCHA and Furukawa Med hHA, respectively. In summary, for Takiron Co. group case studies there were no differences in composite samples degradation behaviour regardless of the changes in degradation protocol. Pure polymer samples experienced a longer delay in molecular weight drop with an in vitro degradation protocol.

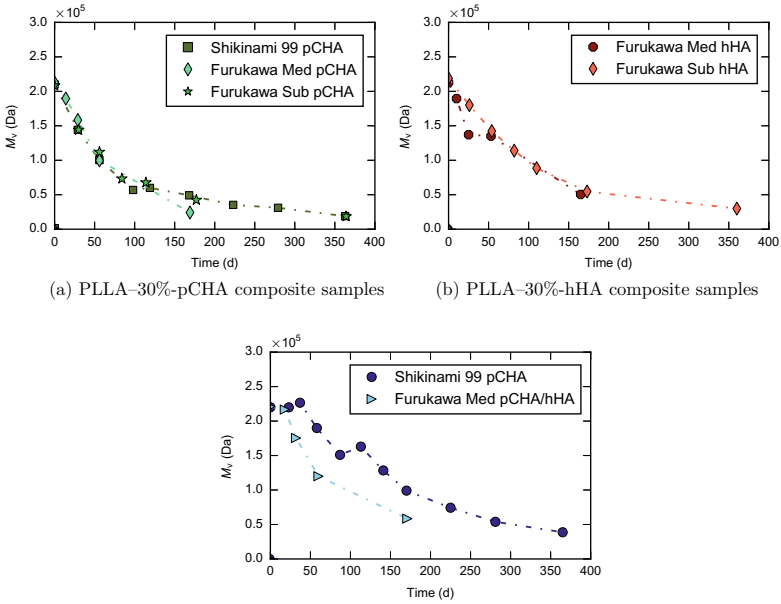

(a) PLLA–30%-pCHA composite samples

(b) PLLA–30%-hHA composite samples

(c) 100% poly(L-lactide) samples

Fig. 5.21 Degradation data (M_v over time) reporting the influence of in vitro versus in vivo protocols on degradation for case studies belonging to the Takiron Co. group [8, 9]. M_v is the viscosity average molecular weight. Data replotted from [8, 9]. Dash-dotted lines are shown for clarity only. Markers and colours are specific of this visual representation

Dense composites made of poly(L-lactide) and highly crystalline pure hydroxyapatite were also employed by Verheyen et al. [5]. In this study, the Verheyen 92 Vit hHA case, with a in vitro degradation protocol (PBS at 37 °C, weekly replacement and 40 mL/sample) showed higher values of polymer degradation rates than the Verheyen 92 Viv hHA case, with a in vivo degradation protocol (subcutaneous implantation in mature female goats). The decrease in variation of molecular weight over time was similar in both pure polymer and composite samples [5].

Several case studies part of the Southwest Jiaotong University group data [18] (green shade markers in Fig. 5.20) were used to also assess the differences between in vitro and in vivo degradation protocols in a different polymer-ceramic system. Cases degraded in vitro (PBS with the addition of sodium azide at 37 °C and 20 mL/sample) showed much lower values of polymer degradation constants k_1 and k_2' than cases with in vivo degradation (subcutaneous implantation in male dogs). Composites had a poly(D,L-lactide) matrix and in-situ-grown non-stoichiometric partially crystalline hydroxyapatite with a porous structure. Although morphology of the in vivo cases was different, the discrepancies in degradation behaviour are believed to originate mainly from degradation protocol as the two morphologies were achieved using the same electrospun mats. Although in all these cases ceramic addition caused a non-buffering effect, the same trend was found for pure polymer samples.

Case studies by Dunn et al. [39] were employed to investigate the effect of buffer replacement on in vitro degradation with sterile water kept at 37 °C. For the cases with a higher fraction of ε-caprolactone (Dunn CLs hHA and Dunn CLd hHA) the buffer replacement had no effect, whereas, in cases with a higher poly(lactide-co-glycolide) content (Dunn LGs hHA and Dunn LGd hHA) the degradation in static conditions (no buffer replacement) was slower than the degradation in dynamic conditions (buffer replacement).

Conclusions

The general analysis of the influence of in vitro versus in vivo protocols on HA composites degradation did not show great promise as distributions of protocols were heavily one-sided for most matrixes. These uneven distributions in the different analysed groups produced results governed by the inherent degradation behaviour of the case studies members of the group instead of reflecting the protocol influence.

On the contrary, the numerous direct comparisons provided interesting insights. In dense samples the differences between in vitro and in vivo protocols ranged from non-existent to mild whereas for porous samples the differences were significant, pointing towards the importance of the compound effect of sample porosity and degradation protocol. Furthermore the discrepancies in behaviour did not follow always the same trend. In vivo degradation resulted in an important increase in molecular weight reduction rate when compared with in vitro degradation for porous sample, whereas conflicting information appeared for dense samples with one event reporting a mild decrease and another event reporting a mild increase but only for the pure polymer samples.

Lastly, the influence of degradation protocol was found to be dependent on polymer chemistry with those having higher degradation rate experiencing a more prominent variation in behaviour with changes in degradation protocol.

5.6 Conclusions for the Hydroxyapatite Composites Analysis

This chapter presented the analysis of hydroxyapatite composites degradation data harvested from literature using the computational model for hydroxyapatite composites presented in Sect. 3.2.2. Firstly, all the necessary information was reported, including both composite degradation data harvested from literature and hydroxyapatite specific parameters employed by the computational model. Secondly, the results from the simulations carried out for all the HA case studies along with the necessary information for the analyses were presented. Finally, the analysis of the results was carried out divided in an overview and four main sections: hydroxyapatite dissolution, effect of HA addition on composite degradation, influence of sample porosity and lastly, influence of in vitro versus in vivo degradation protocols.

The analysis of the hydroxyapatite dissolution showed a dually unexpected behaviour with both extremely high dissolution rates, when compared to the rates measured in free drift experiments at 37 °C and pH ranging from 3.0 to 7.4 [48], and increasing dissolution values for hydroxyapatite types with expected decreasing values. These discrepancies were partially accounted for by both the presence of a polymeric matrix in composites and the influence of particle size. Additionally, this behaviour could suggest an issue with the characterisation of small particles within the composite.

The analysis of the effect of hydroxyapatite addition on composite degradation provided a significant amount of information. The case studies, which displayed a wide range of composite degradation behaviours, were classified into two categories: case studies presenting a buffering effect and case studies presenting a non-buffering effect, with a 63% of the 57 HA cases showing a buffering effect as predicted by the HA composites degradation model, pointing towards its validity especially at high polymer degradation rates.

For the compliant case studies, the computational model highlighted the wide range of degradation constants and buffering effects that could be achieved by different combinations of polymeric matrix and hydroxyapatite resulting in a plethora of degradation behaviours. The analysis also pointed to the existence of behaviour discrepancies within similar case studies belonging to different data groups, suggesting the need for a more comprehensive characterisation of both the employed hydroxyapatite type filler and polymeric matrix in order to identify the factors responsible for these variations. Conversely, the model emphasised the similarities in degradation behaviour for data coming from the same group as seen in the clustering displayed by those cases. The model also showed the ability to capture these degradation similarities even when they were hidden by different initial molecular weights.

For case studies in which the computational model was unable to capture the degradation behaviour a number of plausible causes were identified. These reasons entailed violations of the computational model in-built assumptions generating the mismatches between the expected and the experimentally reported behaviours. In a significant number of cases the broken assumption was the presence of sufficient water to guarantee that water is not a limiting factor in polymer hydrolysis.

The analysis of the influence of porosity in HA composites degradation behaviour provided a complex picture. A part of the data, including the only direct comparison, showed an unforeseen behaviour, whereas the remaining data revealed a behaviour compliant with the characteristic diffusional length $L_{H^+\text{–buffer}}$ hypothesis. This coexistence of conflicting findings suggested that some factors, intrinsically linked to sample structure, such as water penetration or mechanical integrity, played an important role in degradation behaviour that could overshadow the porosity effect.

The general analysis of the influence of in vitro versus in vivo protocols on HA composites degradation did not provide general information but the numerous direct comparisons provided interesting insights such as non-existent to mild differences in both directions between the in vitro and in vivo protocols for dense samples and significant differences with much faster in vivo degradation for porous samples, pointing towards the importance of the compound effect of sample porosity and degradation protocol.

Chapter 7 is the third and last one dealing with the harvest and analysis of experimental degradation data using the computational models derived from the general framework and presented in Chap. 3. After studying tricalcium phosphate in Chap. 4 and hydroxyapatite in the present chapter, this work stream closes in Chap. 7 considering case studies with calcium carbonate as ceramic filler.

But before providing the final piece of the computational composite degradation analysis, the next chapter, Chap. 6, discusses the experimental characterisation of the degradation of biocomposites made of poly(D,L-lactide-co-glycolide)(50:50) and nano-sized calcium carbonate.

References

1. Wang, Y., Liu, L., & Guo, S. (2010b). Characterization of biodegradable and cytocompatible nano-hydroxyapatite/polycaprolactone porous scaffolds in degradation in vitro. *Polymer Degradation and Stability*, *95*(2), 207–213.
2. Huang, J., Xiong, J., Liu, J., Zhu, W., & Wang, D. (2013). Investigation of the in vitro degradation of a novel polylactide/nanohydroxyapatite composite for artificial bone. *Journal of Nanomaterials*, *2013*, 3.
3. Wang, Z., Wang, Y., Ito, Y., Zhang, P., & Chen, X. (2016). A comparative study on the in vivo degradation of poly(L-lactide) based composite implants for bone fracture fixation. *Scientific Reports*, *6*.
4. Zhou, H., Touny, A. H., & Bhaduri, S. B. (2011). Fabrication of novel PLA/CDHA bionanocomposite fibers for tissue engineering applications via electrospinning. *Journal of Materials Science: Materials in Medicine*, *22*(5), 1183–1193.
5. Verheyen, C., De Wijn, J., Van Blitterswijk, C., & De Groot, K. (1992). Evaluation of hydroxylapatite/poly(L-lactide) composites: Mechanical behavior. *Journal of Biomedical Materials Research*, *26*(10), 1277–1296.
6. Verheyen, C., Klein, C., de Blieck-Hogervorst, J., Wolke, J., Van Blitterswijn, C., & De Groot, K. (1993). Evaluation of hydroxylapatite/poly(L-lactide) composites: Physico-chemical properties. *Journal of Materials Science: Materials in Medicine*, *4*(1), 58–65.
7. Díaz, E., Sandonis, I., Puerto, I., & Ibáñez, I. (2014). In vitro degradation of PLLA/nHA composite scaffolds. *Polymer Engineering and Science*, *54*(11), 2571–2578.
8. Shikinami, Y., & Okuno, M. (1999). Bioresorbable devices made of forged composites of hydroxyapatite (HA) particles and poly-L-lactide (PLLA): Part I. Basic characteristics. *Biomaterials*, *20*(9), 859–877.
9. Furukawa, T., Matsusue, Y., Yasunaga, T., Shikinami, Y., Okuno, M., & Nakamura, T. (2000). Biodegradation behavior of ultra-high-strength hydroxyapatite/poly(L-lactide) composite rods for internal fixation of bone fractures. *Biomaterials*, *21*(9), 889–898.
10. Ishii, S., Tamura, J., Furukawa, T., Nakamura, T., Matsusue, Y., Shikinami, Y., et al. (2003). Long-term study of high-strength hydroxyapatite/poly(L-lactide) composite rods for the internal fixation of bone fractures: A 2-4-year follow-up study in rabbits. *Journal of Biomedical Materials Research Part B: Applied Biomaterials*, *66*(2), 539–547.
11. Shikinami, Y., & Okuno, M. (2001). Bioresorbable devices made of forged composites of hydroxyapatite (HA) particles and poly L-lactide (PLLA). Part II: Practical properties of miniscrews and miniplates. *Biomaterials*, *22*(23), 3197–3211.
12. Deng, X., Sui, G., Zhao, M., Chen, G., & Yang, X. (2007). Poly(L-lactic acid)/hydroxyapatite hybrid nanofibrous scaffolds prepared by electrospinning. *Journal of Biomaterials Science, Polymer Edition*, *18*(1), 117–130.
13. Sui, G., Yang, X., Mei, F., Hu, X., Chen, G., Deng, X., et al. (2007). Poly-L-lactic acid/hydroxyapatite hybrid membrane for bone tissue regeneration. *Journal of Biomedical Materials Research Part A*, *82*(2), 445–454.

14. Xu, X., Chen, X., Liu, A., Hong, Z., & Jing, X. (2007). Electrospun poly(L-lactide)-grafted hydroxyapatite/poly(L-lactide) nanocomposite fibers. *European Polymer Journal*, *43*(8), 3187–3196.
15. Rakmae, S., Lorprayoon, C., Ekgasit, S., & Suppakarn, N. (2013). Influence of heat-treated bovine bone-derived hydroxyapatite on physical properties and in vitro degradation behavior of poly(lactic acid) composites. *Polymer-Plastics Technology and Engineering*, *52*(10), 1043–1053.
16. Rakmae, S., Ruksakulpiwat, Y., Sutapun, W., & Suppakarn, N. (2012). Effect of silane coupling agent treated bovine bone based carbonated hydroxyapatite on in vitro degradation behavior and bioactivity of PLA composites. *Materials Science and Engineering: C*, *32*(6), 1428–1436.
17. Van der Meer, S., De Wijn, J., & Wolke, J. (1996). The influence of basic filler materials on the degradation of amorphous D-and L-lactide copolymer. *Journal of Materials Science: Materials in Medicine*, *7*(6), 359–361.
18. Zou, B., Chen, X., Zhi, W., Liu, Y., Cui, W., Hu, S., et al. (2012). Promoted healing of femoral defects with in situ grown fibrous composites of hydroxyapatite and poly(DL-lactide). *Journal of Biomedical Materials Research Part A*, *100*(6), 1407–1418.
19. Zou, B., Li, X., Zhuang, H., Cui, W., Zou, J., & Chen, J. (2011). Degradation behaviors of electrospun fibrous composites of hydroxyapatite and chemically modified poly(DL-lactide). *Polymer Degradation and Stability*, *96*(1), 114–122.
20. Hasegawa, S., et al. (2005). In vivo evaluation of a porous hydroxyapatite/poly-DL-lactide composite for use as a bone substitute. *Journal of Biomedical Materials Research Part A*, *75*(3), 567–579.
21. Chen, L., Tang, C. Y., Tsui, C. P., et al. (2013). Mechanical properties and in vitro evaluation of bioactivity and degradation of dexamethasone-releasing poly-D-L-lactide/nano-hydroxyapatite composite scaffolds. *Journal of the Mechanical Behavior of Biomedical Materials*, *22*, 41–50.
22. Hile, D. D., Doherty, S. A., & Trantolo, D. J. (2004). Prediction of resorption rates for composite polylactide/hydroxylapatite internal fixation devices based on initial degradation profiles. *Journal of Biomedical Materials Research Part B: Applied Biomaterials*, *71*(1), 201–205.
23. Díaz, E., & Puerto, I. (2015). In vitro degradation of PLCL/nHA biodegradable scaffolds. *Polymer-Plastics Technology and Engineering*, *54*(6), 556–564.
24. Ural, E., Kesenci, K., Fambri, L., Migliaresi, C., & Piskin, E. (2000). Poly(D, L-cactide/ε-caprolactone)/hydroxyapatite composites. *Biomaterials*, *21*(21), 2147–2154.
25. Tsunoda, M. (2003). Degradation of poly(DL-lactic acid-co-glycolic acid) containing calcium carbonate and hydroxyapatite fillers-effect of size and shape of the fillers. *Dental Materials Journal*, *22*(3), 371–382.
26. Li, H., & Chang, J. (2005). pH-compensation effect of bioactive inorganic fillers on the degradation of PLGA. *Composites Science and Technology*, *65*(14), 2226–2232.
27. Díaz, E., Puerto, I., & Sandonis, I. (2015). The effects of bioactive nanoparticles on the degradation of DLGA. *International Journal of Polymeric Materials and Polymeric Biomaterials*, *64*(1), 38–46.
28. Agrawal, C. M., & Athanasiou, K. A. (1997). Technique to control pH in vicinity of biodegrading PLA-PGA implants. *Journal of Biomedical Materials Research*, *38*(2), 105–114.
29. Naik, A., Shepherd, D. V., Shepherd, J. H., Best, S. M., & Cameron, R. E. (2017). The effect of the type of HA on the degradation of PLGA/HA composites. *Materials Science and Engineering: C*, *70*, 824–831.
30. Naik, A. (2012). *Effect of calcination and silanisation on the degradation of poly(DL Lactic-co-glycolic acid)-hydroxyapatite composites*. Ph.D. thesis, Department of Materials Science and Metallurgy, University of Cambridge.
31. Naik, A., Best, S. M., & Cameron, R. E. (2015). The influence of silanisation on the mechanical and degradation behaviour of PLGA/HA composites. *Materials Science and Engineering: C*, *48*, 642–650.
32. Ege, D. (2012). *Mechanical and degradation properties of calcium phosphate/biodegradable polymer composites*. Ph.D. thesis, Department of Materials Science and Metallurgy, University of Cambridge.

33. Ege, D., Best, S., & Cameron, R. (2014). The degradation behaviour of nanoscale HA/PLGA and α-TCP/PLGA composites. *Bioinspired, Biomimetic and Nanobiomaterials*, *3*, BBN2.
34. Lee, J. B., Kim, S. E., Heo, D. N., Kwon, I. K., & Choi, B.-J. (2010). In vitro characterization of nanofibrous PLGA/gelatin/hydroxyapatite composite for bone tissue engineering. *Macromolecular Research*, *18*(12), 1195–1202.
35. Liuyun, J., Chengdong, X., Lixin, J., & Lijuan, X. (2013). Degradation behavior of hydroxyapatite/poly(lactic-co-glycolic) acid nanocomposite in simulated body fluid. *Materials Research Bulletin*, *48*(10), 4186–4190.
36. Ban, S., Watanabe, T., Itoh, T., Nakamura, H., Tsuruta, S., & Kawai, T. (2004). Development of biodegradable composite membrane containing oriented needle-like apatites. *Journal of Oral Tissue Engineering*, *2*(1), 1–13.
37. Rodenas-Rochina, J., Vidaurre, A., Cortázar, I. C., & Lebourg, M. (2015). Effects of hydroxyapatite filler on long-term hydrolytic degradation of PLLA/PCL porous scaffolds. *Polymer Degradation and Stability*, *119*, 121–131.
38. Ji, W., Yang, F., Seyednejad, H., Chen, Z., Hennink, W. E., Anderson, J. M., et al. (2012). Biocompatibility and degradation characteristics of PLGA-based electrospun nanofibrous scaffolds with nanoapatite incorporation. *Biomaterials*, *33*(28), 6604–6614.
39. Dunn, A. S., Campbell, P. G., & Marra, K. G. (2001). The influence of polymer blend composition on the degradation of polymer/hydroxyapatite biomaterials. *Journal of Materials Science: Materials in Medicine*, *12*(8), 673–677.
40. Pan, J., Han, X., Niu, W., & Cameron, R. E. (2011). A model for biodegradation of composite materials made of polyesters and tricalcium phosphates. *Biomaterials*, *32*(9), 2248–2255.
41. Bates, R. G. (1951). First dissociation constant of phosphoric acid from 0° to 60°C: Limitations of the electromotive force method for moderately strong acids. *Journal of Research of the National Bureau of Standards*, *47*, 127–134.
42. Bates, R. G., & Acree, S. (1943). pH values of certain phosphate-chloride mixtures, and the second dissociation constant of phosphoric acid from 0° to 60°C. *Journal of Research of the National Bureau of Standards*, *30*, 129–155.
43. Vanderzee, C. E., & Quist, A. S. (1961). The third dissociation constant of orthophosphoric acid. *The Journal of Physical Chemistry*, *65*(1), 118–123.
44. Marshall, W. L., & Franck, E. (1981). Ion product of water substance, 0–1000°C, 1–10,000 bars new international formulation and its background. *Journal of Physical and Chemical Reference Data*, *10*(2), 295–304.
45. PubChem, (2005). *CID*: 14781. Retrieved September 1, 2016 from https://pubchem.ncbi.nlm.nih.gov/compound/14781#section=Top.
46. Dorozhkin, S. V., & Epple, M. (2002). Biological and medical significance of calcium phosphates. *Angewandte Chemie International Edition*, *41*(17), 3130–3146.
47. Ito, A., Maekawa, K., Tsutsumi, S., Ikazaki, F., & Tateishi, T. (1997). Solubility product of OH-carbonated hydroxyapatite. *Journal of Biomedical Materials Research Part A*, *36*(4), 522–528.
48. Nair, M. (2016). *Modelling and study of the dissolution rate of calcium-based fillers in composites for orthopaedic applications*. Part III individual research project, Department of Materials Science and Metallurgy, University of Cambridge.
49. Neuendorf, R., Saiz, E., Tomsia, A., & Ritchie, R. (2008). Adhesion between biodegradable polymers and hydroxyapatite: Relevance to synthetic bone-like materials and tissue engineering scaffolds. *Acta Biomaterialia*, *4*(5), 1288–1296.
50. Middleton, J. C., & Tipton, A. J. (2000). Synthetic biodegradable polymers as orthopedic devices. *Biomaterials*, *21*(23), 2335–2346.
51. Bohner, M. (2000). Calcium orthophosphates in medicine: From ceramics to calcium phosphate cements. *Injury*, *31*, D37–D47.
52. Daculsi, G., LeGeros, R., LeGeros, J., & Mitre, D. (1991). Lattice defects in calcium phosphate ceramics: High resolution TEM ultrastructural study. *Journal of Applied Biomaterials*, *2*(3), 147–152.

53. LeGeros, R. Z. (1993). Biodegradation and bioresorption of calcium phosphate ceramics. *Clinical Materials*, *14*(1), 65–88.
54. Christoffersen, J., Christoffersen, M. R., & Kjaergaard, N. (1978). The kinetics of dissolution of calcium hydroxyapatite in water at constant pH. *Journal of Crystal Growth*, *43*(4), 501–511.
55. Hyakuna, K., Yamamuro, T., Kotoura, Y., Oka, M., Nakamura, T., Kitsugi, T., et al. (1990). Surface reactions of calcium phosphate ceramics to various solutions. *Journal of Biomedical Materials Research Part A*, *24*(4), 471–488.
56. Yamamuro, T., Shikata, J., Kakutani, Y., Yoshii, S., Kitsugi, T., & Ono, K. (1988). Novel methods for clinical applications of bioactive ceramics. *Annals of the New York Academy of Sciences*, *523*(1), 107–114.
57. Higashi, S., Yamamuro, T., Nakamura, T., Ikada, Y., Hyon, S.-H., & Jamshidi, K. (1986). Polymer-hydroxyapatite composites for biodegradable bone fillers. *Biomaterials*, *7*(3), 183–187.
58. Kobayashi, S., & Yamaji, S. (2014). Analytical prediction of hydrolysis behavior of tricalcium phosphate/poly-L-lactic acid composites in simulated body environment. *Advanced Composite Materials*, *23*(3), 211–223.
59. Lam, C. X., Hutmacher, D. W., Schantz, J.-T., Woodruff, M. A., & Teoh, S. H. (2009). Evaluation of polycaprolactone scaffold degradation for 6 months in vitro and in vivo. *Journal of Biomedical Materials Research Part A*, *90*(3), 906–919.

Chapter 6
Experimental Degradation Study of PLGA–$CaCO_3$ Nanocomposites

This chapter presents the study of the degradation of nanocomposites made of poly(D,L-lactide-co-glycolide) and calcium carbonate. The first section of the chapter describes the materials and methods employed in this work. The second section includes the characterisation of the raw materials followed by the characterisation of the undegraded and degraded composites in the third and fourth sections, respectively. The discussion of the results is reported in the fifth section and lastly, the conclusions in the sixth and final section.

As mentioned before, the need to provide well-parametrised experimental degradation data in order to test the computational model assumptions concerning the effect of both the ceramic particle size and weight fraction on composite degradation seems paramount. To fulfil these requirements, a degradation study with nano-structured poly(D,L-lactide-co-glycolide)–calcium carbonate (PLGA–$CaCO_3$) composites was carried out in which calcium carbonate nanoparticles of different sizes were used in various polymer-ceramic ratios. This polymer-ceramic combination was chosen for two reasons: first and foremost, the existence of commercially available CC particles with extremely narrow particle size distributions in two different sizes and secondly, the relative scarcity of CC composites data when compared with TCP or HA composites.

The generation of carefully characterised and controlled composite degradation data will allow a more insightful application of the model in order to characterise the effect of particle size and ceramic weight fraction. Although the harvested $CaCO_3$ composites literature data, which will be presented and analysed in Chap. 7, provided many insights, the presence of pitfalls in the ceramic characterisation such as agglomeration [1] or poorly defined particle size [2–4] emphasised the necessity of this study.

I. Moreno-Gomez, *A Phenomenological Mathematical Modelling Framework for the Degradation of Bioresorbable Composites*, Springer Theses, https://doi.org/10.1007/978-3-030-04990-4_6

6.1 Materials and Methods

This section contains the description of the materials and methods employed in this degradation study. Firstly, a description of the polymeric matrix and ceramic filler is presented. The composite manufacture method is then described, followed by the experimental design, the in vitro degradation protocol and lastly, a description of the techniques used to characterise raw materials and both undegraded and degraded composites.

6.1.1 Polymeric Matrix

A copolymer of the poly(D,L-lactide-co-glycolide) family was chosen as the matrix for the composite samples investigated in this study. PLGA with a mid-range molecular weight and a 50:50 molar ratio of D,L-lactide:glycolide capped with lauryl alcohol resulting in lauryl ester end groups (Product name: PLGA 5050 DLG 5E) was purchased in pellet form (Lakeshore Biomaterials™, Evonik Industries; Alabama USA). Table 6.1 shows the properties, as reported by the manufacturer, of the batch (Lot Number: LP-836) used in this work.

6.1.2 Ceramic Filler

Calcium carbonate nano-structured particles were chosen as inorganic filler for the composite samples. $CaCO_3$ in two different formats, cubes of 80 and 150 nm of nominal size, were obtained from Shiraishi Calcium Kaisha, Ltd.; Japan. For conciseness the 80 nm and the 150 nm cubes are named C80 and C150, respectively. Table 6.2 reports several ceramic properties as characterised by the manufacturer.

Table 6.1 Specifications of purchased PLGA, provided by the manufacturer. Inherent viscosity was measured at 0.5% w/v in $CHCl_3$ at 30 °C. M_{w0} is the initial weight-average molecular weight and M_{n0} is the initial number-average molecular weight

Property	Value
Inherent viscosity ($I.V.(t_0)$)	0.48 dL g^{-1}
Residual D,L-lactide monomer	1.0 wt %
Residual glycolide monomer	0.2 wt %
D,L-lactide mole ratio	50 mol %
Glycolide mole ratio	50 mol %
M_{w0}	70 kDa
M_{n0}	42 kDa
Dispersity ($Đ(t_0)$)	1.7

Table 6.2 Specifications of purchased $CaCO_3$, provided by the manufacturer

Property	C80 value	C150 value
Moisture (%)	0.8	0.4
Whiteness (%)	97	99
Nominal particle size (nm)	80	150
Particle shape	Cubic	Cubic

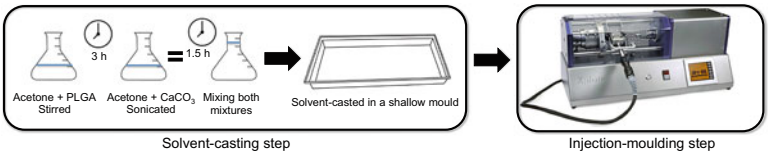

Fig. 6.1 Illustration of the two-steps composite manufacture process

6.1.3 Composite Manufacture

Figure 6.1 illustrates the two-step process used to make PLGA–$CaCO_3$ composites based on a modified version of Yang et al.'s protocol, which resulted in an even ceramic distribution without agglomerates for PLGA–α-TCP nanocomposites [5]. The first step encompassed the making of thin composite films through a solvent casting route. Firstly, the desired quantity of ceramic particles were placed in a 100 ml volumetric flask, then 40 ml of acetone were added and the flask was placed in a sonication bath for 90 min in order to achieve a good and homogeneous dispersion of the particles in the solvent. Simultaneously, the desired quantity of polymer was dissolved in a beaker containing acetone, 40 ml for composite samples and 80 ml for pure polymer samples, with the help of a magnetic stirrer for 90 min. Both mixtures were then placed in the same beaker and stirred together for 120 min more. The mixture was poured into a shallow silicone tray mould and left to dry overnight. The film was then peeled off the tray and placed in the vacuum oven at 40 °C overnight.

The second step of the process consisted of the sample injection moulding to attain the desired shape. Once the films were dried, they were chopped into small pieces to create composite pellets. The pellets were then fed into the barrel and injection-moulded into rods using a DSM Xplore 5.5 ml injection moulding machine (DSM Research) and a cylindrical mould with a diameter of 3.5 mm and a length of 4 cm. Table 6.3a shows the pressure and time parameters used in the three different stages of the injection moulding process and Table 6.3b shows the temperatures of the different injection-moulder parts and the loading process temperature and time parameters.

The injection-moulded rods were cut into their final shape, cylinders of 2 mm of length and 3.5 mm of diameter, using a Struers Accutom-5 automatic saw fitted with a 1224 cutting wheel. The cutting method used rotation without water cooling,

Table 6.3 Setting used in the Xplore 5.5 ml injection-moulding machine and loading process parameters for pure polymer and PLGA-$CaCO_3$ composite samples manufacture

(a) Pressure and time for the different stages in the injection-moulding process

Step	Pressure (bar)	Time (s)
Injection	5	6
Filling	2	4
Holding	2	4

(b) Injection-moulder temperatures and feeding process parameters

Parameter	Value
Barrel temperature	135 °C
Mould temperature	35 °C
Loading temperature	85 °C
Barrel residence time	<120 s

Table 6.4 Summary of the different manufactured pure polymer and composite samples indicating the polymer and ceramic parameters

Sample name	Polymer type	Ceramic			
		Type	Nominal weight fraction (%)	Shape	Nominal particle size (nm)
Pure PLGA	P(D,L)LGA (50:50)	None	0	–	–
PLGA-10%C80	P(D,L)LGA (50:50)	C80	10	Cubic	80
PLGA-20%C80	P(D,L)LGA (50:50)	C80	20	Cubic	80
PLGA-10%C150	P(D,L)LGA (50:50)	C150	10	Cubic	150

medium cutting force, a rotational speed of 3000 rpm and a penetration cutting speed of 0.1 mm s^{-1}. The cut debris was removed with a pair of tweezers and the samples were then stored in a desiccator prior to the degradation study.

6.1.4 Experimental Design

In order to test the model assumptions, several composite types were manufactured. Pure polymer samples were used as control. Two different ceramics were used to investigate the influence of filler specific surface area on degradation behaviour. Different weight fractions, for one of the ceramics, were included to assess the effect of filler quantity. Table 6.4 summarizes the different sample types and their characteristics. For each composite type the nominal ceramic weight fraction is specified, being the reminder pure polymer.

6.1.5 In vitro Degradation Protocol

Pure PLGA and PLGA–$CaCO_3$ disks (3.5 mm in diameter and 2 mm in thickness), with the specifications reported in Table 6.4, were prepared as described in Sect. 6.1.3

for this degradation study. 0.01 M phosphate buffered saline (PBS) was prepared dissolving one pouch of phosphate buffered saline powder, pH = 7.4 from Sigma Aldrich (Product Number: P3813, Lot: SLBK5765V) in one litre of ultra-deionized water with a quality of 18.2 MΩ cm^{-1} (Select Fusion water purification system, Purite) at a time. The PBS density at room temperature was measured to be (1.005 ± 0.001) g cm^{-3} using a density hydrometer (BS718:1991 density hydrometer M100 250 mm, Brannan).

Each sample was placed in a sterile 7 ml polystyrene Bijou bottle (Appleton Woods Ltd.) and the corresponding mass of PBS to attain a ratio of sample to buffer media of 6 mg ml^{-1} was added. The Bijou containers were then sealed and placed in an incubator (Incucell 111, MMM) at (37 ± 0.2) °C. No agitation, media buffer change or replenishment was applied to the samples during degradation. 6 to 8 samples were degraded per polymer-ceramic combination per timepoint.

6.1.6 General Characterisation Techniques

A series of characterisation techniques were employed with raw materials and both undegraded and degraded samples. The methods used for those characterisation techniques are described below.

Particle Morphology

The particle morphology of the ceramic samples was analysed using a FEI Nano Nova Scanning Electron Microscope (SEM). The samples were coated with a gold layer using a sputter coater (EmiTech K550). The deposition process employed a 20 mA sputtering current for 80 s with continuous sample rotation at a working distance of 36.5 mm. According to the manufacturer [6], these settings corresponded to a deposition rate of approximately 12 nm min^{-1} giving an estimated coating thickness in the vicinity of 15 nm. Several micrographs were taken in back-scattered electron (BSE) mode with a 5 kV gun voltage at a magnification of 30,000 times.

Specific Surface Area

A TriStar 3000 (Micromeritics Instrument Corporation) was employed to determine the specific surface area (SSA) of the ceramics. Around 0.3 g per sample were degassed overnight in a vacuum oven and then introduced in the measuring vessel accompanied by a liquid nitrogen (N_2) dewar. The infiltration and adsorption of gaseous N_2 onto the sample surface was measured as a function of the gas pressure and the specific surface area computed using both the Brunauer–Emmett–Teller (BET) and Langmuir theories.

Each sample was subjected to an adsorption-desorption cycle, the adsorption stage spanned from a relative pressure (P/P_0 with a saturation pressure, P_0, of 775 mmHg) of 0.01 to 0.99, and the desorption stage spanned from 0.99 to 0.15. The relative pressure steps were evenly distributed: increments of 0.02 were used for relative pressures less than 0.20 and greater than 0.80 and increments of 0.05 for relative

pressures in the 0.20 to 0.80 interval. The equilibration interval was 10 s for each step. Each complete cycle totalled 55 measurements used to calculate the BET and Langmuir specific surface areas.

Mass and Size Measurements

The mass measurements of undegraded and degraded composites were performed in triplicate for each sample using a lab analytical balance (Sartorius CP124S, d = 0.1 mg). The size measurements of undegraded samples were performed in duplicate for each sample using a digital Vernier caliper (Neiko Stainless Steel Digital Caliper, accuracy of 0.02 mm).

Density Analysis

The density of the ceramic particles and both undegraded and degraded samples was measured using a pycnometer (AccuPyc^{TM} 1330, Micromeritics) equipped with a 1 cm^3 measurement chamber. Prior to the analysis, the two-step calibration was performed with an empty measurement chamber and a known-volume spherical reference [7]. Moreover, ceramic samples were stored in a vacuum oven at 50 °C overnight and dry degraded composites were stored in a desiccator. For the density analysis, the measurement chamber was filled up to three quarters of its height with a known mass, either ceramic powder or 4–6 disks of undegraded, degraded just after removal from the buffer or degraded after drying samples, and the volume was measured. For degraded composites, when the available samples did not amount to at least half of the volume of the measuring chamber (0.5 cm^3), a known-volume plastic stub was used as a filler for the measurements.

For each measurement, helium is admitted to the measuring chamber containing the sample and the gas gauge pressure is measured (P_{1g}), then the gas is also admitted to the expansion chamber and the gauge pressure measured again (P_{2g}). The sample volume, V_{samp}, is calculated as:

$$V_{samp} = V_{cell} - \frac{V_{exp}}{\frac{P_{1g}}{P_{2g}} - 1}$$

where V_{cell} is the volume of the empty measurement chamber, V_{exp} the volume of the expansion chamber and P_{1g} and P_{2g} the measured gas gauge pressures [7]. The apparent density was calculated as mass divided by volume. For each sample the measurement was repeated ten times.

Visual Analysis

The visual appearance of the undegraded and degraded samples was documented using a Canon reflex camera, with the samples placed on top of a flat surface next to a ruler, used as a reference, and shooting from above at a fixed distance.

Phase Identification

X-ray diffraction (XRD) was employed to identify the crystalline phases present in the ceramic samples, as-made and degraded composite samples. A Philips PW1820 $\theta/2\theta$ diffractometer with Bragg-Brentano para-focusing geometry was used with the instrument configuration presented in Table 6.5.

Table 6.5 Parameters of the Philips PW1820 diffractometer configuration used for XRD measurements of the ceramic particles

Parameter	Value
Divergence slit	½ °
Receiving slit	0.2°
Anti-scatter slit	½ °
Mask	5 mm
Step size	0.01°
Time per step	2 s

The 2θ scan typically ranged from 10° to 75°. For ceramic samples, an aluminium well sample holder was back-filled to minimize orientation effects. For composites, a single crystal silicon wafer was used. Several samples were secured on top of the holder with a smear of petroleum jelly. The holder was then levelled to align the top surfaces of the composites in the same horizontal plane. For degraded composites, the samples were flattened using the minimum load in a manual press to counteract the outer surface roughness developed during degradation prior to securing them onto the holder. The spectra of the samples were analysed using X'pert Highscore Plus software (PANalytical). Correction procedures to remove the $K_{\alpha 2}$ peaks and subtract the background were applied. Patterns from the International Centre for Diffraction Data (ICDD) were used for phase identification.

Differential Scanning Calorimetry

Differential scanning calorimetry (DSC) was performed using a Q2000 DSC (TA Instruments) on as-received polymer and both undegraded and degraded composites. Approximately 5 mg of sample were placed in a DSC pan and equilibrated at 0 °C prior to a temperature ramp to 250 °C at a heating rate of 15 °C min^{-1}. The collected heat flow data were analysed using Universal Analysis 2000 software (TA Instruments) to determine the glass transition temperature (T_g).

Thermogravimetric Analysis

Thermogravimetric analysis (TGA) was performed on the as-received polymer, ceramic samples, and both undegraded and degraded samples using a Q500 thermogravimetric analyser (TA Instruments) in order to investigate thermal degradation, weight fraction of ceramic present in the as-made undegraded samples and the influence of degradation on ceramic-weight ratio evolution over time. A TGA palladium pan was tared and then a quantity of around 40 mg for as-received polymer and undegraded samples, 8 mg for ceramic samples and 10 mg for degraded samples, was placed in the pan. The sample was then subjected to a temperature ramp from room temperature (approximately 20 °C) to 550 °C at a heating rate of 10 °C min^{-1} in a nitrogen atmosphere. For ceramic samples, the ramp ended at 800 °C with a heating rate of 15 °C min^{-1}.

6.1.7 Degraded Samples Characterisation Techniques

In addition to the general techniques mentioned above, some other techniques were employed only with the degraded samples.

At the designated degradation timepoint, each sample was removed from the buffer media and placed in a paper towel. The sample was gently dabbed to remove the outer layer of media and its value of wet mass, M_{wet}, was recorded. Then, all the repeats of a particular system were employed to calculate its wet density and the visual appearance was recorded. After completion of the wet characterisation, the samples were placed in a vacuum oven to allow for media evaporation. During the drying process, the mass was monitored at regular time intervals. The dry analysis which included dry mass, M_{dry}, dry volume and visual appearance was carried out once the dry mass became stable. The samples were then prepared for the analyses of phase composition and thermal properties following the protocols described in Sect. 6.1.6.

The pH of the degradation media was measured using a calibrated pH-meter (HI-4222 pH-meter fitted with a HI-1131B general purpose laboratory pH electrode and calibrated prior to the measurements with HI-7004L pH 4.01, HI-7007L pH 7.01 and HI-7010L pH 10.01 buffers, all from Hanna Instruments). The mass loss, M_L, water uptake, W_U, and water absorption, W_A were computed for each sample, using the following expressions:

$$M_L = \left(\frac{M_{init} - M_{dry}}{M_{init}} \right) \times 100 \quad (\%) \quad (6.1)$$

$$W_U = \left(\frac{M_{wet} - M_{dry}}{M_{init}} \right) \times 100 \quad (\%) \quad (6.2)$$

$$W_A = \left(\frac{M_{wet} - M_{dry}}{M_{dry}} \right) \times 100 \quad (\%) \quad (6.3)$$

with M_{init}, the sample initial mass, i.e. before degradation; M_{dry}, the dry mass of the degraded sample and M_{wet}, the wet mass of the degraded sample.

6.2 Characterisation of the Raw Materials

This section contains the results from the characterisation of the raw materials including particle morphology, specific surface area, phase identification and density of the ceramic samples, polymer DSC analysis and TGA analysis for both polymer and ceramics.

6.2.1 Particle Morphology

Figure 6.2 shows a representative micrograph of each ceramic and Table 6.6 presents the analysis of all the micrographs taken, giving a mean particle size with standard deviation, after correcting for coating thickness, for the two $CaCO_3$ samples.

The analysis showed that the morphology of both the C80 and C150 samples was extremely consistent in terms of shape and individual particle size at the nano-scale.

6.2.2 Specific Surface Area

Table 6.7 reports the BET and Langmuir SSA values for the two $CaCO_3$ samples. Although both C80 and C150 presented high values of specific surface area, the SSA values halved from C80 (higher value) to C150 (lower value).

6.2.3 Phase Identification

Calcium carbonate presents three allotropes: β -$CaCO_3$ or calcite (trigonal, $R\bar{3}c$ [8]), λ-$CaCO_3$ or aragonite (orthorhombic, $Pmcn$ [9]) and μ-$CaCO_3$ or vaterite (hexagonal $P6_3/mmc$ [10]). Figure 6.3 shows the spectra of the C80 and C150 samples with the calcite (ICDD Pattern 00-005-0586) peaks indicated. For both C80 and C150 all

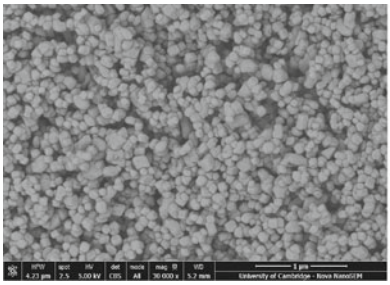

(a) C80 particles

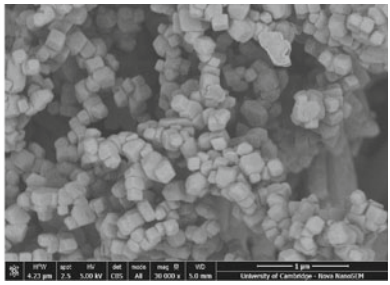

(b) C150 particles

Fig. 6.2 Back-scattered electrons micrographs of the two different $CaCO_3$ particles

Table 6.6 Estimated size, expressed as mean ± standard deviation, of the two different $CaCO_3$ particles from the back-scattered electrons micrographs

Sample	Size (nm)
C80	88 ± 19
C150	164 ± 33

Table 6.7 BET and Langmuir specific surface areas of the two different types of $CaCO_3$ particles

Sample	BET SSA ($m^2\ g^{-1}$)	Langmuir SSA ($m^2\ g^{-1}$)
C80	16.9990 ± 0.0695	21.6877 ± 0.4505
C150	8.3318 ± 0.0138	10.6792 ± 0.2731

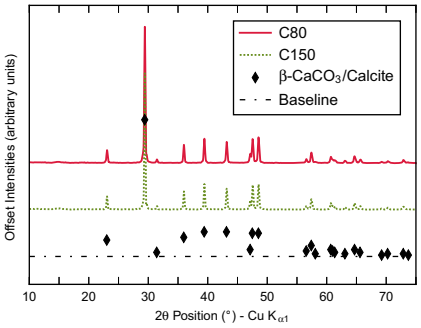

Fig. 6.3 XRD spectra of the $CaCO_3$ samples (C80 and C150) after the removal of the $K_{\alpha 2}$ peaks with calcite reference peaks indicated. The spectra have been normalised and the background noise smoothed with a Savitzky–Golay filter to facilitate cross-comparison between samples. Height, measured from the baseline, of the calcite reference peaks is proportional to the relative intensities reported in the ICDD pattern

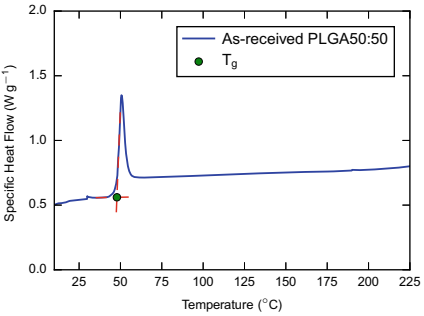

Fig. 6.4 Differential scanning calorimetry analysis of as-received PLGA50:50. Exothermic process down. The glass transition temperature, T_g, was found at the intersection between the specific heat flow baseline extrapolated forward and the step slope extrapolated backwards (dashed red lines)

the peaks of the spectra were accounted for solely with the calcite pattern, indicating pure monophasic composition.

6.2.4 Density

Table 6.8 includes the absolute and relative apparent density values measured for both C80 and C150 using a density value for calcite of $2.710 \times 10^3\,kg\,m^{-3}$ [11] in

the relative density calculations. The relative density values pointed to fully dense nano-particles, with the discrepancies arising from the particle packing efficiency in the measurement chamber.

6.2.5 Differential Scanning Calorimetry

Figure 6.4 depicts the DSC thermogram for the as-received polymer. The glass transition appeared as a step in the specific heat flow curve and corresponded to a temperature of $(48.10 \pm 0.35)\,^{\circ}C$, expressed as mean $\pm$ standard deviation for two different samples.

6.2.6 Thermogravimetric Analysis

Figure 6.5 includes the results of the thermogravimetric analysis for the as-received polymer. The thermal degradation of the polymer started at around 220 °C and finished around 500 °C when the remaining polymer mass was negligible: $(0.33 \pm 0.05)\%$, expressed as mean $\pm$ standard deviation for two different samples. The derivative of the weight loss with respect to temperature had a value of zero until the thermal degradation started, then increased and reached its peak value. A decrease followed until it reached a null value again when the degradation finished.

Figure 6.6 presents the TGA results for the two $CaCO_3$ samples. Both samples showed a similar behaviour, with no signs of thermal degradation below 640 °C. From 640 °C up to 765 °C, C80 and C150 experienced significant degradation which ended when the remaining weight had a value of approximately 55% of the initial weight for both samples. The derivative of the weight loss with respect to temperature had a value of zero until the thermal degradation started, then increased until it peaked and then decreased to zero again.

Table 6.8 Absolute and relative apparent density values, expressed as mean $\pm$ standard deviation, of the two different types of $CaCO_3$ particles

Sample	Density ($kg\,m^{-3}$)	Relative density (1)
C80	$(2.667 \pm 0.008) \times 10^3$	0.984 ± 0.003
C150	$(2.658 \pm 0.012) \times 10^3$	0.980 ± 0.005

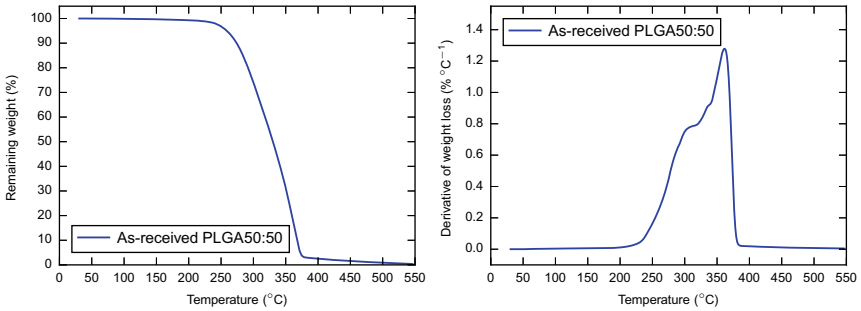

(a) Remaining weight percentage

(b) Derivative of the weight loss percentage with respect to temperature

Fig. 6.5 Thermogravimetric analysis of as-received PLGA50:50 indicating both the percentage of remaining weight as a function of temperature and the derivative of the weight loss percentage with respect to temperature as a function of temperature

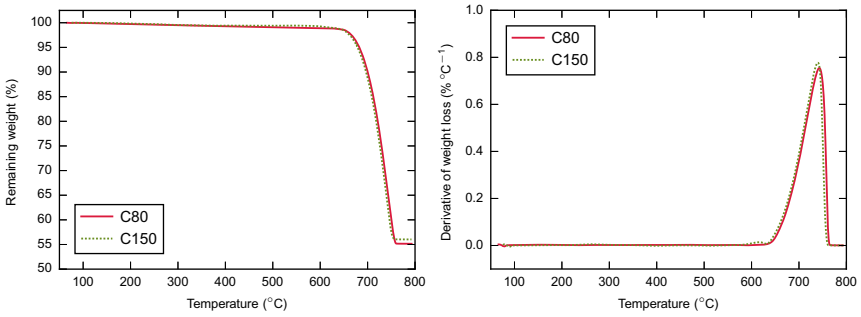

(a) Remaining weight percentage

(b) Derivative of the weight loss percentage with respect to temperature

Fig. 6.6 Thermogravimetric analysis of the $CaCO_3$ samples indicating both the percentage of remaining weight as a function of temperature and the derivative of the weight loss percentage with respect to temperature as a function of temperature

6.3 Characterisation of Undegraded Pure Polymer and Composite Samples

This section contains the results from the characterisation of the undegraded samples. Firstly, the mass and size of the generated samples are reported, followed by density, visual analysis, phase composition, differential scanning calorimetry and lastly, thermogravimetric analysis.

Table 6.9 Mass and size of the undegraded pure polymer and composite samples. Measurements are reported as mean ± standard deviation with a minimum n = 60. D_{max} is the maximum sample diameter, D_{min} the minimum sample diameter, H_{max} is the maximum sample height and H_{min} the minimum sample height

Sample	Mass (mg)	D_{max} (mm)	D_{min} (mm)	H_{max} (mm)	H_{min} (mm)
Pure PLGA	27.8 ± 1.4	3.85 ± 0.11	3.72 ± 0.09	2.22 ± 0.14	2.00 ± 0.08
PLGA-10%C80	29.4 ± 1.1	3.84 ± 0.09	3.66 ± 0.11	2.35 ± 0.18	1.99 ± 0.06
PLGA-20%C80	30.8 ± 0.9	3.86 ± 0.07	3.70 ± 0.09	2.45 ± 0.17	2.01 ± 0.04
PLGA-10%C150	28.6 ± 1.4	3.88 ± 0.08	3.71 ± 0.08	2.37 ± 0.15	1.98 ± 0.08

Table 6.10 Density of the undegraded pure polymer and composite samples. Measurements are reported as mean ± standard deviation

Sample	Density ($kg\,m^{-3}$)
Pure PLGA	1348 ± 35
PLGA-10%C80	1410 ± 32
PLGA-20%C80	1490 ± 29
PLGA-10%C150	1405 ± 31

6.3.1 Mass and Size

As a basic initial physical characterisation, the mass and size of the samples were measured prior to the start of the degradation study, in order to ensure consistency of the manufacture process. Table 6.9 includes the mass and size of the undegraded pure polymer and composite samples. Samples that deviated more than 10% from the mean were discarded. The samples had standard deviation values of less than 5% of the mean pointing to a manufacture process with high reproducibility.

6.3.2 Density

Table 6.10 reports the measured density for the undegraded pure polymer and composite samples. Pure PLGA samples presented the lowest value of density, followed by the PLGA-10%C150 and PLGA-10%C80 and lastly, PLGA-20%C80 with the highest value.

6.3.3 Visual Analysis

Figure 6.7 shows appearance and morphology of a typical sample. Due to the cutting method the samples presented a slight lack of parallelism between the top and bottom facets.

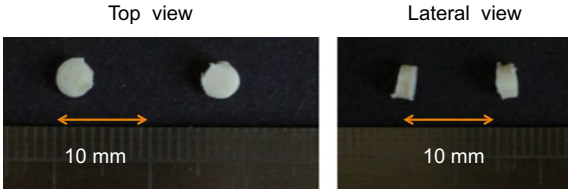

Fig. 6.7 Plan and side views of a typical PLGA–$CaCO_3$ composite sample

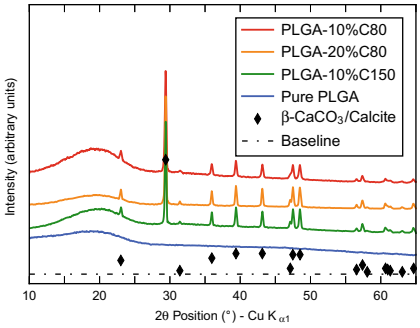

Fig. 6.8 XRD spectra of the undegraded pure polymer and composite samples after the removal of the $K_{\alpha 2}$ peaks with calcite reference peaks indicated. Height, measured from the baseline, of the calcite reference peaks is proportional to the relative intensities reported in the ICDD pattern

6.3.4 Phase Identification

Figure 6.8 shows the XRD spectra of the undegraded pure polymer and composite samples with the calcite reference peaks indicated. For PLGA-10%C80, PLGA-20%C80 and PLGA-10%C150 all the peaks were accounted for solely with the calcite pattern indicating the absence of crystalline impurities. All the samples presented a broad peak at low angles produced by the polymeric matrix. This broad peak was the only one found in the pure PLGA spectrum indicating that the polymer maintained its amorphous structure during processing.

6.3.5 Differential Scanning Calorimetry

Figure 6.9 shows the DSC thermograms, including the glass transition temperature, of the different undegraded pure polymer and composite samples. Table 6.11 reports the measured values of the glass transition temperature for the different samples. The pure PLGA sample presented a lower value of T_g than the as-received polymer and the composite samples presented lower values than the pure PLGA sample.

6.3.6 Thermogravimetric Analysis

Figure 6.10 includes the results of the thermogravimetric analysis for the different samples, depicting one representative TGA run per sample type. The remaining

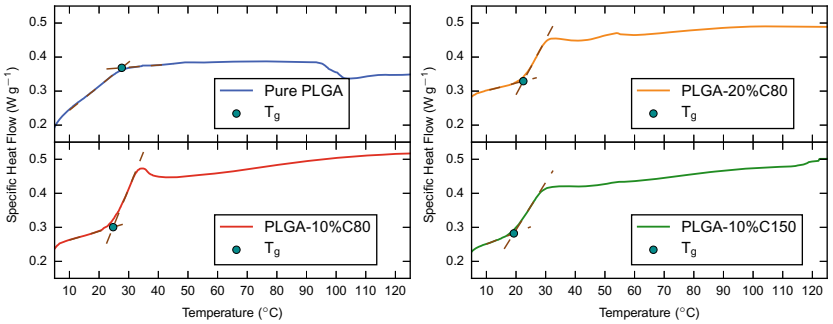

(a) Pure PLGA and PLGA-10%C80 (b) PLGA-20%C80 and PLGA-10%C150

Fig. 6.9 Differential scanning calorimetry analysis of the undegraded pure polymer and composite samples. Exothermic process down. The glass transition temperature, T_g, of each sample was found at the intersection between the specific heat flow baseline extrapolated forward and the step slope extrapolated backwards (dashed brown lines)

Table 6.11 Glass transition temperature (T_g) for undegraded pure polymer and composite samples. Measurements are reported as mean ± standard deviation for three repeats per composite type. Each repeat was taken from a different injection-moulded rod

Sample	T_g (°C)
Pure PLGA	28.41 ± 0.77
PLGA-10%C80	23.31 ± 1.54
PLGA-20%C80	22.04 ± 1.99
PLGA-10%C150	20.95 ± 1.67

weight percentage at 550 °C is considered to be the ceramic weight fraction in the undegraded composite samples as the initial polymer and ceramic analyses showed complete polymer decomposition at around 500 °C and no ceramic decomposition below 640 °C.

Pure PLGA was almost fully disintegrated at temperatures above 370 °C giving a final residue weight of (0.60 ± 0.13)wt % at 550 °C (n = 3). This residue was slightly higher than the residue found in as-received PLGA. All the composite samples presented a similar TGA thermogram profile with weight reduction starting at approximately 220 °C and stabilisation at around 330 °C. Table 6.12 includes the ceramic weight fraction for the different composite samples. The real ceramic weight fraction were fairly close to the intended weight fractions pointing to an accurate manufacture process.

6.4 Characterisation of Degraded Pure Polymer and Composite Samples

This section presents the characterisation of the degraded samples. Firstly, the media pH, mass loss, water uptake and water absorption are presented. Secondly, the wet

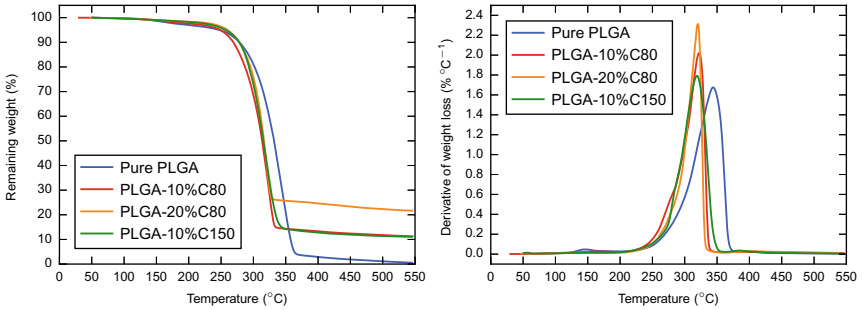

(a) Remaining weight for pure PLGA, PLGA-10%C80, PLGA-20%C80 and PLGA-10%C150

(b) Derivative with respect to temperature of weight loss for pure PLGA, PLGA-10%C80, PLGA-20%C80 and PLGA-10%C150

Fig. 6.10 Thermogravimetric analysis of the undegraded pure polymer and composite samples indicating both the percentage of remaining weight as a function of temperature and the derivative of the weight loss percentage with respect to temperature as a function of temperature

Table 6.12 Ceramic weight fraction for undegraded composite samples. Measurements are reported as mean ± standard deviation for three repeats per composite type. Each repeat was taken from a different injection-moulded rod

Sample	Ceramic weight fraction (wt %)
PLGA-10%C80	11.07 ± 0.30
PLGA-20%C80	21.88 ± 0.37
PLGA-10%C150	11.26 ± 0.18

and dry densities and visual analysis are included and lastly, the phase identification, differential scanning calorimetry and thermogravimetric analysis are reported.

6.4.1 Media pH

Figure 6.11 shows the degradation media pH data for pure polymer and composite samples. The onset of pH drop happened first for the pure PLGA samples, followed by the PLGA-10%C150, PLGA-10%C80 and lastly PLGA-20%C80 samples. The shaded region corresponds roughly to a mass loss, reported in Sect. 6.4.2, of 10 to 20% for the different samples. The final value of the pH plateau ranged from 2.525 to 3.544, with pure PLGA presenting the lowest value, followed by PLGA-10%C150 and PLGA-10%C80, both with a value within 0.001 pH units of 3.153 and lastly, PLGA-20%C80 with the highest value.

The analysis of the media pH values is included in Fig. 6.12, with the normalised and centred curves in Fig. 6.12a and the derivative of pH with respect to time in Fig. 6.12b. To facilitate the comparison, the pH curves were normalised to a 0 to 1 range and centred with a value of 0.5 at the time origin. To compute the derivative of the pH curves, linear splines were fitted to the data and smoothed using a

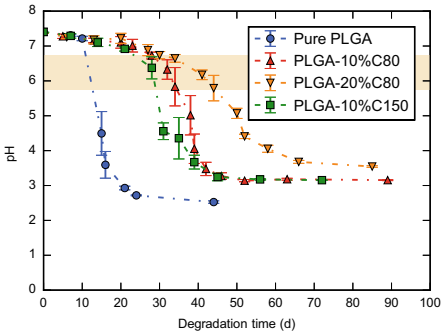

Fig. 6.11 Evolution of degradation media pH over time for pure polymer and composite samples, expressed as mean values ± standard deviation for a minimum of five repeats per timepoint. Dash-dot lines are shown for clarity only. The beige stripe corresponds to a mass loss, reported in Sect. 6.4.2, of 10–20% for the different samples

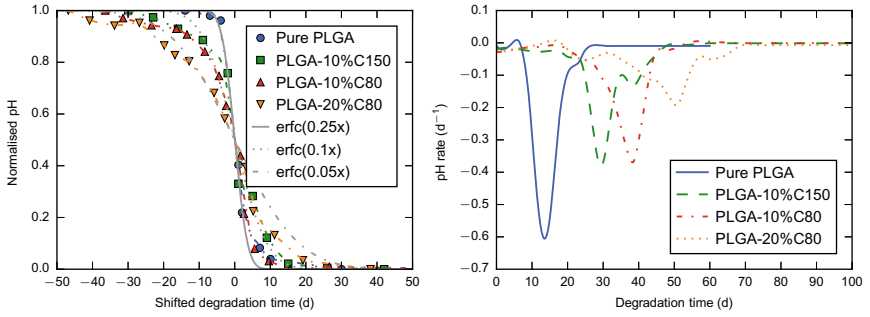

(a) Normalised and centred pH curves (b) Time derivative of media pH

Fig. 6.12 Analysis of media pH values for degraded pure polymer and composite samples including normalised and centred pH curves and pH derivative with respect to time

Savitzky-Golay filter, then quadratic splines were fitted using the smoothed data. The pH derivatives were computed as linear splines resulting from the analytical derivation of the quadratic splines.

All the pH curves presented the shape of the complementary error function, or complementary sigmoid function, as can be seen in Fig. 6.12a, with no or little pH change in the initial stage, followed by a sudden drop until a plateau of minimum value is reached, with different samples presenting variable abruptness in the changes. The pH derivatives, found in Fig. 6.12b, had an initial zero value, followed by a peak and a second stage at null value. The derivative of pure PLGA presented the shortest initial stage and highest absolute value of the peak, followed by PLGA-10%C150 and PLGA-10%C80 with longer initial stages and shorter peaks and lastly, PLGA-20%C80 with the longest initial stage and shortest peak. Both analyses suggested that

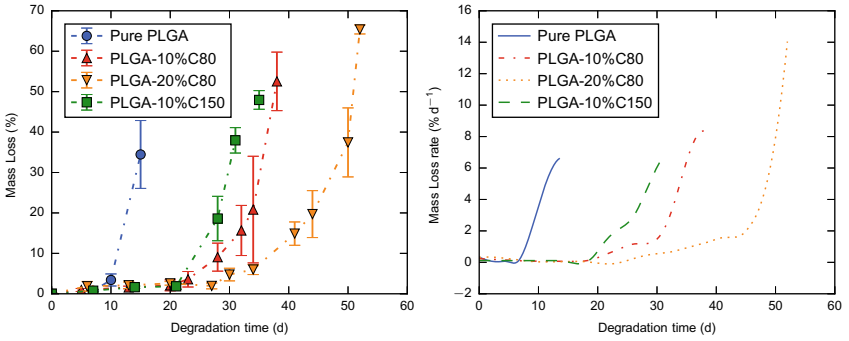

(a) Mass loss (b) Mass loss rate

Fig. 6.13 Evolution of mass loss and mass loss derivative with respect to time (mass loss rate) over degradation time for pure polymer and composite samples, expressed as mean values ± standard deviation for a minimum of three repeats per timepoint for mass loss. Dash-dot lines are shown for clarity only. Mass loss rate computed from mass loss data

the addition of C80 and C150 caused a decrease in the degradation kinetics, resulting in delayed and smoother changes, with a more pronounced effect for smaller particles and higher weight fractions.

6.4.2 Mass Loss

Figure 6.13 presents the mass loss and mass loss rate for pure polymer and composite samples while the samples maintained their mechanical integrity. The onset of mass loss, depicted in Fig. 6.13a, followed the same sequence as the pH drop onset: first pure PLGA, followed by PLGA-10%C150, PLGA-10%C80 and lastly PLGA-20%C80. All the mass loss curves showed a similar behaviour with a initial stage of almost negligible mass loss followed by an stage where mass loss became more significant resulting in the collapse of the sample. The mass loss rate, computed from the mass loss data using fitted quadratic splines, is shown in Fig. 6.13b. All curves presented an initial stage with zero value followed by an incremental increase. Pure PLGA had the earliest and sharpest increase, followed by PLGA-10%C150 and PLGA-10%C80 and lastly, PLGA-20%C80 with the latest and smoothest increase.

6.4.3 Water Uptake and Water Absorption

The water uptake and water absorption for pure polymer and composite samples are included in Fig. 6.14. Water uptake, depicted in Fig. 6.14a followed a similar trend in all the samples with an initial monotonic increase, followed by a plateau before

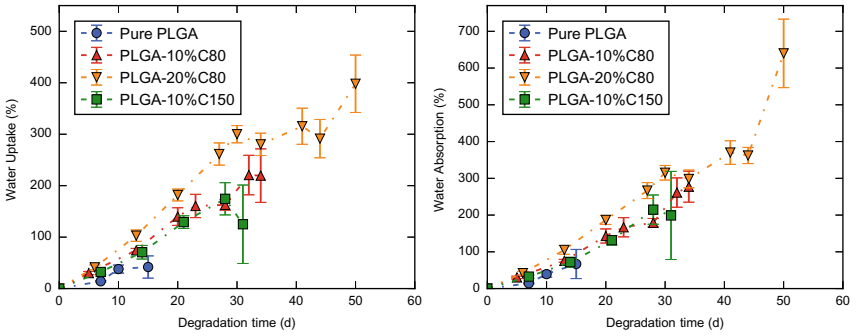

(a) Water uptake (b) Water absorption

Fig. 6.14 Evolution of water uptake and water absorption over degradation time for pure polymer and composite samples, expressed as mean values ± standard deviation for a minimum of three repeats per timepoint. Dash-dot lines are shown for clarity only

sample collapse. The trend in water absorption, presented in Fig. 6.14a was similar to the water uptake trend, only deviating in the final stage when mass loss became significant, causing a lack of final plateau.

6.4.4 Wet and Dry Density

Figure 6.15 shows the evolution of both the wet (Fig. 6.15a) and dry (Fig. 6.15b) densities for the pure polymer and composite samples. All the samples presented a similar wet density pattern with an initial decrease followed by a plateau. Conversely, the dry density pattern displayed by the composites presented an initial increase followed by a decrease.

6.4.5 Visual Analysis

Figure 6.16 depicts the visual appearance over degradation time for pure polymer and composite samples using one representative sample per studied timepoint. All the PLGA–β-$CaCO_3$ composite samples displayed a similar behaviour characterised by an initial swelling (◆) of the sample, causing an increase in sample diameter while still maintaining circular shape. Then, the composites presented a concave appearance (▲) as a result of the faster inner degradation, followed by a flatter aspect (■) caused by further degradation. Immediately after the collapse, the sample presented a hollow shell structure (⬢) and lastly, the degradation of the shell gave a viscous behaviour to the remains of the sample (☆). The pure PLGA went from swelling directly to viscous remains.

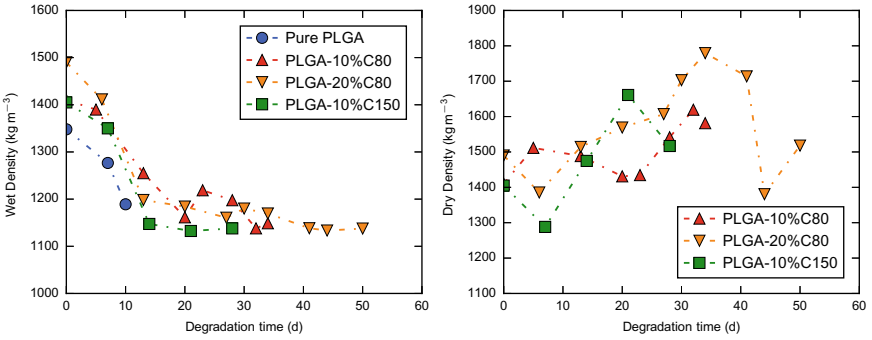

(a) Wet density for pure PLGA, PLGA-10%C80, PLGA-20%C80 and PLGA-10%C150

(b) Dry density for PLGA-10%C80, PLGA-20%C80 and PLGA-10%C150

Fig. 6.15 Evolution of wet and dry density over degradation time for pure polymer and composite samples. Dash-dot lines are shown for clarity only

6.4.6 Phase Identification

The XRD spectrum of the PLGA-20%C80 after 44 days of degradation is included in Fig. 6.17 with the calcite reference peaks indicated. All the peaks were accounted for solely with the calcite pattern indicating the absence of crystalline phases from the reprecipitation of the dissolved Ca^{2+} and CO_3^{2-} ions.

6.4.7 Differential Scanning Calorimetry

Figure 6.18 contains the value of the glass transition temperature, measured from the DSC analyses, for composite samples. All the PLGA–$CaCO_3$ composites experienced the same trend with an initial stage characterised by a T_g increase, followed by a decrease to a value in the vicinity of the initial.

The DSC thermograms of selected PLGA-20%C80 composite samples, indicating the value of T_g, are included in Fig. 6.19. Although all the timepoints showed a similar pattern, there was a clear change in the value of the glass transition temperature over time.

6.4.8 Thermogravimetric Analysis

The evolution of the ceramic weight percentage over degradation time for only two of the composite samples, PLGA-20%C80 and PLGA-10%C150, is shown in Fig. 6.20. Both composites displayed a similar behaviour with an increase in ceramic-polymer ratio during the first half of their degradation time followed by a decrease in the second half, finishing in close proximity of the initial values.

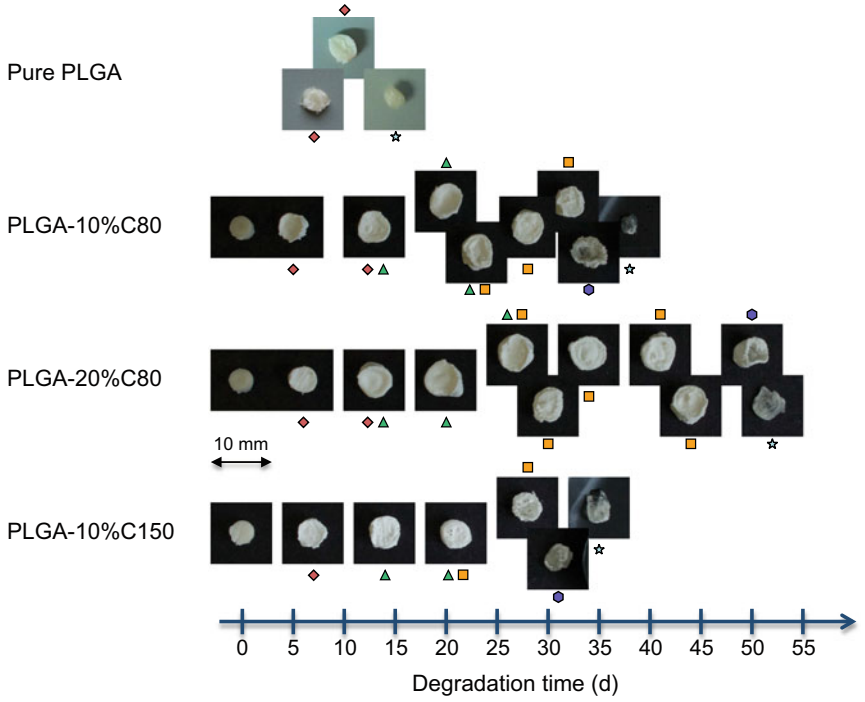

Fig. 6.16 Evolution of visual appearance over degradation time for pure polymer and composite samples. The horizontal coordinate of the centre of each depicted sample indicates its degradation time. PLGA images were taken as part of the wet analysis and composite images were taken as part of the dry analysis. The different morphological stages experienced by the samples are indicated using symbols: swelling (◆), concave surfaces (▲), flat surfaces (■), hollow shell (⬢) and viscous remains (☆)

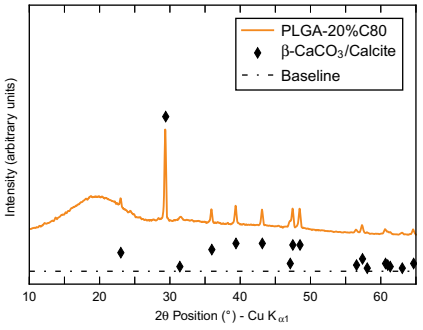

Fig. 6.17 XRD spectrum of degraded PLGA-20%C80 after the removal of the $K_{\alpha 2}$ peaks with calcite reference peaks indicated. Height, measured from the baseline, of the calcite reference peaks is proportional to the relative intensities reported in the ICDD pattern

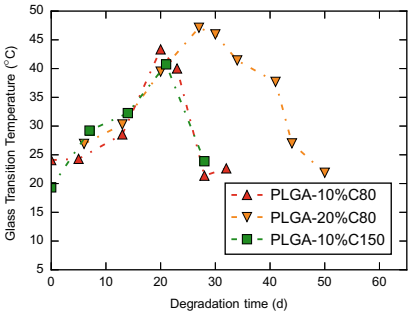

Fig. 6.18 Evolution of the glass transition temperature in composite samples over degradation time with only one repeat per timepoint. Dash-dot lines are shown for clarity only

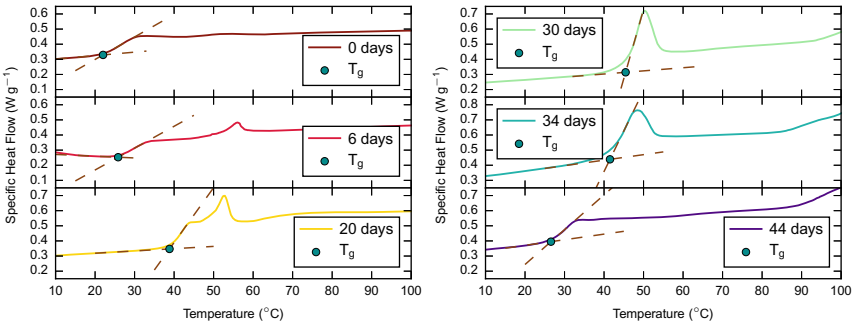

(a) Specific heat flow for samples degraded for 0, 6 and 20 days

(b) Specific heat flow for samples degraded for 30, 34 and 44 days

Fig. 6.19 Differential scanning calorimetry analysis of selected degraded PLGA-20%C80 composite samples with different values of degradation time. Exothermic process down. The glass transition temperature, T_g, of each sample was found at the intersection between the specific heat flow baseline extrapolated forward and the step slope extrapolated backwards (dashed brown lines)

Figure 6.21 contains the thermograms obtained for the different analysed PLGA-20%C80 timepoints including the remaining weight as a function of temperature and the derivative of the weight loss with respect to temperature. As degradation proceeded the polymer degradation started and finished at lower temperature values.

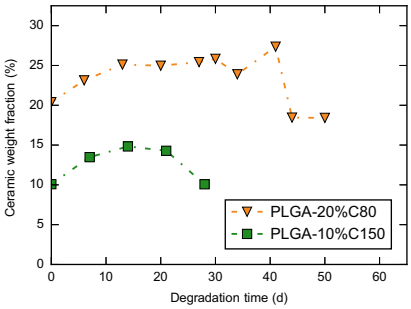

Fig. 6.20 Evolution of the ceramic weight percentage in PLGA-20%C80 and PLGA-10%C150 composite samples over degradation time with only one repeat per timepoint. Dash-dot lines are shown for clarity only

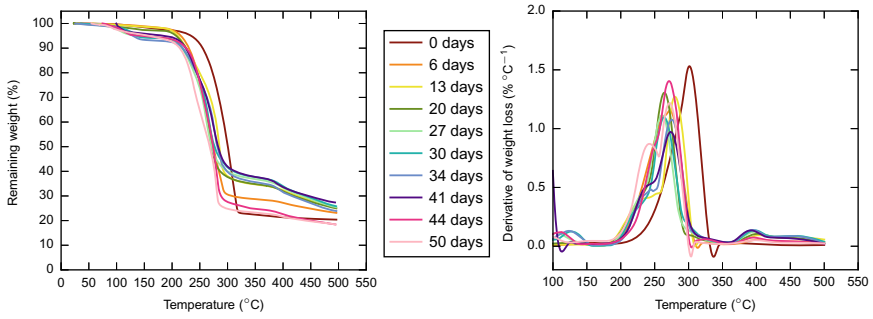

(a) Remaining weight for different timepoints

(b) Derivative with respect to temperature of weight loss for different timepoints

Fig. 6.21 Thermogravimetric analysis of the degraded PLGA-20%C80 composite samples indicating both the percentage of remaining weight as a function of temperature and the derivative of the weight loss percentage with respect to temperature as a function of temperature for different values of degradation time

6.5 Discussion of PLGA–$CaCO_3$ Degradation

This section discusses the characteristics of the PLGA–$CaCO_3$ nanocomposites using the information presented in Sects. 6.2, 6.3 and 6.4.

6.5.1 Raw Materials

The chosen raw materials were a medium molecular weight poly(D,L-lactide-co-glycolide)(50:50) with amorphous structure and a glass transition temperature above

physiological value (DSC analysis in Sect. 6.2.5), thermally stable up to 220 °C with a negligible residue at 500 °C (TGA analysis in Sect. 6.2.6), and two types of calcium carbonate particles, namely C80 and C150, with a monophasic calcite composition (XRD analysis in Sect. 6.2.3), an uniform cubic shape, particle sizes of (88 ± 19) nm (C80) and (164 ± 33) nm (C150) and a really narrow particle size distribution (SEM analysis in Sect. 6.2.1), fully dense (pycnometer analysis in Sect. 6.2.4), with C80 doubling C150 in specific surface area value (SSA analysis in Sect. 6.2.2) and showing thermal instability only above 640 °C (TGA analysis in Sect. 6.2.6).

6.5.2 Manufacturing Process

The employed manufacturing process, described in Sect. 6.1.3 and shown to provide an even distribution of nanoparticles throughout the matrix [5], yielded pure polymer and composite disks with a whitish appearance (visual analysis in Sect. 6.3.3), slightly bigger than the used mould in a reproducible manner in terms of mass and size (mass and size analysis in Sect. 6.3.1), density values increasing with ceramic content and similar to the ones measured by Barrett and Cameron [12, 13] for dense PLGA(50:50)–α-TCP composites suggesting dense structure (density analysis in Sect. 6.3.2), no crystalline impurities or crystalline regions in the polymer phase (XRD results in Sect. 6.3.4), a decrease of the glass transition temperature for all samples when compared with the as-received PLGA pointing to some expected polymer degradation during injection-moulding and with composites T_g values lower than pure polymer values as previously reported by Wilberforce and co-workers for PLGA(50:50)–α-TCP composites and attributed to the large interfacial area and poor polymer-ceramic bonding [14, 15] (DSC analysis in Sect. 6.3.5), slightly higher than intended ceramic weight fractions and well-distributed fillers, as indicated by the ceramic weight fraction reproducibility (TGA analysis in Sect. 6.3.6).

6.5.3 Degradation Behaviour

The discussion of the degradation behaviour is structured in two different parts. Firstly, the common trends, applicable to all the samples are listed while secondly, the specific changes resulting from different parameters such as presence of ceramic, ceramic size and ceramic weight fraction are presented. To facilitate the discussion, the comparisons between pH and mass loss, and mass change and water uptake are included in Fig. 6.22.

General Degradation Pattern

All the analysed samples presented a similar degradation pattern. Firstly, water started entering the samples (Sect. 6.4.3), causing swelling (Sect. 6.4.5) and a decrease in wet density (Sect. 6.4.4), while the pH remained relatively constant at physiological

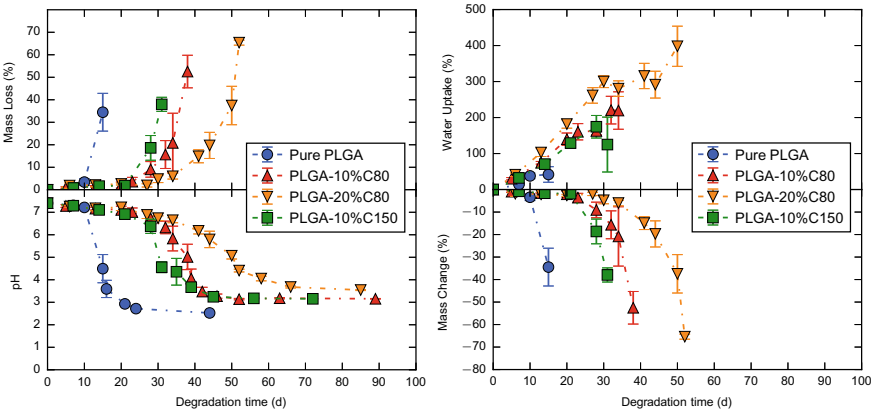

(a) Media pH and mass loss comparison (b) Mass change and water uptake comparison

Fig. 6.22 Comparisons between the evolution of media pH and mass loss, and mass change and water uptake over degradation time for pure polymer and composite samples. Mass change is mass loss expressed in a negative axis. Dash-dot lines are shown for clarity only

value (Sect. 6.4.1) and there was no mass loss (Sect. 6.4.2). As water penetrated, both the PLGA and the β-$CaCO_3$ started experiencing degradation, by means of hydrolysis in the polymer matrix and dissolution in the ceramic filler. During a period of time, degradation continued, preferentially in the sample core where the degradation products accumulated, causing samples to increase its water content, decrease its wet density until it plateaued and show first concave surfaces and later flat facets when dried, with the samples maintaining their mechanical integrity and little change in both pH and mass loss. When the samples reached a critical point, a perforation of the outer shell caused the collapse of the samples with the subsequent release of the acidic degradation products into the buffering media causing a simultaneous drop in pH and increase in mass loss. Then, the outer shell continued degrading resulting in remains with a viscous behaviour. By the end of degradation there was no mass left and the media pH of the media had a stable value.

The samples experienced heterogeneous bulk degradation as previously seen for TCP composites with a similar polymeric matrix by Barrett [12, 13] and Bennett [16]. The core degraded much faster than the outer layer due to the inability of the inner hydrogen ions to diffuse out of the samples, resulting in hollow composite shells as commonly reported for polymeric and composite devices made of poly(α-hydroxy-acids) [17–20].

Analysis of the Specific Differences

The results showed that the addition of nano-structured β-$CaCO_3$ particles, a sparingly soluble calcium-based ceramic, to the poly(D,L-lactide-co-glycolide) matrix caused a reduction in degradation kinetics, referred in this work as buffering effect, resulting in a delayed onset of both mass loss and subsequent pH drop as shown by

the analysis of media pH, including a cross-comparison between samples and the derivative with respect to time (Sect. 6.4.1), and the mass loss analysis, including mass loss rate (Sect. 6.4.2), as previously reported in literature [1–4].

The sample degradation happened in the following order: pure PLGA, PLGA-10%C150, PLGA-10%C80 and lastly, PLGA-20%C80 suggesting two phenomena:

- When two samples had the same ceramic weight fraction, f_{wCer0}, using particles with a smaller representative ceramic particle size, d_0, resulted in a higher buffering effect as previously reported [20, 21], in agreement with the unit cell analysis included in Sect. 3.3.
- When two samples had the representative ceramic particle size, d_0, using a higher ceramic weight fraction, f_{wCer0}, resulted in a higher buffering effect as previously reported [12, 13, 20–22], also in agreement with the unit cell analysis included in Sect. 3.3.

Using a ceramic with smaller d_0 or a higher f_{wCer0} caused a similar effect, because both changes increased the overall ratio of ceramic surface area per unit of polymer volume as captured in the modelling framework unit cell.

The final value of the media pH (Sect. 6.4.1) showed that both β-$CaCO_3$ samples, C80 and C150, possessed the same total buffering potential as both PLGA-10%C80 and PLGA-10%C150, with the same polymer-ceramic ratio and thus, same ratio of acidity to buffering sources, presented the same final pH value, higher than pure PLGA final and lower than PLGA-20%C80. However, the evolution of the media pH value was different, as mentioned above, highlighting the importance of the role of particle size in the accessibility of the buffering potential.

Tsunoda carried out a similar experimental study with nanocomposites made of poly(D,L-lactide-co-glycolide)(44.6:55.4) and calcite cubes of three different sizes with disk-shaped samples and a ceramic weight fraction $f_{wCer0} = 50\%$ with significant agglomeration. The study showed almost no difference in the variation of pH media over time among the three employed particle sizes: 0.7, 1.7 and 3.0 μm, suggesting saturation of the buffering effect due to a high f_{wCer0} [1]. Conversely, the variation of media pH in the present study suggested that the highest employed f_{wCer0} value was below the saturation point.

The water uptake and absorption values (Sect. 6.4.3) were slightly lower for pure polymer than for composite samples as previously seen by Naik and co-workers [23–25], which in a water-controlled hydrolysis scenario would mean that the buffering effect of the calcite particles is even greater than measured. The evolution of the dry density in composites (Sect. 6.4.4) could be explained by an initial compaction of the samples during polymer degradation followed by an increasing loss of mass while maintaining the volume. The XRD analysis (Sect. 6.4.6) showed no recombination of the dissolved ceramic ions into a crystalline phase suggesting their availability for buffering the polymer acidity. As expected, the TGA analysis (Sect. 6.4.8) showed a decrease in polymer degradation temperature boundary with degradation time.

To facilitate the discussion of the changes over degradation time in glass transition temperature, T_g, and ceramic weight fraction, f_{wCer0}, for the composite samples,

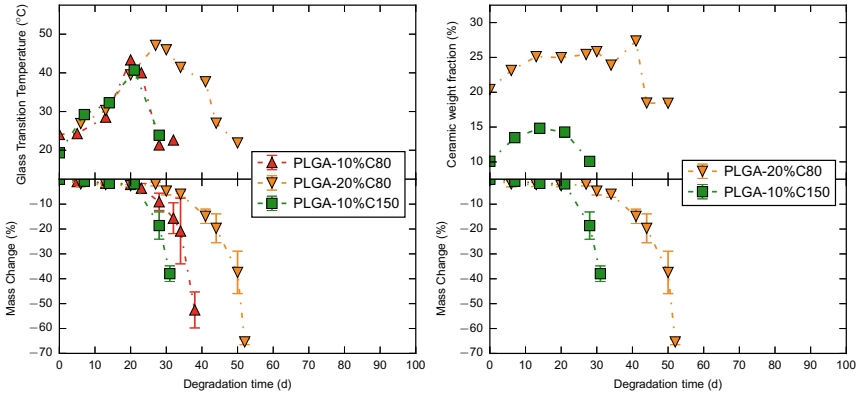

(a) Mass change and Tg comparison

(b) Mass change and ceramic weight fraction comparison

Fig. 6.23 Comparisons between the evolution of mass change and glass transition temperature, and mass change and ceramic weight fraction over degradation time for composite samples. Dash-dot lines are shown for clarity only

Fig. 6.23 includes the comparisons between mass change, defined as $-M_L$, T_g and f_{wCer0}.

The pattern followed by the ceramic weight fraction for both PLGA-20%C80 and PLGA-10%C150 (Sect. 6.4.8) could be explained considering the different degradation stages. While there was no significant mass loss, faster polymer degradation when compared to ceramic dissolution caused an increase in the ceramic-polymer ratio. When mass loss started to become significant, the ceramic weight fraction decreased as the released composite mass was ceramic rich, leaving behind a composite mass with a greater representation of the undegraded outer shell as seen before by Ege [26].

The T_g pattern was unusual, with an initial increase during the first half of the degradation time followed by a decrease, while literature data showed an initial decrease followed by an increase for PLGA(50:50) data [27, 28] with the initial decrease reflecting a drop in molecular weight [29]. Considering that poly(D,L-lactide) has a T_g of 50…60 °C and poly(glycolide) of 35 °C, the increase in T_g could be partially explained by a preferential degradation of the glycolic units [30, 31] coupled with the reported mass change although further research is needed to clarify it.

6.6 Conclusions

The main conclusions from the experimental study of the degradation behaviour of PLGA–$CaCO_3$ nanocomposites are listed below:

- Both PLGA and PLGA–β-$CaCO_3$ composites experienced heterogeneous bulk degradation.
- The addition of nano-structured calcite, a sparingly soluble calcium-based ceramic, in two different sizes and weight fractions to the polymeric matrix caused a buffering effect during composite degradation, causing a delay of all the associated degradation phenomena such as mass loss and pH drop onset.
- The use of particles with a smaller representative particle size d_0 or the use of a higher ceramic weight fraction f_{wCer0} increased the extent of the observed buffering effect pointing to a proportionality between buffering effect and ceramic surface area per unit of polymer volume.

In summary, this chapter has studied the degradation behaviour of PLGA–$CaCO_3$ nanocomposites, including two different particle sizes and ceramic weight fractions. The ceramic filler, extremely consistent in both particle size and shape, presents a good opportunity for an exhaustive analysis of the role of particle size and ceramic weight fraction in composite degradation. Said analysis, carried out with the CC composites degradation model reported in the next chapter, employs a combination of pH and mass loss data as detailed in Sect. 3.5. In addition to this analysis, Chap. 7 contains the remaining harvested and analysed CC composites degradation data.

References

1. Tsunoda, M. (2003). Degradation of poly(DL-lactic acid-co-glycolic acid) containing calcium carbonate and hydroxyapatite fillers-effect of size and shape of the fillers. *Dental Materials Journal*, *22*(3), 371–382.
2. Ara, M., Watanabe, M., & Imai, Y. (2002). Effect of blending calcium compounds on hydrolytic degradation of poly(DL-lactic acid-co-glycolic acid). *Biomaterials*, *23*(12), 2479–2483.
3. Agrawal, C. M., & Athanasiou, K. A. (1997). Technique to control pH in vicinity of biodegrading PLA-PGA implants. *Journal of Biomedical Materials Research*, *38*(2), 105–114.
4. Cotton, N. J., Egan, M. J., & Brunelle, J. E. (2008). Composites of poly(DL-lactide-co-glycolide) and calcium carbonate: In vitro evaluation for use in orthopedic applications. *Journal of Biomedical Materials Research Part A*, *85*(1), 195–205.
5. Yang, Z., Thian, E., Best, S., & Cameron, R. (2007). A novel way of dispersing fine ceramic particles in PLGA matrix. *Key engineering materials* (Vol. 330, pp. 511–514). Stafa-Zuerich: Trans Tech Publications.
6. Quorum EmiTech (1999). *Instruction manual for EmiTech K550 sputter coater*.
7. Micromeritics (1996). *Instruction manual for AccuPyc 1330 pycnometer*.
8. Graf, D. (1961). Crystallographic tables for the rhombohedral carbonates. *American Mineralogist*, *46*(11–2), 1283–1316.
9. De Villiers, J. P. R. (1967). *The crystal structures of aragonite, strontianite, and witherite*. Ph.D. thesis, University of Illinois at Urbana-Champaign.
10. Kamhi, S. R. (1963). On the structure of vaterite, $CaCO_3$. *Acta Crystallographica*, *16*(8), 770–772.
11. Mindat Online Database (2016b). *Calcite*. Retrieved September 1, 2016, from http://www.mindat.org/min-859.html.

12. Barrett, C. E., & Cameron, R. E. (2014). X-ray microtomographic analysis of α-tricalcium phosphate-poly(lactic-co-glycolic) acid nanocomposite degradation. *Polymer*, *55*(16), 4041–4049.
13. Barrett, C. E. (2013). *The degradation behaviour of tricalcium phosphate - poly(lactide-co-glycolide) nanocomposites*. Ph.D. thesis, Department of Materials Science and Metallurgy, University of Cambridge.
14. Wilberforce, S. I., Best, S. M., & Cameron, R. E. (2010). A dynamic mechanical thermal analysis study of the viscoelastic properties and glass transition temperature behaviour of bioresorbable polymer matrix nanocomposites. *Journal of Materials Science: Materials in Medicine*, *21*(12), 3085–3093.
15. Wilberforce, S. I., Finlayson, C. E., Best, S. M., & Cameron, R. E. (2011). The influence of the compounding process and testing conditions on the compressive mechanical properties of poly(D, L-lactide-co-glycolide)/α-tricalcium phosphate nanocomposites. *Journal of the Mechanical Behavior of Biomedical Materials*, *4*(7), 1081–1089.
16. Bennett, S. M. (2012). *Degradation mechanisms of PLGA/α-TCP composites for orthopaedic applications*. Ph.D. thesis, Department of Materials Science and Metallurgy, University of Cambridge.
17. Li, S., Garreau, H., & Vert, M. (1990a). Structure-property relationships in the case of the degradation of massive poly(α-hydroxy acids) in aqueous media. Part 1: Poly(DL-lactic acid). *Journal of Materials Science: Materials in Medicine*, *1*, 123–130.
18. Li, S., Garreau, H., & Vert, M. (1990b). Structure-property relationships in the case of the degradation of massive poly(α-hydroxy acids) in aqueous media. Part 2: Degradation of lactide-glycolide copolymers: PLA37.5GA25 and PLA75GA25. *Journal of Materials Science: Materials in Medicine*, *1*(3), 131–139.
19. Grizzi, I., Garreau, H., Li, S., & Vert, M. (1995). Hydrolytic degradation of devices based on poly(DL-lactic acid) size-dependence. *Biomaterials*, *16*(4), 305–311.
20. Yang, Z., Best, S. M., & Cameron, R. E. (2009). The influence of α-tricalcium phosphate nanoparticles and microparticles on the degradation of poly(D, L-lactide-co-glycolide). *Advanced Materials*, *21*(38–39), 3900–3904.
21. Yang, Z. (2009). *Development and characterisation of bioactive, bioresorbable α-tricalcium phosphate/poly(D,L-lactide-co-glycolide) nanocomposites for bone substitution and fixation*. Ph.D. thesis, Department of Materials Science and Metallurgy, University of Cambridge.
22. Ehrenfried, L. M., Patel, M. H., & Cameron, R. E. (2008). The effect of tri-calcium phosphate (TCP) addition on the degradation of polylactide-co-glycolide (PLGA). *Journal of Materials Science: Materials in Medicine*, *19*(1), 459–466.
23. Naik, A., Best, S. M., & Cameron, R. E. (2015). The influence of silanisation on the mechanical and degradation behaviour of PLGA/HA composites. *Materials Science and Engineering: C*, *48*, 642–650.
24. Naik, A., Shepherd, D. V., Shepherd, J. H., Best, S. M., & Cameron, R. E. (2017). The effect of the type of HA on the degradation of PLGA/HA composites. *Materials Science and Engineering: C*, *70*, 824–831.
25. Naik, A. (2012). *Effect of calcination and silanisation on the degradation of poly(DL Lactic-co-glycolic acid)-hydroxyapatite composites*. Ph.D. thesis, Department of Materials Science and Metallurgy, University of Cambridge.
26. Ege, D. (2012). *Mechanical and degradation properties of calcium phosphate/biodegradable polymer composites*. Ph.D. thesis, Department of Materials Science and Metallurgy, University of Cambridge.
27. Schliecker, G., Schmidt, C., Fuchs, S., Wombacher, R., & Kissel, T. (2003). Hydrolytic degradation of poly(lactide-co-glycolide) films: Effect of oligomers on degradation rate and crystallinity. *International Journal of Pharmaceutics*, *266*(1–2), 39–49.
28. Vey, E., Roger, C., Meehan, L., Booth, J., Claybourn, M., Miller, A. F., et al. (2008). Degradation mechanism of poly(lactic-co-glycolic) acid block copolymer cast films in phosphate buffer solution. *Polymer Degradation and Stability*, *93*(10), 1869–1876.

29. Fox, T. G, Jr., & Flory, P. J. (1950). Second-order transition temperatures and related properties of polystyrene. I. Influence of molecular weight. *Journal of Applied Physics*, *21*(6), 581–591.
30. Alexis, F., Venkatraman, S., Kumar Rath, S., & Gan, L.-H. (2006). Some insight into hydrolytic scission mechanisms in bioerodible polyesters. *Journal of Applied Polymer Science*, *102*(4), 3111–3117.
31. Hakkarainen, M., Albertsson, A.-C., & Karlsson, S. (1996). Weight losses and molecular weight changes correlated with the evolution of hydroxyacids in simulated in vivo degradation of homo-and copolymers of PLA and PGA. *Polymer Degradation and Stability*, *52*(3), 283–291.

Chapter 7
Degradation of Bioresorbable Composites: Calcium Carbonate Case Studies

This chapter includes the analysis of the degradation of calcium carbonate (CC) composites employing the CC composites degradation model described in Sect. 3.2.3. In addition, it presents a second analysis of the experimental data presented in Chap. 6 using an extended method which takes advantage of the detailed nature of the data. Chapter 7 is the third and last chapter dealing with the use of the ceramic-specific degradation models, derived from the general modelling framework, to analyse the degradation of biocomposites and thus, presents a structure similar to Chaps. 4 and 5. The first section, Sect. 7.1, presents the calcium carbonate composite degradation data harvested from literature. Section 7.2 reports the different types of calcium carbonate encountered in the harvested data and the values of the ceramic-dependent constant for each one of them. Similarly to Chap. 5, the values of the polymer-dependent constants are not included. Those values can be found in Sect. 4.3. The values at the time origin of the variables employed in the CC composites degradation model are included in Sect. 7.3. The results of the degradation simulations are presented in Sect. 7.4, followed by the discussion in Sect. 7.5. Section 7.6 contains the conclusions derived from the different analyses of the degradation of calcium carbonate composites. The detailed analysis of Chap. 6 data is presented in Sect. 7.7. And lastly, in addition to the calcium carbonate specific conclusions, Sect. 7.8 contains a summary of the core insights derived from the composite degradation analyses carried out in Chaps. 4, 5 and 7 with the three ceramic-specific computational models.

7.1 Degradation Data from Calcium Carbonate Composites and Composite-Dependent Constants for the Calcium Carbonate Composites Model

This section includes the calcium carbonate composites experimental data harvested from literature. Firstly, several composite-dependent constants in addition to other composite degradation characteristics are presented in a tabular form, as they are

I. Moreno-Gomez, *A Phenomenological Mathematical Modelling Framework for the Degradation of Bioresorbable Composites*,
Springer Theses, https://doi.org/10.1007/978-3-030-04990-4_7

different for each case study. Secondly, the remaining composite-dependent constants, which are common across all the calcium carbonate case studies, are discussed. The harvested data resulted from a search of the available literature conducted according to the method described in Sect. 3.5.2. Following the structure employed in Chaps. 4 and 5, the harvested data can be grouped in two different categories: polymer characteristics and ceramic characteristics. The first category includes several characterising parameters of the polymeric matrix: polymer type, molar ratio of monomers for the case of copolymers, initial number-average molecular weight, M_{n0} (kDa) and type of reported data reflecting composite degradation. The second category includes several characterising parameters of the ceramic filler: ceramic type, initial ceramic weight fraction of the composite samples, f_{w0} (wt%); ceramic representative particle size, d_0(μm) and ceramic data available to compute the ceramic representative particle size. The extracted data were processed as described in Sect. 3.5.2.

Other relevant degradation information, mostly concerning composite characteristics rather than polymer or ceramic characteristics, was also harvested for each studied calcium carbonate composite degradation case. Those characteristics included fabrication method, sample morphology and structure, as well as sample degradation protocol and are presented in Appendix B.3 alongside the results for each analysed case study as they are not considered explicitly in the modelling framework.

Table 7.1 presents the above-mentioned input information employed to analyse the degradation of calcium carbonate composites using the CC composites degradation model described in Sect. 3.2.3. The data are ordered alphabetically by polymer type including first the homopolymers, followed by copolymers and blends. For similar polymer types, enantiopure matrixes are presented first. When several cases concerned the same polymeric matrix the cases were ordered according to ceramic type and initial polymer molecular weight. Each row in the table represents one case study and is separated from the rest by either a solid or a dashed line. A dashed line is used when consecutive cases were generated by the same author or research group and a solid line is used when there is no known author relationship. Calcium carbonate type is described using abbreviations. Briefly, CC stands for calcium carbonate and the preceding Greek letter indicates the allotrope. A complete list of calcium carbonate types including full denominations can be found in Table 7.2.

Having now presented three of the composite-dependent constants for each calcium carbonate case study in Table 7.1, the values of the remaining nine composite-dependent constants are discussed here. Similarly to the TCP composites degradation model, the CC composites degradation model does not considered water self-ionisation and therefore the value of the initial hydroxide ions concentration, $\Delta C_{OH_0^-}$ (mol m^{-3}), is not necessary.

As the polymer chains acid dissociation is the only hydrogen ions source considered in the model, the initial hydrogen ions concentration not resulting from carboxylic end groups dissociation, $\Delta C_{H_0^+}$, takes the value 0 mol m^{-3}. The calcium carbonate case studies employed a mixture of random and end scission, previously used by Pan et al. [8], and characterised by:

Table 7.1 Summary of data found in literature on degradation of composites made of biodegradable polymer and calcium carbonate. *CMR* is the molar ratio of the different monomers in a copolymer, M_{n0} is the sample initial number-average molecular weight, f_{w0} is the initial ceramic weight fraction of a composite sample and d_0 is the ceramic representative particle size of the undegraded composite sample. Further abbreviations employed in columns labelled "Data" can be found in Sect. 3.5.2. Abbreviations used to specify the calcium carbonate type can be found in Table 7.2. A dashed line between rows indicates that data displayed in those consecutive rows belong to the same researcher or research group. A solid line between rows indicates no known author relationship for the data

Polymer characteristics				Ceramic characteristics				Case code and reference
Type	CMR (mol %)	M_{n0} (kDa)	Data	Type	f_{w0} (wt %)	d_0 (μm)	Data	
Poly(L-lactide)	–	145.00	$M_n(t)$	μ-CC	60	1	d_{mean} in text	Wakita K μ-CC [1]
Poly(L-lactide)	–	211.00	$M_n(t)$	μ-CC	60	1	d_{mean} in text	Wakita M μ-CC [1]
Poly(L-lactide)	– –	127.00 127.00	$M_n(t)$	– λ-CC	0 20	– 17.5	d_{mean} in text	Liu λ-CC [2]
Poly(L-lactide)	– –	127.00 127.00	$M_n(t)$	– μ-CC	0 20	– 17.5	d_{mean} in text	Liu λ-CC [2]
Poly(D,L-lactide)	50:50 50:50	98.26 98.26	$M_w(t)$ and $PDI(t_0)$	– λ-CC	0 60	– 388	$f_n(300, 450)$ μm	Li λ-CC [3]
Poly(D,L-lactide-co-glycolide)	44.6:55.4 44.6:55.4	8.60 9.00	$\%M_w(t)$ and $PDI(t_0)$	– β-CC	0 30	– 30	Assumed	Ara β-CC [4]

(continued)

Table 7.1 (continued)

Polymer characteristics				Ceramic characteristics				Case code and reference
Type	CMR (mol%)	M_{n0} (kDa)	Data	Type	f_{w0} (wt%)	d_0 (μm)	Data	
Poly(D,L-lactide-co-glycolide)	44.6:55.4 44.6:55.4 44.6:55.4 44.6:55.4	11.40 9.70 9.00 8.60	$M_n(t)$	– β-CC β-CC β-CC	0 50 50 50	– 0.7 1.3 3.0	d_{cube} in text	Tsunoda β-CC [5]
Poly(D,L-lactide-co-glycolide)	44.6:55.4 44.6:55.4	11.40 6.90	$M_n(t)$	– λ-CC	0 50	– 1.13	$f_a(0.75, 0.75, 20, 30)$ μm	Tsunoda λ-CC [5]
Poly(D,L-lactide-co-glycolide)	50:50 50:50	30.29 30.29	$\%M_w(t)$ and $M_w(t_0)$	– β-CC	0 42	– 80	Assumed	Agrawal β-CC [6]
Poly(D,L-lactide-co-glycolide)	50:50 50:50 50:50 50:50	35.70 35.70 35.70 35.70	$pH(t)$ and $W_L(t)$	– β-CC β-CC β-CC	0 11.07 21.88 11.26	– 0.088 0.088 0.164	Analysis in Chap. 6	Ch6 β-CC [Chap. 6]
Poly(D,L-lactide-co-glycolide)	85:15 85:15 85:15 85:15	60.76 65.45 70.80 70.95	– β-CC β-CC β-CC	$M_w(t)$ and $PDI(t_0)$	0 15.8 36.1 50.6	– 10 10 10	d_{mean} in text	Cotton β-CC [7]

Table 7.2 Abbreviations and descriptions of the different types of calcium carbonate encountered in the harvested degradation data

Abbreviation	Description
β-CC	Calcite or beta-calcium carbonate with high crystallinity
λ-CC	Aragonite or lambda-calcium carbonate with high crystallinity
μ-TCP	Vaterite or mu-calcium carbonate with high crystallinity

- Empirical rate of production of short chains by chain scission, $\alpha = 0.4(1)$.
- Empirical exponent of production of short chains by chain scission, $\beta = 1(1)$.
- Average degree of pseudo-polymerisation of the short chains, $m = 4(1)$.

Obtaining the defining values of the last four composite-dependent parameters, the composite degradation constants k_1, k_2', A_d and θ, for each case study is the aim of the harvested data analysis process. The values of the composite degradation constant for each calcium carbonate case study are reported in Sect. 7.4.

7.2 Calcium Carbonate Information and Ceramic-Dependent Constants for the Calcium Carbonate Composites Degradation Model

This section presents the different types of calcium carbonate encountered in the harvested data and the values of the ceramic-dependent parameters for these types of calcium carbonate. Similarly to the TCP and HA composites degradation model, the CC composites computational model, introduced in Sect. 3.2.3, employs chemical relationships to characterise the interactions between ceramic filler and polymeric matrix resulting in a model capable of dealing with several different types of calcium carbonate.

Calcium carbonate (CC), whose chemical formula is $CaCO_3$, presents several allotropes, namely β, λ and μ. μ-CC is metastable with respect to β and λ-CC, which have a greater biological importance [9]. Although the three allotropes share the exact same chemical composition ($CaCO_3$) and therefore release both Ca_2^+ and $(CO_3)^{2-}$ ions during dissolution, the polymorphs have different crystallographic properties with β-CC or calcite having a trigonal space group $R\bar{3}c$ [10], λ-CC or aragonite, an orthorhombic space group *Pmcn* [11] and μ-CC or vaterite, a hexagonal space group $P6_3/mmc$ [12]. These differences in structure affect the ceramic parameters used in the computational model. The abbreviations used to designate the different types of calcium carbonate found in the the harvested calcium carbonate composites degradation data can be found in Table 7.2.

As summarised in Sect. 3.4, the computational models derived from the general modelling framework employ a series of parameters that are ceramic-dependent, such as ceramic molar mass, M_{cer}; ceramic density, ρ_{cer}; ceramic molar volume, Ω_{cer}; ceramic solubility expressed as a negative base 10 logarithm of the ionic product at equilibrium, $-\log_{10}(K_{sp})$; ceramic calcium equilibrium concentration, $[Ca^{2+}]_{eq|cer}$

Table 7.3 Ceramic specific parameters used in the calcium carbonate model. Acid dissociation expressed as the negative base 10 logarithm of the acid dissociation constant, $pK_i = -\log_{10}(K_i)$ with K_i in mol dm^{-3}. Solubility expressed as the negative base 10 logarithm of the ionic product at equilibrium of $CaCO_3$ with concentrations in mol dm^{-3}. $|_{\beta/\lambda/\mu}$ used to denote the value of a magnitude particularised for a specific CC polymorph

Constant (unit)	Quantity	Value	Reference
pK_1 (1)	First logarithmic carbonic acid dissociation constant at 37 °C	6.30	[13]
pK_2 (1)	Second logarithmic carbonic acid dissociation constant at 37 °C	10.24	[14]
M_{CC} (g mol^{-1})	CC molar mass	100.087	[15]
$-\log_{10}(K_{sp})\|_\beta$ (1)	β-CC solubility at 37 °C	8.56	[16]
$-\log_{10}(K_{sp})\|_\lambda$ (1)	λ-CC solubility at 37 °C	8.42	[16]
$-\log_{10}(K_{sp})\|_\mu$ (1)	μ-CC solubility at 37 °C	8.02	[16]
$[Ca^{2+}]_{eq}\|_\beta$ (mol m^{-3})	β-CC equilibrium calcium concentration at 37 °C	5.248×10^{-2}	Appendix A.2.4
$[Ca^{2+}]_{eq}\|_\lambda$ (mol m^{-3})	λ-CC equilibrium calcium concentration at 37 °C	6.166×10^{-2}	Appendix A.2.4
$[Ca^{2+}]_{eq}\|_\mu$ (mol m^{-3})	μ-CC equilibrium calcium concentration at 37 °C	9.772×10^{-2}	Appendix A.2.4
$\rho_{CC}\|_\beta$ (kg m^{-3})	β-CC density	2710	[17]
$\rho_{CC}\|_\lambda$ (kg m^{-3})	λ-CC density	2947	[18]
$\rho_{CC}\|_\mu$ (kg m^{-3})	μ-CC density	2645	[19]
$\Omega_{CC}\|_\beta$ (m^3 mol^{-1})	β-CC molar volume	3.693×10^{-5}	*
$\Omega_{CC}\|_\lambda$ (m^3 mol^{-1})	λ-CC molar volume	3.396×10^{-5}	*
$\Omega_{CC}\|_\mu$ (m^3 mol^{-1})	μ-CC molar volume	3.784×10^{-5}	*

* Calculated as the ratio between M_{CC} and ρ_{CC} ($\Omega_{CC} = M_{CC}/\rho_{CC}$)

and acid dissociation constants associated to the released anions, pK_i. The values taken by the different types of calcium carbonated present in the degradation data can be found in Table 7.3.

To avoid duplication, the polymer-dependent constants employed by the CC composites degradation model are not listed here as they are common for all the models derived from the general framework. A completed list of these constants can be found in Table 4.4.

7.3 Initial Values for the CC Composites Degradation Model Variables

In order to run the degradation simulations of calcium carbonate composites, the initial values of the CC composites degradation model variables are needed, in addition to the values of the composite-dependent, ceramic-dependent and polymer-dependent constants reported Sects. 7.1, 7.2 and 4.3 respectively.

The values of the ten degradation variables at the time origin, presented in this section and found below, arise from two assumptions: firstly, that both ceramic dissolution and polymer scission start at the time origin and secondly, that the polymer phase has attained carboxylic end acid dissociation equilibrium at the time origin in addition to the existence of only one source of hydrogen ions, namely polymer acid dissociation, as given by the value of the initial hydrogen ions concentration not resulting from carboxylic end groups dissociation, $\Delta C_{H_0^+} = 0\,\text{mol}\,\text{m}^{-3}$.

- $x_1|_{t=0} = R_{s0} = 0$, initial concentration of polymer chain scissions (mol m^{-3}).
- $x_2|_{t=0} = [H^+]_0 = C_{H_0^+} = -0.5K_\text{a} + \sqrt{0.25K_\text{a}^2 + K_\text{a}C_{\text{chain0}}}$, initial concentration of hydrogen ions (mol m^{-3}).
- $x_3|_{t=0} = [Ca^{2+}]_0 = 0$, initial concentration of calcium ions (mol m^{-3}).
- $x_4|_{t=0} = [CO_3^{2-}]_0 = 0$, initial concentration of carbonate ions (mol m^{-3}).
- $x_5|_{t=0} = [R-COOH]_0 = C_{\text{chain0}} - \left(-0.5K_\text{a} + \sqrt{0.25K_\text{a}^2 + K_\text{a}C_{\text{chain0}}}\right)$, initial concentration of non-dissociated carboxylic end group chains (mol m^{-3}).
- $x_6|_{t=0} = [R-COO^-]_0 = -0.5K_\text{a} + \sqrt{0.25K_\text{a}^2 + K_\text{a}C_{\text{chain0}}}$, initial concentration of dissociated carboxylic end group chains (mol m^{-3}).
- $x_7|_{t=0} = [HCO_3^-]_0 = 0$, initial concentration of hydrogen carbonate ions (mol m^{-3}).
- $x_8|_{t=0} = [H_2CO_3]_0 = 0$, initial concentration of carbonic acid (mol m^{-3}).
- $x_9|_{t=0} = a_{\text{CC0}} = \frac{\pi d_0^2}{V_{\text{unit}}}$, initial concentration of calcium carbonate interfacial area in the composite ($\text{m}^2\,\text{m}^{-3}$).
- $x_{10}|_{t=0} = M_{\text{n0}}$, initial polymer number-average molecular weight (Da).

where the concentrations $x_1, \ldots, x_8$ are defined in the polymer phase, K_a is the polymer acid dissociation constant at 37 °C (mol m^{-3}); C_{chain0}, the polymer chains concentration at the time origin (mol m^{-3}); d_0, the representative particle size (m) and V_{unit}, the volume of the representative unit cell (m^3).

7.4 Results of the Calcium Carbonate Composites Degradation Model

The results output by the CC composites degradation model after running the simulations with the CC degradation data reported in Sect. 7.1 are presented in this section. Due to the low number of case studies all of them are presented together using three different graphs: a polymer degradation map, a ceramic degradation map and a 3D plot exploring the polymer-ceramic degradation space. The polymer degradation map provides information about degradation aspects of the matrix by representing each case as a point by their duplet (k_1, k_2') in the k_1–k_2' plane. In a similar fashion, the ceramic degradation map provides information about degradation aspects of the calcium carbonate filler by representing each case as a point by their duplet (A_d, θ) in the A_d–θ plane. Finally, each case is represented as a triplet (k_1, k_2', A_d) in the (k_1–k_2'–A_d) degradation space. Each analysed calcium carbonate composite degradation case is always represented by the same unique combination of marker

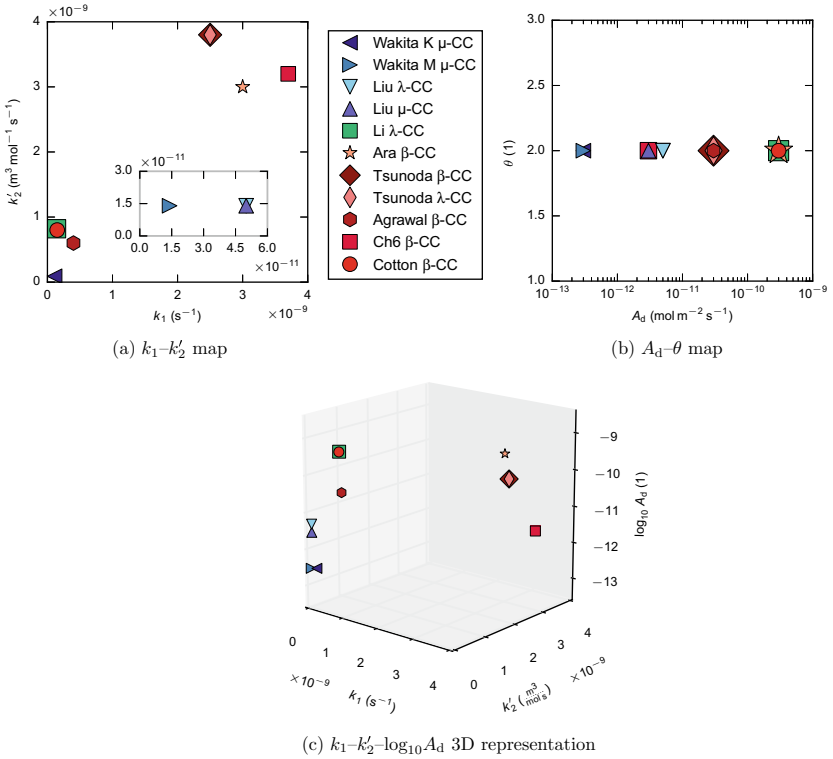

(a) k_1–k_2' map

(b) A_d–θ map

(c) k_1–k_2'–$\log_{10}A_d$ 3D representation

Fig. 7.1 Results output by the CC composites degradation model for all analysed case studies. k_1 is the non-catalytic polymer degradation rate, k_2' is the autocatalytic polymer degradation rate, A_d is the ceramic dissolution rate and θ is the power ceramic dissolution law exponent. The calcium carbonate type used in each case study is indicated in the legend by the abbreviation found at the end of the case study code. The meaning of the abbreviations can be found in Table 7.2. Grey inset plots correspond to zoomed-up regions included to avoid amalgamation of results around the origin

and colour, with the colour shade being an indication of the polymeric matrix group the case belongs to: blue for poly(L-lactide), green for poly(D,L-lactide) and red for poly(lactide-co-glycolide). The legend included in each visual representation of the results is common for the three displayed graphs: k_1–k_2' map, A_d–θ plane and k_1–k_2'–A_d plot.

Uniqueness of model parameters, k_1, k_2', A_d and θ: As explained in Sect. 4.5, there is a possibility of having multiple solutions for a given case. For CC cases with multiple solutions, the chosen and reported (k_1, k_2', A_d, θ) 4-tuple was also selected considering typical dissolution profiles, in terms of remaining ceramic weight fraction, of similar CC composites from literature.

Figure 7.4 shows the visual representation of the modelling results for all the CC case studies. This visual representation consists of three degradation maps: a polymer degradation map, showing the obtained k_1 and k_2' values, in Fig. 7.1a, a

ceramic degradation map, with the A_d and θ values in Fig. 7.1b and lastly, a representation of the 3D degradation space (k_1–k_2'–A_d) in Fig. 7.1c. The CC composites group contained data from Wakita et al. (◀, ▶) [1] with a poly(L-lactide) matrix, data from Liu et al. (▽, △) [2] also with a poly(L-lactide) matrix, data from Li and Vert (■) [3] with a poly(D,L-lactide) matrix and data from Ara et al. (☆) [4], Tsunoda (◆, ◊) [5], Agrawal and Athanasiou (⬢) [6], and Cotton et al. (●) [7], all of them with a poly(D,L-lactide-co-glycolide) matrix. Data from Chap. 6 with a poly(D,L-lactide-co-glycolide) matrix is also included (■) [Chap. 6].

The polymer degradation map shown in Fig. 7.6a contained two clusters with the poly(D,L-lactide-co-glycolide) data split between both. Similarly, the ceramic map shown in Fig. 7.6b presented four different clusters. Appendix B.3 contains the presented CC results in a tabular format, in addition to several composite characteristics for each analysed case, necessary for the following discussion.

7.5 Discussion of the Modelling Results for Calcium Carbonate Composites Degradation Data

In a similar fashion to Chaps. 4 and 5, this section presents the analysis and discussion of the results included in Sect. 7.4 employing the ideas listed in Sect. 4.6.1 on the ideal model usage. The smaller size of the CC degradation data sample causes a shorter than usual overview of the results and initial discussion. These considerations are followed by the characterisation of calcium carbonate dissolution. Also due to the size of the data sample, the discussion of the in-depth analyses, namely effect of calcium carbonate addition, sample structure and degradation protocol on composite degradation behaviour is presented jointly. Lastly, a short summary of the main traits of the degradation of calcium carbonate biocomposites is included.

7.5.1 Initial Discussion

Figure 7.2 includes the CC composites degradation results with the usual presentation style, employed in the initial overview Sects. 4.6.2 and 5.5.1, which includes coloured regions enclosing cases with poly(L-lactide), poly(D,L-lactide) and poly(lactide-co-glycolide) matrixes.

The polymer degradation map, included in Fig. 7.2a, presented a significant spread for both k_1 (s^{-1}), the non-catalytic degradation rate and k_2' ($m^3\ mol^{-1}\ s^{-1}$), the autocatalytic polymer degradation rate, spanning nearly three orders of magnitude, from 10^{-11} to 10^{-8} despite the low number of CC case studies. PLLA showed the lowest values of k_1 and k_2', followed by PDLLA and lastly PLGA, matching the typical behaviour reported by Neuendorf et al. [21] and Middleton and Tipton [22]. All the CC analysed cases lie in the region surrounding the map diagonal, which pointed

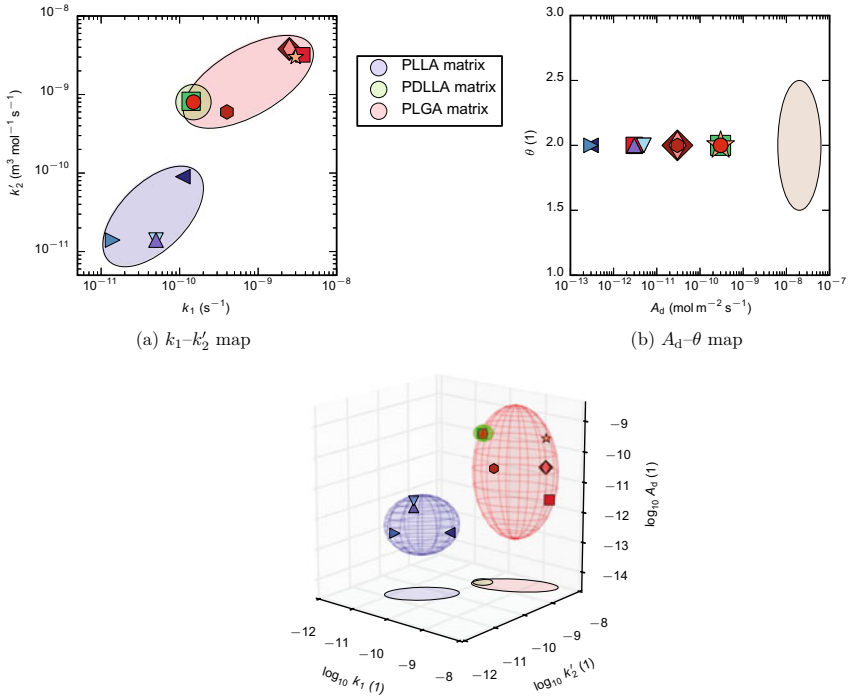

(a) k_1–k_2' map

(b) A_d–θ map

(c) $\log_{10}k_1$–$\log_{10}k_2'$–$\log_{10}A_d$ 3D representation

Fig. 7.2 Global degradation maps containing results output by the CC composites degradation model for all the analysed case studies. k_1 is the non-catalytic polymer degradation rate, k_2' is the autocatalytic polymer degradation rate, A_d is the ceramic dissolution rate and θ is the power ceramic dissolution law exponent. Coloured ellipses, for the k_1–k_2' map, or ellipsoids, for the $\log_{10}k_1$–$\log_{10}k_{2'}$–$\log_{10}A_d$ plot, enclose the majority of the case studies for usual polymeric matrixes. The beige coloured region in the A_d–θ map represents experimental dissolution data for calcite measured at 25 °C and a constant pH = 3.7 in a 0.7 M KCl solution with different rotating speeds by Sjöberg and Rickard [20]

to a coexistence of both types of polymer degradation although some cases showed a marked non-catalytic behaviour, such as Liu μ-CC (▲) [2] and Liu λ-CC (▽) [2], both with $k_1/k_2' > 3.5$, while others showed a marked autocatalytic behaviour such as Li λ-CC (■) [23] and Cotton β-CC (●) [7] both with $k_1/k_2' < 0.2$. At the low degradation end, Wakita M μ-CC (▶) [1], a porous poly(L-lactide)–μ-CC composite, experienced a reduction in M_n of only 7% after 4 weeks of degradation. Conversely, on the opposite k_1–k_2' map corner, Ch6 β-CC (▽) [Chap. 6], a dense poly(D,L-lactide-co-glycolide)(50:50)–β-CC composite, whose pure polymer occurrence reached the critical M_n in a little over 2 weeks.

The ceramic degradation map, shown in Fig. 7.2b, presented values of dissolution rate A_d (mol m^{-2} s^{-1}) spanning almost four orders of magnitude, from 10^{-13} to over 10^{-9}. The power dissolution law exponent θ (1) was equal to 2 for all the CC cases in

a similar fashion to the TCP and HA case studies. The data pointed to a relationship between polymeric matrix, expressed by the marker colours, and the CC dissolution rate A_d. The beige region represents dissolution data for calcite measured at 25 °C and a constant pH = 3.7 in a 0.7 M KCl solution with different rotating speeds by Sjöberg and Rickard [20]. The obtained A_d values were significantly lower than those enclosed by the beige region. A series of detailed analyses, trying to explain these observations, using all the available information about the different types of employed calcium carbonate follows in Sect. 7.5.2.

Lastly, Fig. 7.2c includes the 3D degradation space plot for calcium carbonate biocomposites. Due to the limited number of CC case studies, there was little overlap between ellipsoids, which encompassed the cases with poly(L-lactide), poly(D,L-lactide) and poly(lactide-co-glycolide) matrixes, and no region presented a specially high concentration of data.

7.5.2 Characterisation of Calcium Carbonate Dissolution

Calcium carbonate experiences degradation by dissolution in an aqueous media [9]. $CaCO_3$, a sparingly soluble ceramic, presents low solubility in all its allotropes as indicated by its solubility products at 37 °C of $-\log_{10}(K_{sp}) = 8.56$ for β-CC [16], $-\log_{10}(K_{sp}) = 8.42$ for λ-CC [16] and $-\log_{10}(K_{sp}) = 8.02$ for μ-CC [16]. There are a variety of factors, in addition to the abovementioned crystal structure, which affect CC dissolution such as crystallinity, environmental pH [16] and media composition [24]. The collated analyses of calcium carbonate dissolution are presented in Fig. 7.3.

The influence of CC type is presented in Fig. 7.3a. The dissolution rate of the different $CaCO_3$ did not follow the expected behaviour, included in the legend. μ-CC had the lowest dissolution rate while both λ-CC and β-CC had higher values. Furthermore all the dissolution rate values were significantly lower than those reported by Sjöberg and Rickard for calcite [20].

The influence on dissolution rate A_d of polymer matrix and buffering effect is presented in Fig. 7.3b while the influence of particle size is included in Fig. 7.3c. The presence of buffering effect in all cases with both pure polymer and composite occurrences added no information. As discussed in Chap. 3, polymer degradation causes an increase in acidity during composite degradation. Having lower dissolution values than the ones reported by Sjöberg and Rickard for calcite measured at 25 °C and a constant pH = 3.7 in a 0.7 M KCl solution with sample rotation [20] could be explained by the less harsh environment found in CC composites, without rotation and with, at least during the initial phase, a higher pH. Furthermore the clear correlation between particle size and A_d pointed to a heavy influence of the particle size on the local environment, in a similar fashion to the TCP (Sect. 4.6.3) and HA (Sect. 5.5.2) analyses.

The initial apparent relationship between polymeric matrix and dissolution rate seen in the global A_d–θ map (Fig. 7.2b) could be explained by the scarcity of the CC degradation data as the polymeric matrix–particle size combinations were extremely limited.

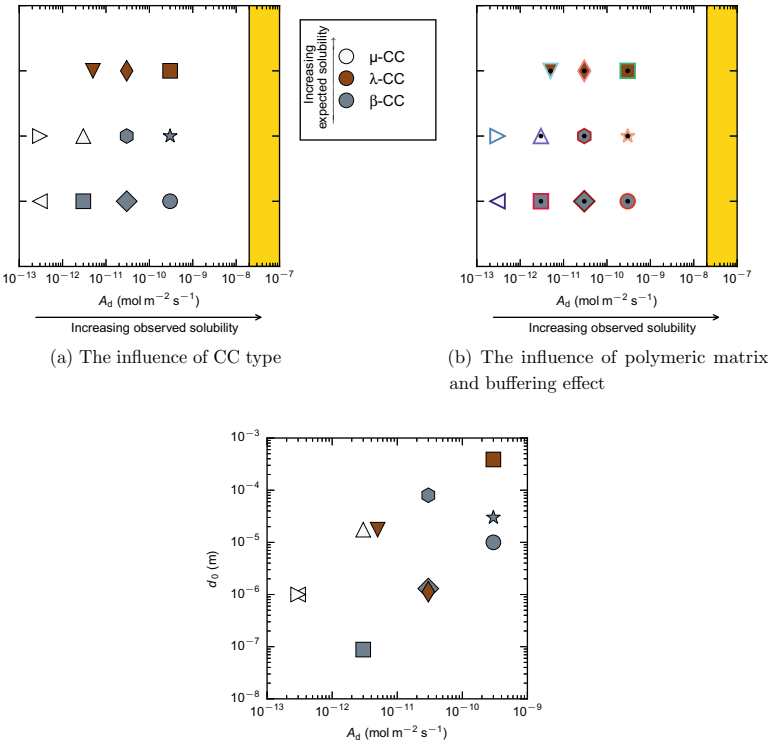

(a) The influence of CC type

(b) The influence of polymeric matrix and buffering effect

(c) The influence of particle size

Fig. 7.3 Calcium carbonate dissolution rate for all the analysed case studies: influence of tricalcium phosphate type, influence of polymeric matrix and presence of buffering effect and influence of particle size. A_d is the ceramic dissolution rate. d_0 is the ceramic representative particle size of the undegraded composite sample. The golden stripe corresponds to the range of dissolution rates measured by Sjöberg and Rickard for calcite at 25 °C and a constant pH = 3.7 in a 0.7 M KCl solution with different rotating speeds [20]. The edge colours of the markers indicate the polymeric matrix used in the case studies following the colour convention used in Sect. 7.4. Black dots represent case studies with a buffering effect, whereas white dots represent case studies with a non-buffering effect

7.5.3 *Effect of Calcium Carbonate Addition, Sample Porosity and Degradation Protocol on Composite Degradation Behaviour*

The different studies of the CC composites degradation results are included in Fig. 7.4 with their respective analyses in Table 7.4.

The effect of calcium carbonate addition is shown in Fig. 7.4a with the analysis included in the first row of Table 7.4. As explained in Sect. 4.6.1, the expected result of the addition of a ceramic such as $CaCO_3$ is the presence of a buffering effect. The 9 analysed CC case studies showed the predicted buffering effect, pointing to a extremely good capture of the CC composites degradation behaviour by the computational model.

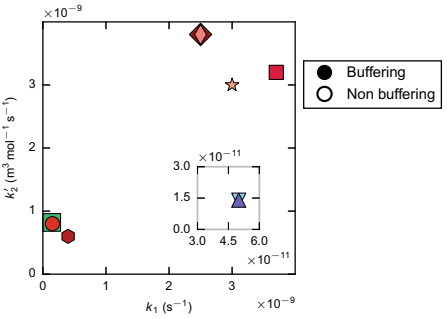

(a) Effect of calcium carbonate addition

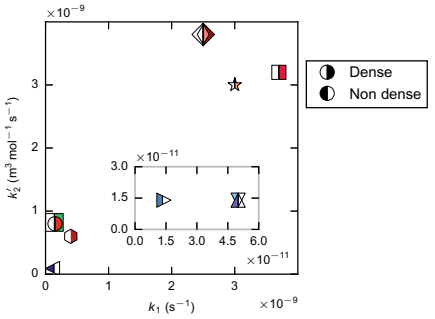

(b) The influence of sample porosity

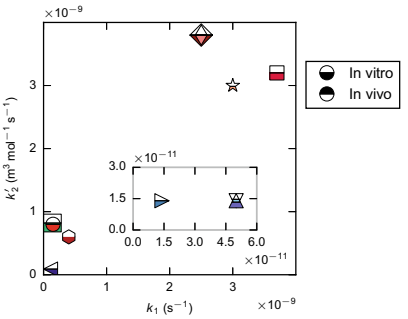

(c) The influence of in vitro vs. in vivo protocols

Fig. 7.4 Analyses of the CC modelling results: effect of calcium carbonate addition, influence of sample porosity and influence of in vitro versus in vivo protocols on composite degradation for all analysed case studies. k_1 is the non-catalytic polymer degradation rate and k_2' is the autocatalytic polymer degradation rate. Full markers represent case studies showing a buffering effect, whereas hollow markers represent case studies showing a non-buffering effect. Right-hand side filled markers represent dense case studies, whereas left-hand side filled markers represent non dense case studies. Bottom side filled markers represent in vitro case studies, whereas top side filled markers represent in vivo case studies. Grey inset plots correspond to zoomed-up regions included to avoid amalgamation of results around the origin

Table 7.4 Analysis of calcium carbonate addition effect, influence of sample porosity and influence of in vitro versus in vivo protocols on composite degradation for all the analysed calcium carbonate case studies. k_1 is the non-catalytic polymer degradation rate and k_2' is the autocatalytic polymer degradation rate, with both reported as geometric mean ⁎ geometric standard deviation

Case studies	k_1 (s^{-1})	k_2' (m^3 mol^{-1}s^{-1})	Percentage of cases (%)	Number of cases
Buffering	$(4.8 \divideontimes 6.1) \times 10^{-10}$	$(6.0 \divideontimes 9.5) \times 10^{-10}$	100	9
Dense	$(9.3 \divideontimes 4.3) \times 10^{-10}$	$(1.8 \divideontimes 2.3) \times 10^{-9}$	64	7
Non-dense	$(4.4 \divideontimes 2.3) \times 10^{-11}$	$(2.2 \divideontimes 2.5) \times 10^{-11}$	36	4
In vitro	$(3.1 \divideontimes 7.1) \times 10^{-10}$	$(3.6 \divideontimes 10.5) \times 10^{-10}$	100	11

The extent of the buffering effect, understood as the decrease of the molecular weight reduction rate in the composite occurrences when compared to the pure polymer data, varied significantly. Liu λ-CC (▽) [2] and Liu μ-CC (▲) [2] displayed an extremely low buffering effect while Agrawal β-TCP (⬢) [6] and Ara β-CC (☆) [4] presented a mild one.

Some other cases with a PLGA matrix displayed a high buffering effect such as Ch6 β-CC (■) [Chap. 6] or Tsunoda β-CC (◆) [5] and Tsunoda λ-CC (◊) [5], in which there was a 10 weeks delay in the time needed to reach the critical molecular weight $M_{\text{n crit}}$. In the two cases with the highest autocatalytic behaviour, Li λ -CC (■) [3] and Cotton β-CC (●) [7], the addition of calcium carbonate caused a extremely high buffering effect delaying the time to reach the critical molecular weight, $M_{\text{n crit}}$, in more than 28 and 22 weeks respectively.

The influence of sample porosity on CC degradation behaviour is shown in Fig. 7.4b with the analysis reported in the second row of Table 7.4. Although initially the results seemed to agree with the length $L_{H^+\text{–buffer}}$ hypothesis, explained in Sect. 4.6.5, they were heavily influenced by the types of polymeric matrix, as only poly(L-lactide) cases presented a porous structure.

Lastly, the influence of degradation protocol is presented in Fig. 7.4c with the respective analysis in the third row of Table 7.4. As all the data had in vitro degradation no useful information emerged from this analysis.

7.6 Conclusions for the Calcium Carbonate Composites Analysis

This chapter discussed the analysis of calcium carbonate composites degradation data harvested from literature using the CC composites degradation model presented in Sect. 3.2.3. Following the usual structure, all the necessary degradation data and the calcium carbonate specific parameters were reported. Then, the simulations results in addition to analyses looking at the calcium carbonate dissolution, effect of CC addition and the influences of sample porosity and in vitro versus in vivo degradation protocols were presented.

The analysis of the calcium carbonate dissolution showed a dually unexpected behaviour, with increasing dissolution rate values for $CaCO_3$ types with expected decreasing values and values lower than those measured by Sjöberg and Rickard [20] for calcite at 25°C and a constant pH = 3.7 in a 0.7 M KCl solution with different rotating speeds [20]. These discrepancies were accounted for by the existence of a milder environment in composites, caused by the degradation of the polymeric matrix, that the one in the reference data [20] and by the influence of the particle size on said environment in a similar fashion to the TCP and HA analyses.

The analysis of the effect of calcium carbonate addition on composite degradation provided several insights. A 100% of the 9 analysed CC cases presented a buffering effect as predicted by the model, pointing to a better representation of the sparingly

soluble calcium filler whose allotropes had higher solubility product K_{sp} values. The computational model highlighted the wide range of degradation constants and buffering effects that could be achieved by different combinations of polymeric matrix and calcium carbonate with a relatively low number of case studies.

Sadly, the analyses of the influences of porosity and in vitro versus in vivo degradation protocols did not provide any useful insights due to the scarcity of CC composites data.

7.7 Detailed Analysis of Chap. 6 Experimental Data

The outcome of the usual analysis of Chap. 6 experimental data is included in Sect. 7.4. Although this analysis provided a significant amount of information, the nature of the data allowed a more detailed analysis of the degradation behaviour of the calcium carbonate bionanocomposites. This detailed analysis of the data is presented in this section. Firstly, the method of analysis is briefly described with emphasis in the differences with the original method. Secondly, the necessary additional data employed in this detailed analysis is presented. And lastly, the results and discussion are included.

This detailed analysis was more complex and time consuming than the original approach. In addition, it required a significant amount of extra information. These reasons precluded the use of this method with all the harvested degradation data. The characteristics of the biocomposites presented in Chap. 6, in addition to their extensive characterisation, made them a good candidate for trying this extended method. The matrix, previously used by other CCMM members, was a commercially available polymer which ensured consistency and reproducibility and the commercial available ceramic had a really narrow particle size distribution.

7.7.1 Method of Analysis for the Detailed Analysis

Figure 7.5 shows an schematic of the detailed analysis data fitting process. Said process, divided in three different stages, aims to find the best set of values for the degradation constants k_1, k_2', A_d and θ similarly to the usual analysis process.

The expression used to characterise the polymer degradation, $\frac{dR_x}{dt} = k_1 C_e + k_2' C_e C_{H+}$, employed two polymer degradation constants: a non-catalytic one, k_1, and an autocatalytic one, k_2'. Examining the expression, it is apparent that the autocatalytic degradation rate only plays a relevant role in polymer degradation when the concentration of hydrogen ions, C_{H+}, is significant. Thus, it is hypothesised that the analysis of polymer degradation data, in which the distance travelled by the hydrogen ions to diffuse out into the degradation media is small enough to ensure no H^+ build up, would yield information solely about the non-catalytic degradation rate k_1.

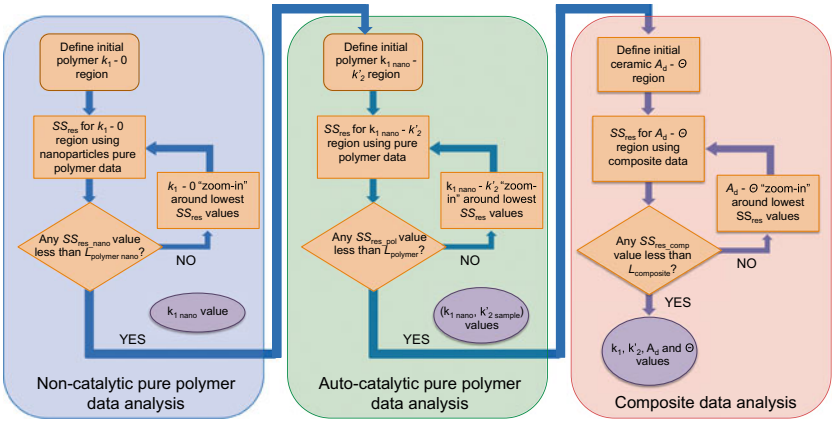

Fig. 7.5 Flow chart depicting the detailed analysis data fitting process

1. The first stage, shown in a blue shade, dealt with the "Non-catalytic pure polymer data analysis" using polymer degradation data from nanoparticles in order to find the value of the non-catalytic polymer degradation constant k_1.
2. The second stage, in a green shade, dealt with the "Autocatalytic pure polymer data analysis" using the case study own pure polymer degradation data and the previously found k_1 value in order to find the value of the autocatalytic polymer degradation constant k'_2.
3. In the third and last stage, in a red shade and labelled "Composite data analysis", the usual procedure was followed to find the values of the values of the ceramic dissolution rate A_d and exponent θ using the previously found values of k_1 and k'_2.

7.7.2 Necessary Data for the Detailed Analysis

The polymer nanoparticles degradation data, employed in the detailed analysis in order to find the value of the non-catalytic polymer degradation rate k_1, are presented here. Fu et al. observed the presence of an acidic environment within poly(D,L-lactide-co-glycolide)(50:50) microspheres during degradation, with the smallest analysed particles of 14 μm presenting a significantly less acidic centre than bigger particles [25], pointing to the necessity of including nanoparticles with a size of less than 14 μm in the data for the non-catalytic pure polymer analysis. Table 7.5 summarises the main characteristics of the poly(D,L-lactide-co-glycolide)(50:50) nanoparticles degradation data harvested from diverse sources in literature, in addition to their corresponding k_1 values obtained in the non-catalytic pure polymer analysis.

Table 7.5 Summary of data found in literature on degradation of poly(D,L-lactide-co-glycolide)(50:50) nanoparticles and obtained values of the non-catalytic polymer degradation constant k_1. M_{n0} is the sample initial number-average molecular weight, d_P is the representative particle size of the pure polymer particles and k_1 is the non-catalytic polymer degradation rate. Further abbreviations employed in columns labelled "Data" can be found in Sect. 3.5.2. A dashed line between rows indicates that data displayed in those consecutive rows belong to the same researcher or research group. A solid line between rows indicates no known author relationship for the data

End-group	Manufacturer	M_{n0} (kDa)	Degradation data	d_p (nm)	k_1 (s^{-1})	Case code and reference
Unknown	Boehringer Ingelheim, Germany	21.25	$M_w\%(t)$	18000	2.8×10^{-9}	Blanco 98 [26]
Unknown	Sigma Aldrich	24.20	$M_n(t)$	900	4.8×10^{-9}	Blanco 06 [27]
Ester capped	Resomer RG504, Boehringer Ingelheim; Germany	26.20	$M_p(t)$	530	1.2×10^{-9}	Dunne [28]
Ester capped	Resomer RG502, Boehringer Ingelheim; Germany	6.72	$M_w\%(t)$	76	4.7×10^{-10}	Musyanovych [29]
Unknown	Birmingham Polymers, USA	113.13	$M_w(t)$	110	2.9×10^{-10}	Panyam 0.1 μm [30]
Unknown	Birmingham Polymers, USA	113.13	$M_w(t)$	1100	1.1×10^{-10}	Panyam 1 μm [30]
Uncapped	Purac, The Netherlands	25.70	$M_n(t)$	300	1.9×10^{-9}	Samadi COOH [31]
Lauryl capped	Purac, The Netherlands	25.90	$M_n(t)$	320	1.0×10^{-9}	Samadi capped [31]

7.7.3 *Results and Discussion from the Detailed Analysis*

The results from the detailed analysis and the subsequent discussion are presented below. Figure 7.6 shows a comparison between Ch6 β-CC [Chap. 6] results from the detailed and typical analyses. In addition, another three comparisons are also included for case studies with the same poly(D,L-lactide-co-glycolide)(50:50) matrix employed in Ch6 β-CC. For all these case studies, a value for the non-catalytic degradation rate $k_1 = 1.1 \times 10^{-9}\,s^{-1}$ was employed. This value was chosen from the non-catalytic pure polymer analysis reported in Table 7.5, as the most similar case studies in terms of end-group and degradation protocol presented k_1 values in the $(1.0\ldots1.2) \times 10^{-9}\,s^{-1}$ range.

The polymer degradation map, included in Fig. 7.6a, showed a better capture of the influence of sample thickness using the detailed analysis. Having a fixed k_1 value, the relationship between the obtained k_2' values and the sample thickness became more obvious. Barrett α-TCP DA (⬣) [32, 33], with a thickness of 900 μm had the lowest k_2' value, followed by Yang Z. 5050 mC α-TCP DA (▶) [34, 35] and Bennett

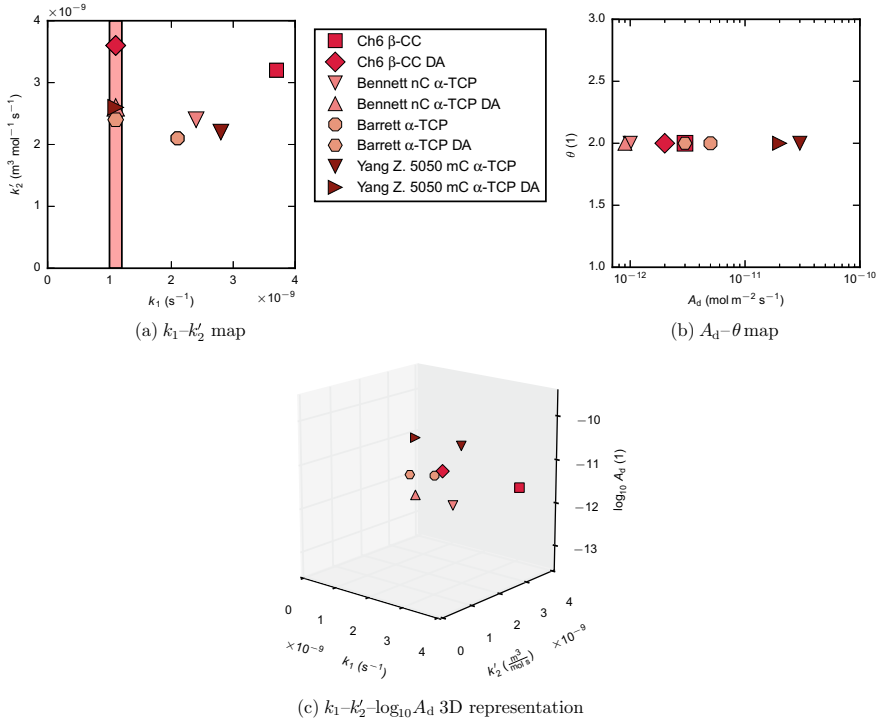

(a) k_1–k_2' map

(b) A_d–θ map

(c) k_1–k_2'–$\log_{10} A_d$ 3D representation

Fig. 7.6 Results output by the CC and TCP composites degradation model for several case studies using the detailed analysis method. k_1 is the non-catalytic polymer degradation rate, k_2' is the autocatalytic polymer degradation rate, A_d is the ceramic dissolution rate and θ is the power ceramic dissolution law exponent. β-CC is calcite or beta-calcium carbonate with high crystallinity and α-TCP is highly crystalline alpha tricalcium phosphate. DA stands for "Detailed Analysis"

nC α-TCP DA (▲) [36], both with a thickness of 1 mm and lastly, Ch6 β-CC DA (◆) [Chap. 6] with the highest k_2' value and a thickness of 2 mm. Likewise, the similarities amongst case studies became even more apparent using the detailed analysis instead of the usual one. Figure 7.6b contains the ceramic degradation map, which showed a slight shift in the values of ceramic dissolution rate A_d for the detailed analysis, as a result of the change in k_1/k_2' ratio to lower values, indicating that samples had a more autocatalytic behaviour than previously thought. Lastly, the 3D representation of the results is presented in Fig. 7.6c showing the differences between both methods of analysis. The use of the detailed method produced fittings as good as the ones generated with the usual method.

In summary, the use of the detailed analysis method provided a more accurate characterisation of the composite degradation behaviour, being able to capture more precisely the influence of sample porosity and the similarities amongst case studies. These features pointed to an improvement in model performance with the use of the active model but with a significant extra cost. As a consequence, the use of this detailed method may be indicated solely for a subset of composites with specific characteristics of interest.

7.8 General Composite Degradation Data Conclusions

Chapters 4, 5 and the present chapter reported the analysis of the degradation of calcium based biocomposites containing three different ceramic fillers: tricalcium phosphate, hydroxyapatite and calcium carbonate. For these three ceramics, quantitative degradation data were harvested and then, analysed with the computational models derived from the general modelling framework presented in Chap. 3. Several analyses were carried out for all the degradation data. These analyses included ceramic dissolution, effect of ceramic addition on composite dissolution, influence of sample porosity and influence of degradation protocol.

The analysis of the ceramic dissolution showed a behaviour consistent with ceramic dissolution in highly acidic environments, with dissolution rates higher than those measured in free drift experiments for highly crystalline samples and lower than those measured in extremely low pH, high molar concentration and with rotation of the ceramic sample, indicating the necessity of using a tailored dissolution protocol to ensure the validity of the obtained information about ceramic dissolution when said information is intended for use in the ceramic-specific computational models.

In addition, the ceramic dissolution analysis pointed to the important influence of both the acidic environment caused by the polymeric matrix and the ceramic particle size on ceramic dissolution rate. The strong particle size dependence of the obtained A_d values, despite the use of surface adimensionalisation resulting in units of mol m^{-2} s^{-1}, with bigger particle reporting higher A_d values, or in other words, with smaller particles being more efficient, could be partially explained by the influence of particle size on the definition of the environment surrounding said particle during composite degradation as explained in Sect. 3.3, but could also point to small particles having less effective surface area available than considered by the model resulting in artificially low A_d values, i.e. the representative particle size found in real composites is bigger than the value reported by the ceramic characterisation processes.

The analysis of the effect of ceramic addition on composite degradation was extremely fruitful. The analysed case studies displayed a wide variety of behaviours that were categorised into two different types: case studies presenting a buffering effect, as predicted by the modelling framework, and case studies presenting a non-buffering effect. Overall, 76% of the 107 cases showed a buffering effect suggesting a good capture of the degradation behaviour of biocomposites by the general modelling framework. By calcium-based filler, the presence of a buffering effect was noticed in a 63% of the 57 HA cases, a 88% of the 41 TCP cases and a 100% of the 9 CC cases. The differences amongst calcium-based fillers pointed to the presence of less deviation from the expected behaviour with higher ceramic solubilities, expressed as solubility product K_{sp}.

For case studies with a buffering effect, the ceramic-specific computational models emphasised the diversity present in the degradation behaviours of the different studied combinations of polymeric matrix and calcium-based ceramic filler. Those differences were represented by the wide range of degradation constants and the

extent of the buffering effects. The analysis revealed the existence of dissimilar behaviours, that could not be accounted for by the expected k_2' variations, for a priori, similar case studies such as two case studies sharing nominally the same matrix and filler. This behaviour dissimilarity suggested the need for a more comprehensive characterisation of both the employed calcium-based filler and polymeric matrix in order to identify the factors responsible for these variations. Conversely, the model highlighted the similarities in degradation behaviour for data coming from the same research group as seen in the clustering displayed by those cases. The use of the detailed analysis method showed an even better capture of the similarities amongst case studies and the relationship between sample thickness and k_2' values, although at a significant extra cost.

For case studies with a non-buffering effect, the analysis done with the ceramic-specific computational models helped identifying potential causes for those behaviours. In most of the cases, the causes concerned violations of the computational models in-built assumptions. Amongst them, the most common cause was the absence of sufficient water to guarantee water-independent polymer hydrolysis. Other causes were poor composite sample structural integrity and the existence of considerable differences between pure polymer and composite samples.

The analysis of the influence of porosity on the degradation behaviour of biocomposites provided an ambiguous picture. A significant portion of the data supported the initial hypothesis of higher degradation rate for samples with a higher characteristic diffusional length $L_{H^+\text{–buffer}}$, such as dense samples, while the remaining data did not support it, suggesting a greater importance, in some cases, of factors intrinsically linked to sample structure, such as water penetration and mechanical integrity, on the degradation behaviour.

Lastly, the analysis of the influence of in vitro versus in vivo protocols on the biocomposites degradation did not provide a general trend but revealed interesting insights concerning the effect of protocol differences for particular polymer-ceramic combinations.

References

1. Wakita, T., Nakamura, J., Ota, Y., Obata, A., Kasuga, T., & Ban, S. (2011). Effect of preparation route on the degradation behavior and ion releasability of siloxane-poly(lactic acid)-vaterite hybrid nonwoven fabrics for guided bone regeneration. *Dental Materials Journal*, *30*(2), 232–238.
2. Liu, Y., Huang, Q., Kienzle, A., Müller, W., & Feng, Q. (2014). In vitro degradation of porous PLLA/pearl powder composite scaffolds. *Materials Science and Engineering: C*, *38*, 227–234.
3. Li, S., & Vert, M. (1996). Hydrolytic degradation of coral/poly(DL-lactic acid) bioresorbable material. *Journal of Biomaterials Science, Polymer Edition*, *7*(9), 817–827.
4. Ara, M., Watanabe, M., & Imai, Y. (2002). Effect of blending calcium compounds on hydrolytic degradation of poly(DL-lactic acid-co-glycolic acid). *Biomaterials*, *23*(12), 2479–2483.
5. Tsunoda, M. (2003). Degradation of poly(DL-lactic acid-co-glycolic acid) containing calcium carbonate and hydroxyapatite fillers-effect of size and shape of the fillers. *Dental Materials Journal*, *22*(3), 371–382.

6. Agrawal, C. M., & Athanasiou, K. A. (1997). Technique to control pH in vicinity of biodegrading PLA-PGA implants. *Journal of Biomedical Materials Research*, *38*(2), 105–114.
7. Cotton, N. J., Egan, M. J., & Brunelle, J. E. (2008). Composites of poly(DL-lactide-co-glycolide) and calcium carbonate: In vitro evaluation for use in orthopedic applications. *Journal of Biomedical Materials Research Part A*, *85*(1), 195–205.
8. Pan, J., Han, X., Niu, W., & Cameron, R. E. (2011). A model for biodegradation of composite materials made of polyesters and tricalcium phosphates. *Biomaterials*, *32*(9), 2248–2255.
9. Morse, J. W., Arvidson, R. S., & Lüttge, A. (2007). Calcium carbonate formation and dissolution. *Chemical Reviews*, *107*(2), 342–381.
10. Graf, D. (1961). Crystallographic tables for the rhombohedral carbonates. *American Mineralogist*, *46*(11–2), 1283–1316.
11. De Villiers, J. P. R. (1967). *The crystal structures of aragonite, strontianite, and witherite*. Ph.D. thesis, University of Illinois at Urbana-Champaign.
12. Kamhi, S. R. (1963). On the structure of vaterite, $CaCO_3$. *Acta Crystallographica*, *16*(8), 770–772.
13. Harned, H. S., & Davis, R, Jr. (1943). The ionization constant of carbonic acid in water and the solubility of carbon dioxide in water and aqueous salt solutions from 0 to 50°. *Journal of the American Chemical Society*, *65*(10), 2030–2037.
14. Harned, H. S., & Scholes, S. R, Jr. (1941). The ionization constant of HCO_3^- from 0 to 50°. *Journal of the American Chemical Society*, *63*(6), 1706–1709.
15. PubChem (2005a). *CID*: 10112. Retrieved September 1, 2016, from https://pubchem.ncbi.nlm.nih.gov/compound/calcium_carbonate#section=Top.
16. Plummer, L. N., & Busenberg, E. (1982). The solubilities of calcite, aragonite and vaterite in CO_2-H_2O solutions between 0 and 90°C, and an evaluation of the aqueous model for the system $CaCO_3$-CO_2-H_2O. *Geochimica et Cosmochimica Acta*, *46*(6), 1011–1040.
17. Mindat Online Database (2016b). *Calcite*. Retrieved September 1, 2016, from http://www.mindat.org/min-859.html.
18. Mindat Online Database (2016a). *Aragonite*. Retrieved September 1, 2016, from http://www.mindat.org/min-307.html.
19. Mindat Online Database (2016c). *Vaterite*. Retrieved September 1, 2016, from http://www.mindat.org/min-4161.html.
20. Sjöberg, E. L., & Rickard, D. T. (1984). Temperature dependence of calcite dissolution kinetics between 1 and 62°C at pH 2.7–8.4 in aqueous solutions. *Geochimica et Cosmochimica Acta*, *48*(3), 485–493.
21. Neuendorf, R., Saiz, E., Tomsia, A., & Ritchie, R. (2008). Adhesion between biodegradable polymers and hydroxyapatite: Relevance to synthetic bone-like materials and tissue engineering scaffolds. *Acta Biomaterialia*, *4*(5), 1288–1296.
22. Middleton, J. C., & Tipton, A. J. (2000). Synthetic biodegradable polymers as orthopedic devices. *Biomaterials*, *21*(23), 2335–2346.
23. Li, H., & Chang, J. (2005). pH-compensation effect of bioactive inorganic fillers on the degradation of PLGA. *Composites Science and Technology*, *65*(14), 2226–2232.
24. Feely, R., Sabine, C., Lee, K., Millero, F., Lamb, M., Greeley, D., et al. (2002). In situ calcium carbonate dissolution in the Pacific Ocean. *Global Biogeochemical Cycles*, *16*(4), 91-1.
25. Fu, K., Pack, D. W., Klibanov, A. M., & Langer, R. (2000). Visual evidence of acidic environment within degrading poly(lactic-co-glycolic acid) (PLGA) microspheres. *Pharmaceutical Research*, *17*(1), 100–106.
26. Blanco, D., & Alonso, M. J. (1998). Protein encapsulation and release from poly(lactide-co-glycolide) microspheres: Effect of the protein and polymer properties and of the co-encapsulation of surfactants. *European Journal of Pharmaceutics and Biopharmaceutics*, *45*(3), 285–294.
27. Blanco, M. D., Sastre, R. L., Teijón, C., Olmo, R., & Teijón, J. M. (2006). Degradation behaviour of microspheres prepared by spray-drying poly(D, L-lactide) and poly(D, L-lactide-co-glycolide) polymers. *International Journal of Pharmaceutics*, *326*(1), 139–147.

28. Dunne, M., Corrigan, O., & Ramtoola, Z. (2000). Influence of particle size and dissolution conditions on the degradation properties of polylactide-co-glycolide particles. *Biomaterials*, *21*(16), 1659–1668.
29. Musyanovych, A., & Landfester, K. (2012). Biodegradable polyester-based nanoparticle formation by miniemulsion technique. *Material Matters*, *7*(3), 30–34.
30. Panyam, J., Dali, M. M., Sahoo, S. K., Ma, W., Chakravarthi, S. S., Amidon, G. L., et al. (2003). Polymer degradation and in vitro release of a model protein from poly (D, L-lactide-co-glycolide) nano-and microparticles. *Journal of Controlled Release*, *92*(1), 173–187.
31. Samadi, N., Abbadessa, A., Di Stefano, A., Van Nostrum, C., Vermonden, T., Rahimian, S., et al. (2013). The effect of lauryl capping group on protein release and degradation of poly(D, L-lactic-co-glycolic acid) particles. *Journal of Controlled Release*, *172*(2), 436–443.
32. Barrett, C. E., & Cameron, R. E. (2014). X-ray microtomographic analysis of α-tricalcium phosphate-poly(lactic-co-glycolic) acid nanocomposite degradation. *Polymer*, *55*(16), 4041–4049.
33. Barrett, C. E. (2013). *The degradation behaviour of tricalcium phosphate - poly(lactide-co-glycolide) nanocomposites*. Ph.D. thesis, Department of Materials Science and Metallurgy, University of Cambridge.
34. Yang, Z. (2009). *Development and characterisation of bioactive, bioresorbable* α*-tricalcium phosphate/poly(D,L-lactide-co-glycolide) nanocomposites for bone substitution and fixation*. Ph.D. thesis, Department of Materials Science and Metallurgy, University of Cambridge.
35. Yang, Z., Best, S. M., & Cameron, R. E. (2009). The influence of α-tricalcium phosphate nanoparticles and microparticles on the degradation of poly(D, L-lactide-co-glycolide). *Advanced Materials*, *21*(38–39), 3900–3904.
36. Bennett, S. M. (2012). *Degradation mechanisms of PLGA/*α*-TCP composites for orthopaedic applications*. Ph.D. thesis, Department of Materials Science and Metallurgy, University of Cambridge.

Chapter 8
Conclusions and Future Work

In this final chapter, the main conclusions stemming from this research are presented, followed by a series of suggestions for future work.

8.1 Conclusions

The principal conclusions drawn from the work presented in this thesis are listed below:

- As understanding of composite degradation is paramount and time consuming, the use of already published data became necessary and the employment of a computational tool for its analysis seemed to present significant advantages.
- The most thorough and up-to-date compilation of quantitative degradation data from biocomposites containing tricalcium phosphate, hydroxyapatite and calcium carbonate was generated. The compiled 131 case studies represented over 60 nominally different polymer-ceramic combinations.
- A general modelling framework for the degradation of bioresorbable composites with calcium-based fillers, which used mathematical expression to characterise the interwoven degradation phenomena, was developed from a generalisation of the degradation model for composites made of biodegradable polyesters and tricalcium phosphates proposed by Pan et al. [1, 2].
- Three ceramic-specific models were generated through the particularisation of the general modelling framework for three different calcium-based fillers, namely tricalcium phosphate (TCP), hydroxyapatite (HA) and calcium carbonate (CC). Implementations of the three ceramic-specific models were programmed in C++ and Python.
- The ceramic-specific models were employed to analyse the 131 different case studies and evaluate the ceramic dissolution, the effect of the ceramic addition on

I. Moreno-Gomez, *A Phenomenological Mathematical Modelling Framework for the Degradation of Bioresorbable Composites*, Springer Theses, https://doi.org/10.1007/978-3-030-04990-4_8

composite degradation, the influence of sample porosity on degradation and lastly, the influence of in vitro versus in vivo protocols on degradation.

- The computational models predicted a decrease in molecular weight reduction rate for composites with the addition of a sparingly soluble ceramic filler, which in this work was termed presence of "a buffering effect", found in 76% of the 107 analysed case studies: 88% of the 41 TCP cases, 63% of the 57 HA cases and a totality of the 9 CC cases which suggested less deviation from the expected behaviour for ceramics with higher solubility product K_{sp}.
- The analysis of composite degradation data highlighted the wide range of both degradation constants and buffering effect extents that could be achieved by different combinations of polymeric matrix and tricalcium phosphate, hydroxyapatite or calcium carbonate, resulting in a plethora of degradation behaviours. Furthermore, the existence of discrepancies in degradation behaviour between a priori similar bioresorbable composites became apparent, highlighting the high number of hidden factors affecting composite degradation such as polymer tacticity or ceramic impurities.
- The analysis of the case studies which displayed a buffering effect showed that the three types of biocomposites, namely TCP, HA and CC shared the same degradation mechanisms and that those were captured by the modelling framework. In general terms, the extent of the buffering effect was dependent on the filler with CC giving the most pronounced buffering effect, followed by TCP and lastly, HA. Additionally, the analysis also showed that practically all the cases presented a combination of both non-catalytic and autocatalytic degradation.
- Several causes were identified in the analysis of cases with a non-buffering effect, such as limited water content during composite degradation, poor composite sample structural integrity and presence of significant differences between pure polymer and composite samples.
- The analysis of ceramic dissolution showed dissolution values which pointed to a significant influence of both polymeric matrix, acting as a source of acidity, and ceramic particle size on the definition of the environment surrounding a ceramic particle during composite degradation. Additionally, it suggested the advisability of further research on the characterisation of ceramic particle sizes within composites and the use of a more complete set up for the experimental study of dissolution when ceramics fillers are analysed outside composites.
- The porosity analysis showed, in a majority of the cases, an agreement with the initial hypothesis of a direct relation between degradation and characteristic diffusional length $L_{H^+\text{–buffer}}$. The degradation protocols analysis did not provide a clear general picture.
- PLGA and three PLGA-β-$CaCO_3$ composites were fabricated with regular uniform nano-sized β-$CaCO_3$ particles employing two different sizes and ceramic weight fractions. The in vitro degradation of all the samples was found to proceed by heterogeneous bulk degradation and the addition of β-$CaCO_3$ resulted in a marked buffering effect proportional to the ceramic surface area per unit of polymer volume, in line with the model predictions.

8.2 Future Work

After the presentation of the main conclusions, the following recommendations, that could serve as a guide for future work, are included. These recommendations are divided into two different categories.

The first group of suggestions includes a series of improvements for the modelling framework and the derived ceramic-specific models presented in Chap. 3 including improvements for both the model and the composite data processing, which are listed below:

- Addition of a water concentration factor to the polymer scission rate equation: the modelling framework assumes an excess of water during polymer scission. However, some of the analysed case studies showed water-controlled composite degradation, thus their behaviour was not well captured by the ceramic-specific models. The addition of the water concentration C_{H_2O} (mol m^{-3}) to both the non-catalytic and the autocatalytic parts of the polymer scission rate equation could improve the performance when dealing with case studies with water-limited degradation.
- Adaptation of the modelling framework for polymers with high degree of crystallinity: the modelling framework does not consider the presence of crystalline phase in the polymeric matrix and therefore, failed to characterise cases with a high degree of crystallinity, a significant increase of crystallinity during degradation or different crystallinity values for pure polymer and composite samples. This misrepresentation happened due to the difference in polymer degradation rate between amorphous and crystalline phases [3, 4]. As biodegradable polyesters usually present certain degree of crystallinity [5], including modifications to deal with the crystalline phase would result in an increase in the versatility of the models. The needed modifications could follow, for example, the theory proposed by Han and Pan [2, 6, 7] or the simplified version proposed by Gleadall et al. [8].
- Inclusion of a characterisation of the transport mechanisms for the different species present during composite degradation: the modelling framework assumes negligible diffusion out of the composite sample and sufficient diffusion within the unit cell of both polymer degradation products such as monomers, oligomers and hydrogen ions, and ceramic dissolution products such as calcium ions and specific ceramic anions. Including the possibility for these degradation products of experiencing controlled diffusion within the composite, and particularly, out of the composite sample would dramatically improve the characterisation of similar biocomposites with different shapes and porosities providing a true value for the autocatalytic polymer degradation rate k_2'. A starting point for the inclusion of the diffusion of polymer degradation products could be the model initially proposed by Wang et al. [9] and modified by Pan [2]. Further analysis would be necessary to include the transport mechanisms of the ceramic dissolution products.
- As a simpler alternative to the inclusion of the polymer degradation products diffusion mechanisms, a database with all the obtained k_2' values for similar biocomposites with different sample shape or porosity could be built and analysed

using a mathematical expression that related the measured values of the autocatalytic polymer degradation rate k_2' to the real value with a factor f_{shape}, function of the characteristic diffusional length $L_{H^+\text{–buffer}}$.

- Use of a pH dependent law to characterise ceramic dissolution: the modelling framework uses a power law to characterise ceramic dissolution with constant A_d and θ values. During composite degradation, the pH of the environment surrounding the ceramic particle changed with degradation time and thus, the use of pH dependent ceramic dissolution rate A_d and exponent θ would result in a more accurate description of the ceramic dissolution behaviour.
- Addition of a non-stoichiometry factor to the ceramic dissolution rate equation: the modelling framework assumes stoichiometric ceramic dissolution but the in-house hydroxyapatite dissolution studies showed a non-stoichiometric dissolution behaviour [10]. Including a factor $k_{\text{non-stoi}}$, representing the ratio of dissolved ceramic anions to calcium cations, would allow a more realistic characterisation of case studies with non-stoichiometric ceramic dissolution.
- Development of a 3D version of the model that could be added to the modelling environment COMSOL Multiphysics enabling the study of real 3D degradation data obtained with micro X-ray computed tomography and handled with Simpleware for geometries of particular interest such as plates or pins using the approach employed by Shine et al. for polymeric scaffolds [11].
- Development of a kinetic Monte Carlo based model to characterised polymer hydrolysis and ceramic dissolution coupled with finite differences for diffusion, which would enable a better understanding of the initial polymer molecular weight distribution and ceramic particle size distribution as well as their evolutions over time. The model could follow the approach employed by Han and Pan for biodegradable polymers [12, 13].
- Addition of the effect of polymer end-group: the initial concentration of hydrogen ions was computed assuming that all the polymer chains ended in free carboxylic acids which could be ionised. A more accurate characterisation could be achieved by considering the polymer end-group and its ionising capability, if any.
- Generation of a database of values of the non-catalytic polymer degradation rate k_1 extracted from nanoparticles degradation data from different polymeric matrixes. Such database would facilitate the use of the detailed analysis method.
- Generation of a database of scission types experienced by the different polymeric matrixes: the modelling framework can accommodate different scission types by changing α (1) and β (1), the empirical parameters used to characterise the polymer scission type and subsequent production of short chains by chain scission. Such database would ensure the use of the correct scission type with each polymer improving the characterisation of the composite degradation behaviour.
- Study of the values of representative particle size within composite samples: a study relating the value of representative particle size within a composite and the value of representative particle size within the ceramic phase before composite making would result in an improvement of ceramic characterisation.
- Selection of a particular subset of the analysed degradation data with potentially interesting clinical application for in-depth analysis of that particular polymer and

ceramic in terms of polymer scission type, non-catalytic polymer degradation, water diffusion, ceramic dissolution under several pH values, etc., which would facilitate the development of a predictive model.

The second group of recommendations contains completely different approaches that could be used with the significant amount of harvested composite degradation data.

- Development of a neural network for classification/prediction of the composite degradation behaviour and study of the relevance of each composite parameter extracted during the data harvest in the displayed composite degradation.
- Development of a model with a binary yes/no outcome stating the suitability for a specific clinical application of a given particular bioresorbable composite.

In summary, this thesis has presented a modelling framework for the degradation of bioresorbable composites, enabling a global approach for the analysis of data with different calcium-based ceramics, resulting in an up-to-date picture of the current understanding of biocomposite degradation which could be used for a better implant design or as a stepping-stone towards a predictive model for customisation of biocomposite implants in clinical use.

References

1. Pan, J., Han, X., Niu, W., & Cameron, R. E. (2011). A model for biodegradation of composite materials made of polyesters and tricalcium phosphates. *Biomaterials*, *32*(9), 2248–2255.
2. Pan, J. (2014). *Modelling degradation of bioresorbable polymeric medical devices*. Elsevier.
3. Tsuji, H., Nakahara, K., & Ikarashi, K. (2001). Poly(L-lactide), 8. High-temperature hydrolysis of poly(L-lactide) films with different crystallinities and crystalline thicknesses in phosphate-buffered solution. *Macromolecular Materials and Engineering*, *286*(7), 398–406.
4. Tsuji, H., Ikarashi, K., & Fukuda, N. (2004). Poly(L-lactide): XII. Formation, growth, and morphology of crystalline residues as extended-chain crystallites through hydrolysis of poly(L-lactide) films in phosphate-buffered solution. *Polymer Degradation and Stability*, *84*(3), 515–523.
5. Van de Velde, K., & Kiekens, P. (2002). Biopolymers: Overview of several properties and consequences on their applications. *Polymer Testing*, *21*(4), 433–442.
6. Han, X., & Pan, J. (2009). A model for simultaneous crystallisation and biodegradation of biodegradable polymers. *Biomaterials*, *30*(3), 423–430.
7. Han, X., Pan, J., Buchanan, F., Weir, N., & Farrar, D. (2010). Analysis of degradation data of poly(L-lactide-co-L, D-lactide) and poly(L-lactide) obtained at elevated and physiological temperatures using mathematical models. *Acta Biomaterialia*, *6*(10), 3882–3889.
8. Gleadall, A., Pan, J., & Atkinson, H. (2012). A simplified theory of crystallisation induced by polymer chain scissions for biodegradable polyesters. *Polymer Degradation and Stability*, *97*(9), 1616–1620.
9. Wang, Y., Pan, J., Han, X., Sinka, C., & Ding, L. (2008). A phenomenological model for the degradation of biodegradable polymers. *Biomaterials*, *29*(23), 3393–3401.
10. Nair, M. (2016). *Modelling and study of the dissolution rate of calcium-based fillers in composites for orthopaedic applications*. Part III individual research project: Department of Materials Science and Metallurgy, University of Cambridge.

11. Shine, R., Shirazi, R. N., Ronan, W., Sweeney, C. A., Kelly, N., Rochev, Y. A., et al. (2017). Modeling of biodegradable polyesters with applications to coronary stents. *Journal of Medical Devices*, *11*(2), 021007.
12. Han, X., & Pan, J. (2011). Polymer chain scission, oligomer production and diffusion: A two-scale model for degradation of bioresorbable polyesters. *Acta Biomaterialia*, *7*(2), 538–547.
13. Han, X. (2011). *Degradation models for polyesters and their composites*. Ph.D. thesis, Univeristy of Leicester.

Appendix A

A.1 Carbonated Hydroxyapatite (CHA)

For carbonated hydroxyapatite (CHA), with the formula: $Ca_{10}(PO_4)_6(CO_3)_x(OH)_{2-2x}$, a fraction of $x = 0.4$ was chosen to accommodate the reduction in carbonate content experienced during heat treatment by bone, which usually has $CO_3 = (4...6)\%$. The chosen value, $x = 0.4$, represents a $CO_3 \approx 2.4\%$ and a $CO_2 \approx 1.7\%$, with the latter value needed to calculate the K_{sp} value according to Ito et al. [1].

The CHA molar mass can be expressed as a function of pure hydroxyapatite molar mass, M_{HA}, and the carbonate content, x, as:

$$\begin{aligned} M_{CHA} &= 10M_{Ca} + 6(M_P + 4M_O) + x(M_C + 3M_O) + (2 - 2x)(M_H + M_O) \\ &= M_{HA} + x(M_O + M_C - 2M_H) \\ &= 1004.6162 + x(25.994) \\ &= 1004.6162 + 0.4(25.994) \\ &= 1015.010 \qquad \text{g mol}^{-1} \end{aligned} \tag{A.1}$$

A.2 Solubility Product (K_{sp}) and Equilibrium Calcium Concentration ($[Ca^{2+}]_{eq}$)

The general equilibrium equation for the dissolution of a sparingly soluble ionic compound MX_ν is given by the following expression from [2]:

$$MX_\nu(s) \rightleftharpoons M^{\nu+}(aq) + \nu X^-(aq) \tag{A.2}$$

The solubility product (K_{sp}) can be defined as:

I. Moreno-Gomez, *A Phenomenological Mathematical Modelling Framework for the Degradation of Bioresorbable Composites*, Springer Theses, https://doi.org/10.1007/978-3-030-04990-4

$$K_{sp} = [M^+][X^-]^\nu \tag{A.3}$$

with $[M^+]$, the concentration of M^+ ions in water and $[X^-]$, the concentration of X^- ions in water.

A generalised version can be expressed as:

$$K_{sp} = \prod_{i=1}^{n} C_i^{m_i}|_{eq} \tag{A.4}$$

with $C_i|_{eq}$ the concentration of constituents ions at equilibrium and m_i, their respective coefficients in the ionic compound.

A.2.1 Tricalcium Phosphate (TCP)

Tricalcium phosphate (TCP), whose chemical formula is $Ca_3(PO_4)_2$, has the following dissolution reaction:

$$Ca_3(PO_4)_2\ (s) \overset{37\ ^\circ C}{\rightleftharpoons} 3Ca^{2+}(aq) + 2(PO_4^{3-})(aq) \tag{A.5}$$

Assuming stoichiometric dissolution: $[PO_4^{3-}]_{eq} = \frac{2}{3}[Ca^{2+}]_{eq}$ and the solubility product can be expressed as:

$$\begin{aligned} K_{sp} &= ([Ca^{2+}]_{eq})^3([PO_4^{3-}]_{eq})^2 \\ &= ([Ca^{2+}]_{eq})^3\left(\frac{2}{3}\right)^2([Ca^{2+}]_{eq})^2 \\ &= \frac{4}{9}([Ca^{2+}]_{eq})^5 \qquad (mol^5\,dm^{-15}) \end{aligned} \tag{A.6}$$

Thus, the equilibrium calcium concentration is:

$$\begin{aligned} [Ca^{2+}]_{eq} &= \left(\frac{9}{4}K_{sp}\right)^{\frac{1}{5}} \\ &= \left(\frac{9}{4}10^{-(-\log_{10}K_{sp})}\right)^{\frac{1}{5}} \qquad (mol\,dm^{-3}) \end{aligned} \tag{A.7}$$

A.2.2 Pure Hydroxyapatite (HA_p)

Pure hydroxyapatite, whose chemical formula is $Ca_{10}(PO_4)_6(OH)_2$, has the following dissolution reaction:

$$Ca_{10}(PO_4)_6(OH)_2\ (s) \overset{37\ ^\circ C}{\rightleftharpoons} 10Ca^{2+}(aq) + 6(PO_4^{3-})(aq) + 2(OH^-)(aq) \quad (A.8)$$

Assuming stoichiometric dissolution: $[PO_4^{3-}]_{eq} = \frac{3}{5}[Ca^{2+}]_{eq}$ and $[OH^-]_{eq} = \frac{1}{5}[Ca^{2+}]_{eq}$, and K_{sp} can be expressed as:

$$\begin{aligned} K_{sp} &= ([Ca^{2+}]_{eq})^{10}([PO_4^{3-}]_{eq})^6([OH^-]_{eq})^2 \\ &= ([Ca^{2+}]_{eq})^{10}\left(\frac{3}{5}\right)^6([Ca^{2+}]_{eq})^6\left(\frac{1}{5}\right)^2([Ca^{2+}]_{eq})^2 \\ &= \frac{3^6}{5^8}([Ca^{2+}]_{eq})^{18} \qquad (mol^{18}\,dm^{-54}) \end{aligned} \quad (A.9)$$

Thus, the equilibrium calcium concentration is:

$$\begin{aligned} [Ca^{2+}]_{eq} &= \left(\frac{5^8}{3^6}K_{sp}\right)^{\frac{1}{18}} \\ &= \left(\frac{5^8}{3^6}10^{-(-\log_{10}K_{sp})}\right)^{\frac{1}{18}} \qquad (mol\,dm^{-3}) \end{aligned} \quad (A.10)$$

A.2.3 Carbonated Hydroxyapatite (CHA)

Carbonated hydroxyapatite (CHA), with the formula: $Ca_{10}(PO_4)_6(CO_3)_x(OH)_{2-2x}$ with x = 0.4, has the following dissolution reaction:

$$\begin{aligned} Ca_{10}(PO_4)_6(CO_3)_x(OH)_{2-2x}\ (s) \overset{37\,^\circ C}{\rightleftharpoons} 10Ca^{2+}(aq) + 6(PO_4^{3-})(aq) \\ + 0.4(CO_3^{2-})(aq) + 1.2(OH^-)(aq) \end{aligned} \quad (A.11)$$

Assuming stoichiometric dissolution: $[PO_4^{3-}]_{eq} = \frac{3}{5}[Ca^{2+}]_{eq}$, $[CO_3^{2-}]_{eq} = \frac{x}{10}[Ca^{2+}]_{eq}$ and $[OH^-]_{eq} = \frac{1-x}{5}[Ca^{2+}]_{eq}$, and K_{sp} can be expressed as:

$$\begin{aligned} K_{sp} &= ([Ca^{2+}]_{eq})^{10}([PO_4^{3-}]_{eq})^6([CO_3^{2-}]_{eq})^x([OH^-]_{eq})^{(2-2x)} \\ &= ([Ca^{2+}]_{eq})^{10}\left(\frac{3}{5}\right)^6([Ca^{2+}]_{eq})^6\left(\frac{x}{5}\right)^x([Ca^{2+}]_{eq})^x\left(\frac{1-x}{5}\right)^{(2-2x)}([Ca^{2+}]_{eq})^{(2-2x)} \\ &= \frac{3^6(2.5x)^x(1-x)^{(2-2x)}}{5^8}([Ca^{2+}]_{eq})^{(18-x)} \qquad (mol^{18-x}\,dm^{-(54-1.2x)}) \end{aligned} \quad (A.12)$$

Thus, the equilibrium calcium concentration is:

$$[Ca^{2+}]_{\text{eq}} = \left(\frac{5^8}{3^6(2.5\text{x})^{\text{x}}(1-\text{x})^{(2-2\text{x})}} K_{\text{sp}}\right)^{\frac{1}{18-\text{x}}}$$
$$= \left(\frac{5^8}{3^6(2.5\text{x})^{\text{x}}(1-\text{x})^{(2-2\text{x})}} 10^{-(-\log_{10} K_{\text{sp}})}\right)^{\frac{1}{18-\text{x}}}$$
$$= \left(\frac{5^8}{3^6 1^{0.4} 0.6^{1.2}} 10^{-(-\log_{10} K_{\text{sp}})}\right)^{\frac{1}{17.6}} \quad (\text{mol dm}^{-3}) \quad \text{(A.13)}$$

A.2.4 Calcium Carbonate (CC)

Calcium carbonate, whose chemical formula is $CaCO_3$, has the following dissolution reaction:

$$CaCO_3\ (s) \overset{37\ ^\circ\text{C}}{\rightleftharpoons} Ca^{2+}(aq) + (CO_3^{2-})(aq) \quad \text{(A.14)}$$

Assuming stoichiometric dissolution: $[Ca^{2+}]_{\text{eq}} = [CO_3^{2-}]_{\text{eq}}$, and K_{sp} can be expressed as:

$$K_{\text{sp}} = [Ca^{2+}]_{\text{eq}}[CO_3^{2-}]_{\text{eq}}$$
$$= ([Ca^{2+}]_{\text{eq}})^2 \quad (\text{mol}^2\ \text{dm}^{-6}) \quad \text{(A.15)}$$

Thus, the equilibrium calcium concentration is:

$$[Ca^{2+}]_{\text{eq}} = (K_{\text{sp}})^{\frac{1}{2}}$$
$$= \left(10^{-(-\log_{10} K_{\text{sp}})}\right)^{\frac{1}{2}} \quad (\text{mol dm}^{-3}) \quad \text{(A.16)}$$

A.3 Polymer Dissociation Constant (pK_{a}) for Copolymers and Blends

The dissociation constant K_{a} of a copolymer or polymer blend can be computed using the K_{a} values of their individual components, usually reported in literature, as shown for a two-components case:

$$K_{\text{a1}} = \frac{[H^+][R_1\text{-}COO^-]}{[R_1\text{-}COOH]} \quad \text{(A.17)}$$

$$K_{\text{a2}} = \frac{[H^+][R_2\text{-}COO^-]}{[R_2\text{-}COOH]} \quad \text{(A.18)}$$

The overall K_a value can be expressed as:

$$K_a = \frac{[H^+][R\text{-}COO^-]}{[R\text{-}COOH]} = \frac{[H^+]\left([R_1\text{-}COO^-] + [R_2\text{-}COO^-]\right)}{[R_1\text{-}COOH] + [R_2\text{-}COOH]} \tag{A.19}$$

Assuming random polymerisation, the possibility of finding a specific monomer at the end of a chain is equal to the molar fraction of said monomer:

$$[R_1\text{-}COOH] + [R_1\text{-}COO^-] = \frac{\alpha_1}{\alpha_2}([R_2\text{-}COOH] + [R_2\text{-}COO^-]) \tag{A.20}$$

As the ratio of undissociated to dissociated chains is large, the relationship can be approximated as:

$$[R_1\text{-}COOH] = \frac{\alpha_1}{\alpha_2}[R_2\text{-}COOH] \tag{A.21}$$

Given the following expression for the overall K_a value:

$$\begin{aligned} K_a &= \frac{[H^+][R\text{-}COO^-]}{[R\text{-}COOH]} = \frac{[H^+][R_1\text{-}COO^-] + [H^+][R_2\text{-}COO^-]}{[R_1\text{-}COOH] + [R_2\text{-}COOH]} \\ &= \frac{K_{a1}[R_1\text{-}COOH] + K_{a2}[R_2\text{-}COO^-]}{[R_1\text{-}COOH] + [R_2\text{-}COOH]} \\ &= \frac{K_{a1}[R_1\text{-}COOH] + K_{a2}\frac{\alpha_2}{\alpha_1}[R_1\text{-}COOH]}{[R_1\text{-}COOH] + \frac{\alpha_2}{\alpha_1}[R_1\text{-}COOH]} \\ &= \frac{K_{a1} + K_{a2}\frac{\alpha_2}{\alpha_1}}{1 + \frac{\alpha_2}{\alpha_1}} = \frac{K_{a1}\alpha_1 + K_{a2}\alpha_2}{\alpha_1 + \alpha_2} = \alpha_1 K_{a1} + \alpha_2 K_{a2} \end{aligned} \tag{A.22}$$

Resulting in a dissociation constant value for a copolymer or polymer blend of $pK_a = -\log_{10}(\alpha_1 K_{a1} + \alpha_2 K_{a2})$ with α_1 and α_2, the molar/ ratios of the two components of the copolymer or blend and K_{a1} and K_{a2}, their corresponding values of dissociation constant.

A.4 Initial Degree of Pseudo-polymerisation

N_{dp0} (Da Da^{-1}), the initial degree of pseudo-polymerisation, can be expressed as a function of M_{unit}, the molar mass associated to one ester bond (Da) and M_{n0}, the number-average molecular weight at the time origin (Da); or C_{e0}, the concentration of ester bonds in long chains at the time origin in the polymer phase (mol m^{-3}) and C_{chain0}, the initial concentration of long polymer chains in the polymer phase (mol m^{-3}) using $C_{e0} = \frac{\rho_{pol}}{M_{unit}}$ and $C_{chain0} = \frac{\rho_{pol}}{M_{n0}}$ with ρ_{pol}, the polymer density (kg m^{-3}):

$$\frac{C_{\text{chain0}}}{C_{\text{e0}}} = \frac{\text{Initial number of chains}}{\text{Initial number of ester bonds}} = \frac{\frac{\rho_{\text{pol}}}{M_{\text{n0}}}}{\frac{\rho_{\text{pol}}}{M_{\text{unit}}}} = \frac{M_{\text{unit}}}{M_{\text{n0}}} = N_{\text{dp0}}^{-1} \tag{A.23}$$

A.5 Sauter Mean Diameter

Assuming spherical particles, the diameter which characterises the distribution in terms of volume and surface area, d_{eq}, would satisfy:

$$\begin{aligned}\frac{\text{Overall volume of particles}}{\text{Overall surface of particles}} &= \frac{\sum_{i=1}^{N} V_i}{\sum_{i=1}^{N} A_i} = \frac{\sum_{i=1}^{N} \frac{\pi}{6} d_i^3}{\sum_{i=1}^{N} \pi d_i^2} \\ &= \frac{N\frac{\pi}{6} d_{\text{eq}}^3}{N\pi d_{\text{eq}}^2} = \frac{d_{\text{eq}}}{6} \quad \text{(m)}\end{aligned} \tag{A.24}$$

being V_i (m^3), A_i (m^2) and d_i (m), the volume, surface area and diameter of the ith particle respectively.

The Sauter Mean diameter, (*SMD* or $D[2, 3]$ or d_{32}), is defined as:

$$\begin{aligned}SMD = D[2,3] = d_{32} = \frac{d_{\text{v}}^3}{d_{\text{s}}^2} = \frac{N d_{\text{v}}^3}{N d_{\text{s}}^2} == \frac{\sum_{i=1}^{N} d_i^3}{\sum_{i=1}^{N} d_i^2} \\ = 6\frac{\sum_{i=1}^{N} \frac{\pi}{6} d_i^3}{\sum_{i=1}^{N} \pi d_i^2} = 6\frac{\sum_{i=1}^{N} V_i}{\sum_{i=1}^{N} A_i} \quad \text{(m)}\end{aligned} \tag{A.25}$$

with d_{v} (m), the volume equivalent particle diameter and d_{s} (m), the surface equivalent particle diameter.

Thus, $d_{\text{eq}} = SMD = D[2, 3] = d_{32}$.

A.6 Geometric Mean and Geometric Standard Deviation

The geometric mean of a set of numbers $\{x_1, x_2, \ldots, x_N\}$ can be defined as:

$$\mu_{\text{g}} = \left(\prod_{i=1}^{N} x_i\right)^{\frac{1}{N}} = \sqrt[N]{x_1 x_2 \ldots x_N} \tag{A.26}$$

And the geometric standard deviation, more appropriately called geometric SD factor [3], can be calculated as:

$$\sigma_g = \exp\left(\sqrt{\frac{\sum_{i=1}^{N}\left(\ln\frac{x_i}{\mu_g}\right)^2}{N-1}}\right) \tag{A.27}$$

With $\{x_1, x_2, \ldots, x_N\}$ characterised by $(\mu_g \divideontimes \sigma_g)$

A.7 Characterisation of Poly(ethylene:hexamethylene/sebacate)

Figure A.1 includes the different repeating units of the poly(ethylene:hexamethylene/sebacate) block [4]. The copolymer had an estimated 50 mol% sebacic acid, a 25 mol% ethylene glycol and a 25 mol% hexamethylene glycol [5].

A random copolymerisation yields, on average, 1.75 ester bonds available per repeating unit, resulting in a M_{unit} value of:

$$\begin{aligned} M_{unit} &= \frac{\text{Molar mass of the average repeating unit}}{\text{Number of ester bonds per repeating unit}} \\ &= \frac{0.5M_{\text{sebacic acid}} + 0.25M_{\text{ethylene}} + 0.25M_{\text{hexamethylene}}}{1.75} \\ &= 146.481 \text{ Da} \end{aligned} \tag{A.28}$$

with $M_{\text{sebacic acid}}$, M_{ethylene} and $M_{\text{hexamethylene}}$, the molar masses of the different monomer repeating units.

Table A.1 includes the values of the polymer-specific parameters for poly(ethylene:hexamethylene/sebacate) block copolymer.

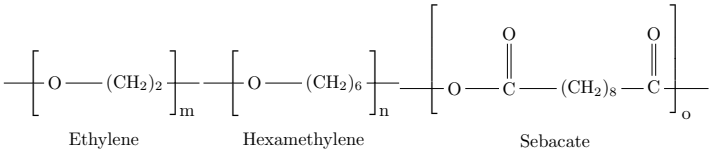

Fig. A.1 Structure of the repeating units of poly(ethylene:hexamethylene/sebacate) block copolymer, taken from [4]

Table A.1 Polymer-specific parameters for poly(ethylene:hexamethylene/sebacate) block copolymer. M_{unit} is the average molar mass associated to one ester bond, $\text{p}K_{\text{a}}$ is the negative base 10 logarithm of the sebacate segment acid dissociation constant at 25 °C and ρ_{pol} is the polymer density reported as midpoint of the typical density interval

Property	Value	Reference
M_{unit}	146.481 Da	See above
$\text{p}K_{\text{a}}$ at 25 °C	4.59	[6]
ρ_{pol}	1085 kg m^{-3}	[7]

Appendix B

This appendix contains information of all the analysed case studies in tabular format. Presented divided by ceramic filler and subdivided by polymeric matrix, each case study occupies a row containing the values of the four composite degradation constants (k_1, k_2', A_d and θ), in addition to several relevant characteristics. These characteristics are split into three different groups: polymer characteristics, such as polymer type and manufacturer; ceramic characteristics, such as ceramic type and manufacturer; and general sample characteristics, such as structure and morphology, fabrication method and degradation protocol. The TCP case studies can be found in Appendix B.1, followed by HA cases in Appendix B.2 and lastly, CC cases in Appendix B.3.

B.1 Tricalcium Phosphate Case Studies Modelling Results

TCP case studies with a poly(L-lactide) matrix are included in Appendix B.1.1, (Table B.1), followed by cases with a poly(D,L-lactide) homo- or copolymer matrix in Appendix B.1.2, (Table B.2), cases with poly(lactide-co-glycolide) matrix in Appendix B.1.3, (Table B.3), and lastly, cases with miscellaneous polymers matrixes in Appendix B.1.4, (Table B.4).

I. Moreno-Gomez, *A Phenomenological Mathematical Modelling Framework for the Degradation of Bioresorbable Composites*, Springer Theses, https://doi.org/10.1007/978-3-030-04990-4

B.1.1 Poly(L-lactide) Matrix

Table B.1 Results output by the TCP composites degradation model for cases with a poly(L-lactide) matrix. k_1 is the non-catalytic polymer degradation rate, k_2' is the autocatalytic polymer degradation rate, A_d is the ceramic dissolution rate and θ is the power ceramic dissolution law exponent. Abbreviations used to specify the tricalcium phosphate type can be found in Table 4.2. A dashed line between rows indicates that data displayed in those consecutive rows belong to the same researcher or research group. A solid line between rows indicates no known author relationship for the data

Polymer characteristics				Ceramic characteristics				Sample characteristics			
Type	Manufacturer	k_1 (s^{-1})	k_2' ($m^3\ mol^{-1}\ s^{-1}$)	Type	Manufacturer	A_d ($mol\ m^{-2}\ s^{-1}$)	θ (1)	Structure and Morphology	Fabrication method	Degradation protocol	Case code and reference
Poly(L-lactide)	Shimadzu Co., Ltd.; Kyoto, Japan (Lacty#5000)	1.4×10^{-11} (3.7×10^{-12})	2.1×10^{-11} (4.30×10^{-12})	β-TCP	Taihei Chemical Industrial Co., Ltd., Osaka, Japan	5.0×10^{-12}	2.0	Dense film: $10 \times 100\ mm^2 \times 4\ mm$	Polymer and ceramic dry-mixed + injection-moulded into final shape	In vitro: PBS (pH = 7.4) at 37°C, w/o shaking, w/o replacement	Kobayashi β-TCP [8]
Poly(L-lactide)	Purac Biomaterials B.V.; Gorinchem, The Netherlands	4.0×10^{-10} (1.1×10^{-11})	3.8×10^{-10} (1.0×10^{-11})	β-TCP	In-house production: granulated + sintered at 1000°C in air	1.0×10^{-12}	2.0	Dense cylinder: $\Phi = 6$ mm, $L = 10$ mm	Polymer and ceramic mixed in air at 60°C for 24 h + injection-moulded into final shape + γ-irradiation 25 kGy	In vivo: femoral implantation in rabbits following Kathagen protocol	Aunoble β-TCP [9]
Poly(L-lactide)	Purac Biomaterials B.V.; Gorinchem, The Netherlands	5.0×10^{-12}	1.3×10^{-11}	β-TCP	Degradable Solution AG, Switzerland	7.0×10^{-14}	2.0	Dense bar: $60 \times 9\ mm^2 \times 1.5\ mm$	Polymer and ceramic mixed in twin-screw extruder at 200°C+ milled to powder in liquid N_2 + compression-moulded into final shape + sterilised w ethylene oxide	In vitro: Simulated body fluid (SBF) (pH = 7.4) at 37°C, w/o shaking, w/o replacement	Adamus β-TCP [10]

(continued)

Table B.1 (continued)

Polymer characteristics				Ceramic characteristics				Sample characteristics			
Type	Manufacturer	k_1 (s^{-1})	k'_2 ($m^3\ mol^{-1}\ s^{-1}$)	Type	Manufacturer	A_d ($mol\ m^{-2}\ s^{-1}$)	θ (1)	Structure and Morphology	Fabrication method	Degradation protocol	Case code and reference
Poly(L-lactide)	Chengdu Organic Chemicals Co. Ltd, China	3.2×10^{-11}	3.8×10^{-11}	β-TCP	In-house production: wet chemistry route using $CaCO_3$ and H_3PO_4 + calcining at 950 °C for 2 h	3.0×10^{-14}	2.0	Porous (60%) cylinder: Φ = 5 mm, L = 10 mm	Polymer dissolved in chloroform + ceramic and porogen addition + composite precipitation in acetone and ethanol + compression moulding at 7 MPa and 25 °C + porogen leaching	In vitro: SBF (pH = 7.4) at 37 °C, w shaking, w replacement of 30 mL every 2 days, 100 mL/sample	Kang 07 S β-TCP [11]
Poly(L-lactide)	Chengdu Organic Chemicals Co. Ltd, China	2.2×10^{-11}	2.2×10^{-11}	β-TCP	In-house production: same as Kang 07 S	3.0×10^{-14}	2.0	Porous (60%) cylinder: Φ = 5 mm, L = 10 mm	Same as Kang 07 S	In vitro: SBF (pH = 7.4) at 37 °C, w constant buffer replacement at a flow rate of 0.02 mL/(mL min)	Kang 07 F β-TCP [11]
Poly(L-lactide)	Chengdu Organic Chemicals Co. Ltd, China	2.8×10^{-11}	3.4×10^{-11}	β-TCP	In-house production: same as Kang 07 S	3.0×10^{-14}	2.0	Porous (60%) cylinder: Φ = 5 mm, L = 10 mm	Same as Kang 07 S	In vitro: same as Kang 07 F	Kang 09 F β-TCP [12]
Poly(L-lactide)	Chengdu Organic Chemicals Co. Ltd, China	4.2×10^{-11}	5.8×10^{-11}	β-TCP	In-house production: same as Kang 09 F	3.0×10^{-14}	2.0	Porous (60%) cylinder: Φ = 5 mm, L = 10 mm	Same as Kang 07 S	In vitro: SBF (pH = 7.4) at 37 °C, w constant buffer replacement at a flow rate of 0.02 mL/(mL min) and dynamic loading at 0.6 Hz and 0.1 MPa	Kang 09 FL β-TCP [12]

B.1.2 Poly(D,L-lactide) Homo- and Copolymers Matrixes

Table B.2 Results output by the TCP composites degradation model for cases with a poly(D,L-lactide) or a poly(D,L-lactide) copolymer matrix. k_1 is the non-catalytic polymer degradation rate, k_2' is the autocatalytic polymer degradation rate, A_d is the ceramic dissolution rate and θ is the power ceramic dissolution law exponent. Abbreviations used to specify the tricalcium phosphate type can be found in Table 4.2. A dashed line between rows indicates that data displayed in those consecutive rows belong to the same researcher or research group. A solid line between rows indicates no known author relationship for the data

Polymer characteristics				Ceramic characteristics				Sample characteristics			
Type	Manufacturer	k_1 (s^{-1})	k_2' ($m^3\ mol^{-1}\ s^{-1}$)	Type	Manufacturer	A_d ($mol\ m^{-2}\ s^{-1}$)	θ (1)	Structure and Morphology	Fabrication method	Degradation protocol	Case code and reference
Poly(D,L-lactide)(4:96)	Purac Biochem B.V.; Gorinchem, The Netherlands	5.0×10^{-11}	5.0×10^{-11}	β-TCP	Biomatlante SA; Vigneux de Bretagne, France	5×10^{-12}	2.0	Dense cylinder: $\Phi = 6$ mm; L = 8 mm	Polymer + ceramic fed to twin-screw extruder + extruded into cylindrical billet at 50 rpm and (225...235) °C for 2.5 min + self-reinforcing + machined into final shape + γ-radiation (25 kGy)	In vitro: PBS (pH = 7.4) at 37 °C, w fortnightly replacement	Daculsi Vit β-TCP [13]
Poly(D,L-lactide)(4:96)	Purac Biochem B.V.; Gorinchem, The Netherlands	7.0×10^{-11}	7.0×10^{-11}	β-TCP	Biomatlante SA; Vigneux de Bretagne, France	1.0×10^{-11}	2.0	Dense cylinder: $\Phi = 6$ mm; L = 8 mm	Same as Daculsi Vit β-TCP	In vivo: condylar implantation in adult New Zealand white rabbits	Daculsi Viv β-TCP [13]
Poly(D,L-lactide)(4:96)	Purac Biochem B.V.; Gorinchem, The Netherlands (Purasorb PLD9655)	4.8×10^{-11}	4.8×10^{-11}	β-TCP	CAM Implants B.V., Leiden, The Netherlands	3.0×10^{-11}	2.0	Dense cylinder: Pure Polymer: Φ = (2.6...2.7) mm; Composite: Φ = (2.9...3.0) mm; L = 30 mm	Polymer granules mixed w ceramic particles + melt-extrusion into cylindrincal billet + solid state die-drawing at 120 °C to final diameter + γ-radiation (25 kGy)	In vitro: PBS (pH = 7.4) at 37 °C, w/o shaking, w fortnightly replacement	Niemela LD β-TCP [14]

(continued)

Table B.2 (continued)

Polymer characteristics				Ceramic characteristics				Sample characteristics			
Type	Manufacturer	k_1 (s^{-1})	k_2' ($m^3\,mol^{-1}\,s^{-1}$)	Type	Manufacturer	A_d ($mol\,m^{-2}\,s^{-1}$)	θ (1)	Structure and Morphology	Fabrication method	Degradation protocol	Case code and reference
Poly(D,L-lactide)(50:50)	In-house production: ring-opening polymerisation of D,L-lactide	7.6×10^{-10}	7.2×10^{-10}	aβ-TCP	In-house production: wet chemistry route	7.0×10^{-12}	2.0	Dense film: 4 × $8\,mm^2$ × 1 mm	Polymer dissolved in chloroform + ceramic dispersed in ethanol + addition of ceramic dispersion + press moulding at 85 °C and (10...15) MPa for 10 min	In vitro: PBS (pH = 7.4) at 37 °C, w shaking at 100 rpm, 100 $mL\,g^{-1}$	Zheng aβ-TCP [15]
Poly(D,L-lactide)(50:50)	Merck; Darmstadt, Germany	2.6×10^{-10}	4.2×10^{-10}	β-TCP	In-house production: as-received TCP (Merck; Darmstadt, Germany) granulated and calcined at 1200 °C for 2 h + crushing, milling and sieving	7.0×10^{-10}	2.0	Dense cylinder: Φ = 5 mm, L = 40 mm	Polymer melted + mixed w ceramic + sintered at 90 °C and (50...80)mPa for 30 min	In vitro: saline at 37 °C	Lin β-TCP [16]
Poly(D,L-lactide)(50:50)	Boehringer Ingelheim, Germany (Resomer R270)	1.0×10^{-10}	9.0×10^{-11}	β-TCP (Assumed)	In-house production: as-received TCP (Fluka AG, Switzerland) milled in ethanol	7.0×10^{-13}	2.0	Dense rod: 20 × $3\,mm^2$ × 2 mm	Polymer and ceramic mixing + injection moulding + γ-irradiation 25 kGy	In vivo: dorsal muscles implantation in rats	Heidemann β-TCP [17]

(continued)

Table B.2 (continued)

Polymer characteristics				Ceramic characteristics				Sample characteristics			
Type	Manufacturer	k_1 (s^{-1})	k_2' ($m^3\ mol^{-1}\ s^{-1}$)	Type	Manufacturer	A_d ($mol\ m^{-2}\ s^{-1}$)	θ (1)	Structure and Morphology	Fabrication method	Degradation protocol	Case code and reference
Poly(L-co-D,L-lactide)(70:30)	Boehringer Ingelheim; Ingelheim am Rhein, Germany (Resomer LR70x family)	9.8×10^{-11}	9.6×10^{-11}	β-TCP	CAM Implants B.V., Leiden, The Netherlands	3.0×10^{-11}	2.0	Dense cylinder: Pure Polymer: $\Phi =$ (2.6...2.7) mm; Composite: $\Phi =$ (2.9...3.0) mm; L = 30 mm	Polymer granules mixed w ceramic particles + melt-extrusion into cylindrincal billet + solid state die-drawing at 120 °C to final diameter + γ-radiation (25 kGy)	In vitro: PBS (pH = 7.4) at 37 °C, w/o shaking, w fortnightly replacement	Niemela LDL β-TCP [18]
Poly(L-co-D,L-lactide)(70:30)	Boehringer Ingelheim; Ingelheim am Rhein, Germany (Resomer LR70x family)	5.4×10^{-11}	5.4×10^{-11}	α-TCP	Not reported	3.0×10^{-12}	2.0	Porous (42 %) cylinder: $\Phi = 10$ mm, L = 15 mm	Ceramic and polymer granules mixed + sintered at 145 °C to final shape + γ-radiation (25 kGy)	In vitro: Sörensen buffer (pH = 7.4) at 37 °C, 50 mL/sample, pH kept constant at 7.4	Ignatius P α-TCP [19]
Poly(L-co-D,L-lactide)(70:30)	Biovision; Ilmenau, Germany (PolyPIN 2.0) and Boehringer Ingelheim; Ingelheim am Rhein, Germany (Resomer LR70x family)	4.5×10^{-11} (3.0×10^{-11})	3.2×10^{-11} (2.0×10^{-11})	β-TCP	Not reported	3.0×10^{-11}	2.0	Dense cylinder: $\Phi = 2$ mm, L = 35 mm	Ceramic granules added to heated polymer + injection-moulding at 210 °C + γ-radiation (28 kGy)	In vitro: Sörensen buffer (pH = 7.4) at 37 °C, 200 $mL\ g^{-1}$, pH kept constant at 7.4	Ignatius D β-TCP [19]

(continued)

Table B.2 (continued)

Polymer characteristics				Ceramic characteristics				Sample characteristics			
Type	Manufacturer	k_1 (s^{-1})	k_2' ($m^3\,mol^{-1}\,s^{-1}$)	Type	Manufacturer	A_d ($mol\,m^{-2}\,s^{-1}$)	θ (1)	Structure and Morphology	Fabrication method	Degradation protocol	Case code and reference
Poly(L-co-D,L-lactide)(70:30)	Purac Biochem B.V.; Gorinchem, The Netherlands (Purasorb PLDL7028)	1.9×10^{-11}	1.8×10^{-11}	β-TCP	Plasma Biotal Ltd.; Tideswell, United Kingdom	5.0×10^{-11}	2.0	Porous disk: Φ= 15 mm, t = 3 mm	Polymer dissolved in dioxane at 3 wt % + ceramic addition + stirring of the mixture + freeze drying	In vitro: PBS (pH = 7.4) at 37 °C, 10 mL/sample	Haaparanta 3w β-TCP [20]
Poly(L-co-D,L-lactide)(70:30)	Purac Biochem B.V.; Gorinchem, The Netherlands (Purasorb PLDL7028)	2.7×10^{-11}	2.5×10^{-11}	β-TCP	Plasma Biotal Ltd.; Tideswell, United Kingdom	5.0×10^{-11}	2.0	Porous disk: Φ= 15 mm, t = 3 mm	Polymer dissolved in dioxane at 2 wt % + ceramic addition + stirring of the mixture + freeze drying	In vitro: PBS (pH = 7.4) at 37 °C, 10 mL/sample	Haaparanta 2w β-TCP [20]

B.1.3 Poly-lactide-co-glycolide Matrix

Table B.3 Results output by the TCP composites degradation model for cases with a poly(lactide-co-glycolide) matrix. k_1 is the non-catalytic polymer degradation rate, k_2' is the autocatalytic polymer degradation rate, A_d is the ceramic dissolution rate and θ is the power ceramic dissolution law exponent. Abbreviations used to specify the tricalcium phosphate type can be found in Table 4.2. A dashed line between rows indicates that data displayed in those consecutive rows belong to the same researcher or research group. A solid line between rows indicates no known author relationship for the data

Polymer characteristics				Ceramic characteristics				Sample characteristics			
Type	Manufacturer	k_1 (s^{-1})	k_2' ($m^3\ mol^{-1}\ s^{-1}$)	Type	Manufacturer	A_d ($mol\ m^{-2}\ s^{-1}$)	θ (1)	Structure and Morphology	Fabrication method	Degradation protocol	Case code and reference
Poly(L-lactide-co-glycolide) (70:30)	In-house production: ring-opening polymerisation of L-lactide and glycolide w stannous octoate	4.2×10^{-10}	2.8×10^{-10}	β-TCP (Assumed)	Forth Reagent Factory; Shanghai, China	3.0×10^{-11}	2.0	Porous (90 %) slab: 6 × 6 mm^2, L = 13 mm	Polymer dissolved in dioxane + ceramic addition + mixing + low-temperature deposition of the slurry using a computer-driven nozzle + freeze-drying	In vitro: distilled water w NaN_3 at 37 °C, w/o shaking, w/o replacement, 50 $mL\ g^{-1}$	Yang F. β-TCP [21]
Poly(L-lactide-co-glycolide) (70:30)	Changchun Institute of Applied Chemistry; Chinese Academy of Sciences, China	3.2×10^{-10}	3.2×10^{-10}	β-TCP	National Engineering Research Centre for Biomaterials; Sichuan University, China	3.0×10^{-13}	2.0	Porous cylinder: Φ = 6 mm, L = 12 mm	Polymer dissolved in chloroform + ceramic and porogen addition + freezing + solvent extraction w ethanol at −18 °C + porogen leached w water	In vitro: PBS (pH = 7.4) at 37 °C, w shaking at 50 rpm, weekly replacement, 4 mL/sample	Yang Y. S β-TCP [21]

(continued)

Table B.3 (continued)

Polymer characteristics				Ceramic characteristics				Sample characteristics			
Type	Manufacturer	k_1 (s^{-1})	k_2' ($m^3\,mol^{-1}\,s^{-1}$)	Type	Manufacturer	A_d ($mol\,m^{-2}\,s^{-1}$)	θ (1)	Structure and Morphology	Fabrication method	Degradation protocol	Case code and reference
Poly(L-lactide-co-glycolide) (70:30)	Changchun Institute of Applied Chemistry; Chinese Academy of Sciences, China	3.5×10^{-10}	3.5×10^{-10}	β-TCP	National Engineering Research Centre for Biomaterials; Sichuan University, China	3.0×10^{-13}	2.0	Porous cylinder: $\Phi = 6$ mm, $L = 12$ mm	Polymer dissolved in chloroform + ceramic and porogen addition + freezing + solvent extraction w ethanol at −18 °C + porogen leached w water	In vitro: PBS (pH = 7.4) at 37 °C, w 8 $h\,d^{-1}$ of cyclic loading at 1 Hz and (0.5...0.6) mm displacement and w 16 $h\,d^{-1}$ of shaking at 50 rpm, weekly buffer replacement, 4 mL/sample	Yang Y. D β-TCP [22]
Poly(L-lactide-co-glycolide) (70.7:29.3)	In-house production: polymerisation using preset microwave power of L-lactide and glycolide w stannous octoate	2.0×10^{-9} (1.5×10^{-9})	2.2×10^{-9} (1.5×10^{-9})	β-TCP	In-house production: wet chemistry route using $Ca(NO_3)\cdot 4H_2O$ and $(NH_4)_2HPO_4$ + aging, filtering and drying + calcining at 800 °C for 2 h	7.0×10^{-12}	2.0	Semi-dense cylinder: $\Phi = 13$ mm, $L = 12$ mm	Ceramic added to initiator and monomers solution + polymerisation using microwave power	In vitro: SBF (pH = 7.4) at 37 °C, w/o shaking, w/o replacement, 15 mL/sample	Jin β-TCP [23]
Poly(D,L-lactide-co-glycolide) (44.6:55.4)	Mitsui Chemicals; Tokyo, Japan: polymerisation of D,L-lactide and glycolide using stannous octoate	3.0×10^{-9}	3.0×10^{-9}	β-TCP (Assumed)	Wako Pure Chemical Industries; Tokyo, Japan	5.0×10^{-11}	2.0	Dense film: 15 × 15 mm^2 × 0.5 mm	Polymer dissolved in dioxane + ceramic addition + freeze-drying of the solvent cast solution + compression moulding at 60 °C and 4.9 MPa	In vitro: PBS (pH = 7.4) at 37 °C, w/o shaking, weekly replacement, 40 mL/sample	Ara β-TCP [24]

(continued)

Table B.3 (continued)

Polymer characteristics				Ceramic characteristics				Sample characteristics			
Type	Manufacturer	k_1 (s^{-1})	k_2' ($m^3\ mol^{-1}\ s^{-1}$)	Type	Manufacturer	A_d ($mol\ m^{-2}\ s^{-1}$)	θ (1)	Structure and Morphology	Fabrication method	Degradation protocol	Case code and reference
Poly(D,L-lactide-co-glycolide) (50:50)	Lakeshore Biomaterials; Birmingham, Alabama, USA (5050 DLG 5E)	2.4×10^{-9}	2.4×10^{-9}	α-TCP	In-house production: wet chemistry route using $Ca(OH)_2$ and H_3PO_4 + aging for 1 d and drying + grinding + calcining at 1400 °C for 4 h + quenching + grinding and sieving through a 100 μm mesh + ball-milling for 1 h in acetone	1.0×10^{-12}	2.0	Dense disk: $\Phi = 3.5$ mm, t = 1 mm	Polymer dissolved in acetone + ceramic addition + solvent casting + injection-moulding at 135 °C and 0.5 MPa into cylinders + cut into final shape	In vitro: PBS (0.01 M, pH = 7.4) at 37 °C, w/o shaking, w/o replacement, 166 $mL\ g^{-1}$	Bennett nC α-TCP [25]
Poly(D,L-lactide-co-glycolide) (50:50)	Lakeshore Biomaterials; Birmingham, Alabama, USA (5050 DLG 5E)	1.4×10^{-9}	1.4×10^{-9}	α-TCP	In-house production: wet chemistry route. Same as Bennett nC α-TCP	5.0×10^{-13}	2.0	Dense disk: $\Phi = 3.5$ mm, t = 1 mm	Same as Bennett nC α-TCP	In vitro: PBS (0.01 M, pH = 7.4) w 50 % v/v of D_2O at 37 °C, w/o shaking, w/o replacement, 166 $mL\ g^{-1}$	Bennett nC D_2 50 α-TCP [25]
Poly(D,L-lactide-co-glycolide) (50:50)	Lakeshore Biomaterials; Birmingham, Alabama, USA (5050 DLG 5E)	5.9×10^{-10}	5.9×10^{-10}	α-TCP	In-house production: wet chemistry route. Same as Bennett nC α-TCP	3.0×10^{-13}	2.0	Dense disk: $\Phi = 3.5$ mm, t = 1 mm	Same as Bennett nC α-TCP	In vitro: PBS (0.01 M, pH = 7.4) w 100 % v/v of D_2O at 37 °C, w/o shaking, w/o replacement, 166 $mL\ g^{-1}$	Bennett nC D_2 100 α-TCP [25]

(continued)

Table B.3 (continued)

Polymer characteristics				Ceramic characteristics				Sample characteristics			
Type	Manufacturer	k_1 (s^{-1})	k'_2 ($m^3\ mol^{-1}\ s^{-1}$)	Type	Manufacturer	A_d ($mol\ m^{-2}\ s^{-1}$)	θ (1)	Structure and Morphology	Fabrication method	Degradation protocol	Case code and reference
Poly(D,L-lactide-co-glycolide) (50:50)	Lakeshore Biomaterials; Birmingham, Alabama, USA (5050 DLG 5E)	2.4×10^{-9}	2.4×10^{-9}	α-TCP	In-house production: wet chemistry route using $Ca(OH)_2$ and H_3PO_4 + aging for 1 d and drying + grinding into powder + calcining at 1400 °C for 4 h + grinding and sieving through a 38 μm mesh	3.0×10^{-12}	2.0	Dense disk: $\Phi = 3.5$ mm, t = 1 mm	Polymer dissolved in acetone + ceramic addition + solvent casting + injection-moulding at 135 °C and 0.5 MPa into cylinders + cut into final shape	In vitro: same as Bennett mC α-TCP	Bennett iC α-TCP [25]
Poly(D,L-lactide-co-glycolide) (50:50)	Lakeshore Biomaterials; Birmingham, Alabama, USA (5050 DLG 5E)	2.4×10^{-9}	2.4×10^{-9}	α-TCP	In-house production: wet chemistry route using $Ca(OH)_2$ and H_3PO_4 + aging for 1 d and drying + grinding into powder + calcining at 1400 °C for 4 h + quenching + grinding and sieving through a 100 μm mesh	1.0×10^{-10}	2.0	Dense disk: $\Phi = 3.5$ mm, t = 1 mm	Polymer dissolved in acetone + ceramic addition + solvent casting + injection-moulding at 135 °C and 0.5 MPa into cylinders + cut into final shape	In vitro: PBS (0.01 M, pH = 7.4) at 37 °C, w/o shaking, w/o replacement, 166 $mL\ g^{-1}$	Bennett mC α-TCP [25]
Poly(D,L-lactide-co-glycolide) (50:50)	Lakeshore Biomaterials; Birmingham, Alabama, USA (5050 DLG 5E)	1.4×10^{-9}	1.4×10^{-9}	α-TCP	In-house production: same as Bennett mC	5.0×10^{-11}	2.0	Dense disk: $\Phi = 3.5$ mm, t = 1 mm	Same as Bennett mC α-TCP	In vitro: PBS (0.01 M, pH = 7.4) at 37 °C w 50 % v/v of D_2O, w/o shaking, w/o replacement, 166 $mL\ g^{-1}$	Bennett mC D_2 50 α-TCP [25]

(continued)

Table B.3 (continued)

Polymer characteristics				Ceramic characteristics				Sample characteristics			
Type	Manufacturer	k_1 (s^{-1})	k'_2 ($m^3\ mol^{-1}\ s^{-1}$)	Type	Manufacturer	A_d ($mol\ m^{-2}\ s^{-1}$)	θ (1)	Structure and Morphology	Fabrication method	Degradation protocol	Case code and reference
Poly(D,L-lactide-co-glycolide) (50:50)	Lakeshore Biomaterials; Birmingham, Alabama, USA (5050 DLG 5E)	5.9×10^{-10}	5.9×10^{-10}	α-TCP	In-house production: same as Bennett mC	1.0×10^{-11}	2.0	Dense disk: $\Phi = 3.5$ mm, t = 1 mm	Same as Bennett mC α-TCP	In vitro: PBS (0.01 M, pH = 7.4) at 37 °C w 100 % v/v of D_2O, w/o shaking, w/o replacement, 166 mL g^{-1}	Bennett mC D_2 100 α-TCP [25]
Poly(D,L-lactide-co-glycolide) (50:50)	SurModics Pharmaceuticals, USA	1.0×10^{-9}	1.8×10^{-9}	α-TCP	In-house production: wet chemistry route using $Ca(OH)_2$ and H_3PO_4 + aging for 1 d and drying + calcining at 1400 °C for 4 h + quenching + grinding and sieving to 75 µm	3.0×10^{-13}	2.0	Dense disk: $\Phi = 6$ mm, t = 2 mm	Ceramic dispersed in polymer using a co-rotating twin screw extruder + cut into pellets + injection-moulded to cylinders at 130 °C and 0.5 MPa + cut into final shape	In vitro: PBS (0.01 M, pH = 7.4) at 37 °C, w/o shaking, w/o replacement	Ege α-TCP [26, 27]
Poly(D,L-lactide-co-glycolide) (50:50)	Lakeshore Biomaterials; Birmingham, Alabama, USA	2.8×10^{-9}	2.2×10^{-9}	α-TCP	In-house production: wet chemistry route using $Ca(OH)_2$ and H_3PO_4 + aging for 1 d and drying + calcining at 1300 °C for 4 h + quenching + grinding and sieving to 75 µm + attritor-milled for 4 h in acetone	9.0×10^{-13}	2.0	Dense film: 8 × 8 mm^2 × 1 mm	Polymer addition to milled ceramic + solvent casting + hot-pressed at 150 °C into sheets + cut into final shape	In vitro: PBS (0.01 M, pH = 7.4) at 37 °C, w/o shaking, w/o replacement, 166 mL g^{-1}	Yang Z. 5050 nC α-TCP [28, 29]

(continued)

Table B.3 (continued)

Polymer characteristics				Ceramic characteristics				Sample characteristics			
Type	Manufacturer	k_1 (s^{-1})	k'_2 ($m^3\ mol^{-1}\ s^{-1}$)	Type	Manufacturer	A_d ($mol\ m^{-2}\ s^{-1}$)	θ (1)	Structure and Morphology	Fabrication method	Degradation protocol	Case code and reference
Poly(D,L-lactide-co-glycolide) (50:50)	Lakeshore Biomaterials; Birmingham, Alabama, USA	2.8×10^{-9}	2.2×10^{-9}	α-TCP	In-house production: wet chemistry route using $Ca(OH)_2$ and H_3PO_4 + aging for 1 d and drying + calcining at 1300 °C for 4 h + quenching + grinding and sieving to 75 µm	3.0×10^{-11}	2.0	Dense film: 8 × 8 mm^2 × 1 mm	Ceramic and polymer mixed + solvent casting + hot-pressed at 150 °C into sheets + cut into final shape	In vitro: PBS (0.01 M, pH = 7.4) at 37 °C, w/o shaking, w/o replacement, 166 $mL\ g^{-1}$	Yang Z. 5050 mC α-TCP [28, 29]
Poly(D,L-lactide-co-glycolide) (50:50)	Alkermes Medisorb; Cincinnati, USA	4.5×10^{-9}	2.9×10^{-9}	α-TCP	In-house production: wet chemistry route + drying for 2 d + grinding into powder + calcining at 1200 °C for 4 h + ball-milling for 11 h + sieving through a 75 µm mesh	3.0×10^{-11}	2.0	Dense disk: Φ = 15 mm, t = 2.3 mm	Polymer and ceramic kneading at 200 °C+ hot-pressed at 200 °C into final shape	In vitro: PBS (0.03 M, pH = 7.4) at 37 °C, w periodic agitation, w/o replacement, 30 mL/sample	Mellon α-TCP [30]
Poly(D,L-lactide-co-glycolide) (50:50)	Lakeshore Biomaterials; Alabama, USA	2.1×10^{-9}	2.1×10^{-9}	α-TCP	In-house production: wet chemistry route using $Ca(OH)_2$ and H_3PO_4 + aging for 1 d and drying + ball-milling for 4 h + sieving using a 75 µm mesh + calcining at 1400 °C for 4 h + attritor-milled in acetone for 4 h	5.0×10^{-12}	2.0	Dense disk: Φ = 8 mm, t = 900 µm	Polymer addition to milled ceramic + drying + hot-pressed at 90 °C into sheets + cut w a circular punch into final shape	In vitro: distilled-deionised water at 37 °C, w/o shaking, w/o replacement, 40 mL/sample	Barrett α-TCP [31, 32]

(continued)

Table B.3 (continued)

Polymer characteristics				Ceramic characteristics				Sample characteristicsSample characteristics			
Type	Manufacturer	k_1 (s^{-1})	k'_2 ($m^3\,mol^{-1}\,s^{-1}$)	Type	Manufacturer	A_d ($mol\,m^{-2}\,s^{-1}$)	θ (1)	Structure and Morphology	Fabrication method	Degradation protocol	Case code and reference
Poly(D,L-lactide-co-glycolide) (50:50)	SurModics Pharmaceuticals, USA	3.0×10^{-9}	2.4×10^{-9}	α-TCP	In-house production: wet chemistry route using $Ca(OH)_2$ and H_3PO_4 + aging for 1 d and drying + grinding and sieving using a 75 µm mesh + calcining at 1200 °C for 4 h + grinding and sieving to 75 µm	5.0×10^{-10}	2.0	Dense disk: Φ = 10 mm, t = 1.5 mm	Polymer and ceramic kneading at 200 °C + hot-pressed at 200 °C into final shape	In vitro: PBS (0.01 M, pH = 7.4) at 37 °C, w periodic agitation, w/o replacement, 166 $mL\,g^{-1}$	Ehrenfried α-TCP [33]
Poly(D,L-lactide-co-glycolide) (50:50)	SurModics Pharmaceuticals, USA	1.0×10^{-9}	1.8×10^{-9}	β-TCP	In-house production: wet chemistry route using $Ca(OH)_2$ and H_3PO_4 + aging for 1 d and drying + calcining at 1100 °C for 4 h + grinding and sieving to 75 µm	7.0×10^{-13}	2.0	Dense disk: Φ = 6 mm, t = 2 mm	Ceramic dispersed in polymer using a co-rotating twin screw extruder + cut into pellets + injection-moulded to cylinders at 130 °C and 0.5 MPa + cut into final shape	In vitro: PBS (0.01 M, pH = 7.4) at 37 °C, w/o shaking, w/o replacement	Ege β-TCP [26]
Poly(D,L-lactide-co-glycolide) (50:50)	Alkermes Medisorb; Cincinnati, USA	4.5×10^{-9}	2.9×10^{-9}	β-TCP	In-house production: wet chemistry route + drying for 2 d + grinding into powder + calcining at 1000 °C for 4 h + ball-milling for 11 h + sieving through a 75 µm mesh	9.0×10^{-12}	2.0	Dense disk: Φ = 15 mm, t = 2.3 mm	Polymer and ceramic kneading at 200 °C+ hot-pressed at 200 °C into final shape	In vitro: PBS (0.03 M, pH = 7.4) at 37 °C, w periodic agitation, w/o replacement, 30 mL/sample	Mellon β-TCP [30]

(continued)

Table B.3 (continued)

Polymer characteristics				Ceramic characteristics				Sample characteristics			
Type	Manufacturer	k_1 (s^{-1})	k_2' ($m^3\ mol^{-1}\ s^{-1}$)	Type	Manufacturer	A_d ($mol\ m^{-2}\ s^{-1}$)	θ (1)	Structure and Morphology	Fabrication method	Degradation protocol	Case code and reference
Poly(D,L-lactide-co-glycolide) (75:25)	Lakeshore Biomaterials; Birmingham, Alabama, USA	1.6×10^{-9}	1.1×10^{-9}	α-TCP	In-house production: wet chemistry route using $Ca(OH)_2$ and H_3PO_4 + aging for 1 d and drying + calcining at 1300 °C for 4 h + quenching + grinding and sieving to 75 µm + attritor-milled for 4 h in acetone	7.0×10^{-13}	2.0	Dense film: 8 × 8 mm^2 × 1 mm	Polymer addition to milled ceramic + solvent casting + hot-pressed at 150 °C into sheets + cut into final shape	In vitro: PBS (0.01 M, pH = 7.4) at 37 °C, w/o shaking, w/o replacement, 166 $mL\ g^{-1}$	Yang Z. 7525 nC α-TCP [29]
Poly(D,L-lactide-co-glycolide) (75:25)	Lakeshore Biomaterials; Birmingham, Alabama, USA	1.6×10^{-9}	1.1×10^{-9}	α-TCP	In-house production: wet chemistry route using $Ca(OH)_2$ and H_3PO_4 + aging for 1 d and drying + calcining at 1300 °C for 4 h + quenching + grinding and sieving to 75 µm	3.0×10^{-11}	2.0	Dense film: 8 × 8 mm^2 × 1 mm	Ceramic and polymer mixed + solvent casting + hot-pressed at 150 °C into sheets + cut into final shape	In vitro: PBS (0.01 M, pH = 7.4) at 37 °C, w/o shaking, w/o replacement, 166 $mL\ g^{-1}$	Yang Z. 7525 mC α-TCP [29]

B.1.4 Miscellaneous Polymers Matrixes

Table B.4 Results output by the TCP composites degradation model for cases with a miscellaneous polymer matrix. k_1 is the non-catalytic polymer degradation rate, k_2' is the autocatalytic polymer degradation rate, A_d is the ceramic dissolution rate and θ is the power ceramic dissolution law exponent. Abbreviations used to specify the tricalcium phosphate type can be found in Table 4.2. A dashed line between rows indicates that data displayed in those consecutive rows belong to the same researcher or research group. A solid line between rows indicates no known author relationship for the data

Polymer characteristics				Ceramic characteristics				Sample characteristics			
Type	Manufacturer	k_1 (s^{-1})	k_2' ($m^3\ mol^{-1}\ s^{-1}$)	Type	Manufacturer	A_d ($mol\ m^{-2}\ s^{-1}$)	θ (1)	Structure and Morphology	Fabrication method	Degradation protocol	Case code and reference
Poly(L-lactide- co-ε-caprolactone)(70:30)	Purac Biomaterials, The Netherlands (Purasorb PLC7015)	7.4×10^{-10}	3.4×10^{-10}	β-TCP	Plasma Biotal Ltd., United Kingdom	3.0×10^{-12}	2.0	Dense cylinder: $\Phi = 2.5$ mm, L = 2.5 mm	Polymer and ceramic fed to a co-rotating twin screw-extruder and processed at (25...130) °C into rod shape billets + cut to final shape + γ-irradiation (25 kGy)	In vitro: Sörensen buffer (pH = 7.4) at 37 °C, w shaking, w replacement every 2 days, 66 $mL\ g^{-1}$	Ahola 13 β-TCP [34]
Poly(L-lactide- co-ε-caprolactone)(70:30)	Purac Biomaterials, The Netherlands (Purasorb PLC7015)	5.8×10^{-10} (4.0×10^{-10})	3.8×10^{-10} (2.6×10^{-10})	β-TCP	Plasma Biotal Ltd., United Kingdom	3.0×10^{-12}	2.0	Dense cylinder: $\Phi = 2.5$ mm, L = 2.5 mm	Same as Ahola 13	In vitro: Sörensen buffer (pH = 7.4) at 37 °C, w shaking, w fortnightly replacement, 66 $mL\ g^{-1}$	Ahola 12 β-TCP [35]
Poly(L-lactide-co-ε-caprolactone)(92:8)	In-house production: bulk copolymerisation of L-lactide and ε-caprolac-tone using stannous 2-ethylhexanoate	1.8×10^{-10}	1.4×10^{-10}	β-TCP	In-house production: wet chemistry route using $Ca(OH)_2$ and H_3PO_4 + aging, drying at 120 °C, pelletised in 125 μm + calcining at 800 °C	3.0×10^{-12}	2.0	Dense film: 5 × 20 mm^2 × 200 μm	Polymer and ceramic kneaded in a milled at 180 °C and 30 rpm for 10 min + cooled in air for 15 min + hot-pressed at 180 °C	In vitro: physiological saline (pH = 7.4) at 37 °C, w/o shaking, w/o replacement	Kikuchi PLCL β-TCP [36]

(continued)

Table B.4 (continued)

Polymer characteristics				Ceramic characteristics				Sample characteristics			
Type	Manufacturer	k_1 (s^{-1})	k_2' ($m^3\ mol^{-1}\ s^{-1}$)	Type	Manufacturer	A_d ($mol\ m^{-2}\ s^{-1}$)	θ (1)	Structure and Morphology	Fabrication method	Degradation protocol	Case code and reference
Poly(L-lactide)/poly(ethylene: hexamethylene/sebacate) block copolymer (75.3:24.7)	In-house production: ring-opening polymerisation of L-lactide in the presence of poly(ethylene: hexamethylene/sebacate) (60:40 in weight) using stannous octoate	2.3×10^{-10}	2.8×10^{-10}	β-TCP	Taihei Chemical; Tokyo, Japan	5.0×10^{-12}	2.0	Dense film: 20 × 30 mm^2 × 100 μm	Blending polymer and ceramic in a plastomill mixer at 180 °C and 50 rpm for 10 min + compression moulding at 180 °C and 19.6 MPa	In vitro: PBS (pH = 7.4) at 37 °C, w/o shaking, weekly replacement, 50 mL/sample	Imai L100 β-TCP [37]
Poly(L-lactide)/poly(ethylene: hexamethylene/sebacate) block copolymer (75.3:24.7)	In-house production: same as Imai L100	4.8×10^{-10}	4.9×10^{-10}	β-TCP	Taihei Chemical; Tokyo, Japan	1.0×10^{-11}	2.0	Dense film: 20 × 30 mm^2 × 250 μm	Same as Imai L100	In vitro: same as Imai L100	Imai L250 β-TCP [37]
Poly(L-lactide)/poly(ethylene: hexamethylene/sebacate) block copolymer (75.3:24.7)	In-house production: ring-opening polymerisation of L-lactide in the presence of poly(ethylene: hexamethylene/sebacate) (60:40 in weight) using stannous octoate	1.0×10^{-10}	1.2×10^{-10}	β-TCP	In-house production: wet chemistry route + calcining at 800 °C	5.0×10^{-14}	2.0	Dense film: 5 × 20 mm^2 × 3 mm	Blending polymer and ceramic in mill mixer at 180 °C and 20 rpm for 10 min + cooled in air to room temperature + compression moulding at 180 °C and 30 MPa + cutting to final shape	In vitro: physiological saline (pH = 7.4) at 37 °C, w/o shaking, 100 mL/sample	Kikuchi T800 β-TCP [38]
Poly(L-lactide)/poly(ethylene: hexamethylene/sebacate) block copolymer (75.3:24.7)	In-house production: same as Kikuchi T800	5.0×10^{-11}	1.4×10^{-10}	β-TCP	In-house production: wet chemistry route + calcining at 1100 °C	5.0×10^{-13}	2.0	Dense film: 5 × 20 mm^2 × 3 mm	Same as Kikuchi T800	In vitro: same as Kikuchi T800	Kikuchi T1100 β-TCP [38]

(continued)

Table B.4 (continued)

Polymer characteristics				Ceramic characteristics				Sample characteristics			
Type	Manufacturer	k_1 (s^{-1})	k'_2 ($m^3\ mol^{-1}\ s^{-1}$)	Type	Manufacturer	A_d ($mol\ m^{-2}\ s^{-1}$)	θ (1)	Structure and Morphology	Fabrication method	Degradation protocol	Case code and reference
Poly(L-lactide)/poly(ethylene: hexamethylene/sebacate) block copolymer (98.3:1.7)	In-house production: ring-opening polymerisation of L-lactide in the presence of poly(ethylene: hexamethylene/sebacate) (97:3 in weight) using stannous octoate	6.0×10^{-11}	2.2×10^{-11}	β-TCP	Taihei Chemical; Tokyo, Japan	3.0×10^{-12}	2.0	Dense film: 20 × 30 mm^2 × 100 μm	Blending polymer and ceramic in a plastomill mixer at 180 °C and 50 rpm for 10 min + compression moulding at 180 °C and 19.6 MPa	In vitro: PBS (pH = 7.4) at 37 °C, w/o shaking, weekly replacement, 50 mL/sample	Imai H100 β-TCP [4]
Poly(L-lactide)/poly(ethylene: hexamethylene/sebacate) block copolymer (98.3:1.7)	In-house production: same as Imai H100	6.8×10^{-11}	7.0×10^{-11}	β-TCP	Taihei Chemical; Tokyo, Japan	5.0×10^{-12}	2.0	Dense film: 20 × 30 mm^2 × 250 μm	Same as Imai H100	In vitro: same as Imai H100	Imai H250 β-TCP [4]
Poly(L-lactide-co-glycolide-co-ε-caprolactone)(75:11:14)	In-house production: bulk copolymerisation of L-lactide, glycolide and ε-caprolactone using stannous 2-ethylhexanoate	2.2×10^{-10}	2.8×10^{-10}	β-TCP	In-house production: wet chemistry route using $Ca(OH)_2$ and H_3PO_4 + aging, drying at 120 °C, pelletised in 125 μm + calcining at 800 °C	5.0×10^{-12}	2.0	Dense film: 5 × 20 mm^2 × 200 μm	Polymer and ceramic kneaded in a milled at 180 °C and 30 rpm for 10 min + cooled in air for 15 min + hot-pressed at 180 °C	In vitro: physiological saline (pH = 7.4) at 37 °C, w/o shaking, w/o replacement	Kikuchi PLGC β-TCP [36]

B.2 Hydroxyapatite Case Studies Modelling Results

HA case studies with a poly(L-lactide) matrix are included in Appendix B.2.1, (Table B.5), followed by cases with a poly(D,L-lactide) matrix in Appendix B.2.2, (Table B.6), cases with poly(lactide-co-glycolide) matrix in Appendix B.2.3, (Table B.7) and lastly, cases with miscellaneous polymers matrixes in Appendix B.2.4, (Table B.8).

B.2.1 Poly(L-lactide) Matrix

Table B.5 Results output by the HA composites degradation model for cases with a poly(L-lactide) matrix. k_1 is the non-catalytic polymer degradation rate, k_2' is the autocatalytic polymer degradation rate, A_d is the ceramic dissolution rate and θ is the power ceramic dissolution law exponent. Abbreviations used to specify the hydroxyapatite type can be found in Table 5.2. A dashed line between rows indicates that data displayed in those consecutive rows belong to the same researcher or research group. A solid line between rows indicates no known author relationship for the data

Polymer characteristics				Ceramic characteristics				Sample characteristics			
Type	Manufacturer	k_1 (s^{-1})	k_2' ($m^3\ mol^{-1}\ s^{-1}$)	Type	Manufacturer	A_d ($mol\ m^{-2}\ s^{-1}$)	θ (1)	Structure and Morphology	Fabrication method	Degradation protocol	Case code and reference
Poly(L-lactide)	In-house production: ring-opening polymerisation of L-lactide at 140 °C	4.6×10^{-10}	2.0×10^{-10}	hHA	In-house production: wet chemistry route using $Ca(NO_3)_2$ and NH_4PO_3 + sintered + milled	5.0×10^{-14}	2.0	Dense cylinder: $\Phi = 5$ mm, L = 10 mm	Polymer and ceramic mixed at 160 °C+ compression moulded	In vitro: PBS (pH = 7.4) at 37 °C, w shaking at 100 rpm	Huang hHA [39]
Poly(L-lactide)	In-house production: ring-opening polymerisation of L-lactide using stannous octoate	8.0×10^{-11} (1.2×10^{-11})	8.0×10^{-11} (1.2×10^{-11})	lHA	In-house production: wet chemistry route w $Ca(OH)_2$ and H_3PO_4	2.0×10^{-14}	2.0	Dense bar: 30 × 5 mm^2 × 2 mm	Polymer and ceramic blended at 190 °C for 5 min in the rheometer + hot press moulded at 190 °C and 15 MPa + annealed at 115 °C for 1 h	In vivo: intramuscular implantation in New Zealand white rabbits	Wang lHA [40]
Poly(L-lactide)	In-house production: same as Wang lHA	8.0×10^{-11} (1.2×10^{-11})	8.0×10^{-11} (1.2×10^{-11})	gP-lHA	In-house production: same as Wang nHA + PLLA polymerised on the nHA	5.0×10^{-15}	2.0	Dense bar: 30 × 5 mm^2 × 2 mm	Same as Wang nHA	In vivo: same as Wang nHA	Wang gP-lHA [40]
Poly(L-lactide)	Jamplast; Ellisville, Missouri, USA	3.5×10^{-10} (1.2×10^{-10})	2.3×10^{-10} (8.0×10^{-11})	lCCDHA	In-house production: wet chemistry route using Tris-base SBF	1.0×10^{-15}	2.0	Porous fibrous mat (t: NR)	Polymer dissolved in chloroform + ceramic added + ultrasonicated for 1 h + electrospinning	In vitro: standard conditions (PBS at 37 °C, 25 mL/sample)	Zhou lCCDHA [41]

(continued)

Table B.5 (continued)

Polymer characteristics				Ceramic characteristics				Sample characteristics			
Type	Manufacturer	k_1 (s^{-1})	k_2' ($m^3\ mol^{-1}\ s^{-1}$)	Type	Manufacturer	A_d ($mol\ m^{-2}\ s^{-1}$)	θ (1)	Structure and Morphology	Fabrication method	Degradation protocol	Case code and reference
Poly(L-lactide)	Purac Biochem B.V.; Gorinchem, The Netherlands: polymerised after mixing HA w L-lactide	3.0×10^{-10}	2.4×10^{-10}	hHA	Merck; Darmstadt, Germany: as-received HA + sintered in N_2 + crushed and milled	1.0×10^{-12}	2.0	Dense film: 15 × $10\,mm^2$ × 3 mm	Polymerised in an ampule w ceramic + machined to desired dimensions	In vitro: PBS at 37 °C, weekly replacement, 40 mL/sample	Verheyen 92 Vit hHA [42]
Poly(L-lactide)	Purac Biochem B.V.; Gorinchem, The Netherlands: see Verheyen 92 Vit	1.3×10^{-10}	2.6×10^{-10}	hHA	Merck; Darmstadt, Germany: see Verheyen 92 Vit	5.0×10^{-12}	2.0	Dense film: 15 × $10\,mm^2$ × 3 mm	Same as Verheyen 92 Vit	In vitro: PBS at 37 °C, weekly replacement, w shaking, 10 mL/sample	Verheyen 93 hHA [43]
Poly(L-lactide)	Purac Biochem B.V.; Gorinchem, The Netherlands: see Verheyen 92 Vit	3.0×10^{-10}	2.0×10^{-10}	hHA	Merck; Darmstadt, Germany: see Verheyen 92 Vit	3.0×10^{-12}	2.0	Dense film: 15 × $10\,mm^2$ × 3 mm	Same as Verheyen 92 Vit	In vivo: subcutaneous implantation in mature female goats	Verheyen 92 Viv hHA [42]
Poly(L-lactide)	Biomer, Germany (L9000)	1.6×10^{-10}	1.0×10^{-10}	bnHA	Aldrich Chemistry, USA	1.0×10^{-14}	2.0	Porous (90 %) disk: $\Phi = 15$ mm, t: NR	Polymer dissolved in dioxane + blended w ceramic + freeze drying	In vitro: standard conditions (PBS at 37 °C, w/o shaking, 10 mL/sample)	Diaz PP/C bnHA [44]
Poly(L-lactide)	Biomer, Germany (L9000)	2.0×10^{-10} (1.6×10^{-10})	1.2×10^{-10} (1.0×10^{-10})	bnHA	Aldrich Chemistry, USA	1.0×10^{-14}	2.0	Porous (90 %) disk: $\Phi = 15$ mm, t: NR	Same as Diaz PP/C	In vitro: same as Diaz PP/C	Diaz C bnHA [44]

(continued)

Table B.5 (continued)

Polymer characteristics				Ceramic characteristics				Sample characteristics			
Type	Manufacturer	k_1 (s^{-1})	k_2' ($m^3\ mol^{-1}\ s^{-1}$)	Type	Manufacturer	A_d ($mol\ m^{-2}\ s^{-1}$)	θ (1)	Structure and Morphology	Fabrication method	Degradation protocol	Case code and reference
Poly(L-lactide)	In-house production: ring-opening polymerisation of L-lactide using tin octoate and lauryl alcohol	1.2×10^{-10} (2.6×10^{-11})	6.0×10^{-11} (1.3×10^{-11})	pCHA	In-house production: wet chemistry route w $CaHPO_4$ and $CaCO_3$ in aqueous solution at 90 °C+ filtered and dried + milled and sieved	3.0×10^{-13}	2.0	Dense cylinder: $\Phi = 3.2$ mm, L = 30 mm	Ceramic and polymer mixed + extruded + compression moulded at 103 °C+ lathing	In vitro: standard conditions (PBS (pH = 7.4) at 37 °C, w/o shaking)	Shikinami 99 pCHA [45]
Poly(L-lactide)	In-house production: see Shikinami 99	1.2×10^{-10} (7.5×10^{-11})	3.0×10^{-11} (1.7×10^{-11})	pCHA	In-house production: see Shikinami 99	3.0×10^{-13}	2.0	Dense cylinder: $\Phi = 3.2$ mm, L = 30 mm	Same as Shikinami 99	In vivo: medullary cavity implantation in Japanese white rabbits	Furukawa Med pCHA [46]
Poly(L-lactide)	In-house production: same as Shikinami 99	1.2×10^{-10}	3.0×10^{-11}	pCHA	In-house production: same as Shikinami 99	3.0×10^{-13}	2.0	Dense cylinder: $\Phi = 3.2$ mm, L = 50 mm	Same as Shikinami 99	In vivo: subcutis implantation in Japanese white rabbits	Furukawa Sub pCHA [46]
Poly(L-lactide)	In-house production: same as Shikinami 99	1.2×10^{-10}	3.0×10^{-11}	pCHA	In-house production: same as Shikinami 99	3.0×10^{-13}	2.0	Dense cylinder: $\Phi = 3.2$ mm, L = 30 mm	Same as Shikinami 99	In vivo: intercondylar implantation in male Japanese white rabbits	Ishii pCHA [47]
Poly(L-lactide)	In-house production: same as Shikinami 99	8.0×10^{-11}	4.0×10^{-11}	pCHA	In-house production: same as Shikinami 99	5.0×10^{-13}	2.0	Dense screw: $\Phi = 1.6$ mm, L = 8 mm	Same as Shikinami 99	In vitro: standard conditions	Shikinami 01 pCHA [48]

(continued)

Table B.5 (continued)

Polymer characteristics				Ceramic characteristics				Sample characteristics			
Type	Manufacturer	k_1 (s^{-1})	k_2' ($m^3\ mol^{-1}\ s^{-1}$)	Type	Manufacturer	A_d ($mol\ m^{-2}\ s^{-1}$)	θ (1)	Structure and Morphology	Fabrication method	Degradation protocol	Case code and reference
Poly(L-lactide)	In-house production: see Shikinami 99	1.2×10^{-10} (7.5×10^{-11})	3.0×10^{-11} (1.7×10^{-11})	hHA	In-house production: pCHA production (see Shikinami 99) + calcined at 900 °C	5.0×10^{-13}	2.0	Dense cylinder: $\Phi = 3.2$ mm, L = 30 mm	Same as Shikinami 99	Same as Furukawa Med CHA	Furukawa Med hHA [46]
Poly(L-lactide)	In-house production: same as Shikinami 99	8.0×10^{-11}	5.0×10^{-11}	hHA	In-house production: same as Furukawa Med HA	5.0×10^{-13}	2.0	Dense cylinder: $\Phi = 3.2$ mm, L = 50 mm	Same as Shikinami 99	In vivo: same as Furukawa Sub CHA	Furukawa Sub hHA [46]
Poly(L-lactide)	In-house production: same as Shikinami 99	8.0×10^{-11}	5.0×10^{-11}	hHA	In-house production: same as Furukawa Med HA	1.1×10^{-12}	2.0	Dense cylinder: $\Phi = 3.2$ mm, L = 30 mm	Same as Shikinami 99	In vivo: same as Ishii CHA	Ishii hHA [47]
Poly(L-lactide)	In-house production: same as Shikinami 99	1.2×10^{-10}	2.0×10^{-11}	hHA	In-house production: same as Furukawa Med HA	1.0×10^{-13}	2.0	Dense miniplate: t = 1 mm	Same as Shikinami 99	In vitro: standard conditions	Shikinami 01 hHA [48]
Poly(L-lactide)	Shang Dong Institute (Dept. of Med. Pol.), China	6.0×10^{-12}	3.0×10^{-12}	lHA	In-house production: wet chemistry route using $Ca(NO_3)_2{\cdot}4H_2O$ and $(NH_4)_2HPO_4$ w ultrasonic stirring	3.0×10^{-15}	2.0	Dense film: 20 × 20 mm^2 × 0.05 mm	Polymer-ceramic mixture solvent casting	In vitro: PBS (pH = 7.4) at 37 °C, w/o shaking, 15 mL/sample	Deng SC lHA [49]
Poly(L-lactide)	Shang Dong Institute (Dept. of Med. Pol.), China	1.0×10^{-11}	1.1×10^{-11}	lHA	In-house production: same as Deng SC	9.0×10^{-15}	2.0	Porous fibrous mat: 20 × 20 mm^2 × 0.05 mm	Polymer-ceramic mixture electrospinning	In vitro: same as Deng SC	Deng ES lHA [49]
Poly(L-lactide)	Shang Dong Institute (Dept. of Med. Pol.), China	8.0×10^{-12}	1.9×10^{-11}	lHA	In-house production: same as Deng SC	9.0×10^{-15}	2.0	Porous fibrous mat: 20 × 20 mm^2 × 0.05 mm	Polymer-ceramic mixture electrospinning	In vitro: same as Deng SC	Sui lHA [50]

(continued)

Table B.5 (continued)

Polymer characteristics				Ceramic characteristics				Sample characteristics			
Type	Manufacturer	k_1 (s^{-1})	k_2' ($m^3\ mol^{-1}\ s^{-1}$)	Type	Manufacturer	A_d ($mol\ m^{-2}\ s^{-1}$)	θ (1)	Structure and Morphology	Fabrication method	Degradation protocol	Case code and reference
Poly(L-lactide)	In-house production: ring-opening polymerisation of L-lactide	5.2×10^{-10}	4.8×10^{-10}	gP-lHA	In-house production: wet chemistry route + grafting with PLLA	2.0×10^{-14}	2.0	Porous fibrous mat: 20 × 20 mm^2 × 0.2 mm	Polymer dissolved in chloroform + ceramic added + electrospinning	In vitro: PBS (pH = 7.4) at 37 °C, w shaking at 90 rpm, 40 mL/sample)	Xu PP/C gP-lHA [51]
Poly(L-lactide)	In-house production: same as Xu PP/C	1.1×10^{-9} (5.2×10^{-10})	8.0×10^{-10} (4.8×10^{-10})	gP-lHA	In-house production: same as Xu PP/C	4.0×10^{-15}	2.0	Porous fibrous mat: 20 × 20 mm^2 × 0.2 mm	Same as Xu PP/C	In vitro: same as Xu PP/C	Xu C gP-lHA [51]

B.2.2 Poly(D,L-lactide) Matrix

Table B.6 Results output by the HA composites degradation model for cases with a poly(D,L-lactide) matrix. k_1 is the non-catalytic polymer degradation rate, k_2' is the autocatalytic polymer degradation rate, A_d is the ceramic dissolution rate and θ is the power ceramic dissolution law exponent. Abbreviations used to specify the hydroxyapatite type can be found in Table 5.2. A dashed line between rows indicates that data displayed in those consecutive rows belong to the same researcher or research group. A solid line between rows indicates no known author relationship for the data

Polymer characteristics				Ceramic characteristics				Sample characteristics			
Type	Manufacturer	k_1 (s^{-1})	k_2' ($m^3\,mol^{-1}\,s^{-1}$)	Type	Manufacturer	A_d ($mol\,m^{-2}\,s^{-1}$)	θ (1)	Structure and Morphology	Fabrication method	Degradation protocol	Case code and reference
Poly(D,L-lactide)(4:96)	Nature Works LLC (#4042D)	1.7×10^{-10} (3.5×10^{-11})	1.7×10^{-10} (3.4×10^{-11})	lCHA	In-house production: wet chemistry route using bovine bone derived precursors	5.0×10^{-15}	2.0	Dense slab: 10 × 10 mm^2 × 4 mm	Ceramic and polymer mixed at 170 °C for 10 min + hot pressed at 180 °C and 14 MPa for 5 min	In vitro: SBF (pH = 7.4) at 37 °C, weekly replacement, 11.6 mL/sample	Rakmae 13 lCHA [52]
Poly(D,L-lactide)(4:96)	Nature Works LLC (#4042D)	1.7×10^{-10} (3.5×10^{-11})	1.7×10^{-10} (3.4×10^{-11})	pCHA	In-house production: above-mentioned lCHA heat treated at 800 °C for 3 h	1.1×10^{-13}	2.0	Dense slab: 10 × 10 mm^2 × 4 mm	Same as Rakmae 13 lCHA	In vitro: same as Rakmae 13 lCHA	Rakmae 13 pCHA [52]
Poly(D,L-lactide)(4:96)	Nature Works LLC (#4042D)	1.7×10^{-10} (3.5×10^{-11})	1.7×10^{-10} (3.4×10^{-11})	hHA	In-house production: above-mentioned lCHA heat treated at 1100 °C for 3 h	7.0×10^{-14}	2.0	Dense slab: 10 × 10 mm^2 × 4 mm	Same as Rakmae 13 lCHA	In vitro: same as Rakmae 13 lCHA	Rakmae 13 hHA [52]

(continued)

Table B.6 (continued)

Polymer characteristics				Ceramic characteristics				Sample characteristics			
Type	Manufacturer	k_1 (s^{-1})	k_2' ($m^3\,mol^{-1}\,s^{-1}$)	Type	Manufacturer	A_d ($mol\,m^{-2}\,s^{-1}$)	θ (1)	Structure and Morphology	Fabrication method	Degradation protocol	Case code and reference
Poly(D,L-lactide)(4:96)	Nature Works LLC (#4042D)	7.0×10^{-11}	1.6×10^{-10}	hCHA	In-house production: ground and ball-milled bovine bone heat treated at 1100 °C for 3 h	7.0×10^{-14}	2.0	Dense slab: 60 × 10 mm^2 × 4 mm	Ceramic and polymer mixed at 170 °C for 10 min + heated to 180 °C for 15 min + hot pressed at 180 °C and 14 MPa for 5 min	In vitro: PBS (0.1 M, pH = 7.4) at 37 °C, weekly replacement, 11.6 mL/sample	Rakmae 12 hCHA [53]
Poly(D,L-lactide)(4:96)	Nature Works LLC (#4042D)	6.0×10^{-11}	1.7×10^{-10}	sA-hCHA	In-house production: above-mentioned hCHA modified with APES (3-Aminopropyl-triethoxysilane)	5.0×10^{-12}	2.0	Dense slab: 60 × 10 mm^2 × 4 mm	Same as Rakmae 12 C	In vitro: same as Rakmae 12 hCHA	Rakmae 12 sA-hCHA [53]
Poly(D,L-lactide)(4:96)	Nature Works LLC (#4042D)	6.0×10^{-11}	1.7×10^{-10}	sM-hCHA	In-house production: above-mentioned hCHA modified with MPTS (3-methacryloxy-propyltrimetho-xysilane)	5.0×10^{-12}	2.0	Dense slab: 60 × 10 mm^2 × 4 mm	Same as Rakmae 12 hCHA	In vitro: same as Rakmae 12 hCHA	Rakmae 12 sM-hCHA [53]
Poly(D,L-lactide)(15:85)	Purac Biochem BV, The Netherlands	2.0×10^{-10}	2.5×10^{-9}	hHA	Not reported: sintered, milled and sieved	3.0×10^{-11}	2.0	Dense film: t = (0.3...0.5) mm	Polymer dissolved in chloroform, ceramic added and mixture stirred + solvent evaporation	In vitro: PBS (pH = 7.2) at 37 °C, w/o replacement, w shaking, 11 mL/sample	Van der Meer hHA [54]

(continued)

Table B.6 (continued)

Polymer characteristics				Ceramic characteristics				Sample characteristics			
Type	Manufacturer	k_1 (s^{-1})	k_2' ($m^3\ mol^{-1}\ s^{-1}$)	Type	Manufacturer	A_d ($mol\ m^{-2}\ s^{-1}$)	θ (1)	Structure and Morphology	Fabrication method	Degradation protocol	Case code and reference
Poly(D,L-lactide)(50:50)	In-house production: ring-opening polymerisation of racemic D,L-lactide	2.1×10^{-10}	5.0×10^{-11}	pCHA	In-house production: wet chemistry route	1.0×10^{-13}	2.0	Porous cylinder $\Phi = 6$ mm, L = 15 mm	Composite fiber precipitation	In vivo: male Japanese white rabbits	Hasegawa pCHA [55]
Poly(D,L-lactide)(50:50)	In-house production: ring-opening polymerisation of D,L-lactide + modification with gellatin	4.3×10^{-10} (2.6×10^{-10})	8.0×10^{-11} (5.0×10^{-11})	Mixture of pHA and ns-lHA	In-house production: grown in-situ with SBF	5.0×10^{-14}	2.0	Porous fibrous disk: $\Phi = 11$ mm, t = (250...300) µm	Electrospun fibrous mats w in-situ grown ceramic	In vitro: PBS (pH = 7.4) w sodium azide at 37 °C, 20 mL/sample	Zou 12 Vit pns-lHA [56]
Poly(D,L-lactide)(50:50)	In-house production: same as Zou 12 Vit pns-lHA	1.4×10^{-10} (9.0×10^{-11})	1.5×10^{-10} (1.0×10^{-10})	Mixture of pHA and ns-lHA	In-house production: same as Zou 12 Vit pns-lHA	5.0×10^{-15}	2.0	Porous fibrous disk: $\Phi = 11$ mm, t = (250...300) µm	Re-electrospun after dissolving above-mentioned mat	In vitro: same as Zou 12 Vit pns-lHA	Zou 12 Vit R pns-lHA [56]
Poly(D,L-lactide)(50:50)	In-house production: same as Zou 12 Vit pns-lHA	4.4×10^{-10} (3.7×10^{-10})	4.7×10^{-10} (1.8×10^{-10})	Mixture of pHA and ns-lHA	In-house production: same Zou 12 Vit pns-lHA	5.0×10^{-15}	2.0	Porous fibrous cylinder: $\Phi = 5$ mm, L = 15 mm	Electrospun fibrous mats w in-situ grown ceramic	In vivo: subcutaneous implantation in male dogs	Zou 12 Viv pns-lHA [56]
Poly(D,L-lactide)(50:50)	In-house production: same as Zou 12 Vit pns-lHA	2.5×10^{-10} (2.0×10^{-10})	5.2×10^{-10} (2.0×10^{-10})	Mixture of pHA and ns-lHA	In-house production: same as Zou 12 Vit pns-lHA	1.1×10^{-14}	2.0	Porous fibrous cylinder: $\Phi = 5$ mm, L = 15 mm	Re-electrospun after dissolving above-mentioned mat	In vivo: same as Zou 2 Viv pns-lHA	Zou 12 Viv R pns-lHA [56]
Poly(D,L-lactide)(50:50) modified with carboxyl groups	In-house production: ring-opening polymerisation of D,L-lactide + modification with carboxyl groups	4.9×10^{-10}	2.3×10^{-10}	Mixture of pHA and ns-lHA	In-house production: grown in-situ using concentrated SBF	3.0×10^{-13}	2.0	Porous fibrous mat: t = 0.5 mm	Electrospun mats with in-situ grown ceramic	In vitro: PBS w sodium azide at 37 °C, w shaking at 100 rpm	Zou 11 C pns-lHA [57]

(continued)

Table B.6 (continued)

Polymer characteristics				Ceramic characteristics				Sample characteristics			
Type	Manufacturer	k_1 (s^{-1})	k'_2 ($m^3\ mol^{-1}\ s^{-1}$)	Type	Manufacturer	A_d ($mol\ m^{-2}\ s^{-1}$)	θ (1)	Structure and Morphology	Fabrication method	Degradation protocol	Case code and reference
Poly(D,L-lactide)(50:50) modified with carboxyl groups	In-house production: same as Zou 11 C pns-lHA	2.3×10^{-10}	2.9×10^{-10}	Mixture of pHA and ns-lHA	In-house production: same as Zou 11 C pns-lHA	3.0×10^{-13}	2.0	Porous fibrous mat: t = 0.5 mm	Re-electrospun after dissolving above-mentioned mat	In vitro: same as Zou 11 C	Zou 11 CR pns-lHA [57]
Poly(D,L-lactide)(50:50) modified with hydroxyl and carboxyl groups	In-house production: ring-opening polymerisation of D,L-lactide + modification with hydroxyl and carboxyl groups	2.8×10^{-10} (2.2×10^{-10})	2.5×10^{-10} (2.1×10^{-10})	Mixture of pHA and ns-lHA	In-house production: same as Zou 11 C pns-lHA	3.0×10^{-14}	2.0	Porous fibrous mat: t = 0.5 mm	Electrospun mats with in-situ grown ceramic	In vitro: same as Zou 11 C pns-lHA	Zou 11 HC [57]
Poly(D,L-lactide)(50:50) modified with amino, carboxyl and hydroxyl groups	In-house production: ring-opening polymerisation of D,L-lactide + modification with amino, hydroxyl and carboxyl groups	3.5×10^{-10} (2.0×10^{-10})	2.9×10^{-10} (1.8×10^{-10})	Mixture of pHA and ns-lHA	In-house production: same as Zou 11 C pns-lHA	1.1×10^{-14}	2.0	Porous fibrous mat: t = 0.5 mm	Electrospun mats with in-situ grown ceramic	In vitro: same as Zou 11 C pns-lHA	Zou 11 AHC pns-lHA [57]
Poly(D,L-lactide)(NR)	Jinan Daigang Bio-Technology Co. Ltd., China	6.0×10^{-11}	6.2×10^{-11}	bnHA	Berkeley Advanced Biomaterials Inc, USA	7.0×10^{-15}	2.0	Porous (80 %) cylinder: $\Phi = 10$ mm, L = 5 mm	Polymer dissolved in chloroform + ceramic and NaCl addition and dispersion + compression at 10 MPa and 25 °C	In vitro: SBF (pH = 7.4) at 37 °C, weekly replacement, w/o shaking	Chen PP/C bnHA [58]
Poly(D,L-lactide)(NR)	Jinan Daigang Bio-Technology Co. Ltd., China	8.0×10^{-11} (6.0×10^{-11})	9.0×10^{-11} (6.2×10^{-11})	bnHA	Berkeley Advanced Biomaterials Inc, USA	3.0×10^{-15}	2.0	Porous (80 %) cylinder: $\Phi = 10$ mm, L = 5 mm	Same as Chen PP/C	In vitro: same as Chen PP/C	Chen C bnHA [58]

B.2.3 Poly-lactide-co-glycolide Matrix

Table B.7 Results output by the HA composites degradation model for cases with a poly(lactide-co-glycolide) matrix. k_1 is the non-catalytic polymer degradation rate, k_2' is the autocatalytic polymer degradation rate, A_d is the ceramic dissolution rate and θ is the power ceramic dissolution law exponent. Abbreviations used to specify the hydroxyapatite type can be found in Table 5.2. A dashed line between rows indicates that data displayed in those consecutive rows belong to the same researcher or research group. A solid line between rows indicates no known author relationship for the data

Polymer characteristics				Ceramic characteristics				Sample characteristics			
Type	Manufacturer	k_1 (s^{-1})	k_2' ($m^3\ mol^{-1}\ s^{-1}$)	Type	Manufacturer	A_d ($mol\ m^{-2}\ s^{-1}$)	θ (1)	Structure and Morphology	Fabrication method	Degradation protocol	Case code and reference
Poly(D,L-lactide-co-glycolide) (44.6:55.4)	Mitsui Chemicals Co.; Tokio, Japan	2.5×10^{-9}	3.8×10^{-9}	hHA	Maruo Calcium Co.; Akashi, Japan	2.0×10^{-12}	2.0	Dense disk: $\Phi = 5$ mm, t = 0.5 mm	Polymer dissolved in dioxane + ceramic addition + freeze-drying of the solvent cast solution + compression moulding at 60 °C and 4.9 MPa	In vitro: PBS (0.01 M, pH = 7.4) at 37 °C, weekly replacement, w/o shaking, 30 mL/sample	Tsunoda hHA [59]
Poly(D,L-lactide-co-glycolide) (44.6:55.4)	Shang Dong Institute (Dept. of Med. Dev.), China	3.2×10^{-10} (2.8×10^{-10})	5.2×10^{-10} (3.2×10^{-10})	hHA	In-house production: wet chemistry route + calcining at 1100 °C for 6 h	1.1×10^{-11}	2.0	Porous (≈ 90 %) disk: $\Phi = 6$ mm, t = 2 mm	Polymer-ceramic mixture solvent casting + particulate leaching using NaCl	In vitro: standard conditions (PBS (pH = 7.4) at 37 °C w/o shaking) 20 mL/sample	Li hHA [60]
Poly(D,L-lactide-co-glycolide) (47:53)	Purac Biomaterials BV, The Netherlands (Purasorb PDLG 5004)	1.7×10^{-9}	1.5×10^{-9}	bnHA	Aldrich Chemistry, USA	3.0×10^{-13}	2.0	Porous (≈ 90 %) film: 0.5 cm^2 × t (t: NR)	Polymer dissolved in dioxane + blended w ceramic + freeze drying	In vitro: standard conditions (PBS at 37 °C w/o shaking) 20 mL/sample	Diaz PLGA bnHA [61]
Poly(D,L-lactide-co-glycolide) (50:50)	Birmingham Polymers Inc.; Birmingham, Alabama, USA	4.0×10^{-10}	6.0×10^{-10}	hHA	Sigma Chemicals; St. Louis, Missouri, USA	7.0×10^{-12}	2.0	Dense cylinder: $\Phi = 5$ mm, L = 5 mm	Polymer dissolved in acetone + precipitated in ethanol + mixed w ceramic + compression moulding into final shape	In vitro: distilled water at 37 °C w/o shaking, w/o replacement, 10 mL/sample	Agrawal hHA [62]

(continued)

Table B.7 (continued)

Polymer characteristics				Ceramic characteristics				Sample characteristics			
Type	Manufacturer	k_1 (s^{-1})	k'_2 ($m^3\ mol^{-1}\ s^{-1}$)	Type	Manufacturer	A_d ($mol\ m^{-2}\ s^{-1}$)	θ (1)	Structure and Morphology	Fabrication method	Degradation protocol	Case code and reference
Poly(D,L-lactide-co-glycolide) (50:50)	SurModics Pharmaceuticals, USA	1.1×10^{-9}	2.0×10^{-9}	pCHA	In-house production: wet chemistry route using $Ca(OH)_2$ and H_3PO_4 + ground, milled and sieved using a 180 μm mesh	1.0×10^{-12}	2.0	Dense disk: $\Phi = 2$ mm, t = 2 mm	Polymer and ceramic mixed in acetone + dried at 40 °C overnight + injection-moulded into cylinders at 140 °C and 0.5 MPa + cut into final shape	In vitro: PBS (0.01 M, pH = 7.4) at 37 °C,w/o shaking, w/o replacement, 166mL g^{-1}	Naik pCHA [63]
Poly(D,L-lactide-co-glycolide) (50:50)	SurModics Pharmaceuticals, USA	1.1×10^{-9}	2.0×10^{-9}	hCHA	In-house production: same as Naik pCHA + calcined at 800 °C for 4 h in an air atmosphere	5.0×10^{-12}	2.0	Dense disk: $\Phi = 2$ mm, t = 2 mm	Same as Naik pCHA	In vitro: same as Naik pCHA	Naik ca hCHA [63]
Poly(D,L-lactide-co-glycolide) (50:50)	SurModics Pharmaceuticals, USA	1.1×10^{-9}	2.0×10^{-9}	hCHA	In-house production: same as Naik pCHA + calcined at 800 °C for 4 h in a wet argon atmosphere	3.0×10^{-12}	2.0	Dense disk: $\Phi = 2$ mm, t = 2 mm	Same as Naik pCHA	In vitro: same as Naik pCHA	Naik cw hCHA [63]

(continued)

Table B.7 (continued)

Polymer characteristics				Ceramic characteristics				Sample characteristics			
Type	Manufacturer	k_1 (s^{-1})	k_2' ($m^3\ mol^{-1}\ s^{-1}$)	Type	Manufacturer	A_d ($mol\ m^{-2}\ s^{-1}$)	θ (1)	Structure and Morphology	Fabrication method	Degradation protocol	Case code and reference
Poly(D,L-lactide-co-glycolide) (50:50)	SurModics Pharmaceuticals, USA	1.1×10^{-9}	2.0×10^{-9}	sMP-pCHA	In-house production: same as Naik pCHA + treatment w physisorbed 1 wt % mercaptopropyl trimethoxy silane (MPTMS) for 1 h	3.0×10^{-11}	2.0	Dense disk: $\Phi = 2$ mm, t = 2 mm	Same as Naik pCHA	In vitro: same as Naik pCHA	Naik f sMP-pCHA [64]
Poly(D,L-lactide-co-glycolide) (50:50)	SurModics Pharmaceuticals, USA	1.1×10^{-9}	2.0×10^{-9}	sMP-pCHA	In-house production: same as Naik pCHA + treatment w chemisorbed 1 wt % mercaptopropyl trimethoxy silane (MPTMS) for 1 h	3.0×10^{-11}	2.0	Dense disk: $\Phi = 2$ mm, t = 2 mm	Same as Naik pCHA	In vitro: same as Naik pCHA	Naik c sMP-pCHA [64]
Poly(D,L-lactide-co-glycolide) (50:50)	SurModics Pharmaceuticals, USA	1.1×10^{-9}	2.0×10^{-9}	sMP-hCHA	In-house production: same as Naik ca-hCHA + treatment w physisorbed 1 wt % mercaptopropyl trimethoxy silane (MPTMS) for 1 h	1.0×10^{-11}	2.0	Dense disk: $\Phi = 2$ mm, t = 2 mm	Same as Naik pCHA	In vitro: same as Naik pCHA	Naik fca sMP-hCHA [64]
Poly(D,L-lactide-co-glycolide) (50:50)	SurModics Pharmaceuticals, USA	1.1×10^{-9}	2.0×10^{-9}	sMP-hCHA	In-house production: same as Naik ca-hCHA + treatment w chemisorbed 1 wt % mercaptopropyl trimethoxy silane (MPTMS) for 1 h	1.0×10^{-11}	2.0	Dense disk: $\Phi = 2$ mm, t = 2 mm	Same as Naik pCHA	In vitro: same as Naik pCHA	Naik cca sMP-hCHA [64]

(continued)

Table B.7 (continued)

Polymer characteristics				Ceramic characteristics				Sample characteristics			
Type	Manufacturer	k_1 (s^{-1})	k_2' ($m^3\ mol^{-1}\ s^{-1}$)	Type	Manufacturer	A_d ($mol\ m^{-2}\ s^{-1}$)	θ (1)	Structure and Morphology	Fabrication method	Degradation protocol	Case code and reference
Poly(D,L-lactide-co-glycolide) (50:50)	SurModics Pharmaceuticals, USA	1.0×10^{-9}	1.8×10^{-9}	hCHA	In-house production: wet chemistry route using $Ca(OH)_2$ and H_3PO_4 + aged for 1 d and dried + calcined at 800 °C for 2 h + ground and sieved using a 75 µm mesh	3.0×10^{-14}	2.0	Dense disk: $\Phi = 6$ mm, t = 2 mm	Ceramic dispersed in polymer using a co-rotating twin screw extruder + cut into pellets + injection-moulded into cylinders at 130 °C and 0.5 MPa + cut into final shape	In vitro: PBS (0.01 M, pH = 7.4) at 37 °C, w/o shaking, w/o replacement	Ege hCHA [27]
Poly(D,L-lactide-co-glycolide) (50:50)	SurModics Pharmaceuticals, USA	1.0×10^{-9}	1.8×10^{-9}	hHA	In-house production: wet chemistry route using $Ca(OH)_2$ and H_3PO_4 + aged for 1 d and dried + calcined at 1200 °C for 2 h + ground and sieved using a 75 µm mesh	1.0×10^{-13}	2.0	Dense disk: $\Phi = 6$ mm, t = 2 mm	Same as Ege hCHA	In vitro: same as Ege hCHA	Ege hHA [26] [27]
Poly(D,L-lactide-co-glycolide) (75:25)	Boehringer Ingelheim, Germany (Resomer RG750S)	3.4×10^{-10}	2.4×10^{-10}	hHA	Sigma Aldrich; St. Louis, Missouri, USA	1.0×10^{-13}	2.0	Porous fibrous mat: 20 × $5mm^2$ × t (t: NR)	Polymer dissolved in HFIP + blended w ceramic + electrospinning	In vitro: standard conditions (PBS (0.01 M) at 37 °C w/o shaking) 5 mL/sample	Lee hHA [65]
Poly(lactide-co-glycolide) (95:05)	In-house production	1.5×10^{-10} (2.8×10^{-11})	1.0×10^{-10} (1.9×10^{-11})	lHA	In-house production	1.0×10^{-14}	2.0	Dense bar: 60 × $6mm^2$ × 4 mm	Solution mixing + pressed + annealed at 110 °C for 30 min	In vitro: SBF at 37 °C (buffered to pH = 7.4), w shaking, 20 mL/sample	Liuyun lHA [66]
Poly(lactide-co-glycolide) (NR)	Not reported	6.6×10^{-10}	4.8×10^{-10}	hHA	In-house production: hydrothermal-electrochemical deposition using an electrolyte containing the precursors	3.0×10^{-13}	2.0	Dense film: 5 × $5mm^2$ × (0.05...0.08) mm	Polymer solvent casting on a Ti substrate w grown HA + delaminating	In vitro: SBF at 37 °C	Ban hHA [67]

B.2.4 Miscellaneous Polymers Matrixes

Table B.8 Results output by the HA composites degradation model for cases with a miscellaneous polymer matrix. k_1 is the non-catalytic polymer degradation rate, k_2' is the autocatalytic polymer degradation rate, A_d is the ceramic dissolution rate and θ is the power ceramic dissolution law exponent. Abbreviations used to specify the hydroxyapatite type can be found in Table 5.2. A dashed line between rows indicates that data displayed in those consecutive rows belong to the same researcher or research group. A solid line between rows indicates no known author relationship for the data

Polymer characteristics				Ceramic characteristics				Sample characteristics			
Type	Manufacturer	k_1 (s^{-1})	k_2' ($m^3\,mol^{-1}\,s^{-1}$)	Type	Manufacturer	A_d ($mol\,m^{-2}\,s^{-1}$)	θ (1)	Structure and Morphology	Fabrication method	Degradation protocol	Case code and reference
Poly(ε-caprolactone)	Daicel Polymer Ltd.; Tokyo, Japan	6.0×10^{-12} (1.0×10^{-12})	2.3×10^{-11} (4.0×10^{-12})	bnHA	Nanjing Emperor Nano Material Co. Ltd., China	3.0×10^{-16}	2.0	Porous (≈ 70 %) film: 10 × 10 mm^2 × 3 mm	Polymer, ceramic and porogen mixed at 100 °C and 90 rpm for 15 min + compression moulding at 80 °C+ porogen leaching w distilled water	In vitro: PBS (pH = 7.4) at 37 °C, monthly replacement, w shaking	Wang PCL bnHA[68]
Poly(L-co-D,L-lactide)(70:30) and poly(L-lactide) for pure polymer sample	Boehringer Ingelheim, Germany (Resomer LR708)	4.4×10^{-11} (6.0×10^{-11})	4.4×10^{-11} (5.8×10^{-11})	hHA	CamCeram Coating Powder; Leiden, The Netherlands	3.0×10^{-13}	2.0	Dense screw: Φ = (2.62...4.5) mm, L = 30 mm	Polymer and ceramic mixed in a rotary blender + injection moulded into screw shape	In vitro: PBS (0.01 M, pH = 7.4) at 37 °C, w shaking at 60 rpm, 50 mL g^{-1}	Hile hHA [69]
Poly(L-lactide-co-ε-caprolactone) (70:30)	Purac Biomaterials BV., The Netherlands (Purasorb PLC 7015)	1.5×10^{-10}	2.8×10^{-10}	bnHA	Aldrich Chemistry, USA	1.0×10^{-14}	2.0	Porous (≈ 90 %) film (dimensions: NR)	Polymer dissolved in dioxane + blended w ceramic + freeze drying	In vitro: standard conditions (PBS at 37 °C w/o shaking) 10 mL/sample	Diaz PLCL bnHA [70]

(continued)

Table B.8 (continued)

Polymer characteristics				Ceramic characteristics				Sample characteristics			
Type	Manufacturer	k_1 (s^{-1})	k'_2 ($m^3\ mol^{-1}\ s^{-1}$)	Type	Manufacturer	A_d ($mol\ m^{-2}\ s^{-1}$)	θ (1)	Structure and Morphology	Fabrication method	Degradation protocol	Case code and reference
Poly(D,L-lactide-co-ε-caprolactone) (60:40)	In-house production: ring-opening polymerisation at 145 °C in N_2 atmosphere for 3 h	1.5×10^{-9}	1.2×10^{-9}	hHA	De Puy, Bioland, France (BRKO)	7.0×10^{-12}	2.0	Dense dogbone: DIN Standard 53448 F.2. Smallest dimension < 5 mm	Polymer dissolved in methylene chloride + mixed w ceramic + compression moulded at (70...90) °C and (2500...4500) kg	In vitro: Ringer solution (pH = (5.5...7.0)) at 37 °C, w shaking	Ural NS hHA[71]
Poly(D,L-lactide-co-ε-caprolactone) (60:40)	In-house production: ring-opening polymerisation at 145 °C under vacuum for 19 h	1.5×10^{-9}	1.2×10^{-9}	hHA	De Puy, Bioland, France (BRKO)	5.0×10^{-12}	2.0	Dense dogbone: DIN Standard 53448 F.2. Smallest dimension < 5 mm	Same as Ural NS hHA	In vitro: same as Ural NS hHA	Ural VL hHA [71]
Poly(L-lactide) and poly(ε-caprolactone) blend (28.4:71.6)	Cargill-Dow and Polysciences	8.0×10^{-12}	2.4×10^{-11}	bnHA	Sigma Aldrich	3.0×10^{-15}	2.0	Porous (≈ 90 %) disk: Φ = 6 mm, t = 3.5 mm	Polymer dissolved in dioxane + ceramic dispersed in solvent + mixed + freeze-drying + porogen leaching	In vitro: Phosphate buffer (pH = 7.4) at 37 °C, replacement every 2 weeks, w shaking, 200 $mL\,g^{-1}$	Rodenas CL bnHA [72]
Poly(L-lactide) and poly(ε-caprolactone) blend (86.4:13.6)	Cargill-Dow and Polysciences	2.6×10^{-11}	1.2×10^{-11}	bnHA	Sigma Aldrich	3.0×10^{-15}	2.0	Porous (≈ 90 %) disk: Φ = 6 mm, t = 3.5 mm	Same as Rodenas CL bnHA	In vitro: same as Rodenas CL bnHA	Rodenas LA bnHA [72]
Poly(D,L-lactide-co-glycolide)(50:50) and poly(ε-caprolactone) blend (84:16)	Purac Biomaterials BV; Gorinchem, The Netherlands (Purasorb PDLG 5010) and Sigma Aldrich; St. Louis, Missouri, USA	7.8×10^{-10}	9.4×10^{-10}	bnHA	Donated by Prof. Marc Bohner (Budenheim, Tri-Cafos P/C53-80)	1.0×10^{-14}	2.0	Porous mat (dimensions: NR)	Ceramic suspended in solvent + polymer added + electrospinning of the solution	In vitro: PBS (pH = 7.4) at 37 °C, w/o replacement, w shaking at 60 rpm 2 mL/sample	Ji bnHA [73]

(continued)

Table B.8 (continued)

Polymer characteristics				Ceramic characteristics				Sample characteristics			
Type	Manufacturer	k_1 (s^{-1})	k'_2 ($m^3\ mol^{-1}\ s^{-1}$)	Type	Manufacturer	A_d ($mol\ m^{-2}\ s^{-1}$)	θ (1)	Structure and Morphology	Fabrication method	Degradation protocol	Case code and reference
Poly(D,L-lactide-co-glycolide)(65:35) and poly(ε-caprolactone) blend (71.8:28.2)	Aldrich and Aldrich	2.2×10^{-10}	1.8×10^{-10}	hHA	Aldrich	9.0×10^{-12}	2.0	Porous (80 %) film: 5 × 5 mm^2 × 1 mm	Polymers dissolved in tetrahydrofuran + NaCl and ceramic addition + solvent evaporation + pressed at (41.4...68.9) MPa	In vitro: sterile water at 37 °C, no replacement	Dunn CLs hHA [74]
Poly(D,L-lactide-co-glycolide)(65:35) and poly(ε-caprolactone) blend (71.8:28.2)	Aldrich and Aldrich	2.2×10^{-10}	1.8×10^{-10}	hHA	Aldrich	3.0×10^{-11}	2.0	Porous (80 %) film: 5 × 5 mm^2 × 1 mm	Same as Dunn CLs hHA	In vitro: sterile water at 37 °C, replacement every 2/3 days	Dunn CLd hHA [74]
Poly(D,L-lactide-co-glycolide)(65:35) and poly(ε-caprolactone) blend (93.9:6.1)	Aldrich and Aldrich	3.0×10^{-10}	1.6×10^{-10}	hHA	Aldrich	3.0×10^{-12}	2.0	Porous (80 %) film: 5 × 5 mm^2 × 1 mm	Same as Dunn CLs hHA	In vitro: sterile water at 37 °C, no replacement	Dunn LGs hHA [74]
Poly(D,L-lactide-co-glycolide)(65:35) and poly(ε-caprolactone) blend (93.9:6.1)	Aldrich and Aldrich	3.0×10^{-10}	2.6×10^{-10}	hHA	Aldrich	5.0×10^{-12}	2.0	Porous (80 %) film: 5 × 5 mm^2 × 1 mm	Same as Dunn CLs hHA	In vitro: sterile water at 37 °C, replacement every 2/3 days	Dunn LGd hHA [74]

B.3 Calcium Carbonate Case Studies Modelling Results

Table B.9 Results output by the CC composites degradation model for all analysed case studies. k_1 is the non-catalytic polymer degradation rate, k_2' is the autocatalytic polymer degradation rate, A_d is the ceramic dissolution rate and θ is the power ceramic dissolution law exponent. Abbreviations used to specify the calcium carbonate type can be found in Table 7.2. A dashed line between rows indicates that data displayed in those consecutive rows belong to the same researcher or research group. A solid line between rows indicates no known author relationship for the data

Polymer characteristics				Ceramic characteristics				Sample characteristics			
Type	Manufacturer	k_1 (s^{-1})	k_2' ($m^3\ mol^{-1}\ s^{-1}$)	Type	Manufacturer	A_d ($mol\ m^{-2}\ s^{-1}$)	θ (1)	Structure and Morphology	Fabrication method	Degradation protocol	Case code and reference
Poly(L-lactide)	Purac Biochem B.V.; Gorinchem, The Netherlands (Purasorb)	1.1×10^{-10}	9.0×10^{-11}	μ-CC	In-house production: mixture of $Ca(OH)_2$ + aminopropyl-triethoxysilane (APTES) + methanol in a CO_2 atmosphere + dried at 110 °C	3.0×10^{-13}	2.0	Porous mat	Polymer and ceramic kneaded at 200 °C for 10 min + mixture dissolved in chloroform + electrospinning of the polymer and ceramic mix	In vitro: 5 mmol/L NaOH solution, w/o shaking, w/o replacement	Wakita K μ-CC [75]
Poly(L-lactide)	Purac Biochem B.V.; Gorinchem, The Netherlands (Purasorb)	1.4×10^{-11}	1.4×10^{-11}	μ-CC	In-house production: mixture of $Ca(OH)_2$ + aminopropyl-triethoxysilane (APTES) + methanol in a CO_2 atmosphere + dried at 110 °C	3.0×10^{-13}	2.0	Porous mat	Ceramic dispersed in chloroform + polymer dissolved in the mixture + electrospinning of the polymer and ceramic mix	In vitro: same as Wakita K μ-CC	Wakita M μ-CC [75]

(continued)

Table B.9 (continued)

Polymer characteristics				Ceramic characteristics				Sample characteristics			
Type	Manufacturer	k_1 (s^{-1})	k'_2 ($m^3\ mol^{-1}\ s^{-1}$)	Type	Manufacturer	A_d ($mol\ m^{-2}\ s^{-1}$)	θ (1)	Structure and Morphology	Fabrication method	Degradation protocol	Case code and reference
Poly(L-lactide)	Shandong Medical Device Company, China	5.0×10^{-11}	1.4×10^{-11}	λ-CC	In-house production: freshwater cultured lack luster pearls (*H. cumingii*) ground into powder using a grinder	5.0×10^{-12}	2.0	Porous cylinder: $\Phi = 9$ mm, L = 18 mm	Polymer dissolver in 1,4-dioxane + ceramic addition + stirring and sonication + freezing at −20 °C for 24 h + lyophilisation at −60 °C for 48 h + drying in a vacuum oven for 72 h	In vitro: PBS (pH = 7.4) at 37 °C, w shaking at 60 rpm, weekly replacement, 15 mL/sample	Liu λ-CC [76]
Poly(L-lactide)	Shandong Medical Device Company, China	5.0×10^{-11}	1.4×10^{-11}	μ-CC	In-house production: freshwater cultured lustrous pearls (*H. cumingii*) ground into powder using a grinder	3.0×10^{-12}	2.0	Porous cylinder: $\Phi = 9$ mm, L = 18 mm	Same as Liu λ-CC	In vitro: same as Liu λ-CC	Liu μ-CC [76]
Poly(D,L-lactide) (50:50)	In-house production: bulk ring-opening polymerisation of D,L-lactide at 145 °C using zinc powder	1.4×10^{-10}	8.2×10^{-10}	λ-CC	Inoteb; France (Biocoral)	3.0×10^{-10}	2.0	Dense film: 12 × $12\,mm^2$ (PDLLA) × 2.1 mm (PDLLA–λ-CC) × 1.4 mm	Polymer dissolved in acetone + blended w ceramic + vacuum drying at 40 °C for 2 d + compression at 10 MPa and 130 °C+ cut at 80 °C into final shape	In vitro: PBS (0.13 M, pH = 7.4) w 0.02 % NaN_3 at 37 °C, w/o shaking, w/o replacement, 30 mL/sample	Li λ-CC [77]

(continued)

Table B.9 (continued)

Polymer characteristics				Ceramic characteristics				Sample characteristics			
Type	Manufacturer	k_1 (s^{-1})	k'_2 ($m^3\ mol^{-1}\ s^{-1}$)	Type	Manufacturer	A_d ($mol\ m^{-2}\ s^{-1}$)	θ (1)	Structure and Morphology	Fabrication method	Degradation protocol	Case code and reference
Poly(D,L-lactide-co-glycolide) (44.6:55.4)	Mitsui Chemicals; Tokyo, Japan: polymerisation of D,L-lactide and glycolide using stannous octoate	3.0×10^{-9}	3.0×10^{-9}	β-CC (Assumed)	Wako Pure Chemical Industries; Tokyo, Japan	3.0×10^{-10}	2.0	Dense film: 15 × $15\,mm^2$ × 0.5 mm	Polymer dissolved in dioxane + ceramic addition + freeze-drying of the solvent cast solution + compression moulding at 60 °C and 4.9 MPa	In vitro: PBS (pH = 7.4) at 37 °C, w/o shaking, weekly replacement, 40 mL/sample	Ara β-CC [24]
Poly(D,L-lactide-co-glycolide) (44.6:55.4)	Mitsui Chemicals Co.; Tokio, Japan	2.5×10^{-9}	3.8×10^{-9}	β-CC	Maruo Calcium Co.; Akashi, Japan	3.0×10^{-11}	2.0	Dense disk: Φ = 5 mm, t = 0.5 mm	Polymer dissolved in dioxane + ceramic addition + freeze-drying of the solvent cast solution + compression moulding at 60 °C and 4.9 MPa	In vitro: PBS (0.01 M, pH = 7.4) at 37 °C, weekly replacement, w/o shaking, 30 mL/sample	Tsunoda β-CC [59]
Poly(D,L-lactide-co-glycolide) (44.6:55.4)	Mitsui Chemicals Co.; Tokio, Japan	2.5×10^{-9}	3.8×10^{-9}	λ-CC	Maruo Calcium Co.; Akashi, Japan	3.0×10^{-11}	2.0	Dense disk: Φ = 5 mm, t = 0.5 mm	Same as Tsunoda β-CC	In vitro: same as Tsunoda β-CC	Tsunoda λ-CC [59]
Poly(D,L-lactide-co-glycolide) (50:50)	Birmingham Polymers Inc.; Birmingham, Alabama, USA	4.0×10^{-10}	6.0×10^{-10}	β-CC (Assumed)	Sigma Chemicals; St. Louis, Missouri, USA	3.0×10^{-11}	2.0	Dense cylinder: Φ = 5 mm, L = 5 mm	Polymer dissolved in acetone + precipitated in ethanol + mixed w ceramic + compression moulding into final shape	In vitro: distilled water at 37 °C w/o shaking, w/o replacement, 10 mL/sample	Agrawal β-CC [62]

(continued)

Table B.9 (continued)

Polymer characteristics				Ceramic characteristics				Sample characteristics			
Type	Manufacturer	k_1 (s^{-1})	k_2' ($m^3\ mol^{-1}\ s^{-1}$)	Type	Manufacturer	A_d ($mol\ m^{-2}\ s^{-1}$)	θ (1)	Structure and Morphology	Fabrication method	Degradation protocol	Case code and reference
Poly(D,L-lactide-co-glycolide) (50:50)	Lakeshore Biomaterials; Birmingham, Alabama, USA (5050 DLG 5E)	3.7×10^{-9}	3.2×10^{-9}	β-CC	Shiraishi Calcium Kaisha Ltd; Japan	3.0×10^{-12}	2.0	Dense disk: $\Phi = 3.5$ mm, t = 2 mm	Polymer dissolved in acetone + ceramic sonicated in acetone + mixing + solvent casting + cut into pellets + injection-moulding at 135 °C and 0.5 MPa into cylinders + cut into final shape	In vitro: PBS (0.01 M, pH = 7.4) at 37 °C, w/o shaking, w/o replacement, 166 mL g^{-1}	Ch6 β-CC [Chapter 6]
Poly(D,L-lactide-co-glycolide) (85:15)	Purac Biochem B.V.; Gorinchem, The Netherlands	1.5×10^{-10}	8.0×10^{-10}	β-CC (Assumed)	Sigma; St. Louis, Missouri, USA (SigmaUltra Grade)	3.0×10^{-10}	2.0	Dense screw: $\Phi = 9$ mm, L = 30 mm	Polymer dried under vacuum for 3 h at 40 °C+ blended w ceramic in a co-rotating twin extruder + injection moulded into screw shape	In vitro: PBS (0.05 M, pH = 7.4) at 37 °C, w/o shaking, w/o replacement, 250 mL/sample	Cotton β-CC [78]

References

1. Ito, A., Maekawa, K., Tsutsumi, S., Ikazaki, F., & Tateishi, T. (1997). Solubility product of OH-carbonated hydroxyapatite. *Journal of Biomedical Materials Research Part A*, *36*(4), 522–528.
2. Atkins, P. (2010). *Shriver and Atkins' inorganic chemistry*. USA: Oxford University Press.
3. Kirkwood, T. B. (1979). Geometric means and measures of dispersion. *Biometrics*, *35*, 908–909.
4. Imai, Y., Nagai, M., & Watanabe, M. (1999b). Degradation of composite materials composed of tricalcium phosphate and a new type of block polyester containing a poly(L-lactic acid) segment. *Journal of Biomaterials Science, Polymer Edition*, *10*(4), 421–432.
5. Ebato, H., Oya, S., Kakizawa, Y., Furuta, H., and Arai, K. (1995). Process for producing lactic acid-based copolyester and packaging material. US Patent 5,403,897.
6. Speight, J. G., et al. (2005). *Lange's handbook of chemistry* (Vol. 1). New York: McGraw-Hill.
7. Scientific Polymer, Inc. (2013). *Polymer density data*. Retrieved September 1, 2016 from http://scientificpolymer.com/density-of-polymers-by-density/.
8. Kobayashi, S., & Yamaji, S. (2014). Analytical prediction of hydrolysis behavior of tricalcium phosphate/poly-L-lactic acid composites in simulated body environment. *Advanced Composite Materials*, *23*(3), 211–223.
9. Aunoble, S., Clément, D., Frayssinet, P., Harmand, M. F., & Le Huec, J. C. (2006). Biological performance of a new β-TCP/PLLA composite material for applications in spine surgery: in vitro and in vivo studies. *Journal of Biomedical Materials Research Part A*, *78*(2), 416–422.
10. Adamus, A., Jozwiakowska, J., Wach, R., Suarez-Sandoval, D., Ruffieux, K., & Rosiak, J. (2012). In vitro degradation of β-tricalcium phosphate reinforced poly (L-lactic acid). In *Materials Science Forum* (Vol. 714, pp. 283–290). Trans Tech Publication
11. Kang, Y., Xu, X., Yin, G., Chen, A., Liao, L., Yao, Y., et al. (2007). A comparative study of the in vitro degradation of poly(L-lactic acid)/β-tricalcium phosphate scaffold in static and dynamic simulated body fluid. *European Polymer Journal*, *43*(5), 1768–1778.
12. Kang, Y., Yao, Y., Yin, G., Huang, Z., Liao, X., Xu, X., et al. (2009). A study on the in vitro degradation properties of poly(L-lactic acid)/β-tricalcuim phosphate (PLLA/β-TCP) scaffold under dynamic loading. *Medical Engineering & Physics*, *31*(5), 589–594.
13. Daculsi, G., Goyenvalle, E., Cognet, R., Aguado, E., & Suokas, E. O. (2011). Osteoconductive properties of poly(96L/4D-lactide)/beta-tricalcium phosphate in long term animal model. *Biomaterials*, *32*(12), 3166–3177.
14. Niemelä, T. (2005). Effect of β-tricalcium phosphate addition on the in vitro degradation of self-reinforced poly-L,D-lactide. *Polymer Degradation and Stability*, *89*(3), 492–500.

I. Moreno-Gomez, *A Phenomenological Mathematical Modelling Framework for the Degradation of Bioresorbable Composites*,
Springer Theses, https://doi.org/10.1007/978-3-030-04990-4

15. Zheng, X., Zhou, S., Yu, X., Li, X., Feng, B., Qu, S., et al. (2008). Effect of in vitro degradation of poly(D, L-lactide)/β-tricalcium composite on its shape-memory properties. *Journal of Biomedical Materials Research Part B: Applied Biomaterials*, *86*(1), 170–180.
16. Lin, F.-H., Chen, T.-M., Lin, C.-P., & Lee, C.-J. (1999). The merit of sintered PDLLA/TCP composites in management of bone fracture internal fixation. *Artificial Organs*, *23*(2), 186–194.
17. Heidemann, W., Jeschkeit, S., Ruffieux, K., Fischer, J. H., Wagner, M., Krüger, G., et al. (2001). Degradation of poly(D, L)lactide implants with or without addition of calciumphosphates in vivo. *Biomaterials*, *22*(17), 2371–2381.
18. Niemelä, T., Kellomäki, M., & Törmälä, P. (2004). In vitro degradation of osteoconductivepoly-L/DL-lactide/β-TCP composites.In *Key Engineering Materials* (Vol. 254, pp. 509–512). Trans Tech Publication
19. Ignatius, A. A., Augat, P., & Claes, L. E. (2001a). Degradation behavior of composite pins made of tricalcium phosphate and poly(L, DL-lactide). *Journal of Biomaterials Science, Polymer Edition*, *12*(2), 185–194.
20. Haaparanta, A.-M., Haimi, S., Ellä, V., Hopper, N., Miettinen, S., Suuronen, R., et al. (2010). Porous polylactide/β-tricalcium phosphate composite scaffolds for tissue engineering applications. *Journal of Tissue Engineering and Regenerative Medicine*, *4*(5), 366–373.
21. Yang, F., Cui, W., Xiong, Z., Liu, L., Bei, J., & Wang, S. (2006). Poly(L, L-lactide-co-glycolide)/tricalcium phosphate composite scaffold and its various changes during degradation in vitro. *Polymer Degradation and Stability*, *91*(12), 3065–3073.
22. Yang, Y., Zhao, Y., Tang, G., Li, H., Yuan, X., & Fan, Y. (2008). In vitro degradation of porous poly(L-lactide-co-glycolide)/β-tricalcium phosphate (PLGA/β-TCP) scaffolds under dynamic and static conditions. *Polymer Degradation and Stability*, *93*(10), 1838–1845.
23. Jin, H.-H., Min, S.-H., Song, Y.-K., Park, H.-C., & Yoon, S.-Y. (2010). Degradation behavior of poly(lactide-co-glycolide)/β-TCP composites prepared using microwave energy. *Polymer Degradation and Stability*, *95*(9), 1856–1861.
24. Ara, M., Watanabe, M., & Imai, Y. (2002). Effect of blending calcium compounds on hydrolytic degradation of poly(DL-lactic acid-co-glycolic acid). *Biomaterials*, *23*(12), 2479–2483.
25. Bennett, S. M. (2012). *Degradation mechanisms of PLGA/*α*-TCP composites for orthopaedic applications*. Ph.D. thesis, Department of Materials Science and Metallurgy, University of Cambridge.
26. Ege, D., Best, S., & Cameron, R. (2014). The degradation behaviour of nanoscale HA/PLGA and α-TCP/PLGA composites. *Bioinspired, Biomimetic and Nanobiomaterials*, *3*, BBN2.
27. Ege, D. (2012). *Mechanical and degradation properties of calcium phosphate/biodegradable polymer composites*. Ph.D. thesis, Department of Materials Science and Metallurgy, University of Cambridge.
28. Yang, Z., Best, S. M., & Cameron, R. E. (2009). The influence of α-tricalcium phosphate nanoparticles and microparticles on the degradation of poly(D, L-lactide-co-glycolide). *Advanced Materials*, *21*(38–39), 3900–3904.
29. Yang, Z. (2009). *Development and characterisation of bioactive, bioresorbable* α*-tricalcium phosphate/poly(D,L-lactide-co-glycolide) nanocomposites for bone substitution and fixation*. Ph.D. thesis, Department of Materials Science and Metallurgy, University of Cambridge.
30. Mellon, V. (2003). *Degradation study of poly(lactide-co-glycolic) acid and alpha or beta tricalcium phosphate composites - non porous*. Unpublished research at University of Cambridge.
31. Barrett, C. E., & Cameron, R. E. (2014). X-ray microtomographic analysis of α-tricalcium phosphate-poly(lactic-co-glycolic) acid nanocomposite degradation. *Polymer*, *55*(16), 4041–4049.
32. Barrett, C. E. (2013). *The degradation behaviour of tricalcium phosphate - poly(lactide-co-glycolide) nanocomposites*. Ph.D. thesis, Department of Materials Science and Metallurgy, University of Cambridge.
33. Ehrenfried, L. M., Patel, M. H., & Cameron, R. E. (2008). The effect of tri-calcium phosphate (TCP) addition on the degradation of polylactide-co-glycolide (PLGA). *Journal of Materials Science: Materials in Medicine*, *19*(1), 459–466.

34. Ahola, N., Männistö, N., Veiranto, M., Karp, M., Rich, J., Efimov, A., et al. (2013). An in vitro study of composites of poly(L-lactide-co-ε-caprolactone), β-tricalcium phosphate and ciprofloxacin intended for local treatment of osteomyelitis. *Biomatter*, *3*(2), e23162.
35. Ahola, N., Veiranto, M., Rich, J., Efimov, A., Hannula, M., Seppälä, J., et al. (2012). Hydrolytic degradation of composites of poly(L-lactide-co-ε-caprolactone)70/30 and β-tricalcium phosphate. *Journal of Biomaterials Applications*, *28*(4), 529–543.
36. Kikuchi, M., Koyama, Y., Yamada, T., Imamura, Y., Okada, T., Shirahama, N., et al. (2004). Development of guided bone regeneration membrane composed of β-tricalcium phosphate and poly(L-lactide-co-glycolide-co-ε-caprolactone) composites. *Biomaterials*, *25*(28), 5979–5986.
37. Imai, Y., Fukuzawa, A., & Watanabe, M. (1999a). Effect of blending tricalcium phosphate on hydrolytic degradation of a block polyester containing poly(L-lactic acid) segment. *Journal of Biomaterials Science, Polymer Edition*, *10*(7), 773–786.
38. Kikuchi, M., Koyama, Y., Takakuda, K., Miyairi, H., Shirahama, N., & Tanaka, J. (2002). In vitro change in mechanical strength of β-tricalcium phosphate/copolymerized poly-L-lactide composites and their application for guided bone regeneration. *Journal of Biomedical Materials Research*, *62*(2), 265–272.
39. Huang, J., Xiong, J., Liu, J., Zhu, W., & Wang, D. (2013). Investigation of the in vitro degradation of a novel polylactide/nanohydroxyapatite composite for artificial bone. *Journal of Nanomaterials*, *2013*, 3.
40. Wang, Z., Wang, Y., Ito, Y., Zhang, P., & Chen, X. (2016). A comparative study on the in vivo degradation of poly(L-lactide) based composite implants for bone fracture fixation. *Scientific Reports*, *6*.
41. Zhou, H., Touny, A. H., & Bhaduri, S. B. (2011). Fabrication of novel PLA/CDHA bionanocomposite fibers for tissue engineering applications via electrospinning. *Journal of Materials Science: Materials in Medicine*, *22*(5), 1183–1193.
42. Verheyen, C., De Wijn, J., Van Blitterswijk, C., & De Groot, K. (1992). Evaluation of hydroxylapatite/poly(L-lactide) composites: Mechanical behavior. *Journal of Biomedical Materials Research*, *26*(10), 1277–1296.
43. Verheyen, C., Klein, C., de Blieck-Hogervorst, J., Wolke, J., Van Blitterswijn, C., & De Groot, K. (1993). Evaluation of hydroxylapatite/poly(L-lactide) composites: Physico-chemical properties. *Journal of Materials Science: Materials in Medicine*, *4*(1), 58–65.
44. Díaz, E., Sandonis, I., Puerto, I., & Ibáñez, I. (2014). In vitro degradation of PLLA/nHA composite scaffolds. *Polymer Engineering & Science*, *54*(11), 2571–2578.
45. Shikinami, Y., & Okuno, M. (1999). Bioresorbable devices made of forged composites of hydroxyapatite (HA) particles and poly-L-lactide (PLLA): Part I Basic characteristics. *Biomaterials*, *20*(9), 859–877.
46. Furukawa, T., Matsusue, Y., Yasunaga, T., Shikinami, Y., Okuno, M., & Nakamura, T. (2000). Biodegradation behavior of ultra-high-strength hydroxyapatite/poly(L-lactide) composite rods for internal fixation of bone fractures. *Biomaterials*, *21*(9), 889–898.
47. Ishii, S., Tamura, J., Furukawa, T., Nakamura, T., Matsusue, Y., Shikinami, Y., et al. (2003). Long-term study of high-strength hydroxyapatite/poly(L-lactide) composite rods for the internal fixation of bone fractures: A 2–4-year follow-up study in rabbits. *Journal of Biomedical Materials Research Part B: Applied Biomaterials*, *66*(2), 539–547.
48. Shikinami, Y., & Okuno, M. (2001). Bioresorbable devices made of forged composites of hydroxyapatite (HA) particles and poly L-lactide (PLLA). Part II: Practical properties of miniscrews and miniplates. *Biomaterials*, *22*(23), 3197–3211.
49. Deng, X., Sui, G., Zhao, M., Chen, G., & Yang, X. (2007). Poly(L-lactic acid)/hydroxyapatite hybrid nanofibrous scaffolds prepared by electrospinning. *Journal of Biomaterials Science, Polymer Edition*, *18*(1), 117–130.
50. Sui, G., Yang, X., Mei, F., Hu, X., Chen, G., Deng, X., et al. (2007). Poly-L-lactic acid/hydroxyapatite hybrid membrane for bone tissue regeneration. *Journal of Biomedical Materials Research Part A*, *82*(2), 445–454.

51. Xu, X., Chen, X., Liu, A., Hong, Z., & Jing, X. (2007). Electrospun poly(L-lactide)-grafted hydroxyapatite/poly(L-lactide) nanocomposite fibers. *European Polymer Journal*, *43*(8), 3187–3196.
52. Rakmae, S., Lorprayoon, C., Ekgasit, S., & Suppakarn, N. (2013). Influence of heat-treated bovine bone-derived hydroxyapatite on physical properties and in vitro degradation behavior of poly(lactic acid) composites. *Polymer-Plastics Technology and Engineering*, *52*(10), 1043–1053.
53. Rakmae, S., Ruksakulpiwat, Y., Sutapun, W., & Suppakarn, N. (2012). Effect of silane coupling agent treated bovine bone based carbonated hydroxyapatite on in vitro degradation behavior and bioactivity of PLA composites. *Materials Science and Engineering: C*, *32*(6), 1428–1436.
54. Van der Meer, S., De Wijn, J., & Wolke, J. (1996). The influence of basic filler materials on the degradation of amorphous D-and L-lactide copolymer. *Journal of Materials Science: Materials in Medicine*, *7*(6), 359–361.
55. Hasegawa, S., Tamura, J., Neo, M., Goto, K., Shikinami, Y., Saito, M., et al. (2005). In vivo evaluation of a porous hydroxyapatite/poly-DL-lactide composite for use as a bone substitute. *Journal of Biomedical Materials Research Part A*, *75*(3), 567–579.
56. Zou, B., Chen, X., Zhi, W., Liu, Y., Cui, W., Hu, S., et al. (2012). Promoted healing of femoral defects with in situ grown fibrous composites of hydroxyapatite and poly(DL-lactide). *Journal of Biomedical Materials Research Part A*, *100*(6), 1407–1418.
57. Zou, B., Li, X., Zhuang, H., Cui, W., Zou, J., & Chen, J. (2011). Degradation behaviors of electrospun fibrous composites of hydroxyapatite and chemically modified poly(DL-lactide). *Polymer Degradation and Stability*, *96*(1), 114–122.
58. Chen, L., Tang, C. Y., Tsui, C. P., et al. (2013). Mechanical properties and in vitro evaluation of bioactivity and degradation of dexamethasone-releasing poly-D-L-lactide/nano-hydroxyapatite composite scaffolds. *Journal of the Mechanical Behavior of Biomedical Materials*, *22*, 41–50.
59. Tsunoda, M. (2003). Degradation of poly(DL-lactic acid-co-glycolic acid) containing calcium carbonate and hydroxyapatite fillers-effect of size and shape of the fillers. *Dental Materials Journal*, *22*(3), 371–382.
60. Li, H., & Chang, J. (2005). pH-compensation effect of bioactive inorganic fillers on the degradation of PLGA. *Composites Science and Technology*, *65*(14), 2226–2232.
61. Díaz, E., Puerto, I., & Sandonis, I. (2015). The effects of bioactive nanoparticles on the degradation of DLGA. *International Journal of Polymeric Materials and Polymeric Biomaterials*, *64*(1), 38–46.
62. Agrawal, C. M., & Athanasiou, K. A. (1997). Technique to control pH in vicinity of biodegrading PLA-PGA implants. *Journal of Biomedical Materials Research*, *38*(2), 105–114.
63. Naik, A., Shepherd, D. V., Shepherd, J. H., Best, S. M., & Cameron, R. E. (2017). The effect of the type of HA on the degradation of PLGA/HA composites. *Materials Science and Engineering: C*, *70*, 824–831.
64. Naik, A., Best, S. M., & Cameron, R. E. (2015). The influence of silanisation on the mechanical and degradation behaviour of PLGA/HA composites. *Materials Science and Engineering: C*, *48*, 642–650.
65. Lee, J. B., Kim, S. E., Heo, D. N., Kwon, I. K., & Choi, B.-J. (2010). In vitro characterization of nanofibrous PLGA/gelatin/hydroxyapatite composite for bone tissue engineering. *Macromolecular Research*, *18*(12), 1195–1202.
66. Liuyun, J., Chengdong, X., Lixin, J., & Lijuan, X. (2013). Degradation behavior of hydroxyapatite/poly(lactic-co-glycolic) acid nanocomposite in simulated body fluid. *Materials Research Bulletin*, *48*(10), 4186–4190.
67. Ban, S., Watanabe, T., Itoh, T., Nakamura, H., Tsuruta, S., & Kawai, T. (2004). Development of biodegradable composite membrane containing oriented needle-like apatites. *Journal of Oral Tissue Engineering*, *2*(1), 1–13.
68. Wang, Y., Liu, L., & Guo, S. (2010b). Characterization of biodegradable and cytocompatible nano-hydroxyapatite/polycaprolactone porous scaffolds in degradation in vitro. *Polymer Degradation and Stability*, *95*(2), 207–213.

69. Hile, D. D., Doherty, S. A., & Trantolo, D. J. (2004). Prediction of resorption rates for composite polylactide/hydroxylapatite internal fixation devices based on initial degradation profiles. *Journal of Biomedical Materials Research Part B: Applied Biomaterials*, *71*(1), 201–205.
70. Díaz, E., & Puerto, I. (2015). In vitro degradation of PLCL/nHA biodegradable scaffolds. *Polymer-Plastics Technology and Engineering*, *54*(6), 556–564.
71. Ural, E., Kesenci, K., Fambri, L., Migliaresi, C., & Piskin, E. (2000). Poly(D, L-cactide/ε-caprolactone)/hydroxyapatite composites. *Biomaterials*, *21*(21), 2147–2154.
72. Rodenas-Rochina, J., Vidaurre, A., Cortázar, I. C., & Lebourg, M. (2015). Effects of hydroxyapatite filler on long-term hydrolytic degradation of PLLA/PCL porous scaffolds. *Polymer Degradation and Stability*, *119*, 121–131.
73. Ji, W., Yang, F., Seyednejad, H., Chen, Z., Hennink, W. E., Anderson, J. M., et al. (2012). Biocompatibility and degradation characteristics of PLGA-based electrospun nanofibrous scaffolds with nanoapatite incorporation. *Biomaterials*, *33*(28), 6604–6614.
74. Dunn, A. S., Campbell, P. G., & Marra, K. G. (2001). The influence of polymer blend composition on the degradation of polymer/hydroxyapatite biomaterials. *Journal of Materials Science: Materials in Medicine*, *12*(8), 673–677.
75. Wakita, T., Nakamura, J., Ota, Y., Obata, A., Kasuga, T., & Ban, S. (2011). Effect of preparation route on the degradation behavior and ion releasability of siloxane-poly(lactic acid)-vaterite hybrid nonwoven fabrics for guided bone regeneration. *Dental Materials Journal*, *30*(2), 232–238.
76. Liu, Y., Huang, Q., Kienzle, A., Müller, W., & Feng, Q. (2014). In vitro degradation of porous PLLA/pearl powder composite scaffolds. *Materials Science and Engineering: C*, *38*, 227–234.
77. Li, S., & Vert, M. (1996). Hydrolytic degradation of coral/poly(DL-lactic acid) bioresorbable material. *Journal of Biomaterials Science, Polymer Edition*, *7*(9), 817–827.
78. Cotton, N. J., Egan, M. J., & Brunelle, J. E. (2008). Composites of poly(DL-lactide-co-glycolide) and calcium carbonate: In vitro evaluation for use in orthopedic applications. *Journal of Biomedical Materials Research Part A*, *85*(1), 195–205.